frontiers | Research Topics

Cellular and molecular mechanisms that govern assembly, plasticity, and function of GABAergic inhibitory circuits in the mammalian brain

Edited by
Hiroki Taniguchi, Goichi Miyoshi, Anirban Paul and Yasufumi Hayano

Published in
Frontiers in Cellular Neuroscience

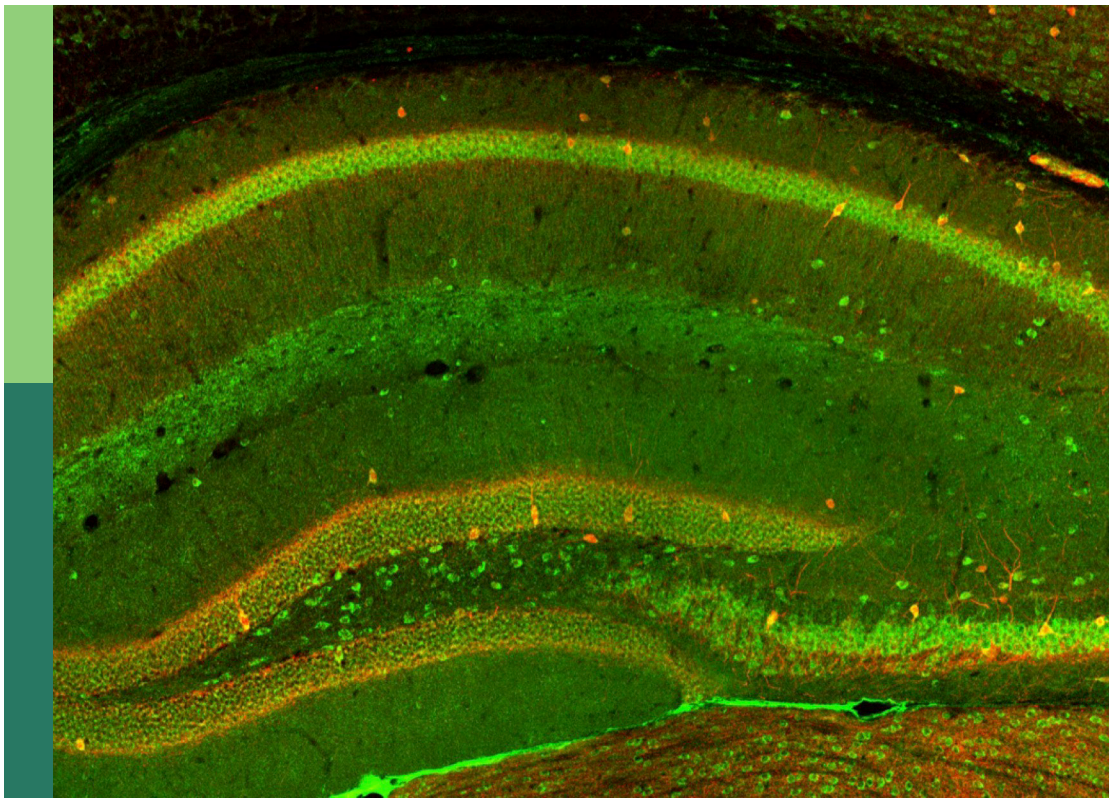

ISSN 1664-8714
ISBN 978-2-8325-6079-2
DOI 10.3389/978-2-8325-6079-2

About Frontiers

Frontiers is more than just an open access publisher of scholarly articles: it is a pioneering approach to the world of academia, radically improving the way scholarly research is managed. The grand vision of Frontiers is a world where all people have an equal opportunity to seek, share and generate knowledge. Frontiers provides immediate and permanent online open access to all its publications, but this alone is not enough to realize our grand goals.

Frontiers journal series

The Frontiers journal series is a multi-tier and interdisciplinary set of open-access, online journals, promising a paradigm shift from the current review, selection and dissemination processes in academic publishing. All Frontiers journals are driven by researchers for researchers; therefore, they constitute a service to the scholarly community. At the same time, the *Frontiers journal series* operates on a revolutionary invention, the tiered publishing system, initially addressing specific communities of scholars, and gradually climbing up to broader public understanding, thus serving the interests of the lay society, too.

Dedication to quality

Each Frontiers article is a landmark of the highest quality, thanks to genuinely collaborative interactions between authors and review editors, who include some of the world's best academicians. Research must be certified by peers before entering a stream of knowledge that may eventually reach the public - and shape society; therefore, Frontiers only applies the most rigorous and unbiased reviews. Frontiers revolutionizes research publishing by freely delivering the most outstanding research, evaluated with no bias from both the academic and social point of view. By applying the most advanced information technologies, Frontiers is catapulting scholarly publishing into a new generation.

What are Frontiers Research Topics?

Frontiers Research Topics are very popular trademarks of the *Frontiers journals series*: they are collections of at least ten articles, all centered on a particular subject. With their unique mix of varied contributions from Original Research to Review Articles, Frontiers Research Topics unify the most influential researchers, the latest key findings and historical advances in a hot research area.

Find out more on how to host your own Frontiers Research Topic or contribute to one as an author by contacting the Frontiers editorial office: frontiersin.org/about/contact

Cellular and molecular mechanisms that govern assembly, plasticity, and function of GABAergic inhibitory circuits in the mammalian brain

Topic editors

Hiroki Taniguchi — The Ohio State University, United States
Goichi Miyoshi — Gunma University, Japan
Anirban Paul — The Pennsylvania State University, United States
Yasufumi Hayano — The Ohio State University, United States

Citation

Taniguchi, H., Miyoshi, G., Paul, A., Hayano, Y., eds. (2025). *Cellular and molecular mechanisms that govern assembly, plasticity, and function of GABAergic inhibitory circuits in the mammalian brain*. Lausanne: Frontiers Media SA.
doi: 10.3389/978-2-8325-6079-2

Table of contents

04 Editorial: Cellular and molecular mechanisms that govern assembly, plasticity, and function of GABAergic inhibitory circuits in the mammalian brain
Yasufumi Hayano, Goichi Miyoshi, Anirban Paul and Hiroki Taniguchi

08 Acute stress modulates hippocampal to entorhinal cortex communication
Azat Nasretdinov, David Jappy, Alina Vazetdinova, Fliza Valiullina-Rakhmatullina and Andrei Rozov

19 Distinct mechanisms of allopregnanolone and diazepam underlie neuronal oscillations and differential antidepressant effect
Keiko Takasu, Yosuke Yawata, Ryoichi Tashima, Hiroyuki Aritomi, Shinji Shimada, Tsukasa Onodera, Teruhiko Taishi and Koichi Ogawa

35 Loss of Ezh2 in the medial ganglionic eminence alters interneuron fate, cell morphology and gene expression profiles
Christopher T. Rhodes, Dhanya Asokumar, Mira Sohn, Shovan Naskar, Lielle Elisha, Parker Stevenson, Dongjin R. Lee, Yajun Zhang, Pedro P. Rocha, Ryan K. Dale, Soohyun Lee and Timothy J. Petros

57 Region and layer-specific expression of $GABA_A$ receptor isoforms and KCC2 in developing cortex
Kirill Zavalin, Anjana Hassan, Yueli Zhang, Zain Khera and Andre H. Lagrange

86 $GABA_A$ receptors and neuroligin 2 synergize to promote synaptic adhesion and inhibitory synaptogenesis
Yusheng Sui, Martin Mortensen, Banghao Yuan, Martin W. Nicholson, Trevor G. Smart and Jasmina N. Jovanovic

102 Genetic approaches to elucidating cortical and hippocampal GABAergic interneuron diversity
Robert Machold and Bernardo Rudy

119 Vasoactive intestinal peptide-expressing interneurons modulate the effect of behavioral state on cortical activity
Ehsan Sabri and Renata Batista-Brito

126 The function of *Mef2c* toward the development of excitatory and inhibitory cortical neurons
Claire Ward, Lucas Sjulson and Renata Batista-Brito

137 Developmental regression of novel space preference in an autism spectrum disorder model is unlinked to GABAergic and social circuitry
Hirofumi Asano, Masaya Arai, Aito Narita, Takayuki Kuroiwa, Mamoru Fukuchi, Yuhei Yoshimoto, Soichi Oya and Goichi Miyoshi

frontiers | Frontiers in Cellular Neuroscience

TYPE Editorial
PUBLISHED 11 February 2025
DOI 10.3389/fncel.2025.1568845

OPEN ACCESS

EDITED AND REVIEWED BY
Arianna Maffei,
Stony Brook University, United States

*CORRESPONDENCE
Hiroki Taniguchi
✉ hiroki.taniguchi@osumc.edu

RECEIVED 30 January 2025
ACCEPTED 31 January 2025
PUBLISHED 11 February 2025

CITATION
Hayano Y, Miyoshi G, Paul A and Taniguchi H (2025) Editorial: Cellular and molecular mechanisms that govern assembly, plasticity, and function of GABAergic inhibitory circuits in the mammalian brain.
Front. Cell. Neurosci. 19:1568845.
doi: 10.3389/fncel.2025.1568845

Editorial: Cellular and molecular mechanisms that govern assembly, plasticity, and function of GABAergic inhibitory circuits in the mammalian brain

Yasufumi Hayano[1,2], Goichi Miyoshi[3], Anirban Paul[4] and Hiroki Taniguchi[1,2]*

[1]Department of Pathology, The Ohio State University Wexner Medical Center, Columbus, OH, United States, [2]Chronic Brain Injury Program, The Ohio State University Wexner Medical Center, Columbus, OH, United States, [3]Department of Developmental Genetics and Behavioral Neuroscience, Gunma University Graduate School of Medicine, Maebashi, Japan, [4]Department of Neural and Behavioral Sciences, College of Medicine, Pennsylvania State University, Hershey, PA, United States

KEYWORDS

inhibitory interneuron, GABA, neurodevelopmental disorder, cell type, circuit assembly, neuronal circuit

Editorial on the Research Topic
Cellular and molecular mechanisms that govern assembly, plasticity, and function of GABAergic inhibitory circuits in the mammalian brain

Inhibitory regulations by GABAergic interneurons (INs) play an essential role in intricate neural computations in normal brains, and their malformation and malfunction lead to a variety of brain disorders (Del Pino et al., 2018; Frye et al., 2016; Kepecs and Fishell, 2014; Takano, 2015; Taniguchi, 2014; Tremblay et al., 2016; Wang et al., 2016). Over the past two decades, there has been a remarkable progress in understanding development, plasticity, function, and pathological relevance of GABAergic inhibitory circuits. In particular, along with recent rapid technological advances in single-cell omics, genetic targeting, *in vivo* imaging, functional manipulations, and behavioral assays, our knowledge on IN subtypes has been explosively expanded. A Research Topic of articles including seven original research papers and two reviews, organized under the theme "Cellular and Molecular Mechanisms that Govern Assembly, Plasticity, and Function of GABAergic Inhibitory Circuits in the Mammalian Brain," highlights just how far we've come—and where we need to go next. These reports comprehensively discuss topics on the GABAergic inhibitory system ranging from cell type specification, synaptic assembly, and functional diversity to its role in health and disease. The overarching goal is to untangle how myriad of INs weave themselves into functional circuits—a puzzle central to understanding the power and vulnerability of cortical inhibition.

The challenging but essential tasks for dissecting the inhibitory system is to disentangle intricate inhibitory circuits consisting of diverse GABAergic IN subtypes (Bandler et al., 2017; Hu et al., 2017; Lodato and Arlotta, 2015; Miyoshi, 2019; Pelkey et al., 2017). Machold and Rudy review the emerging view on cortical and hippocampal IN subtypes defined by transcriptomics and developmental origin and highlight a genetic toolkit for targeting specific IN subtypes, along with the technical considerations inherent to each approach.

The authors provide gene expression heatmaps illustrating transcriptomic identity of cortical and hippocampal IN subtypes as well as a table summarizing Cre/Flp driver lines and Cre/Flp-dependent reporter lines for investigating IN subtypes that are currently available. Expanding genetic toolkit allowing for targeting more specific IN subtypes will further deepen our understanding of IN specification, assembly, and function and facilitate gaining novel insight into brain diseases. Yet, pinpointing these subtypes is only half the story—each interneuron lineage arises from a dynamic mix of genetic and epigenetic codes where the interplay of chromatin modifiers can direct interneuron destinies, reshaping the fundamental map of inhibitory identity.

It is fundamental to ask how genetic and epigenetic regulators orchestrate generation and specification of inhibitory cell types, and Rhodes et al. demonstrate that loss of histone methyltransferase Ezh2 in the medial ganglionic eminence (MGE) disrupts H3K27me3 levels, leading to significant changes in interneuron fate, with increased somatostatin-expressing (SST+) INs and decreased parvalbumin-expressing (PV+) INs, indicating that the MGE is not a uniform source of PV+ INs and SST+ INs simply marching along a preordained path. Instead, these progenitors rely on nuanced chromatin remodeling to steer them toward particular fates. By perturbing Ezh2, the authors reveal how epigenetic mechanisms bias lineage outcomes, ultimately capable of altering interneuron composition and circuit-level consequences. This aligns with a growing literature showing that interneuron progenitor domains—from MGE to CGE—are not static templates, but dynamic entities whose transcriptional and epigenetic landscapes are continuously shaped by internal gene regulatory networks and external signaling cues.

While epigenetic codes inscribe interneuron destinies, GABA itself can orchestrate a variety of developmental maturational processes in the brain such as neuronal migration, synapse formation, neurite elongation, and circuit integration (Bortone and Polleux, 2009; Kilb, 2021; Peerboom and Wierenga, 2021). $GABA_A$ receptors ($GABA_A$Rs) and K-Cl transporter 2 (KCC2) play a major role in this regulation. Zavalin et al. tracks the developmental expression patterns of $GABA_A$R subunits and KCC2. The discovery of region- and layer-specific changes in receptor composition during early postnatal maturation exemplifies how the inhibitory system is constructed in phases—akin to a building whose scaffolding and wiring are put in place step-by-step rather than all at once. This temporal and spatial refinement is pivotal for stabilizing nascent circuits, ensuring that as excitatory inputs proliferate and refine, the inhibitory networks are calibrated in lockstep, achieving a balanced interplay that underlies the cortex's computational prowess.

Development and maturation of inhibitory synapses are key cellular processes to establish functional GABAergic synaptic transmission in neuronal networks. Establishing robust inhibitory synapses requires an additional layer of coordination—a molecular dialogue at the synapse itself. Here Sui et al. reveals the synergy between Neuroligin-2 (NL2) and $GABA_A$Rs and how their conversation dictates inhibitory circuit assembly. NL2 and $GABA_A$Rs, inhibitory postsynaptic cell surface proteins, have been demonstrated to synergistically recruit inhibitory synapses in a heterologous co-culture system containing HEK cells and striatal GABAergic medium spiny neurons (Fuchs et al., 2013). Sui et al. extend this finding by investigating the effect of different types of $GABA_A$Rs on NL2 synaptogenic activity using the same assay system as well as conducting structure/function analysis of $GABA_A$Rs. The authors find that the synaptic type $GABA_A$Rs ($\alpha2\beta2\gamma2$-$GABA_A$Rs) have a significantly greater effect in facilitating the NL2-dependent induction of synapses than the prototypical extrasynaptic type $GABA_A$Rs ($\alpha4\beta3\delta$-$GABA_A$Rs). They show that this synergistic effect of $GABA_A$Rs on NL2-dependent inhibitory synapse recruitment is independent of $GABA_A$R channel activity. Furthermore, they demonstrate that the synergism between $GABA_A$Rs and NL2 is dependent on the $\gamma2$ subunit interaction with NL2, and the intracellular domain of this subunit is necessary for this interaction. These findings reveal the molecular logic underlying the $GABA_A$Rs and NL2 interaction that mediates morphological and functional coordination in inhibitory synapse development.

Finely-tuned synaptic elements modulate circuit activity across behavioral contexts, reflecting a dynamic dialogue between interneurons and the overall brain state—a hallmark of GABAergic control. However, much is not known about the cortical mechanisms behind the modulation of neuronal activity across behavioral states. Sabri and Batista-Brito, utilizing chemogenetics and multi-cell spike recording, demonstrate that inhibiting vasoactive intestinal peptide (VIP)-expressing (VIP+) INs throughout the brain reduces the correlation between the mouse facial motion and the spiking activity of individual neurons in the primary visual cortex. The authors also find that inhibiting VIP+ INs during the quiet state results in enhanced slow rhythms while reducing fast spike synchrony. Their findings suggest that VIP interneurons modulate cortical activity in a behavior-dependent manner across different behavioral states.

Even beyond moment-to-moment states, key transcription factors guide the balance between excitation and inhibition over the course of development, and small disruptions in this orchestration can reverberate into neurodevelopmental disorders, as we now observe. Myocyte enhancement factor 2c (MEF2C), a transcription factor expressed in both excitatory PNs and inhibitory INs throughout the life in mice, have been implicated in various neurodevelopmental disorders (NDDs) such as autism spectrum disorder (ASD), schizophrenia, and bipolar disorder (Assali et al., 2019; Harrington et al., 2016; Rajkovich et al., 2017; Tu et al., 2017). In a minireview, Ward et al. review how MEF2C loss-of-function (LOF) impacts excitatory and inhibitory cortical circuit development and highlight how brain dysfunction and altered behavior may derive from the dysfunction of specific cortical circuits at specific developmental times along with a table showing cellular and behavioral phenotypes in MEF2C LOF mouse models. These more nuanced studies in MEF2C LOF mice could provide a suggestive hint for identifying prognostic biomarkers and developing early intervention in NDDs.

As outlined by the above review, a mutation in one risk factor gene for NDDs could differentially impact development and functional maturation of distinct cell types and neuronal circuits, and thus distinct behavioral deficits in NDDs that involve dysfunction in different sets of circuit modules may be attributable to separate pathological landscapes. Asano et al. address this

line of question using the ASD mouse model with FOXG1 haploinsufficiency. The authors find that in the ASD model, while social behavior deficits are evident from the early juvenile stages, novel space preference is initially established during early juvenile stages but regresses by postnatal week 6. Furthermore, they demonstrate that in contrast to their previous finding that reducing GABAergic tone decreased social scores in wildtype mice and exacerbated social deficits in the ASD model (Miyoshi et al., 2021), this reduction has no impact on novel space preference in either wildtype or ASD model mice. This dissociation underscores that the relationship between developmental inhibitory dysfunction and resulting behavioral phenotypes is not one-size-fits-all. Different aspects of behavior and cognition may rely on distinct inhibitory subtypes or specific developmental time windows. To devise effective therapeutic strategies, it is crucial to identify the circuit elements relevant to particular symptoms and determine the optimal timing for interventions to achieve meaningful outcomes.

If altered inhibitory tone can selectively affect social and spatial behaviors, it is just as crucial to understand how environmental stress tangles with these microcircuits. At the circuit level, information processing relies on excitatory circuits operating under precise modulation by GABAergic inhibition. In the current Research Topic, Nasretdinov et al. show that CB1 receptor-expressing (CB1R+) INs in layer V of the entorhinal cortex are modulated by stress. These INs regulate excitatory flow within the hippocampal-entorhinal loop while contributing minimally to local feedback inhibition. Consequently, CB1R+ INs in the deep layers of the entorhinal cortex function as a key relay station, translating hippocampal excitation into effective inhibition of cortical pyramidal cells. This provides circuit- and cellular-level mechanisms for linking environmental stress to neuronal activity.

Such sensitivity to both internal and external cues underscores the therapeutic potential of targeting GABAergic elements. In fact, we are beginning to see evidence of how subtle receptor differences can open distinct avenues for pharmacological intervention. Developing effective drugs for brain disorders is one of important missions for neuroscientists. Takasu et al. investigate the effect of allopregnanolone and diazepam, two positive modulators of $GABA_AR$s on abnormal social behaviors and cortical oscillations in social defeat model mice. The authors find that allopregnanolone's selective engagement of extrasynaptic δ-subunit-containing receptors leads to unique changes in circuit oscillations within the basolateral amygdala and medial prefrontal cortex, producing rapid antidepressant-like effects that benzodiazepines cannot replicate. This result echoes a central tenet of our field: subtle differences in receptor composition and localization matter immensely for how interneurons regulate circuit states linked to mood and cognition.

These diverse set of articles coalesce into a powerful message: GABAergic circuits, in all their complexity, underwrite the brain's astonishing adaptability—yet they remain intriguingly susceptible to brain states and stressors. We now see a system in which genetic specification, epigenetic shaping, receptor diversity, and synaptic adhesion cooperate to produce circuits that are robust, plastic, and finely attuned to the ever-shifting computational landscape of the brain. Moving forward, novel approaches combining genetic access, multiomic profiling, and advanced imaging and electrophysiological methods with continuous behavioral monitoring paradigms will provide comprehensive insights linking the molecular logic underlying circuit assembly, cell types, and circuit mechanisms to animal behaviors in health and disease. The NIH SSPSyGene Consortium has taken a bold step toward this ambitious goal by launching a massive initiative to generate and multi-dimensionally profile 100 mouse gene knockouts for neurodevelopmental and psychiatric disorder risk genes—systematically building an accessible catalog of genotypes and phenotypes for open exploration (https://sspsygene.ucsc.edu). The continuous effort on elucidating complexity and specificity inherent in inhibitory neuron biology holds great promise for gaining the power to not only describe cortical circuits in detail, but also to correct their pathological deviations and restore proper function.

Author contributions

YH: Writing – original draft, Writing – review & editing. GM: Writing – original draft, Writing – review & editing. AP: Writing – original draft, Writing – review & editing. HT: Writing – original draft, Writing – review & editing.

Conflict of interest

The authors declare that the research was conducted in the absence of any commercial or financial relationships that could be construed as a potential conflict of interest.

The author(s) declared that they were an editorial board member of Frontiers, at the time of submission. This had no impact on the peer review process and the final decision.

Publisher's note

References

Assali, A., Harrington, A. J., and Cowan, C. W. (2019). Emerging roles for MEF2 in brain development and mental disorders. *Curr. Opin. Neurobiol.* 59, 49–58. doi: 10.1016/j.conb.2019.04.008

Bandler, R. C., Mayer, C., and Fishell, G. (2017). Cortical interneuron specification: the juncture of genes, time and geometry. *Curr. Opin. Neurobiol.* 42, 17–24. doi: 10.1016/j.conb.2016.10.003

Bortone, D., and Polleux, F. (2009). KCC2 expression promotes the termination of cortical interneuron migration in a voltage-sensitive calcium-dependent manner. *Neuron* 62, 53–71. doi: 10.1016/j.neuron.2009.01.034

Del Pino, I., Rico, B., and Marin, O. (2018). Neural circuit dysfunction in mouse models of neurodevelopmental disorders. *Curr. Opin. Neurobiol.* 48, 174–182. doi: 10.1016/j.conb.2017.12.013

Frye, R. E., Casanova, M. F., Fatemi, S. H., Folsom, T. D., Reutiman, T. J., Brown, G. L., et al. (2016). Neuropathological mechanisms of seizures in autism spectrum disorder. *Front. Neurosci.* 10:192. doi: 10.3389/fnins.2016.00192

Fuchs, C., Abitbol, K., Burden, J. J., Mercer, A., Brown, L., Iball, J., et al. (2013). GABA(A) receptors can initiate the formation of functional inhibitory GABAergic synapses. *Eur. J. Neurosci.* 38, 3146–3158. doi: 10.1111/ejn.12331

Harrington, A. J., Raissi, A., Rajkovich, K., Berto, S., Kumar, J., Molinaro, G., et al. (2016). MEF2C regulates cortical inhibitory and excitatory synapses and behaviors relevant to neurodevelopmental disorders. *Elife* 5:e20059. doi: 10.7554/eLife.20059.023

Hu, J. S., Vogt, D., Sandberg, M., and Rubenstein, J. L. (2017). Cortical interneuron development: a tale of time and space. *Development* 144, 3867–3878. doi: 10.1242/dev.132852

Kepecs, A., and Fishell, G. (2014). Interneuron cell types are fit to function. *Nature* 505, 318–326. doi: 10.1038/nature12983

Kilb, W. (2021). When are depolarizing GABAergic responses excitatory? *Front. Mol. Neurosci.* 14:747835. doi: 10.3389/fnmol.2021.747835

Lodato, S., and Arlotta, P. (2015). Generating neuronal diversity in the mammalian cerebral cortex. *Annu. Rev. Cell Dev. Biol.* 31, 699–720. doi: 10.1146/annurev-cellbio-100814-125353

Miyoshi, G. (2019). Elucidating the developmental trajectories of GABAergic cortical interneuron subtypes. *Neurosci. Res.* 138, 26–32. doi: 10.1016/j.neures.2018.09.012

Miyoshi, G., Ueta, Y., Natsubori, A., Hiraga, K., Osaki, H., Yagasaki, Y., et al. (2021). FoxG1 regulates the formation of cortical GABAergic circuit during an early postnatal critical period resulting in autism spectrum disorder-like phenotypes. *Nat. Commun.* 12:3773. doi: 10.1038/s41467-021-23987-z

Peerboom, C., and Wierenga, C. J. (2021). The postnatal GABA shift: a developmental perspective. *Neurosci. Biobehav. Rev.* 124, 179–192. doi: 10.1016/j.neubiorev.2021.01.024

Pelkey, K. A., Chittajallu, R., Craig, M. T., Tricoire, L., Wester, J. C., McBain, C. J., et al. (2017). Hippocampal GABAergic inhibitory interneurons. *Physiol. Rev.* 97, 1619–1747. doi: 10.1152/physrev.00007.2017

Rajkovich, K. E., Loerwald, K. W., Hale, C. F., Hess, C. T., Gibson, J. R., Huber, K. M., et al. (2017). Experience-dependent and differential regulation of local and long-range excitatory neocortical circuits by postsynaptic Mef2c. *Neuron* 93, 48–56. doi: 10.1016/j.neuron.2016.11.022

Takano, T. (2015). Interneuron dysfunction in syndromic autism: recent advances. *Dev. Neurosci.* 37, 467–475. doi: 10.1159/000434638

Taniguchi, H. (2014). Genetic dissection of GABAergic neural circuits in mouse neocortex. *Front. Cell. Neurosci.* 8:8. doi: 10.3389/fncel.2014.00008

Tremblay, R., Lee, S., and Rudy, B. (2016). GABAergic interneurons in the neocortex: from cellular properties to circuits. *Neuron* 91, 260–292. doi: 10.1016/j.neuron.2016.06.033

Tu, S., Akhtar, M. W., Escorihuela, R. M., Amador-Arjona, A., Swarup, V., Parker, J., et al. (2017). NitroSynapsin therapy for a mouse MEF2C haploinsufficiency model of human autism. *Nat. Commun.* 8:1488. doi: 10.1038/s41467-017-01563-8

Wang, Y., Zhang, P., and Wyskiel, D. R. (2016). Chandelier cells in functional and dysfunctional neural circuits. *Front. Neural Circuits* 10:33. doi: 10.3389/fncir.2016.00033

frontiers | Frontiers in Cellular Neuroscience

TYPE Brief Research Report
PUBLISHED 07 December 2023
DOI 10.3389/fncel.2023.1327909

OPEN ACCESS

EDITED BY
Goichi Miyoshi,
Gunma University, Japan

REVIEWED BY
Hiroyuki Miyawaki,
Osaka City University, Japan
Paul George Anastasiades,
University of Bristol, United Kingdom

*CORRESPONDENCE
Andrei Rozov
✉ rozov1511@gmail.com

RECEIVED 25 October 2023
ACCEPTED 24 November 2023
PUBLISHED 07 December 2023

CITATION
Nasretdinov A, Jappy D, Vazetdinova A, Valiullina-Rakhmatullina F and Rozov A (2023) Acute stress modulates hippocampal to entorhinal cortex communication. *Front. Cell. Neurosci.* 17:1327909. doi: 10.3389/fncel.2023.1327909

Acute stress modulates hippocampal to entorhinal cortex communication

Azat Nasretdinov[1], David Jappy[2,3], Alina Vazetdinova[1,2], Fliza Valiullina-Rakhmatullina[1,2] and Andrei Rozov[2,4]*

[1]Laboratory of Neurobiology, Kazan Federal University, Kazan, Russia, [2]Federal Center of Brain Research and Neurotechnologies, Moscow, Russia, [3]Institute of Neuroscience, Lobachevsky State University of Nizhny Novgorod, Nizhny Novgorod, Russia, [4]Department of Physiology and Pathophysiology, Heidelberg University, Heidelberg, Germany

Feed-forward inhibition is vital in the transfer and processing of synaptic information within the hippocampal–entorhinal loop by controlling the strength and direction of excitation flow between different neuronal populations and individual neurons. While the cellular targets in the hippocampus that receive excitatory inputs from the entorhinal cortex have been well studied, and the role of feedforward inhibitory neurons has been attributed to neurogliafom cells, the cortical interneurons providing feed-forward control over receiving layer V in the entorhinal cortex remain unknown. We used sharp-wave ripple oscillations as a natural excitatory stimulus of the entorhinal cortex, driven by the hippocampus, to study the function of synaptic interactions between neurons in the deep layers of the entorhinal cortex. We discovered that CB1R-expressing interneurons in the deep layers of the entorhinal cortex constitute the major relay station that translates hippocampal excitation into efficient inhibition of cortical pyramidal cells. The impact of inhibition provided by these interneurons is under strong endocannabinoid control and can be drastically reduced either by enhanced activity of postsynaptic targets or by stress-induced elevation of cannabinoids.

KEYWORDS

feed-forward inhibition, CB1R, SPW-R, stress, endocannabinoids

Introduction

The hippocampal-entorhinal loop plays an important role in episodic memory, storing spatial and temporal information about the occurrence of past events. Over the past decade, significant progress has been made in understanding the function and postsynaptic targets of projections from the entorhinal cortex (EC) to the hippocampus (Zhang et al., 2013, 2014; Kitamura et al., 2015; López-Madrona and Canals, 2021). However, until recently, little was known about projection pattern of the hippocampus to the EC (Sürmeli et al., 2015; Witter et al., 2017). Moreover, while local excitatory/inhibitory circuitries in the hippocampus (Freund and Buzsáki, 1996; Freund and Katona, 2007) and upper layers of EC (Varga et al., 2010; Armstrong et al., 2016; Witter et al., 2017) have been investigated and specific functional roles assigned to given types of interneurons, nearly nothing is known about feed-back and feed-forward inhibition in the deep layers of EC.

In our previous study we characterized the functional connectivity between the ventral hippocampus and the deep layers of the medial entorhinal cortex (mEC) (Rozov et al., 2020).

Besides direct projections to two types of layer V pyramidal cells, we discovered that deep layer fast-spiking interneurons (FS-IN) also receive hippocampal excitatory inputs. It was suggested that during rhythmic activity FS-IN can be recruited into hippocampal-driven feed-forward inhibition. Indeed, during sharp-wave ripples (SPW-R) we observed IPSCs in LVa and LVb pyramidal neurons (held at 0 mV) with a characteristic disynaptic delay relative to the onset of hippocampal SPW-R. However, IPSC-coupling, calculated as the percentage of SPW-R followed by IPSCs in both types of pyramidal cells was significantly lower than EPSC-coupling when measured from the same cell (Rozov et al., 2020). A close look at the coupling and amplitude dynamics of SPW-R driven IPSCs revealed that right after depolarization nearly every SPW-R event was followed by a high amplitude IPSC, but then both amplitude and coupling probability drastically declined reaching steady state values within 30 s. In the present study we found that suppression of SPW-R associated IPSC amplitudes and coupling probabilities were occluded by application of the CB1 receptor antagonist AM-251 (2 μM), suggesting involvement of CB1-positive interneurons in SPW-R driven feed-forward inhibition (Gatley et al., 1996; **Figure 1**). Thus, one can assume the following: (i) depolarization of the postsynaptic neuron triggered synthesis of endocannabinoids, which selectively blocked GABA release from CB1R expressing terminals; (ii) CB1R-positive interneurons (CB1-IN) also receive direct hippocampal innervation and are involved in signal processing within the hippocampal-entorhinal loop.

Interestingly, differential roles of CB1-INs and FS-INs in the control of neuronal populations involved in propagation of information within the hippocampal-entorhinal loop have been previously suggested for both the hippocampus (Yap et al., 2021) and upper layers of EC (Witter et al., 2017). Expression of CB1R equips the circuitries controlled by CB1-INs with the possibility of activity dependent modulation of the inhibitory impact of these interneurons (Dubruc et al., 2013). Moreover, the strength of CB1-IN - mediated inhibition can be altered by circulating endocannabinoids, and the concentration of the latter can be elevated by salient aversive experiences and acute stress (Ney et al., 2021; Vecchiarelli et al., 2022; Kondev et al., 2023a,b).

Therefore, in this study we explore: (i) the integration of the deep layer EC CB1INs in long distance (hippocampal-entorhinal loop) and local (layer V) networks; and (ii) the impact of stress-dependent endocannabinoid modulation in feed-forward CB1IN-mediated inhibition.

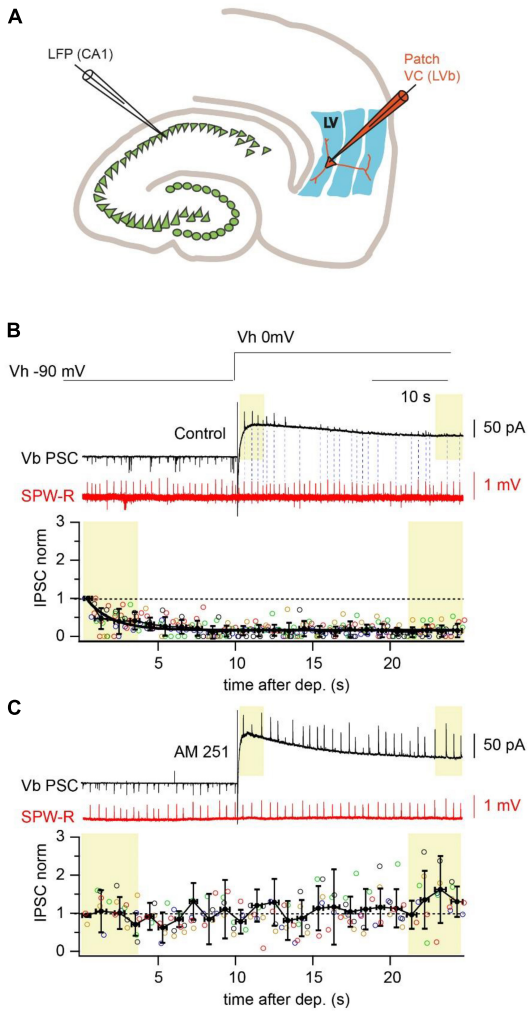

FIGURE 1
Depolarization reduces amplitude and propagation probability of SPW-R driven IPSCs. **(A)** Schematic representation of a horizontal hippocampal–EC slice with the position of the LFP recording site in the CA1 region and a LVb pyramidal neuron in layer V of EC recorded in whole cell voltage-clamp mode. **(B)** Spontaneous SPW-Rs (red) in CA1 and associated PSCs (black) in mEC LVb recorded at the reversal potentials of $GABA_A$ (−90 mV) and iGluR (0 mV). Experiments were done with a low-Cl^- internal solution. Note that right after the depolarization step IPSCs are well detectable. However, both IPSC amplitude and propagation probability rapidly decline at the depolarized holding potential. Dotted lines connect SPW-Rs with corresponding small amplitude IPSCs. The time course of depolarization induced reduction of IPSC amplitudes is plotted underneath. Data from different neurons are shown in different colors ($n = 5$; $p < 0.01$). For statistical analysis the IPSC amplitudes within the first and the last 3 s windows (yellow boxes) after depolarization were compared. **(C)** The same as in panel **(A)** recorded in the presence of a CB1R blocker (AM251; 2 μM). Application of the CB1R antagonist completely occludes the effect of depolarization on IPSC amplitude ($n = 5$; $p > 0.05$).

Results

Synaptic integration of CB1R-positive interneurons into the layer V mEC network

Screening the different interneurons located in layer V of mEC we found a population of cells that have firing properties similar to those described for CB1R-positive hippocampal basket cells (Pawelzik et al., 2002). In response to a 1 s depolarizing current injection these interneurons fire action potentials with a characteristic initial burst followed by lower frequency regular spiking (**Figure 2A**). The neurons were located in layer Va, the size and the appearance of the cell body on the IR-image was similar to that of Va pyramidal cells. Therefore, all experiments that required direct recordings from CB1R-expressing interneurons were performed in slices from GAD67-GFP mice.

To confirm expression of presynaptic CB1Rs in these neurons we tested for the ability to exhibit depolarization-induced suppression of inhibition (Kreitzer and Regehr, 2001;

10.3389/fncel.2023.1327909

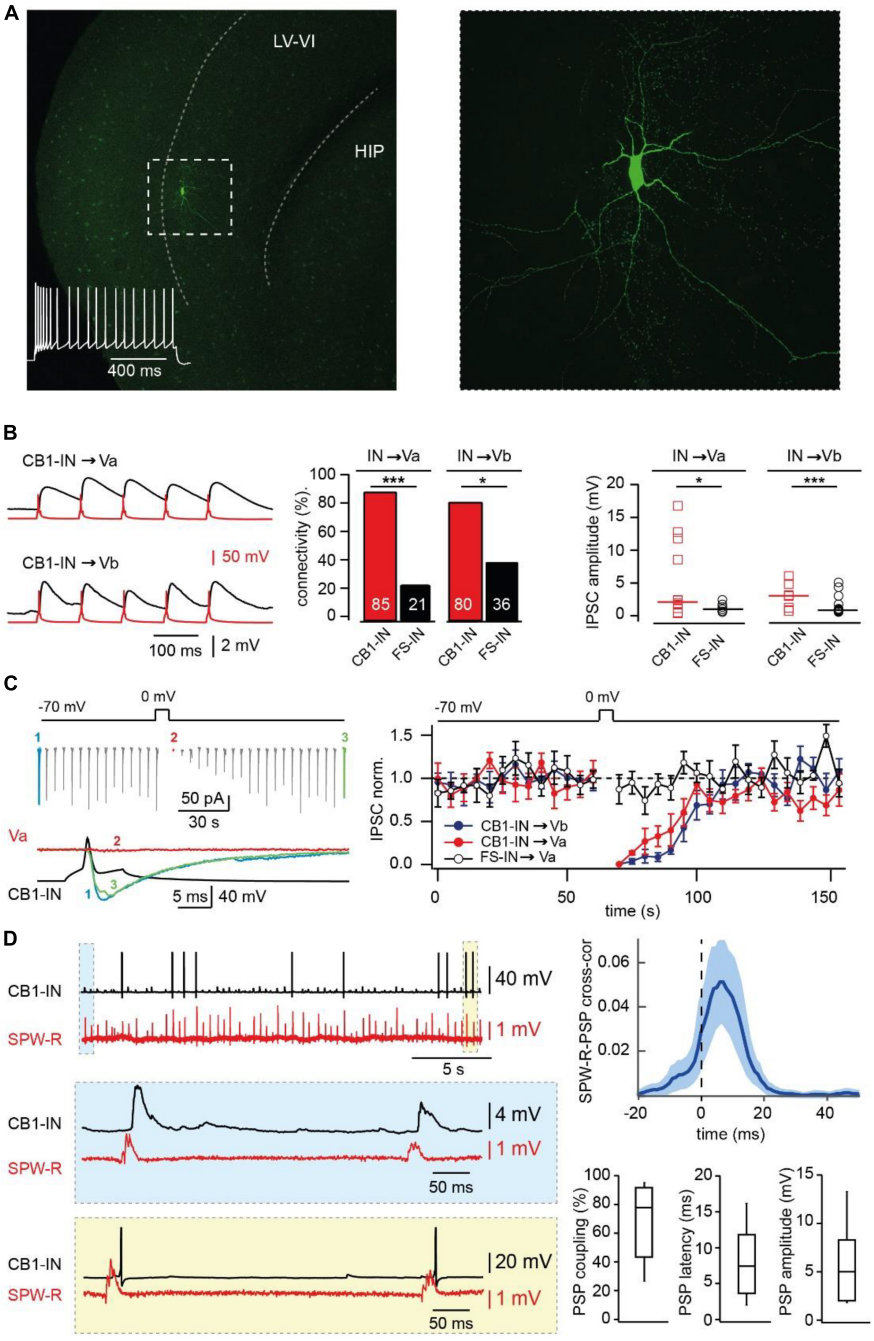

FIGURE 2
Synaptic integration of deep layer entorhinal cortex CB1R positive interneurons into local and long-distance networks. **(A)** z-Projected confocal images of a biocytin-filled mEC layer V CB1-IN at low (left) and high (right) magnification. The characteristic firing pattern is shown on the left panel. **(B)** Connectivity and efficacy of inhibitory connections from CB1-INs to LV pyramidal neurons in comparison with the properties of corresponding FS-INs connections. The left panel shows example traces recorded from connected CB1-IN to Va and Vb pyramidal neurons. The bar histogram (center) compares connectivity from two types of mEC LV interneurons to local pyramidal cells. The number of trials for different types of connections are as follows: CB1-IN to Va (n = 20), CB1-IN to Vb (n = 20), FS-IN to Va (n = 29) and FS-IN to Vb (n = 27). The significance of the differences was assessed by Fisher's exact test (*p < 0.05; ***p < 0.001). The right plot compares individual amplitudes of IPSPs and median values at: CB1-IN to Va (n = 12), CB1-IN to Vb (n = 7), FSIN to Va (n = 6) and FSIN to Vb (n = 15) connections. The significance of the differences was assessed by Mann-Whitney test (*p < 0.05; ***p < 0.001). For calculating amplitude distribution, we used only those experiments which were done in CC mode. For calculating connectivity, we used both experiments done in VC and CC modes. Data on connectivity rate and synaptic efficacy at connections formed by FS-INs were taken from Rozov et al. (2020). **(C)** DSI at CB1-IN to Va and Vb cell synapses. An example experiment is shown on the left. The plot on the right compares depolarization-induced changes in synaptic efficacy at the following synapses: red–CB1-IN to Va (n = 5; p < 0.001), blue - CB1-IN to Vb (n = 5; p < 0.001) and black–FS-IN to Va (n = 5; p > 0.05) pyramidal cells. For statistical analysis the IPSC amplitudes within the 10 s windows prior to depolarization and right after depolarization were compared. **(D)** Propagation of SPW-Rs to mEC LV CB1-INs. PSPs of mEC CB1-IN (red trace) during spontaneous SPW-Rs in CA1 (black trace). Expanded traces of subthreshold SPW-R driven PSPs (blue box) and SPW-R driven APs (yellow box) are shown underneath. Averaged cross-correlograms between SPW-Rs and PSPs in CB1-INs (upper right plot; peak values: mean ± SD; n = 8). **(C)** Box plots show pooled data on PSP coupling, PSP latency, and PSP amplitude for SPW-R driven responses (n = 8). Data are presented as the median (P25; P75).

Wilson et al., 2001) (DSI) at their synapse onto local pyramidal LVa and LVb cells. The connectivity of the interneurons to both types of LV pyramidal cells was very high, being 85% (17 out of 20 tested pairs) for connection to LVa pyramids and 80% (16 out of 20 tested pairs) for connection to LVb pyramids (**Figure 2B**). In all tested cases depolarization of the postsynaptic pyramidal cell caused strong DSI lasting for more than 30 s (**Figure 2C**), confirming CB1R expression in these interneurons (CB1-IN). Another feature that was similar between hippocampal and mEC CB1-INs was profound asynchronous GABA release in response to high frequency stimulation (Hefft and Jonas, 2005; Ali and Todorova, 2010; **Supplementary Figure 1A**).

Involvement of CB1R-positive interneurons in SPW-R driven feed-forward inhibition

Next, we assessed whether CB1-INs in mEC LV receive direct excitatory drive during SPW-Rs. Oscillatory activity was measured extracellularly in the CA1 region of the hippocampus simultaneously with whole cell current clamp recordings of cortical CB1-INs identified by firing properties (Hájos and Mody, 2009; Rozov et al., 2020; **Figure 2D**). In all cases (n = 8) hippocampal SPW-R could trigger subthreshold responses in interneurons with characteristic propagation success and latencies that were very similar to those found for mEC FS-Ins (Rozov et al., 2020). Moreover, in 37.5% of recorded CB1-INs, SPW-R driven responses could reach suprathreshold values and trigger action potentials (APs). The high excitability of CB1-INs (**Supplementary Figure 2**) together with their high connectivity rate to layer V mEC pyramidal neurons strongly suggest that these interneurons play a significant role in feed-forward inhibition, which was overlooked in our previous study, since the depolarization used for IPSC separation leads to DSI and selectively occluded the contribution of CB1-INs. To test this hypothesis, we evaluated the effects of CB1R blockade on amplitude and coupling probability of SPW-R driven EPSCs and IPSCs. As expected, application of AM251 did not affect EPSCs, while both amplitude and coupling frequency of IPSCs recorded at 0 mV in LVa and LVb pyramidal cells after drug application were substantially higher relative to control (**Figure 3A**).

Thus, CB1-INs are indeed among the major players in hippocampal feed-forward inhibition of layer V mEC. Moreover, given that we didn't find any excitatory connections from LVb pyramidal cells to CB1-IN (n = 20) and only one connection from LVa (n = 20) to CB1-INs, hippocampal glutamatergic projections might constitute the main source of excitatory drive to CB1-INs, which makes the role of these interneurons within the hippocampal-mEC loop significant.

Endocannabinoid modulation of CB1-IN feed-forward inhibition

To assess the possible specific function of CB1-INs in signal transduction between these two structures we first tested if depolarization can reduce the contribution of CB1-INs to SPW-R driven IPSCs. This task was rather challenging since pharmacological isolation of IPSCs by blocking excitation would also block rhythmic activity (Maier et al., 2003). To overcome that problem, we used a high Cl^- internal solution (38 mM). In this case E_{GABA} is around −40 mV, while at −90 mV the direction of IPSCs and EPSCs is the same. Thus, DSI selectively reducing IPSCs would also suppress the amplitude of compound SPW-R driven responses (PSC) recorded at −90 mV. Indeed, 5 s depolarization of postsynaptic LVa (n = 7) and LVb (n = 7) pyramidal cells to 0 mV led to significant temporal reduction of SPW-R driven PSC amplitudes (**Figure 3B**). The DSI-like effect was totally occluded by application of the CB1 antagonist AM251 (2 μM; **Supplementary Figure 3**). To exclude possible effects of depolarization on the excitatory component of PSCs we repeated the same experiments with a low Cl^- internal solution (4 mM; $E_{GABA} \sim -90$ mV). Under these conditions depolarization didn't have any significant effect on PSCs recorded at −90 mV (**Figure 2B**; n = 7 for both LVa and LVb neurons). We then tested whether endocannabinoids could modulate the amplitude and duration of SPW-R driven PSPs under more physiological conditions, namely: in current clamp mode with a low intracellular Cl^- concentration (4 mM) and the use of burst firing (Dubruc et al., 2013) instead of sustained depolarization to trigger DSI. These experiments were done on LVb pyramidal cells, since they have shorter afterhyperpolarization and recover back to resting membrane potential faster than LVa pyramidal neurons. Prior to firing activity most PSPs had prominent depolarizing and hyperpolarizing components, however, within 10–20 s of postsynaptic burst firing, the contribution of the GABA-mediated inhibitory component was significantly reduced, which led to enhancement of the amplitude and duration of PSPs (**Figure 3C**). Application of the CB1R antagonist completely occluded the DSI-like effect of postsynaptic cell firing on SPW-R driven IPSP (**Supplementary Figure 4**) We separately analyzed the excitatory and inhibitory components of PSPs (Antoine et al., 2019) (for details see method; **Supplementary Figure 5**). The time course of suppression of inhibition was very similar to the durations of DSIs observed for IPSCs in connected cell pairs and for SPW-R driven PSCs. Thus, endocannabinoid-dependent suppression of CB1-IN-mediated feed-forward inhibition should be more pronounced in pyramidal cells that receive stronger excitatory inputs, therefore, promoting further firing activity in more active neurons.

Acute stress reduces the impact of CB1-IN-mediated feed-forward inhibition via activation of presynaptic CB1Rs

In the DSI-like phenomenon, endocannabinoid synthesis is triggered by activity of individual neurons, however, certain levels of endocannabinoids are persistently present in the brain tissue causing detectable suppression of GABA release via partial activation of CB1Rs (Neu et al., 2007; Ali and Todorova, 2010; Lee et al., 2010). The concentration of circulating endocannabinoids can increase in response to various adverse stimuli for example: acute stress (Ney et al., 2021; Vecchiarelli et al., 2022; Kondev et al., 2023a,b), tissue injury (Vered et al., 2023) and inflammation (Bouchet et al., 2023). Therefore, we

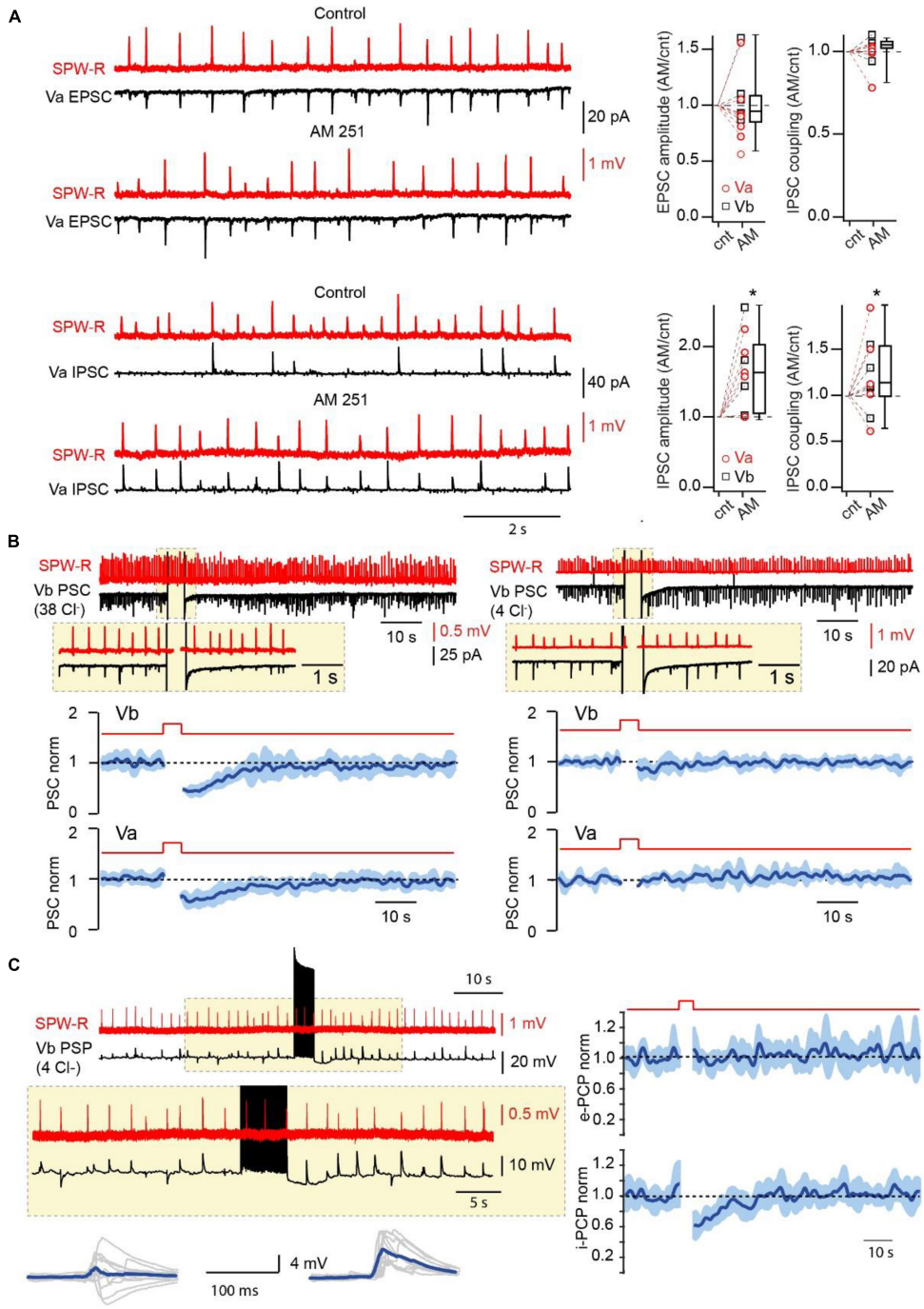

FIGURE 3
Endocannabinoids control the amplitude and probability of SPW-R driven inhibition. **(A)** Effect of CB1R blockade on the amplitude and coupling probability of SPW-R driven EPSCs and IPSCs. Traces on the left show spontaneous SPW-Rs in CA1 and associated EPSC (V_h −90 mV) and IPSC (V_h 0 mV) in mEC LVa cells before and after application of the CB1R antagonist AM251 (2 μM). The experiment was done with a low-Cl^- internal solution. Box plots on the right show normalized (AM251/control) amplitude and coupling probability values in individual cells and pooled data (presented as the median; P25; P75). The significance of the differences was assessed by Wilcoxon Signed Rank Test (*$p < 0.05$). Note, that application of AM251 did not have any effect on EPSCs but caused significant enhancement of the amplitude and coupling probability of IPSCs. **(B)** Effects of short-lasting (5 s) depolarization on the amplitude of compound SPW-R driven PSCs depends on internal Cl^- concentration. Traces on the left represent spontaneous SPW-Rs (red) in CA1 and associated PSC (Vm −90 mV) in mEC LVb recorded with a high-Cl^- (38 mM) internal solution. Depolarization of the postsynaptic cell led to temporal reduction of PSC amplitudes. Plots underneath show averaged time course (mean ± SEM) of induced by depolarization suppression of PSC efficacy in Va ($n = 7$; $p < 0.01$) and Vb ($n = 7$; $p < 0.01$) pyramidal cells. The traces and the plots on the right represent data obtained with a low-Cl^- (4 mM) internal solution. Each plot represents data from 7 cells ($p > 0.05$). For statistical analysis the PSC amplitudes within the 5 s windows prior to depolarization and right after depolarization were compared. **(C)** Postsynaptic cell burst firing triggers a DSI-like effect. Traces on the left represent spontaneous SPW-Rs (red) in CA1 and associated PSPs (black; Vm −65 mV) in mEC LVb ($n = 7$) recorded with a low-Cl^- internal solution. A train (5 s) of high frequency APs in the postsynaptic cell temporally enhances amplitude and duration of PSPs. Traces underneath show 10 individual PSPs (gray) and averaged responses (blue) before and after the AP burst. Plots on the right show averages of normalized amplitudes of excitatory (e-PSP; $p > 0.05$) and inhibitory (i-PSP; $p < 0.01$) components of SPW-R driven responses. For statistical analysis the e-PSP and i-PSP amplitudes within the 5 s windows prior to depolarization and right after depolarization were compared.

investigated the effects of acute unavoidable stress (Paré and Glavin, 1986; Glavin et al., 1994; Zimprich et al., 2014) on feed-forward inhibition in the hippocampal-EC loop mediated by CB1-INs. Mice were restrained for 1 h prior to decapitation. First, we compared the levels of sustained suppression of GABA release at CB1-IN to LVb cell synapses in naïve and stressed animals. This was achieved by measuring the effects of CB1-R antagonist application on the amplitude of IPSCs recorded from connected pairs of neurons. In slices from naïve mice AM251 caused small, but significant enhancement of IPSC amplitudes (**Supplementary Figure 1B**). However, in pairs recorded from stressed animals, CB1R antagonist administration resulted in significantly stronger amplification of IPSCs (**Supplementary Figure 1B**), suggesting that acute stress leads to long lasting activation of CB1Rs. Thus, stress induced elevation of endocannabinoid levels may facilitate SPW-R driven excitation of LV pyramidal cells in mEC via selective suppression of CB1-IN mediated feed-forward inhibition. To test this hypothesis, we compared the amplitudes and halfwidth of compound SPW-R driven PSPs before and after AM251 application in slices from stressed and naïve mice. In LVa and LVb cells of naive animals where we expected minimal modulation of CB1-IN IPSPs by tissue endocannabinoids, drug administration didn't produce any significant alteration of PSP amplitude and duration (**Figures 4A, C**). However, in stressed animals, CB1R antagonist application strongly reduced the amplitude and halfwidth of compound SPW-R driven responses, suggesting that relief from endocannabinoid block enhanced the IPSP component (**Figures 4B, D**). In similar experiments performed with depolarizing IPSPs (high Cl^- internal solution) AM251 application in stressed animals led to enhancement of PSP amplitude without significant alteration of duration, proving that block of CB1Rs affects SPW-R driven inhibition (**Supplementary Figure 6**).

Discussion

In this paper we describe, for the first time, the role of CB1 receptor expressing interneurons located in layer V of entorhinal cortex (EC) in control of excitation flow within the hippocampal-entorhinal loop and show that these interneurons can be modulated by stress. We describe the basic and synaptic properties of Layer V EC CB1-INs. Similarly to layer V EC parvalbumin positive fast spiking interneurons, CB1-INs receive direct excitatory drive from the hippocampus during the hippocampal rhythmic activity, sharp wave-ripple oscillations (Rozov et al., 2020). However, we didn't find any evidence of the existence of excitatory connections from local Va and Vb, pyramidal to layer V CB1-INs. The domination of distal, hippocampal excitation over local excitatory inputs strongly suggests involvement of CB1-INs in hippocampal-driven feed-forward inhibition. This assumption is further supported by the very high connectivity rates (>80%) and the strength of the GABAergic connection from presynaptic CB1-INs to Va and Vb pyramidal cells. Comparing the synaptic interaction of either CB1-INs or FS-INs with the surrounding layer V pyramidal neurons, we found that both CB1-IN connectivity and the efficacy of inhibition at their synapses were significantly higher than for connections formed by FS-INs. Thus, summarizing the existing data on layer V interneurons we can conclude that CB1-INs are substantially involved in hippocampus-driven feed-forward "GABAergic control" of layer V entorhinal cortex circuitry, and they do not contribute much to local feed-back inhibition.

Expression of CB1 receptors equips the feed-forward inhibitory chain made by these interneurons with activity sensitive gain control. Endocannabinoid modulation of GABAergic synapses can occur at the several levels and different time scales. The first level is DSI-like reduction of CB1-IN-mediated inhibition at given synapses. Enhanced subthreshold activity in the target postsynaptic Va and Vb pyramidal neurons could be translated into temporal, on a tenths of seconds timescale, endocannabinoid-dependent suppression of CB1-IN-mediated inhibition. Selective reduction of inhibition of those layer V pyramidal cells that receive stronger hippocampal excitatory drive may contribute to the formation of neuronal engrams similar to that observed in the hippocampus and other brain regions (Kim et al., 2013; Morrison et al., 2016; Stefanelli et al., 2016; Han et al., 2022). Interestingly, rearrangement of CB1-IN- and FS-IN-mediated inhibition has been shown for hippocampal CA1 pyramidal cells which were "engaged into new object memory formation." Perisomatic inhibition of *Fos*-expressing CA1 pyramidal neurons by local parvalbumin expressing FS-INs was enhanced, while perisomatic inhibition by hippocampal CB1-INs was reduced (Yap et al., 2021). The possibility of similar long lasting tuning of efficacy at layer V CB1-INs synapses triggered by stimuli that can lead to formation of new engrams should be addressed by combining behavioral, molecular and electrophysiological experiments.

The second way that endocannabinoids may influence the impact of CB1-IN mediated inhibition is more global and arises from glucocorticoid modulation of endocannabinoid production. It is known that the concentration of circulating 2-arachidonoyl glycerol increases in various brain regions including the hippocampus in response to glucocorticoid administration or as a result or acute, restraint, stress (Hill and McEwen, 2010; Morena et al., 2016; Balsevich et al., 2017). CB1R-mediated components of the stress response and stress adaptation have also been observed at the behavioral level (Atsak et al., 2012; Santori et al., 2020). In this study we tested whether 1 h of restraint stress can influence the weight of CB1-INs in the net SPW-R driven inhibition of layer V EC pyramidal cells. Indeed, while in naïve animals application of a CB1R antagonist did not have any effect on the amplitude and halfwidth of triggered PSPs in Va and Vb pyramidal neurons, in slices from the brains of stressed animals CB1R blockade caused significant reduction of both the amplitude and duration of SPW-R driven responses. The effects of AM251 on amplitude and kinetics were also observed in cells recorded with a "high Cl^-" internal solution, that excludes possible effects of CB1R occlusion on the excitatory component of SPW-R triggered PSPs. These data suggest that acute stress results in sustained activation of CB1Rs at GABAergic synapses onto Va and Vb neurons, that greatly reduces net inhibition, which in turn promotes the efficiency of hippocampus-driven excitation to the deep layers of EC. Hence, depending on the mechanism, endocannabinoid production CB1-INs can either "allow" preferential information flow from the hippocampus to the most active receiving excitatory neurons in layer V EC or rapidly reduce inhibitory control of the entire population of deep layer pyramidal cells. As a future extension of this study,

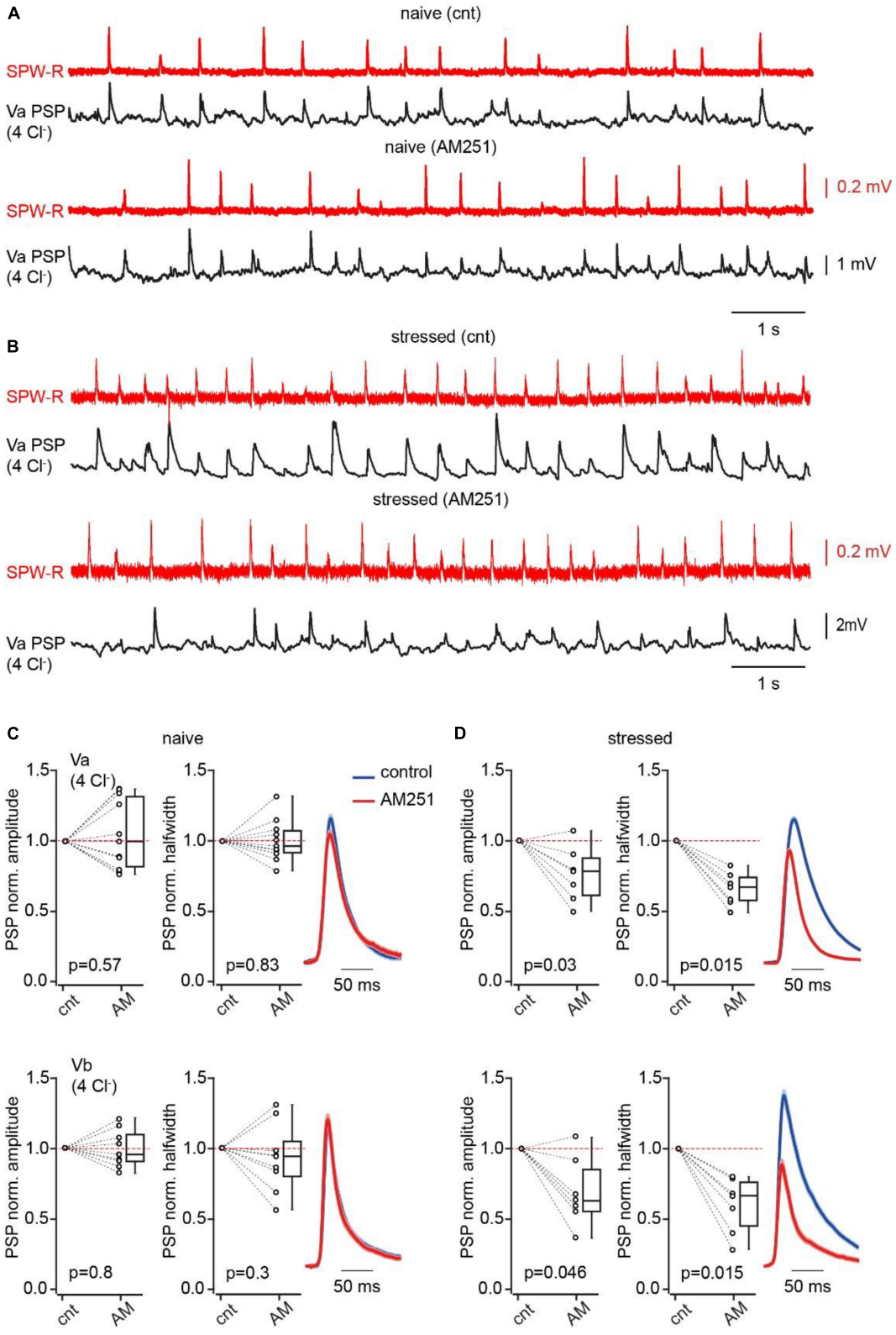

FIGURE 4
Acute stress suppresses CB1IN mediated feed-forward inhibition. **(A)** Spontaneous SPW-Rs (red) in CA1 and associated PSPs (black; Vm −65 mV) in mEC LVa recorded in a slice from a naive animal before and after AM251 application. **(B)** The same as in panel **(A)** recorded in the brain slice of the mouse that was stressed prior to decapitation. **(C)** Plots show normalized (AM251/control) amplitude (left) and halfwidth (right) values in individual cells and pooled data (presented as the median; P25; P75) obtained in Va (upper plots; *n* = 11) and Vb (bottom plots; *n* = 9) pyramidal cells, recorded in brain slices of naïve mice. **(D)** The same as in panel **(A)** recorded in brain slices of stressed mice (Va *n* = 7; Vb *n* = 7). Note that in both types of pyramidal neurons blockade of CB1R results in significant reduction of PSP amplitude and duration in slices obtained from stressed mice. The significance of the differences was assessed by the Wilcoxon signed-rank test, p values are indicated on the plots.

it would be interesting to evaluate the role of CB1-INs and endocannabinoid signaling in controlling the generation and propagation of epileptiform activity.

Thus, this study provides valuable and novel information about: (i) integration of CB1-INs into the local network in layer V of the entorhinal cortex; (ii) the organization of hippocampal inhibitory control over information processing in the entorhinal cortex and (iii) the cellular mechanisms for translating environmental stress to neuronal activity.

Materials and methods

Preparation of mouse brain slices

Horizontal brain slices (450 μm thick) containing the hippocampus and entorhinal cortex were obtained from male C57BL/6N mice or genetically modified reporter mice B6.Cg-Gad1^{TM1Tama} (GAD67-GFP) 10–12 weeks of age using a standard procedure (Roth et al., 2016). All experimental protocols were approved by the State Government of Baden-Württemberg (Projects T100/15 and G188/15) or by the Local Ethical Committee of Kazan Federal University (#24/22.09.2020). Mice were killed under deep CO_2-induced anesthesia. After decapitation, brains were rapidly removed and placed in cold (1–4°C) oxygenated artificial CSF (ACSF) containing the following (in mM): 124 NaCl, 3 KCl, 1.6 $CaCl_2$, 1.8 $MgSO_4$, 10 glucose, 1.25 NaH_2PO_4, and 26 $NaHCO_3$, saturated with carbogen (95% O_2 and 5% CO_2), with pH 7.4 at 34°C. Horizontal brain slices containing the intermediate/ventral portion of the hippocampus and connected areas of the entorhinal cortex were cut using a vibratome slicer (VT1200S, Leica). Section level was between approximately -3.7 and -5 mm along the dorsoventral axis. To better preserve connectivity between the hippocampus and entorhinal cortex, slices were cut with an angle of ∼15° toward the ventral side. Before electrophysiological recordings, slices were allowed to recover for at least 2 h. Slices that were used for the registration of oscillatory activity were transferred into a Haas-type interface chamber (Haas et al., 1979), and superfused with ACSF at a rate of 1.5–2 ml/min at 34 ± 1°C. Otherwise, slices were stored in a submerged incubation chamber at room temperature.

Examining connectivity of ec layer V CB1-INs and their sensitivity to endocannabinoids

Dual whole-cell recordings were performed at 32 ± 1°C. Slices were continuously superfused with an extracellular solution containing the following (in mM): 125 NaCl, 2.5 KCl, 25 glucose, 25 $NaHCO_3$, 1.25 NaH_2PO_4, 2 $CaCl_2$, and 1 $MgCl_2$, bubbled with 95% O_2/5% CO_2. The pipette solution contained the following (in mM): 110 K-gluconate, 30 KCl, 8 NaCl, 10 HEPES, 4 Mg-ATP, 0.3 Na-GTP, and 10 Na_2-phosphocreatine, adjusted to pH 7.3 with KOH. To study synaptic connections, presynaptic cells were stimulated with a 10 Hz train of five suprathreshold current pulses, which were repeated every 10 s. All paired recordings used for connectivity analysis were conducted in CC mode. During recordings, cells were held at resting membrane potential. Averages of 50–100 consecutive sweeps were used for the analysis of postsynaptic responses. Depolarization induced suppression of inhibition at synapses formed by CB1-INs were tested in a separate set of experiments where postsynaptic Va and Vb pyramidal neurons were dialyzed with a Cs^+-based "high Cl^-" internal solution. DSI was induced by depolarization of the postsynaptic cell to 0 mV for 2 s.

The effect of acute stress on the magnitude of endocannabinoid-dependent chronic suppression of inhibition at synapses formed by CB1-INs was assessed by comparing the enhancement of IPSC amplitudes upon application the CB1R antagonist AM251 (2 mM). Postsynaptic cells were recorded with a Cs^+-based "high Cl^-" internal solution and held at −70 mV. The effect of AM251 was measured 15 min after drug application.

Simultaneous recordings of SPW-Rs and postsynaptic responses from LV neurons

After resting in an interface chamber, slices were transferred into a modified double perfusion submerged chamber (Hájos and Mody, 2009) and perfused with ACSF at a rate of 9–10 ml/min at 32 ± 1°C. Extracellular local field potentials (FPs) were recorded from stratum pyramidale of hippocampal area CA1 using ACSF-filled borosilicate glass electrodes with a tip diameter of 3–5 μm. Following this protocol, submerged hippocampal slices showed spontaneously occurring SPW-Rs (Maier et al., 2003), which could be reliably observed for at least 2 h. Extracellular FPs were amplified 100 × with an EXT 10-2F amplifier (npi electronics). Signals were digitized at 10 kHz with an analog-to-digital converter [ADC; MICRO 1401 mkII, Cambridge Electronic Design (CED)] and saved on a computer using PATCHMASTER software (HEKA) for offline analysis. Patch-clamp recordings were performed using two EPC7 amplifiers (HEKA). Layer V neurons (Va and Vb excitatory cells, FS-INs and CB1-INs) were identified by their location in the slice, the appearance of the cell body on the IR-image and characteristic firing pattern.

Whole-cell current-clamp (CC) recordings were performed using borosilicate glass pipettes with resistances of 5–7 MΩ containing depending on experimental needs either "low Cl^-" or "High Cl^-" intracellular solutions. The low Cl^- solution consisted of (in mM): 144 K-gluconate, 4 KCl, 10 HEPES, 4 Mg-ATP, 0.3 Na-GTP, and 10 Na_2-phosphocreatine, adjusted to pH 7.3 with KOH. The high Cl^- solution consisted of (in mM): 110 K-gluconate, 30 KCl, 8 NaCl, 10 HEPES, 4 Mg-ATP, 0.3 Na-GTP, and 10 Na_2-phosphocreatine, adjusted to pH 7.3 with KOH. During recordings, cells were held at resting membrane potential, unless otherwise indicated.

For recordings of postsynaptic currents patch pipettes were filled with a Cs^+-based "low Cl^-"or "High Cl^-" internal solution. In the Cs^+-based internal solutions K^+ was substituted with an equimolar concentration of Cs^+. In Voltage-clamp experiments holding membrane potentials were corrected for the liquid junction potential of approximately -15 mV.

In the experiments studying the effects of depolarization on the inhibitory components of SPW-R-driven postsynaptic currents, the postsynaptic neurons were depolarized to 0 mV for 5 s. The

postsynaptic pyramidal cells in this case were recorded with Cs^+-based internal solutions. To study the effect of postsynaptic high frequency firing on the inhibitory components of SPW-R-driven PSPs, neurons dialyzed with K^+-based internal solutions were injected with 5 s depolarizing current pulses (300–350 pA). The concentration of Cl^- in the intracellular solution was determined by experimental needs and is stated in the main text.

Stress protocol

Animals of the stress group were restrained in well-ventilated 50 ml tubes and left undisturbed a separate room from the other animals for 1 h (Zimprich et al., 2014). After the restraint period the mice were sacrificed, then brains were dissected and sliced as described above.

Data analysis

Raw data were digitally filtered using the RC (resistor–capacitor) filter routine of MATLAB [bandpass: 1–80 Hz for SPW-Rs; 1–500 Hz for postsynaptic potentials (PSPs); and 0.1–500 Hz for postsynaptic currents (PSCs)]. For signal detection, a two-threshold method was applied as follows. First, events exceeding three SDs of the most silent 10-s period of the full-length recording were considered as SPW-Rs, PSPs, or PSCs, respectively. Second, approximate onsets and offsets of the SPW-R events were defined as times when the signal intersected a threshold of 1 SDs of the most silent 10-s period. Exact SPW-R onset was defined as the time when the first derivative of the FP (low-pass filtered at 40 Hz) reached a threshold of 0.02 mV/ms. For PSP detection, approximate onsets and offsets of the signals were defined as the time when the signal intersected a threshold of 1 SD. Exact PSP onset was defined as the time when the first signal derivative (low-pass filtered 500 Hz) reached a threshold of 0.1 mV/ms. For PSCs, approximate onsets and offsets were defined as times when the signal intersected a threshold of 0.5 SDs. Exact PSC onset was defined as the time when the first signal derivative (low-pass filtered at 500 Hz) reached a threshold of 10 pA/ms. The correlation between SPW-Rs and PSPs or PSCs was calculated based on cross-correlograms of onsets. Event amplitudes were estimated as the maximum value between onset and approximate offset with subtraction of baseline level (median value from a 3 ms window before onset). Event half-width was estimated as the duration at the half-amplitude level. Latencies between SPW-Rs in CA1 and PSPs/PSCs in the mEC were defined as the time interval between onset of field-SPW-R and onset of postsynaptic events. PSPs or PSCs in the mEC were considered SPW-R driven if their onset time was < 50 ms following the beginning of an SPW-R event in CA1.

For ripple-associated PSPs, the first derivative of potential was calculated to estimate the contribution from excitatory and inhibitory current components (e-PSP and i-PSP). The corresponding amplitudes were calculated as the maximum and minimum peak values of the first derivative of potential during PSP (**Supplementary Figure 5**).

All data were analyzed offline using PatchMaster (HEKA), SigmaPlot (Systat) and MATLAB R2012 (MathWorks). Values of EPSP/PSP amplitudes of connected pairs were calculated from averaged first synaptic responses in trains of 5.

Statistical analysis

Quantitative data from multiple slices are given as the median (P_{25}; P_{75}). Data in figures are presented as medians (P_{25}; P_{75}) and individual values. Whiskers show minimum and maximum values. Statistical analysis was performed using SigmaPlot (Systat), GraphPad (InStat, GraphPad Software) or Matlab Statistics Toolbox. Mann–Whitney *U test*, Wilcoxon Rank Sum test or Fisher's exact test were used for statistical comparisons as indicated in the text. A p value < 0.05 was regarded as significant (for all data: $^*p < 0.05$, $^{***}p < 0.001$, ns, not significant).

Data availability statement

The raw data supporting the conclusions of this article will be made available by the authors, without undue reservation.

Ethics statement

The animal study was approved by the State Government of Baden-Württemberg (Projects T100/15 and G188/15) and the Local Ethical Committee of Kazan Federal University (#24/22.09.2020). The study was conducted in accordance with the local legislation and institutional requirements.

Author contributions

AN: Investigation, Formal analysis, Writing—review and editing. DJ: Investigation, Writing—original draft, Validation. AV: Investigation, Writing—original draft. FV-R: Investigation, Writing—original draft. AR: Funding acquisition, Investigation, Supervision, Writing—original draft.

Funding

The author(s) declare financial support was received for the research, authorship, and/or publication of this article. This work was supported by RSF grant 22-15-00293 (to AV, FV-R, and AR) and by the "Center of Photonics" funded by the Ministry of Science and Higher Education of the Russian Federation (contract no. 075-15-2022-293) to DJ.

Acknowledgments

We thank Andreas Draguhn and Mark Cunningham for invaluable suggestions, Tina Sackmann and Nadine Zuber for immunocytochemistry support.

Conflict of interest

The authors declare that the research was conducted in the absence of any commercial or financial relationships that could be construed as a potential conflict of interest.

Publisher's note

All claims expressed in this article are solely those of the authors and do not necessarily represent those of their affiliated organizations, or those of the publisher, the editors and the reviewers. Any product that may be evaluated in this article, or claim that may be made by its manufacturer, is not guaranteed or endorsed by the publisher.

Supplementary material

The Supplementary Material for this article can be found online at: https://www.frontiersin.org/articles/10.3389/fncel.2023.1327909/full#supplementary-material

References

Ali, A. B., and Todorova, M. (2010). Asynchronous release of GABA via tonic cannabinoid receptor activation at identified interneuron synapses in rat CA1. *Eur. J. Neurosci.* 31, 1196–1207. doi: 10.1111/j.1460-9568.2010.07165.x

Antoine, M. W., Langberg, T., Schnepel, P., and Feldman, D. E. (2019). Increased excitation-inhibition ratio stabilizes synapse and circuit excitability in four autism mouse models. *Neuron* 101, 648–661.e1. doi: 10.1016/j.neuron.2018.12.026

Armstrong, C., Wang, J., Yeun Lee, S., Broderick, J., Bezaire, M. J., Lee, S. H., et al. (2016). Target-selectivity of parvalbumin-positive interneurons in layer II of medial entorhinal cortex in normal and epileptic animals. *Hippocampus* 26, 779–793. doi: 10.1002/hipo.22559

Atsak, P., Hauer, D., Campolongo, P., Schelling, G., McGaugh, J. L., and Roozendaal, B. (2012). Glucocorticoids interact with the hippocampal endocannabinoid system in impairing retrieval of contextual fear memory. *Proc. Natl. Acad. Sci. U. S. A.* 109, 3504–3509. doi: 10.1073/pnas.1200742109

Balsevich, G., Petrie, G. N., and Hill, M. N. (2017). Endocannabinoids: Effectors of glucocorticoid signaling. *Front. Neuroendocrinol.* 47:86–108. doi: 10.1016/j.yfrne.2017.07.005

Bouchet, C. A., McPherson, K. B., Coutens, B., Janowsky, A., and Ingram, S. L. (2023). Monoacylglycerol lipase protects the presynaptic cannabinoid 1 receptor from desensitization by endocannabinoids after persistent inflammation. *J. Neurosci.* 43, 5458–5467. doi: 10.1523/JNEUROSCI.0037-23.2023

Dubruc, F., Dupret, D., and Caillard, O. (2013). Self-tuning of inhibition by endocannabinoids shapes spike-time precision in CA1 pyramidal neurons. *J. Neurophysiol.* 110, 1930–1944. doi: 10.1152/jn.00099.2013

Freund, T. F., and Buzsáki, G. (1996). Interneurons of the hippocampus. *Hippocampus* 6, 347–470.

Freund, T. F., and Katona, I. (2007). Perisomatic inhibition. *Neuron* 56, 33–42.

Gatley, S. J., Gifford, A. N., Volkow, N. D., Lan, R., and Makriyannis, A. (1996). 123I-labeled AM251: a radioiodinated ligand which binds in vivo to mouse brain cannabinoid CB1 receptors. *Eur. J. Pharmacol.* 307, 331–338. doi: 10.1016/0014-2999(96)00279-8

Glavin, G. B., Paré, W. P., Sandbak, T., Bakke, H. K., and Murison, R. (1994). Restraint stress in biomedical research: an update. *Neurosci. Biobehav. Rev.* 18, 223–249.

Haas, H. L., Schaerer, B., and Vosmansky, M. (1979). A simple perfusion chamber for the study of nervous tissue slices in vitro. *J. Neurosci. Methods* 1, 323–325. doi: 10.1016/0165-0270(79)90021-9

Hájos, N., and Mody, I. (2009). Establishing a physiological environment for visualized in vitro brain slice recordings by increasing oxygen supply and modifying aCSF content. *J. Neurosci. Methods* 183, 107–113. doi: 10.1016/j.jneumeth.2009.06.005

Han, D. H., Park, P., Choi, D. I., Bliss, T. V. P., and Kaang, B. K. (2022). The essence of the engram: Cellular or synaptic? *Semin. Cell Dev. Biol.* 125, 122–135.

Hefft, S., and Jonas, P. (2005). Asynchronous GABA release generates long-lasting inhibition at a hippocampal interneuron-principal neuron synapse. *Nat. Neurosci.* 8, 1319–1328. doi: 10.1038/nn1542

Hill, M. N., and McEwen, B. S. (2010). Involvement of the endocannabinoid system in the neurobehavioural effects of stress and glucocorticoids. *Prog. Neuropsychopharmacol. Biol. Psychiatry* 34, 791–797. doi: 10.1016/j.pnpbp.2009.11.001

Kim, D., Paré, D., and Nair, S. S. (2013). Assignment of model amygdala neurons to the fear memory trace depends on competitive synaptic interactions. *J. Neurosci.* 33, 14354–14358. doi: 10.1523/JNEUROSCI.2430-13.2013

Kitamura, T., Macdonald, C. J., and Tonegawa, S. (2015). Entorhinal-hippocampal neuronal circuits bridge temporally discontiguous events. *Learn. Mem.* 22, 438–443. doi: 10.1101/lm.038687.115

Kondev, V., Najeed, M., Loomba, N., Brown, J., Winder, D. G., Grueter, B. A., et al. (2023a). Synaptic and cellular endocannabinoid signaling mechanisms regulate stress-induced plasticity of nucleus accumbens somatostatin neurons. *Proc. Natl. Acad. Sci. U. S. A.* 120:e2300585120. doi: 10.1073/pnas.2300585120

Kondev, V., Najeed, M., Yasmin, F., Morgan, A., Loomba, N., Johnson, K., et al. (2023b). Endocannabinoid release at ventral hippocampal-amygdala synapses regulates stress-induced behavioral adaptation. *Cell Rep.* 42:113027. doi: 10.1016/j.celrep.2023.113027

Kreitzer, A. C., and Regehr, W. G. (2001). Cerebellar depolarization-induced suppression of inhibition is mediated by endogenous cannabinoids. *J. Neurosci.* 21:Rc174.

Lee, S. H., Földy, C., and Soltesz, I. (2010). Distinct endocannabinoid control of GABA release at perisomatic and dendritic synapses in the hippocampus. *J. Neurosci.* 30, 7993–8000. doi: 10.1523/JNEUROSCI.6238-09.2010

López-Madrona, V. J., and Canals, S. (2021). Functional interactions between entorhinal cortical pathways modulate theta activity in the hippocampus. *Biology* 10:692.

Maier, N., Nimmrich, V., and Draguhn, A. (2003). Cellular and network mechanisms underlying spontaneous sharp wave-ripple complexes in mouse hippocampal slices. *J. Physiol.* 550, 873–887.

Morena, M., Patel, S., Bains, J. S., and Hill, M. N. (2016). Neurobiological interactions between stress and the endocannabinoid system. *Neuropsychopharmacology* 41, 80–102.

Morrison, D. J., Rashid, A. J., Yiu, A. P., Yan, C., Frankland, P. W., and Josselyn, S. A. (2016). Parvalbumin interneurons constrain the size of the lateral amygdala engram. *Neurobiol. Learn. Mem.* 135, 91–99. doi: 10.1016/j.nlm.2016.07.007

Neu, A., Földy, C., and Soltesz, I. (2007). Postsynaptic origin of CB1-dependent tonic inhibition of GABA release at cholecystokinin-positive basket cell to pyramidal cell synapses in the CA1 region of the rat hippocampus. *J. Physiol.* 578, 233–247. doi: 10.1113/jphysiol.2006.115691

Ney, L., Stone, C., Nichols, D., Felmingham, K., Bruno, R., and Matthews, A. (2021). Endocannabinoid reactivity to acute stress: Investigation of the relationship between salivary and plasma levels. *Biol. Psychol.* 159:108022. doi: 10.1016/j.biopsycho.2021.108022

Paré, W. P., and Glavin, G. B. (1986). Restraint stress in biomedical research: a review. *Neurosci. Biobehav. Rev.* 10, 339–370.

Pawelzik, H., Hughes, D. I., and Thomson, A. M. (2002). Physiological and morphological diversity of immunocytochemically defined parvalbumin- and cholecystokinin-positive interneurones in CA1 of the adult rat hippocampus. *J. Comp. Neurol.* 443, 346–367. doi: 10.1002/cne.10118

Roth, F. C., Beyer, K. M., Both, M., Draguhn, A., and Egorov, A. V. (2016). Downstream effects of hippocampal sharp wave ripple oscillations on medial entorhinal cortex layer V neurons in vitro. *Hippocampus* 26, 1493–1508. doi: 10.1002/hipo.22623

Rozov, A., Rannap, M., Lorenz, F., Nasretdinov, A., Draguhn, A., and Egorov, A. V. (2020). Processing of hippocampal network activity in the receiver network of the medial entorhinal cortex layer V. *J. Neurosci.* 40, 8413–8425. doi: 10.1523/JNEUROSCI.0586-20.2020

Santori, A., Morena, M., Hill, M. N., and Campolongo, P. (2020). Hippocampal 2-arachidonoyl glycerol signaling regulates time-of-day- and stress-dependent effects on rat short-term memory. *Int. J. Mol. Sci.* 21:7316. doi: 10.3390/ijms21197316

Stefanelli, T., Bertollini, C., Lüscher, C., Muller, D., and Mendez, P. (2016). Hippocampal somatostatin interneurons control the size of neuronal memory ensembles. *Neuron* 89, 1074–1085. doi: 10.1016/j.neuron.2016.01.024

Sürmeli, G., Marcu, D. C., McClure, C., Garden, D. L. F., Pastoll, H., and Nolan, M. F. (2015). Molecularly defined circuitry reveals input-output segregation in deep layers of the medial entorhinal cortex. *Neuron* 88, 1040–1053.

Varga, C., Lee, S. Y., and Soltesz, I. (2010). Target-selective GABAergic control of entorhinal cortex output. *Nat. Neurosci.* 13, 822–824. doi: 10.1038/nn.2570

Vecchiarelli, H. A., Morena, M., Lee, T. T. Y., Nastase, A. S., Aukema, R. J., Leitl, K. D., et al. (2022). Sex and stressor modality influence acute stress-induced dynamic changes in corticolimbic endocannabinoid levels in adult Sprague Dawley rats. *Neurobiol. Stress* 20:100470. doi: 10.1016/j.ynstr.2022.100470

Vered, S., Beiser, A. S., Sulimani, L., Sznitman, S., Gonzales, M. M., Aparicio, H. J., et al. (2023). The association of circulating endocannabinoids with neuroimaging and blood biomarkers of neuro-injury. *Alzheimers Res. Ther.* 15:154. doi: 10.1186/s13195-023-01301-x

Wilson, R. I., Kunos, G., and Nicoll, R. A. (2001). Presynaptic specificity of endocannabinoid signaling in the hippocampus. *Neuron* 31, 453–462.

Witter, M. P., Doan, T. P., Jacobsen, B., Nilssen, E. S., and Ohara, S. (2017). Architecture of the entorhinal cortex a review of entorhinal anatomy in rodents with some comparative notes. *Front. Syst. Neurosci.* 11:46. doi: 10.3389/fnsys.2017.00046

Yap, E. L., Pettit, N. L., Davis, C. P., Nagy, M. A., Harmin, D. A., Golden, E., et al. (2021). Bidirectional perisomatic inhibitory plasticity of a Fos neuronal network. *Nature* 590, 115–121. doi: 10.1038/s41586-020-3031-0

Zhang, S. J., Ye, J., Couey, J. J., Witter, M., Moser, E. I., and Moser, M. B. (2014). Functional connectivity of the entorhinal-hippocampal space circuit. *Philos. Trans. R Soc. Lond. B Biol. Sci.* 369:20120516.

Zhang, S. J., Ye, J., Miao, C., Tsao, A., Cerniauskas, I., Ledergerber, D., et al. (2013). Optogenetic dissection of entorhinal-hippocampal functional connectivity. *Science* 340:1232627. doi: 10.1126/science.1232627

Zimprich, A., Garrett, L., Deussing, J. M., Wotjak, C. T., Fuchs, H., Gailus-Durner, V., et al. (2014). A robust and reliable non-invasive test for stress responsivity in mice. *Front. Behav. Neurosci.* 8:125. doi: 10.3389/fnbeh.2014.00125

frontiers | Frontiers in Cellular Neuroscience

TYPE Original Research
PUBLISHED 08 January 2024
DOI 10.3389/fncel.2023.1274459

OPEN ACCESS

EDITED BY
Anirban Paul,
The Pennsylvania State University, United States

REVIEWED BY
Benjamin Gunn,
University of California, United States
Isabella Ferando,
University of Miami, United States

*CORRESPONDENCE
Koichi Ogawa
✉ kouichi.ogawa@shionogi.co.jp

RECEIVED 08 August 2023
ACCEPTED 29 November 2023
PUBLISHED 08 January 2024

CITATION
Takasu K, Yawata Y, Tashima R, Aritomi H, Shimada S, Onodera T, Taishi T and Ogawa K (2024) Distinct mechanisms of allopregnanolone and diazepam underlie neuronal oscillations and differential antidepressant effect.
Front. Cell. Neurosci. 17:1274459.
doi: 10.3389/fncel.2023.1274459

Distinct mechanisms of allopregnanolone and diazepam underlie neuronal oscillations and differential antidepressant effect

Keiko Takasu[1], Yosuke Yawata[1], Ryoichi Tashima[1], Hiroyuki Aritomi[2], Shinji Shimada[2], Tsukasa Onodera[1], Teruhiko Taishi[1] and Koichi Ogawa[1]*

[1]Laboratory for Drug Discovery and Disease Research, Shionogi Pharmaceutical Research Center, Shionogi & Co., Ltd., Osaka, Japan, [2]Shionogi TechnoAdvance Research, Osaka, Japan

The rapid relief of depressive symptoms is a major medical requirement for effective treatments for major depressive disorder (MDD). A decrease in neuroactive steroids contributes to the pathophysiological mechanisms associated with the neurological symptoms of MDD. Zuranolone (SAGE-217), a neuroactive steroid that acts as a positive allosteric modulator of synaptic and extrasynaptic δ-subunit-containing $GABA_A$ receptors, has shown rapid-onset, clinically effective antidepressant action in patients with MDD or postpartum depression (PPD). Benzodiazepines, on the other hand, act as positive allosteric modulators of synaptic $GABA_A$ receptors but are not approved for the treatment of patients with MDD. It remains unclear how differences in molecular mechanisms contribute to the alleviation of depressive symptoms and the regulation of associated neuronal activity. Focusing on the antidepressant-like effects and neuronal activity of the basolateral amygdala (BLA) and medial prefrontal cortex (mPFC), we conducted a head-to-head comparison study of the neuroactive steroid allopregnanolone and the benzodiazepine diazepam using a mouse social defeat stress (SDS) model. Allopregnanolone but not diazepam exhibited antidepressant-like effects in a social interaction test in SDS mice. This antidepressant-like effect of allopregnanolone was abolished in extrasynaptic $GABA_A$ receptor δ-subunit knockout mice (δKO mice) subjected to the same SDS protocol. Regarding the neurophysiological mechanism associated with these antidepressant-like effects, allopregnanolone but not diazepam increased theta oscillation in the BLA of SDS mice. This increase did not occur in δKO mice. Consistent with this, allopregnanolone potentiated tonic inhibition in BLA interneurons via δ-subunit-containing extrasynaptic $GABA_A$ receptors. Theta oscillation in the mPFC of SDS mice was also increased by allopregnanolone but not by diazepam. Finally, allopregnanolone but not diazepam increased frontal theta activity in electroencephalography recordings in naïve and SDS mice. Neuronal network alterations associated with MDD showed decreased frontal theta and beta activity in depressed SDS mice. These results demonstrated that, unlike benzodiazepines, neuroactive steroids increased theta oscillation in the BLA and mPFC through the activation of δ-subunit-containing $GABA_A$ receptors, and this change was associated with antidepressant-like effects in the SDS model. Our findings

support the notion that the distinctive mechanism of neuroactive steroids may contribute to the rapid antidepressant effects in MDD.

KEYWORDS

neuroactive steroid, benzodiazepine, extrasynaptic $GABA_A$ receptor, social defeat stress model, antidepressant-like effect, theta activity, basolateral amygdala

Introduction

Major depressive disorder (MDD) is a psychiatric disorder characterized by an episode of core depressive symptoms lasting at least 2 weeks, including pervasive low mood or loss of interest or pleasure in normally enjoyable activities (American Psychiatric Association, 2013). Approved drugs for MDD take at least 4–8 weeks to show efficacy (Rush et al., 2006). A delayed onset of response has been associated with decreased treatment adherence, leading to incomplete remission and relapse (Habert et al., 2016). Rapid relief of depressive symptoms through effective treatment is therefore an important medical requirement for improving the quality of life of patients with MDD.

Brexanolone (allopregnanolone) and zuranolone (SAGE-217) are neuroactive steroids that are used clinically as fast-acting antidepressant agents; these compounds act on synaptic and extrasynaptic $GABA_A$ receptors (Edinoff et al., 2021; Ali et al., 2023; Kato et al., 2023). Previous studies have reported decreased plasma or brain concentrations of the endogenous neuroactive steroid allopregnanolone in patients with MDD, which correlates with the severity of depressive symptoms (Uzunova et al., 1998; Agis-Balboa et al., 2014). Increased plasma concentrations of allopregnanolone with antidepressant treatment are associated with the relief of depressive symptoms (Romeo et al., 1998). Therefore, the potentiation of $GABA_A$ receptors by increasing neuroactive steroids may contribute to fast-acting antidepressant effects in patients with MDD. In contrast, benzodiazepines also act as positive allosteric modulators of the $GABA_A$ receptor but are not approved for the treatment of patients with MDD (Lim et al., 2020). The differences in efficacies in patients with MDD may be caused by distinct molecular mechanisms. There are two subtypes of $GABA_A$ receptors, namely, synaptic and extrasynaptic $GABA_A$ receptors. Most δ-subunit-containing $GABA_A$ receptors seem to be purely extrasynaptic, although there are various subunit compositions (Brickley and Mody, 2012). In addition to the difference of the subunits, neuroactive steroids specifically enhance a tonic inhibitory conductance that is mediated by δ-subunit-containing $GABA_A$ receptors at lower concentrations, and then they also start to potentiate phasic inhibition at higher concentrations (Stell et al., 2003; Belelli and Lambert, 2005; Farrant and Nusser, 2005; Brickley and Mody, 2012; Martinez et al., 2017). It has also been reported that neuroactive steroids potentiate both synaptic and extrasynaptic (δ-subunit-containing) $GABA_A$ receptors by binding to α and β subunits, which are common to both types of receptors (Sigel, 2002; Hosie et al., 2006; Carver and Reddy, 2013; Nuss, 2015; Alvarez and Pecci, 2018). In contrast, benzodiazepines primarily activate synaptic $GABA_A$ receptors by binding to α and γ subunits (Carver and Reddy, 2013; Nuss, 2015). Therefore, based on differences in the binding and activation mode, δ-subunit-containing $GABA_A$ receptors could largely contribute to differences in efficacies in patients with MDD. However, it remains unclear how differences in molecular mechanisms contribute to alleviating depressive symptoms and modulating neuronal network activity.

The dysregulation of neural network activity in brain regions is associated with depressive symptoms in patients with MDD (Drevets, 2000; Phillips et al., 2003; Northoff et al., 2011). The amygdala is one of the regions with high concentrations of neuroactive steroids involved in the pathology of MDD (Bixo et al., 2018). Altered neuronal activity between the amygdala and its regulated brain regions, including the prefrontal cortex, in MDD patients has been implicated in stress vulnerability and negative emotions (Drevets, 2000; Phillips et al., 2003). Neuroactive steroids regulate emotional cognition by altering the functional connectivity of the amygdala and frontal cortex (Sripada et al., 2014). Recent preclinical studies have demonstrated that increased basolateral amygdala (BLA) theta activity via potentiation of δ-subunit-containing $GABA_A$ receptors on interneurons can contribute to the antidepressant effects of neuroactive steroids in chronic unpredictable stress model mice (Antonoudiou et al., 2022; Luscher et al., 2023; Walton et al., 2023). The benzodiazepine diazepam also acts on the amygdala but does not increase theta activity in naïve mice (Antonoudiou et al., 2022). BLA theta activity is therefore thought to be related to differential antidepressant effects between neuroactive steroids and benzodiazepines. However, there have been no reports of direct comparisons between neuroactive steroids and benzodiazepines under identical conditions using a preclinical model of depression.

In the present study, we used the social interaction test (SIT) in a mouse social defeat stress (SDS) model and collected *in vivo* recordings of oscillation in the BLA and medial prefrontal cortex (mPFC) to assess differences in the effect of allopregnanolone, a neuroactive steroid, and diazepam, a benzodiazepine drug, by direct comparison. Allopregnanolone, but not diazepam, potentiates δ-subunit-containing $GABA_A$ receptors in BLA interneurons and increases theta oscillation in the BLA and mPFC. This mechanism may contribute to the development of antidepressant-like effects in depressed SDS mice.

Materials and methods

Animals

Experiments were performed using C57BL/6 J Jcl mice, $GABA_A$ receptor δ-subunit knockout mice (δKO mice, $Gabrd^{-/-}$ mice), and Crl:CD1 (ICR) retired mice. ICR mice (male) and $Gabrd^{-/-}$ mice (male) were purchased from Jackson Laboratory. $Gabrd^{-/-}$ mice are homozygous null for Gabrd (Mihalek et al., 1999). The breeding of

Gabrd$^{-/-}$ mice was approved by the Animal Care and Use Committee of Shionogi Research Laboratories and was in accordance with the Association for Assessment and Accreditation of Laboratory Animal Care (AAALAC) International guidelines. C57BL/6 J Jcl mice (male) were purchased from CLEA Japan Inc. and were used as wild-type controls. The body weights of C57BL/6 J Jcl mice were 20–30 g. Mice aged 2–4 months were used. The mice were housed under controlled temperature and humidity with a 12/12-h light/dark cycle (light from 8:00 to 20:00). Less than three mice were housed in a cage (W 235 mm, D 353 mm, H 160 mm) with a paper-chip bedding (SLC Japan, Inc.) and Nesting Sheets™ (Bio-Serv, United States) as environmental enrichment. Mice were allowed *ad libitum* access to food (CE-2, CLEA Japan, Inc.) and clean water (filtered at 5 mm from Toyonaka City, Japan) under SPF conditions. All procedures were approved by the Animal Care and Use Committee of Shionogi Research Laboratories, Osaka, Japan. Electrophysiological assessments were performed according to the AAALAC International guidelines.

Drugs

Allopregnanolone was purchased from Toronto Research Chemicals (Canada). Diazepam and methyl cellulose were purchased from Fujifilm (Japan). Escitalopram was purchased from MedChemExpress (United States). Hydroxypropyl-β-cyclodextrin was purchased from Tokyo Chemical Industry (Japan). Allopregnanolone and diazepam were dissolved in 15% hydroxypropyl-β-cyclodextrin in distilled water. Escitalopram was dissolved in methyl cellulose. Allopregnanolone and diazepam were administered intraperitoneally. Escitalopram was administered by oral gavage.

Preparation of the SDS model

A C57BL/6 J Jcl mouse was defeated by a larger stranger ICR mouse. Each individual defeat lasted 10 min. If the mice developed severe injuries or extreme weakness during the 10-day defeat procedure, they were euthanized at the veterinarian's discretion (Figure 1A). After the 10-day defeat procedure, SIT was conducted to select the mice with depression-like behavior with a series of 3 sequential tests: (1) Each C57BL/6 J Jcl mouse was placed in an open-field chamber (40 × 30 × 20 cm) with an empty wire mesh box at one end, and the mouse was allowed to freely explore the chamber for 150 s while being recorded on video. This session was defined as test 1. (2) After that day, the C57BL/6 J Jcl mouse was placed in an open-field chamber where a novel male ICR mouse was enclosed in a wire mesh box at one end, and the mouse was allowed to freely explore the chamber for 150 s while being recorded on video. This session was defined as test 2. (3) After that day, the same test (test 2) was conducted. This session was defined as test 3. In each test, the time that each mouse spent in the interaction zone (around the wire mesh box with or without the ICR mouse) was calculated by tracking the mass of the mouse with the EthoVision XT video-tracking system (Noldus Information Technology, Wageningen, The Netherlands). The times in tests 1, 2, and 3 were defined as direct SIT time 1 (dSIT1), direct SIT time 2 (dSIT2), and direct SIT time 3 (dSIT3), respectively. A mouse whose dSIT2 and dSIT3 were both lower than dSIT1 was regarded as a depression-like mouse. Depression-like mice were used for further studies, including the SIT, the tail suspension test (TST), a patch-clamp assay in BLA slices, and *in vivo* electrophysiological studies with local field potential (LFP) and electroencephalogram (EEG) recordings.

Social interaction test

In depression-like mice, the SIT was conducted to evaluate the efficacy of the test substance. Each depression-like C57BL/6 J Jcl mouse was placed in an open-field chamber where a novel male ICR mouse was enclosed in a wire mesh box at one end, and the mouse was allowed to freely explore the chamber for 150 s while being recorded on video. The time that each mouse spent in the direct interaction zone (close to the wire mesh box with the ICR mouse) was calculated by tracking the center of mass of the mouse with an EthoVision XT video-tracking system (Figure 1A). A different ICR mouse was used for each trial to reduce the influence of habituation on social behavior. Allopregnanolone, diazepam, or vehicle was intraperitoneally administered once daily for 7 days. The day when dSIT3 was measured was defined as "pre." The day of the initial injection was defined as Day 1. In the direct comparison study between allopregnanolone and diazepam, SIT at days 1, 3, and 7 was conducted approximately 30 min after the injection of the drug. The data represent the time that each mouse spent in the direct interaction zone. Analysis was conducted using Tukey's test for multiple groups and using Sidak's test for two groups. A value of $p < 0.05$ was considered statistically significant.

Tail suspension test

In mice with depression-like behavior, the TST was conducted to evaluate the efficacy of the test substance. Each depression-like C57BL/6 J Jcl mouse was suspended in a chamber for 10 min. The time that each mouse spent immobile was calculated by tracking the center of mass of the mouse with an EthoVision XT video-tracking system. In the depression-like mice after SIT for 7 days and the following washout periods for 5–10 days, a tail suspension test was conducted. Allopregnanolone, diazepam, or vehicle was intraperitoneally administered approximately 30 min prior to the test. The data represent the immobility time for each mouse over 8 min. Analysis was conducted using Dunnett's test. A value of $p < 0.05$ was considered statistically significant.

Open field test for the assessment of locomotor activity

To identify non-sedative doses of allopregnanolone and diazepam, locomotor activity was assessed in naïve mice. Immediately after the injection of allopregnanolone or diazepam, the C57BL/6 J Jcl mouse was placed in an open-field chamber (40 × 30 × 20 cm), and the mouse was allowed to freely explore the chamber for 40 min while being recorded on video. The distance that each mouse traveled in the chamber was calculated by tracking the mass of the mouse with an EthoVision XT video-tracking system. The data represent the distance that each mouse moved in the chamber for 40 min. Analysis was conducted using Dunnett's test. A p-value of <0.05 was considered statistically significant.

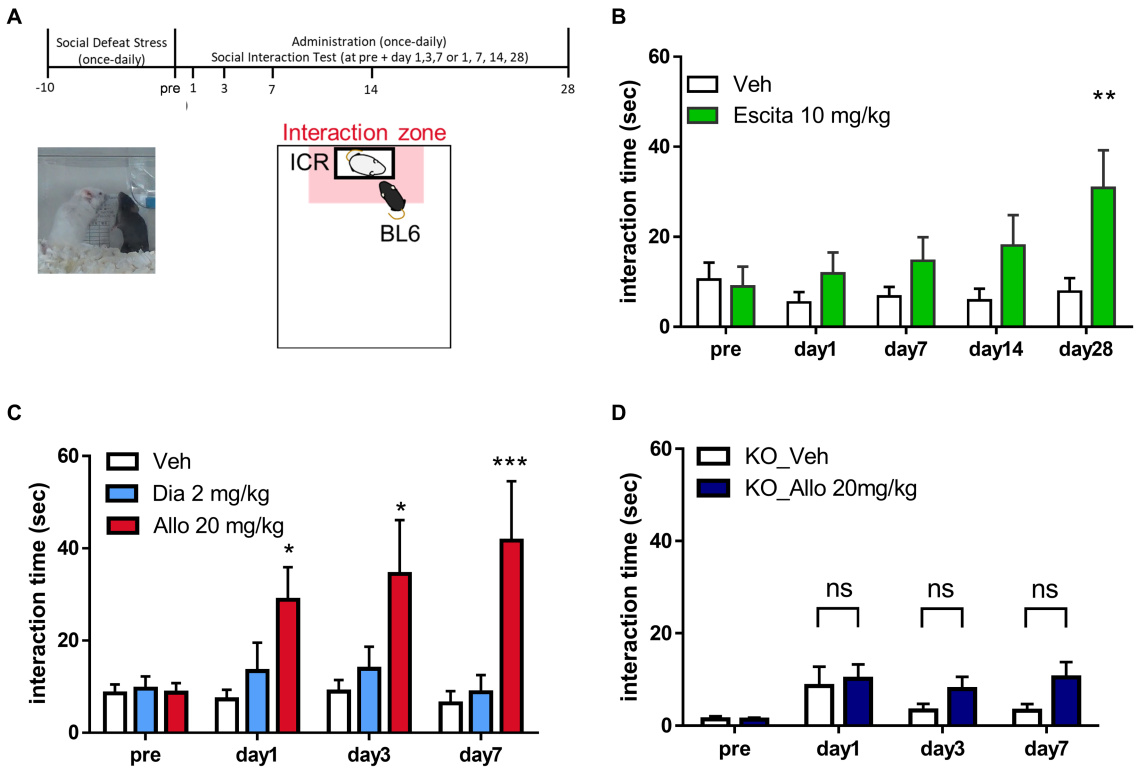

FIGURE 1
Antidepressant-like effects of allopregnanolone, in contrast to diazepam. **(A)** Behavioral paradigm of antidepressant assessment in the social interaction test (SIT) of the social defeat stress (SDS) model. A C57BL/6 J Jcl mouse was defeated by a larger ICR mouse for 10 days. SIT was conducted for the purpose of identifying depression-like mice and assessing antidepressant effects following drug administration. Data are expressed as the interaction time that each mouse spent in the direct interaction zone (close to the box with the ICR mouse, depicted in the pale red zone). **(B)** Time course of the interaction time before and after the administration of vehicle (Veh, white column) and a selective serotonin reuptake inhibitor escitalopram (Escita, green column) in wild-type mice with the SDS model. Data are represented as the mean ± SEM. *$p = 0.003$, $n = 9$–10 mice, Sidak's test. **(C)** Time course of the interaction time before and after administration of the vehicle (Veh, white column), the benzodiazepine diazepam (Dia, blue column), and the neuroactive steroid allopregnanolone (Allo, red column) in wild-type mice with the SDS model. Data are represented as the mean ± SEM. *$p = 0.038$ at day 1, *$p = 0.011$ at day 3, ***$p = 0.0003$ at day 7, $n = 13$ mice, Tukey's test. **(D)** Time course of the interaction time before and after the administration of Veh (white column) and Allo (dark blue column) in $GABA_A$ receptor δ-subunit knockout mice (δKO mice) with the SDS model. Data are represented as the mean ± SEM. $p = 0.985$ at day 1, $p = 0.573$ at day 3, $p = 0.163$ at day 7, $n = 20$ mice, Sidak's test.

Open field test for the assessment of the anxiolytic effects of diazepam

To evaluate the anxiolytic effects of diazepam, an open-field device (SCANET MV-40, MELQUEST, Japan) was used. Each mouse was placed in the device 30 min after the injection of diazepam. The time that each mouse stayed in a 30 cm square area in the center area of the device (45× 45×12 cm) and the movement in the chamber were measured by the number of squares crossed with the four paws for 10 min. The data represent the total time that each mouse stayed in the center area of the chamber for 10 min. Analysis was conducted using Dunnett's test. A p-value of <0.05 was considered statistically significant.

Patch clamp assay in BLA slices

Preparation of BLA Slices

The mice were euthanized by cervical dislocation. The brains were then quickly removed and placed in ice-cold, low-sodium artificial CSF (cerebrospinal fluid) containing 100 mM choline-Cl, 13 mM NaCl, 3 mM KCl, 1 mM NaH_2PO_4, 25 mM $NaHCO_3$, 11 mM D-glucose, 1 mM $CaCl_2$, and 5 mM $MgCl_2$ (pH 7.4 after bubbling with 95% O_2 and 5% CO_2). Coronal slices (300 µm thick) were prepared using a vibratome (VT1200S, Leica, Germany) and then maintained for at least 60 min in standard artificial CSF containing 113 mM NaCl, 3 mM KCl, 1 mM NaH_2PO_4, 25 mM $NaHCO_3$, 11 mM d-glucose, 2 mM $CaCl_2$, and 1 mM $MgCl_2$ (pH 7.4, after bubbling with 95% O_2 and 5% CO_2 at 30–32°C). Slices were transferred to a recording chamber mounted on the stage of a microscope (BX51WI, Olympus, Japan) and superfused with standard artificial CSF (flow rate of 2.5 mL min^{-1} at 30–32°C).

Patch-clamp recording

Whole-cell voltage-clamp recordings were made from visually identified interneurons in the BLA area using an upright microscope with infrared differential interference contrast optics. The recorded neurons exhibited sustained fast spiking activity following the current injection (Figure 2A), consistent with a previous study (Park et al., 2007; Perumal and Sah, 2022). Patch electrodes (2.5–3.0 µm tip diameter) were pulled from borosilicate glass capillaries and had a resistance of 3–5 MΩ when filled with an internal solution consisting of 135 mM KCl, 10 mM HEPES, 1.1 mM EGTA, 2 mM $MgCl_2$,

3 mM Mg-ATP, and 0.3 mM Li–GTP, pH 7.3, adjusted with KOH. Membrane voltage was recorded with a patch clamp system (EPC-10, HEKA, Darmstadt, Germany) and PowerLab (ADInstruments, Dunedin, New Zealand), low-pass filtered at 4 kHz, and digitized at 40 kHz for computer analysis using Pulse software (HEKA) and LabChart software (ADInstruments). All experiments were performed at 30–32°C. To block excitatory postsynaptic currents, 10 μM CNQX and 50 μM D-AP5 were added to standard artificial CSF. To unmask the contribution of tonic current, 10 μM bicuculline was perfused at the end of each recording.

Data analysis

The magnitude of the tonic current was calculated as previously described (Antonoudiou et al., 2022). The mean current was measured

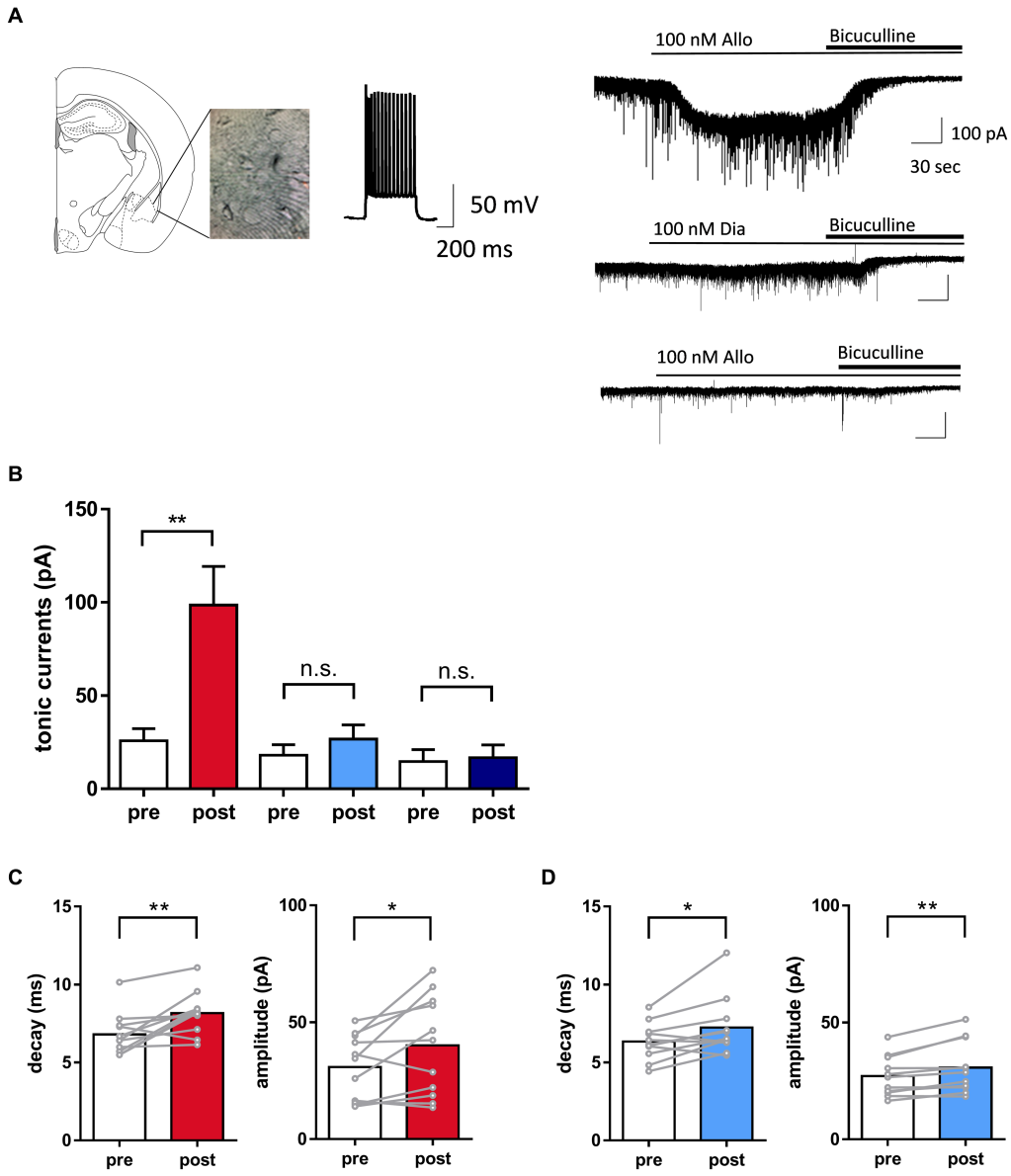

FIGURE 2
Distinct potentiation of tonic currents by allopregnanolone in basolateral amygdala (BLA) interneurons, in contrast to diazepam. **(A)** Left panel. A representative image illustrating the mouse BLA slice and the recording interneuron with fast-spiking activity. Right panel. Representative traces indicated that allopregnanolone (Allo, 100 nM) potentiated tonic currents, as shown by inward currents (upper trace), while diazepam (Dia, 100 nM) had no effect on the BLA interneuron in wild-type mice with the SDS model (middle trace). In the $GABA_A$ receptor δ-subunit knockout mouse (δKO mouse) with the SDS model, allopregnanolone (Allo, 100 nM) did not potentiate tonic currents in the BLA interneuron (bottom trace). Application of bicuculine (10 μM) abolished inhibitory postsynaptic currents. **(B)** Allo (depicted in red) significantly potentiated tonic currents. *$p = 0.0028$, $n = 11$ slices from wild-type mice with the SDS model, paired t-test. Dia (depicted in blue) did not significantly increase tonic currents. $n = 11$ slices from wild-type mice with the SDS model. Allo (depicted in dark blue) had no effect on tonic currents. $n = 6$ slices from δKO mice with the SDS model. **(C)** Left panel. Summary of the significant increase in the decay of inhibitory postsynaptic currents (IPSCs) by allopregnanolone (100 nM) in BLA interneurons from wild-type mice with the SDS model. **$p = 0.0067$, $n = 11$, unpaired t-test. Right panel. Summary of the significant increase of the amplitude of IPSCs by allopregnanolone (100 nM) in BLA interneurons from wild-type mice with the SDS model. **$p = 0.0347$, $n = 11$, unpaired t-test. **(D)** The same as **(C)**, but for diazepam (100 nM). *$p = 0.0251$ for the decay, *$p = 0.0044$ for the amplitude, $n = 11$, unpaired t-test.

during 10 ms epochs collected every 100 ms throughout the recording. A histogram of the holding currents (30 s before the application of bicuculline) and in the presence of bicuculline (30 s after bicuculline blockade) were fit with a Gaussian, and the difference in the mean of the fitted curve was defined as posttonic currents. Pretonic currents were measured by calculating the bicuculline-induced shift in holding currents from baseline (prior to the application of allopregnanolone or diazepam). Regarding the analysis of spontaneous inhibitory postsynaptic currents (sIPSCs), the data of amplitude, frequency, and decay were analyzed using easy electrophysiology (Easy Electrophysiology Ltd., London, United Kingdom). The amplitude, frequency, and decay of sIPSCs for 30 s during pre- and post-treatment of allopregnanolone and diazepam were calculated by averaging the values of individual sIPSCs, which were detected based on criteria. Decay was measured as τ by fitting individual sIPSCs with exponential functions. Data are expressed as pre- and post-treatment parameters. Statistical analysis was conducted using a paired *t*-test for pre- and post-treatment comparisons. For statistical analysis for comparisons between naïve mice and SDS models, an unpaired *t*-test was performed using pre-treatment parameters for each group. Cells were excluded from the analysis if series resistance or whole-cell capacitance changed >30% during the course of the recording.

In vivo electrophysiological assessment

Surgery

Surgery was performed to implant electrodes for recording LFPs, EEGs, and electromyography (EMG) signals from mice. The detailed surgical procedures have been previously described in Okada et al., 2017; Sasaki et al., 2017; Shikano et al., 2018, and Yawata et al., 2023. Briefly, LFP electrode devices consisting of a core body and a custom-made electrical interface board accommodating 6–12 LFP channels, 2 EMG channels, and 1 ground/reference channel were assembled for LFP recordings before surgery. For the surgery, mice were anesthetized with 1–2.5% isoflurane gas. After anesthesia, a midline incision was made from the area between the eyes to the incised neck area, and two stainless-steel EMG electrodes with a tip diameter of 147 µm (AS633; Cooner Wire Company) in which the PTFE coating at the tip (~5.0 mm) was peeled off were sutured to the dorsal neck muscles. Circular craniotomies with a diameter of ~1 mm were made using a high-speed drill above the mPFC (1.9 mm anterior and 0.2 mm right to the bregma), BLA (1.6 mm posterior and 3.0 mm right to the bregma), and cerebellum (5.8 mm posterior ±1.0 mm lateral to the bregma) for the ground/reference. The dura was surgically removed. The tips of the BLA electrodes were inserted 3.85 mm from the brain surface. Stainless-steel screws were implanted on the surface of the cerebellum (5.8 mm posterior and 1.0 mm right/left to the bregma) as ground/reference electrodes. All the wires and the electrode assembly were secured to the skull using dental cement.

Socket pins (ME-3-1, MAC8 Co., Ltd.) were used for the EEG electrodes. An EMG electrode to use in conjunction with EEG recordings was created by soldering the socket pin to a wire (0.26ETFE2X7, Junkosya, Ibaraki, Japan). Electrode implantation surgery was similar to EEG and LFP recording. However, electrodes implanted above the frontal cortex (1.5 mm anterior and ± 0.2 mm lateral to the bregma), parietal cortex (2.0 mm posterior and ± 2.5 mm lateral to the bregma), and cerebellum (5.8 mm posterior ±1.0 mm lateral to the bregma) were used for the ground/reference.

In vivo electrophysiological recording

Approximately 1 week after surgery, each mouse was connected to recording equipment to record *in vivo* LFP and EEG signals. Recordings were conducted within a copper-shielded room to remove 60-Hz hum noise. LFPs were sampled at 2 kHz using Cerebus (Blackrock Microsystems, Salt Lake City, Utah, United States), and EEG data were sampled at 400 Hz using the PowerLab system (ADInstruments, Dunedin, New Zealand). The LFP data were filtered between 0.1 and 500 Hz. Home-cage recordings were conducted for 60 min. After a baseline recording for 30 min, the mice were administered vehicle, diazepam (2 mg/kg), or allopregnanolone (20 mg/kg) intraperitoneally, and recording continued for an additional 30 min.

Histology

After all recordings and behavioral tests, mice implanted with LFP electrodes were euthanized with an overdose of isoflurane and perfused intracardially with PBS, followed by 4% paraformaldehyde in PBS. Brains were removed, postfixed overnight in 4% paraformaldehyde, and equilibrated in 30% sucrose in PBS overnight. Frozen coronal sections (50 µm) were cut using a cryostat (NX50, PHC Corporation) and mounted with a DAPI-containing mounting medium (VECTASHIELD Vibrance Antifade Mounting Medium, Funakoshi). Fluorescence images were captured using an all-in-one microscope (BZ-X710; Keyence, Osaka, Japan). LFP recordings were excluded from the data analysis unless the electrode was in the mPFC and BLA.

Data analysis

To analyze LFP and EEG signals within the physiological range, periods in which the LFPs for 1-s bins exceeded 2 mV were excluded from the analysis. In home-cage recordings, we included data from mice with excluded time periods comprising less than 10% of the total. Moreover, to identify periods containing noise from mouse movement, EMG was used as previously described (Konno et al., 2022). Briefly, a high-pass filter with a cutoff frequency of 100 Hz was applied to the EMG signal, and the root mean square was calculated for 1-s bins (rmsEMG). The mean plus one standard deviation of rmsEMG was used as a threshold, and periods in which the rmsEMG exceeded the threshold were excluded from the analysis. The missing values during the excluded periods were filled using linear interpolation. The Fourier transform was applied to LFP and EEG signals, and the intensity of each frequency was calculated for every 1-s bin. The definitions of each frequency band were based on previous studies (Antonoudiou et al., 2022) and set as follows: theta wave (6–12 Hz) and beta wave (15–30 Hz). LFP and EEG power were computed using the NeuroExplorer (Plexon Inc., Dallas, Texas, United States) and the LabChart Reader (ADInstruments), respectively. The power values were normalized for each time point across the total power. The average power from 0 to 15 min before drug administration was defined as the preadministration period, and the average power from 15 to 30 min after administration was defined as the postadministration period. Differences between groups were analyzed for statistical significance with the paired *t*-test for two groups in LFP recordings from wild-type mice with the SDS model.

Regarding LFP recordings from Gabrd$^{-/-}$ mice with the SDS model and EEG recordings from naïve mice and SDS mice, unpaired *t*-tests were used for two groups. In the EEG analysis with naïve mice and SDS mice, Tukey's test was used for multiple groups. A *p*-value of <0.05 was taken to indicate statistical significance. All data are expressed as the means ± SEMs.

Results

Rapid onset of the antidepressant-like effects of allopregnanolone, in contrast to diazepam

To investigate the differences in effects on depression-like behavior, we conducted a direct comparison study with the neuroactive steroid allopregnanolone and the benzodiazepine diazepam by using SIT in SDS model mice. This model features a variety of symptoms and pathologies of MDD and allows testing of the antidepressant-like effects of drugs (Petković and Chaudhury, 2022). Consistently, mice showed robust decreased social behavior time as a depressive symptom due to stress exposure compared to non-stress mice or before stress (Supplementary Figure 1). To conduct direct comparison studies, we utilized frontal beta oscillation with EEGs, a marker of $GABA_A$ receptor potentiation. The dose of diazepam at 2 mg/kg (i.p.) employed in this study was established based on a notable enhancement in frontal beta activity (Supplementary Figure 2) and the manifestation of the anxiolytic-like effects (Supplementary Figure 4) at a non-sedative dosage (Supplementary Figures 3, 4). These results indicate $GABA_A$ receptor potentiation subsequent to brain exposure (Friedman et al., 1992; Bhatt et al., 2013; Shahnouri et al., 2016; Antonoudiou et al., 2022). Similarly, the dose of allopregnanolone at 20 mg/kg (i.p.) in this study was non-sedating (Supplementary Figure 3) and determined by the observed increase in beta activity (Supplementary Figure 2). This setting dose of each drug is based on previous reports (Brot et al., 1997; Doukkali et al., 2016; Shahnouri et al., 2016; Holmberg et al., 2018; Dornellas et al., 2020; Antonoudiou et al., 2022; Choudhary et al., 2022). Before a direct comparison study between these agents, we first investigated whether the SIT was suitable for evaluating antidepressant-like effects by administering escitalopram, a selective serotonin reuptake inhibitor (SSRI) antidepressant, to mice to examine whether it improved their social interaction. Based on a previous study (Burstein et al., 2017), escitalopram at a dose of 10 mg/kg (p.o.) for 4 weeks increased social interaction, confirming that the SIT can be used to evaluate the antidepressant-like effects of SDS model mice (Figure 1B). This result also demonstrated the delayed onset of the antidepressant-like effects of escitalopram. With this behavioral test, we assessed the antidepressant-like effects of allopregnanolone and diazepam. Allopregnanolone at a dose of 20 mg/kg (i.p.) induced a rapid onset of antidepressant-like effects in the SIT of SDS mice (Figure 1C). In contrast, diazepam at a dose of 2 mg/kg (i.p.) had no effect at each time point from day 1 to day 7 (Figure 1C). Since escitalopram elicited a delayed onset of antidepressant-like effects in the SIT (Figure 1B), and diazepam, at a dose of anxiolytic-like effects, had no effects in the SIT test (Figure 1C), the effects in SIT could reflect efficacy on social interaction impairment or a lack of motivation to interact with novel conspecifics as dysregulated essential behaviors in rodents after social defeat stress (Petković and Chaudhury, 2022). With the TST, allopregnanolone (20 mg/kg, i.p.) but not diazepam (2 mg/kg, i.p.) elicited antidepressant-like effects (Supplementary Figure 5). The effects of the TST could reflect efficacy on behavioral despair and helplessness under unbearable environmental stressful conditions (Hao et al., 2019). These results demonstrated that allopregnanolone elicited antidepressant-like effects, while diazepam had no effect on depressive-like symptoms. Regarding the molecular mechanism underlying this different antidepressant-like effect, previous studies have reported that neuroactive steroids act on both extra and synaptic $GABA_A$ receptors, while benzodiazepines primarily act on synaptic $GABA_A$ receptors (Carver and Reddy, 2013; Althaus et al., 2020). Therefore, we investigated whether the potentiation of δ-subunit-containing $GABA_A$ receptors might contribute to the *in vivo* efficacy of allopregnanolone by using Gabrd$^{-/-}$ mice with SDS. The antidepressant-like effect of allopregnanolone was abolished in Gabrd$^{-/-}$ mice (Figure 1D). This result demonstrated that δ-subunit-containing $GABA_A$ receptors are involved in the rapid antidepressant-like effect of allopregnanolone.

Increase in tonic inhibition in BLA interneurons with allopregnanolone, in contrast to diazepam

Signaling through δ-subunit-containing $GABA_A$ receptors strongly influences network activity due to the role of tonic GABA currents in controlling the excitability of inhibitory interneurons (Vida et al., 2006; Lee and Maguire, 2014; Pavlov et al., 2014). A previous study demonstrated that allopregnanolone-induced potentiation of δ-subunit-containing $GABA_A$ receptors in BLA interneurons could be related to its antidepressant-like effect (Antonoudiou et al., 2022; Luscher et al., 2023; Walton et al., 2023). This potentiation of δ-subunit-containing $GABA_A$ receptors could be measured as tonic GABA currents in neurons (Vida et al., 2006; Lee and Maguire, 2014; Pavlov et al., 2014). Therefore, in the present study, we first performed whole-cell patch-clamp recording from BLA interneurons, which were visually identified and exhibited fast spiking activity by current injections, in slices prepared from SDS mice with depressive symptoms (Figure 2A). Allopregnanolone significantly potentiated tonic currents compared with diazepam in BLA slices from wild-type mice with the SDS model (Figure 2B, $P = 0.0028$, $n = 11$ slices, paired *t*-test). The augmentation of tonic currents induced by allopregnanolone was not observed in Gabrd−/− mice with the SDS model, thereby confirming the involvement of δ-subunit-containing $GABA_A$ receptors in the currents (Figure 2B, $N = 6$ slices). Regarding phasic currents, both allopregnanolone and diazepam exhibited an augmentation of the amplitude and decay of IPSCs in BLA slices from wild-type mice with the SDS model (Figures 2C,D). The result obtained from this experiment confirms our understanding of the compound concentrations required for the potentiation of synaptic $GABA_A$ receptors. Of greater significance, there was a notable reduction in the frequency of IPSCs in BLA interneurons from SDS mice during the pre-treatment period when compared to those from naïve mice (Supplementary Figure 6). This suggests that GABA release from presynaptic terminals might be diminished in a depressive state. Regarding the amplitude and decay of sIPSCs and tonic currents

during the pre-treatment period, there were no significant changes between SDS and naïve mice (Supplementary Figure 6). Based on these findings, in conjunction with behavior outcomes, it can be inferred that the enhancement of extrasynaptic $GABA_A$ receptors in BLA interneurons plays a role in the antidepressant-like effects of allopregnanolone, which diverge from the effects of diazepam.

Distinct effect of allopregnanolone on resting BLA theta activity, in contrast to diazepam

A previous study reported that orchestrating the neural network centered around the amygdala is important for the mechanism of action of the antidepressant effects of neuroactive steroids (Antonoudiou et al., 2022). In particular, theta oscillations (6–12 Hz) in the BLA are essential for them as optogenetically induced theta oscillations in the BLA reduce immobility time in the TST (Antonoudiou et al., 2022). Moreover, previous studies have reported that theta oscillation in the mPFC is also involved in the regulation of depression (Kuga et al., 2022). Thus, to compare the effect of the neuroactive steroid allopregnanolone and benzodiazepine diazepam on the oscillation of these brain regions in SDS mice, we simultaneously recorded LFPs from the BLA and mPFC (Figure 3A). We recorded LFPs of SDS mice in their home cages for 30 min as a baseline, followed by the administration of vehicle, diazepam, and allopregnanolone, and continued recording for another 30 min (Figure 3B). According to a previous study (Antonoudiou et al., 2022), we focused on theta oscillations as the activity related to antidepressant effects and beta oscillations (15–30 Hz) as a marker of functional activation of the $GABA_A$ receptor. The BLA theta power significantly increased after the administration of allopregnanolone (Figures 3C,D; $P = 0.026$, $n = 7$ mice, paired t-test) but was not changed after the administration of vehicle or diazepam. The BLA beta power increased after the administration of diazepam and allopregnanolone (Figures 3E,F; $P = 0.011$ and 0.0014, respectively, $n = 7$ mice, paired t-test) but was not changed in the vehicle condition. Similarly, we analyzed mPFC theta and beta oscillations. The mPFC theta power significantly increased after the administration of allopregnanolone (Figures 4A,B; $P = 0.034$, $n = 8$ mice, paired t-test), while theta power was not changed after the administration of vehicle or diazepam. The PFC beta power increased after the administration of diazepam and allopregnanolone (Figures 4C,D; $P = 0.034$ and 0.0004, respectively, $n = 8$ mice, paired t-test) but was not changed in the vehicle condition. These results demonstrate that allopregnanolone increases both theta and beta oscillations in the BLA and mPFC, while diazepam increases only beta activity. Moreover, when combined with our behavioral data in the SIT and TST, theta activity might be associated with the antidepressant effects of allopregnanolone.

Involvement of δ-subunit-containing $GABA_A$ receptors in the increase in resting theta activity in the BLA and mPFC due to allopregnanolone but not in beta activity

To evaluate whether δ-subunit-containing $GABA_A$ receptors are involved in oscillation due to allopregnanolone as well as its antidepressant effect, we assessed the effects of allopregnanolone on BLA and mPFC activity in $Gabrd^{-/-}$ mice with SDS. The increase in theta activity in the BLA and mPFC due to allopregnanolone was significantly attenuated in $Gabrd^{-/-}$ mice in the SDS model compared with wild-type mice in the SDS model (Figures 5A,B; $P = 0.0097$, $n_{WT} = 8$ mice, $n_{KO} = 5$ mice, unpaired t-test). Beta activity was also attenuated but not significantly (Figures 5A,C; $P = 0.088$, $n_{WT} = 8$ mice, $n_{KO} = 5$ mice, unpaired t-test). Similar results were obtained in mPFC theta (Figures 5D,E; $P = 0.031$, $n_{WT} = 9$ mice, $n_{KO} = 6$ mice, unpaired t-test) and beta activity (Figures 5D,F; $P = 0.013$, $n_{WT} = 9$ mice, $n_{KO} = 6$ mice, unpaired t-test). Thus, theta activity in the BLA and mPFC mediated by δ-subunit-containing $GABA_A$ receptors is essentially involved in the antidepressant effects of allopregnanolone.

Distinct effect of allopregnanolone on frontal theta and beta activity, in contrast to diazepam

A previous study reported that neuroactive steroids such as zuranolone increase the theta activity of the frontal cortex in healthy volunteers based on EEG recordings (Antonoudiou et al., 2022), while benzodiazepines such as diazepam do not (Friedman et al., 1992). Regarding the increase in frontal beta activity, reflecting the functional activation of $GABA_A$ receptors in the brain, both neuroactive steroids and benzodiazepine have effects in healthy volunteers (Friedman et al., 1992; van Broekhoven et al., 2007; Antonoudiou et al., 2022). However, no clinical evidence has been reported as direct comparison data between them in the same protocol. Therefore, in reference to these clinical studies, we evaluated the effects of allopregnanolone and diazepam on frontal theta and beta activity in EEG recordings from naïve mice and the SDS model (Figures 6A,B). In SDS model mice, allopregnanolone significantly increased frontal theta activity (Figures 6C,D; $P = 0.0003$, $p < 0.0001$ for vehicle versus allopregnanolone and diazepam versus allopregnanolone, respectively, $n = 14$ mice, Tukey's test), while diazepam did not. Regarding frontal beta activity, both allopregnanolone and diazepam significantly increased it (Figures 6E,F; $P = 0.040$, $p < 0.0001$, 0.0001 for vehicle versus diazepam, diazepam versus allopregnanolone and vehicle versus allopregnanolone, respectively, $n = 14$ mice, Tukey's test). A similar result was obtained in naïve mice (Supplementary Figure 2). Thus, we have demonstrated that there is a difference in theta and beta activity in the frontal cortex between allopregnanolone and diazepam in a direct comparison study with EEG recordings from naïve and SDS model mice.

Decrease in frontal beta and theta activities in the depressive state

Finally, we evaluated changes in theta and beta activity in the frontal cortex of SDS model mice. Several previous studies reported that dysfunction of GABAergic inhibition, such as the amount of GABA in the frontal cortex and the expression of $GABA_A$ receptors or their function, is reduced not only in animal models but also in depressed patients (Luscher et al., 2011). Furthermore, allopregnanolone increased frontal theta and beta activity in depressed SDS mice. Therefore, we hypothesized that theta activity and beta

10.3389/fncel.2023.1274459

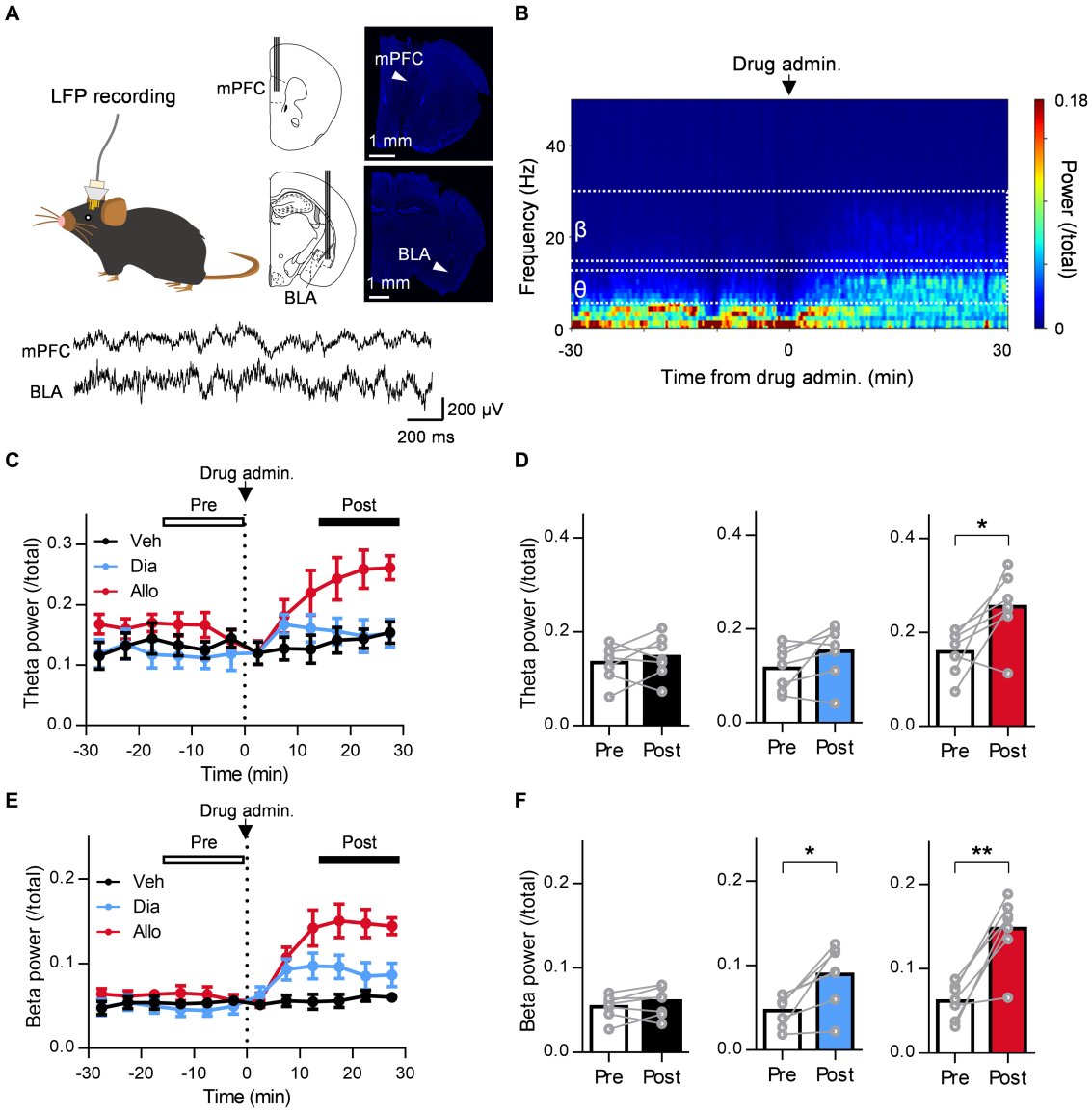

FIGURE 3
A distinct effect of allopregnanolone, in contrast to diazepam, on resting theta activity in the BLA. **(A)** Local field potentials (LFPs) were recorded from the medial frontal cortex (mPFC) and BLA of SDS mice. The arrowhead in the macrographs indicates the location of the electrode tip. The nuclei were counterstained with DAPI. The bottom panel demonstrates a representative trace of LFPs in the mPFC and BLA. **(B)** Representative power spectrogram of BLA LFPs before and after allopregnanolone administration. The LFP power was normalized for each time point across the total power and plotted on a pseudocolor scale. **(C)** Time course of BLA theta oscillation (6–12 Hz) power before and after administration of vehicle (Veh, depicted in black), diazepam (Dia, 2 mg/kg, depicted in blue), and allopregnanolone (Allo, 20 mg/kg, depicted in red). The dashed line indicates the timing of drug administration. Power values were normalized by total power and shown as ratios. The average power from 0 to 15 min before drug administration was defined as the preadministration period, and the average from 15 to 30 min after administration was defined as the postadministration period. Data are represented as the mean ± SEM of seven mice. **(D)** BLA theta power during the preadministration and postadministration periods with Veh (black), Dia (blue), and Allo (red). *$p = 0.026$, $n = 7$ mice, paired t-test. Power values were normalized by total power and shown as ratios. **(E,F)** The same as **(C,D)** but for the beta oscillation (15–30 Hz) power. *$p = 0.011$, **$p = 0.0014$, $n = 7$ mice, paired t-test.

activity in the frontal cortex of SDS model mice were lower than those of naïve mice. We calculated the theta power and beta power during the preadministration period as baseline activity and compared them between naïve and SDS model mice (Figures 7A,C). As a result, both theta power and beta power in the frontal cortex of SDS mice were significantly lower than those of naïve mice (Figures 7B,D; $P = 0.0004$ and 0.0127 for theta power and beta power, respectively, $n = 14$ mice each, unpaired t-test). These results showed that baseline activity in the theta and beta bands decreases in the SDS model.

Discussion

Rapid onset of antidepressant-like effects of allopregnanolone, in contrast to diazepam

In the present study, allopregnanolone elicited antidepressant-like effects in the SIT and TST of the SDS model. In contrast, diazepam had no effect on depression-like behaviors. The dose of

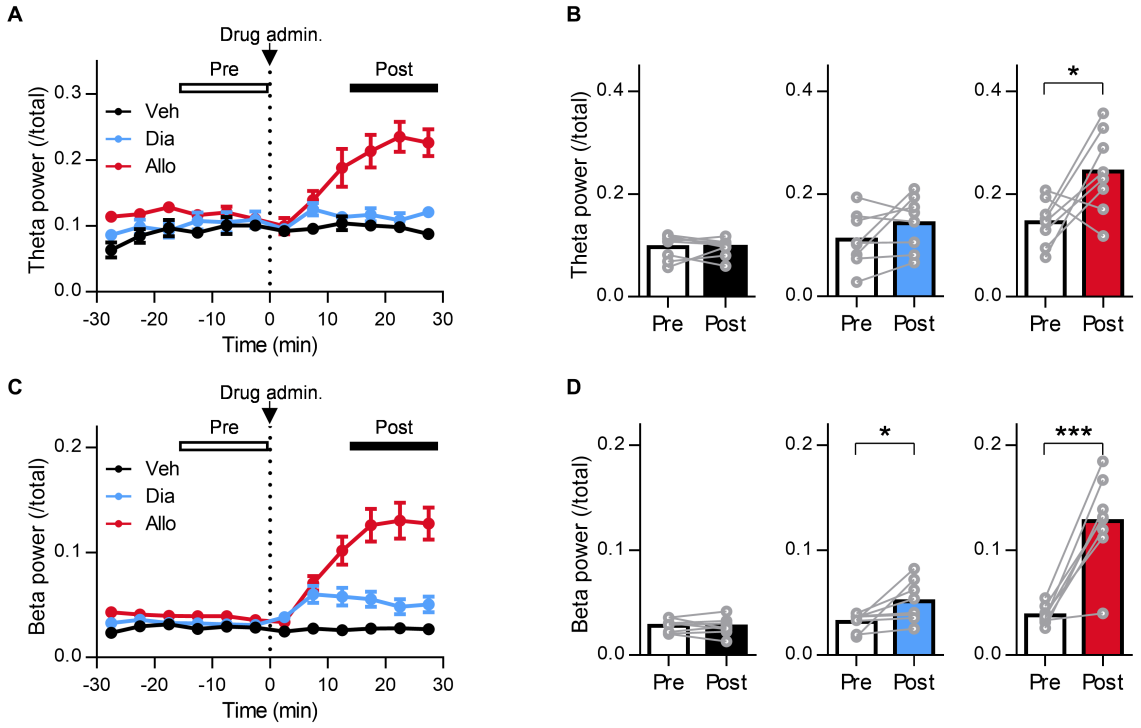

FIGURE 4
A distinct effect of allopregnanolone, in contrast to diazepam, on resting theta activity in the mPFC. **(A)** Time course of mPFC theta power before and after administration of vehicle (Veh, depicted in black), diazepam (Dia, depicted in blue), and allopregnanolone (Allo, depicted in red). The dashed line indicates the timing of drug administration. Data are represented as the mean ± SEM of eight mice. **(B)** mPFC theta power during the preadministration and postadministration periods for Veh (black), Dia (blue), and Allo (red). *$p = 0.03$, $n = 8$ mice, paired t-test. Power values were normalized by total power and are shown as ratios. **(C,D)** The same as **(A,B)** but for beta power. *$p = 0.034$, ***$p = 0.0004$, $n = 8$ mice, paired t-test.

diazepam used in the present study was determined by its anxiolytic-like effects and increased beta activity of the frontal cortex without sedation, which is within a range of previous studies (Bhatt et al., 2013; Shahnouri et al., 2016; Antonoudiou et al., 2022). Similarly, the dosage of allopregnanolone was set to increase beta activity without sedation. The present result of the locomotor assessment and EEG confirms our understanding of the dose of compound required for the potentiation of $GABA_A$ receptors and antidepressant or anxiolytic effects without sedation. In the SIT of the SDS model, we demonstrated that allopregnanolone elicited rapid-onset antidepressant-like effects. Diazepam, at a dose eliciting anxiolytic-like effects, had no effect on the SIT of SDS mice. Escitalopram for 4 weeks elicited significant antidepressant-like effects. Based on these results, the present study demonstrated rapid onset effects of allopregnanolone on depression-like behavior in the SIT of the SDS model, in contrast to diazepam and escitalopram. This corresponds to clinical evidence of the efficacy profile of these drugs on depressive symptoms in MDD patients (Rush et al., 2006; Lim et al., 2020; Edinoff et al., 2021). More importantly, this antidepressant-like effect of allopregnanolone in SIT was abolished in δKO mice. These data demonstrated that δ-subunit-containing $GABA_A$ receptors are critical for the antidepressant-like effects of allopregnanolone. Both diazepam and allopregnanolone are positive allosteric modulators of $GABA_A$ receptors, exhibiting relatively little α-subunit selectivity. Diazepam acts on the benzodiazepine site of α1, 2, 3, and α5-containing $GABA_A$ receptors (Carver and Reddy, 2013; Nuss, 2015). Allopregnanolone is a non-selective neuroactive steroid acting on α1, 2, 3, 4, 5, and α6-containing $GABA_A$ receptors (Sigel, 2002; Hosie et al., 2006; Carver and Reddy, 2013; Nuss, 2015; Alvarez and Pecci, 2018). In combination with genetically modified animals, the relationship between each α subunit and behavior has been shown, particularly regarding the effects of benzodiazepines; for example, the α1 subunit for sedation and the α2 subunit for anxiolysis (Engin et al., 2018). In the present study, the relief of depressive symptoms by allopregnanolone is associated with δ-subunit-containing $GABA_A$ receptors. Particularly, recent studies report that not only δ-subunit-containing $GABA_A$ receptors but also other subtypes of $GABA_A$ receptors such as the α5-subunit have been related to behaviors such as affective and cognitive function in the depression model (Piantadosi et al., 2016; Luscher et al., 2023). Thus, each subunit-selective behavioral profile and their associated neuronal activities remain to be clarified in future studies. Although potentiation of δ-subunit-containing $GABA_A$ receptors by allopregnanolone may be critical for mediating the rapid antidepressant effects, it could not be excluded that phasic inhibition via synaptic $GABA_A$ receptors by allopregnanolone could contribute to antidepressant effects. Future studies with the effects of DS2, which is a selective compound for δ-subunit-containing $GABA_A$ receptors, are needed in the SDS model. Moreover, previous studies have shown that SSRIs elicit moderate and slow increases in allopregnanolone, associated with the initiation of their antidepressant effects (Romeo et al., 1998). Further studies of the effects of SSRIs, combined with δKO mice in the SDS model, are needed to clarify the involvement of δ-subunit-containing $GABA_A$ receptors in the effects of SSRIs.

10.3389/fncel.2023.1274459

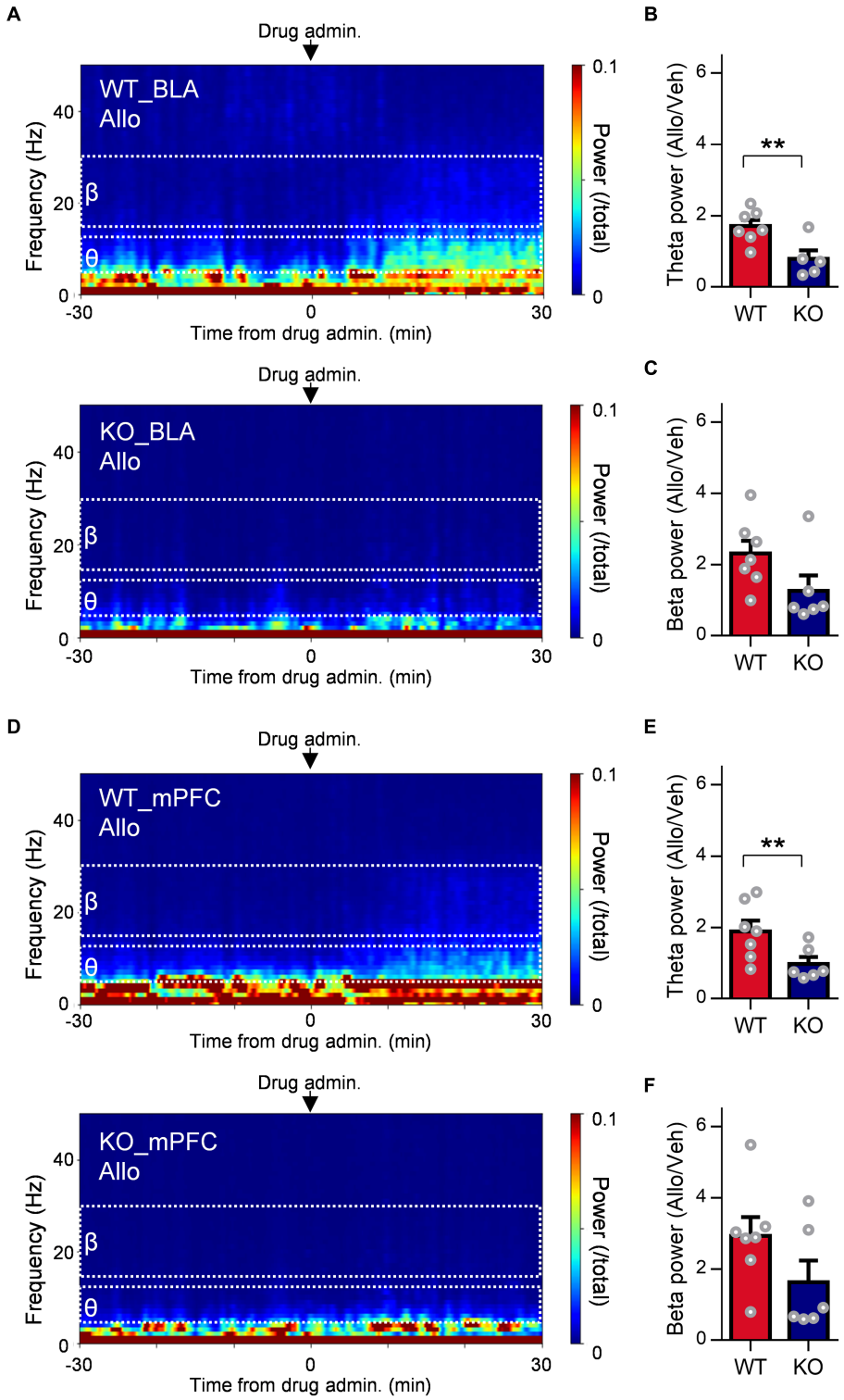

FIGURE 5
Involvement of extrasynaptic $GABA_A$ receptors in the increase in resting theta activity in the BLA due to allopregnanolone. **(A)** Representative power spectrogram of BLA LFPs before and after allopregnanolone (Allo, 20 mg/kg) administration in a WT mouse (top) and a $GABA_A$ receptor δ-subunit KO mouse (bottom). The LFP power was normalized for each time point across the total power and plotted on a pseudocolor scale. **(B)** The ratio of BLA theta power after the administration of Allo to that after the administration of vehicle (Veh) in WT (red) and KO (dark blue) mice. $^{**}p = 0.0097$, $n_{WT} = 8$ mice, $n_{KO} = 5$ mice, unpaired *t*-test. **(C)** The same as **(B)**, but for the ratio of BLA beta power. $p = 0.088$, $n_{WT} = 8$ mice, $n_{KO} = 5$ mice, unpaired *t*-test. **(D)** The same as **(A)** but for the mPFC LFPs. **(E)** The same as **(B)** but for mPFC theta power. $^{*}p = 0.031$, $n_{WT} = 9$ mice, $n_{KO} = 6$ mice, unpaired *t*-test. **(F)** The same as **(C)** but for mPFC beta power. $p = 0.13$, $n_{WT} = 9$ mice, $n_{KO} = 6$ mice, unpaired *t*-test.

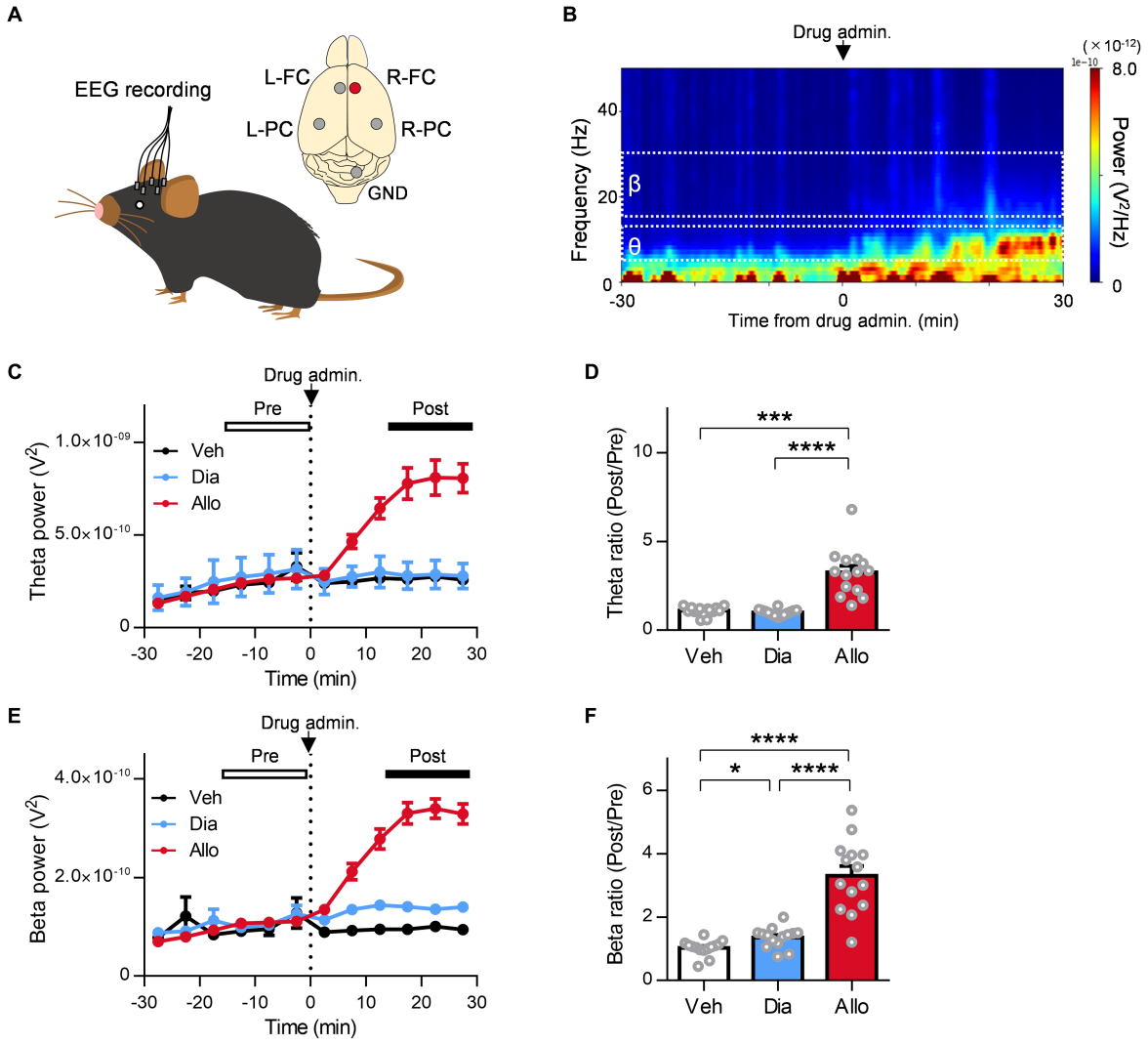

FIGURE 6
Distinct effect of allopregnanolone compared with diazepam on resting frontal EEG theta activity in SDS model mice. **(A)** Electroencephalograms (EEGs) were recorded from the bilateral frontal cortex (FC) and parietal cortex (PC) of naïve and SDS model mice. The EEGs of the right FC (R-FC) were used for the analysis. GND, ground electrode. **(B)** Representative power spectrogram of R-FC EEGs before and after allopregnanolone administration. **(C)** Time course of R-FC theta power before and after the administration of vehicle (Veh, depicted in black), diazepam (Dia, depicted in blue), and allopregnanolone (Allo, depicted in red). The dashed line indicates the timing of drug administration. Data are represented as the mean ± SEM of 14 mice. **(D)** The ratio of R-FC theta power during the postadministration to the preadministration for Veh (black), Dia (blue), and Allo (red). ***$p = 0.0003$ and ****$p < 0.0001$ for vehicle versus allopregnanolone and diazepam versus allopregnanolone, respectively, $n = 14$ mice, Tukey's test. **(E,F)** The same as **(C,D)**, but for beta power. *$p = 0.040$, ****$p < 0.0001$, $n = 14$ mice, Tukey's est.

Distinct neurophysiological mechanism of allopregnanolone acting on BLA oscillation, in contrast to diazepam

The amygdala is one of the abundant regions with a high concentration of neuroactive steroids (Bixo et al., 2018) and is involved in vigilance attention and learning biologically relevant signals such as negative emotional stimuli (Tzovara et al., 2019). Altered amounts of neuroactive steroids have been implicated in amygdala reactivity to negative emotional stimuli and stress vulnerability (Pisu et al., 2022). Dysregulation of neural network activity involving the amygdala is associated with depressive symptoms in patients with MDD (Drevets, 2000, Phillips et al., 2003). Recent studies demonstrated that neuroactive steroid treatment increased BLA theta activity in stress model mice and elicited antidepressant-like effects (Antonoudiou et al., 2022; Luscher et al., 2023; Walton et al., 2023). In addition, optogenetic stimulation of BLA interneurons at a theta frequency of 8 Hz caused antidepressant effects in a chronic unpredictable stress mouse model (Antonoudiou et al., 2022). The antidepressant-like effects of allopregnanolone were abolished in δKO mice (Antonoudiou et al., 2022). Thus, the activation of δ-subunit-containing $GABA_A$ receptors in BLA interneurons is believed to contribute to the antidepressant-like effects of allopregnanolone by triggering an increase in BLA theta activity. In the present study, several differences between allopregnanolone and diazepam may contribute to antidepressant-like effects. Focusing on BLA interneurons, allopregnanolone potentiated tonic inhibition via potentiation of δ-subunit-containing $GABA_A$ receptors. In addition, allopregnanolone but not diazepam increased

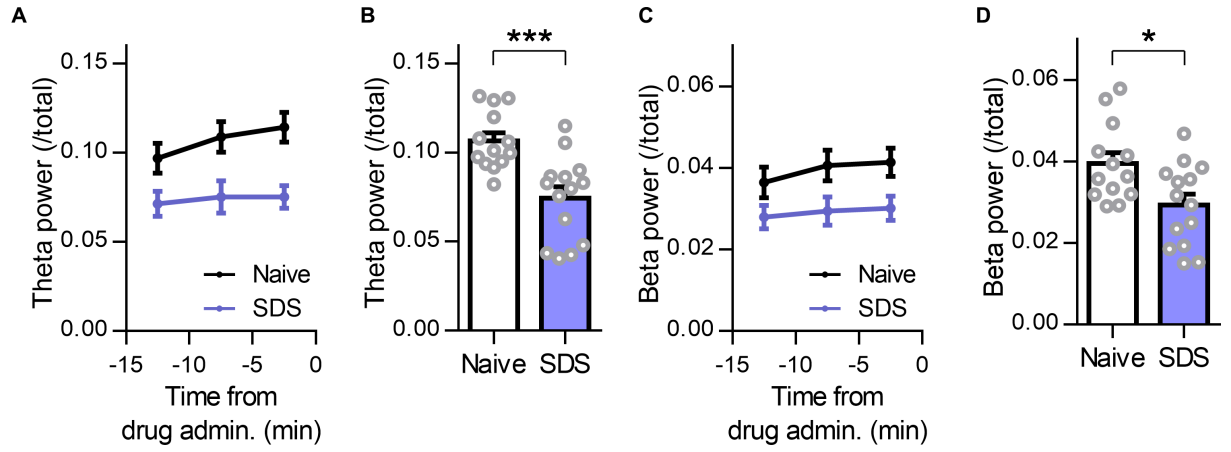

FIGURE 7
Decrease in frontal beta and theta activities in the depressive state. **(A)** Time course of the R-FC theta power of naïve (black) and SDS (purple) mice before administration of the drug. The average preadministration period of all drugs (vehicle, diazepam, and allopregnanolone) was used. The data are represented as the mean ± SEM of 14 mice each. **(B)** The R-FC theta power of naïve and SDS mice during the preadministration period of drugs. ***$p = 0.0004$, $n = 14$ mice each, unpaired t-test. **(C,D)** The same as **(A, B)**, but for beta power. *$p = 0.013$, n naïve = 13 mice, $n_{SDS} = 14$ mice, unpaired t-test.

theta activity in the BLA during the resting state in SDS mice. Increased theta activity was attenuated in δKO mice. Allopregnanolone has been reported to act on δ-subunit-containing $GABA_A$ receptors only in BLA interneurons but not in principal neurons (Antonoudiou et al., 2022). Thus, allopregnanolone-induced increases in the theta activity of the BLA through δ-subunit-containing $GABA_A$ receptors in BLA interneurons may lead to a shift from fear to a normal state and reduced depression-like behaviors in the SDS model. With regard to beta activity within BLA, both allopregnanolone and diazepam exhibited enhancements, indicating that the augmentation of beta power resulted from the activation of synaptic $GABA_A$ receptors in BLA interneurons. These results align with our observed potentiation of IPSC decay and amplitude in BLA interneurons by allopregnanolone and diazepam. In the present study, the allopregnanolone-induced increase in beta activity was slightly attenuated in δKO mice but not significantly. This implies that δ-subunit-containing $GABA_A$ receptors are also involved in both beta and theta activities in the BLA increased by allopregnanolone, which is consistent with a previous study (Antonoudiou et al., 2022). Considering the significant correlation between increased BLA theta activity and antidepressant effects from neuroactive steroids (Antonoudiou et al., 2022) and the increase in beta activity alone by diazepam without antidepressant-like effects, an increase in BLA theta activity via δ-subunit-containing $GABA_A$ receptors may be important for the antidepressant-like effects of allopregnanolone. Of course, the possible involvement of beta activity in the antidepressant-like effects of allopregnanolone cannot be excluded. At the very least, the differences in the antidepressant-like effects of allopregnanolone and diazepam could be largely attributed to differences in the theta oscillation of the BLA. In addition to BLA activity, mPFC theta activity was increased by allopregnanolone but not by diazepam. This increase in theta activity in the mPFC was attenuated in δKO mice. As for mPFC beta activity, both allopregnanolone and diazepam demonstrated an increase in activity. Consequently, not only theta activity in the BLA but also in the mPFC might be implicated in the antidepressant-like effects of allopregnanolone. Previous investigations have established that augmented theta activity in the mPFC and BLA plays a role in the regulation and discrimination of negative stimuli or emotions (Calhoon and Tye, 2015; Tovote et al., 2015). Specifically, it has been reported that BLA firing activity becomes synchronized with input from the mPFC, indicating that the BLA is selectively tuned to mPFC input, which potentially contributes to memory retrieval, fear responses, and extinction (Likhtik et al., 2014). It is worth noting that the function of the mPFC has also been associated with amygdala output (Senn et al., 2014). Indeed, allopregnanolone regulates the functional connectivity between the human frontal cortex and amygdala, which is involved in the relief of fear memory or cognition of negative stimuli (Sripada et al., 2014). In addition, an increase in theta activity in the mPFC and BLA in mice is also involved in approach behavior to communicate with other mice (Kuga et al., 2022). As an underlying neurological mechanism, modulation of interneuron activity not only in the BLA but also in the mPFC has been reported to contribute to antidepressant-like effects in preclinical models (Fogaça et al., 2021; Antonoudiou et al., 2022). This implies that allopregnanolone could affect not only emotional cognition but also motivational behavior. This is supported by previous reports that the amygdala and frontal cortex are involved in the regulation of motivational behavior via dopamine signaling pathways, which could be regulated by allopregnanolone (Rougé-Pont et al., 2002; Phillips et al., 2003; Holmberg et al., 2018). Thus, allopregnanolone, unlike diazepam, could ameliorate negative emotion and motivational affect, which is regulated by BLA-PFC theta activity.

Distinct modulation of frontal theta and beta EEG activity by allopregnanolone, in contrast to diazepam, as a translational biomarker

Previous studies with EEGs have shown that neuroactive steroids such as zuranolone, but not benzodiazepines such as diazepam, increase frontal cortex theta activity in healthy volunteers

(Romano-Torres et al., 2002; Saletu et al., 2006; Antonoudiou et al., 2022). Regarding frontal beta activity, a marker of central $GABA_A$ receptor activation, both neuroactive steroids and benzodiazepines increased this activity (Friedman et al., 1992; Romano-Torres et al., 2002; Saletu et al., 2006; van Broekhoven et al., 2007; Antonoudiou et al., 2022). Interestingly, the increase in beta activity has been suggested to be more potent with allopregnanolone compared to diazepam, but no report has verified it in a head-to-head comparison under the same conditions. In the present study, we used an SDS model and naïve mice to demonstrate the difference in the effect of both agents in enhancing frontal theta activity by direct comparison verification. Furthermore, regarding beta activity, we observed that both allopregnanolone and diazepam increased this activity and that allopregnanolone exhibited a significant increase compared with diazepam. Thus, we have demonstrated distinct EEG profiles for allopregnanolone and diazepam, supported by previous studies (Visser et al., 2003; Antonoudiou et al., 2022; Hammond et al., 2022). This EEG result using the SDS model and naïve mice not only supports the results of the BLA and mPFC theta activity assessment in LFP recordings but also could be important as translational evidence forming a bridge from non-clinical evidence to human evidence. It is implied that frontal theta activity, similar to that in the BLA, is related to the mechanism of action of neuroactive steroids and may potentially contribute to the superior antidepressant-like effects of allopregnanolone. It has also been clinically reported that changes in frontal theta power could predict antidepressant efficacy in responders (Wade and Iosifescu, 2016; Wu et al., 2020). Since we did not investigate the causal relationship between theta activity and antidepressant effects, an additional study will be needed to examine the effects of theta activity on the downstream signals, such as stress responses, and its influence on antidepressant-like effects in depression model mice. Indeed, it has been reported that the optogenetically induced theta oscillations in the BLA have an antidepressant-like effect in the TST (Antonoudiou et al., 2022).

The decrease in beta and theta activities in a depressive state and their increase in response to allopregnanolone, related to extrasynaptic $GABA_A$ receptors

Decreased frontal beta and theta activities have been reported to correlate with the severity of depressive symptoms in patients with MDD (Saletu et al., 2010). Similarly, a decrease in frontal beta and theta activities was observed in SDS mice compared to non-stressed naïve mice, as evidenced by EEG recordings. Neuronal oscillation is potently regulated by GABAergic signaling through synaptic and extrasynaptic $GABA_A$ receptors (Luscher et al., 2011). In particular, signaling through δ-subunit-containing $GABA_A$ receptors strongly impacts network activity due to tonic inhibition regulating inhibitory interneuron excitability. Inhibitory interneurons are key regulators of rhythmic brain network activity (Vida et al., 2006; Mann and Paulsen, 2007). Recently, dysfunction of GABAergic inhibition has been reported in the pathology of MDD, such as a decrease in the concentration of GABA and/or allopregnanolone (Perlman et al., 2021), changes in the subunit expression of the $GABA_A$ receptor (Luscher et al., 2011), and the excitability of GABAergic interneurons (Jie et al., 2018) in several brain areas including mPFC and BLA. Our present findings further support these reports as we observed a decrease in presynaptic GABA release in BLA slices from SDS mice. While the specific alterations in neuronal oscillation within the BLA during a depressive state remain to be fully elucidated, it is plausible that these mechanisms contribute to the observed decrease in frontal beta and theta activities in SDS mice. Importantly, our results demonstrated that allopregnanolone potentiated PFC-BLA beta and theta activities in SDS mice, and δ-subunit-containing $GABA_A$ receptors are important mechanisms of action of allopregnanolone. In terms of molecular mechanisms, previous studies reported that δ-subunit-containing $GABA_A$ receptors enable neurons to sense the low ambient GABA concentrations present in the extracellular space, leading to tonic inhibition and both cell and network behavior (Carver and Reddy, 2013; Feng and Forman, 2018). Additionally, neuroactive steroids, including allopregnanolone and zuranolone, can enhance the surface expression of $GABA_A$ receptors, thereby amplifying GABA currents through multiple mechanisms (Abramian 2014; Modgil 2017). Thus, dysregulated neuronal network activity under a depressive state could be shifted to a normal state by treatment with neuroactive steroids. Additionally, several mood disorders, such as bipolar disorder, premenstrual dysphoric disorder, and postpartum depression, have dysregulated neuronal networks, along with changes in the concentration of allopregnanolone (Porcu et al., 2016; Karademir et al., 2023). Neuroactive steroids with the potentiation of synaptic and extrasynaptic $GABA_A$ receptors may therefore present a potential therapeutic target for the treatment of major depressive disorder.

Data Availability Statement

The raw data supporting the conclusions of this article will be made available by the authors, without undue reservation.

Ethics Statement

The animal study was approved by All procedures were approved by the Animal Care and Use Committee of Shionogi Research Laboratories, Osaka, Japan. Electrophysiological assessments were performed according to the AAALAC International guidelines. The study was conducted in accordance with the local legislation and institutional requirements.

Author contributions

KT: Conceptualization, Data curation, Investigation, Writing – original draft, Writing – review & editing. YY: Data curation, Formal analysis, Investigation, Methodology, Writing – original draft. RT: Data curation, Formal analysis, Investigation, Methodology, Writing – original draft, Writing – review & editing. HA: Data curation, Writing – review & editing. SS: Data curation, Writing – review & editing. TO: Project administration, Writing – review & editing. TT: Conceptualization, Project administration, Writing – review &

editing. KO: Conceptualization, Investigation, Project administration, Writing – review & editing.

Funding

The author(s) declare that no financial support was received for the research, authorship, and/or publication of this article.

Conflict of interest

KT, YY, RT, TO, TT, and KO are employees belonging to Shionogi & Co., Ltd. HA and SS are employed by the company Shionogi TechnoAdvance Research.

Publisher's note

Supplementary material

The Supplementary material for this article can be found online at: https://www.frontiersin.org/articles/10.3389/fncel.2023.1274459/full#supplementary-material

References

Abramian, A. M., Comenencia-Ortiz, E., Modgil, A., Vien, T. N., Nakamura, Y., Moore, Y. E., et al. (2014). Neurosteroids promote phosphorylation and membrane insertion of extrasynaptic $GABA_A$ receptors. *Proc Natl Acad Sci U S A.* 111, 7132–7137. doi: 10.1073/pnas.1403285111

Agis-Balboa, R. C., Guidotti, A., and Pinna, G. (2014). 5α-reductase type I expression is downregulated in the prefrontal cortex/Brodmann's area 9 (BA9) of depressed patients. *Psychopharmacology* 231, 3569–3580. doi: 10.1007/s00213-014-3567-5

Ali, M., Ullah, I., Diwan, M. N., Aamir, A., Awan, H. A., Waris Durrani, A., et al. (2023). Zuranolone and its role in treating major depressive disorder: a narrative review. *Horm. Mol. Biol. Clin. Invest.* 44, 229–236. doi: 10.1515/hmbci-2022-0042

Althaus, A. L., Ackley, M. A., Belfort, G. M., Gee, S. M., Dai, J., Nguyen, D. P., et al. (2020). Preclinical characterization of zuranolone (SAGE-217), a selective neuroactive steroid $GABA_A$ receptor positive allosteric modulator. *Neuropharmacology* 181:108333. doi: 10.1016/j.neuropharm.2020.108333

Alvarez, L. D., and Pecci, A. (2018). Structure and dynamics of neurosteroid binding to the $\alpha_1\beta_2\gamma_2$ $GABA_A$ receptor. *J. Steroid Biochem. Mol. Biol.* 182, 72–80. doi: 10.1016/j.jsbmb.2018.04.012

American Psychiatric Association. *Diagnostic and Statistical Manual of Mental Disorders* (*Fifth edition*), US: American Psychiatric Association (2013).

Antonoudiou, P., Colmers, P. L. W., Walton, N. L., Weiss, G. L., Smith, A. C., Nguyen, D. P., et al. (2022). Allopregnanolone Mediates Affective Switching Through Modulation of Oscillatory States in the Basolateral Amygdala. *Biol. Psychiatry* 91, 283–293. doi: 10.1016/j.biopsych.2021.07.017

Belelli, D., and Lambert, J. J. (2005). Neurosteroids: endogenous regulators of the $GABA_A$ receptor. *Nat. Rev. Neurosci.* 6, 565–575. doi: 10.1038/nrn1703

Bhatt, S., Mahesh, R., Devadoss, T., and Jindal, A. K. (2013). Anxiolytic-like effect of (4-benzylpiperazin-1-yl)(3-methoxyquinoxalin-2-yl)methanone (6g) in experimental mouse models of anxiety. *Indian J. Pharm.* 45, 248–251. doi: 10.4103/0253-7613.111923

Bixo, M., Johansson, M., Timby, E., Michalski, L., and Bäckström, T. (2018). Effects of GABA active steroids in the female brain with a focus on the premenstrual dysphoric disorder. *J. Neuroendocrinol.* 30. doi: 10.1111/jne.12553

Brickley, S. G., and Mody, I. (2012). Extrasynaptic $GABA_A$ receptors: Their function in the CNS and implications for disease. *Neuron* 73, 23–34. doi: 10.1016/j.neuron.2011.12.012

Brot, M. D., Akwa, Y., Purdy, R. H., Koob, G. F., and Britton, K. T. (1997). The anxiolytic-like effects of the neurosteroid allopregnanolone: interactions with $GABA_A$ receptors. *Eur. J. Pharmacol.* 325, 1–7. doi: 10.1016/S0014-2999(97)00096-4

Burstein, O., Franko, M., Gale, E., Handelsman, A., Barak, S., Motsan, S., et al. (2017). Escitalopram and NHT normalized stress-induced anhedonia and molecular neuroadaptations in a mouse model of depression. *PLoS One* 12:e0188043. doi: 10.1371/journal.pone.0188043

Calhoon, G. G., and Tye, K. M. (2015). Resolving the neural circuits of anxiety. *Nat. Neurosci.* 18, 1394–1404. doi: 10.1038/nn.4101

Carver, C. M., and Reddy, D. S. (2013). Neurosteroid interactions with synaptic and extrasynaptic $GABA_A$ receptors: regulation of subunit plasticity, phasic and tonic inhibition, and neuronal network excitability. *Psychopharmacology* 230, 151–188. doi: 10.1007/s00213-013-3276-5

Choudhary, D., Sasibhushana, R. B., Shankaranarayana Rao, B. S., and Srikumar, B. N. (2022). Mifepristone blocks the anxiolytic- and antidepressant-like effects of allopregnanolone in male rats. *Int. J. Neurosci.* 1-10. doi: 10.1080/00207454.2022.2153047

Dornellas, A. P. S., Macedo, G. C., McFarland, M. H., Gómez-A, A., O'Buckley, T. K., da Cunha, C., et al. (2020). Allopregnanolone decreases evoked dopamine release differently in rats by sex and estrous stage. *Front. Pharmacol.* 11:608887. doi: 10.3389/fphar.2020.608887

Doukkali, Z., Taghzouti, K., Bouidida, E. L. H., Kamal, R., Jemli, M., Belatar, B., et al. (2016). Evaluation of its anxiolytic effect in the elevated plus-maze and open field. *Ann Clin Lab Res.* 2016:1. doi: 10.1016/j.jep.2004.06.022

Drevets, W. C. (2000). Functional anatomical abnormalities in limbic and prefrontal cortical structures in major depression. *Prog. Brain Res.* 126, 413–431. doi: 10.1016/S0079-6123(00)26027-5

Edinoff, A. N., Odisho, A. S., Lewis, K., Kaskas, A., Hunt, G., Cornett, E. M., et al. (2021). Brexanolone, a $GABA_A$ Modulator, in the Treatment of Postpartum Depression in Adults: A Comprehensive Review. *Front. Psychol.* 12:699740. doi: 10.3389/fpsyt.2021.699740

Engin, E., Benham, R. S., and Rudolph, U. (2018). An Emerging Circuit Pharmacology of $GABA_A$ Receptors. *Trends Pharmacol. Sci.* 39, 710–732. doi: 10.1016/j.tips.2018.04.003

Farrant, M., and Nusser, Z. (2005). Variations on an inhibitory theme: phasic and tonic activation of $GABA_A$ receptors. *Nat. Rev. Neurosci.* 6, 215–229. doi: 10.1038/nrn1625

Feng, H. J., Forman, S. (2018). Comparison of αβδ and αβγ GABAA receptors: Allosteric modulation and identification of subunit arrangement by site-selective general anesthetics. *Pharmacol Res.* 133, 289–300. doi: 10.1016/j.phrs.2017.12.031

Fogaça, M. V., Wu, M., Li, C., Li, X. Y., Picciotto, M. R., and Duman, R. S. (2021). Inhibition of GABA interneurons in the mPFC is sufficient and necessary for rapid antidepressant responses. *Mol. Psychiatry* 26, 3277–3291. doi: 10.1038/s41380-020-00916-y

Friedman, H., Greenblatt, D. J., Peters, G. R., Metzler, C. M., Charlton, M. D., Harmatz, J. S., et al. (1992). Pharmacokinetics and pharmacodynamics of oral diazepam: effect of dose, plasma concentration, and time. *Clin. Pharmacol. Ther.* 52, 139–150. doi: 10.1038/clpt.1992.123

Habert, J., Katzman, M. A., Oluboka, O. J., McIntyre, R., McIntosh, D., MacQueen, G., et al. (2016). Functional Recovery in Major Depressive Disorder: Focus on Early Optimized Treatment. *Prim Care Companion CNS Disord.* 18. doi: 10.4088/PCC.15r01926

Hammond, R. S., Althaus, A. L., Farley, B. J., Smith, A. C., Lotarski, S. M., Koralek, A. C., et al. (2022). Differential network activity of benzodiazepines and neuroactive steroids observed with cortical EEG in rat. *Neuroscience*

Hao, Y., Ge, H., Sun, M., and Gao, Y. (2019). Selecting an Appropriate Animal Model of Depression. *Int. J. Mol. Sci.* 20:4827. doi: 10.3390/ijms20194827

Holmberg, E., Sjöstedt, J., Malinina, E., Johansson, M., Turkmen, S., Ragagnin, G., et al. (2018). Allopregnanolone involvement in feeding regulation, overeating and obesity. *Front. Neuroendocrinol.* 48, 70–77. doi: 10.1016/j.yfrne.2017.07.002

Hosie, A. M., Wilkins, M. E., da Silva, H. M., and Smart, T. G. (2006). Endogenous neurosteroids regulate GABAA receptors through two discrete transmembrane sites. *Nature* 444, 486–489. doi: 10.1038/nature05324

Jie, F., Yin, G., Yang, W., Yang, M., Gao, S., Lv, J., et al. (2018). Stress in Regulation of GABA Amygdala System and Relevance to Neuropsychiatric Diseases. *Front. Neurosci.* 12:562. doi: 10.3389/fnins.2018.00562

Karademir, M., Beyazyüz, E., Beyazyüz, M., Yılmaz, A., and Albayrak, Y. (2023). Decreased serum allopregnanolone and progesterone levels in male patients with bipolar disorder and their effects on cognitive functions. *Eur. Arch. Psychiatry Clin. Neurosci.* doi: 10.1007/s00406-023-01607-9

Kato, M., Nakagome, K., Baba, T., Sonoyama, T., Okutsu, D., Yamanaka, H., et al. (2023). Efficacy and safety of zuranolone in Japanese adults with major depressive disorder: A double-blind, randomized, placebo-controlled, phase 2 clinical trial. *Psychiatry Clin. Neurosci.* 77, 497–509. doi: 10.1111/pcn.13569

Konno, D., Ikegaya, Y., and Sasaki, T. (2022). Weak representation of awake/sleep states by local field potentials in aged mice. *Sci. Rep.* 12:7766. doi: 10.1038/s41598-022-11888-0

Kuga, N., Abe, R., Takano, K., Ikegaya, Y., and Sasaki, T. (2022). Prefrontal-amygdalar oscillations related to social behavior in mice. *elife* 11:e78428. doi: 10.7554/eLife.78428

Lee, V., and Maguire, J. (2014). The impact of tonic $GABA_A$ receptor-mediated inhibition on neuronal excitability varies across brain region and cell type. *Front Neural Circuits.* 8:3. doi: 10.3389/fncir.2014.00003

Likhtik, E., Stujenske, J. M., Topiwala, M. A., Harris, A. Z., and Gordon, J. A. (2014). Prefrontal entrainment of amygdala activity signals safety in learned fear and innate anxiety. *Nat. Neurosci.* 17, 106–113. doi: 10.1038/nn.3582

Lim, B., Sproule, B. A., Zahra, Z., Sunderji, N., Kennedy, S. H., and Rizvi, S. J. (2020). Understanding the effects of chronic benzodiazepine use in depression: a focus on neuropharmacology. *Int. Clin. Psychopharmacol.* 35, 243–253. doi: 10.1097/YIC.0000000000000316

Luscher, B., Maguire, J. L., Rudolph, U., and Sibille, E. (2023). $GABA_A$ receptors as targets for treating affective and cognitive symptoms of depression. *Trends Pharmacol.* 44, 586–600. doi: 10.1016/j.tips.2023.06.009

Luscher, B., Shen, Q., and Sahir, N. (2011). The GABAergic deficit hypothesis of major depressive disorder. *Mol. Psychiatry* 16, 383–406. doi: 10.1038/mp.2010.120

Mann, E. O., and Paulsen, O. (2007). Role of GABAergic inhibition in hippocampal network oscillations. *Trends Neurosci.* 30, 343–349. doi: 10.1016/j.tins.2007.05.003

Martinez, B. G., Salituro, F. G., Harrison, B. L., Beresis, R. T., Bai, Z., Blanco, M. J., et al. (2017). Neuroactive Steroids. 2. 3α-Hydroxy-3β-methyl-21-(4-cyano-1H-pyrazol-1′-yl)-19-nor-5β-pregnan-20-one (SAGE-217): A Clinical Next Generation Neuroactive Steroid Positive Allosteric Modulator of the $(\gamma\text{-Aminobutyric Acid})_A$ Receptor. *J. Med. Chem.* 60, 7810–7819. doi: 10.1021/acs.jmedchem.7b00846

Mihalek, R. M., Banerjee, P. K., Korpi, E. R., Quinlan, J. J., Firestone, L. L., Mi, Z. P., et al. (1999). Attenuated sensitivity to neuroactive steroids in gamma-aminobutyrate type A receptor delta subunit knockout mice. *Proc. Natl. Acad. Sci. U. S. A.* 96, 12905–12910. doi: 10.1073/pnas.96.22.12905

Modgil, A., Parakala, M. L., Ackley, M. A., Doherty, J. J., Moss, S. J., Davies, P. A.. (2017). Endogenous and synthetic neuroactive steroids evoke sustained increases in the efficacy of GABAergic inhibition via a protein kinase C-dependent mechanism. *Neuropharmacology*. 113, 314–322. doi: 10.1016/j.neuropharm.2016.10.010

Northoff, G., Wiebking, C., Feinberg, T., and Panksepp, J. (2011). The 'resting-state hypothesis' of major depressive disorder-a translational subcortical-cortical framework for a system disorder. *Neurosci. Biobehav. Rev.* 35, 1929–1945. doi: 10.1016/j.neubiorev.2010.12.007

Nuss, P. (2015). Anxiety disorders and GABA neurotransmission: a disturbance of modulation. *Neuropsychiatr. Dis. Treat.* 11, 165–175. doi: 10.2147/NDT.S58841

Okada, S., Igata, H., Sasaki, T., and Ikegaya, Y. (2017). Spatial Representation of Hippocampal Place Cells in a T-Maze with an Aversive Stimulation. *Front Neural Circuits.* 11:101. doi: 10.3389/fncir.2017.00101

Park, K., Lee, S., Kang, S. J., Choi, S., and Shin, K. S. (2007). Hyperpolarization-activated currents control the excitability of principal neurons in the basolateral amygdala. *Biochem. Biophys. Res. Commun.* 361, 718–724. doi: 10.1016/j.bbrc.2007.07.064

Pavlov, I., Savtchenko, L. P., Song, I., Koo, J., Pimashkin, A., Rusakov, D. A., et al. (2014). Tonic $GABA_A$ conductance bidirectionally controls interneuron firing pattern and synchronization in the CA3 hippocampal network. *Proc. Natl. Acad. Sci. U. S. A.* 111, 504–509. doi: 10.1073/pnas.1308388110

Perlman, G., Tanti, A., and Mechawar, N. (2021). Parvalbumin interneuron alterations in stress-related mood disorders: A systematic review. *Neurobiol Stress.* 15:100380. doi: 10.1016/j.ynstr.2021.100380

Perumal, M. B., and Sah, P. (2022). A protocol to investigate cellular and circuit mechanisms generating sharp wave ripple oscillations in rodent basolateral amygdala using ex vivo slices. *STAR Protoc.* 3:101085. doi: 10.1016/j.xpro.2021.101085

Petković, A., and Chaudhury, D. (2022). Encore: Behavioural animal models of stress, depression and mood disorders. *Front. Behav. Neurosci.* 16:931964. doi: 10.3389/fnbeh.2022.931964

Phillips, M. L., Drevets, W. C., Rauch, S. L., and Lane, R. (2003). Neurobiology of emotion perception II: Implications for major psychiatric disorders. *Biol. Psychiatry* 54, 515–528. doi: 10.1016/S0006-3223(03)00171-9

Piantadosi, S. C., French, B. J., Poe, M. M., Timić, T., Marković, B. D., Pabba, M., et al. (2016). Sex-Dependent Anti-Stress Effect of an α5 Subunit Containing $GABA_A$ Receptor Positive Allosteric Modulator. *Front. Pharmacol.* 7:446. doi: 10.3389/fphar.2016.00446

Pisu, M. G., Concas, L., Siddi, C., Serra, M., and Porcu, P. (2022). The Allopregnanolone Response to Acute Stress in Females: Preclinical and Clinical Studies. *Biomol. Ther.* 12:1262. doi: 10.3390/biom12091262

Porcu, P., Barron, A. M., Frye, C. A., Walf, A. A., Yang, S. Y., He, X. Y., et al. (2016). Neurosteroidogenesis Today: Novel Targets for Neuroactive Steroid Synthesis and Action and Their Relevance for Translational Research. *J. Neuroendocrinol.* 28:12351. doi: 10.1111/jne.12351

Romano-Torres, M., Borja-Lascurain, E., Chao-Rebolledo, C., del-Río-Portilla, Y., and Corsi-Cabrera, M. (2002). Effect of diazepam on EEG power and coherent activity: sex differences. *Psychoneuroendocrinology* 27, 821–833. doi: 10.1016/s0306-4530(01)00082-8

Romeo, E., Ströhle, A., Spalletta, G., di Michele, F., Hermann, B., Holsboer, F., et al. (1998). Effects of antidepressant treatment on neuroactive steroids in major depression. *Am. J. Psychiatry* 155, 910–913. doi: 10.1176/ajp.155.7.910

Rougé-Pont, F., Mayo, W., Marinelli, M., Gingras, M., Le Moal, M., and Piazza, P. V. (2002). The neurosteroid allopregnanolone increases dopamine release and dopaminergic response to morphine in the rat nucleus accumbens. *Eur. J. Neurosci.* 16, 169–173. doi: 10.1046/j.1460-9568.2002.02084.x

Rush, A. J., Trivedi, M. H., Wisniewski, S. R., Nierenberg, A. A., Stewart, J. W., Warden, D., et al. (2006). Acute and longer-term outcomes in depressed outpatients requiring one or several treatment steps: a STAR*D report. *Am. J. Psychiatry* 163, 1905–1917. doi: 10.1176/ajp.2006.163.11.1905

Saletu, B., Anderer, P., and Saletu-Zyhlarz, G. M. (2006). EEG topography and tomography (LORETA) in the classification and evaluation of the pharmacodynamics of psychotropic drugs. *Clin. EEG Neurosci.* 37, 66–80. doi: 10.1177/155005940603700205

Saletu, B., Anderer, P., and Saletu-Zyhlarz, G. M. (2010). EEG topography and tomography (LORETA) in diagnosis and pharmacotherapy of depression. *Clin. EEG Neurosci.* 41, 203–210. doi: 10.1177/155005941004100407

Sasaki, T., Nishimura, Y., and Ikegaya, Y. (2017). Simultaneous Recordings of Central and Peripheral Bioelectrical Signals in a Freely Moving Rodent. *Biol. Pharm. Bull.* 40, 711–715. doi: 10.1248/bpb.b17-00070

Senn, V., Wolff, S. B., Herry, C., Grenier, F., Ehrlich, I., Gründemann, J., et al. (2014). Long-range connectivity defines behavioral specificity of amygdala neurons. *Neuron* 81, 428–437. doi: 10.1016/j.neuron.2013.11.006

Shahnouri, M., Abouhosseini, T. M., and Araghi, A. (2016). Neuropharmacological properties of farnesol in Murine model. *Iran J Vet Res.* 17, 259–264.

Shikano, Y., Sasaki, T., and Ikegaya, Y. (2018). Simultaneous Recordings of Cortical Local Field Potentials, Electrocardiogram, Electromyogram, and Breathing Rhythm from a Freely Moving Rat. *J. Vis. Exp.* 134:56980. doi: 10.3791/56980

Sigel, E. (2002). Mapping of the benzodiazepine recognition site on GABAA receptors. *Curr. Top. Med. Chem.* 2, 833–839. doi: 10.2174/1568026023393444

Sripada, R. K., Welsh, R. C., Marx, C. E., and Liberzon, I. (2014). The neurosteroids allopregnanolone and dehydroepiandrosterone modulate resting-state amygdala connectivity. *Hum. Brain Mapp.* 35, 3249–3261. doi: 10.1002/hbm.22399

Stell, B., Brickley, S., Tang, C. Y., Farrant, M., and Mody, I. (2003). Neuroactive steroids reduce neuronal excitability by selectively enhancing tonic inhibition mediated by δ subunit-containing GABAAreceptors. *Proc. Natl. Acad. Sci. U. S. A.* 100, 14439–14444. doi: 10.1073/pnas.2435457100

Tovote, P., Fadok, J. P., and Lüthi, A. (2015). Neuronal circuits for fear and anxiety. *Nat. Rev. Neurosci.* 16, 317–331. doi: 10.1038/nrn3945

Tzovara, A., Meyer, S. S., Bonaiuto, J. J., Abivardi, A., Dolan, R. J., Barnes, G. R., et al. (2019). High-precision magnetoencephalography for reconstructing amygdalar and hippocampal oscillations during prediction of safety and threat. *Hum. Brain Mapp.* 40, 4114–4129. doi: 10.1002/hbm.24689

Uzunova, V., Sheline, Y., Davis, J. M., Rasmusson, A., Uzunov, D. P., Costa, E., et al. (1998). Increase in the cerebrospinal fluid content of neurosteroids in patients with unipolar major depression who are receiving fluoxetine or fluvoxamine. *Proc. Natl. Acad. Sci. U. S. A.* 95, 3239–3244. doi: 10.1073/pnas.95.6.3239

van Broekhoven, F., Bäckström, T., van Luijtelaar, G., Buitelaar, J. K., Smits, P., and Verkes, R. J. (2007). Effects of allopregnanolone on sedation in men, and in women on oral contraceptives. *Psychoneuroendocrinology* 32, 555–564. doi: 10.1016/j.psyneuen.2007.03.009

Vida, I., Bartos, M., and Jonas, P. (2006). Shunting inhibition improves robustness of gamma oscillations in hippocampal interneuron networks by homogenizing firing rates. *Neuron* 49, 107–117. doi: 10.1016/j.neuron.2005.11.036

Visser, S. A., Wolters, F. L. C., Gubbens-Stibbe, J. M., Tukker, E., van der Graaf, P. H., Peletier, L. A., et al. (2003). Mechanism-based pharmacokinetic/pharmacodynamic modeling of the electroencephalogram effects of $GABA_A$ receptor modulators: in vitro-in vivo correlations. *J. Pharmacol. Exp. Ther.* 304, 88–101. doi: 10.1124/jpet.102.042341

Wade, E. C., and Iosifescu, D. V. (2016). Using electroencephalography for treatment guidance in major depressive disorder. *Biol Psychiatry Cogn Neurosci Neuroimag.* 1, 411–422. doi: 10.1016/j.bpsc.2016.06.002

Walton, N. L., Antonoudiou, P., Barros, L., Dargan, T., DiLeo, A., Evans-Strong, A., et al. (2023). Impaired Endogenous Neurosteroid Signaling Contributes to Behavioral Deficits Associated With Chronic Stress. *Biol. Psychiatry* S0006-3223, 00050–00051. doi: 10.1016/j.biopsych.2023.01.022

Wu, W., Zhang, Y., Jiang, J., Lucas, M. V., Fonzo, G. A., Rolle, C. E., et al. (2020). An electroencephalographic signature predicts antidepressant response in major depression. *Nat. Biotechnol.* 38, 439–447. doi: 10.1038/s41587-019-0397-3

Yawata, Y., Shikano, Y., Ogasawara, J., Makino, K., Kashima, T., Ihara, K., et al. (2023). Mesolimbic dopamine release precedes actively sought aversive stimuli in mice. *Nat. Commun.* 14:2433. doi: 10.1038/s41467-023-38130-3

frontiers | Frontiers in Cellular Neuroscience

TYPE Original Research
PUBLISHED 14 February 2024
DOI 10.3389/fncel.2024.1334244

OPEN ACCESS

EDITED BY
Goichi Miyoshi,
Gunma University, Japan

REVIEWED BY
Santos Franco,
University of Colorado Anschutz Medical Campus, United States
Shigeyuki Esumi,
Kumamoto University, Japan

*CORRESPONDENCE
Timothy J. Petros
✉ tim.petros@nih.gov

†These authors have contributed equally to this work

RECEIVED 06 November 2023
ACCEPTED 31 January 2024
PUBLISHED 14 February 2024

CITATION
Rhodes CT, Asokumar D, Sohn M, Naskar S, Elisha L, Stevenson P, Lee DR, Zhang Y, Rocha PP, Dale RK, Lee S and Petros TJ (2024) Loss of Ezh2 in the medial ganglionic eminence alters interneuron fate, cell morphology and gene expression profiles. *Front. Cell. Neurosci.* 18:1334244. doi: 10.3389/fncel.2024.1334244

Loss of Ezh2 in the medial ganglionic eminence alters interneuron fate, cell morphology and gene expression profiles

Christopher T. Rhodes[1], Dhanya Asokumar[1,2†], Mira Sohn[3†], Shovan Naskar[4†], Lielle Elisha[1], Parker Stevenson[4], Dongjin R. Lee[1], Yajun Zhang[1], Pedro P. Rocha[2,5], Ryan K. Dale[3], Soohyun Lee[4] and Timothy J. Petros[1*]

[1]Unit on Cellular and Molecular Neurodevelopment, *Eunice Kennedy Shriver* National Institute of Child Health and Human Development (NICHD), NIH, Bethesda, MD, United States, [2]Unit on Genome Structure and Regulation, *Eunice Kennedy Shriver* National Institute of Child Health and Human Development (NICHD), NIH, Bethesda, MD, United States, [3]Bioinformatics and Scientific Programming Core, *Eunice Kennedy Shriver* National Institute of Child Health and Human Development (NICHD), NIH, Bethesda, MD, United States, [4]Unit on Functional Neural Circuits, National Institute of Mental Health (NIMH), NIH, Bethesda, MD, United States, [5]National Cancer Institute (NCI), NIH, Bethesda, MD, United States

Introduction: Enhancer of zeste homolog 2 (Ezh2) is responsible for trimethylation of histone 3 at lysine 27 (H3K27me3), resulting in repression of gene expression. Here, we explore the role of Ezh2 in forebrain GABAergic interneuron development.

Methods: We removed *Ezh2* in the MGE by generating *Nkx2-1Cre;Ezh2* conditional knockout mice. We then characterized changes in MGE-derived interneuron fate and electrophysiological properties in juvenile mice, as well as alterations in gene expression, chromatin accessibility and histone modifications in the MGE.

Results: Loss of *Ezh2* increases somatostatin-expressing (SST+) and decreases parvalbumin-expressing (PV+) interneurons in the forebrain. We observe fewer MGE-derived interneurons in the first postnatal week, indicating reduced interneuron production. Intrinsic electrophysiological properties in SST+ and PV+ interneurons are normal, but PV+ interneurons display increased axonal complexity in *Ezh2* mutant mice. Single nuclei multiome analysis revealed differential gene expression patterns in the embryonic MGE that are predictive of these cell fate changes. Lastly, CUT&Tag analysis revealed that some genomic loci are particularly resistant or susceptible to shifts in H3K27me3 levels in the absence of *Ezh2*, indicating differential selectivity to epigenetic perturbation.

Discussion: Thus, loss of Ezh2 in the MGE alters interneuron fate, morphology, and gene expression and regulation. These findings have important implications for both normal development and potentially in disease etiologies.

KEYWORDS

interneurons, medial ganglionic eminence (MGE), EZH2 (enhancer of zeste homolog 2), epigenetics, neurodevelopment, single cell sequencing, Cut&Tag, histone methylation

1 Introduction

Inhibitory GABAergic interneurons are a heterogeneous cell population with dozens of subtypes displaying distinct morphologies, connectivity, electrophysiology properties, neurochemical markers and gene expression profiles (Bandler et al., 2017; Hu et al., 2017b; Lim et al., 2018; Williams and Riedemann, 2021). Perturbation of interneuron development and inhibition is associated with a range of disorders including epilepsy, schizophrenia and autism (Valiente and Marin, 2010; Bozzi et al., 2012; Inan et al., 2013; Contractor et al., 2021), and many disease-associated genes are enriched in prenatal immature interneurons and affect their development (Schork et al., 2019; Trevino et al., 2020; Paulsen et al., 2022). Forebrain interneurons originate from two transient structures in the embryonic ventral forebrain, the medial and caudal ganglionic eminences (MGE and CGE, respectively), and mature over the course of embryonic and postnatal development (Bandler et al., 2017; Hu et al., 2017b; Miyoshi, 2019; Williams and Riedemann, 2021). The MGE gives rise to distinct, non-overlapping interneuron subtypes, parvalbumin- (PV+) and somatostatin-expressing (SST+) interneurons (fast-spiking (FS) and non-fast spiking (NFS) interneurons, respectively).

Several factors regulate initial interneuron fate decisions within the MGE, including gradients of diffusible cues, spatial location of progenitors, temporal birthdates and the mode of neurogenesis (Flames et al., 2007; Glickstein et al., 2007; Wonders et al., 2008; Inan et al., 2012; Petros et al., 2015; Bandler et al., 2017, 2021; Mi et al., 2018; Allaway et al., 2021). The advent of single cell sequencing technologies over the last decade has generated a transcriptional and epigenetic 'ground truth' in the ganglionic eminences in mice (Mayer et al., 2018; Mi et al., 2018; Allaway et al., 2021; Bandler et al., 2021; Lee et al., 2022a; Rhodes et al., 2022), and more recently, in primates and humans (Nowakowski et al., 2017; Eze et al., 2021; Shi et al., 2021; Yu et al., 2021; Braun et al., 2022; Schmitz et al., 2022; Velmeshev et al., 2022; Zhao et al., 2022). With this baseline in place, researchers can better characterize how genetic and epigenetic perturbations affect the fate and maturation of GABAergic interneurons.

Epigenetic mechanisms play critical roles in gene expression during neurogenesis, and modifications of the chromatin landscape regulate cell state changes during neurodevelopment (Hirabayashi and Gotoh, 2010; Yao et al., 2016; Podobinska et al., 2017; Albert and Huttner, 2018). Alterations in epigenetic regulation can be associated with numerous neurodevelopmental disorders (Sokpor et al., 2017; Dall'Aglio et al., 2018; Wang et al., 2018). Enhancer of Zeste Homolog 2 (Ezh2) is the primary methyltransferase component of the Polycomb Repressive Complex 2 (PRC2) that is critical for trimethylation of histone 3 at lysine 27 (H3K27me3) resulting in gene repression (Muller, 1995; Cao et al., 2002; Aranda et al., 2015). *Ezh2* is an evolutionary conserved gene that is aberrantly overexpressed in several forms of cancerous tumors (Sun et al., 2022; Zeng et al., 2022). *Ezh2* expression is enriched in neural precursor cells where it represses target genes crucial to cell fate decisions and, in concert with other epigenetic marks, generates a transcriptional memory of specific gene expression patterns through cell divisions (Rice and Allis, 2001; Zaidi et al., 2011; Aranda et al., 2015). *EZH2* variants can lead to Weaver Syndrome, a complex disease with variable degrees of intellectual disability (Tatton-Brown et al., 2013; Cohen et al., 2016), and dysregulation of H3K27me3 may be the primary driver in ataxia-telangiectasia (Li et al., 2013). Loss of *Ezh2* can lead to ectopic exiting of the cell cycle and premature neuronal differentiation (Pereira et al., 2010; Zemke et al., 2015; Kim et al., 2018; Buontempo et al., 2022; Wu et al., 2022), neuronal migration defects (Di Meglio et al., 2013; Zhao et al., 2015), altered neuronal fate (Zemke et al., 2015; Feng et al., 2016; Wever et al., 2019) and changes in neuronal morphology and cognitive defects (von Schimmelmann et al., 2016; Zhang et al., 2019). Thus, Ezh2 is an important player in epigenetic regulation of neuronal fate and maturation, but a role for Ezh2 in forebrain GABAergic interneurons has not been explored.

We generated conditional *Ezh2* knockout (cKO) mice to remove *Ezh2* from the MGE and observed an increase in SST+ and decrease in PV+ interneurons across multiple brain regions. These fate changes were due to *Ezh2* loss in cycling neural progenitors, as removing *Ezh2* in post-mitotic cells did not alter interneuron fate. While the intrinsic physiology of MGE-derived interneurons in *Ezh2* cKO mice was normal, fast-spiking cells displayed an increase in axonal length and branching. Fewer cortical MGE-derived interneurons were observed during the first postnatal week, which likely indicates decreased neurogenesis compared to WT mice. Single nuclei transcriptome analysis revealed an increase in *SST* expression and a decrease in genes predictive of PV-fated cells in the MGE of *Ezh2* cKO mice, consistent with the fate changes observed in the adult. Lastly, while a global downregulation of H3K27me3 was observed in the *Ezh2* cKO MGE, we observed that specific genomic loci were more susceptible to loss of *Ezh2* while other loci were more resistant, indicating that global loss of *Ezh2* had a differential effect of H3K27me3 at specific loci. In sum, we demonstrate that loss of *Ezh2* disrupts H3K27me3, alters gene expression and cell proliferation in the MGE, which in turn disrupts the normal balance of SST+ and PV+ interneurons in the forebrain.

2 Materials and methods

2.1 Animals

All experimental procedures were conducted in accordance with the National Institutes of Health guidelines and were approved by the NICHD Animal Care and Use Committee (protocol #20-047). The following mouse lines were used in this study: *Nkx2-1-Cre* (Jax# 008661) (Xu et al., 2008), $Ezh2^{F/F}$ (Jax# 022616) (Shen et al., 2008), *Dlx5/6-Cre* (Jax# 008199) (Monory et al., 2006) and *Ai9* (Jax# 007909) (Madisen et al., 2010). *Ezh2* genotyping was performed as previously described (Shen et al., 2008). For timed matings, noon on the day a vaginal plug was observed was denoted E0.5. Both embryonic and adult male and female embryonic mice were used without bias for all experiments.

2.2 Harvesting and fixing brain tissue

MGE dissections: E12.5 and E15.5 embryos were removed and placed in ice-cold carbogenated ACSF. Tails were clipped for PCR genotyping. During genotyping, embryonic brains were harvested

and MGEs were dissected from each embryo and stored in ice-cold carbogenated artificial cerebral spinal fluid (ACSF, in mM: 87 NaCl, 26 $NaHCO_3$, 2.5 KCl, 1.25 NaH_2PO_4, 0.5 $CaCl_2$, 7 $MgCl_2$, 10 glucose, 75 sucrose, saturated with 95% O_2, 5% CO_2, pH 7.4). For E12.5, the entire MGE was removed as previously described (Lee et al., 2022b). For E15.5, the MGE was dissected under a fluorescent dissecting microscope to ensure collection of only Tom+ MGE cells and minimize collection of post-mitotic MGE-derived cells in the striatum anlage and other ventral forebrain structures. Upon obtaining genotyping results (∼90 min), MGEs from embryos of the same genotype were combined (when applicable) to generate single nuclei dissociations.

Postnatal brain fixations: All mice ≥ P5 were terminally anesthetized with an i.p. injection of Euthasol (270 mg/kg, 50 μl injection per 30 g mouse) and perfused with 4% paraformaldehyde (PFA). In some cases, tail snips were collected for genotyping prior to perfusion. Brains were removed and post-fixed in 4% PFA O/N at 4°C, then cryoprotected in 30% sucrose in PBS O/N at 4°C before embedding in OCT. Brains were sectioned at 30 μm on a CryoStar™ NX50 cryostat and stored as floating sections in antifreeze solution (30% ethylene glycol, 30% glycerol, 40% PBS) at −20°C in 96-well plates.

Embryonic brain fixations: Pregnant dams were terminally anesthetized with an i.p. injection of Euthasol (270 mg/kg, 50 μl injection per 30 g mouse). E12.5-E15.5 embryos were removed and placed in ice cold carbogenated ACSF. Embryonic brains were removed and incubated in 4% PFA O/N at 4°C. In some cases, tail snips were collected for genotyping. Brains were washed in PBS, transferred to 30% sucrose in PBS and embedded in OCT upon sinking. Brains were sectioned at 14–16 μm, mounted directly onto Permafrost slides, and stored at −80°C.

2.3 Immunohistochemistry and fluorescent *in situ* hybridizations (FISH)

30 μm free floating sections from P30-40 brains were washed in PBS to remove antifreeze solution and incubated in blocking solution (10% Normal Donkey Serum in PBS + 0.3% Triton X-100) for 1–2 h. Sections were incubated with primary antibodies in blocking solution for 48 h at 4°C, then washed in PBS for 2–4 h at RT. Sections were incubated with secondary antibodies with DAPI in blocking solution O/N at 4°C, washed in PBS, mounted and imaged.

Cryosectioned E12.5-E15.5 brains sections were incubated with blocking buffer (10% Normal Donkey Serum in PBS + 0.1% Triton X-100) for 1 h at RT, then incubated in primary antibody solution in blocking buffer O/N at 4°C, washed in PBS for 1–2 h, then incubated with secondary antibodies with DAPI in blocking solution for 2 h at RT or O/N at 4°C. Slides were washed in PBS and imaged. The following antibodies were used in this study: rabbit-anti H3K27me3 (1:100, Cell Signaling 9733T), rat-anti SST (1:300, Millipore MAB354), goat-anti PV (1:1000, Swant PVG213), rabbit-anti PV (1:1000, Swant PV27), rabbit-anti nNos (1:500, Millipore MAB5380), rabbit anti-Olig2 (1;500, Millipore AB9610). Species-specific fluorescent secondary antibodies used were conjugated to AlexaFluor® 488, 647 and 790, and all used at 1:500.

RNAscope ISH assays™ (Advanced Cell Diagnostics) were performed on E12.5-E13.5 brain sections according to the manufacturer's instructions. The following probes were used in this study: *Nkx2-1* (434721), *Ezh2* (802751-C3), *Ezh1* (895231) and *tdTomato* (317041-C2).

All images were captured at 20X on a Zeiss Axioimager.M2 with ApoTom.2 (with Zen Blue software) or an Olympus VS200 Slide Scanner (VS200 ASW). Image post-processing was performed with Adobe Photoshop and ImageJ software.

2.4 Western blots and analysis

Core histone proteins from E13.5 MGE samples (pooled from 2 to 4 brains per genotype) were extracted using EpiQuik Total Histone Extraction kit (Epigentek# OP-0006). We obtained 40–80 μg of histone proteins per extraction and loaded 20 μg of protein onto a 4–12% Bis-Tris Plus mini gel (Invitrogen# NW04120BOX). Gels were run for ∼20 min at 200V using the Invitrogen mini gel tank with Blot MES SDS Running buffer. Gels were transferred to iBlot2 polyvinylidene difluoride (PVDF) membranes (Invitrogen# IB24001) in the iblot2 at 20V for 7 min. Blots were incubated with the primary antibody, mouse anti-H3 (Cell Signaling Technology# 3638S; 1:1000) and Rabbit anti-H3K27me3 (Cell Signaling Technology# 9733S; 1:500) overnight at 4°C, and then incubated with secondary anti-mouse-Starbright Blue-520 (Bio-Rad# 64456855; 1:2000) and anti-Rabbit-Starbright Blue-700 (Bio-Rad# 64484700; 1:2000) for 1 h at room temperature. Blots were imaged on a Bio-Rad ChemiDoC MP imaging system.

For analysis, a box was drawn around the ROI in each lane, with the same sized box used for both H3 and H3K27me3 signals for the WT, Het and cKO lanes in each blot. The average (mean) gray value was calculated in each box, then a lane-specific background signal taken just below each ROI was subtracted from each value. For normalization, each H3K27me3 value was divided by the corresponding H3 value for each lane (e.g., WT H3K27me3/WT H3). Then these Het and cKO values were divided by the WT value to determine the % of H3K27me3 signal compared to WT.

2.5 Cell counting

Adult brains: All cell counts were performed by hand and blind to genotypes. Total brains counted for *Nkx2-1-Cre;Ezh2;Ai9* mice: WT = 5, Het = 5, cKO = 6, from 4 different litters. Total brains counted for *Dlx5/6-Cre;Ezh2;Ai9* mice: WT = 4, Het = 3, cKO = 5, from 3 different litters. Counted cells consisted of either Tom+, Tom+/SST+, or Tom+/PV+ (and in the hippocampus, Tom+/nNos+); any SST+, PV+ or nNos+ cells that were Tom- were excluded from counts since they likely did not recombine at the *Ezh2* (or Ai9) locus. For all sections, area was calculated using "Measurement" function in Photoshop, and all average areas described below include WT, het and cKO brains. Cortex: Counts were performed in somatosensory cortex on 3 non-consecutive sections per brain, then averaged together. Individual cortical images were divided into superficial and deep sections using DAPI staining to define the layer III-IV boundary. Average cortical area/section = 0.85 mm^2. Striatum: Counts were performed on 3

sections per brain, one section each through the anterior, middle and posterior striatum, then averaged together. Average striatal area/section = 3.15 mm^2. Hippocampus: Counts were performed on 8 non-consecutive sections per brain, then averaged together. More hippocampal sections were counted per brain due to the comparatively low number and section-to-section variability of Tom+ cells in the hippocampus. Sections were restricted to the anterior and middle hippocampus; the posterior hippocampus was excluded due to greater variability in interneuron density in this region. Hippocampal sections were divided into CA1, CA2/3 and DG regions using DAPI staining. Small Tom+ cell bodies (identified as oligodendrocytes) in CA2/3 were excluded from interneuron counts and counted as separate group. Average CA1 area/section = 0.98 mm^2, average CA2/3 area/section = 0.49 mm^2, average DG area/section = 0.60 mm^2.

P5 brains: All cell counts were performed by hand and blind to genotypes. Total brains counted for *Nkx2-1-Cre;Ezh2;Ai9* mice: WT = 4 and cKO = 4, from 4 different litters. Counts were performed in somatosensory cortex on 3 non-consecutive sections per brain, then averaged together. Individual cortical images were divided into superficial and deep sections using DAPI staining. Average cortical area/section = 0.92 mm^2.

2.6 *In vitro* electrophysiology

Slice preparation: P30-P40 *Nkx2-1-Cre*;*Ezh2* WT and cKO mice were anesthetized with isoflurane [5% isoflurane (vol/vol) in 100% oxygen], perfused transcardially with an ice-cold sucrose solution containing (in mM) 75 sucrose, 87 NaCl, 2.5 KCl, 26 $NaHCO_3$, 1.25 NaH_2PO_4, 10 glucose, 0.5 $CaCl_2$, and 2 $MgSO_4$, saturated with 95% O_2 and 5% CO_2 and decapitated. Brain was rapidly removed from the skull and transferred to a bath of ice-cold sucrose solution. Coronal slices of 300 μm were made using a vibratome (Leica Biosystems) and were stored in the same solution at 35°C for 30 min and at room temperature (RT) for an additional 30–45 min before recording.

Electrophysiology: Whole-cell patch clamp recordings on tdTomato+ cells in cortical layers V/VI cells were performed in oxygenated ACSF containing (in mM) 125 NaCl, 2.5 KCl, 26 $NaHCO_3$, 1.25 NaH_2PO_4, 10 glucose, 2 $CaCl_2$ and 1 $MgCl_2$. The ACSF was equilibrated with 95% O_2 and 5% CO_2 throughout an entire recording session which typically lasted between 30 min to 1 h to ensure sufficient permeation of neurobiotin. Recordings were performed at 30°C–33°C. Electrodes (3–7 MΩ) were pulled from borosilicate glass capillary (1.5 mm OD). The pipette intracellular solution contained (in mM) 130 potassium gluconate, 6.3 KCl, 0.5 EGTA, 10 HEPES, 5 sodium phosphocreatine, 4 Mg-ATP, 0.3 Na-GTP and 0.3% neurobiotin (pH 7.4 with KOH, 280–290 mOsm). Membrane potentials were not corrected for the liquid junction potential. During patching, cell-attached seal resistances were > 1 GΩ. Once whole-cell configuration was achieved, uncompensated series resistance was usually 5–30 MΩ and only cells with stable series resistance (<20% change throughout the recording) were used for analysis. Data were collected using a Multiclamp 700B amplifier (Molecular Devices), low-pass filtered at 10 kHz and digitally sampled at 20 kHz, and analyzed with pClamp10 (Molecular Devices). To characterize the intrinsic membrane properties of neurons, hyperpolarizing and depolarizing current steps were injected at 0.1 Hz under current-clamp configuration.

Data analysis: All intrinsic properties were measured in current-clamp configuration and calculated from 800 millisecond-long current injections unless noted otherwise. The resting membrane potential (in mV) was measured with 0 pA current injection a few minutes after entering whole-cell configuration. All other properties were measured holding the cell at −70 mV. Input resistance (in MΩ) was calculated using Ohm's law from averaged traces of 100 ms long negative current injections of −20 pA. Action potential (AP) threshold was calculated as the potential when voltage change over time was 10 mV/ms using the first observed spike. AP amplitude (in mV) was calculated as the time difference in potential from the spike peak to spike threshold. AP/spike half-width (in ms) was calculated as the difference in time between the ascending and descending phases of a putative spike at the voltage midpoint between the peak of spike and spike threshold. Adaptation ratio was calculated as the ratio of the number of APs in the number of spikes in the last 200 ms over the number of APs in the first 200 ms of a positive current injection that elicited approximately 20 Hz firing. Afterhyperpolarization (AHP) amplitude was calculated as the difference between AP threshold and the most negative membrane potential after the AP, measured on the response to the smallest current step evoking an AP (Rheobase). Membrane time constant (in ms) was determined from a monoexponential curve best fitting the falling phase of the response to a small hyperpolarizing current step.

2.7 CUBIC clearing and streptavidin staining

After performing electrophysiological recordings, brain slices were fixed in 4% PFA in 0.1M PB and kept overnight at 4°C and then kept in 20% sucrose (in PB). The brain slices were processed for CUBIC (Clear, Unobstructed Brain/Body Imaging Cocktails and Computational analysis) clearing (Susaki et al., 2014). Slices were first washed with 0.1M PB (3 times for 10 min) at RT, followed by immersion in CUBIC reagent 1 for 2 days at 4°C. After 2 days of incubation, slices were washed with 0.1M PB (4 times for 30 min) at RT to ensure complete removal of CUBIC reagent 1. Slices were then incubated in fluorophore-conjugated streptavidin (1:500; ThermoFisher Scientific) in 0.1M PB (0.5% TritonX-100) overnight at 4°C. Slices were subsequently washed with 0.1M PB (4 times, 30 min) at RT and mounted with CUBIC reagent 1. Filled neurons were imaged with a Nikon A1R confocal microscope. Z-stacked images (each stack 1 μm) were acquired with a 40X oil-immersion objective.

2.8 Sholl analysis

Neurobiotin-filled neurons were processed and reconstructed using the Neurolucida 360 software (NL360) (MBF Biosciences). Briefly, image stack files were converted to JPEG 2000 file format with a MicroFile+ software, and the converted images were loaded

into the NL360 software package. Neurites of PV were then traced manually in a 2D environment. Among the traced neurites, dendrites were easily distinguishable from axons, whose extensive ramifications maintained a constant diameter and had varicosities. Branched structure and Sholl analysis were performed using the built-in functions of the Neurolucida explorer, in which a series of concentric spheres (10 μm interval between radii) were created around the middle point (soma of the traced neuron).

2.9 Generating single nuclei suspensions for CUT&Tag and multiome experiments

Single nuclei suspensions were prepared as previously described (Lee et al., 2022a,b) with slight modifications. CUT&Tag: MGEs were transferred to a 1 mL Dounce homogenizer containing DNA Lysis Buffer (10 mM Tris–HCl (Ph.7.4), 10 mM NaCl, 3 mM $CaCl_2$, 0.1% Tween-20, 1.5% BSA and 0.1% IGEPAL CA-630 in nuclease-free water, 1 mL per sample). Cells were dounced with pestle A and pestle B, ∼10–15 times each, and pipetted through a 40 μm filter onto a pre-chilled 50 mL conical tube on ice and wet with 1 mL of DNA Nuclei Wash Buffer [in mM: 10 Tris–HCl (Ph.7.4), 10 NaCl, 3 $CaCl_2$, with 0.1% Tween-20 and 1.5% BSA in nuclease-free water, 5 mL per sample]. Lysed nuclei suspensions were then passed through a pre-wetted filter, and dounce was rinsed with 1 mL Nuclei Wash Buffer and passed through filter. After filtering, nuclei suspension was divided into 2 pre-chilled 2 mL tubes and spun at 500 g for 5 min at 4°C. After removing supernatant, nuclei pellet was washed once with 1 mL Nuclei Wash Buffer and then with 1 mL of 1X CUT&Tag Wash Buffer (from Active Motif CUT&Tag IT Assay kit), spinning with same conditions above. CUT&Tag Wash Buffer was removed, leaving ∼30–50 μL in each tube, and solutions were triturated and combined. Nuclei concentration was determined on Countess II FL Automated Cell Counter. 100,000–125,000 nuclei were used for each CUT&Tag reaction using the CUT&Tag IT Assay Kit (Active Motif, #53610) per manufacturer's instructions. Primary antibody was rabbit-anti H3K27me3 (Cell Signaling, #9733T, 1:50) or rabbit-anti H3K27ac (Cell Signaling, #8173; 1:50), and secondary antibody was guinea pig anti-rabbit (Active Motif, 105465 from CUT&Tag IT kit, 1:100).

10x Genomics Multiome kit: MGEs were transferred to a 1 mL Dounce homogenizer containing Multiome Lysis Buffer [in mM: 10 Tris–HCl (Ph.7.4), 10 NaCl, 3 $CaCl_2$, 1 DTT, with 0.1% Tween-20, 1.5% BSA and 0.1% IGEPAL CA-630 in nuclease-free water, 1 mL per sample]. Cells were lysed by douncing with pestle A and pestle B, ∼10–15 times each. A 40 μm filter was placed onto a pre-chilled 50 mL conical tube on ice and wet with 1 mL of Multiome Nuclei Wash Buffer [in mM: 10 Tris–HCl (Ph.7.4), 10 NaCl, 3 $CaCl_2$, 1 DTT, with 0.1% Tween-20, 1.5% BSA and 1 U/μL in nuclease-free water, 5 mL per sample]. Nuclei suspension was then passed through pre-wetted filter, and dounce was rinsed with 1 mL Multiome Wash Buffer and passed through filter. After filtering, nuclei suspension was divided into 2 pre-chilled 2 mL tubes and spin at 500 g for 5 min at 4°C. After removing supernatant, nuclei pellet was washed twice with 1 mL Multiome Wash Buffer and spun as above. Multiome Wash Buffer was removed, leaving ∼20–30 μL of solution in each tube. Solution was then triturated to dissociate pellets and nuclei suspensions combined into 1 tube. Nuclei concentration was determined on Countess II FL Automated Cell Counter. Nuclei suspensions were diluted to ∼3,000–4,000 nuclei/μL, with 5 μL being used for 10x Genomics Multiome kit per manufacturer's instructions. E15.5 data: MGE from 4 WT, Het and cKO embryos from 2 different E15.5 litters were combined to generate 1 biological rep. E12.5 data: MGE from 1 WT, Het and cKO mouse from a single E12.5 litter were used to generate 1 biological rep. Total cell numbers that passed QC: E12.5 WT = 6,391; E12.5 Het = 6,608; E12.5 cKO = 8,546; E15.5 WT = 11,477; E15.5 Het = 10,027; E15.5 cKO = 8,607.

2.10 CUT&Tag sequencing and analysis

Following library amplification, DNA quantity was determined with a Qubit and library quality characterized with an Agilent Tapestation. Libraries were balanced for DNA content and pooled before performing a final SPRI select bead 1x left size selection and paired-end sequenced (50 x 50 bp) on an Illumina NovaSeq. Sequencing read depths per library are detailed in **Supplementary Table 5**.

Paired-end run Illumina NovaSeq produced 2 compressed fastq.gz files for each replicate. For each age (E12.5 and E15.5) and each genotype, a total of 3 different biological reps from 3 different experiments were combined. Adaptor sequences were removed using cutadapt (Martin, 2011) v3.4 with the following parameters: -a AGATCGGAAGAGCACACGTCTGAACTCCAGTCA -A AGATCGGAAGAGCGTCGTGTAGGGAAAGAGTGT -q 20 –minimum-length 25. Trimmed reads were mapped to mouse reference genome (GRCm38/mm10) using bowtie2 (Langmead and Salzberg, 2012) v2.4.2 with the following parameters: –no-unal -N 1 –no-mixed –no-discordant –very-sensitive-local –local –phred33 -I 10. Aligned reads in sam files were further processed to remove multimappers if MAPQ was less than 10 (-q 10) and then sorted using samtools (Danecek et al., 2021) v1.12. Aligned reads that intersected blacklist regions (Amemiya et al., 2019) were removed and saved to bam files using bedtools (Quinlan and Hall, 2010) v2.30.0. PCR duplicates were removed from the bam files using picard MarkDuplicates v2.25.2.[1] Bigwig files were created from bam files using deepTools (Ramirez et al., 2016) (v3.5.1) bamCoverage with the following parameters: –binSize 5 –normalizeUsing RPKM. Peaks/domains were called using Epic2 (Stovner and Saetrom, 2019) on each bam file with the parameters –genome mm10 –guess-bampe and saved to bed files. Peak widths ranged from 200 bp to 261 kb, with a mean of 5.1 kb and median of 3.2 kb. Peaks were visualized using the Integrative Genomics Viewer (IGV) (Robinson et al., 2011) v2.16.1 by importing bigwig and bed files, respectively.

2.10.1 Differential analysis

Differentially enriched peaks were analyzed using edgeR (Robinson et al., 2010) v3.32.1 implemented in DiffBind (Ross-Innes et al., 2012) v3.0.15 in R v4.0.3.[2] Similarity in raw peak profiling across the samples was analyzed through PCA and a sample correlation heatmap using DiffBind::plotPCA and DiffBind::plot, respectively. For differential testing, CUT&Tag

1 https://broadinstitute.github.io/picard/

2 https://cran.r-project.org/

reads were counted in consensus peaks with default width in DiffBind::dba.count. The counts were subsequently normalized using the TMM (Robinson and Oshlack, 2010) method by setting the normalize argument to DBA_NORM_TMM in DiffBind::dba.normalize. In the TMM method, raw CUT&Tag counts, which were aggregated per consensus peak, were normalized using normalization factors that represented library size for moderately counted peaks. To determine normalization factors, peak-wise proportions of peak abundance in log2 scale were calculated between cKO and WT for individual consensus peaks. These proportions are defined as M values. M values calculated from peaks with extreme abundance were subsequently removed. A normalization factor for a sample is the weighted mean of the trimmed M values, where the weight is the inverse of the consensus peak's approximate variance. The false discovery rate (FDR) was determined using the Benjamini–Hochberg (BH) (Benjamini and Hochberg, 1995) method for multiple hypothesis testing. Peaks with an FDR < 0.1 were considered statistically significant. Given the range of peak sizes, multiple settings for the "summit width" of DiffBind were used: (1) the default of using only reads in the 400 bp around the highest detected position within a peak; (2) extending this width to 2kb; and (3) disabling any summit to use reads from the whole peak/domain. Differential binding results differed slightly but were largely concordant across parameter choices, and the default of 400 bp was selected for further analysis because it best matched biological expectations.

Peaks were annotated to the nearest genes using ChIPseeker package (Yu et al., 2015) in R v4.0.3. For the TxDb and annoDb arguments in ChIPseeker::annotatePeak, we used TxDb.Mmusculus.UCSC.mm10.knownGene (DOI: 10.18129/B9.bioc.TxDb.Mmusculus.UCSC.mm10.knownGene) and org.Mm.eg.db (DOI: 10.18129/B9.bioc.org.Mm.eg.db), respectively. The transcript start site (TSS) region was defined as ranging from −5kb to +5kb. Statistically significant loci were visualized in MA plots (also known as Bland-Altman plots) using ggplot2 v3.3.3 in R.

2.11 Multiome sequencing and analysis

Joint libraries for snRNA-seq and snATAC-seq were created using 10x Genomics Single Cell Multiome ATAC + Gene Expression kit (1000285) by following manufacturer's protocols. Sequencing was conducted with paired-end (50 x 50 bp) using an Illumina HiSeq 2500 (E12.5 snATAC-seq) or NovaSeq 6000 (E12.5 snRNA-seq, E15.5 snATAC-seq, E15.5 snRNA-seq), with detailed sequencing depth data in **Supplementary Table 6**.

The Cell Ranger ARC (v2.0.0) pipeline was used to process sequenced libraries with default parameters unless otherwise noted. Demultiplexed FASTQ files were generated by cellranger-arc mkfastq from BCL files. Reads were aligned to custom-built mouse (GRCm38/mm10) reference genome modified to include tdTomato using cellranger-arc count. Reads with de-duplicated and valid cell barcodes were used to build gene-by-barcode (snRNA-seq) and peak-by-barcode (snATAC-seq) matrices by cellranger-arc count per genotype. Individual matrices were aggregated to a single feature-barcode matrix file containing every genotype using cellranger-arc aggr without depth normalization (–normalize = none).

2.11.1 snRNA-seq data analysis

Seurat: An aggregated feature-barcode matrix was used as input to Seurat (Satija et al., 2015) (v4.0.5[3]) in R (v4.1.1, see text footnote 2). After imputing missing values to zero in metadata, outlier removal was performed on the number of counts per gene and percent reads mapping to mitochondrial genome (mitochondrial percentage). Lower limits for the number of counts per gene and mitochondrial percentage were set to 100 counts per gene and three standard deviations (SD) below the mean, respectively. Upper limits were set to three SD above the mean for both metrics. Negative datapoints created by subtraction of three SD from the mean were reset to 1, while datapoints that exceeded the upper limits were reset to the maximum datapoint. Cells were removed if they were more extreme then the upper/lower limits, or if they were eliminated from the snATAC-seq dataset during QC. The numbers of cells passing QC were: WT E12.5: 6,391; WT E15.5: 11,477; Het E12.5: 6,608; Het E15.5 10,027; cKO E12.5: 8,546; cKO E15.5: 8,607. Remaining cells were proceeded to the normalization workflow using Seurat::SCTransform using default parameters. For integration of snRNA-seq datasets from E12.5 and E15.5, 3,000 variable features were found using Seurat::SelectIntegrationFeatures on SCTransformed data. Prior to integration, anchors were identified using Seurat::FindIntegrationAnchors with the parameters dims, anchors.features, and normalization.method set to 1:30, the 30,000 variable features, and SCT, respectively. The integration was performed using Seurat::IntegrateData with identical dims and normalization.method to those from Seurat::FindIntegrationAnchors, along with the computed anchors. Dimensionality reduction was performed using Seurat::RunPCA and Seurat::RunUMAP with the parameters dims and umap.method set to 1:25 and uwot, respectively, on the integrated data.

2.11.2 snATAC-seq data analysis

Signac: An aggregated peak-by-barcode matrix was used as input to Signac (Stuart et al., 2021) (v1.4.0[4]) pipeline in R (v4.1.1). After imputing missing values in metadata as described above, outlier removal was performed on the number of chromatin accessibility peaks, transcription start site (TSS) enrichment score, and mitochondrial percentage. Lower limits were set to 1,000 counts per feature for the number of peaks and 2 for TSS enrichment score. Lower limit for mitochondrial percentage and all the upper limits were determined as described in the snRNA-seq analysis. Cells were removed if they were more extreme than the lower/upper limits in individual metrics, or if they were eliminated in corresponding snRNA-seq dataset during QC. Peaks were normalized via Term Frequency–Inverse Document Frequency (TF-IDF) method using Signac::RunTFIDF with default parameters. Highly variable peaks were found by Signac::FindTopFeatures with the min.cutoff set to 10. Dimensionality reduction was performed using Signac::RunSVD with default parameters. For integration of snATAC-seq datasets from E12.5 and E15.5, anchors were identified using Seurat::FindIntegrationAnchors with the parameters anchor.features and dims set to all features and

3 https://satijalab.org/seurat/

4 https://stuartlab.org/signac

2:30, respectively. Integration of two snATAC-seq datasets was conducted using Seurat::IntegrateEmbeddings taking advantage of reciprocal LSI projection (RLSI), as instructed by Signac standard workflow. The Seurat::IntegrateEmbeddings ran using the previously computed anchors and 1 to 30 dimensions.

2.11.3 Multimodal analysis

Seurat: Multimodal data integration was started by finding Weighted Nearest Neighbor (WNN) (Hao et al., 2021) using Seurat::FindMultiModalNeighbors on snRNA-seq and snATAC-seq datasets with or without age-specific integration along with reduction lists set to Principal Component Analysis (PCA) (1–25 dimensions) for snRNA-seq and RLSI (1–20 dimensions) for snATAC-seq. Subsequent dimensionality reduction was performed using Seurat::RunUMAP on weighted.nn with default parameters. Cells were clustered on the WNN graph with Leiden algorithm and resolution 0.8 using Seurat::FindClusters. To visualize the DEGs between populations subsetted using Seurat, we employed the EnhancedVolcano tool. For significant determination, parameters were set to pCutoff = $10e^{-6}$ and FCcutoff = 0.2. By default, the Uniform Manifold Approximation and Projection (UMAP) from the age-integrated multimodal analysis was utilized throughout the study. The expression of *Sst* and *Pde1a* genes in was examined on a multimodal UMAP at E15.5 without age integration.

For QC, the TSS enrichment score and the approximate ratio of mononucleosomal to nucleosome-free fragments (nucleosome signal) were computed using the functions Signac::TSSEnrichment and Signac::NucleosomeSignal with default parameters, respectively. The mitochondrial percentage was computed using the function Seurat::PercentageFeatureSet, which matches the pattern of gene names to "^[Mm][Tt]-".

2.11.4 Differential analysis via DA-seq

Single cell DA analysis was conducted using DA-seq (Zhao et al., 2021) (v1.0.0[5]) in R (v4.1.1). The DA-seq used a PCA matrix as input, which was computed by Seurat after the multimodal integration of age-integrated snRNA-seq and snATAC-seq datasets. Cells were projected onto 2D space based on UMAP coordinates, which were computed by Seurat after multimodal integration of age-integrated snRNA-seq and snATAC-seq datasets. DA cells were determined by running DAseq::getDAcells, with the k.vector parameter set to every 50 between 50 and 500, and DAseq::updateDAcells with the pred.thres parameter set to +/- 0.7. DA-seq conducted a random permutation test on abundance scores, using a threshold of +/- 0.7, to identify cells with an abundance score greater than 0.7 or less than −0.7.

2.11.5 Visualization of Multiome data

Uniform Manifold Approximation and Projection coordinates and WNN clustering, computed by Seurat on multimodal integrated datasets with or without age-specific integration, were imported to the Loupe Browser (v6.0.0, 10x Genomics). The expression of genes of interest and multimodal clustering were visualized using the Loupe Browser. DA analysis was visualized on a UMAP created using the functions DAseq::getDAcells and DAseq::updateDAcells in R, which take advantage of ggplot2 (v3.3.5). UMAPs visualizing the genotype and age in the DA analysis were generated using the Seurat::DimPlot. For QC, the following metrics were extracted from the metadata of the Seurat object: the number of ATAC fragments (nCount_ATAC), nucleosome signal (nucleosome_signal), the TSS enrichment score (TSS.enrichment), the number of RNA reads (nCount_RNA) and mitochondrial percentage (percent.mt). These metrics were then visualized using violin plots with the ggplot2 package in R.

To infer the developmental trajectories of E12.5 and E15.5 MGE cells across all conditions, Slingshot (Street et al., 2018) was used to generate trajectories onto UMAP projections. The Slingshot function was applied to the WNN matrix as described above, enabling the identification of neural developmental progression along the inferred trajectories.

2.12 Statistics and reproducibility

Cell counts: All cell counts were performed by hand and blind to genotype. Number of brain sections per mice and mice per genotype are described above and in figure legends. One-way ANOVA was used to compare WT, Het and cKO for all brain regions, followed by Tukey's Multiple Comparison Test to identify significant differences between conditions. All statistical analysis was performed on GraphPad Prism (version 9.4.1). All raw cell counts, ANOVA F- and *P*-values, and results of Tukey's multiple comparison tests related to **Figures 2–4**, **6**, **Supplementary Figures 2–4**, **6** can be found in the Source Data file.

Electrophysiology: Collection of data and analysis were not performed blind and were non-randomized. Data from electrophysiological recordings are presented throughout as mean ± s.e.m unless otherwise noted. Unless indicated, all statistical comparisons were non-parametric. Number of recorded neurons (n) and number of animals (N) used were reported for each figure. All data were analyzed using pClamp10, GraphPad Prism and Neurolucida 360 software.

Sample size determination: No statistical method was used to predetermine sample size. For Western Blots, we desired $n \geq 2$ biological replicates for each genotype to determine the percent of decreased H3K27me3 signal in the *Ezh2* cKO. For cell counts with *Nkx2-1-Cre* mice, we wanted $n \geq 5$ mice per genotype from at least 3 different litters. For cell counts with *Dlx5/6-Cre* mice, we wanted $n \geq 4$ WT and cKO mice per genotype from at least 3 different litters. For electrophysiological recordings, we wanted to record from ≥ 10 neurons for each condition. For the single nuclei Multiome experiments, we wanted a minimum of 5,000 high-quality sequenced nuclei per condition (age and genotype), which should be sufficient to identify significant differences between conditions. This goal required ∼15,000 nuclei input for each sample (with the expectation of recovering ∼30–70% of nuclei/cells for each reaction based on 10x Genomics recommendations and our previous experience). Viable nuclei that passed QC ranged from 6,391 to 11,477 nuclei per condition (see above). Per standard single nuclei sequencing protocols, nuclei that did not pass stringent QC measurements (nCount_RNA and % mitochondria reads for snRNA; nCount_ATAC, nucleosome_signal and TSS enrichment for snATAC) in the Multiome datasets were excluded from analysis (as detailed in **Supplementary Figure 7**). For the CUT&Tag experiments, we strove for 100,000 nuclei for each reaction (actual range from 90,000 to 120,000 per reaction), with $n = 3$ biological

5 https://klugerlab.github.io/DAseq

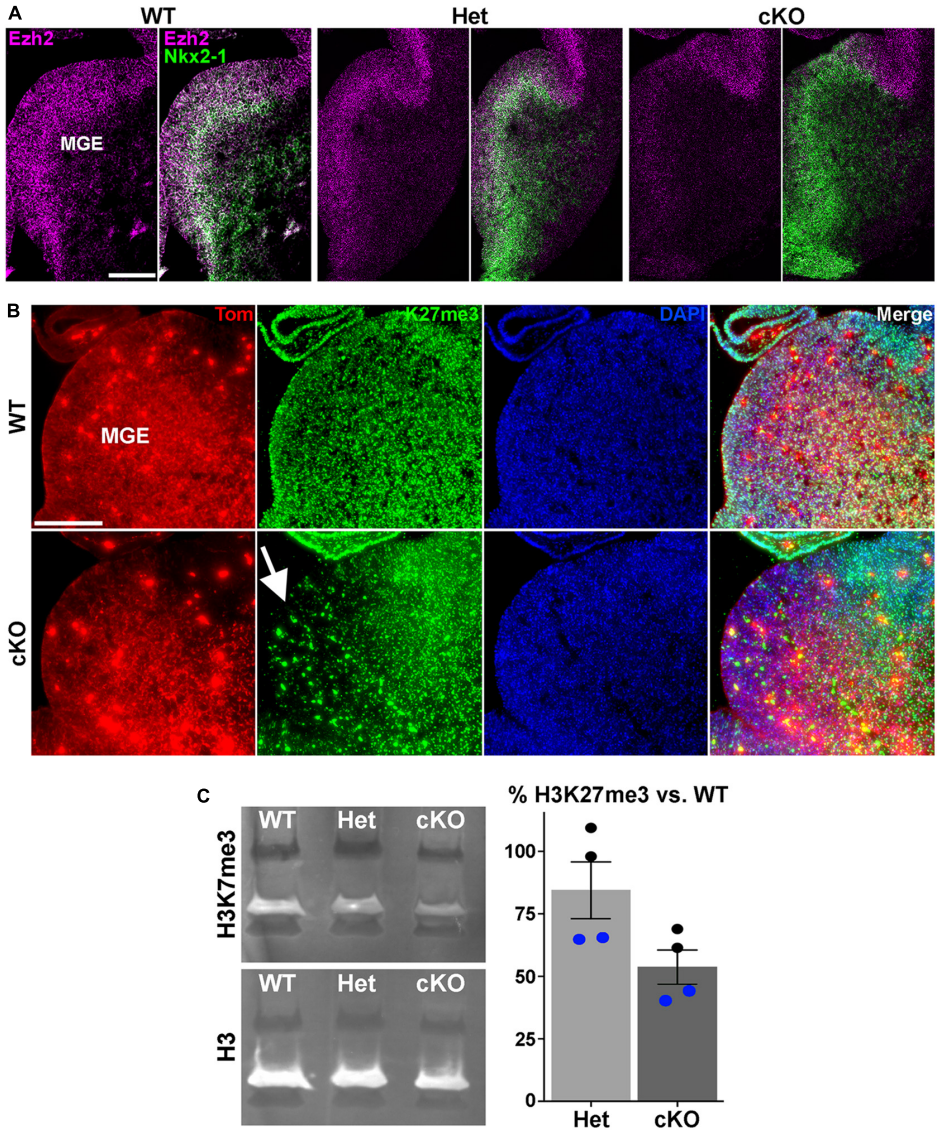

FIGURE 1
Loss of *Ezh2* and H3K27me3 in the MGE of *Ezh2* cKO mice. **(A)** *In situ* hybridizations of *Ezh2* (magenta) and *Nkx2-1* (green) in E12.5 brains of *Nkx2-1-Cre;Ezh2;Ai9* WT, Het and cKO mice. **(B)** Immunostaining in the MGE reveals a strong decrease of H3K27me3 (green) in the MGE of cKO mice (highlighted by white arrow). **(C)** Representative Western Blot showing H3K27me3 and H3 levels in E13.5 WT, Het and cKO MGE (left), and graph summarizing average H3K27me3 decrease in Het and cKO MGE compared to WT (right), with black and blue dots representing 2 different biological reps, with 2 technical reps each. Scale bars in panels **(A,B)** = 200 μm.

replicates for each condition (age and genotype). All computational and statistical analysis are discussed in detail above and/or in the legends of the relevant figures and tables. All attempts at replication were successful.

3 Results

3.1 Loss of *Ezh2* alters MGE-derived interneuron fate in the cortex and striatum

To characterize the function of *Ezh2* in MGE-derived interneurons, we crossed *Nkx2-1-Cre*$^{C/C}$;*Ezh2*$^{F/+}$ males with *Ai9*$^{F/F}$;*Ezh2*$^{F/+}$ females to generate *Nkx2-1-Cre*$^{C/+}$;*Ezh2*;*Ai9*$^{F/+}$ wildtype, heterozygous and conditional knockout mice (hereafter WT, Het and cKO mice, respectively). In these mice, *Ezh2* perturbation is restricted to MGE-derived cells in the telencephalon, and these cells also express tdTomato (Tom+). We first confirmed that *Ezh2* expression is strongly downregulated in the MGE of cKO mice (Figure 1A). Since Ezh2 is critical for tri-methylation at histone H3K27, we also verified a significant reduction in H3K27me3 in the MGE in cKO mice (Figure 1B). To quantify this decrease, we performed Western Blots on MGE tissue from WT, Het and cKO mice. We observed a 15% decrease of H3K27me3 signal in Hets and a 47% decrease in cKO MGE compared to WT levels (Figure 1C). Some of this remaining H3K27me3 in the cKO MGE likely arises from the

10.3389/fncel.2024.1334244

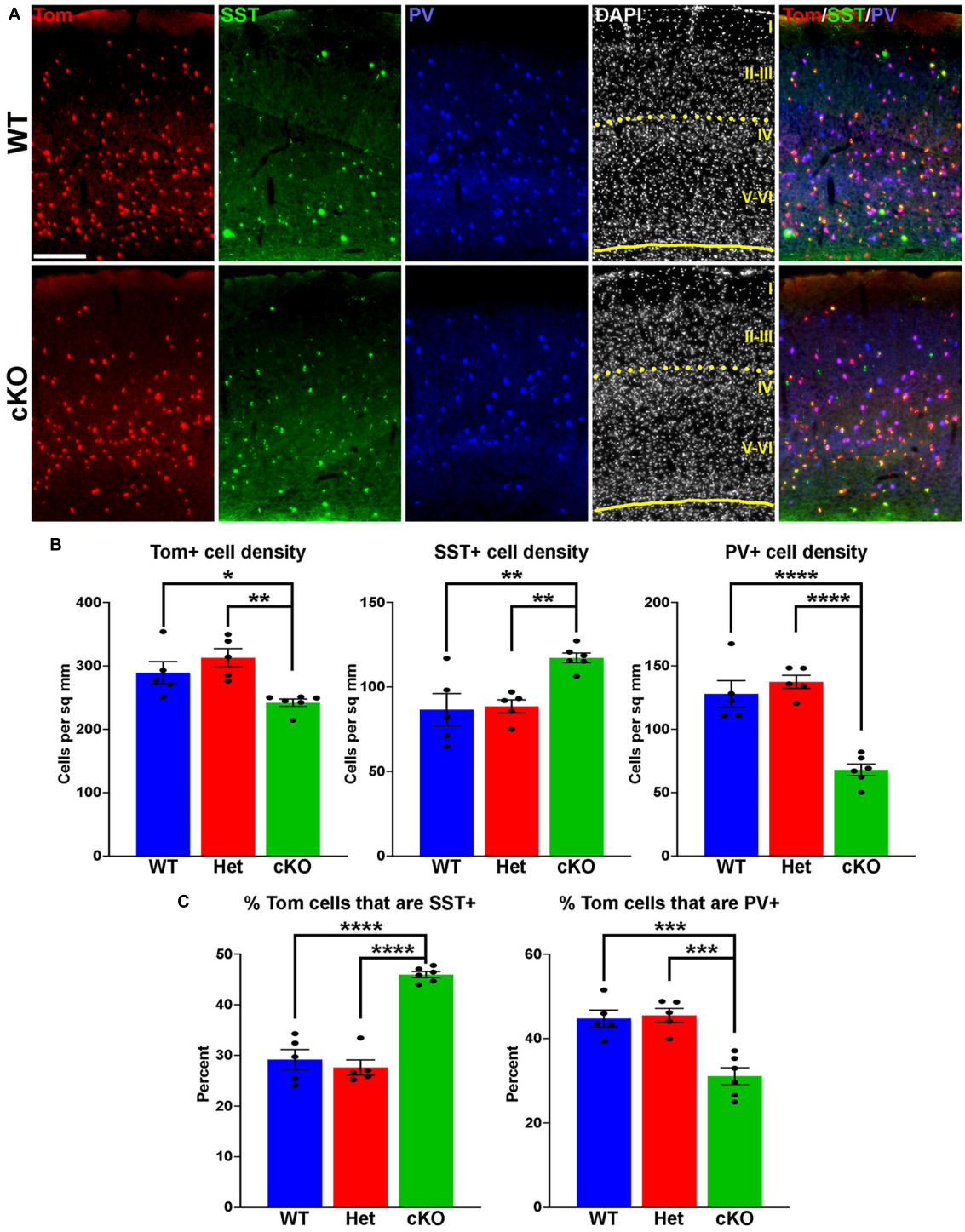

FIGURE 2
Changes in cortical interneuron fate in *Ezh2* cKO mice. **(A)** Representative images through the somatosensory cortex of P30 *Nkx2-1-Cre;Ezh2;Ai9* WT and cKO mice stained for SST (green) and PV (blue). Scale bar = 100 μm. Yellow dotted lines indicate division between superficial (layers I-III) and deep (layers IV-VI) cortical layers defined by DAPI densities. **(B)** Graphs displaying the density of Tom+, SST+ and PV+ cells in WT, Het and cKO mice. **(C)** Graphs displaying the percent of Tom+ cells expressing SST or PV in WT, Het and cKO mice. For all graphs, statistics are one-way ANOVA followed by Tukey's multiple comparison tests: $*p \leq 0.05$, $**p \leq 0.005$, $***p \leq 0.0005$, $****p \leq 0.0001$. n = 5 WT, 5 Het and 6 cKO brains from a total of 4 different litters.

dorsal MGE where Cre expression is lacking in *Nkx2-1-Cre* mice (Xu et al., 2008), and from non-*Nkx2-1* lineage cells within the MGE (endothelial cells, LGE- and CGE-derived cells migrating through this region, etc.). Additionally, the methyltransferase *Ezh1* is ubiquitously expressed and can partially compensate for loss of *Ezh2* in some conditions (Margueron et al., 2008; Shen et al., 2008). We do not observe significant changes in *Ezh1* expression in the MGE of *Ezh2* cKO mice (**Supplementary Figure 1**).

10.3389/fncel.2024.1334244

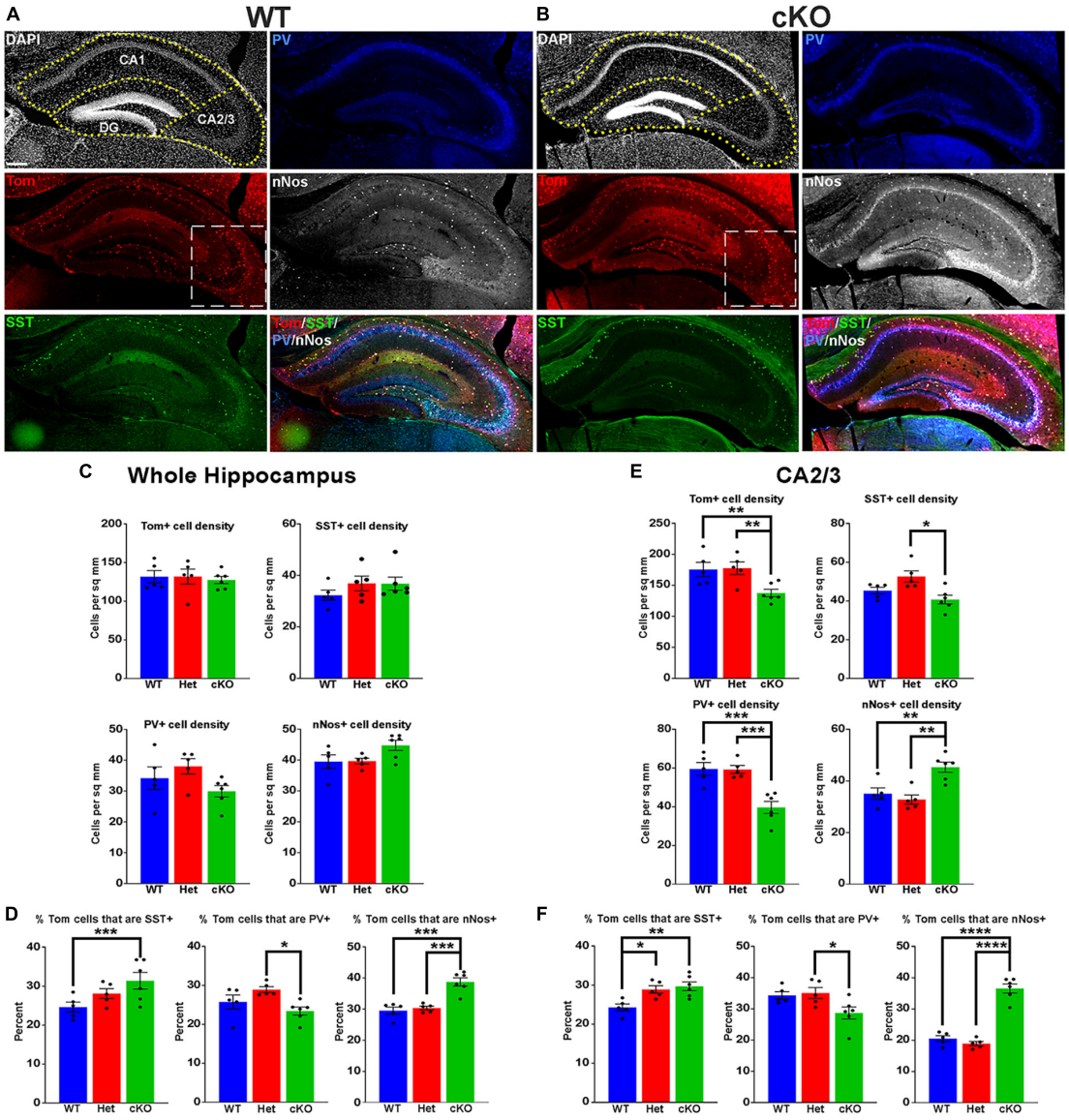

FIGURE 3

Changes in hippocampal interneuron fate in *Ezh2* cKO mice. **(A,B)** Representative hippocampus images of P30 *Nkx2-1-Cre;Ezh2;Ai9* WT **(A)** and cKO **(B)** mice stained for SST (green), PV (blue) and nNos (white). Scale bar = 100 μm. Dotted white box indicates region blown up in Figure 4. **(C,D)** Graphs displaying the density of Tom+, SST+, PV+ and nNos+ cells **(C)** and the percent of Tom+ cells expressing SST, PV or nNos **(D)** in the whole hippocampus of WT, Het and cKO mice. **(E,F)** Graphs displaying the density of Tom+, SST+, PV+ and nNos+ cells **(E)** and the percent of Tom+ cells expressing SST, PV or nNos **(F)** in the CA2/3 region of WT, Het and cKO mice. All stats are one-way ANOVA followed by Tukey's multiple comparison tests: $*p \leq 0.05$, $**p \leq 0.005$, $***p \leq 0.0005$, $****p \leq 0.0001$. n = 5 WT, 5 Het and 6 cKO brains, from 4 different litters.

To determine if loss of *Ezh2* affects interneuron fate, we counted the number of SST+ and PV+ interneurons in the somatosensory cortex, hippocampus and striatum from WT, Het and cKO mice. We observed a moderate but significant decrease in the density of Tom+ MGE-derived cortical interneurons in the cortex of cKO mice. More striking, there was a significant increase in the density of SST+ interneurons and a corresponding decrease in the density of PV+ interneurons in the cortex of cKO mice (Figures 2A, B). This shift in cell fate is also apparent when examining the proportion of Tom+ cells that express either SST or PV (Figure 2C).

To examine if these differences were consistent throughout cortical layers, we divided the somatosensory cortex into superficial (I-III) and deep (IV-VI) layers based on DAPI staining (Figure 2A). There was no significant decrease in the density of Tom+ cells between WT and cKO mice in either the superficial or deep layers (Supplementary Figure 2). The strongest effect in SST and PV fate changes was found in deep cortical layers, whereas superficial layers displayed a more moderate increase in SST+ and decrease in PV+ cells (Supplementary Figure 2). Thus, loss of *Ezh2* in the MGE results in a slight reduction in total MGE-derived cortical neurons, with a significant increase in SST+ and decrease in PV+ cells, most notably in the deeper cortical layers.

MGE-derived SST+ and PV+ interneurons also populate the adult striatum. We observed a significant decrease in the density and proportion of PV+ interneurons in the striatum of cKO

10.3389/fncel.2024.1334244

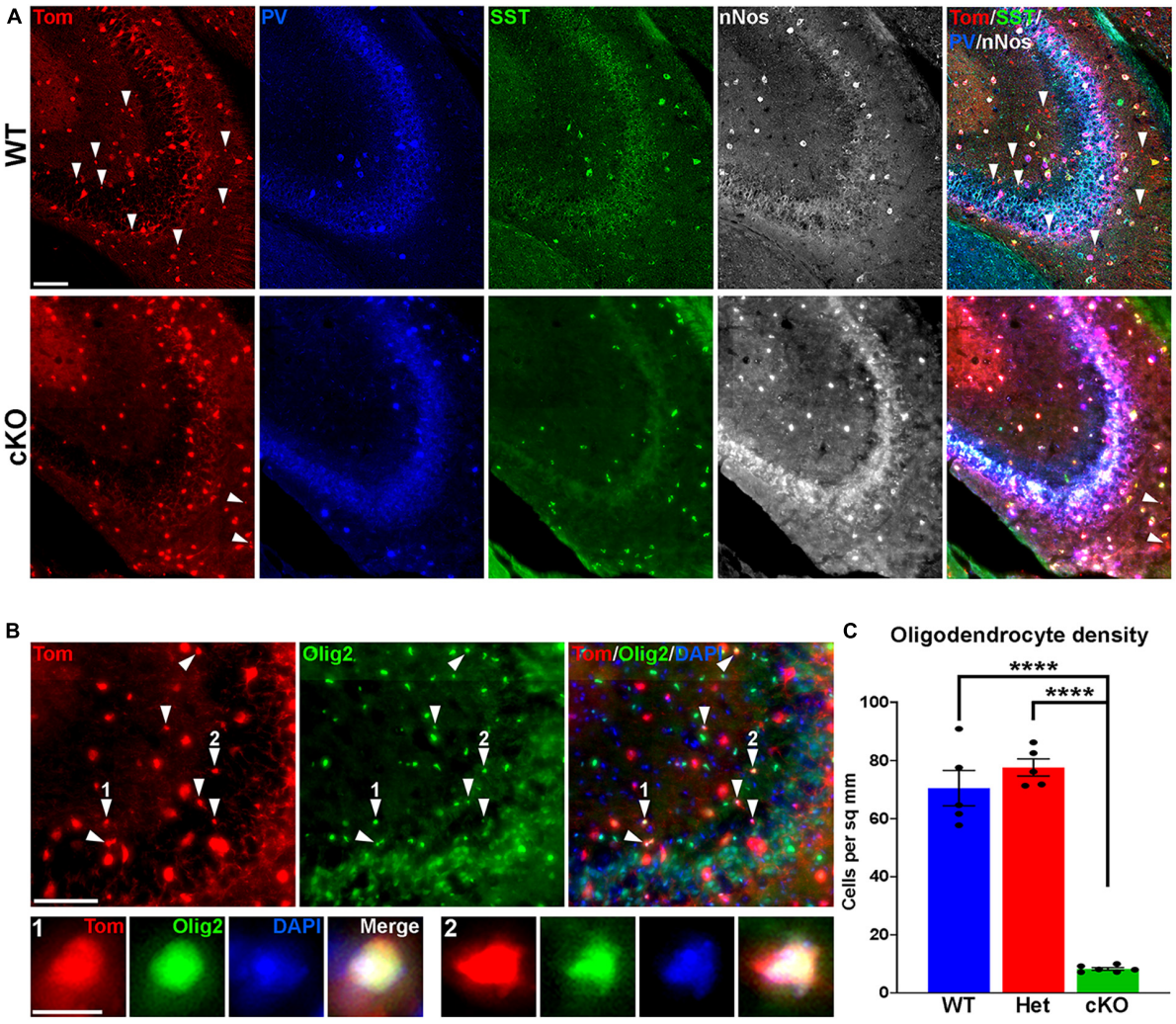

FIGURE 4
Loss of MGE-derived oligodendrocytes in CA2/3 in *Ezh2* cKO mice. **(A)** Representative images through the CA2/3 region of the hippocampus from P30 *Nkx2-1-Cre;Ezh2;Ai9* WT and cKO mice stained for SST (green), PV (blue) and nNos (white). From boxed regions in **Figures 3A, B**. **(B)** Top, CA2/3 from *Nkx2-1-Cre;Ezh2;Ai9* WT mice showing many small Tom+ cells express the oligodendrocyte markers Olig2 (white arrowheads). Bottom, higher magnification images of cells 1 and 2. Scale bars in panels **(A,B)** = 50 μm, scale bar in B1 = 5 μm. **(C)** Graph displaying the density of Tom+ oligodendrocytes in CA2/3 region of WT, Het and cKO mice. All stats are one-way ANOVA followed by Tukey's multiple comparison tests: ****$p \leq 0.0001$. n = 5 WT, 5 Het and 6 cKO brains from a total of 4 different litters.

mice, but no change in the total number of Tom+ or SST+ cells (**Supplementary Figure 3**), indicating this decrease in the density of PV+ interneurons is observed in multiple brain regions.

3.2 Alteration in both hippocampal interneurons and oligodendrocytes in *Ezh2* cKO

The hippocampus contains a population of MGE-derived, neuronal nitric oxide synthase nNos-expressing (nNos+) neurogliaform and ivy cells that are not found in the cortex (Tricoire et al., 2010, 2011; Jaglin et al., 2012). SST+, PV+ and nNos+ interneurons each make up ∼1/3 of MGE-derived hippocampal interneurons (Quattrocolo et al., 2017). We characterized the densities and percentages of SST+, PV+ and nNos+ interneurons throughout the hippocampus (**Figures 3A, B**). No significant differences were found in the densities of Tom+, SST+, PV+ or nNos+ interneurons in the whole hippocampus (**Figure 3C**). However, there was a significant increase in the percentage of Tom+ cells that expressed SST or nNos in cKO mice compared to WT (**Figure 3D**).

Since the prevalence of interneurons differs between the CA1, CA2/3 and dentate gyrus (DG) regions of the hippocampus, we divided hippocampal sections into these three regions based on DAPI staining (**Figures 3A, B**). There were almost no differences in densities or the proportion of subtypes in the CA1, only a slight but significant increase in the percentage of Tom+/nNos+ cells in the cKO (**Supplementary Figure 4A**). This increase in the percentage of nNos+ cells was also detected in the DG. More striking was a strong reduction of both PV+ cell densities and the percentage of Tom+/PV+ in the DG (**Supplementary Figure 4B**).

10.3389/fncel.2024.1334244

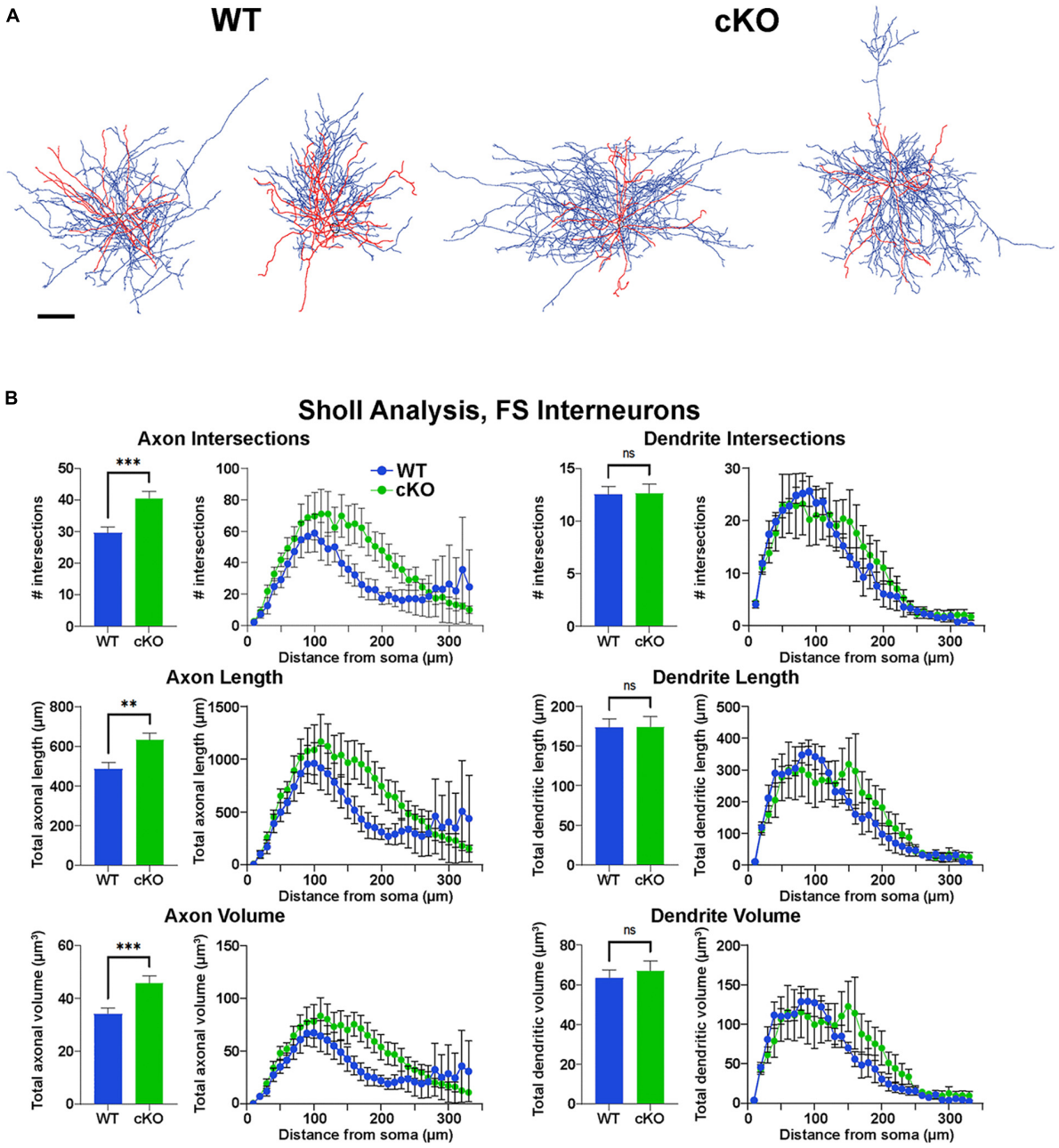

FIGURE 5
Increased axonal complexity of fast-spiking cortical interneurons in *Ezh2* cKO mice. **(A)** Representative morphological reconstructions of biocytin-filled FS cortical interneurons from P30-P40 *Nkx2-1-Cre;Ezh2;Ai9* WT and cKO mice depicting axons (blue) and dendrites (red). Scale bar = 20 µm. **(B)** Sholl analysis reveals increased axon intersections, axon length and axon volume in FS cortical interneurons from cKO mice compared to WT littermates. No significant differences were found in the dendritic arbors. All statistics are two-way ANOVA followed by Holm-Sidak's test: $^{**}p \leq 0.005$, $^{***}p \leq 0.0005$; n = 6 cells from 4 WT mice and 7 cells from 4 cKO mice.

The CA2/3 region displayed the greatest differences between WT and cKO mice, many of which mimicked cell fate changes in the cortex. First, there was a decrease in the total density of CA2/3 Tom+ cells in the cKO compared to WT (Figure 3E). Second, there was a significant decrease in PV+ cell densities in the CA2/3 region of cKO mice, and a corresponding increase in the percentage of Tom+/SST+ (Figures 3E, F). Third, there was a significant increase in the density and percentage of nNos+ cells in CA2/3 region of cKO mice compared to WT (Figures 3E, F). Thus, loss of *Ezh2* in the MGE had both broad and region-specific effects on interneuron fate in the hippocampus: an increase in the proportion of MGE-derived nNos+ cells in all three hippocampal regions, an increase in the percentage of Tom+/SST+ cells specifically in the CA2/3 region (which resulted in a significant increase in the entire hippocampus), and a decrease in PV+ cell density in both CA1 and CA2/3. This decrease in PV cells was observed in the cortex, striatum and hippocampus.

10.3389/fncel.2024.1334244

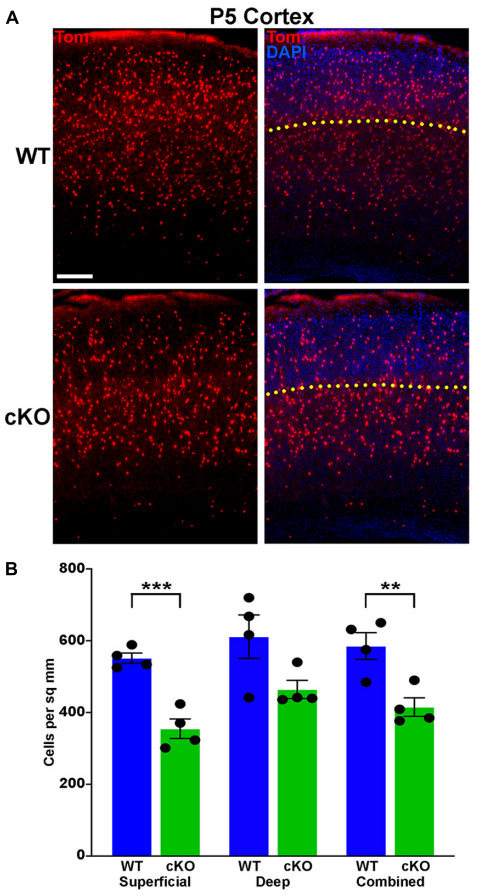

FIGURE 6
Significantly fewer MGE-derived cortical interneurons at P5 in *Ezh2* cKO mice. **(A)** Representative cortical images from P5 *Nkx2-1-Cre;Ezh2;Ai9* WT and cKO mice showing decrease in Tom+ cells in the cKO mouse. Yellow dotted line demarcates superficial and deep layers as defined by DAPI staining. Scale bar = 100 μm. **(B)** Graph displaying the density of Tom+ cells in P5 cortex. All stats are unpaired *t*-tests: ***$p \leq 0.001$, **$p \leq 0.01$. $n = 4$ WT and 4 cKO brains, from 4 different litters.

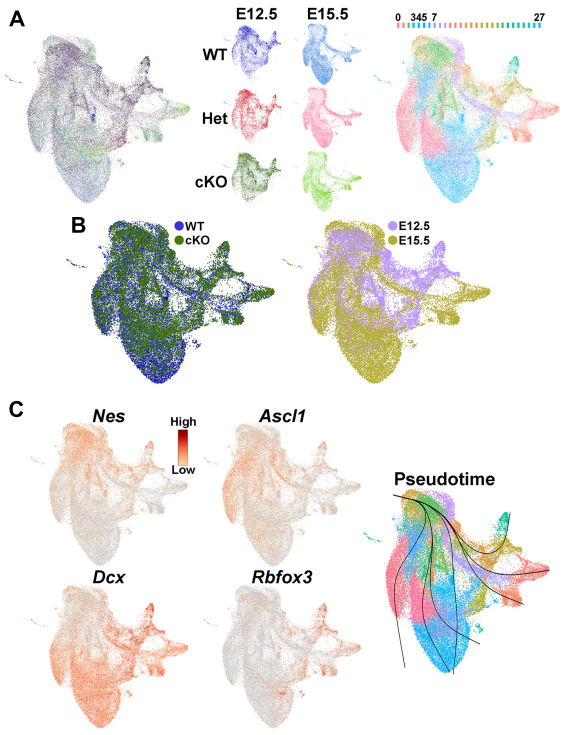

FIGURE 7
Single nuclei Multiome analysis of the MGE *Ezh2* cKO mice. **(A)** UMAP plots of E12.5 and E15.5 integrated single nuclei RNA- and ATAC-seq (Multiome) dataset via weighted nearest neighbor (WNN), annotated by age and genotype (left and middle) or putative cell clusters (right). Labels for putative cell clusters are listed above the UMAP. **(B)** Integrated E12.5+E15.5 RNA and ATAC dataset annotated by genotype (left) and age (right). **(C)** Markers for radial glia cells (*Nes*), cycling GE progenitors (*Ascl1*) and post-mitotic immature neurons (*Dcx*, *Rbfox3*), with general trajectory confirmed by pseudotime in the integrated E12.5+E15.5 UMAP plot.

While performing cell counts in the CA2/3 region, we observed Tom+ cell bodies that were too small to be interneurons, and we did not observe these cells in other brain regions (Figure 4A). Counting these cells separately, we found a very strong reduction of these CA2/3-specific cells in the cKO hippocampus (Figures 4B, C). We stained WT hippocampal sections with various glia and microglia markers and found that many of these small Tom+ cell bodies were Olig2+, indicating that they are likely oligodendrocytes (Figure 4B). This decrease in oligodendrocytes in *Ezh2* cKO mice is consistent with findings demonstrating that loss of *Ezh2* can block or delay gliogenesis (Hirabayashi et al., 2009; Wang et al., 2020).

3.3 Normal intrinsic properties but altered morphology of *Ezh2* cKO interneurons

To characterize the intrinsic physiology of MGE-derived interneurons in cKO mice, we performed patch clamp recording of layer V/VI Tom+ cortical cells in acute brain slices. Cells were classified as FS or NFS based on their intrinsic electrophysiological properties characterized under current clamp-recording. NFS cells had larger half-width, input resistance and membrane time constant/Tau, but smaller rheobase compared to FS cells. We analyzed action potential shapes, resting membrane potential, spike adaptation ratio, afterhyperpolarization (AHP) amplitude, input resistance and rheobase. There were no differences in intrinsic properties of FS or NFS cortical interneurons between WT and cKO mice (Supplementary Figure 5).

However, reconstructions of recorded cells did reveal morphological changes in FS cells. The axonal arbor of FS cells from cKO mice were larger and more complex compared to WT cells (Figure 5A). Sholl analysis revealed a significant increase in axon intersections, axon length and axon volume in FS cKO cells, while there were no changes in dendritic arbors (Figure 5B). This increased axonal arbor is similar to what was observed when trkB signaling was blocked in PV cells (Guyon et al., 2021). Thus, while intrinsic properties of Tom+ MGE-derived cortical interneurons were normal in *Ezh2* cKO mice, FS cells displayed greater complexity in their axonal arbors compared to FS cells from WT mice.

10.3389/fncel.2024.1334244

3.4 Loss of *Ezh2* in cycling progenitors is required for cell fate changes

We next wanted to determine at what stage of development loss of Ezh2 results in cell fate changes. *Ezh2* is enriched in cycling progenitors throughout the embryonic brain (**Figure 1A**), but Ezh2 may play a critical at other stages as well. To investigate this possibility, we generated *Dlx5/6-Cre*;*Ezh2*$^{F/F}$;*Ai9* conditional cKO mice in which loss of *Ezh2* is restricted to post-mitotic neurons arising from the ganglionic eminences. We verified that *Ezh2* is still expressed in MGE ventricular and subventricular zone cycling progenitors in *Dlx5/6-Cre* cKO mice (**Supplementary Figure 6A**). There were no differences in the densities or percent of SST+ and PV+ cells in the cortices of these *Dlx5/6-Cre* cKO mice (**Supplementary Figure 6B**), indicating that *Ezh2* is required in cycling MGE progenitors for proper interneuron fate and maturation.

A wave of programmed apoptosis occurs between the first and second postnatal weeks that eliminates ~20–40% of cortical interneurons (Southwell et al., 2012; Denaxa et al., 2018; Priya et al., 2018; Duan et al., 2020). To determine if there were changes in the overall production of MGE-derived interneurons during embryogenesis, we counted the number of Tom+ cells in the cortex at P5, prior to programmed apoptosis. We found a significant decrease in the number of Tom+ cells in the cKO cortex compared to WT at P5 (**Figures 6A, B**). This finding supports the hypothesis that loss of *Ezh2* in cycling MGE progenitors decreases the overall production of MGE-derived cortical interneurons, which would lead to more prominent loss of PV+ interneurons due to their bias production at later embryonic timepoints compared to SST+ cells (Inan et al., 2012).

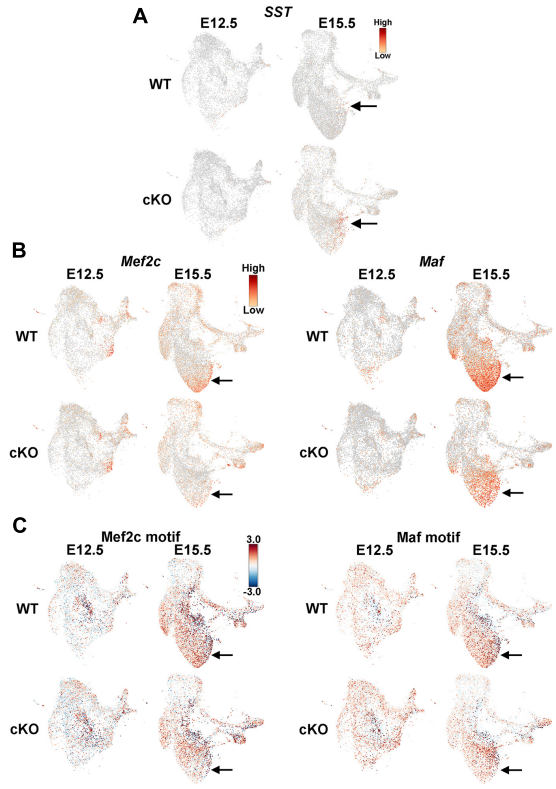

FIGURE 8
Altered expression of *SST*, *Mef2c* and *Maf* in the MGE of *Ezh2* cKO mice. **(A)** *SST* is enriched in E15.5 cKO MGE post-mitotic neurons compared WT MGE. **(B)** Enrichment of *Mef2c* and *Maf*, two genes predictive of PV-fated interneurons, in E15.5 WT MGE compared to cKO. **(C)** Enrichment of *Mef2c* and *Maf* binding motifs in E15.5 WT MGE compared to cKO.

3.5 Changes in gene expression and chromatin accessibility in the MGE of *Ezh2* cKO mice

We then investigated whether transcriptomic and epigenetic changes in the *Ezh2* cKO MGE are predictive of these cell fate changes in the mature forebrain. We generated single nuclei suspensions from E12.5 and E15.5 MGE and used the 10x Genomics Multiome kit to define the gene expression profile and chromatin accessibility within individual cells. We obtained a total of 51,656 nuclei that passed QC (**Supplementary Figure 7A**), with a range of ~6,300–11,500 nuclei per condition. These nuclei can be clustered based on their transcriptome, chromatin accessibility or integrated RNA and ATAC using the Weighted Nearest Neighbor (WNN) function in Seurat (Hao et al., 2021; **Figures 7A, B**; **Supplementary Figure 7B**). Analysis of several genes revealed the expected progression from radial glia cells (*Nes*) to immature neuronal progenitors (*Ascl1*) to post-mitotic neural precursors (*Dcx* and *Rbfox3*), which was verified with pseudotime analysis (**Figure 7C**).

Since there was a general increase in SST+ interneurons in the *Ezh2* cKO mouse, we examined *SST* expression in this single nuclei dataset. While no obvious differences in *SST* expression was apparent at E12.5, we did observe an increase in *SST* expression in the MGE of E15.5 cKO compared to WT (**Figure 8A**). While PV is not expressed in the embryonic mouse brain, two genes that are enriched in PV-fated interneurons and critical for their development are the transcription factors *Mef2c* and *Maf* (Mayer et al., 2018; Pai et al., 2020). We found that both genes are strongly reduced in E15.5 cKO MGEs compared to WT (**Figure 8B**). Complementing this gene expression analysis, the motifs for these transcription factors are enriched in accessible regions of the E15.5 WT MGE compared to cKO mice (**Figure 8C**). Thus, our gene expression analysis reveals an apparent increase in *SST* expression and decrease in *Maf* and *Mef2c* expression in the MGE of E15.5 cKO mice, which is predictive for the increase in SST+ and decrease of PV+ interneurons in *Ezh2* cKO brains.

Additionally, WT and cKO cells appeared to display differential abundance (DA) in specific regions of the UMAP plot, most notably in the E15.5 dataset (**Figure 7B**; **Supplementary Figure 7B**). To confirm this observation, we performed DA analysis using DA-seq (Zhao et al., 2021). DA-seq determines a DA score for each cell, whereby a cell that is surrounded by cKO cells in a k-nearest neighbor (KNN) graph has a score closer to +1, and a cell surrounded by WT cells has a score closer to −1. This DA score does not rely upon previously identified clusters, and it does not require similar cell numbers between different conditions. Our DA-seq analysis revealed that most cells with a DA score above +0.7 or below −0.7 were from the E15.5 MGE (**Figure 9A**), whereas

cells from the E12.5 MGE displayed little differential abundance. Most cells with a DA score below −0.7 (blue, WT bias) were in the clusters enriched for *Maf* and *Mef2c*, which are putative PV+ interneurons, whereas the cluster containing *SST*+ cells contained many cells with DA score above 0.7 (red, cKO bias) (**Figure 9A**). Thus, we observe a differential abundance of WT and cKO cells specifically in the E15.5 dataset, with an increase of cKO cells in clusters expressing *SST* and an increase of WT cells in clusters where *Maf* and *Mef2c* are strongly enriched.

To specifically focus on these clusters enriched for SST- and PV-fated interneurons, we extracted the four clusters containing these cells from the dataset (clusters 3, 4, 5 and 7) (**Figures 7A**, **9B**). Using thresholds of a Log_2 fold change (FC) $> \pm 0.2$ and a false discovery rate (FDR) of -Log_{10} Adjusted *P*-value (-Log_{10}Adj P) $< 10^{-6}$, we identified 66 differentially expressed genes at E12.5 (52 downregulated and 14 upregulated in cKO) and 174 differentially expressed genes at E15.5 (46 downregulated and 128 upregulated in cKO) (**Figure 9C**; **Supplementary Tables 1–2**). Notably, *SST* was significantly upregulated in the E15.5 cKO MGE whereas both *Maf* and *Mef2c* were significantly downregulated in the E15.5 cKO MGE, consistent with the observations above (**Figure 9C**). Additionally, the MGE-specific transcription factors *Nkx2-1* and *Lhx6* were also upregulated in the E15.5 cKO MGE.

Since differentially expressed genes of interest were restricted to E15.5, we reexamined the integrated E15.5 RNA+ATAC dataset alone (**Supplementary Figure 7B**). In this dataset, *SST* was enriched in cluster 10 (**Figure 9D**). The top gene enriched in this cluster was Phosphodiesterase 1A, *Pde1a*, which is also significantly upregulated in the E15.5 cKO MGE (**Figure 9C**). Based on the Allen Brain Institute's single cell transcriptomic adult mouse brain dataset, *Pde1a* is enriched in many SST+ interneuron subtypes while it's excluded from PV+ interneurons (**Figure 9D**), providing additional evidence that there is an increase in SST-fated cells in the MGE of *Ezh2* cKO mouse. In sum, this analysis indicates that the shift in MGE-derived interneuron subtypes is most evident in the E15.5 MGE, with an increase in both *SST* expression levels and the number of *SST*-expressing cells in the MGE of *Ezh2* cKO mice, with a corresponding decrease in PV-fated cells and PV-predictive genes.

3.6 Changes of H3K27me3 at distinct genomic loci in MGE of *Ezh2* cKO mice

H3K27me3 levels are strongly downregulated in the MGE of *Ezh2* cKO mice (**Figure 1**). This downregulation could occur homogenously throughout the genome, or alternatively, there could be differential changes where some loci are more resistant to loss of *Ezh2* while other sites are more susceptible. For example, the promoter-enhancer interaction at the *Sox2* locus is extremely resistant to epigenetic perturbations, possibly due to its critical function in in the epiblast stage of pre-implantation embryos (Chakraborty et al., 2023). To explore differential H3K27me3 changes at specific genomic loci, we performed bulk CUT&Tag (Kaya-Okur et al., 2019) with a H3K27me3 antibody in the MGE of WT and cKO mice. We conducted 3 biological replicates for each age and genotype, using Epic2 (Stovner and Saetrom, 2019) for peak calls and the DiffBind package (Stark and Brown, 2023) with edgeR's trimmed mean of M values (TMM) (Robinson et al., 2010) for comparative analysis.

We hypothesized that H3K27me3 would not be uniformly lost throughout the genome in the MGE of *Ezh2* cKO mice and that some loci might preferentially retain (or lose) H3K27me3. CUT&Tag experiments with global differences between conditions are challenging to interpret. Spike-ins can help, but the amount of added material must be known with high accuracy and precision to avoid propagating measurement error in spike-in concentration to the normalized CUT&Tag data. Without spike-ins, sequencing and library size normalization effectively equalizes any global differences between samples, and the resulting normalized data can be interpreted as relative differences (in this case H3K27me3 levels at specific genomic loci between WT and cKO mice). This interpretation enables us to examine the redistribution of H3K27me3 throughout the genome. We interpret normalized, equalized H3K27me3 signal that is lower in cKO compared to WT to indicate H3K27me3 was preferentially lost from that locus (i.e., a locus more susceptible to loss of *Ezh2*). Conversely, we interpret H3K27me3 signal that is higher in cKO compared to WT as preferentially retained at that locus (i.e., a locus more resistant to loss of *Ezh2*).

Biological replicates were grouped together in both principal component analysis (PCA) and unbiased correlation heatmaps, with age being a greater differentiation factor compared to genotype (**Figures 10A, B**). Comparative analyses revealed significant changes in the distribution of H3K27me3 at 82 loci at E12.5 (59 "decreased" and 23 "increased" loci in cKO) and 51 loci at E15.5 (14 "decreased" and 37 "increased" loci in cKO) (**Figure 10C**; **Supplementary Tables 3–4**). One of the most prominent changes was at the *Foxp4* locus, which is very susceptible to *Ezh2* loss with a strong 'decrease' in H3K27me3 at both E12.5 and E15.5 (**Figures 10C, D**). Despite this significant change, we do not observe a concomitant increase in *Foxp4* gene expression in the cKO MGE (**Figure 10D**). While *Foxp4* is strongly enriched in the LGE (Takahashi et al., 2008), its function in forebrain development has not been explored. Several genes critical for development of MGE-derived interneurons displayed a relative 'increase' in H3K27me3 (and thus increased resistance to loss of *Ezh2*) in the cKO MGE: *Nkx2-1* and the *Dlx1/2* locus were increased at E12.5, and *Lhx6* and the *Dlx5/6* locus were increased at E15.5 (**Figures 10C, E–G**). We did not observe a corresponding decrease in expression levels of these genes in the cKO MGE. In fact, several of these genes were upregulated in the E15.5 cKO MGE (**Figure 9C**), which is likely due to the absolute downregulation of H3K27me3 at these loci.

We identified 240 differentially expressed genes in the Multiome dataset and 133 peaks with significantly different relative H3K27me3 levels in the CUT&Tag dataset. Integrating these two datasets is challenging because (1) the CUT&Tag data represents 'relative' changes in H3K27me3 levels rather than global changes, and (2) we cannot definitively associate H3K27me3 peaks with specific genes. With these caveats, we identified 7 genes/loci that were significantly different between WT and *Ezh2* cKO MGE in both datasets. Three genes displayed increased relative H3K27me3 levels and increased gene expression in the cKO MGE (*Lhx6*, *Myt1l* and *Nkx2-1*). It is intriguing that two of the most important genes for MGE development (*Nkx2-1* and *Lhx6*) display resistance to changes in H3K27me3 levels

10.3389/fncel.2024.1334244

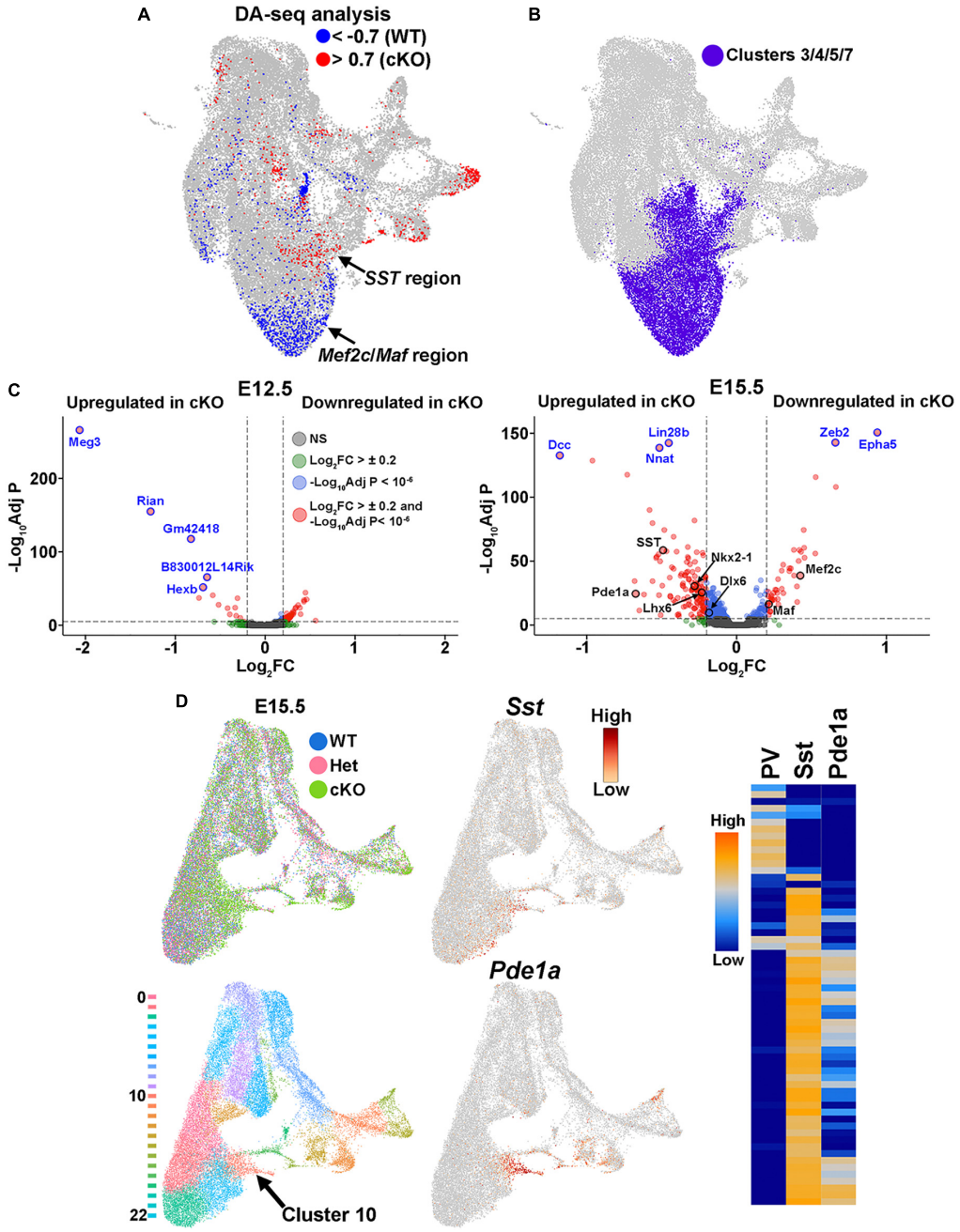

FIGURE 9
Differential abundance of SST- and PV-fated cells in the MGE of *Ezh2* cKO mice. **(A)** Differential abundance (DA) analysis using DA-seq reveals that *SST*+ cells reside in cKO-enriched clusters (red) whereas *Mef2c*- and *Maf*-expressing cells are located in WT-enriched clusters (blue). DA score threshold of +/- 0.7 used for significant enrichment of DA cells in DA-seq analysis. **(B)** Clusters 3, 4, 5, and 7 from panel A that contain PV- and SST-fated cells. **(C)** Volcano plots depicting genes upregulated or downregulated in cKO MGE at E12.5 (left) and E15.5 (right). Thresholds used were Log_2 fold change (FC) > ± 0.2 and a false discovery rate (FDR) of $-Log_{10}AdjustedP < 10^{-6}$. Top five genes with highest FDR are labeled in blue, genes of interest are labeled in black. **(D)** E15.5 integrated RNA and ATAC dataset annotated by genotype (top left) and putative cell clusters (bottom left). The top gene enriched in the cluster harboring *SST*+ cells (Cluster 10, arrow) is *Pde1a*. *Pde1a* is expressed in many SST+ interneuron subtypes in the adult mouse (each row is a mature interneuron subtype), but excluded from PV+ interneurons (right, adapted from the Allen Brain Map Transcriptomics Explorer).

and increased gene expression in *Ezh2* cKO mice. One gene displayed decreased relative H3K27me3 levels and decreased gene expression in the cKO MGE (*Zeb2*). *ZEB2* is co-expressed with *MAF*+ cells in the human MGE (Yu et al., 2021), so decreased of *Zeb2* expression in the cKO MGE is another predictor of decreased PV+ cells. Three genes displayed increased relative H3K27me3 levels and decreased gene expression in the cKO MGE (*Kirrel3*, *Meis1* and *Zfhx3*), which represents a logical correlation between H3K27me3 levels and gene expression. Variants in *KIRREL3* and *ZFHX3* have recently been associated with ASD and neurodevelopmental disorders, respectively (Taylor et al., 2020; Del Rocio Perez Baca et al., 2023), so it will be interesting to

10.3389/fncel.2024.1334244

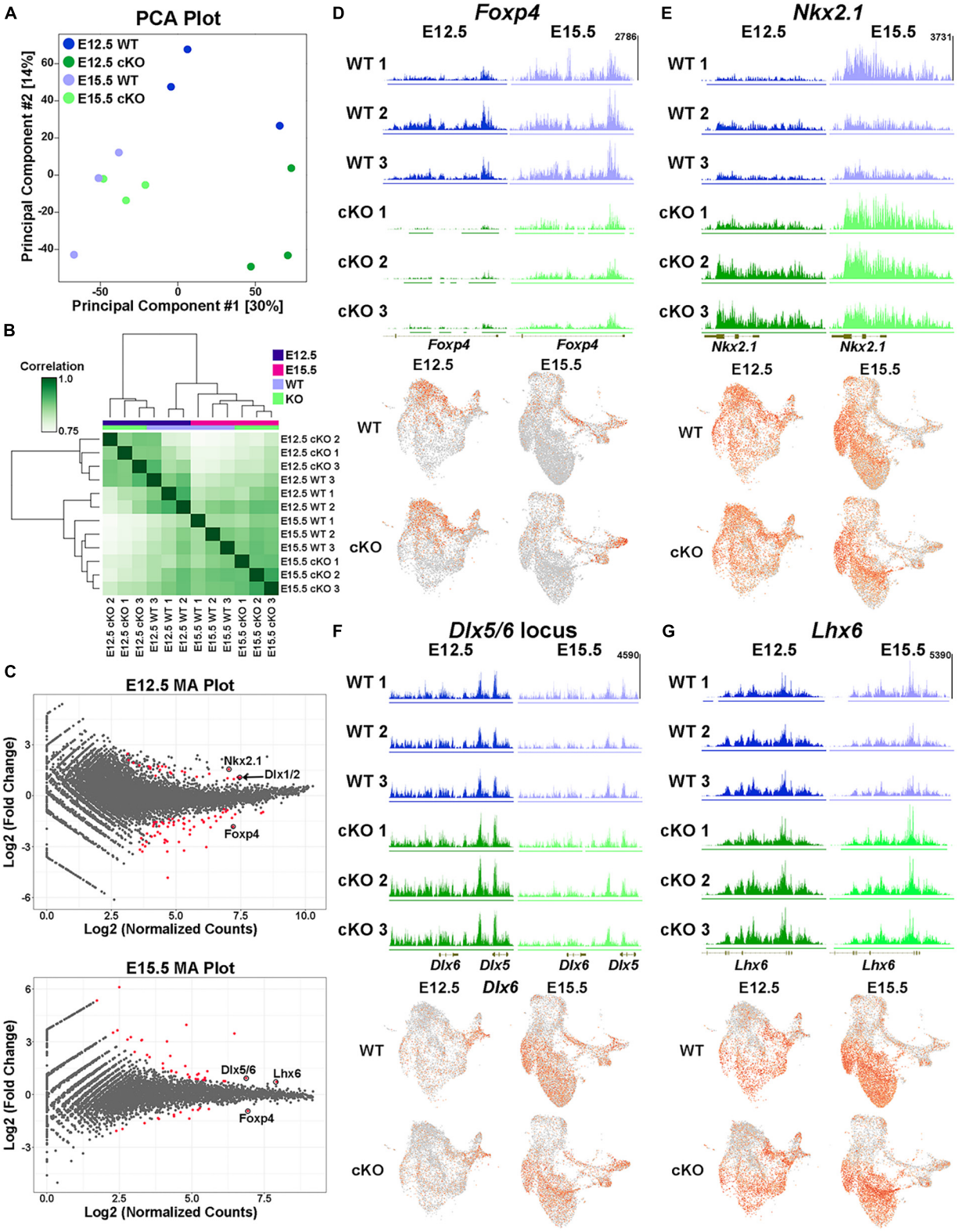

FIGURE 10

Altered H3K27me3 at distinct genomic loci in *Ezh2* cKO MGE. **(A)** PCA plot comparing the E12.5 WT, E12.5 cKO, E15.5 WT and E15.5 cKO CUT&Tag samples, 3 biological replicates each. **(B)** Unbiased hierarchical correlation heatmap comparing differential peaks between all 12 samples. **(C)** MA plots depicting the fold changes vs. mean peak counts for E12.5 (top) and E15.5 (bottom) data, with all significant peaks (FDR $\leq$ 0.1) highlighted in red. **(D–G)** H3K27me3 levels at the *FoxP4* **(D)**, *Nkx2-1* **(E)**, *Dlx5/6* **(F)** and *Lhx6* **(G)** loci in all 12 samples (top) along with the integrated UMAP plots showing gene expression profiles in the four different conditions (bottom).

determine how these genes regulate fate of MGE-derived cells in the future. There were zero genes that displayed decreased relative K27me3 levels and increased gene expression in the cKO MGE.

Even though there is a strong global decrease of H3K27me3 in the *Ezh2* cKO MGE (**Figure 1**), we identified shifts in the relative level of H3K27me3 at various loci in the genome. This indicates that specific genomic loci are more susceptible (e.g., *Foxp4*) or resistant (e.g., *Nkx2-1*) to H3K27me3 loss in the absence of *Ezh2*. The mechanism by which loss of *Ezh2* generates these differential effects at genomic loci, and how these changes in H3K27me3 levels relate to gene expression, require further investigation.

4 Discussion

There is growing evidence that dysregulation of epigenetic mechanisms can lead to a variety of human diseases and neurodevelopmental disorders (Kalish et al., 2014; Sokpor et al., 2017; Dall'Aglio et al., 2018; Qureshi and Mehler, 2018; Wang et al., 2018). For example, postmortem tissue from schizophrenic patients displays alterations in genome organization and other epigenomic characteristics (Kozlenkov et al., 2018; Rajarajan et al., 2018). Additionally, many genes associated with neurological and psychiatric diseases are enriched in immature interneurons during embryonic development (Cross-Disorder Group of the Psychiatric Genomics Consortium, 2019; Grove et al., 2019; Schork et al., 2019; Trevino et al., 2020). Thus, advancing our knowledge of gene regulation mechanisms during interneuron development is critical for understanding both normal development and disease etiologies.

In this study, we find that loss of *Ezh2* in the MGE decreases the density and proportion of PV+ cells, often with a corresponding increase in SST+ cells. This shift in interneuron fate was most prominent in the cortex and the CA2/3 region of the hippocampus, with an overall decrease in total MGE-derived interneurons also observed in the cortex. A decrease in PV+ cells was observed in the CA1, DG and striatum without a significant increase in SST+ cells (**Figures 2–3**; **Supplementary Figures 2–4**). In the hippocampus, we also observe an increase in MGE-derived nNos+ cells in the cKO (**Figure 3**). Unlike PV+ and SST+ interneurons, the spatial and temporal origin of hippocampal nNos+ in the MGE is not well characterized, so it's unclear how loss of *Ezh2* increased nNos+ cells. These phenotypes were due to *Ezh2* function in cycling MGE progenitors, as no changes were observed when *Ezh2* was removed in post-mitotic MGE cells (**Supplementary Figure 6**). This differential severity of interneuron fate changes in specific brain regions highlights the importance of examining interneuron fate in multiple brain regions.

In the hippocampus, CA2/3 displayed the strongest shift in interneuron fate compared to other hippocampal regions, more closely matching changes in the cortex. CA1 and CA2/3 have similar densities and percentages of MGE-derived interneurons (**Figure 3**; **Supplementary Figure 4**), so why these regions display such different phenotypes in the *Ezh2* cKO remains unknown. The severity of CA2/3-specific changes could arise from differences in interneuron migration, cell survivability or specific circuit interactions within this region. Additionally, the high density of MGE-derived oligodendrocytes in the WT CA2/3 was quite striking, as we did not observe these cells in the cortex or other hippocampal regions. MGE-derived oligodendrocytes do migrate into the cortex, but they are almost entirely eliminated during the second postnatal week (Kessaris et al., 2006). We are unaware of any reports describing MGE-derived oligodendrocytes in the hippocampus, and specifically in the CA2/3 region. Further studies are needed to understand why a population of MGE-derived oligodendrocytes perdures in CA2/3 into adulthood. Assuming these MGE-derived oligodendrocytes are generated toward the end of the cell cycle, then loss of this population is consistent with preemptive cell cycle exit in the *Ezh2* cKO mouse and the overall reduced production of MGE-derived cortical interneurons observed at P5 (**Figure 6**).

Previous studies revealed that the spatial origin and temporal birthdates of MGE-derived progenitors play a role in cell fate decisions. Cells born in the dorsal-posterior MGE preferentially give rise to SST+ interneurons whereas PV+ cells predominantly arise from the ventral-anterior MGE (Flames et al., 2007; Fogarty et al., 2007; Wonders et al., 2008; Inan et al., 2012; Taniguchi et al., 2013; McKenzie et al., 2019). Additionally, SST+ cells are preferentially born early (E11.5-E15.5) from apical progenitors whereas PV+ interneurons arise later (E12.5-E17.5) predominantly from basal progenitors (Inan et al., 2012; Taniguchi et al., 2013; Petros et al., 2015). As loss of *Ezh2* has been shown to induce cell cycle exit and neurogenesis (Pereira et al., 2010; Zemke et al., 2015; Kim et al., 2018; Buontempo et al., 2022; Wu et al., 2022), this could in part explain the fate switch in *Ezh2* cKO mice. Premature neurogenesis would generate an excess of neurons at early stages when SST+ interneurons are born, while simultaneously deplete the progenitor pool so that there are fewer neurogenic divisions at later stages when PV+ cells arise. This could also result in an overall decrease in MGE-derived interneurons, as was apparent at P5 (**Figure 6**). Manipulation of cell cycle dynamics has previously been shown to shift the percentage of SST+ or PV+ cells born at a particular timepoint (Inan et al., 2012; Taniguchi et al., 2013; Petros et al., 2015).

Despite these changes in cell fate, mature PV+ and SST+ cortical interneurons displayed normal intrinsic physiological properties. However, cortical PV+ interneurons displayed significantly greater axon length and complexity in the cKO mouse. This could be a form of compensation, as one way to increase inhibition with fewer PV+ cells is for the surviving PV+ interneurons to have increased synaptic contacts. Alternatively, enhanced activation of PV+ interneurons can result in more elaborate axon morphologies (Stedehouder et al., 2018): if individual PV+ interneurons are receiving more glutamatergic inputs because of decreased number of PV+ cells in *Ezh2* cKO mice, than this could in part explain the morphological changes. Additionally, PV+ interneurons normally form exuberant axon projections and synaptic connections during the first two postnatal weeks which are then pruned and retracted during the 3rd and 4th weeks (Micheva et al., 2021). Thus, it's possible that this normal developmental retraction is disrupted in the cKO mouse.

Single nuclei sequencing revealed that these cell fate changes are already apparent in the developing MGE. First, the majority of transcriptome differences were observed in the E15.5 MGE while

the E12.5 MGE from WT and cKO mice were quite similar. This could imply that the loss of *Ezh2* takes time to manifest (due to perdurance of H3K27me3 marks, rate of histone turnover, etc.), with the strongest affects becoming more evident during the second half of MGE neurogenesis. Second, there was an increase in *SST* expression and a decrease in expression of PV-predictive genes *Mef2c* and *Maf* in the *Ezh2* cKO mouse at E15.5 (**Figures 8**, **9C**). Third, differential abundance analysis reveals that there is an enrichment of cells from the cKO MGE in the *SST*-expressing region and an enrichment for WT MGE cells in the *Mef2c*/*Maf*-expressing region (**Figure 9A**). Fourth, the top gene expressed in the *SST*-enriched cluster at E15.5 is *Pde1a*, which is expressed by many mature *SST*+ interneuron subtypes but excluded from *PV*+ interneurons (**Figure 9D**). In sum, these transcriptional and cellular differences in the MGE drive the shifts in SST+ and PV+ interneurons in the adult brain of *Ezh2* cKO mice.

Despite the global downregulation of H3K27me3, we found that specific genomic loci were either more resistant ("increased" H3K27me3) or susceptible ("decreased" H3K27me3) to loss of *Ezh2*. One of the most susceptible regions at both E12.5 and E15.5 with a strong "decrease" in H3K27me3 was the *Foxp4* locus (**Figures 10C, D**). *Foxp4* is enriched in the LGE (Takahashi et al., 2008), but it has not been well-studied in neurodevelopment. In heterologous cell lines, FOXP4 can directly interact with the transcription factors SATB1, NR2F1 and NR2F2, all of which are critical for development of MGE-derived interneurons (Close et al., 2012; Hu et al., 2017a; Estruch et al., 2018). Whether these interactions occur in the developing brain is unclear. A study on medulloblastoma found that *Foxp4* and *Ezh2* are both targets of the microRNA miR-101-3p (Xue et al., 2022), indicating the function of these genes might be linked in some scenarios. Why the *Foxp4* locus is extremely sensitive to *Ezh2* loss requires further study.

In the *Ehz2* cKO MGE, we observed that several genes critical for fate determination of MGE-derived interneurons (*Nkx2-1*, *Lxh6*, *Dlx1/2* and *Dlx5/6*) were more resistant to loss of *Ezh2* (**Figures 10C, E–G**). This raises the possibility that some genes playing critical roles in fate determination may be more resistant to epigenetic changes. As *Nkx2-1* is a 'master regulator' of MGE fate and the *Nkx2-1* locus displays unique chromatin organization specific to the MGE (Rhodes et al., 2022), this locus could be more resistant to epigenetic modifications. The interaction between *Sox2*, a transcription factor essential in the epiblast of pre-implantation embryos, and a critical enhancer downstream is maintained even when artificial boundaries are introduced between these regions (Chakraborty et al., 2023). It will be interesting to explore if this theme of specific genomic loci being resistant to epigenetic modifications holds true at critical fate-determining genes in other tissues and/or stages of development, both in terms of normal development and with respect to neurodevelopmental and psychiatric diseases.

Data availability statement

The datasets presented in this study can be found in online repositories. The names of the repository/repositories and accession number(s) can be found in the article/**Supplementary material**.

Ethics statement

The animal study was approved by the NICHD Animal Use and Care Committee (ACUC). The study was conducted in accordance with the local legislation and institutional requirements.

Author contributions

CR: Conceptualization, Data curation, Formal analysis, Investigation, Methodology, Software, Visualization, Writing—original draft, Writing—review and editing. DA: Data curation, Formal analysis, Investigation, Methodology, Writing—review and editing. MS: Data curation, Formal analysis, Investigation, Methodology, Software, Visualization, Writing—review and editing. SN: Data curation, Formal analysis, Investigation, Methodology, Visualization, Writing—review and editing. LE: Data curation, Formal analysis, Investigation, Writing—review and editing. PS: Formal analysis, Investigation, Visualization, Writing—review and editing. DL: Formal analysis, Methodology, Visualization, Writing—original draft, Writing—review and editing. YZ: Investigation, Visualization, Writing—review and editing. PR: Funding acquisition, Methodology, Supervision, Writing—review and editing. RD: Data curation, Formal analysis, Funding acquisition, Methodology, Supervision, Writing—review and editing. SL: Methodology, Supervision, Writing—review and editing. TP: Conceptualization, Funding acquisition, Resources, Supervision, Visualization, Writing—original draft, Writing—review and editing.

Funding

The author(s) declare financial support was received for the research, authorship, and/or publication of this article. This work was supported by *Eunice Kennedy Shriver* NICHD Intramural Awards to TP, PR, and RD; NIMH Intramural Award to SL; NICHD Scientific Director's Award to TP and PR.

Acknowledgments

We thank S. Coon, F. Faucz, J. Iben, T. Li, and other members of the NICHD Molecular Genomic Core; members of the Petros Lab for helpful discussions and feedback on the manuscript. Further information and requests for resources and reagents should be directed to and will be fulfilled by the Lead Contact, TP (tim.petros@nih.gov).

Conflict of interest

The authors declare that the research was conducted in the absence of any commercial or financial relationships that could be construed as a potential conflict of interest.

The author(s) declared that they were an editorial board member of Frontiers, at the time of submission. This had no impact on the peer review process and the final decision.

Publisher's note

All claims expressed in this article are solely those of the authors and do not necessarily represent those of their affiliated organizations, or those of the publisher, the editors and the reviewers. Any product that may be evaluated in this article, or claim that may be made by its manufacturer, is not guaranteed or endorsed by the publisher.

Supplementary material

The Supplementary Material for this article can be found online at: https://www.frontiersin.org/articles/10.3389/fncel.2024.1334244/full#supplementary-material

References

Albert, M., and Huttner, W. B. (2018). Epigenetic and transcriptional pre-patterning-an emerging theme in cortical neurogenesis. *Front. Neurosci.* 12:359. doi: 10.3389/fnins.2018.00359

Allaway, K. C., Gabitto, M. I., Wapinski, O., Saldi, G., Wang, C. Y., Bandler, R. C., et al. (2021). Genetic and epigenetic coordination of cortical interneuron development. *Nature* 597, 693–697.

Amemiya, H. M., Kundaje, A., and Boyle, A. P. (2019). The ENCODE blacklist: identification of problematic regions of the genome. *Sci. Rep.* 9:9354.

Aranda, S., Mas, G., and Di Croce, L. (2015). Regulation of gene transcription by Polycomb proteins. *Sci. Adv.* 1:e1500737.

Bandler, R. C., Mayer, C., and Fishell, G. (2017). Cortical interneuron specification: the juncture of genes, time and geometry. *Curr. Opin. Neurobiol.* 42, 17–24. doi: 10.1016/j.conb.2016.10.003

Bandler, R. C., Vitali, I., Delgado, R. N., Ho, M. C., Dvoretskova, E., Ibarra Molinas, J. S., et al. (2021). Single-cell delineation of lineage and genetic identity in the mouse brain. *Nature* 601, 404–409. doi: 10.1038/s41586-021-04237-0

Benjamini, Y., and Hochberg, Y. (1995). Controlling the false discovery rate - a practical and powerful approach to multiple testing. *J. R. Stat. Soc. Ser. B Stat. Methodol.* 57, 289–300.

Bozzi, Y., Casarosa, S., and Caleo, M. (2012). Epilepsy as a neurodevelopmental disorder. *Front. Psychiatry* 3:19. doi: 10.3389/fpsyt.2012.00019

Braun, E., Danan-Gotthold, M., Borm, L. E., Vinsland, E., Lee, K. W., Lonnerberg, P., et al. (2022). Comprehensive cell atlas of the first-trimester developing human brain. *bioRxiv [Preprint]* doi: 10.1101/2022.10.24.513487

Buontempo, S., Laise, P., Hughes, J. M., Trattaro, S., Das, V., Rencurel, C., et al. (2022). EZH2-mediated H3K27me3 targets transcriptional circuits of neuronal differentiation. *Front. Neurosci.* 16:814144. doi: 10.3389/fnins.2022.814144

Cao, R., Wang, L., Wang, H., Xia, L., Erdjument-Bromage, H., Tempst, P., et al. (2002). Role of histone H3 lysine 27 methylation in Polycomb-group silencing. *Science* 298, 1039–1043.

Chakraborty, S., Kopitchinski, N., Zuo, Z., Eraso, A., Awasthi, P., Chari, R., et al. (2023). Enhancer–promoter interactions can bypass CTCF-mediated boundaries and contribute to phenotypic robustness. *Nat. Genet.* 55, 280–290. doi: 10.1038/s41588-022-01295-6

Close, J., Xu, H., De Marco Garcia, N., Batista-Brito, R., Rossignol, E., Rudy, B., et al. (2012). Satb1 is an activity-modulated transcription factor required for the terminal differentiation and connectivity of medial ganglionic eminence-derived cortical interneurons. *J. Neurosci.* 32, 17690–17705. doi: 10.1523/JNEUROSCI.3583-12.2012

Cohen, A. S., Yap, D. B., Lewis, M. E., Chijiwa, C., Ramos-Arroyo, M. A., Tkachenko, N., et al. (2016). Weaver syndrome-associated EZH2 protein variants show impaired histone methyltransferase function in vitro. *Hum. Mutat.* 37, 301–307. doi: 10.1002/humu.22946

Contractor, A., Ethell, I. M., and Portera-Cailliau, C. (2021). Cortical interneurons in autism. *Nat. Neurosci.* 24, 1648–1659.

Cross-Disorder Group of the Psychiatric Genomics Consortium (2019). Genomic relationships, novel loci, and pleiotropic mechanisms across eight psychiatric disorders. *Cell* 179, 1469–1482 e1411. doi: 10.1016/j.cell.2019.11.020

Dall'Aglio, L., Muka, T., Cecil, C. A. M., Bramer, W. M., Verbiest, M., Nano, J., et al. (2018). The role of epigenetic modifications in neurodevelopmental disorders: a systematic review. *Neurosci. Biobehav. Rev.* 94, 17–30.

Danecek, P., Bonfield, J. K., Liddle, J., Marshall, J., Ohan, V., Pollard, M. O., et al. (2021). Twelve years of SAMtools and BCFtools. *Gigascience* 10:giab008. doi: 10.1093/gigascience/giab008

Del Rocio Perez Baca, M., Jacobs, E. Z., Vantomme, L., Leblanc, P., Bogaert, E., and Dheedene, A. (2023). A novel neurodevelopmental syndrome caused by loss-of-function of the Zinc Finger Homeobox 3 (ZFHX3) gene. *medRxiv [Preprint]* doi: 10.1101/2023.05.22.23289895

Denaxa, M., Neves, G., Rabinowitz, A., Kemlo, S., Liodis, P., Burrone, J., et al. (2018). Modulation of apoptosis controls inhibitory interneuron number in the cortex. *Cell Rep.* 22, 1710–1721.

Di Meglio, T., Kratochwil, C. F., Vilain, N., Loche, A., Vitobello, A., Yonehara, K., et al. (2013). Ezh2 orchestrates topographic migration and connectivity of mouse precerebellar neurons. *Science* 339, 204–207. doi: 10.1126/science.1229326

Duan, Z. R. S., Che, A., Chu, P., Modol, L., Bollmann, Y., Babij, R., et al. (2020). GABAergic restriction of network dynamics regulates interneuron survival in the developing cortex. *Neuron* 105, 75–92 e75. doi: 10.1016/j.neuron.2019.10.008

Estruch, S. B., Graham, S. A., Quevedo, M., Vino, A., Dekkers, D. H. W., Deriziotis, P., et al. (2018). Proteomic analysis of FOXP proteins reveals interactions between cortical transcription factors associated with neurodevelopmental disorders. *Hum. Mol. Genet.* 27, 1212–1227.

Eze, U. C., Bhaduri, A., Haeussler, M., Nowakowski, T. J., and Kriegstein, A. R. (2021). Single-cell atlas of early human brain development highlights heterogeneity of human neuroepithelial cells and early radial glia. *Nat. Neurosci.* 24, 584–594. doi: 10.1038/s41593-020-00794-1

Feng, X., Juan, A. H., Wang, H. A., Ko, K. D., Zare, H., and Sartorelli, V. (2016). Polycomb Ezh2 controls the fate of GABAergic neurons in the embryonic cerebellum. *Development* 143, 1971–1980. doi: 10.1242/dev.132902

Flames, N., Pla, R., Gelman, D. M., Rubenstein, J. L., Puelles, L., and Marin, O. (2007). Delineation of multiple subpallial progenitor domains by the combinatorial expression of transcriptional codes. *J. Neurosci.* 27, 9682–9695. doi: 10.1523/JNEUROSCI.2750-07.2007

Fogarty, M., Grist, M., Gelman, D., Marin, O., Pachnis, V., and Kessaris, N. (2007). Spatial genetic patterning of the embryonic neuroepithelium generates GABAergic interneuron diversity in the adult cortex. *J. Neurosci.* 27, 10935–10946. doi: 10.1523/JNEUROSCI.1629-07.2007

Glickstein, S. B., Moore, H., Slowinska, B., Racchumi, J., Suh, M., Chuhma, N., et al. (2007). Selective cortical interneuron and GABA deficits in cyclin D2-null mice. *Development* 134, 4083–4093. doi: 10.1242/dev.008524

Grove, J., Ripke, S., Als, T. D., Mattheisen, M., Walters, R. K., and Won, H. (2019). Identification of common genetic risk variants for autism spectrum disorder. *Nat. Genet.* 51, 431–444.

Guyon, N., Zacharias, L. R., Van Lunteren, J. A., Immenschuh, J., Fuzik, J., Martin, A., et al. (2021). Adult trkB signaling in parvalbumin interneurons is essential to prefrontal network dynamics. *J. Neurosci.* 41, 3120–3141. doi: 10.1523/JNEUROSCI.1848-20.2021

Hao, Y., Hao, S., Andersen-Nissen, E., Mauck, W. M., Zheng, S., and Butler, A. (2021). Integrated analysis of multimodal single-cell data. *Cell* 184, 3573–3587 e3529.

Hirabayashi, Y., and Gotoh, Y. (2010). Epigenetic control of neural precursor cell fate during development. *Nat. Rev. Neurosci.* 11, 377–388.

Hirabayashi, Y., Suzki, N., Tsuboi, M., Endo, T. A., Toyoda, T., Shinga, J., et al. (2009). Polycomb limits the neurogenic competence of neural precursor cells to promote astrogenic fate transition. *Neuron* 63, 600–613. doi: 10.1016/j.neuron.2009.08.021

Hu, J. S., Vogt, D., Lindtner, S., Sandberg, M., Silberberg, S. N., and Rubenstein, J. L. R. (2017a). Coup-TF1 and Coup-TF2 control subtype and laminar identity of MGE-derived neocortical interneurons. *Development* 144, 2837–2851. doi: 10.1242/dev.150664

Hu, J. S., Vogt, D., Sandberg, M., and Rubenstein, J. L. (2017b). Cortical interneuron development: a tale of time and space. *Development* 144, 3867–3878. doi: 10.1242/dev.132852

Inan, M., Petros, T. J., and Anderson, S. A. (2013). Losing your inhibition: linking cortical GABAergic interneurons to schizophrenia. *Neurobiol. Dis.* 53, 36–48. doi: 10.1016/j.nbd.2012.11.013

Inan, M., Welagen, J., and Anderson, S. A. (2012). Spatial and temporal bias in the mitotic origins of somatostatin- and parvalbumin-expressing interneuron subgroups and the chandelier subtype in the medial ganglionic eminence. *Cereb. Cortex* 22, 820–827. doi: 10.1093/cercor/bhr148

Jaglin, X. H., Hjerling-Leffler, J., Fishell, G., and Batista-Brito, R. (2012). The origin of neocortical nitric oxide synthase-expressing inhibitory neurons. *Front. Neural Circuits* 6:44. doi: 10.3389/fncir.2012.00044

Kalish, J. M., Jiang, C., and Bartolomei, M. S. (2014). Epigenetics and imprinting in human disease. *Int. J. Dev. Biol.* 58, 291–298.

Kaya-Okur, H. S., Wu, S. J., Codomo, C. A., Pledger, E. S., Bryson, T. D., Henikoff, J. G., et al. (2019). CUT&Tag for efficient epigenomic profiling of small samples and single cells. *Nat. Commun.* 10:1930.

Kessaris, N., Fogarty, M., Iannarelli, P., Grist, M., Wegner, M., and Richardson, W. D. (2006). Competing waves of oligodendrocytes in the forebrain and postnatal elimination of an embryonic lineage. *Nat. Neurosci.* 9, 173–179. doi: 10.1038/nn1620

Kim, H., Langohr, I. M., Faisal, M., Mcnulty, M., Thorn, C., and Kim, J. (2018). Ablation of Ezh2 in neural crest cells leads to aberrant enteric nervous system development in mice. *PLoS One* 13:e0203391. doi: 10.1371/journal.pone.0203391

Kozlenkov, A., Li, J., Apontes, P., Hurd, Y. L., Byne, W. M., Koonin, E. V., et al. (2018). A unique role for DNA (hydroxy)methylation in epigenetic regulation of human inhibitory neurons. *Sci. Adv.* 4:eaau6190. doi: 10.1126/sciadv.aau6190

Langmead, B., and Salzberg, S. L. (2012). Fast gapped-read alignment with Bowtie 2. *Nat. Methods* 9, 357–359. doi: 10.1038/nmeth.1923

Lee, D. R., Rhodes, C., Mitra, A., Zhang, Y., Maric, D., Dale, R. K., et al. (2022a). Transcriptional heterogeneity of ventricular zone cells in the ganglionic eminences of the mouse forebrain. *Elife* 11:e71864. doi: 10.7554/eLife.71864

Lee, D. R., Zhang, Y., Rhodes, C. T., and Petros, T. J. (2022b). Generation of single-cell and single-nuclei suspensions from embryonic and adult mouse brains. *STAR Protoc.* 4:101944. doi: 10.1016/j.xpro.2022.101944

Li, J., Hart, R. P., Mallimo, E. M., Swerdel, M. R., Kusnecov, A. W., and Herrup, K. (2013). EZH2-mediated H3K27 trimethylation mediates neurodegeneration in ataxia-telangiectasia. *Nat. Neurosci.* 16, 1745–1753. doi: 10.1038/nn.3564

Lim, L., Mi, D., Llorca, A., and Marin, O. (2018). Development and functional diversification of cortical interneurons. *Neuron* 100, 294–313.

Madisen, L., Zwingman, T. A., Sunkin, S. M., Oh, S. W., Zariwala, H. A., Gu, H., et al. (2010). A robust and high-throughput Cre reporting and characterization system for the whole mouse brain. *Nat. Neurosci.* 13, 133–140. doi: 10.1038/nn.2467

Margueron, R., Li, G., Sarma, K., Blais, A., Zavadil, J., Woodcock, C. L., et al. (2008). Ezh1 and Ezh2 maintain repressive chromatin through different mechanisms. *Mol. Cell* 32, 503–518.

Martin, M. (2011). Cutadapt removes adapter sequences from high-throughput sequencing reads. *EMBnet J.* 17, 10–12. doi: 10.1089/cmb.2017.0096

Mayer, C., Hafemeister, C., Bandler, R. C., Machold, R., Batista Brito, R., Jaglin, X., et al. (2018). Developmental diversification of cortical inhibitory interneurons. *Nature* 555, 457–462.

McKenzie, M. G., Cobbs, L. V., Dummer, P. D., Petros, T. J., Halford, M. M., Stacker, S. A., et al. (2019). Non-canonical Wnt signaling through Ryk regulates the generation of somatostatin- and parvalbumin-expressing cortical interneurons. *Neuron* 103, 853–864 e854. doi: 10.1016/j.neuron.2019.06.003

Mi, D., Li, Z., Lim, L., Li, M., Moissidis, M., Yang, Y., et al. (2018). Early emergence of cortical interneuron diversity in the mouse embryo. *Science* 360, 81–85.

Micheva, K. D., Kiraly, M., Perez, M. M., and Madison, D. V. (2021). Extensive structural remodeling of the axonal arbors of parvalbumin basket cells during development in mouse neocortex. *J. Neurosci.* 41, 9326–9339. doi: 10.1523/JNEUROSCI.0871-21.2021

Miyoshi, G. (2019). Elucidating the developmental trajectories of GABAergic cortical interneuron subtypes. *Neurosci. Res.* 138, 26–32. doi: 10.1016/j.neures.2018.09.012

Monory, K., Massa, F., Egertova, M., Eder, M., Blaudzun, H., and Westenbroek, R. (2006). The endocannabinoid system controls key epileptogenic circuits in the hippocampus. *Neuron* 51, 455–466. doi: 10.1016/j.neuron.2006.07.006

Muller, J. (1995). Transcriptional silencing by the Polycomb protein in Drosophila embryos. *EMBO J.* 14, 1209–1220.

Nowakowski, T. J., Bhaduri, A., Pollen, A. A., Alvarado, B., Mostajo-Radji, M. A., and Di Lullo, E. (2017). Spatiotemporal gene expression trajectories reveal developmental hierarchies of the human cortex. *Science* 358, 1318–1323. doi: 10.1126/science.aap8809

Pai, E. L., Chen, J., Fazel Darbandi, S., Cho, F. S., Chen, J., Lindtner, S., et al. (2020). Maf and Mafb control mouse pallial interneuron fate and maturation through neuropsychiatric disease gene regulation. *Elife* 9:e54903. doi: 10.7554/eLife.54903

Paulsen, B., Velasco, S., Kedaigle, A. J., Pigoni, M., Quadrato, G., and Deo, A. J. (2022). Autism genes converge on asynchronous development of shared neuron classes. *Nature* 602, 268–273. doi: 10.1038/s41586-021-04358-6

Pereira, J. D., Sansom, S. N., Smith, J., Dobenecker, M. W., Tarakhovsky, A., and Livesey, F. J. (2010). Ezh2, the histone methyltransferase of PRC2, regulates the balance between self-renewal and differentiation in the cerebral cortex. *Proc. Natl. Acad. Sci. U S A.* 107, 15957–15962. doi: 10.1073/pnas.1002530107

Petros, T. J., Bultje, R. S., Ross, M. E., Fishell, G., and Anderson, S. A. (2015). Apical versus basal neurogenesis directs cortical interneuron subclass fate. *Cell Rep.* 13, 1090–1095. doi: 10.1016/j.celrep.2015.09.079

Podobinska, M., Szablowska-Gadomska, I., Augustyniak, J., Sandvig, I., Sandvig, A., and Buzanska, L. (2017). Epigenetic modulation of stem cells in neurodevelopment: the role of methylation and acetylation. *Front. Cell Neurosci.* 11:23. doi: 10.3389/fncel.2017.00023

Priya, R., Paredes, M. F., Karayannis, T., Yusuf, N., Liu, X., Jaglin, X., et al. (2018). Activity regulates cell death within cortical interneurons through a calcineurin-dependent mechanism. *Cell Rep.* 22, 1695–1709. doi: 10.1016/j.celrep.2018.01.007

Quattrocolo, G., Fishell, G., and Petros, T. J. (2017). Heterotopic transplantations reveal environmental influences on interneuron diversity and maturation. *Cell Rep.* 21, 721–731. doi: 10.1016/j.celrep.2017.09.075

Quinlan, A. R., and Hall, I. M. (2010). BEDTools: a flexible suite of utilities for comparing genomic features. *Bioinformatics* 26, 841–842. doi: 10.1093/bioinformatics/btq033

Qureshi, I. A., and Mehler, M. F. (2018). Epigenetic mechanisms underlying nervous system diseases. *Handb. Clin. Neurol.* 147, 43–58.

Rajarajan, P., Jiang, Y., Kassim, B. S., and Akbarian, S. (2018). Chromosomal conformations and epigenomic regulation in schizophrenia. *Prog. Mol. Biol. Transl. Sci.* 157, 21–40.

Ramirez, F., Ryan, D. P., Gruning, B., Bhardwaj, V., Kilpert, F., Richter, A. S., et al. (2016). deepTools2: a next generation web server for deep-sequencing data analysis. *Nucleic Acids Res.* 44, W160–W165. doi: 10.1093/nar/gkw257

Rhodes, C. T., Thompson, J. J., Mitra, A., Asokumar, D., Lee, D. R., Lee, D. J., et al. (2022). An epigenome atlas of neural progenitors within the embryonic mouse forebrain. *Nat. Commun.* 13:4196. doi: 10.1038/s41467-022-31793-4

Rice, J. C., and Allis, C. D. (2001). Histone methylation versus histone acetylation: new insights into epigenetic regulation. *Curr. Opin. Cell Biol.* 13, 263–273.

Robinson, J. T., Thorvaldsdottir, H., Winckler, W., Guttman, M., Lander, E. S., Getz, G., et al. (2011). Integrative genomics viewer. *Nat. Biotechnol.* 29, 24–26.

Robinson, M. D., Mccarthy, D. J., and Smyth, G. K. (2010). edgeR: a bioconductor package for differential expression analysis of digital gene expression data. *Bioinformatics* 26, 139–140.

Robinson, M. D., and Oshlack, A. (2010). A scaling normalization method for differential expression analysis of RNA-seq data. *Genome Biol.* 11:R25.

Ross-Innes, C. S., Stark, R., Teschendorff, A. E., Holmes, K. A., Ali, H. R., and Dunning, M. J. (2012). Differential oestrogen receptor binding is associated with clinical outcome in breast cancer. *Nature* 481, 389–393.

Satija, R., Farrell, J. A., Gennert, D., Schier, A. F., and Regev, A. (2015). Spatial reconstruction of single-cell gene expression data. *Nat. Biotechnol.* 33, 495–502.

Schmitz, M. T., Sandoval, K., Chen, C. P., Mostajo-Radji, M. A., Seeley, W. W., Nowakowski, T. J., et al. (2022). The development and evolution of inhibitory neurons in primate cerebrum. *Nature* 603, 871–877.

Schork, A. J., Won, H., Appadurai, V., Nudel, R., Gandal, M., and Delaneau, O. (2019). A genome-wide association study of shared risk across psychiatric disorders implicates gene regulation during fetal neurodevelopment. *Nat. Neurosci.* 22, 353–361. doi: 10.1038/s41593-018-0320-0

Shen, X., Liu, Y., Hsu, Y. J., Fujiwara, Y., Kim, J., Mao, X., et al. (2008). EZH1 mediates methylation on histone H3 lysine 27 and complements EZH2 in maintaining stem cell identity and executing pluripotency. *Mol. Cell* 32, 491–502. doi: 10.1016/j.molcel.2008.10.016

Shi, Y., Wang, M., Mi, D., Lu, T., Wang, B., and Dong, H. (2021). Mouse and human share conserved transcriptional programs for interneuron development. *Science* 374:eabj6641. doi: 10.1126/science.abj6641

Sokpor, G., Xie, Y., Rosenbusch, J., and Tuoc, T. (2017). Chromatin remodeling BAF (SWI/SNF) complexes in neural development and disorders. *Front. Mol. Neurosci.* 10:243. doi: 10.3389/fnmol.2017.00243

Southwell, D. G., Paredes, M. F., Galvao, R. P., Jones, D. L., Froemke, R. C., Sebe, J. Y., et al. (2012). Intrinsically determined cell death of developing cortical interneurons. *Nature* 491, 109–113.

Stark, R., and Brown, G. D. (2023). *DiffBind: Differential Binding Analysis of ChIP-seq Peak Data*. Cambridge: University of Cambridge.

Stedehouder, J., Brizee, D., Shpak, G., and Kushner, S. A. (2018). Activity-dependent myelination of parvalbumin interneurons mediated by axonal morphological plasticity. *J. Neurosci.* 38, 3631–3642. doi: 10.1523/JNEUROSCI.0074-18.2018

Stovner, E. B., and Saetrom, P. (2019). epic2 efficiently finds diffuse domains in ChIP-seq data. *Bioinformatics* 35, 4392–4393. doi: 10.1093/bioinformatics/btz232

Street, K., Risso, D., Fletcher, R. B., Das, D., Ngai, J., Yosef, N., et al. (2018). Slingshot: cell lineage and pseudotime inference for single-cell transcriptomics. *BMC Genomics* 19:477. doi: 10.1186/s12864-018-4772-0

Stuart, T., Srivastava, A., Madad, S., Lareau, C. A., and Satija, R. (2021). Single-cell chromatin state analysis with signac. *Nat. Methods* 18, 1333–1341.

Sun, S., Yu, F., Xu, D., Zheng, H., and Li, M. (2022). EZH2, a prominent orchestrator of genetic and epigenetic regulation of solid tumor microenvironment and immunotherapy. *Biochim. Biophys. Acta Rev. Cancer* 1877:188700. doi: 10.1016/j.bbcan.2022.188700

Susaki, E. A., Tainaka, K., Perrin, D., Kishino, F., Tawara, T., and Watanabe, T. M. (2014). Whole-brain imaging with single-cell resolution using chemical cocktails and computational analysis. *Cell* 157, 726–739. doi: 10.1016/j.cell.2014.03.042

Takahashi, K., Liu, F. C., Hirokawa, K., and Takahashi, H. (2008). Expression of Foxp4 in the developing and adult rat forebrain. *J. Neurosci. Res.* 86, 3106–3116. doi: 10.1002/jnr.21770

Taniguchi, H., Lu, J., and Huang, Z. J. (2013). The spatial and temporal origin of chandelier cells in mouse neocortex. *Science* 339, 70–74.

Tatton-Brown, K., Murray, A., Hanks, S., Douglas, J., Armstrong, R., and Banka, S. (2013). Weaver syndrome and EZH2 mutations: clarifying the clinical phenotype. *Am. J. Med. Genet. A* 161A, 2972–2980. doi: 10.1002/ajmg.a.36229

Taylor, M. R., Martin, E. A., Sinnen, B., Trilokekar, R., Ranza, E., Antonarakis, S. E., et al. (2020). Kirrel3-mediated synapse formation is attenuated by disease-associated missense variants. *J. Neurosci.* 40, 5376–5388. doi: 10.1523/JNEUROSCI.3058-19.2020

Trevino, A. E., Sinnott-Armstrong, N., Andersen, J., Yoon, S. J., Huber, N., Pritchard, J. K., et al. (2020). Chromatin accessibility dynamics in a model of human forebrain development. *Science* 367:eaay1645. doi: 10.1126/science.aay1645

Tricoire, L., Pelkey, K. A., Daw, M. I., Sousa, V. H., Miyoshi, G., Jeffries, B., et al. (2010). Common origins of hippocampal Ivy and nitric oxide synthase expressing neurogliaform cells. *J. Neurosci.* 30, 2165–2176. doi: 10.1523/JNEUROSCI.5123-09.2010

Tricoire, L., Pelkey, K. A., Erkkila, B. E., Jeffries, B. W., Yuan, X., and Mcbain, C. J. (2011). A blueprint for the spatiotemporal origins of mouse hippocampal interneuron diversity. *J. Neurosci.* 31, 10948–10970. doi: 10.1523/JNEUROSCI.0323-11.2011

Valiente, M., and Marin, O. (2010). Neuronal migration mechanisms in development and disease. *Curr. Opin. Neurobiol.* 20, 68–78.

Velmeshev, D., Perez, Y., Yan, Z., Valencia, J. E., Castaneda-Castellanos, D. R., and Schirmer, L. (2022). Single-cell analysis of prenatal and postnatal human cortical development. *bioRxiv [Preprint]* doi: 10.1101/2022.10.24.513555

von Schimmelmann, M., Feinberg, P. A., Sullivan, J. M., Ku, S. M., Badimon, A., and Duff, M. K. (2016). Polycomb repressive complex 2 (PRC2) silences genes responsible for neurodegeneration. *Nat. Neurosci.* 19, 1321–1330. doi: 10.1038/nn.4360

Wang, D., Liu, S., Warrell, J., Won, H., Shi, X., and Navarro, F. C. P. (2018). Comprehensive functional genomic resource and integrative model for the human brain. *Science* 362:eaat8464.

Wang, W., Cho, H., Kim, D., Park, Y., Moon, J. H., and Lim, S. J. (2020). PRC2 acts as a critical timer that drives oligodendrocyte fate over astrocyte identity by repressing the notch pathway. *Cell Rep.* 32:108147. doi: 10.1016/j.celrep.2020.108147

Wever, I., Wagemans, C., and Smidt, M. P. (2019). EZH2 is essential for fate determination in the mammalian isthmic area. *Front. Mol. Neurosci.* 12:76. doi: 10.3389/fnmol.2019.00076

Williams, R. H., and Riedemann, T. (2021). Development, diversity, and death of MGE-derived cortical interneurons. *Int. J. Mol. Sci.* 22:9297. doi: 10.3390/ijms22179297

Wonders, C. P., Taylor, L., Welagen, J., Mbata, I. C., Xiang, J. Z., and Anderson, S. A. (2008). A spatial bias for the origins of interneuron subgroups within the medial ganglionic eminence. *Dev. Biol.* 314, 127–136.

Wu, Q., Shichino, Y., Abe, T., Suetsugu, T., Omori, A., Kiyonari, H., et al. (2022). Selective translation of epigenetic modifiers affects the temporal pattern and differentiation of neural stem cells. *Nat. Commun.* 13:470. doi: 10.1038/s41467-022-28097-y

Xu, Q., Tam, M., and Anderson, S. A. (2008). Fate mapping Nkx2.1-lineage cells in the mouse telencephalon. *J. Comp. Neurol.* 506, 16–29.

Xue, P., Huang, S., Han, X., Zhang, C., Yang, L., Xiao, W., et al. (2022). Exosomal miR-101-3p and miR-423-5p inhibit medulloblastoma tumorigenesis through targeting FOXP4 and EZH2. *Cell Death Differ.* 29, 82–95. doi: 10.1038/s41418-021-00838-4

Yao, B., Christian, K. M., He, C., Jin, P., Ming, G. L., and Song, H. (2016). Epigenetic mechanisms in neurogenesis. *Nat. Rev. Neurosci.* 17, 537–549.

Yu, G., Wang, L. G., and He, Q. Y. (2015). ChIPseeker: an R/Bioconductor package for ChIP peak annotation, comparison and visualization. *Bioinformatics* 31, 2382–2383. doi: 10.1093/bioinformatics/btv145

Yu, Y., Zeng, Z., Xie, D., Chen, R., Sha, Y., Huang, S., et al. (2021). Interneuron origin and molecular diversity in the human fetal brain. *Nat. Neurosci.* 24, 1745–1756. doi: 10.1038/s41593-021-00940-3

Zaidi, S. K., Young, D. W., Montecino, M., Van Wijnen, A. J., Stein, J. L., Lian, J. B., et al. (2011). Bookmarking the genome: maintenance of epigenetic information. *J. Biol. Chem.* 286, 18355–18361.

Zemke, M., Draganova, K., Klug, A., Scholer, A., Zurkirchen, L., and Gay, M. H. (2015). Loss of Ezh2 promotes a midbrain-to-forebrain identity switch by direct gene derepression and Wnt-dependent regulation. *BMC Biol.* 13:103. doi: 10.1186/s12915-015-0210-9

Zeng, J., Zhang, J., Sun, Y., Wang, J., Ren, C., Banerjee, S., et al. (2022). Targeting EZH2 for cancer therapy: from current progress to novel strategies. *Eur. J. Med. Chem.* 238:114419.

Zhang, M., Zhang, Y., Xu, Q., Crawford, J., Qian, C., and Wang, G. (2019). Neuronal histone methyltransferase EZH2 regulates neuronal morphogenesis, synaptic plasticity, and cognitive behavior of mice. *bioRxiv [Preprint]* doi: 10.1101/582908

Zhao, J., Jaffe, A., Li, H., Lindenbaum, O., Sefik, E., Jackson, R., et al. (2021). Detection of differentially abundant cell subpopulations in scRNA-seq data. *Proc. Natl. Acad. Sci. U S A.* 118:e2100293118.

Zhao, L., Li, J., Ma, Y., Wang, J., Pan, W., Gao, K., et al. (2015). Ezh2 is involved in radial neuronal migration through regulating Reelin expression in cerebral cortex. *Sci. Rep.* 5:15484. doi: 10.1038/srep15484

Zhao, Z., Zhang, D., Yang, F., Xu, M., Zhao, S., Pan, T., et al. (2022). Evolutionarily conservative and non-conservative regulatory networks during primate interneuron development revealed by single-cell RNA and ATAC sequencing. *Cell Res.* 32, 425–436.

frontiers | Frontiers in Cellular Neuroscience

TYPE Original Research
PUBLISHED 04 June 2024
DOI 10.3389/fncel.2024.1390742

OPEN ACCESS

EDITED BY
Goichi Miyoshi,
Gunma University, Japan

REVIEWED BY
Miho Terunuma,
Niigata University, Japan
Guillermo Gonzalez-Burgos,
University of Pittsburgh, United States

*CORRESPONDENCE
Andre H. Lagrange
✉ andre.h.lagrange@vumc.org

†These authors have contributed equally to this work and share first authorship

RECEIVED 23 February 2024
ACCEPTED 13 May 2024
PUBLISHED 04 June 2024

CITATION
Zavalin K, Hassan A, Zhang Y, Khera Z and Lagrange AH (2024) Region and layer-specific expression of $GABA_A$ receptor isoforms and KCC2 in developing cortex.
Front. Cell. Neurosci. 18:1390742.
doi: 10.3389/fncel.2024.1390742

Region and layer-specific expression of $GABA_A$ receptor isoforms and KCC2 in developing cortex

Kirill Zavalin[1†], Anjana Hassan[1†], Yueli Zhang[1], Zain Khera[1] and Andre H. Lagrange[1,2*]

[1]Department of Neurology, Vanderbilt University School of Medicine, Nashville, TN, United States, [2]Department of Neurology, TVH VA Medical Center, Nashville, TN, United States

Introduction: γ-Aminobutyric acid (GABA) type A receptors ($GABA_A$Rs) are ligand-gated Cl-channels that mediate the bulk of inhibitory neurotransmission in the mature CNS and are targets of many drugs. During cortical development, $GABA_A$R-mediated signals are significantly modulated by changing subunit composition and expression of Cl-transporters as part of developmental processes and early network activity. To date, this developmental evolution has remained understudied, particularly at the level of cortical layer-specific changes. In this study, we characterized the expression of nine major $GABA_A$R subunits and K-Cl transporter 2 (KCC2) in mouse somatosensory cortex from embryonic development to postweaning maturity.

Methods: We evaluated expression of α1-5, β2-3, γ2, and δ $GABA_A$R subunits using immunohistochemistry and Western blot techniques, and expression of KCC2 using immunohistochemistry in cortices from E13.5 to P25 mice.

Results: We found that embryonic cortex expresses mainly α3, α5, β3, and γ2, while expression of α1, α2, α4, β2, δ, and KCC2 begins at later points in development; however, many patterns of nuanced expression can be found in specific lamina, cortical regions, and cells and structures.

Discussion: While the general pattern of expression of each subunit and KCC2 is similar to previous studies, we found a number of unique temporal, regional, and laminar patterns that were previously unknown. These findings provide much needed knowledge of the intricate developmental evolution in $GABA_A$R composition and KCC2 expression to accommodate developmental signals that transition to mature neurotransmission.

KEYWORDS

GABA-A receptors, potassium chloride co-transporter 2 (KCC2), developmental expression pattern, cortical development, GABAA subtypes, Western blot (WB), immunohistochemistry (IHC)

Introduction

GABA-A receptors ($GABA_A$Rs) are Cl^--conducting ion channels activated by γ-Aminobutyric acid (GABA) that convey the majority of inhibitory neurotransmission in the adult brain. $GABA_A$R activity appears early in cortical development, preceding the emergence of glutamatergic activity in some brain regions (Wang and Kriegstein, 2008; Chancey et al., 2013; Warm et al., 2022). This early GABAergic signaling regulates many aspects of brain development, including migration of GABAergic interneuron progenitors (Cuzon et al., 2006; Bortone and Polleux, 2009; Cuzon Carlson and Yeh, 2011; Inada et al., 2011; Inamura et al., 2012), formation of synapses (Wang and Kriegstein, 2008, 2011; Oh et al., 2016), neurite extension (Ge et al., 2006; Cancedda et al., 2007; Bouzigues et al., 2010), and circuit integration of immature neurons through concerted high-amplitude

early network oscillations termed "giant depolarizing potentials" (Ben-Ari et al., 2007; Allene et al., 2008); reviewed by Kilb (2021) and Peerboom and Wierenga (2021).

$GABA_A$Rs are pentameric ligand-gated ion channels, commonly comprised of a combination of α, β, and either γ or δ subunits that determine receptor properties and localization. There are multiple isoforms for these subunits, with α1-5, β1-3, γ2, and δ being the most prevalent in mammalian forebrain. Of the most common subunit combinations, α1β2/3γ2, α2β2/3γ2, and α3β2/3γ2 localize to synapses and mediate phasic responses to GABA, while α4βδ and α5βγ2 are typically found in the extrasynaptic space and primarily mediate tonic currents (Chuang and Reddy, 2018; Engin et al., 2018). The α1β2/3γ2 combination is the predominant subunit combination found in mature synapses and the target of many of our most useful drugs used in babies and adults, including anti-seizure medicine and anxiolytics (Möhler, 2006; Engin et al., 2018). In contrast, α4β2δ and α5β3γ2 $GABA_A$Rs that mediate tonic inhibition are sensitive to lower and [GABA] and have slower activation and deactivation kinetics (Lagrange et al., 2018). These receptors are targeted by several general anesthetics and alcohol. Many subunit isoforms have regionally specific distributions (Pirker et al., 2000; Hortnagl et al., 2013).

$GABA_A$R-mediated responses undergo a significant transformation over the course of development that reflects synaptic maturation, but also transient developmental adaptations. Most notably, $GABA_A$R activation during early development can be excitatory, which triggers Ca^{2+} transients that promote cytoskeletal remodeling and synaptic plasticity and appears to be essential for many developmental processes driven by GABA (Kilb, 2021; Peerboom and Wierenga, 2021). On a similar timeline, early GABAergic responses display slow and tonic kinetics conducive to developmental processes (Owens et al., 1999; Daw et al., 2007; Sebe et al., 2010; Le Magueresse and Monyer, 2013; Warm et al., 2022), while fast GABAergic responses optimal for resolution of discrete synaptic events emerge with maturity (Bosman et al., 2002; Kobayashi et al., 2008; Brown et al., 2016; Kroon et al., 2019).

Developmental changes in expression of $GABA_A$R subunits and K-Cl transporter 2 (KCC2) drive many of the changes to GABAergic responses during development. Cl^- extrusion by KCC2 is the primary mechanism for maintaining low intracellular [Cl^-] that drives inhibitory GABAergic responses. Both KCC2 expression and kinase-determined functional state are developmentally regulated to increase KCC2 activity with maturation of GABAergic neurotransmission, resulting in a relatively rapid shift from excitatory to inhibitory GABAergic responses in the second and third week of postnatal life (Fukuda, 2020). Meanwhile, a large body of work has demonstrated that developmental changes in subunit composition of $GABA_A$Rs profoundly modify GABAergic signaling in context of specific developmental processes (Bosman et al., 2002; Serwanski et al., 2006; Giusi et al., 2009; Sebe et al., 2010; Cuzon Carlson and Yeh, 2011; Brady and Jacob, 2015; Hernandez et al., 2019; Lodge et al., 2021).

Given the importance of KCC2 and $GABA_A$R composition during development, a detailed understanding of their developmental expression is of vital importance. Previously, several expression studies (Fritschy et al., 1994; Golshani et al., 1997; Paysan et al., 1997) characterized the general and regional course of $GABA_A$R subunit expression in developing cortex, including an extensive characterization of mRNA expression of thirteen major $GABA_A$R subunits from middle of embryonic development to adulthood in rat brains (Laurie et al., 1992). Unfortunately, these studies are limited by primarily looking only at mRNA expression and missing laminar details, and a need exists for a more comprehensive, detailed characterization of $GABA_A$R subunit protein expression similar to adult expression studies (Pirker et al., 2000; Hortnagl et al., 2013). A lesser knowledge gap exists for developmental expression of KCC2, which has been investigated at the level of mRNA and protein in mouse and human tissue, including regional specificity in adult CNS (Markkanen et al., 2014) and developmental expression (Lu et al., 1999; Rivera et al., 1999; Stein et al., 2004; Uvarov et al., 2009; Murguia-Castillo et al., 2013), specifically including cortex (Dzhala et al., 2005; Vanhatalo et al., 2005; Takayama and Inoue, 2010; Kovács et al., 2014; Sedmak et al., 2016). These studies defined the general trend in KCC2 expression over the course of development, including some laminar and cell-type specificity, such as early interneuron-specific expression we recently reported (Zavalin et al., 2022). However, a more comprehensive study of KCC2 expression in developing cortical lamina is still needed. In this study, we address these knowledge gaps by a comprehensive and focused characterization of expression patterns of major $GABA_A$R subunits and KCC2 from cortical plate formation (E13.5) to more mature brain (P26) in mouse cortex. We paid particular attention to lamina-specific expression within barrel cortex, which showed a rich level of complexity at these ages.

Materials and methods

Experimental mice, background and breeding

Mice were maintained in temperature-controlled housing areas, were adequately fed, hydrated, and kept under 12:12 h of alternating dark/light cycles. All animal handling and procedures were approved by Vanderbilt IACUC and VA ACORP committees. All experiments were performed using both female and male C57BL/6J congenic mice. Experiments requiring interneuron identification used Dlx5/6-Cre-IRES-EGFP mice (Jackson labs stock # 023724) that we had bred into the C57BL/6J congenic line for at least eleven generations. *Gabra3* knockout mice, exhibiting complete loss of $GABA_A$R α3, were generously donated by Uwe Rudolph, maintained by our lab, and used for validating the $GABA_A$R α3 antibody from Alomone labs. For experiments requiring embryonic timepoints, timed pregnancies for dams were carried out by mating them with wild type males from 4 pm to 4 pm next day. The following day in which the vaginal mucous plug was seen was taken as E0.5.

Tissue collection and preparation

Postnatal brain tissues for P1, P5, P12, and P25/26 timepoints were collected from either wildtype or *Dlx5* $GFP^{+/WT}$ mice to label MGE-derived interneurons by decapitation under isoflurane anesthesia, after which the brain and meninges were removed

from the skull. Similarly, E13.5, E15.5, and E17.5 brain tissues were collected from embryos that were dissected from pregnant dams under anesthesia. After dissection, the embryos were quickly decapitated. For Western blot (WB) experiments, brains were dissected in PBS with tweezers under a dissection microscope to separate cortex from subcortical structures, and then processed as described below. For immunohistochemistry (IHC) experiments, embryonic heads and postnatal brain tissue were fixed with a brief immersion in 4% paraformaldehyde in PBS for 7 min. Similarly to previous reports (Schneider Gasser et al., 2006), we found that this light fixation protocol provided much greater detail for $GABA_AR$ studies than the relatively homogenous, non-punctate staining that we typically obtained from cardiac-perfused tissue. Following fixation, postnatal brains and embryonic heads were transferred to 30% sucrose for 24–48 h for cryoprotection, blocked by coronal cuts at the levels of prefrontal cortex and brain stem, and cryo-embedded in OCT compound. Twenty μm-thick sections were obtained for all ages under study using a Leica cryostat and stored in −80°C.

Genotyping, PCR and primers

PCR analysis was performed on tail tissue harvested on E13.5, E15.5, E17.5, P1, P5, or on ear punches for P12 and P25 to determine genotypes. We used Sigma REDExtract-N-Amp tissue PCR kit Cat # XNAT-100RXN for extracting and amplifying the tissue DNA. For genotyping presence of Dlx5/6-Cre-IRES-EGFP in our mice, we used the following primers: Cre Forward 5′-GCA TTA CCG GTC GAT GCA ACG AGT GAT GAG-3′, Cre reverse: 5′-GAG TGA ACG AAC CTG GTC GAA ATC AGT GCG-3′ and the following thermal cycler protocol: 94°C for 3 min, (94°C for 30 seconds, 68°C for 30 seconds, 72°C for 1 min) × 30 cycles to amplify a cre product at 408 bp. For genotyping *Gabra3* knockout mice, we used the following primers: Primer UR75: 5′-GAC AGA CAT GGC ATG ATG AAA GAC TGA AAT−3′, Primer UR106: 5′-ACA AAA TGT AAG AAC AAG AAC CAA GAA AAT-3′ and the following thermal cycler protocol: 96°C for 1 min, (96°C for 15 seconds, 50°C for 10 seconds, 70°C for 1 min) × 40 cycles, 68°C for 5 min and hold at 4°C to amplify a single band at 480 bp for wildtype and two bands at 480 and 520 bp for knockout. Product bands were distinguished by electrophoresis on a 2% agarose gel stained with SYBR Safe DNA gel stain (Invitrogen Cat# P/N S33102) and visualized using Biorad GelDoc EZ.

Antibodies

We chose target proteins and antibodies for this study based on several factors. Firstly, we reviewed known mRNA expression in embryonic/perinatal forebrain (Laurie et al., 1992). We then chose subunits contained in $GABA_AR$ combinations whose pharmacological and kinetic properties have been characterized to allow us to formulate subsequent hypotheses about the potential physiological significance of our results. Finally, we selected commercially available antibodies to improve the generalizable utility of this work for other investigators.

When validating our antibodies, we first screened for subunit specificity using recombinant receptors expressed in HEK 293T cells (Lagrange et al., 2007). Whole cell protein extracts (data not shown) and plated HEK cells (Supplementary Figure 1) were analyzed by immunoblot to find isoform-specific anti-$GABA_AR$ antibodies which detect the appropriately sized protein band for the target protein without cross-reactivity with off-target subunit isoforms. We then further confirmed antibody sensitivity and specificity of non-denatured proteins by immunostaining young adult mouse brain tissue, selecting antibodies that labeled regionally specific patterns of subunit-specific expression found in previously published reports (Pirker et al., 2000; Hortnagl et al., 2013) (Figure 1). The α4 immunostains were sometimes associated with a non-specific punctate signal that we could not entirely prevent, which presented as a patchy, inconsistent signal that was equally present in tissue known to lack expression of α4, such as postnatal white matter. While most antibodies have well-defined patterns of high/low expression, this is not true for the more ubiquitously expressed β3, γ2 subunits, so these antibodies were validated using embryonic brain slices from knockout mice that do not express those proteins, using tissue that was generously provided by Jing-Qiong Kang's lab. We also confirmed specificity of α3 and KCC2 expression using knockout mice. The resulting list of validated antibodies used in our study is presented in Supplementary Table 1.

HEK293T transfection and immunocytochemistry

Human embryonic kidney cells (HEK293T) were maintained in culture and transfected as previously described (Lo et al., 2014). Cells were transfected with a combination of cDNAs, each containing the sequence for one of the rat $GABA_AR$ mRNA. These were done using Fugene with equimolar amounts (1 μg) of each cDNA. For Western blot (WB), cells were then harvested, and protein extracted as described below. For immunocytochemistry, cells were harvested and then replaced at 10K cells per well in a 24-well plate. They were then cultured overnight and then processed for immunocytochemistry. We tested a number of fixation techniques, including methanol, 4% PFA × 5 min, and 4% PFA + 4% sucrose for 15 min. We also tested multiple blocking conditions, including milk, BSA, or donkey/horse serum, with or without Triton X-100. Based on these results, we chose 4% PFA × 5 min, blocked in 10% donkey serum + 0.3% Triton X-100, then overnight incubation with the primary antibody without Triton X-100 at 1:250 to 1:500. These were then stained with the appropriate secondary antibody, as described in the immunofluorescence section. Wells were then washed three times in PBS, followed by imaging at 10× with an upright Zeiss microscope.

Western blots

Tissue was homogenized with a sonicator (QSonica) in a modified RIPA buffer containing (50 mM Tris-HCl pH 7.4, 150 mM

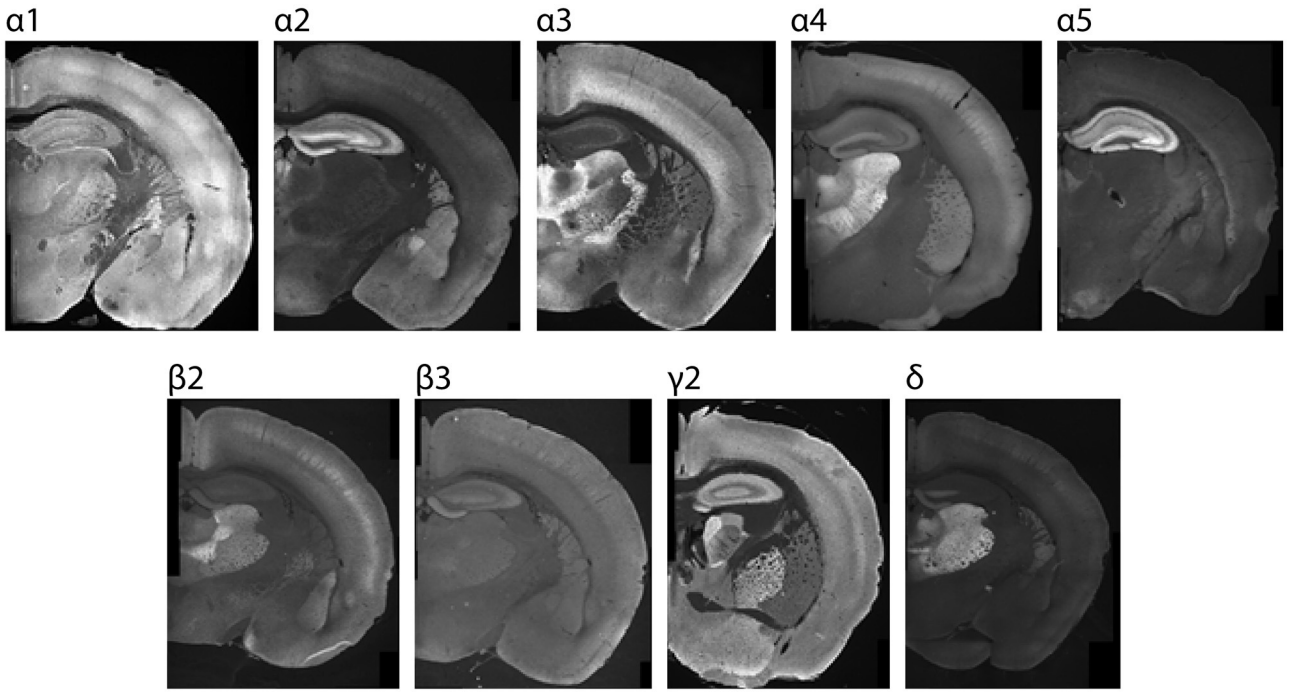

FIGURE 1
Sample P26 images showing region-specific immunolabeling patterns of $GABA_AR$ subunits in the CNS. Regions with the highest expression were used for setting acquisition settings and the maximum grading threshold for quantifying subunit expression within cortex.

NaCl, 1% NP-40, 0.2% sodium deoxycholate, 1 mM EDTA) with 10 μL/mL protease and phosphatase inhibitors (Sigma). Protein concentration was determined with the Bradford assay (Bio-Rad), and samples were diluted to a final concentration of 1 to 3 μg/μL in Laemmli loading buffer (Biorad) containing β-mercaptoethanol. Heat denaturation was skipped due to the delicate nature of transmembrane proteins like $GABA_AR$ subunits. Samples and protein ladder (Cytiva RPN800E) were loaded onto a 10% SDS gel (Invitrogen) and run at 75–85 V for 2.5–3 h. Proteins were transferred in a Tris-glycine transfer buffer (19.2 mM Glycine, 7.5 mM Tris-base, 20% methanol) onto Immobilon-FL PVDF membranes (Millipore) by applying 100 V for 1.5 h. Membranes were then blocked in TBS with 0.1% Tween-20 (TBS-T) with 4% milk for 1 h at room temperature. Membranes were cut into portions containing E6AP (top) and actin/$GABA_AR$ protein (bottom) and incubated with respective primary antibodies in 5% BSA in TBS-T overnight at 4°C. Primary antibodies were the same as those used for immunofluorescent staining of brain slices. Membranes were washed at least three times for 10 min in TBS-T and then incubated with fluorescent secondary antibodies in TBS-T for 2 h at room temperature or overnight at 4°C. Membranes were then washed three times for at least 10 min with TBS-T. Imaging was performed on a LI-COR Odyssey fluorescence scanner, protein expression was quantified with Odyssey imaging software, and further analyzed with MS Excel and GraphPad Prism. E6AP and actin were both evaluated as loading controls, after which E6AP was used to normalize all WB expression data for loading differences. The ratios of $GABA_AR$/E6AP were averaged, and the mean ± SEM were plotted vs. age. Differences in antibody affinity preclude direct comparisons of protein amounts among different subunits. Therefore, the point of maximal expression for each subunit was used to normal WB data for plotting. Data are depicted as arbitrary units (a.u.) relative to the maximal data point.

To minimize experiment-to-experiment variability, several WBs containing a full range of ages were run, probed for a single $GABA_AR$ subunit, and analyzed simultaneously. Typically, at least three measurements from three different mouse samples per developmental timepoint per antibody were collected. On a few occasions, we ran additional gels without the complete range of ages. This was due to either needing additional ages to characterize periods of rapid change, or because there was a loading error with a particular protein sample. In these uncommon cases, we included at least 2 protein samples from previously run gels to confirm consistency in our results. The anti-γ2 antibody here recognized both the long and short splice variants of this protein, but their sizes were too similar to discriminate. Examples of $GABA_AR$ subunit and E6AP WB bands obtained from cortical samples are shown in Supplementary Figure 2. Due to low levels of α4 expression in cortex during development, P36 thalamic and cortical samples were run as controls.

To perform statistical analysis on WB data, expression data was binned into E13.5-P3, P5-P10, and P12-P26 bins to represent generalized developmental stages and avoid type II error from having too many groups. Significance was determined using a one-way ANOVA with Šídák's multiple comparisons test between each of the three bins.

Immunofluorescence

The slides chosen for cortical staining included coronal sections containing somatosensory cortex. In postnatal tissue, this was further defined as coronal sections containing somatosensory and barrel cortex, and dorsal hippocampus. While not reported here, this plane of coronal sections also allowed us to visualize important germinal areas, such as pallial ventricular and subventricular zones (SVZ), median ganglionic eminence (MGE), intermediate zone (IZ), and postnatal hippocampus, thalamus, and basal ganglia. These postnatal areas were chosen based on strong subunit-specific expression for each. This allowed us to quality control for antibody specificity and qualitatively assess relative expression intensity from run to run. These results were used to conservatively optimize image acquisition parameters before imaging. For example, thalamic α3 expression is high in the reticular nucleus, but absent in ventrobasal thalamus. In contrast, α4 and δ expression are high in the ventrobasal thalamus, but not in the reticular nucleus. Specific cortical areas were identified using Prenatal Mouse Brain Atlas (Schambra and Schambra, 2008) and Chemoarchitectonic Atlas of the Developing Mouse Brain (Jacobowitz and Abbott, 1997) for E13.5 and E15.5 mice, Atlas of the Developing Mouse Brain at E17.5, P0, and P6 (Paxinos, 2007) for perinatal mice, and The Mouse Brain in Stereotaxic Coordinates (Paxinos and Franklin, 2004) for sections from mice P12 and older.

In order to minimize inter-run variability, immunolabeling was performed in batches that included multiple age groups: E13.5, E15.5, E17.5, P1, P5, P12, and/or P25/26. Immunolabeling was done between 4–10 times for each antibody, totaling tissue from 3–8 different mice for each age group. We also included a few slides with no primary antibody as control slides. Slides were labeled and circled around the tissue with the hydrophobic Pap Pen, dried at room temperature for 30 min, then washed (1× PBS, 0.2% Triton X-100) for 5 min. Slides were then blocked in blocking buffer (1× PBS, 0.2% Triton X-100, 10% donkey serum) for 1 h, then incubated with the appropriate primary antibody in blocking buffer at 4°C for two nights. Slides were washed 3 times for 5 min, then incubated with the appropriate secondary antibody in blocking buffer for 2 h at room temperature or overnight at 4°C. Sections were washed 3 times for 5 min, mounted and cover slipped with VectaShield HardSet Antifade Mounting Medium with DAPI (Vector Labs, Burlingame, CA), dried for 30 min at room temperature, and stored at 4°C. Images were acquired within 2 to 3 weeks of mounting.

Microscopy

Stained brain sections were imaged using a Leica DM 6000 epifluorescent microscope equipped with a DFC 365 FX digital camera (Leica, Buffalo Grove, IL). Images were acquired using 5× and 10× objectives. Acquisition settings for each antibody were determined using normative regions of interest (ROIs) from P26 brains (Figure 1), and the settings within each run were kept consistent for each subunit. Normative ROIs with maximal subunit expression include: α1: ventrobasal thalamus, α2: dentate gyrus molecular layer, α3: thalamic reticular nucleus, α4 and δ: dentate gyrus molecular layer, α5: CA3 of hippocampus, γ2: globus pallidus, β2: ventrobasal thalamus, and β3: dentate gyrus molecular layer. The grid images were stitched using Fiji Image J stitching plugin (Preibisch et al., 2009): stitching-grid/collection stitching, 30% overlap, maximum intensity fusion method with subpixel accuracy. The fused images were saved as 8-bit TIFF files. Post-stitching modifications included adjustments for contrast and were carried out for display purposes only using Image J. A subset of images was also acquired using higher magnification (20× or 40×), as indicated in the text.

Image analysis

Brain regions were identified using dedicated atlases of embryonic, perinatal, and adult mouse brain (Jacobowitz and Abbott, 1997; Paxinos and Franklin, 2004; Paxinos, 2007; Schambra and Schambra, 2008). When needed, marginal zone (MZ) and subplate (SP) were further identified (Bayer and Altman, 1990). The most superficial layer of the cortical plate (CP) was defined as MZ before P1, and then as layer 1 postnatally. Cortical layers were defined using DAPI staining of our tissue. We then performed semi-quantitative grading of expression based on age and cortical layers by quantifying the mean intensity in at least three randomly selected regions for each region/layer/age. These numeric results for all ages and cortical layers within each run of IHC were collated to determine the distribution of our results. This information was then used to determine the percentile ranks of each data point and were the basis for initial grades (e.g., >90% percentile was considered a "+ + +"). Multiple investigators (AHL, AH, KZ, and ZK) then reviewed these grades and the original source images from multiple runs to form a consensus semi-quantitative grading. Each experimental run included E13.5 to P26 tissue, and the ROIs chosen as the normative reference areas of highest expression were assigned a value of 5, while postnatal white matter as 0. Images from at least three animals per timepoint were used in making these assessments. Some subunits had a pattern of expression that was stronger in either the upper or lower portion of a particular layer. This occurred most commonly with L5. In these situations, we report the upper portion as L5a, the lower portion as L5b. This distinction is based purely on the pattern of expression and may not exactly match sublayers reported in the literature that are based on other patterns of expression or physiology. Composite, multi-age figures were typically created from tissue run at the same time to more accurately convey expression-intensity differences over time.

Laminae in figures and grading tables

In figures, divisions of adult and transient development-specific lamina were defined based on the DAPI signal and were then superimposed on greyscale IHC images. Grading tables used definitions of adult laminae and the transient subplate for ease of tracking laminar changes within a single row. At E13.5-P1, MZ corresponds to L1 in the grading table. CP corresponds to L2-L4 in the grading table for E15.5-P1. Expression for most subunits was ubiquitous in the CP, but when certain banding was

observed at the bottom of the CP, this was distinguished as L4-specific signal at these early stages. For some images at E15.5 when no expression differences were seen between CP, L5, and L6, we did not distinguish these laminae and labeled them all as CP. For images at E13.5, CP corresponded to L2–L6 in the grading table.

Results

We started our investigation by validating $GABA_AR$ subunit specificity for a panel of antibodies for α1-5, β2-3, δ, and γ2 *in vitro* in HEK cells expressing different $GABA_AR$ combinations (Supplementary Figure 1), and showing that regional IHC expression at P26 (Figure 1) matched previous reports (Hortnagl et al., 2013). Next, we used the validated antibodies to create a developmental profile of $GABA_AR$ subunit expression in cortex at different timepoints. Our approach included (1) a quantitative comparison of expression changes associated with each developmental stage by Western blot (WB) across a detailed timeline with statistical analysis performed between three generalized stages (E13.5-P3; P5-P10; P15-P25); and (2) a complimentary layer and region-specific analysis of expression by immunohistochemistry (IHC). Using IHC, we generated a large dataset of immunolabeled tissue, which we used for semi-quantitative grading of laminar expression differences as the development progresses. We designed our semi-quantitative approach (refer to Methods) based on seminal expression studies in our field (Pirker et al., 2000; Hortnagl et al., 2013; Stefanits et al., 2018), which is arguably the most objective approach to quantifying IHC expression while taking into account staining variability and other limitations of IHC. We found that each subunit showed distinct temporal and layer-specific patterns of expression, which are discussed below.

$GABA_AR$ α1

An overview of α1-5 subunit expression is shown in Figure 2. Cortical immunoreactivity of α1 on WB was generally low in embryonic and early postnatal period, but steadily rose to prominent and then high levels in the late postnatal period that showed a statistically significant difference from earlier expression (Figure 3, $^{****}P < 0.0001$ P15-P25 vs. earlier ages). Our IHC experiments corroborated this trend and revealed significant regional and lamina-specific differences (Figures 2, 3). At E13.5, α1 protein expression was essentially absent from the developing cortex and underlying regions, and only very low α1 levels were seen at E15.5. Somewhat higher expression in the cortex and subplate was evident at E17.5 and P1, primarily in marginal zone (MZ)/layer 1 (L1) and layer 4 (L4). At these ages, future somatosensory cortex could be distinguished from adjacent regions by elevated α1 expression in L4. While α1 was low in other layers at E17.5-P1, there were clear α1-positive putative dendrites in L2 that appeared to arise from L4 and end in dendritic tufts in L1 (Figure 2) in a fashion similar to previously reported (Paysan et al., 1997; Paysan and Fritschy, 1998).

The overall α1 expression levels rose dramatically in most cortical areas at P5 but retained a layer-specific pattern. Increased α1 expression in L2/3 made it impossible to distinguish the aforementioned L2/3 dendrites by P5. However, the highest expression remained in L1 and L4, as well as somewhat increased expression at the boundary of L5b/L6a. This gave the appearance of alternating bands of high expression in L1, L4, and L5b/L6a boundary with lower expression in-between. Expression at P12 and P26 continued to rise throughout cortex, becoming most prominent in L1-4 and highest in L3/4 of barrel cortex. Expression within L5/6 was comparatively lower at these ages, but consistently higher in L6 than L5.

$GABA_AR$ α2

WB analysis showed low α2 expression during embryonic and perinatal periods that greatly increased and peaked at P10-P18, coming down to a moderate level of expression at P25 (Figure 4). Our statistical evaluation showed this as a significant steady increase across development ($^{****}P < 0.0001$ E13.5-P3 vs. P5-P10, $^{**}P < 0.01$ P5-P10 vs. P15-P25). Our IHC experiments reflected this general trend but detected multiple instances of localized expression throughout development. At E13.5, there was very faint α2 expression in the MZ and subcortical tissue, but not the somatosensory cortical plate (CP) itself. Expression of α2 within the CP began at E15.5, with diffuse α2 expression mostly in the upper layers of CP (L1-3). Interestingly, most of the α2 signal in the lower CP appeared to be a continuation of radial fibers originating in subcortical tissue. This was more prominent at E17.5, with α2-positive radial fibers arising from the intermediate zone, extending through the subplate and then outward toward the cortical surface. These processes are clearly visible in L5/6 but are lost in the generalized α2 expression in more superficial layers. The identity of these fibers is not entirely clear, but they overlap with projections of RC2-expressing radial glia (Figure 5). At P1, the subcortical α2 signal disappears, but these processes are still visible in L5/6 until P5. Within the superficial layers, expression of α2 increased at P1 along a lateral-to-medial gradient, with a narrow strip of expression primarily in L1 in the far lateral somatosensory cortex that widens to include L1-3 in more medial somatosensory cortex and L1-5 in motor cortex (Figure 2).

By P5, there was an abrupt increase in α2 expression in L4, producing a transient pattern of highly restricted α2 expression to L1 and L4. While other $GABA_AR$ subunit proteins show a specific pattern in L4 somatosensory cortex at this age, the increased α2 expression is more widespread, involving L4 in most cortical areas, such as somatosensory, V1, parietal, auditory, and insular cortices (Figure 2). The one exception remains in adjacent motor cortex, where L4 is poorly distinguished from α2 expression in L2/3. By P12, the α2 expression becomes homogenous in L1-4, though it is still slightly higher in L4. Within L5/6, expression is overall lower, with a subtle band of elevated expression in L5b. This pattern persists at P26, albeit with modestly reduced overall expression. While our WB measurements and previous work (Fritschy et al., 1994) indicate a peak expression during the second or third postnatal week, we did not see a strong drop in tissue immunoreactivity within the somatosensory cortex at P26.

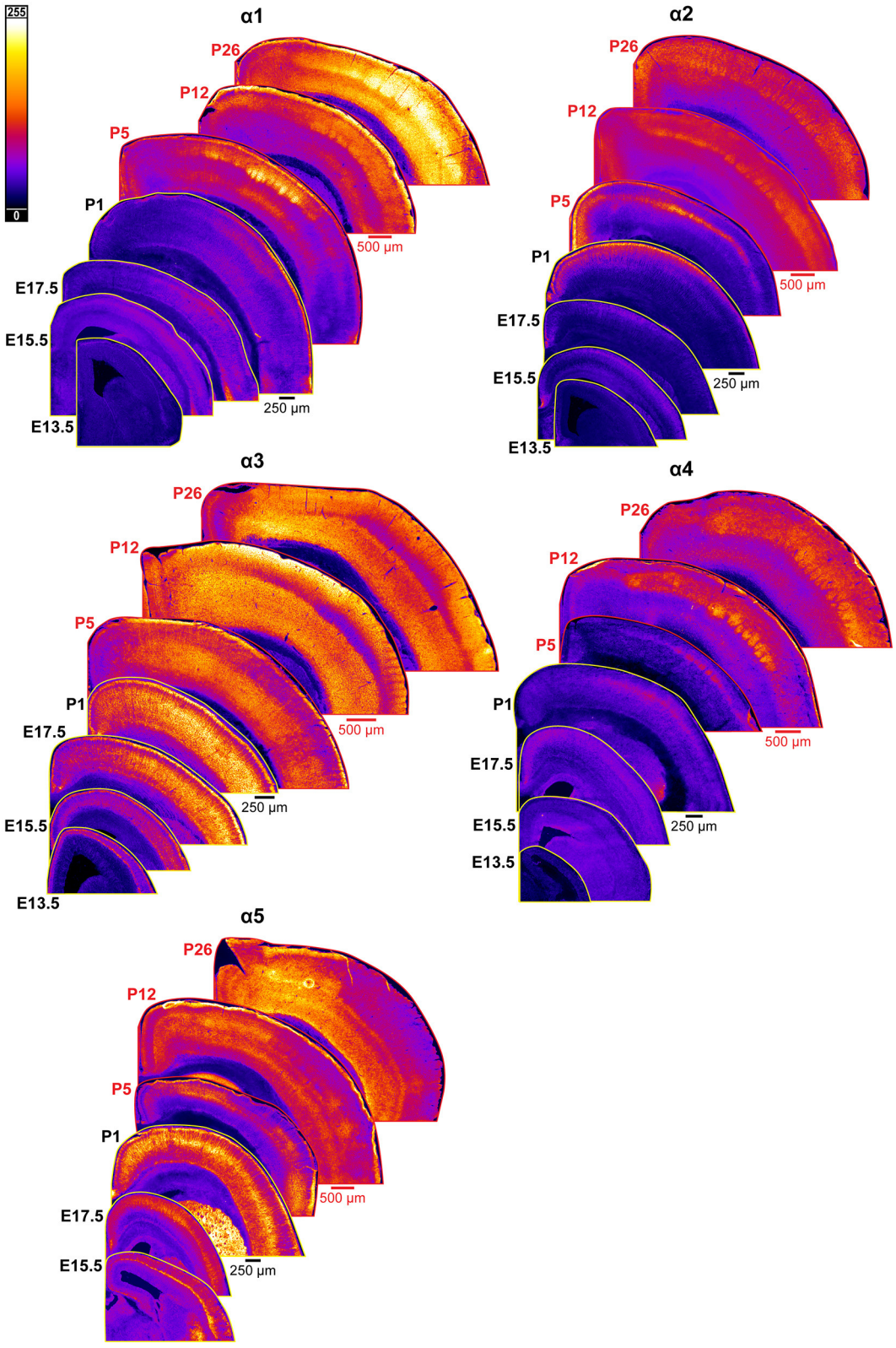

FIGURE 2
Expression of $GABA_AR$ α1-5 subunits in developing cortex. Coronal sections are overlaid from embryonic day E13.5/E15.5 on the bottom left to postnatal day 26 on the top right separately for each α subunit. All sections are oriented from ventral bottom to dorsal top, with lateral cortex on the right. Separate spatial scaling has been used for sections E13.5-P1 (black scale bar) and P5-P26 (red scale bar), separately for each subunit. Signal is represented using a subunit-specific heat map lookup table to highlight differences in regional expression. Heatmap intensity scaling is shown by the bar in top left.

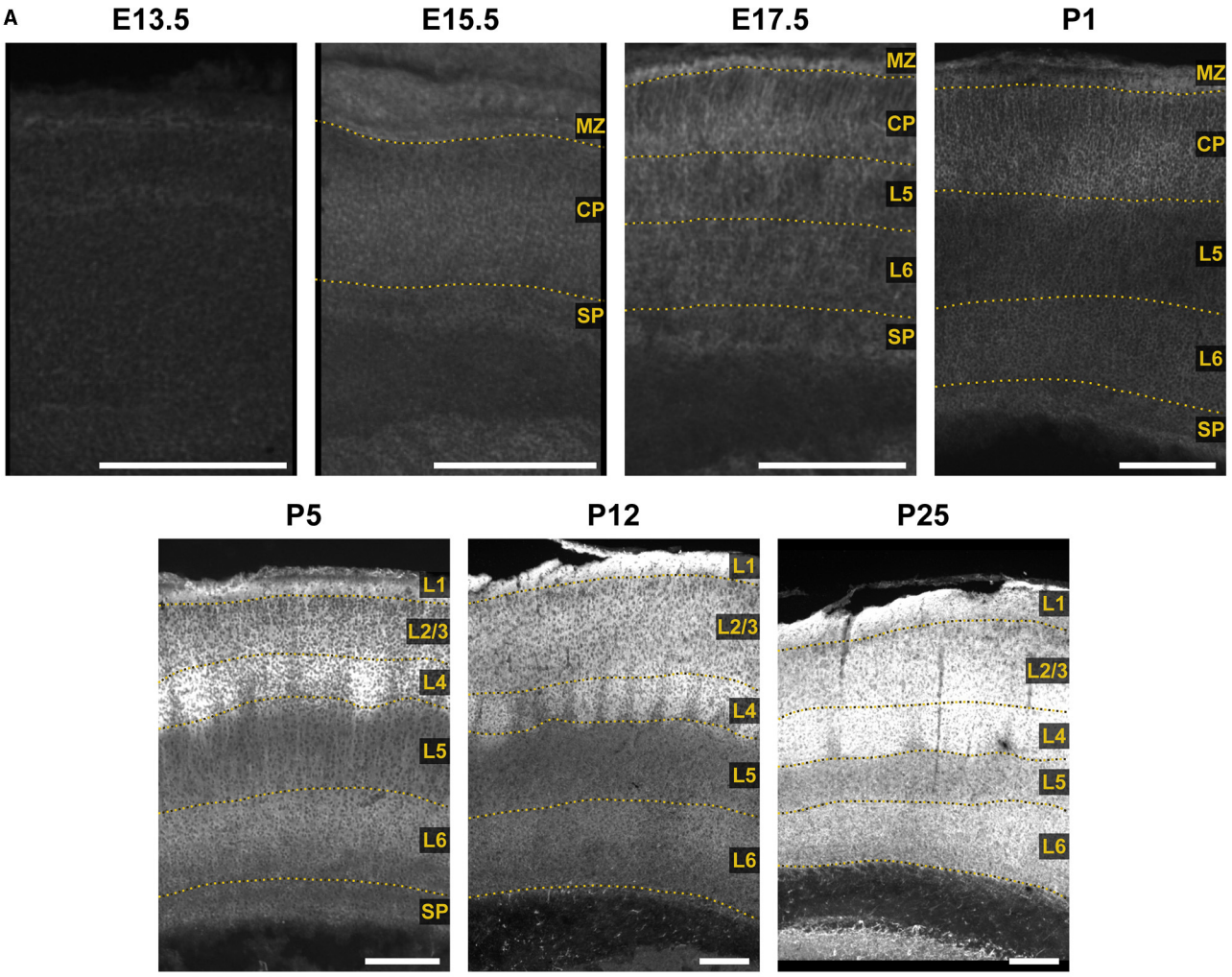

B

GABA$_A$R α1 IF Intensity in Barrel Field Cortex

Lamina	Age						
	E13.5	E15.5	E17.5	P1	P5	P12	P26
L1	ND	-	(+)	(+)	+	++++	++++
L2		-	-	(+)	(+)	++	+++
L3		-	-	(+)	+	+++	++++
L4		-	(+)	+	++	+++	++++
L5		-	(+)	(+)	(+)	+	+
L6a		-	(+)	(+)	(+)	++	++
L6b		-	-	(+)	(+)	+	++
SP		-	(+)	(+)	(+)		

C

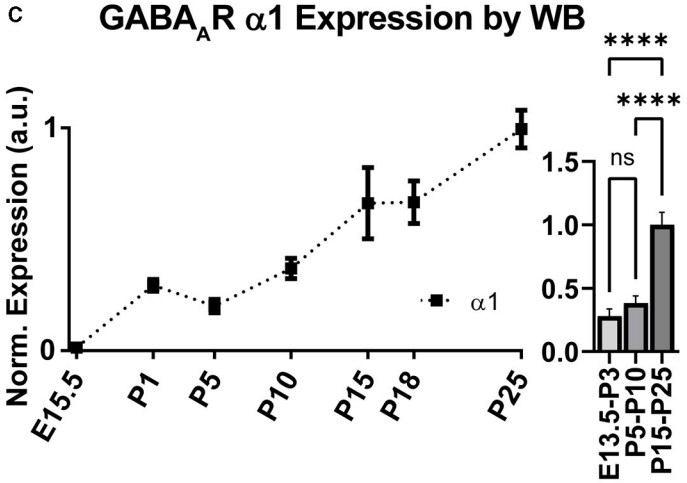

FIGURE 3
GABA$_A$R α1 expression in barrel field cortex from embryonic age to maturity. **(A)** Exemplar images of α1 immunoreactivity in barrel field cortex across development. Scale bar = 250 μm. **(B)** Grading of immunofluorescence intensity across cortical lamina, where + + ++ is the maximal α1 signal that could be detected in brain at P26. **(C)** Quantification of GABA$_A$R α1 protein in cortical samples by Western blot (WB), with a timeline of all points on the left and binned stages tested for significance on the right. $^{****}P < 0.0001$ by one-way ANOVA with Šídák's multiple comparisons; n in mice/age: 3/E15.5, 8/P1, 3/P5, 4/P10, 4/P15, 4/P18, and 4/P25. L1–L6, layer 1–layer 6; MZ, marginal zone; SP, subplate; CP, cortical plate; ND, not determined; also refer to "Lamina in Grading Table and Figures" section in Methods.

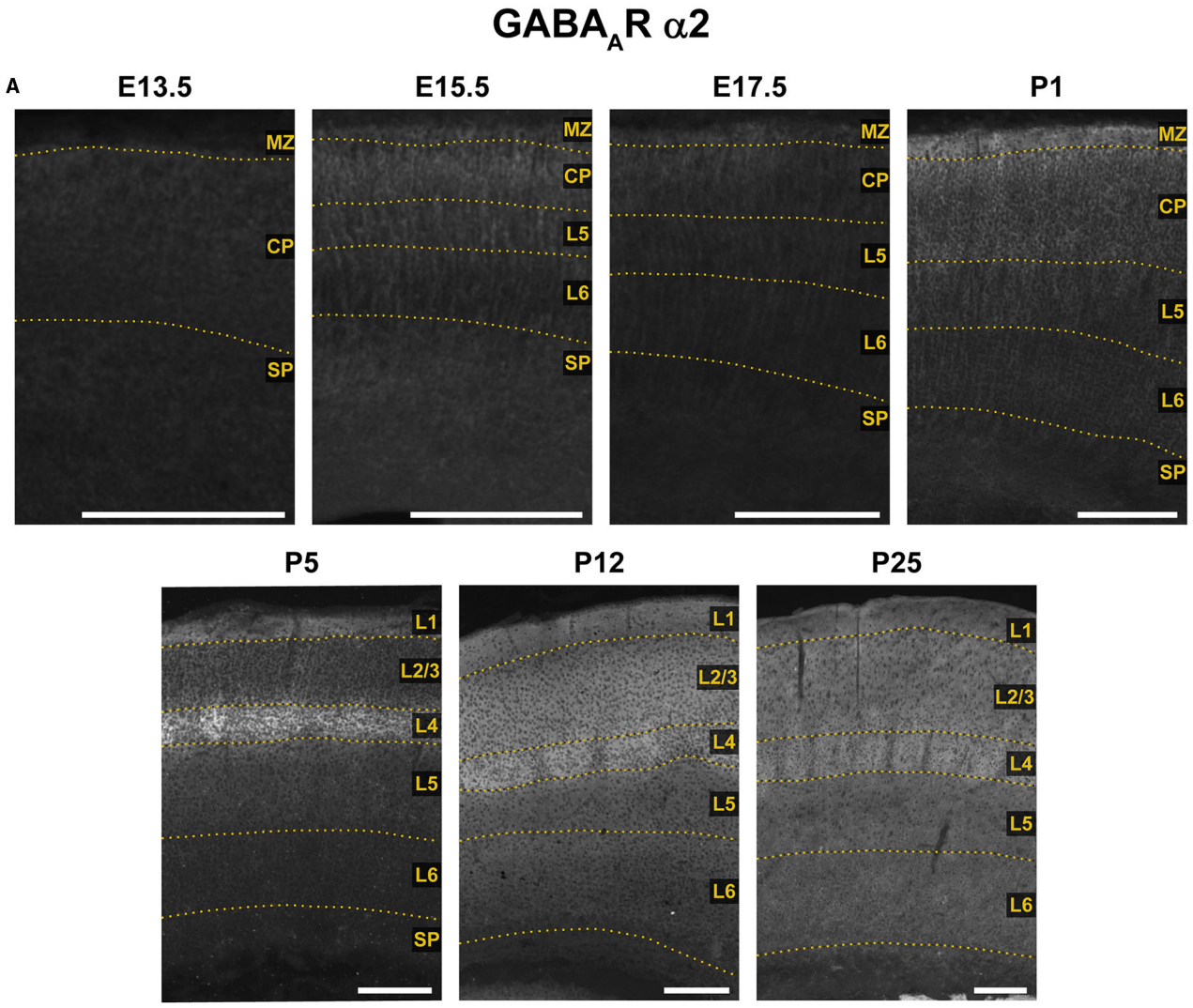

B

GABA$_A$R α2 IF Intensity in Barrel Field Cortex

Lamina	Age						
	E13.5	E15.5	E17.5	P1	P5	P12	P25-P26
L1	+	+	+	++	++	++	+
L2	-	(+)	+	+	(+)	++	++
L3	-	(+)	(+)	(+)	(+)	++	++
L4	-	(+)	(+)	+	++	+++	++
L5	-	-	-	(+)	(+)	+	+
L6	-	-	-	(+)	(+)	(+)	(+)
SP	-	-	-	-	-		

C

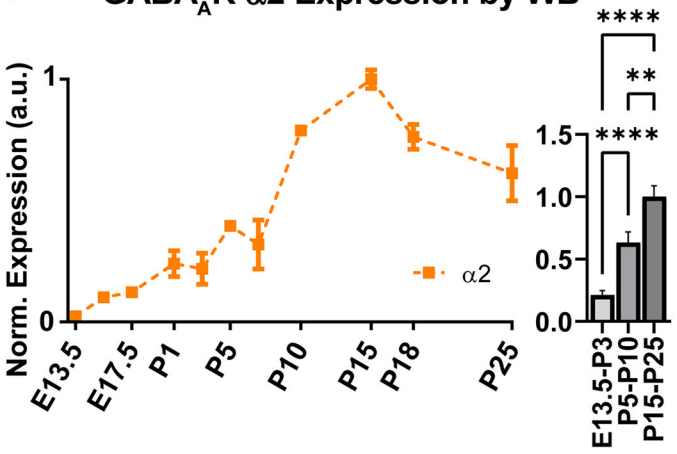

FIGURE 4
GABA$_A$R α2 expression in barrel field cortex from embryonic age to maturity. **(A)** Exemplar images of α2 immunoreactivity in barrel field cortex across development. Scale bar = 250 μm. **(B)** Grading of immunofluorescence intensity across cortical lamina, where + + ++ is the maximal α2 signal that could be detected in brain at P26. **(C)** Quantification of GABA$_A$R α2 protein in cortical samples by Western blot, with a timeline of all points on the left and binned stages tested for significance on the right. $^{****}P < 0.0001$, $^{**}P < 0.01$ by one-way ANOVA with Šídák's multiple comparisons; n in mice/age: 3/E13.5; 3/E15.5, 3/E17.5, 6/P1, 4/P3, 5/P5, 5/P7, 4/P10, 3/P15, 4/P18, and 5/P25. L1–L6, layer 1–layer 6; MZ, marginal zone; SP, subplate; CP, cortical plate; also refer to "Lamina in Grading Table and Figures" section in Methods.

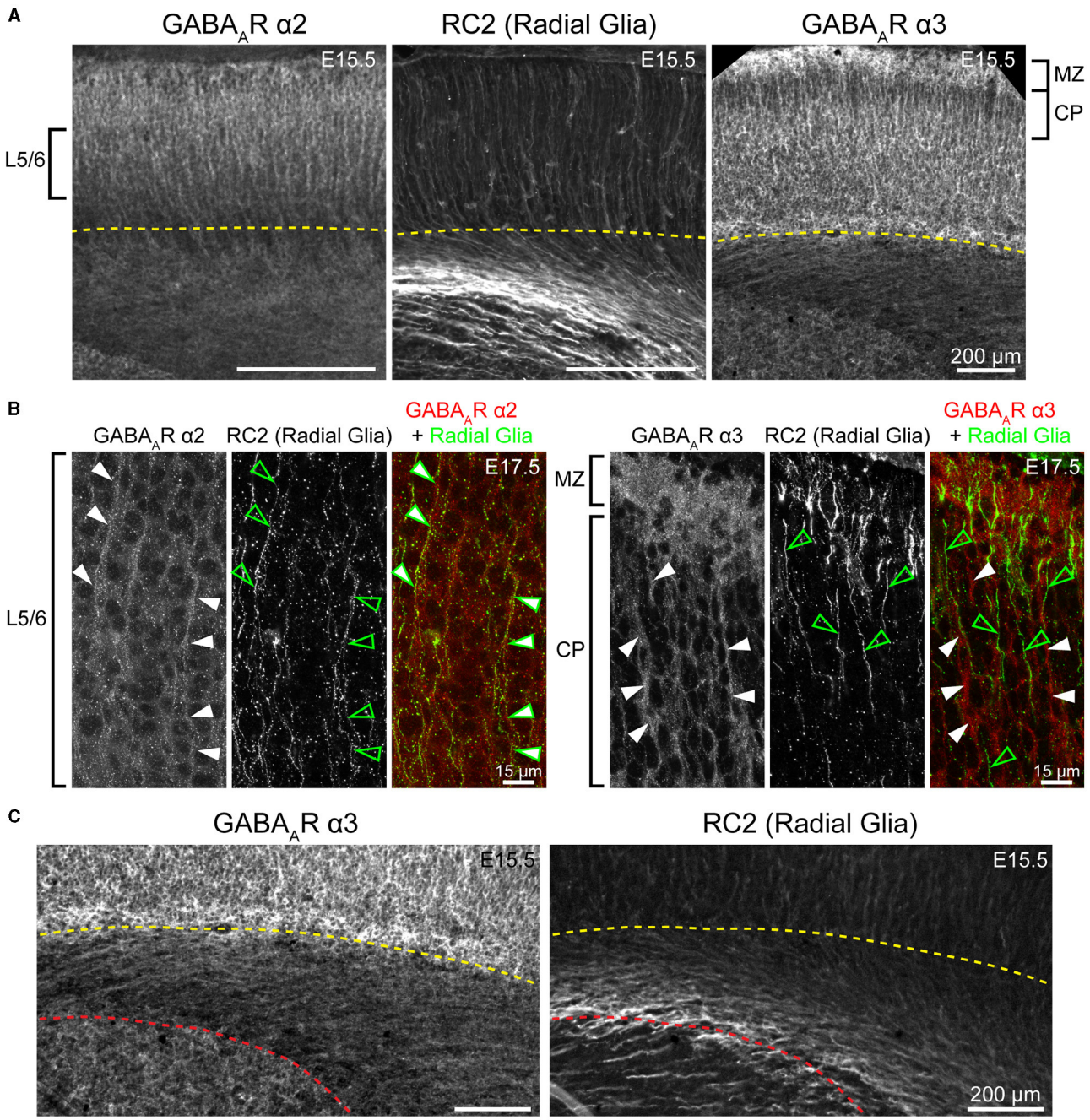

FIGURE 5
Fibers of radial glia co-localize with GABA$_A$R α2, but not GABA$_A$R α3. **(A)** Both GABA$_A$R α2 and α3 immunolabeling showed a pattern of ascending cortical fibers, which are prominent in the CP/developing layers 2/3 for α3 (right) and are found throughout the cortical column for α2 (left) in embryonic and early postnatal period. These fibers resemble radial glia marked by RC2 (middle). **(B)** The radial glia marker RC2 co-localized with α2-immunopositive fibers (left, arrows), but not with α3-immunopositive fibers (right, arrows). Note that white arrows denote fibers immunopositive for α2 and α3, while green empty arrows indicate radial glia fibers. **(C)** Subcortical expression of α3-positive fibers has a different pattern than radial glia. The yellow dotted line in **(A, C)** indicates the basal margin of the subplate, while red dotted line in **(C)** indicates the margin between intermediate zone/white matter and the striatum. All images are oriented basal bottom to apical top.

GABA$_A$R α3

WB analysis showed high cortical levels of α3 during embryonic development, steadily increasing from E13.5 with a plateau between E17.5-P7, then decreasing to a lower plateau at P10 onwards that was significantly different from earlier postnatal expression (Figure 6; $^*P < 0.05$ for P15-P25 vs. P5-P10). Our IHC analysis showed a highly lamina-specific pattern of α3 expression at all timepoints (Figures 2, 6). Expression of α3 first appeared in the MZ and subplate at E13.5 with lower levels throughout the CP. The subcortical band of α3 actually included the subplate and adjacent cell-poor zone below the CP, and this was present

throughout the embryonic ages. Over development, this subplate-specific α3 expression merged with expression in L6 and became indistinguishable from L6 by P5. At E15.5, expression of α3 increased in lower portions of the CP (L5/6) with what appeared to be cytoplasmic expression of many cells superimposed on a more diffuse pattern (details best seen in Figure 5A). In contrast, there was little intrinsic α3 expression in the upper CP, although there were clear radial fibers extending from L5/6 that appeared to end in intensely stained dendritic tufts in L1 (Fritschy et al., 1998). This pattern of robust α3 in the lower CP with presumed dendrites in L2-4 persisted until P5. Compared to α2-positive fibers, these α3-stained fibers differed in a number of features. While α2-positive fibers were narrow and appeared primarily in deep cortical layers and the intermediate zone, the α3 fibers were found in superficial layers, were much thicker and numerous, and did not co-localize with RC2+ processes of radial glia (Figure 5). At P1 and P5, α3 expression levels continued to rise in cortical layers, making individual layers less distinct. Accordingly, the presumed dendrites were no longer visible in L2/3 after P5, although sparsely distributed α3+ fibers traversing across L4 can be seen as late at P26. Expression of α3 remained highest in the lower levels of cortex (L5/6) with a pattern of strong somatic expression in L5/6 that was superimposed on a lower diffuse level of α3 expression. By P12, this somatic pattern evolved to a more diffuse pattern.

In the mature brain, the subcortical white matter is generally devoid of any $GABA_AR$ subunit protein expression. However, between E15.5 and P1, we saw considerable subcortical α3 expression with apparent fiber tracks running parallel to lower margin of the CP. This pattern was most prominent at E17.5 and not seen in tissue from *Gabra3* knockout mice (Figure 7). This was especially conspicuous in the internal capsule fibers seen running between the thalamus and basal ganglia, as well α3+ fascicles running through the caudate. The subcortical α3 signal was most prominent in the thalamocortical tracks passing through the basal ganglia and into the ventrolateral IZ. This signal was also seen in the external capsule, but not in other tracks like corpus callosum or the anterior commissure.

$GABA_AR$ α4

Both WB and IHC data showed low cortical α4 expression in prenatal tissue that began to increase at P5, particularly in L1-4 by immunofluorescence (Figures 2, 8), though a significant difference by WB expression was only detected at P15-P25 compared to earlier ages (Figure 8, $^{****}P < 0.0001$). While α4 mRNA has been reported in embryonic ventricular and sub-ventricular zones (Laurie et al., 1992; Ma and Barker, 1995, 1998), we did not find significant/consistent expression of α4 protein in this area but cannot rule out expression below our level of detection. Similarly, there were very low or negligible α4 levels in the CP and subplate until after P1. By P5, there was distinct α4 expression in L4 of somatosensory cortex, which was slightly more intense in barrels. At P12 and P26, there was increasing α4 expression throughout L1-4 that remained most prominent in L4 of motor and somatosensory cortex. This was especially prominent in the barrels, where α4 expression peaked at P12 and was on par with P26 thalamus, our reference ROI for maximal α4 intensity signal (Figure 1). In L5/6, α4 expression increased slightly at P12 and P26, but remained at a generally low level.

$GABA_AR$ α5

Our WB experiments showed low embryonic and perinatal expression of α5 that suddenly increased and peaked between P1-P10, then decreased to a moderate level from P15 onwards and showed a statistically significant difference between all three developmental stages (Figure 9; $^{****}P < 0.0001$ E13.5-P3 vs. P5-P10 and P15-P25, $^{****}P < 0.0001$ P5-P10 vs. P15-P25). In immunostained sections (Figures 2, 9), the first clear expression of α5 was seen at E13.5 in the subplate, but nowhere else. There was a clear lateral to medial gradient, with highest expression in the lateral subplate and claustrum (Figure 2). Prominent α5 in subplate was a persistent feature at all ages studied. There was even a band of higher α5 signal at the lower edge of L6 as late as P26, although we were unable to distinguish L6b vs. subplate after P5 (Viswanathan et al., 2016). At E15.5, α5 was expressed in the MZ, with lower levels in the mid-CP/L5, creating a trilaminar pattern of MZ/L5/subplate. There was relatively little α5 in other layers. At E17.5/P1, α5 expression increased, especially in the upper portions of L5 (L5a). The pattern of expression was mostly as a perisomatic rim around individual cells overlying a more diffuse pattern of α5 expression. There was relatively little α5 in L2-4, although α5+ dendrites from L5 could be seen traversing L2-4 until about P5.

There were significant changes in α5 expression around P5, with most cortical areas showing increased expression in the upper half of cortex, especially L4. However, a distinctly different pattern was seen in the barrel cortex, where α5 virtually disappeared from L2-4. This created an abrupt margin between barrel cortex and the adjacent somatosensory and motor cortices (Figure 2). A similar loss of α5 in L2-4 was seen in primary visual cortex (V1), but not in adjacent cortices (not shown). This pattern in primary sensory cortex and V1 was also reported by Paysan et al. (1997) at P7, who found it was dependent on early sensory input, and could be prevented by ablation of the ventrobasal or lateral geniculate nuclei of thalamus. At around P5, we could also begin to appreciate more complex sublamina in lower cortex, with moderate levels in L5a and L5c/L6a, but lower levels in L5b and L6. This distinct pattern was first seen at P5, but most clearly at P12. The previously noted pattern of somatic α5 superimposed on a diffuse background of α5 persisted in lower cortex until at least P12, with somewhat more numerous cell bodies in L5b and subplate. However, the distinction between somata and neuropil was never as clear as that seen at E17.5/P1. At P26, α5 expression became more diffuse, and individual dendrites and cell bodies became poorly distinguishable. Expression approached moderate levels in all cortical regions and layers, but previous patterns of α5 expression were still apparent; namely, barrel field cortex had lower expression than other cortical regions, deeper cortical layers showed a complex sublaminar expression pattern, and expression in L2/3 was lower than in other layers.

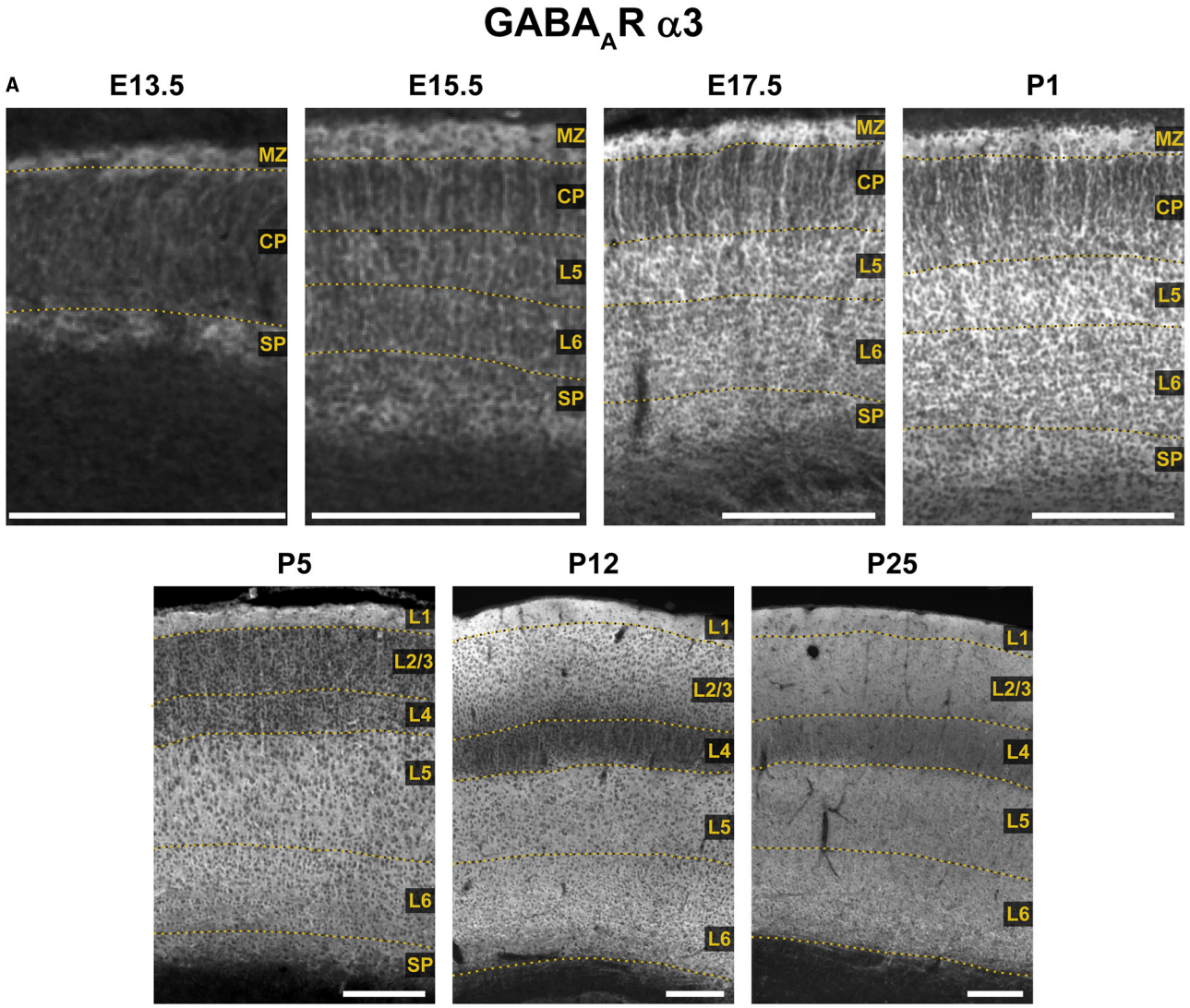

Lamina	Age						
	E13.5	E15.5	E17.5	P1	P5	P12	P26
L1	+	++	++++	++++	+++	++	++
L2	(+)	(+)	+	++	+	++	+
L3	(+)	(+)	+	++	+	++	+
L4	(+)	(+)	++	+++	+	(+)	(+)
L5a	(+)	+	+++	++++	+++	++	+
L5b	(+)	+	+++	++++	+++	+	+
L6	-	(+)	+++	+++	++	+	+
SP	+	+	+++	+++	+++		

FIGURE 6
GABA$_A$R α3 expression in barrel field cortex from embryonic age to maturity. **(A)** Exemplar images of α3 immunoreactivity in barrel field cortex across development. Scale bar = 250 μm. **(B)** Grading of immunofluorescence intensity across cortical lamina, where + + ++ is the maximal α3 signal that could be detected in brain at P26. **(C)** Quantification of GABA$_A$R α3 protein in cortical samples by Western blot, with a timeline of all points on the left and binned stages tested for significance on the right. *$P < 0.05$ by one-way ANOVA with Šídák's multiple comparisons; n in mice/age: 3/E13.5; 3/E15.5, 3/E17.5, 6/P1, 4/P3, 6/P5, 6/P7, 4/P10, 3/P15, 4/P18, 6/P25. L1-L6, layer 1-layer 6; MZ, marginal zone; SP, subplate; CP, cortical plate; also refer to "Lamina in Grading Table and Figures" section in Methods.

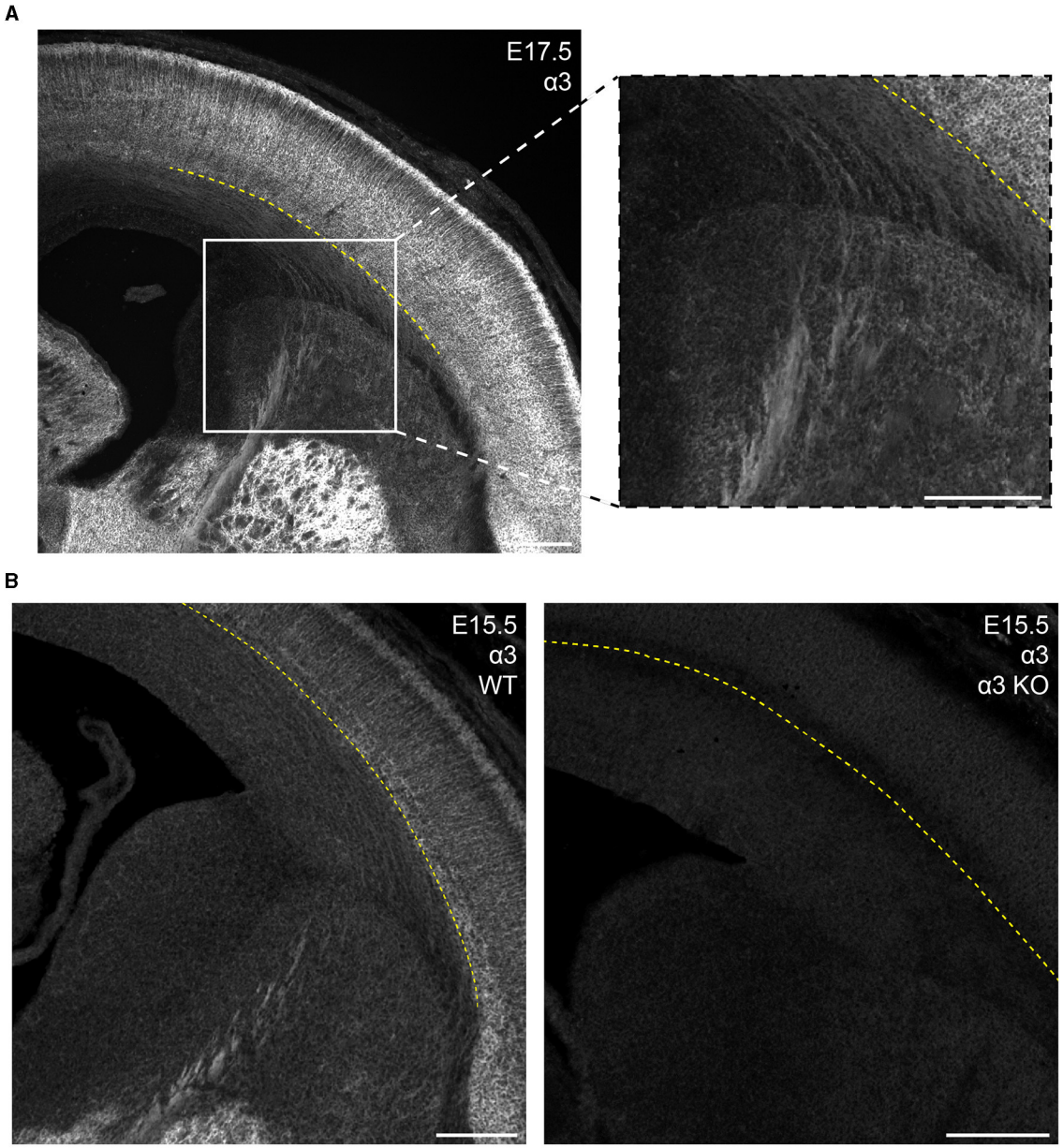

FIGURE 7
$GABA_AR$ α3 expression in fibers of the internal capsule during embryonic development. **(A)** E17.5 coronal section showing prominent α3 immunolabeling of internal capsule fibers in the white matter/intermediate zone located below the subplate and running medioventrally through the striatum. These regions of interest are enlarged in the inset. **(B)** α3-immunolabeled fibers are absent in the α3-knockout mouse (α3 KO, right), but consistently present in sections from wildtype mice (left). The yellow dotted line in **(A, B)** indicates the basal margin of the subplate. All images are oriented ventral bottom to dorsal top, with lateral cortex on the right.

$GABA_AR$ δ

An overview of δ subunit expression is shown together with β2, β3, and γ2 in Figure 10. We detected essentially no embryonic or perinatal expression of the δ subunit in cortex by IHC or WB. By WB, we began to see low cortical expression of δ around P10 that quickly rose to a plateau level at P15-P25, showing a statistically significant difference from earlier ages (Figure 11; $^{****}P < 0.0001$ P15-P25 vs. earlier ages). However, δ IHC expression in sections (Figures 10, 11) first appeared at P5 as a diffuse signal in L4, most prominently in the barrel cortex, with lower levels in the rest of somatosensory cortex. By P12 and P26, this diffuse pattern of expression increased in all layers, but remained highest in L4 in barrels and relatively low in L5/6.

Superimposed upon this diffuse layer-specific pattern of expression, there were scattered δ+ cell bodies in cortex and hippocampus as early as P5, which became much more evident at P12 and P26. However, these cells were somewhat less visually distinct at P26, likely due to increasing background δ subunit expression. Density of these cells was greatest in L4, L5, and subplate but and very sparse in L1 and lower portions of L6.

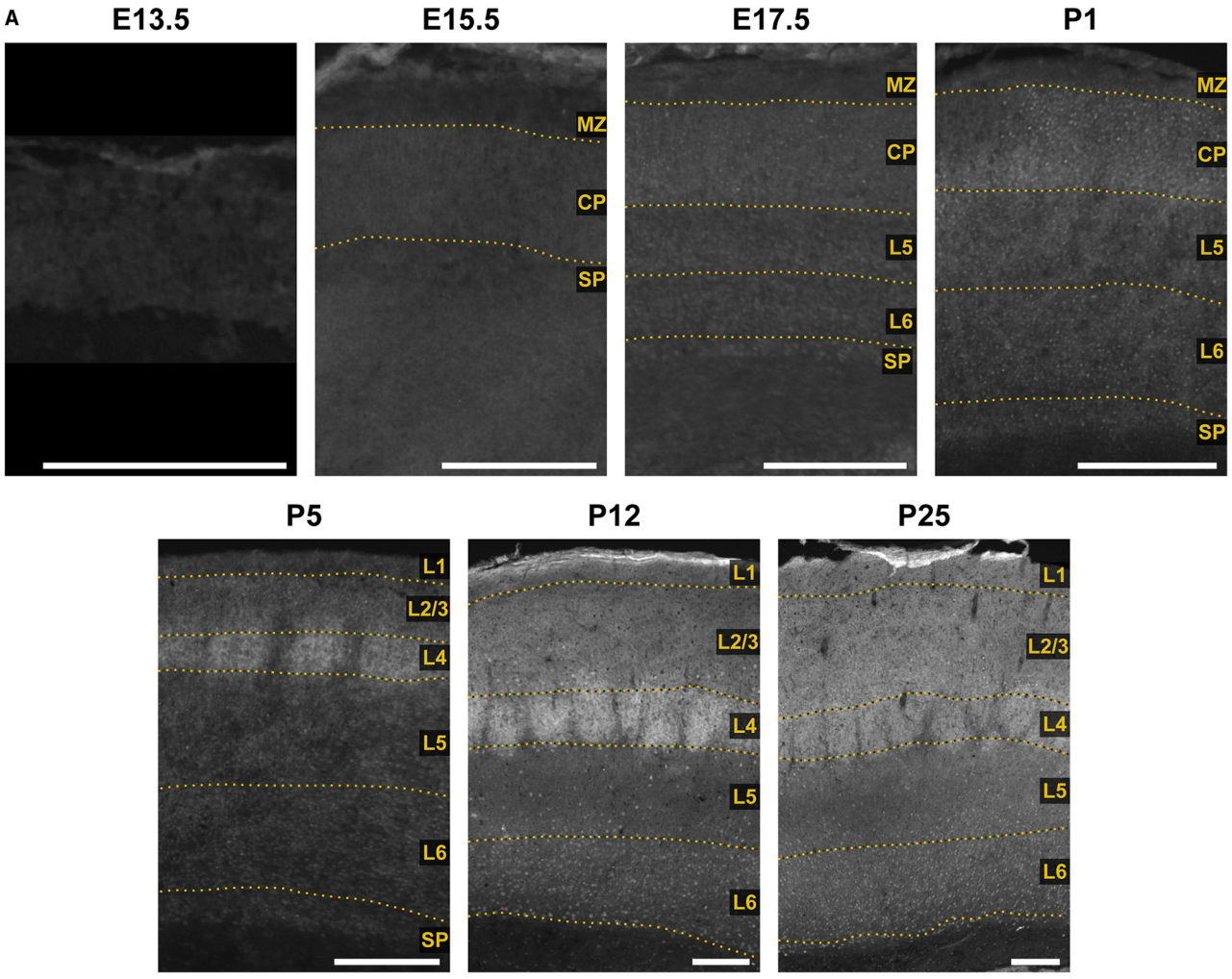

B

GABA$_A$R α4 IF Intensity in Barrel Field Cortex

Lamina	Age						
	E13.5	E15.5	E17.5	P1	P5	P12	P26
L1	-	-	-	-	-	+	+++
L2	-	-	-	-	(+)	+	++
L3	-	-	-	-	(+)	++	++
L4	-	-	-	(+)	++	++++	+++
L5	-	-	-	-	(+)	+	+
L6	-	-	-	(+)	(+)	+	+
SP	-	-	-	-	-		

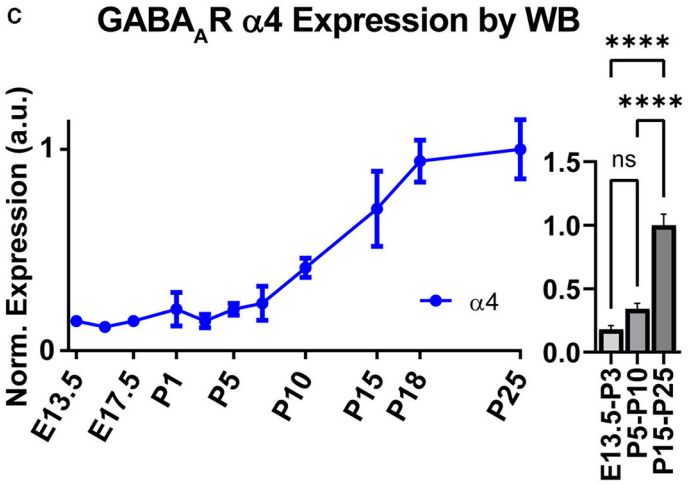

FIGURE 8
GABA$_A$R α4 expression in barrel field cortex from embryonic age to maturity. **(A)** Exemplar images of α4 immunoreactivity in barrel field cortex across development. Scale bar = 250 μm. **(B)** Grading of immunofluorescence intensity across cortical lamina, where + + ++ is the maximal α4 signal that could be detected in brain at P26. **(C)** Quantification of GABA$_A$R α4 protein in cortical samples by Western blot, with a timeline of all points on the left and binned stages tested for significance on the right. $^{****}P < 0.0001$ by one-way ANOVA with Šídák's multiple comparisons; n in mice/age: 3/E13.5; 3/E15.5, 3/E17.5, 6/P1, 3/P3, 4/P5, 3/P7, 6/P10, 3/P15, 5/P18, and 4/P25. L1–L6, layer 1–layer 6; MZ, marginal zone; SP, subplate; CP, cortical plate; also refer to "Lamina in Grading Table and Figures" section in Methods.

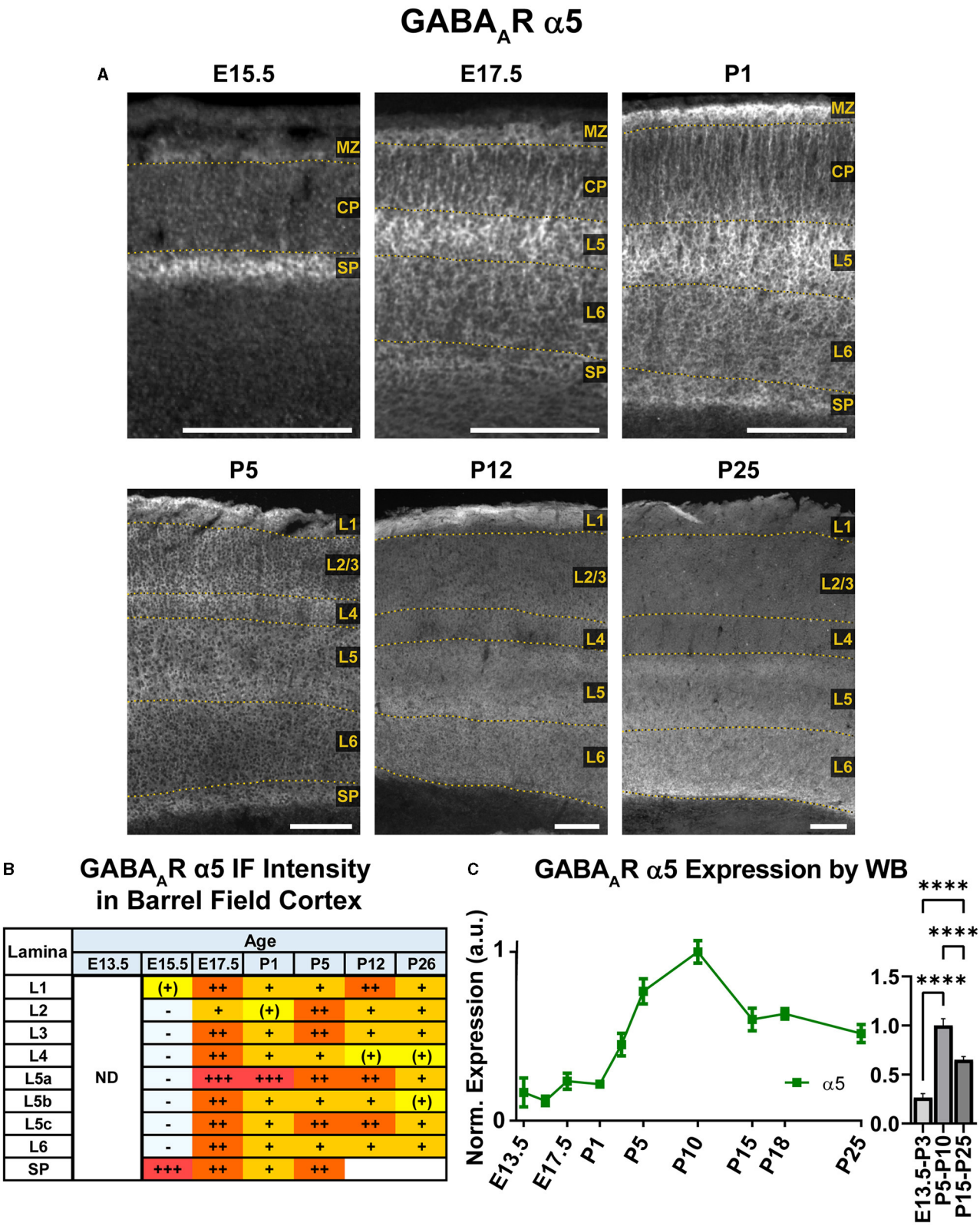

Lamina	Age						
	E13.5	E15.5	E17.5	P1	P5	P12	P26
L1	ND	(+)	++	+	+	++	+
L2		-	+	(+)	++	+	+
L3		-	++	+	++	+	+
L4		-	++	+	+	(+)	(+)
L5a		-	+++	+++	++	++	+
L5b		-	++	+	+	+	(+)
L5c		-	++	+	++	++	+
L6		-	++	+	+	+	+
SP		+++	++	+	++		

FIGURE 9
GABA$_A$R α5 expression in barrel field cortex from embryonic age to maturity. **(A)** Exemplar images of α5 immunoreactivity in barrel field cortex across development. Scale bar = 250 μm. **(B)** Grading of immunofluorescence intensity across cortical lamina, where + + ++ is the maximal α5 signal that could be detected in brain at P26. **(C)** Quantification of GABA$_A$R α5 protein in cortical samples by Western blot, with a timeline of all points on the left and binned stages tested for significance on the right. $^{****}P < 0.0001$ by one-way ANOVA with Šídák's multiple comparisons; n in mice/age: 3/E13.5; 3/E15.5, 3/E17.5, 3/P1, 3/P3, 4/P5, 3/P7, 5/P10, 3/P15, 7/P18, and 6/P25. L1–L6, layer 1–layer 6; MZ, marginal zone; SP, subplate; CP, cortical plate; ND, not determined; also refer to "Lamina in Grading Table and Figures" section in Methods.

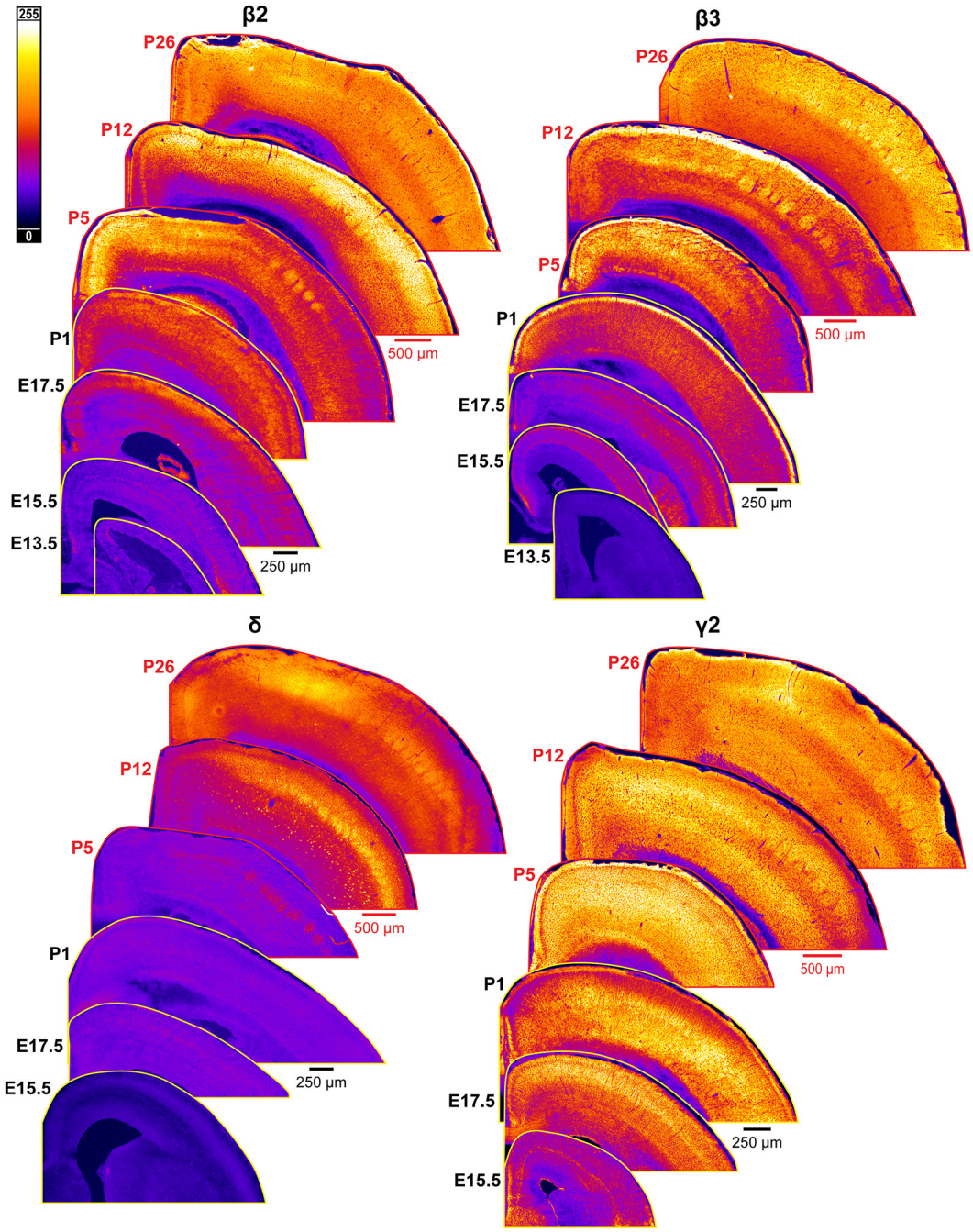

FIGURE 10
Expression of $GABA_AR$ β2, β3, δ, and γ2 subunits in developing cortex. Coronal sections are overlaid from embryonic day E13.5/E15.5 on the bottom left to postnatal day 26 on the top right separately for each subunit. All sections are oriented from ventral bottom to dorsal top, with lateral cortex on the right. Separate scaling has been used for sections E13.5-P1 (black scale bar) and P5-P26 (red scale bar), separately for each subunit. Signal is represented using a heat map lookup table to highlight differences in regional expression. Heatmap intensity scaling is shown by the bar in top left.

$GABA_AR$ γ2

Our WB results showed that γ2 expression begins early in development and exhibits a steady increase from E13.5 to P26 that was statistically significant (Figure 12; $^{**}P < 0.01$ E13.5-P3 vs. P5-P10, $^{***}P < 0.0001$ P15-P25 vs. P5-P10). Immunofluorescent stains showed a layer-specific pattern of γ2 expression (Figures 10, 12). As early as E15.5, we detected low levels of γ2 immunoreactivity in the MZ and subplate. At E17.5 and P1, γ2 was expressed throughout the CP, especially in L5. At P5, expression increased in all layers, but was highest in L4/L5 and was especially pronounced in the L4 barrels. At P12, γ2 expression was prominent in all layers, particularly high in L2-4 and L6. However, at the same time γ2 expression in L5 rose less significantly, so this layer was

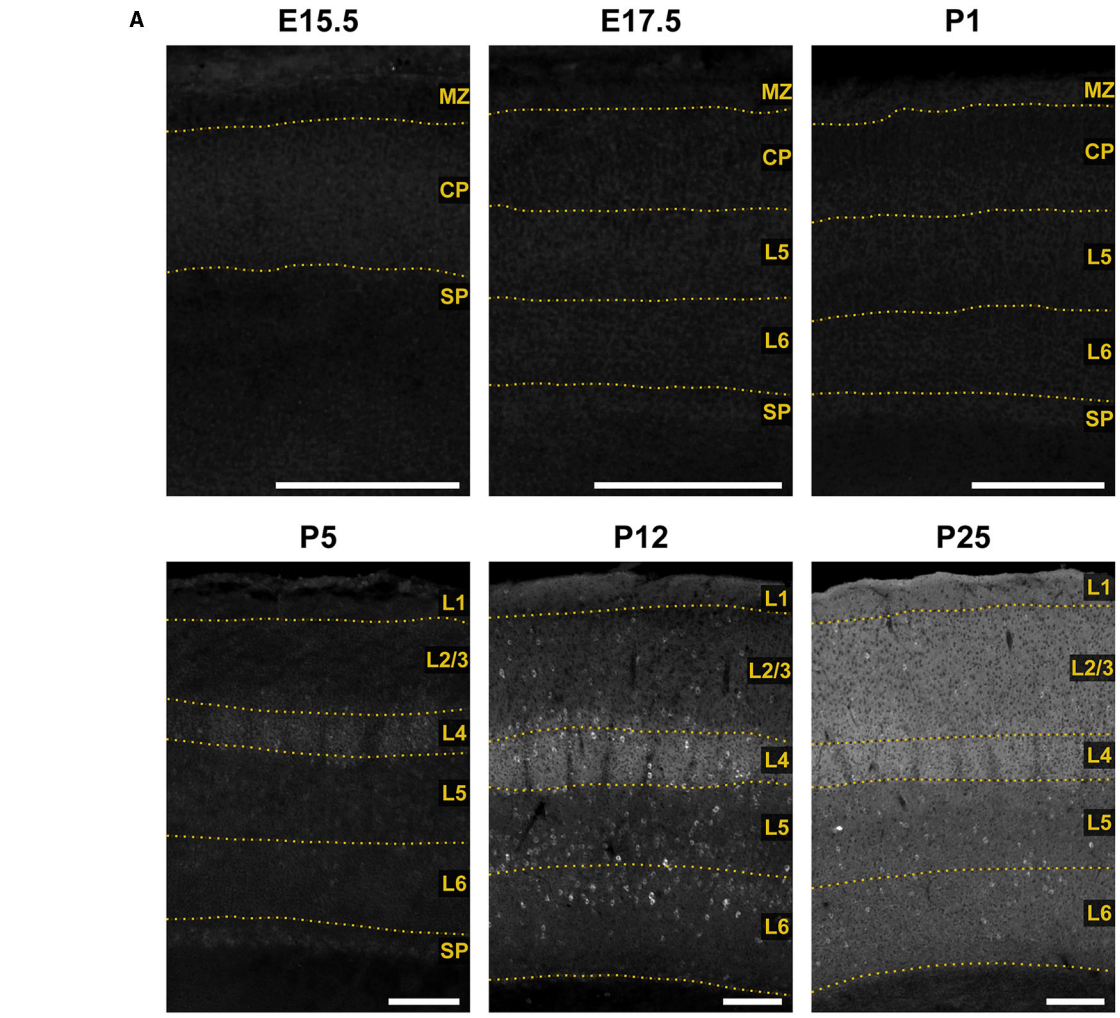

B

GABA$_A$R δ IF Intensity in Barrel Field Cortex

Lamina	Age						
	E13.5	E15.5	E17.5	P1	P5	P12	P26
L1	ND	(+)	-	(+)	-	+	+
L2		(+)	(+)	-	-	+	+
L3		(+)	(+)	-	-	+	+
L4		(+)	(+)	-	+	+++	+++
L5		(+)	(+)	(+)	-	+	+
L6		(+)	-	(+)	-	(+)	(+)
SP		-	-	-	-		

C

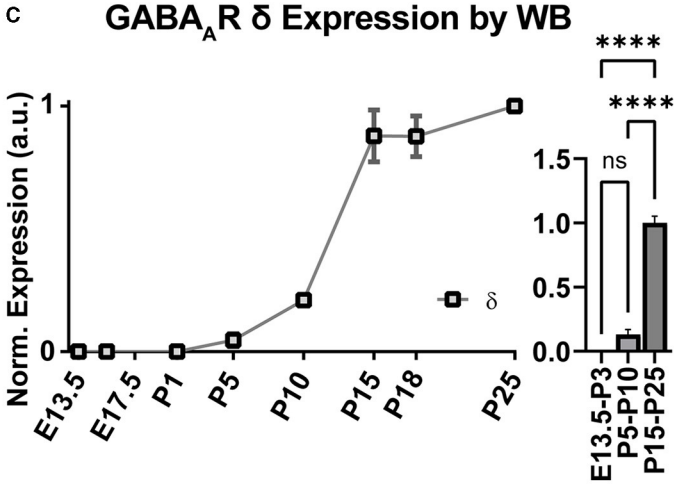

FIGURE 11
GABA$_A$R δ expression in barrel field cortex from embryonic age to maturity. **(A)** Exemplar images of δ immunoreactivity in barrel field cortex across development. Scale bar = 250 μm. **(B)** Grading of immunofluorescence intensity across cortical lamina, where + + ++ is the maximal δ signal that could be detected in brain at P26. **(C)** Quantification of GABA$_A$R δ protein in cortical samples by Western blot, with a timeline of all points on the left and binned stages tested for significance on the right. $^{****}P < 0.0001$ by one-way ANOVA with Šídák's multiple comparisons; n in mice/age: 4/E13.5; 3/E15.5, 4/P1, 4/P5, 3/P10, 4/P15, 5/P18, and 3/P25. L1–L6, layer 1–layer 6; MZ, marginal zone; SP, subplate; CP, cortical plate; ND, not determined; also refer to "Lamina in Grading Table and Figures" section in Methods.

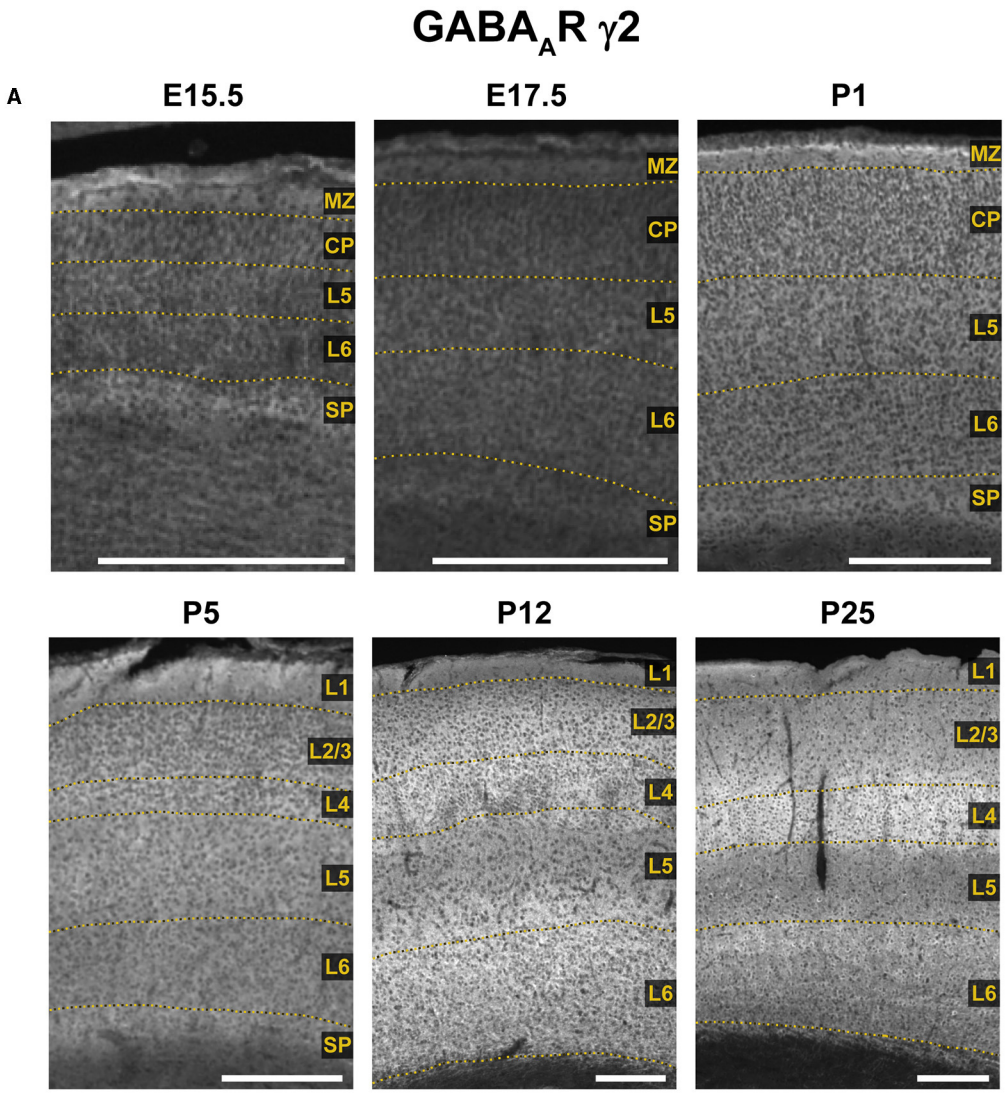

B

GABA$_A$R γ2 IF Intensity in Barrel Field Cortex

Lamina	Age						
	E13.5	E15.5	E17.5	P1	P5	P12	P26
L1	ND	+	++	++	++++	+++	++
L2		(+)	(+)	(+)	+	++	++
L3		(+)	(+)	(+)	+	++	++
L4		(+)	(+)	+	++	+++	++++
L5		(+)	+	+	++	+	+
L6a		-	-	(+)	+	++	++
L6b		-	-	(+)	(+)	(+)	(+)
SP		(+)	+	+	+		

C

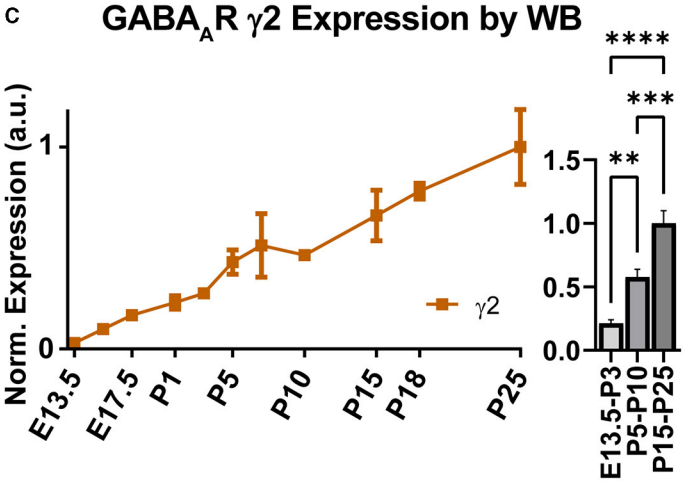

FIGURE 12
GABA$_A$R γ2 expression in barrel field cortex from embryonic age to maturity. **(A)** Exemplar images of γ2 immunoreactivity in barrel field cortex across development. Of note, the sections shown here were stained at the same time, but L1 was damaged in the P12 sections. Scale bar = 250 μm. **(B)** Grading of immunofluorescence intensity across cortical lamina, where + + ++ is the maximal γ2 signal that could be detected in brain at P26. **(C)** Quantification of GABA$_A$R γ2 protein in cortical samples by Western blot, with a timeline of all points on the left and binned stages tested for significance on the right. $^{****}P < 0.0001$, $^{***}P < 0.001$, $^{**}P < 0.01$ by one-way ANOVA with Šídák's multiple comparisons; n in mice/age: 3/E13.5, 3/E15.5, 3/E17.5, 6/P1, 3/P3, 3/P5, 3/P7, 3/P10, 4/P15, 4/P18, and 4/P25. L1–L6, layer 1–layer 6; MZ, marginal zone; SP, subplate; CP, cortical plate; ND, not determined; also refer to "Lamina in Grading Table and Figures" section in Methods.

easily distinguishable from the higher expression in all other layers. Within L6, heightened expression was centered in L6a, but spread into L5c and top of L6b. These P12 patterns were preserved at P26.

$GABA_AR$ β2

WB immunoreactivity showed moderate β2 expression throughout the embryonic period that exhibited a steady increase to high levels in the postnatal period that was statistically significant (Figure 13; $^{***}P < 0.001$ E13.5-P3 vs. P5-P10, $^{****}P < 0.0001$ P5-P10 vs. P15-P25). In immunostained brain sections (Figures 10, 13), expression of β2 was seen as early as E13.5 in the MZ and subplate, followed by low levels of β2 in CP by E15.5/E17.5. This cortical expression was relatively featureless from E15.5 to P1, but showed a steady, progressive increase that was not as readily apparent in the WB data. A distinct subplate could be seen from E13.5–E17.5 but blended into L6 at P1 and later ages. Prominent expression in MZ/L1 became clear at E17.5 and was present at all ages.

Robust β2 expression appeared abruptly in L4 at P5, especially in barrel cortex. By P12, β2 expression expanded into L1–4, with lesser increases in L5/6. There was strong expression in L1–4 and somewhat lower levels in L5/6. By P26, L1–4 still had the highest expression, and weaker expression in L5.

$GABA_AR$ β3

A steady general increase in cortical expression of β3 was apparent on WB, starting in the embryonic period and continuing until P10, when it reached a stable plateau of high expression that showed a statistically significant difference from embryonic/perinatal timepoints, but not across the postnatal period (Figure 14; $^{****}P < 0.0001$ P15-P25 and P5-P10 vs. E13.5-P3). In brain sections (Figures 10, 14), expression of β3 was first detectable at E15.5 in the MZ and subplate. Low expression was also visible in L5/L6 with L5 being slightly higher. While β3 expression is lower in L2–4, there are dendrites extending from L5 through L2/3 and ending in L1. Expression intensity increased from E15.5-P1, but the laminar pattern remained the same. By P5, β3 expression increased in the upper cortex, resulting in a relatively undifferentiated laminar pattern from L2 to the subplate. The one exception is in the barrel cortex, where the L4 barrels had notably higher expression than other layers and adjacent cortices. By P12, a clear, laminar pattern was again re-established throughout somatosensory and motor cortex due to a relatively weak β3 expression in L5, while L1 and L4 barrels had the highest expression. At P26, this general pattern persists, but L1 and L6 decrease in intensity, giving a pattern of high expression in L1-3, higher expression in L4/barrels, and moderate expression in L5-L6.

KCC2

The general pattern of KCC2 expression during rodent cortical development has been previously thoroughly characterized by WB and other techniques, showing low immunoreactivity during embryonic and perinatal life, and then a dramatic increase in the second to fourth postnatal weeks (Rivera et al., 1999; Stein et al., 2004; Dzhala et al., 2005; Uvarov et al., 2009; Takayama and Inoue, 2010; Kovács et al., 2014). Due to these prior studies, we only focused on investigating laminar and regional differences in KCC2 expression by IHC (Figure 15). We detected the earliest cortical KCC2 expression at E15.5 as faint immunoreactivity in the subplate and MZ. At E17.5-P1, KCC2 was robustly expressed in MZ and subplate. Additionally, individual neurons within the CP, particularly within L5, exhibited significant plasmalemmal KCC2 immunoreactivity that corresponds to GABAergic neuron-specific expression we previously reported (Zavalin et al., 2022). Early KCC2 expression within MZ also appeared to be interneuron-specific, since MZ is densely packed with migrating interneurons and similarly lost KCC2 immunoreactivity in the interneuron-specific KCC2 knockout. On the other hand, interneurons did not contribute to KCC2 expression within the subplate, which retained KCC2 immunoreactivity in the knockout (Zavalin et al., 2022). Therefore, with the exception of subplate-specific expression, KCC2 appears to be expressed exclusively by a subset of interneurons until P4-P5, at which point, we saw a marked increase in KCC2 expression within L4 and particularly the barrels, and low emerging expression in L5. At this point, we could also see numerous immunopositive dendrites ascending through L2/3. By P13, KCC2 was diffusely expressed throughout the cortical lamina and had higher expression in L1-4 than L5/6. Higher expression following a similar pattern was present after P18 (Figure 15).

Discussion

Synopsis of $GABA_AR$ subunit and KCC2 expression in developing cortex

In this study, we found unique spatial and temporal patterns of $GABA_AR$ subunits and KCC2 protein expression during cortical development. Generally, expression of α3 and α5 $GABA_AR$ subunits began very early, predominantly in L5/6 and subplate. On the other hand, α1, α2, α4, and δ, as well as KCC2, were primarily expressed at later developmental stages, most strongly in L4 and more superficial layers. In contrast, expression of β2, β3, and γ2 were spatially and temporally more ubiquitous than expression of α subunits but were similarly higher in certain laminae. β3 expression came online early and generally preceded expression of β2, although this difference was less distinct in the barrel field, *per se*.

Rationale for our approach and comparison with other expression studies

While there have been a few studies reporting $GABA_AR$ subunit expression in perinatal cortex, they have been much more limited in scope than our work. For example, Fritschy et al. (1994) described α1 and α2 protein expression in somatosensory and visual cortex at P0, P4, and P20. In addition, Paysan et al. (1997) showed that α1, α2, α3, and α5 $GABA_AR$ expression at P7 in sensory cortex

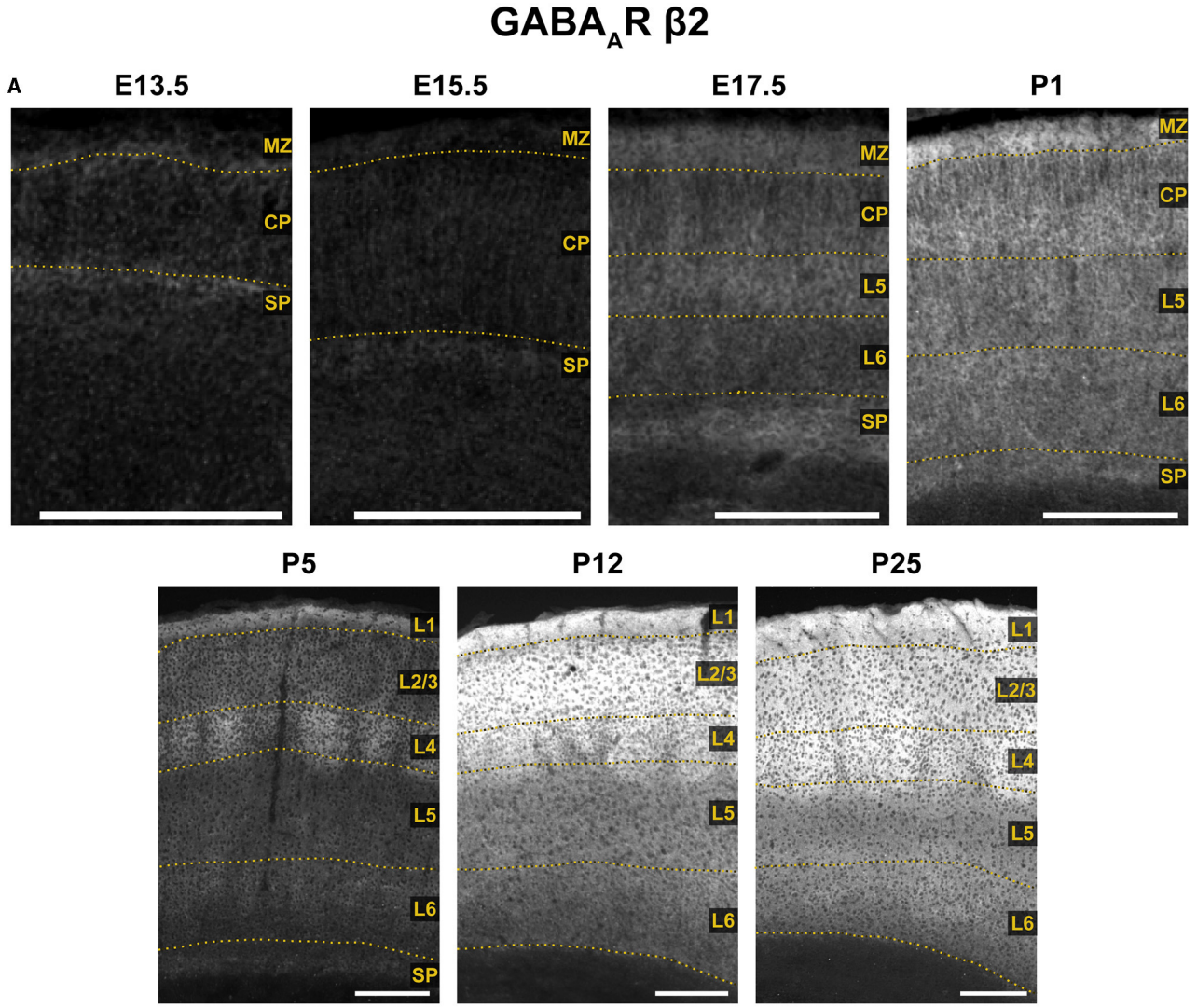

B

GABA$_A$R β2 IF Intensity in Barrel Field Cortex

Lamina	Age						
	E13.5	E15.5	E17.5	P1	P5	P12	P26
L1	+	+	+	+	++	+++	+++
L2	-	-	(+)	(+)	+	+++	+++
L3	-	-	(+)	(+)	+	+++	+++
L4	-	-	(+)	+	+++	+++	++++
L5	-	(+)	-	+	+	++	++
L6	-	-	-	(+)	(+)	+	++
SP	(+)	(+)	(+)	(+)	-		

C

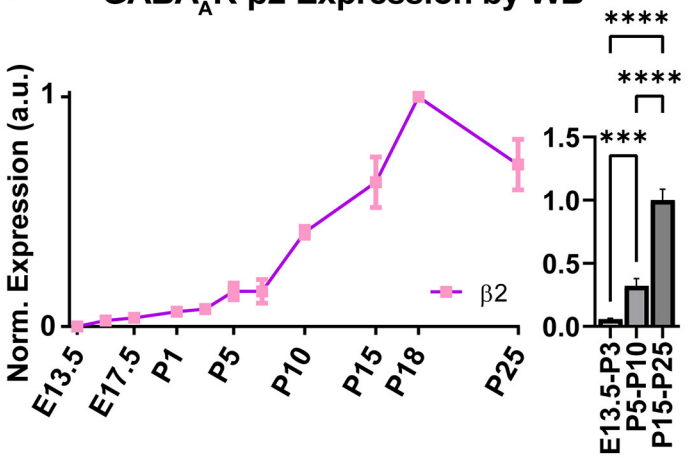

FIGURE 13
GABA$_A$R β2 expression in barrel field cortex from embryonic age to maturity. **(A)** Exemplar images of β2 immunoreactivity in barrel field cortex across development. Scale bar = 250 μm. **(B)** Grading of immunofluorescence intensity across cortical lamina, where + + ++ is the maximal β2 signal that could be detected in brain at P26. **(C)** Quantification of GABA$_A$R β2 protein in cortical samples by Western blot, with a timeline of all points on the left and binned stages tested for significance on the right. $^{****}P < 0.0001$, $^{***}P < 0.001$ by one-way ANOVA with Šídák's multiple comparisons; n in mice/age: 3/E13.5; 3/E15.5, 3/E17.5, 6/P1, 3/P3, 3/P5, 3/P7, 4/P10, 3/P15, 4/P18, and 3/P25. L1–L6, layer 1–layer 6; MZ, marginal zone; SP, subplate; CP, cortical plate; also refer to "Lamina in Grading Table and Figures" section in Methods.

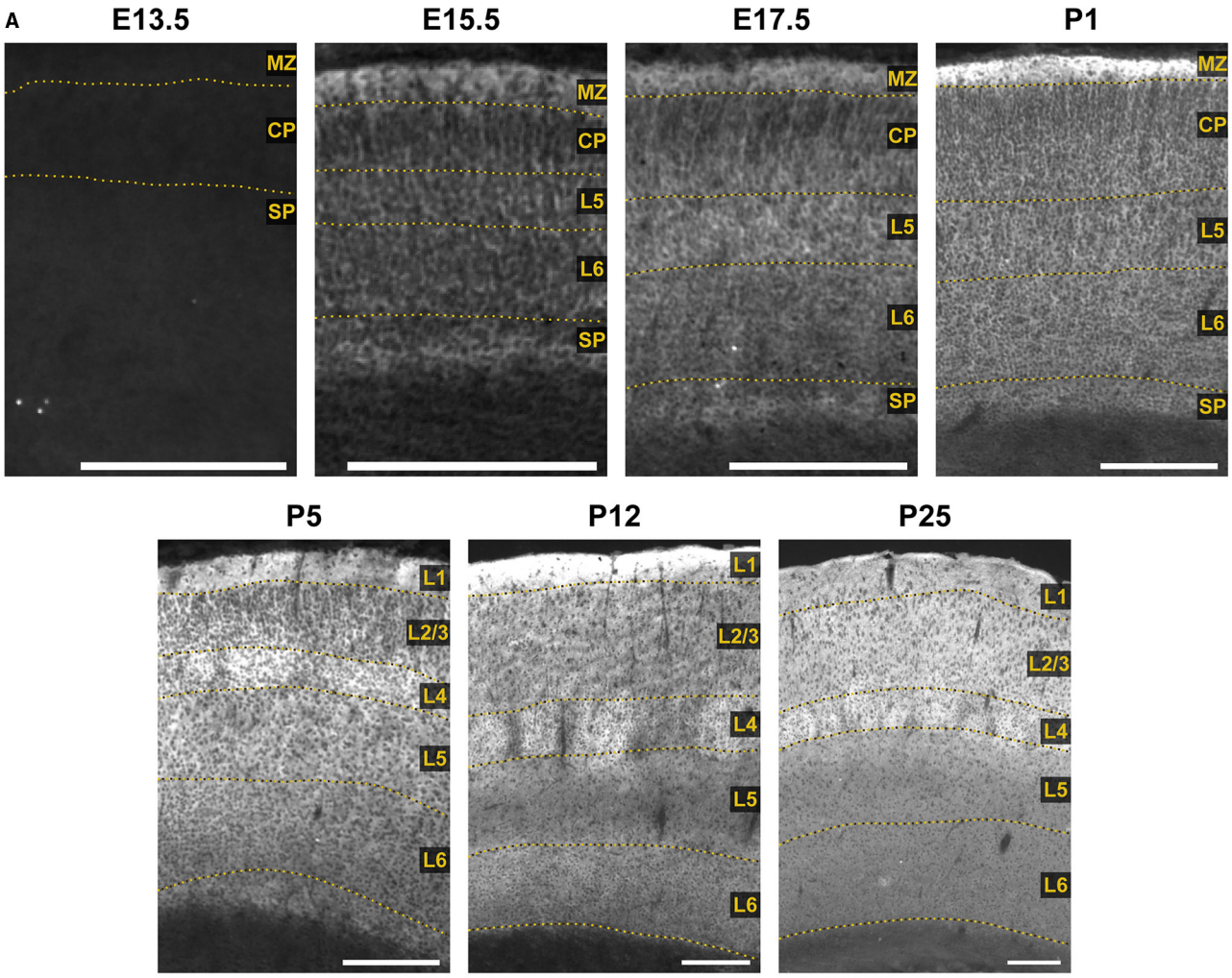

B

GABA$_A$R β3 IF Intensity in Barrel Field Cortex

Lamina	Age						
	E13.5	E15.5	E17.5	P1	P5	P12	P26
L1	(+)	+	+++	+++	+++	+++	++
L2	-	-	(+)	+	+	+	++
L3	-	-	(+)	+	+	+	++
L4	-	-	+	++	+++	+++	+++
L5a	-	-	+	+	+	+	+
L5b	-	-	+	+	++	+	+
L6	-	-	(+)	+	+	++	++
SP	-	+	+	(+)	(+)		

C

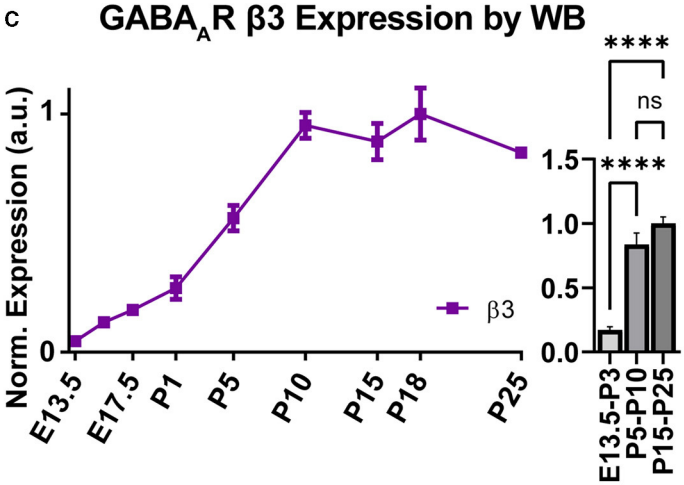

FIGURE 14
GABA$_A$R β3 expression in barrel field cortex from embryonic age to maturity. **(A)** Exemplar images of β3 immunoreactivity in barrel field cortex across development. Scale bar = 250 μm. **(B)** Grading of immunofluorescence intensity across cortical lamina, where + + ++ is the maximal β3 signal that could be detected in brain at P26. **(C)** Quantification of GABA$_A$R β3 protein in cortical samples by Western blot, with a timeline of all points on the left and binned stages tested for significance on the right. $^{****}P < 0.0001$ by one-way ANOVA with Šídák's multiple comparisons; n in mice/age: 4/E13.5, 4/E15.5, 4/E17.5, 4/P1, 4/P5, 4/P10, 4/P15, 4/P18, and 4/P25. L1–L6, layer 1–layer 6; MZ, marginal zone; SP, subplate; CP, cortical plate; also refer to "Lamina in Grading Table and Figures" section in Methods.

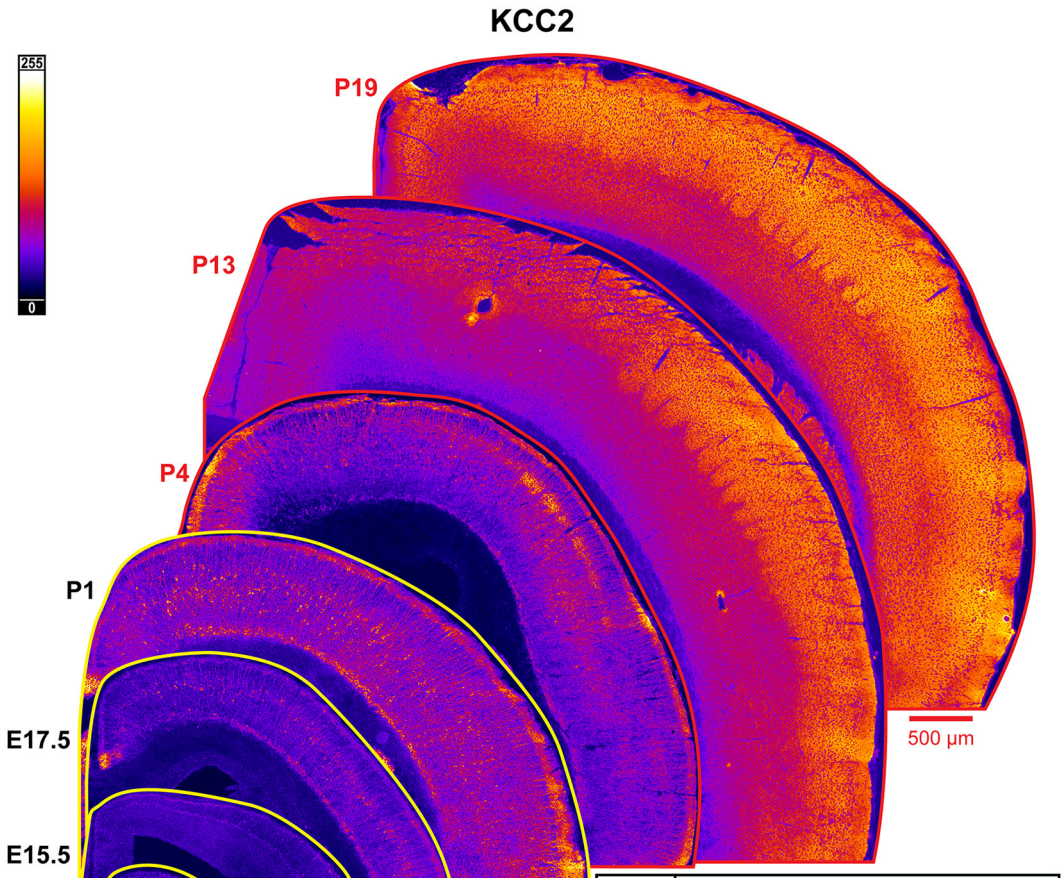

Lamina	Age						
	E13.5	E15.5	E17.5	P0-1	P4-5	P13	P19+
L1	-	(+)	(+)	+	++	++	++++
L2	-	-	-	-	+	++	++++
L3	-	-	-	-	+	++	++++
L4	-	-	-	(+)	+++	++	++++
L5	-	-	(+)	+	++	+	++
L6	-	-	-	(+)	+	(+)	++
SP	-	(+)	+	+	+		

FIGURE 15
KCC2 expression in developing cortex. Coronal sections are overlaid from embryonic day E13.5 on the bottom left to postnatal day 19 on the top right, and concensus grading of immunofluorescence intensity is on bottom right. All sections are oriented from ventral bottom to dorsal top, with lateral cortex on the right. Separate scaling has been used for sections E13.5-P1 (black scale bar) and P4-P19 (red scale bar). Signal is represented using a heat map lookup table to highlight differences in regional expression. Heatmap intensity scaling is shown by the bar in top left. For grading of immunofluorescence intensity, + + ++ is the maximal KCC2 signal that could be detected in brain at P19+. L1–L6, layer 1–layer 6; SP, subplate; also refer to "Lamina in Grading Table and Figures" section in Methods.

depended on perinatal thalamocortical input. More comprehensive evaluations of perinatal mRNA expression have been reported previously (Laurie et al., 1992), but lacked the layer-specific detail reported here. Other *in situ* hybridization studies have reported greater anatomic detail but did not include embryonic expression (Golshani et al., 1997; Fertuzinhos et al., 2014). More importantly, mRNA expression patterns may not match the subcellular distribution of functional $GABA_A$Rs, such as mRNA expression in the somata but protein expression in the dendrites. Moreover, mRNA levels may not reflect quantitative differences in protein expression due to post-transcriptional and post-translational levels of control, such as mRNA editing, $GABA_A$R internalization, and degradation. While our findings usually corroborate these previous publications on $GABA_A$R expression (Laurie et al., 1992; Golshani et al., 1997; Hortnagl et al., 2013; Fertuzinhos et al., 2014) and KCC2 expression (Rivera et al., 1999; Stein et al., 2004; Dzhala et al., 2005; Uvarov et al., 2009; Takayama and Inoue, 2010; Markkanen et al., 2014; Zavalin et al., 2022), our work provides laminar resolution that was previously unknown.

Lamina-specific expression

A summary of expression trajectories of multiple $GABA_A$R subunit proteins within a single lamina is provided in Supplementary Figure 3. However, it is important to realize

that differences in antibody affinity preclude any direct comparison of absolute protein quantity among the various subunits.

Layer 1/marginal zone

MZ/L1 is the site of multiple important development processes, including tangential migration of interneuron progenitors (Li et al., 2008; Bortone and Polleux, 2009; Bartolini et al., 2013), which rely on $GABA_AR$-mediated excitation for motility (Inada et al., 2011). MZ is also populated by a transient neuronal population of Cajal-Retzius neurons, which develop exceptionally early and exhibit strong GABAergic input in the early period, playing a vital role in cortical circuit formation and organization (Kilb and Frotscher, 2016; Molnár et al., 2020). In our experiments, we found clear α2, α3, α5, β3, and γ2 $GABA_AR$ subunit expression in this layer by E15.5 in a generally diffuse pattern. At the time of birth, α1, α4, and δ were essentially absent in L1, but all other $GABA_AR$ subunits and KCC2 were clearly expressed.

Layers 2/3

L2/3 are the latest-maturing laminae in the inside-out sequence of cortical development. While α1, α2, α4, δ, and KCC2 expression was strong at maturity, these subunits were generally first clearly visible in L4 around P5 and then subsequently in more superficial layers by P12. This is concordant with the emergence of synaptic activity L2/3 and a critical period of receptive fields in L2/3 of barrel cortex (Maravall et al., 2004; Kobayashi et al., 2008). Prior to P5; α2, β2, β3, and γ2 were the predominant subunits expressed in L2/3. Additionally, α3 and α5 expression appeared to lie along the ascending dendrites of L4-6 neurons passing through L2/3. This interpretation is supported by previous work showing that α3 and α5 mRNA expression before P6-12 is predominantly in the lower and middle cortical layers, respectively (Laurie et al., 1992). From P5 onwards, the pattern of α3 expression became more diffuse and somewhat weaker, while α5 expression in barrel cortex virtually disappeared by P12.

Layer 4

L4 is the primary input layer for thalamocortical input, and dramatic changes in expression of $GABA_AR$ subunits and KCC2 occurred around the time when thalamocortical afferent fibers reach L4 at P4 and form defined barrels during P4-P8 (Inan and Crair, 2007). Prior to P5, $GABA_AR$ subunit expression in L4 was typically similar to L2/3. β3 and γ2 were consistently expressed in this area at all peri- and postnatal ages. At P5, there was an abrupt onset of strong α1, α2, α4, β2, δ, and KCC2 expression, while α3 and α5 expression was lost, and this pattern was also most prominent in barrel cortex. Expression of α(1,2)β(2,3)γ2 pentamers could allow temporally precise GABAergic signaling for accurate sensory processing during and after the critical period, while extrasynaptic α4βδ receptors may help provide local area regulation of multiple neurons with tonic inhibition.

Layers 5/6

L5/L6 are the earliest-forming cortical layers, and the site of early GABAergic "giant depolarizing potentials" that assist with circuit formation in the first postnatal week (Allene et al., 2008). Prior to P5, $GABA_AR$ subunits α3 and α5 were prominently expressed in L5/6 along with β2, β3, and γ2. KCC2 expression was also seen in L5 as early as E17.5, but was restricted to interneurons in the perinatal period, as previously shown with tissue from interneuron-specific KCC2 knockout mice (Zavalin et al., 2022). After P5, expression of α3 and α5 remained robust, but gained a sublaminar pattern with slightly stronger expression in the superficial L5 (L5a), and the border between L5 and L6 (L5c/L6a). At P12 there were moderate levels of α1 and γ2 expression in L1-4 and L6, but not L5. Finally, while α2, α4, δ, and KCC2 expression began in L5/6 by P12, it remained relatively weak compared to more superficial layers.

Subplate

Like the MZ, subplate hosts a population of transient, early-developing neurons that assist cortical formation by regulating processes like thalamocortical axon pathfinding and radial migration of neurons. Subplate neurons form a layer beneath the CP, with a distinct cell-sparse zone between L6 and the subplate from E15.5 until at least P2 (Torres-Reveron and Friedlander, 2007). Some of these subplate neurons are GABAergic, and prominent GABAergic currents can be evoked in subplate neurons (Unichenko et al., 2015; Ohtaka-Maruyama, 2020). Previous work has shown that after P2-4, a distinct layer of subplate neurons is lost, and these cells become intermixed with the lower portions of L6 (Kast and Levitt, 2019).

We found strong expression of $GABA_AR$ subunits α3, α5, and β2 that began as early as E13.5/E15.5; followed by β3, γ2, and KCC2 expression by E15.5/E17.5; and then low α1 expression by E17.5/P1. In addition, there was faint, primarily somatic δ expression in some subplate neurons as early as P1, as previously reported by Qu et al. (2016). This somatic pattern was most evident at P5 and persisted with fewer cells at P12 in the region where subplate was found earlier, and then was essentially gone by P26.

Previous work has shown *Gabra5* mRNA in the perinatal subplate (Golshani et al., 1997), and we found a consistent band of α5 expression restricted to the subplate. In contrast to other subunits, this expression persisted even into adulthood as a distinct, thin band in the post-subplate region/L6b. In contrast, α3 and β3 had a broader band of expression that included both the subplate, as well as the cell-poor region between the subplate and CP (referred to as "L6b" by Catalano et al., 1991). Unlike *Gabra5*, *Gabra3* mRNA is not known to be expressed in subplate at this age, and some α3 protein expression may be due to afferent/efferent fibers passing through this area, such as thalamocortical input and corticothalamic output. In particular, growing thalamocortical afferents that eventually project to L4 make contact with subplate neurons at E16-E19 (Catalano et al., 1991; Inan and Crair, 2007).

Other notable expression patterns

Subcortical α3+ fiber tracks

While $GABA_AR$ expression is not typically found in the subcortical white matter of a mature brain, we found expression of α3 in fibers of the intermediate zone and internal capsule

in the embryonic brain between E15.5 to P1, which was most evident at E17.5. This expression was no longer present by P5 and was also not seen in tissue from E17.5 *Gabra3*-knockout mice. Embryonic thalamus expresses α3 (Laurie et al., 1992, also visible in Figure 7A), and α3 expression can be seen extending past the striatum and into the subcortical region with a pattern suggestive of thalamocortical fibers (Agmon et al., 1993; Bicknese et al., 1994; Abe et al., 2015). Conversely, L5/6 show robust α3 expression starting in the embryonic period, and the fibers may also mark corticothalamic tracks. Future work will need to be done to more specifically identify the source of this α3 expression and its developmental significance.

Radial glia

α2 $GABA_AR$ protein expression was found in the superficial subcortical tissue, with radially oriented projections extending through the overlying CP in the embryonic and perinatal periods. Our results show that this α2 $GABA_AR$ protein expression overlaps with a subset of RC2-labeled radial glia in dorsal cortex. Previous work has shown that both mature glia and their precursors express functional $GABA_ARs$ (Wang et al., 2005; Muth-Kohne et al., 2010; Renzel et al., 2013). Bergmann glia specifically express *Gabra2* mRNA (Riquelme et al., 2002), and possibly α1, β1, β3, and γ1 (Bovolin et al., 1992). Laurie et al. (1992) also reported mRNA expression of α2 in the lower intermediate zone by E17. Thus, it is possible that our results reflect presence of α2-containing $GABA_ARs$ in the radial glia. However, radial glial processes in embryonic brain are much more widely distributed than the pattern of α2 expression reported here. There were RC2-positive fibers extending centrifugally from both pallial and subpallial ventricular zones, while α2+ fibers lacked this range and appeared to arise from the intermediate zone. Therefore, the identity of these fibers is not entirely clear. It is conceivable that these fibers represent radial processes of a subset of radial glia, but it is just as likely that they are expressed in some other closely associated processes instead. Additionally, it is unclear whether these are functional $GABA_AR$ pentamers, since we did not see this pattern with other $GABA_AR$ proteins.

Somata

Immunolabelling for the δ $GABA_AR$ subunit or KCC2 identified distinct somata in cortex. In the case of KCC2, we were able to corroborate that this represented early KCC2 expression in interneurons (Zavalin et al., 2022). The δ+ somata were most prominent at P12 and P26, but the identity of these cells is unclear. A similar pattern has been reported in hippocampus by other groups, which found discrete α1, β2, and δ co-expressing cell bodies that correspond with parvalbumin interneurons (Peng et al., 2004; Milenkovic et al., 2013). We also found intensely labeled α1+ and β2+ somata in hippocampus from P5-P26 (data not shown), but not in the cortex from the same sections. Therefore, cortical δ+ somata may likewise represent interneurons, but it is unclear which $GABA_AR$ subunits partner with δ in the cortex, although α4β2δ is the subunit combination most commonly found in brain.

Developmental significance of subunit expression patterns

The developmental significance of the expression patterns discussed here is unclear without knowing how those changes will affect GABAergic signaling. Fortunately, there is now a large body of work characterizing the pharmacodynamic properties and subcellular location of different $GABA_AR$ subunit-combination (Chuang and Reddy, 2018; Engin et al., 2018).

γ2-containing $GABA_ARs$

$GABA_ARs$ containing the γ2 subunit are the primary mediators of synaptic responses, since they are often found within the synapse and tend to produce large, rapidly activating and deactivating currents. However, they require relatively high [GABA] (≈ 10–15 μM) for full activation and also desensitize rapidly. We found that ubiquitous γ2 expression begins early in development and ramps up to even higher levels as the brain matures, suggesting that γ2-containing $GABA_ARs$ constitute a sizeable portion of cortical $GABA_ARs$ at all ages. Moreover, some of the α subunits that typically combine with γ2, which include α1, α2, α3, and α5 in adult brain, are also present at early ages. However, expression of each of these α subunits significantly varies by developmental stage and lamina, imparting different properties to γ2-containing $GABA_ARs$ in development and adulthood.

α3 and α5-containing $GABA_ARs$

Among the α subunits, α3 and α5 are expressed particularly early in development in multiple cortical laminae, including the MZ, L5, and subplate. Unlike in adult brain, these subunits often had spatially and temporally overlapping patterns of expression in the developing cortex. $GABA_ARs$ containing either of these subunits tend to have prolonged decay times and slow desensitization. Concordantly, GABAergic currents during embryonic and perinatal period generally have slow phasic or tonic kinetic properties (Le Magueresse and Monyer, 2013; Warm et al., 2022). However, α3- and α5-containing $GABA_ARs$ have notably different sensitivities to GABA (Picton and Fisher, 2007; Rula et al., 2008; Lagrange et al., 2018). For example, α5β3γ2 $GABA_ARs$ are sensitive to low [GABA] (<5–10 μM) and often localize to the extrasynaptic space, allowing them to convey much of the tonic inhibition in some adult brain regions (Caraiscos et al., 2004; Lagrange et al., 2018). In contrast, α3-containing $GABA_ARs$ require very high [GABA] (EC50 30–100 μM) and relatively prolonged or repetitive exposure to GABA for full activation (Rula et al., 2008). Thus, a mixed population of α3βγ2 and α5βγ2 $GABA_ARs$ would provide a pool of highly sensitive α5-containing $GABA_ARs$ to respond to low levels of GABA and another population of α3-containing $GABA_ARs$ tuned to detect repetitive exposure to high [GABA]. The ability of α3-containing $GABA_ARs$ to detect coincident stimulation may be particularly useful in a developmental context, where growth cone stabilization, synaptogenesis, and other developmental processes depend on repetitive $GABA_AR$ activation. Indeed, embryonic α3 expression is required for the formation of certain axo-axonic synapses

in the retina (Sinha et al., 2021). Interestingly, α3 expression may provide an additional, temporally dependent regulation of GABAergic signaling. *Gabra3* is subject to RNA editing during later stages of development (50% edited at P2-5, 90% edited at P7-9). This process converts an isoleucine to methionine in the third transmembrane domain, leading to reduced GABA potency, reduced surface expression, and faster decay (Rula et al., 2008; Daniel et al., 2011), which likely fine-tunes the ability to sum up repetitive stimuli.

On the other hand, α5-containing $GABA_A$Rs may provide GABAergic depolarization when low [GABA] is present. Sebe et al. (2010) found significant α5-mediated tonic current in cortical L5 neurons uniquely at early postnatal timepoints, which excited a minority and inhibited the majority of neurons, but whether similar tonic currents occur in other areas remains to be determined. While α5-containing $GABA_A$Rs tend to be extrasynaptic in adult brain, they have also been found at/near synapses in developing neurons and mediate signals that assist neuronal development (Serwanski et al., 2006; Brady and Jacob, 2015; Hernandez et al., 2019). Previous work has shown that α5-mediated currents promote dendrite and spine development *in vitro* (Giusi et al., 2009; Brady and Jacob, 2015), as well as migration and dendrite development of adult-born granule cells (Deprez et al., 2016; Lodge et al., 2021).

α1 and α2-containing $GABA_A$Rs

In contrast to α3 and α5, α1 and α2-containing $GABA_A$Rs have kinetic properties that are tailored toward phasic signaling associated with mature synaptic signals. The robust upregulation of these two subunits is coincident with a period of maximal synaptic formation during the second and early third postnatal week in mice (Bosman et al., 2002; Kobayashi et al., 2008; Okaty et al., 2009; Lazarus and Huang, 2011; Le Magueresse and Monyer, 2013; Yang et al., 2014).

α1βγ2 is by far the most abundant $GABA_A$R subunit combination found in adult brain and conveys the majority of synaptic inhibition. α1βγ2 $GABA_A$Rs activate very quickly and have moderate rates of deactivation that allow them to convert sub-millisecond GABA transients into currents lasting tens of milliseconds or more. However, these $GABA_A$Rs also desensitize quickly and extensively. Thus, synaptic activity conveyed by α1βγ2 $GABA_A$R is able to respond to sparse synaptic activity with high temporal precision but is also relatively insensitive to high frequency input (Bianchi et al., 2007; Lagrange et al., 2018). Indeed, electrophysiological experiments in L2/3 show a developmental transition of GABAergic synaptic currents toward a fast activation/fast deactivation profile, which is coincident with a decrease of the α3-mediated component and increase in the α1-mediated component (Bosman et al., 2002; Kobayashi et al., 2008).

α2βγ2 have similar activation, deactivation, and desensitization to α1βγ2, but somewhat lower GABA potency and more rapid recovery during frequent stimulation (Picton and Fisher, 2007). While α1βγ2 $GABA_A$Rs are prevalent at the majority of GABAergic synapses (Chuang and Reddy, 2018; Engin et al., 2018), α2βγ2 $GABA_A$Rs appear to be the dominant combination at specific synapses, such as synapses made by parvalbumin+ chandelier interneurons on the axon initial segment and on somatic synapses made by non-parvalbumin basket interneurons, such as cholecystokinin+ interneurons (Nusser et al., 1996; Nyíri et al., 2001; Klausberger et al., 2002).

δ-containing $GABA_A$Rs

In contrast to synaptic γ2-containing $GABA_A$Rs, α5βγ2 and δ-containing $GABA_A$Rs are mediators of tonic GABAergic signaling, partly due to their preferential localization outside of the synapse. The δ subunit tends to partner with α4 *in vivo* to create α4βδ pentamers (Engin et al., 2018; Lagrange et al., 2018), and we found that α4 and δ followed a similar pattern of expression that was quite sparse until the second postnatal week. α4βδ $GABA_A$Rs are the primary mediators of tonic inhibition in response to low levels of extrasynaptic [GABA] found in cortex, thalamus, and hippocampus (usually ≈ 1 μM or even less), activating slowly but maintaining a prolonged tonic current due to slow deactivation and low desensitization (Lagrange et al., 2018). Since α4βδ $GABA_A$Rs are maximally activated at low [GABA], they can only discriminate a relatively narrow range of extrasynaptic [GABA] concentrations (≤1–5 μM). α5β3γ2 $GABA_A$Rs are less sensitive to low [GABA], with EC50s between those of α4βδ and α1βγ2 $GABA_A$Rs (Lagrange et al., 2018). While α4 and α5 subunits are often expressed in different brain regions, there are some areas of overlap (Hortnagl et al., 2013). In these cases, expression of both α4βδ and α5β3γ2 $GABA_A$Rs imparts the ability to fine-tune network activity to a wider range of [GABA] (Scimemi et al., 2005).

However, α4 and α5 subunits often have non-overlapping patterns of expression. As mentioned previously, α5-containing $GABA_A$Rs convey most of the tonic signaling in early life, since α4 and δ subunit expression only appears around P5. Even in the adult cortex, where both subunits are expressed, α5 is expressed highly in L5/6, α4 expression is higher in superficial layers. Neurons throughout the cortical column have been shown to exhibit tonic currents, but subunit composition of $GABA_A$Rs mediating these currents differs by layer (Yamada et al., 2007; Jang et al., 2013). Therefore, while tonic currents in L5 have a prominent α5-mediated component (Yamada et al., 2007), our findings indicate that tonic currents in L4 and superficial layers may have stronger α4 and δ-mediated components.

A small percentage of the α1 subunit can also be found in α1βδ $GABA_A$Rs, which are predominantly expressed on interneurons (Glykys et al., 2007) that could correspond with the immunolabeled somata we observed for both α1 and δ subunits. These pentamers have GABA potency that is similar to α5β3γ2, but also have very fast rates of activation and deactivation, as well as much less desensitization than any other $GABA_A$R subunit combinations studied so far (Bianchi et al., 2002; Lagrange et al., 2018). Their extremely fast deactivation would make them poorly suited to respond to low frequency phasic stimulation. Their minimal desensitization is conducive to tonic inhibition, but kinetic properties make this subunit combination able to respond near-instantaneously to abrupt changes in extrasynaptic GABA. These properties are expected to produce extrasynaptic responses with extremely high temporal precision to presynaptic input, but little overall charge transfer during single events. α1βδ $GABA_A$Rs are well-suited to respond to prolonged, repetitive synaptic input with high temporal fidelity.

KCC2

KCC2 has a strong influence on development through its effect in transitioning GABAergic signaling to mediate inhibition during later stages of development. In agreement with this function, we saw late KCC2 expression in cortex with exception of interneurons, where KCC2 may play an important developmental role (Cuzon et al., 2006; Bortone and Polleux, 2009; Inada et al., 2011; Inamura et al., 2012; Zavalin et al., 2022). While KCC2 expression is a significant factor in heralding a transition to inhibitory GABAergic responses, extensive regulation by kinases further restricts KCC2 activity to late stages of development (Fukuda, 2020; Virtanen et al., 2020, 2021), and additional factors including extracellular matrix proteins influence the polarity of GABAergic responses (Delpire and Staley, 2014; Glykys et al., 2014; Rahmati et al., 2021). Additionally, KCC2 has transport-independent functions that affect dendritic spine formation, apoptosis, and other developmental processes (Llano et al., 2020).

We did not distinguish the two isoforms of KCC2, KCC2a, and KCC2b, which both act as transporters, but have structural differences and significantly vary in temporal and spatial expression (Uvarov et al., 2007, 2009; Markkanen et al., 2014, 2017).

Additional considerations

Our data from P26 mice is generally quite consistent with the published literature. However, we cannot rule out the possibility that tissue from later ages might have revealed greater changes in expression intensity, such as a drop in α2 or α5 expression. We did not measure expression of β1, γ1, and γ3, as we were unable to find a suitably specific antibody for use in WB and IHC experiments.

Unlike other subunits, it is less clear how much β subunit composition affects $GABA_A$Rs properties, and the significance of asynchronous β2 and β3 in cortical signaling is unclear. However, there are some subtle differences between β2 and β3 containing $GABA_A$Rs, such as their sensitivity to some general anesthetics (Zeller et al., 2007), and α4β3δ are less sensitive to low GABA than α4β2δ $GABA_A$Rs (Lagrange et al., 2018). In general, α5 tends to partner with β3 and γ2 *in vivo*, so early expression of β3 and γ2 may be conducive to forming α5β3γ2 $GABA_A$Rs (Mckernan and Whiting, 1996).

The isoform specific $GABA_A$R responses are only one factor mediating GABAergic signaling in the developing brain. The concentration and kinetics of GABA play an equally important role that may vary from very brief synaptic transients to longer bursts of synaptic input, slower transients of intermediate GABA concentrations, and even steady state levels of low GABA (Brickley and Mody, 2012).

This work evaluated the expression of individual $GABA_A$R subunits, and thus is not entirely informative of subunit combinations that form functional $GABA_A$Rs. Though certain frequently-occurring combinations can be predicted from our expression, we cannot address the effects of mixed $GABA_A$R α subunit combinations that are expressed *in vivo* (Sun et al., 2023). For example, it is currently unknown whether α3/α5β3γ2 would have high sensitivity to GABA like α5β3γ2 $GABA_A$Rs, or low like α3β3γ2 $GABA_A$Rs. Furthermore, a number of endogenous $GABA_A$R modulators, such as neurosteroids and endozepines, are also developmentally regulated and regulate $GABA_A$R function (Brown et al., 2016; Tonon et al., 2020). Finally, $GABA_A$R-mediated signals can differ not only by lamina and developmental stage, but by specific neuronal types, circuits, and synapses. Therefore, while our experiments delineate certain trends in cortical $GABA_A$R composition during development, physiology studies that focus on certain neuronal types and synapses may find exceptions and specializations that do not follow these trends.

Data availability statement

The datasets presented in this article are not readily available because imaging and expression data has not been systematically organized for shared use and will not be stored indefinitely. Requests to access the datasets should be directed to AL, andre.h.lagrange@vumc.org.

Ethics statement

Ethical approval was not required for the studies on humans in accordance with the local legislation and institutional requirements because only commercially available established cell lines were used. The animal study was approved by the Vanderbilt University Institutional Animal Care and Use Committee. The study was conducted in accordance with the local legislation and institutional requirements.

Author contributions

KZ: Formal analysis, Investigation, Methodology, Visualization, Writing – original draft, Writing – review & editing. AH: Formal analysis, Investigation, Methodology, Visualization, Writing – review & editing. YZ: Investigation, Methodology, Writing – review & editing. ZK: Investigation, Writing – review & editing. AL: Conceptualization, Formal analysis, Funding acquisition, Investigation, Methodology, Project administration, Supervision, Visualization, Writing – review & editing.

Funding

The author(s) declare financial support was received for the research, authorship, and/or publication of this article. This work was supported by Veteran Affairs Merit grant I01 BX001189.

Conflict of interest

The authors declare that the research was conducted in the absence of any commercial or financial relationships

that could be construed as a potential conflict of interest.

Publisher's note

All claims expressed in this article are solely those of the authors and do not necessarily represent those of their affiliated organizations, or those of the publisher, the editors and the reviewers. Any product that may be evaluated in this article, or claim that may be made by its manufacturer, is not guaranteed or endorsed by the publisher.

Supplementary material

The Supplementary Material for this article can be found online at: https://www.frontiersin.org/articles/10.3389/fncel.2024.1390742/full#supplementary-material

References

Abe, P., Molnar, Z., Tzeng, Y. S., Lai, D. M., Arnold, S. J., and Stumm, R. (2015). Intermediate progenitors facilitate intracortical progression of thalamocortical axons and interneurons through CXCL12 chemokine signaling. *J. Neurosci.* 35, 13053–13063. doi: 10.1523/JNEUROSCI.1488-15.2015

Agmon, A., Yang, L. T., O'dowd, D. K., and Jones, E. G. (1993). Organized growth of thalamocortical axons from the deep tier of terminations into layer IV of developing mouse barrel cortex. *J. Neurosci.* 13, 5365–5382. doi: 10.1523/JNEUROSCI.13-12-05365.1993

Allene, C., Cattani, A., Ackman, J. B., Bonifazi, P., Aniksztejn, L., Ben Ari, Y., et al. (2008). Sequential generation of two distinct synapse-driven network patterns in developing neocortex. *J Neurosci.* 28, 12851–12863. doi: 10.1523/JNEUROSCI.3733-08.2008

Bartolini, G., Ciceri, G., and Marín, O. (2013). Integration of GABAergic interneurons into cortical cell assemblies: lessons from embryos and adults. *Neuron* 79, 849–864. doi: 10.1016/j.neuron.2013.08.014

Bayer, S. A., and Altman, J. (1990). Development of layer I and the subplate in the rat neocortex. *Exp. Neurol.* 107, 48–62. doi: 10.1016/0014-4886(90)90062-W

Ben-Ari, Y., Gaiarsa, J. L., Tyzio, R., and Khazipov, R. (2007). GABA: a pioneer transmitter that excites immature neurons and generates primitive oscillations. *Physiol. Rev.* 87, 1215–1284. doi: 10.1152/physrev.00017.2006

Bianchi, M. T., Botzolakis, E. J., Haas, K. F., Fisher, J. L., and Macdonald, R. L. (2007). Microscopic kinetic determinants of macroscopic currents: insights from coupling and uncoupling of GABAA receptor desensitization and deactivation. *J. Physiol.* 584, 769–787. doi: 10.1113/jphysiol.2007.142364

Bianchi, M. T., Haas, K. F., and Macdonald, R. L. (2002). Alpha1 and alpha6 subunits specify distinct desensitization, deactivation and neurosteroid modulation of GABA(A) receptors containing the delta subunit. *Neuropharmacology* 43, 492–502. doi: 10.1016/S0028-3908(02)00163-6

Bicknese, A. R., Sheppard, A. M., O'leary, D. D., and Pearlman, A. L. (1994). Thalamocortical axons extend along a chondroitin sulfate proteoglycan-enriched pathway coincident with the neocortical subplate and distinct from the efferent path. *J. Neurosci.* 14, 3500–3510. doi: 10.1523/JNEUROSCI.14-06-03500.1994

Bortone, D., and Polleux, F. (2009). KCC2 expression promotes the termination of cortical interneuron migration in a voltage-sensitive calcium-dependent manner. *Neuron* 62, 53–71. doi: 10.1016/j.neuron.2009.01.034

Bosman, L. W., Rosahl, T. W., and Brussaard, A. B. (2002). Neonatal development of the rat visual cortex: synaptic function of $GABA_A$ receptor alpha subunits. *J. Physiol.* 545, 169–181. doi: 10.1113/jphysiol.2002.026534

Bouzigues, C., Holcman, D., and Dahan, M. (2010). A mechanism for the polarity formation of chemoreceptors at the growth cone membrane for gradient amplification during directional sensing. *PLoS ONE* 5:e9243. doi: 10.1371/journal.pone.0009243

Bovolin, P., Santi, M. R., Memo, M., Costa, E., and Grayson, D. R. (1992). Distinct developmental patterns of expression of rat alpha 1, alpha 5, gamma 2S, and gamma 2L gamma-aminobutyric acidA receptor subunit mRNAs *in vivo* and *in vitro*. *J. Neurochem.* 59, 62–72. doi: 10.1111/j.1471-4159.1992.tb08876.x

Brady, M. L., and Jacob, T. C. (2015). Synaptic localization of α5 GABA (A) receptors via gephyrin interaction regulates dendritic outgrowth and spine maturation. *Develop. Neurobiol.* 75, 1241–1251. doi: 10.1002/dneu.22280

Brickley, S. G., and Mody, I. (2012). Extrasynaptic GABA(A) receptors: their function in the CNS and implications for disease. *Neuron* 73, 23–34. doi: 10.1016/j.neuron.2011.12.012

Brown, A. R., Mitchell, S. J., Peden, D. R., Herd, M. B., Seifi, M., Swinny, J. D., et al. (2016). During postnatal development endogenous neurosteroids influence GABA-ergic neurotransmission of mouse cortical neurons. *Neuropharmacology* 103, 163–173. doi: 10.1016/j.neuropharm.2015.11.019

Cancedda, L., Fiumelli, H., Chen, K., and Poo, M. M. (2007). Excitatory GABA action is essential for morphological maturation of cortical neurons *in vivo*. *J. Neurosci.* 27, 5224–5235. doi: 10.1523/JNEUROSCI.5169-06.2007

Caraiscos, V. B., Elliott, E. M., You-Ten, K. E., Cheng, V. Y., Belelli, D., Newell, J. G., et al. (2004). Tonic inhibition in mouse hippocampal CA1 pyramidal neurons is mediated by alpha5 subunit-containing gamma-aminobutyric acid type A receptors. *Proc. Natl. Acad. Sci. U S A* 101, 3662–3667. doi: 10.1073/pnas.0307231101

Catalano, S. M., Robertson, R. T., and Killackey, H. P. (1991). Early ingrowth of thalamocortical afferents to the neocortex of the prenatal rat. *Proc. Natl. Acad. Sci. U S A* 88, 2999–3003. doi: 10.1073/pnas.88.8.2999

Chancey, J. H., Adlaf, E. W., Sapp, M. C., Pugh, P. C., Wadiche, J. I., and Overstreet-Wadiche, L. S. (2013). GABA depolarization is required for experience-dependent synapse unsilencing in adult-born neurons. *J. Neurosci.* 33, 6614–6622. doi: 10.1523/JNEUROSCI.0781-13.2013

Chuang, S.-H., and Reddy, D. S. (2018). Genetic and molecular regulation of extrasynaptic GABA-A receptors in the brain: therapeutic insights for epilepsy. *J. Pharmacol. Exper. Therap.* 364, 180–197. doi: 10.1124/jpet.117.244673

Cuzon Carlson, V. C., and Yeh, H. H. (2011). GABAA receptor subunit profiles of tangentially migrating neurons derived from the medial ganglionic eminence. *Cereb. Cortex* 21, 1792–1802. doi: 10.1093/cercor/bhq247

Cuzon, V. C., Yeh, P. W., Cheng, Q., and Yeh, H. H. (2006). Ambient GABA promotes cortical entry of tangentially migrating cells derived from the medial ganglionic eminence. *Cereb. Cortex* 16, 1377–1388. doi: 10.1093/cercor/bhj084

Daniel, C., Wahlstedt, H., Ohlson, J., Bjork, P., and Ohman, M. (2011). Adenosine-to-inosine RNA editing affects trafficking of the gamma-aminobutyric acid type A (GABA(A)) receptor. *J. Biol. Chem.* 286, 2031–2040. doi: 10.1074/jbc.M110.130096

Daw, M. I., Ashby, M. C., and Isaac, J. T. R. (2007). Coordinated developmental recruitment of latent fast spiking interneurons in layer IV barrel cortex. *Nat. Neurosci.* 10, 453–461. doi: 10.1038/nn1866

Delpire, E., and Staley, K. J. (2014). Novel determinants of the neuronal Cl^- concentration. *J. Physiol.* 592, 4099–4114. doi: 10.1113/jphysiol.2014.275529

Deprez, F., Vogt, F., Floriou-Servou, A., Lafourcade, C., Rudolph, U., Tyagarajan, S. K., et al. (2016). Partial inactivation of $GABA_A$ receptors containing the α5 subunit affects the development of adult-born dentate gyrus granule cells. *Eur. J. Neurosci.* 44, 2258–2271. doi: 10.1111/ejn.13329

Dzhala, V. I., Talos, D. M., Sdrulla, D. A., Brumback, A. C., Mathews, G. C., Benke, T. A., et al. (2005). NKCC1 transporter facilitates seizures in the developing brain. *Nat. Med.* 11, 1205–1213. doi: 10.1038/nm1301

Engin, E., Benham, R. S., and Rudolph, U. (2018). An emerging circuit pharmacology of GABAA receptors. *Trends Pharmacol. Sci.* 39, 710–732. doi: 10.1016/j.tips.2018.04.003

Fertuzinhos, S., Li, M., Kawasawa, Yuka i., Ivic, V., Franjic, D., Singh, D., et al. (2014). Laminar and temporal expression dynamics of coding and noncoding RNAs in the mouse neocortex. *Cell Rep.* 6, 938–950. doi: 10.1016/j.celrep.2014.01.036

Fritschy, J. M., Paysan, J., Enna, A., and Mohler, H. (1994). Switch in the expression of rat GABAA-receptor subtypes during postnatal development: an immunohistochemical study. *J. Neurosci.* 14, 5302–5324. doi: 10.1523/JNEUROSCI.14-09-05302.1994

Fritschy, J. M., Weinmann, O., Wenzel, A., and Benke, D. (1998). Synapse-specific localization of NMDA and $GABA_A$ receptor subunits revealed by antigen-retrieval immunohistochemistry. *J. Comp. Neurol.* 390, 194–210. doi: 10.1002/(SICI)1096-9861(19980112)390:2<194::AID-CNE3>3.0.CO;2-X

Fukuda, A. (2020). Chloride homeodynamics underlying modal shifts in cellular and network oscillations. *Neurosci. Res.* 156, 14–23. doi: 10.1016/j.neures.2020.02.010

Ge, S., Goh, E. L., Sailor, K. A., Kitabatake, Y., Ming, G. L., and Song, H. (2006). GABA regulates synaptic integration of newly generated neurons in the adult brain. *Nature* 439, 589–593. doi: 10.1038/nature04404

Giusi, G., Facciolo, R. M., Rende, M., Alò, R., Di Vito, A., Salerno, S., et al. (2009). Distinct α subunits of the GABAA receptor are responsible for early hippocampal silent neuron-related activities. *Hippocampus* 19, 1103–1114. doi: 10.1002/hipo.20584

Glykys, J., Dzhala, V., Egawa, K., Balena, T., Saponjian, Y., Kuchibhotla, K. V., et al. (2014). Local impermeant anions establish the neuronal chloride concentration. *Science* 343, 670–675. doi: 10.1126/science.1245423

Glykys, J., Peng, Z., Chandra, D., Homanics, G. E., Houser, C. R., and Mody, I. (2007). A new naturally occurring GABA(A) receptor subunit partnership with high sensitivity to ethanol. *Nat. Neurosci.* 10, 40–48. doi: 10.1038/nn1813

Golshani, P., Truong, H., and Jones, E. G. (1997). Developmental expression of GABA(A) receptor subunit and GAD genes in mouse somatosensory barrel cortex. *J. Comp. Neurol.* 383, 199–219. doi: 10.1002/(SICI)1096-9861(19970630)383:2<199::AID-CNE7>3.0.CO;2-W

Hernandez, C. C., Xiangwei, W., Hu, N., Shen, D., Shen, W., Lagrange, A. H., et al. (2019). Altered inhibitory synapses in de novo GABRA5 and GABRA1 mutations associated with early onset epileptic encephalopathies. *Brain* 142, 1938–1954. doi: 10.1093/brain/awz123

Hortnagl, H., Tasan, R. O., Wieselthaler, A., Kirchmair, E., Sieghart, W., and Sperk, G. (2013). Patterns of mRNA and protein expression for 12 GABAA receptor subunits in the mouse brain. *Neuroscience* 236, 345–372. doi: 10.1016/j.neuroscience.2013.01.008

Inada, H., Watanabe, M., Uchida, T., Ishibashi, H., Wake, H., Nemoto, T., et al. (2011). GABA regulates the multidirectional tangential migration of GABAergic interneurons in living neonatal mice. *PLoS ONE* 6:e27048. doi: 10.1371/journal.pone.0027048

Inamura, N., Kimura, T., Tada, S., Kurahashi, T., Yanagida, M., Yanagawa, Y., et al. (2012). Intrinsic and extrinsic mechanisms control the termination of cortical interneuron migration. *J. Neurosci.* 32, 6032–6042. doi: 10.1523/JNEUROSCI.3446-11.2012

Inan, M., and Crair, M. C. (2007). Development of cortical maps: perspectives from the barrel cortex. *Neuroscientist* 13, 49–61. doi: 10.1177/1073858406296257

Jacobowitz, D. M., and Abbott, L. C. (1997). *Chemoarchitectonic Atlas of the Developing Mouse Brain.* New York: CRC Press. doi: 10.1201/9781466593411

Jang, H. J., Cho, K. H., Kim, M. J., Yoon, S. H., and Rhie, D. J. (2013). Layer- and cell-type-specific tonic GABAergic inhibition of pyramidal neurons in the rat visual cortex. *Pflugers Arch.* 465, 1797–1810. doi: 10.1007/s00424-013-1313-1

Kast, R. J., and Levitt, P. (2019). Precision in the development of neocortical architecture: from progenitors to cortical networks. *Progr. Neurobiol.* 175, 77–95. doi: 10.1016/j.pneurobio.2019.01.003

Kilb, W. (2021). When are depolarizing GABAergic responses excitatory? *Front. Molec. Neurosci.* 14:747835. doi: 10.3389/fnmol.2021.747835

Kilb, W., and Frotscher, M. (2016). Cajal-Retzius cells: organizers of cortical development. *e-Neuroforum* 7, 82–88. doi: 10.1007/s13295-016-0031-5

Klausberger, T., Roberts, J. D. B., and Somogyi, P. (2002). Cell type- and input-specific differences in the number and subtypes of synaptic $GABA_A$ receptors in the hippocampus. *J. Neurosci.* 22, 2513–2521. doi: 10.1523/JNEUROSCI.22-07-02513.2002

Kobayashi, M., Hamada, T., Kogo, M., Yanagawa, Y., Obata, K., and Kang, Y. (2008). Developmental profile of GABAA-mediated synaptic transmission in pyramidal cells of the somatosensory cortex. *Eur. J. Neurosci.* 28, 849–861. doi: 10.1111/j.1460-9568.2008.06401.x

Kovács, K., Basu, K., Rouiller, I., and Sík, A. (2014). Regional differences in the expression of K(+)-Cl(-) 2 cotransporter in the developing rat cortex. *Brain Struct. Funct.* 219, 527–538. doi: 10.1007/s00429-013-0515-9

Kroon, T., Van Hugte, E., Van Linge, L., Mansvelder, H. D., and Meredith, R. M. (2019). Early postnatal development of pyramidal neurons across layers of the mouse medial prefrontal cortex. *Sci. Rep.* 9:5037. doi: 10.1038/s41598-019-41661-9

Lagrange, A. H., Botzolakis, E. J., and Macdonald, R. L. (2007). Enhanced macroscopic desensitization shapes the response of alpha4 subtype-containing GABAA receptors to synaptic and extrasynaptic GABA. *J. Physiol.* 578, 655–676. doi: 10.1113/jphysiol.2006.122135

Lagrange, A. H., Hu, N., and Macdonald, R. L. (2018). GABA beyond the synapse: defining the subtype-specific pharmacodynamics of non-synaptic GABAA receptors. *J. Physiol.* 596, 4475–4495. doi: 10.1113/JP276187

Laurie, D. J., Wisden, W., and Seeburg, P. H. (1992). The distribution of thirteen GABAA receptor subunit mRNAs in the rat brain. III. Embryonic and postnatal development. *J. Neurosci.* 12, 4151–4172. doi: 10.1523/JNEUROSCI.12-11-04151.1992

Lazarus, M. S., and Huang, Z. J. (2011). Distinct maturation profiles of perisomatic and dendritic targeting GABAergic interneurons in the mouse primary visual cortex during the critical period of ocular dominance plasticity. *J. Neurophysiol.* 106, 775–787. doi: 10.1152/jn.00729.2010

Le Magueresse, C., and Monyer, H. (2013). GABAergic interneurons shape the functional maturation of the cortex. *Neuron* 77, 388–405. doi: 10.1016/j.neuron.2013.01.011

Li, G., Adesnik, H., Li, J., Long, J., Nicoll, R. A., Rubenstein, J. L. R., et al. (2008). Regional distribution of cortical interneurons and development of inhibitory tone are regulated by Cxcl12/Cxcr4 signaling. *J. Neurosci.* 28, 1085–1098. doi: 10.1523/JNEUROSCI.4602-07.2008

Llano, O., Rivera, C., and Ludwig, A. (2020). "Chapter 6 - KCC2 regulates dendritic spine development," in *Neuronal Chloride Transporters in Health and Disease,* ed. X. Tang (London: Academic Press), 103–132. doi: 10.1016/B978-0-12-815318-5.00006-6

Lo, W.-Y., Lagrange, A. H., Hernandez, C. C., Gurba, K. N., and Macdonald, R. L. (2014). Co-expression of γ2 subunits hinders processing of N-linked glycans attached to the N104 glycosylation sites of GABAA receptor β2 subunits. *Neurochem. Res.* 39, 1088–1103. doi: 10.1007/s11064-013-1187-9

Lodge, M., Hernandez, M.-C., Schulz, J. M., and Bischofberger, J. (2021). Sparsification of AP firing in adult-born hippocampal granule cells via voltage-dependent α5-GABAA receptors. *Cell Rep.* 37:109768. doi: 10.1016/j.celrep.2021.109768

Lu, J., Karadsheh, M., and Delpire, E. (1999). Developmental regulation of the neuronal-specific isoform of K-Cl cotransporter KCC2 in postnatal rat brains. *J. Neurobiol.* 39, 558–568. doi: 10.1002/(SICI)1097-4695(19990615)39:4<558::AID-NEU9>3.0.CO;2-5

Ma, W., and Barker, J. L. (1995). Complementary expressions of transcripts encoding GAD67 and $GABA_A$ receptor a4, b1, and g1 subunits in the proliferative zone of the embryonic rat central nervous system. *J. Neurosci.* 15, 2547–2560. doi: 10.1523/JNEUROSCI.15-03-02547.1995

Ma, W., and Barker, J. L. (1998). GABA, GAD, and $GABA_A$ receptor a4, b1, and g1 subunits are expressed in the late embryonic and early postnatal neocortical germinal matrix and coincide with gliogenesis. *Microsc. Res. Tech.* 40, 398–407. doi: 10.1002/(SICI)1097-0029(19980301)40:5<398::AID-JEMT6>3.0.CO;2-N

Maravall, M., Koh, I. Y. Y., Lindquist, W. B., and Svoboda, K. (2004). Experience-dependent changes in basal dendritic branching of layer 2/3 pyramidal neurons during a critical period for developmental plasticity in rat barrel cortex. *Cerebr. Cortex* 14, 655–664. doi: 10.1093/cercor/bhh026

Markkanen, M., Karhunen, T., Llano, O., Ludwig, A., Rivera, C., Uvarov, P., et al. (2014). Distribution of neuronal KCC2a and KCC2b isoforms in mouse CNS. *J. Compar. Neurol.* 522, 1897–1914. doi: 10.1002/cne.23510

Markkanen, M., Ludwig, A., Khirug, S., Pryazhnikov, E., Soni, S., Khiroug, L., et al. (2017). Implications of the N-terminal heterogeneity for the neuronal K-Cl cotransporter KCC2 function. *Brain Res.* 1675, 87–101. doi: 10.1016/j.brainres.2017.08.034

Mckernan, R. M., and Whiting, P. J. (1996). Which GABAA-receptor subtypes really occur in the brain? *Trends Neurosci.* 19, 139–143. doi: 10.1016/S0166-2236(96)80023-3

Milenkovic, I., Vasiljevic, M., Maurer, D., Höger, H., Klausberger, T., and Sieghart, W. (2013). The parvalbumin-positive interneurons in the mouse dentate gyrus express GABAA receptor subunits α1, β2, and δ along their extrasynaptic cell membrane. *Neuroscience* 254, 80–96. doi: 10.1016/j.neuroscience.2013.09.019

Möhler, H. (2006). GABAA receptors in central nervous system disease: anxiety, epilepsy, and insomnia. *J. Recept. Signal Transd.* 26, 731–740. doi: 10.1080/10799890600920035

Molnár, Z., Luhmann, H. J., and Kanold, P. O. (2020). Transient cortical circuits match spontaneous and sensory-driven activity during development. *Science* 370:eabb2153. doi: 10.1126/science.abb2153

Murguia-Castillo, J., Beas-Zarate, C., Rivera-Cervantes, M. C., Feria-Velasco, A. I., and Urena-Guerrero, M. E. (2013). NKCC1 and KCC2 protein expression is sexually dimorphic in the hippocampus and entorhinal cortex of neonatal rats. *Neurosci. Lett.* 552, 52–57. doi: 10.1016/j.neulet.2013.07.038

Muth-Kohne, E., Terhag, J., Pahl, S., Werner, M., Joshi, I., and Hollmann, M. (2010). Functional excitatory GABAA receptors precede ionotropic glutamate receptors in radial glia-like neural stem cells. *Mol. Cell Neurosci.* 43, 209–221. doi: 10.1016/j.mcn.2009.11.002

Nusser, Z., Sieghart, W., Benke, D., Fritschy, J. M., and Somogyi, P. (1996). Differential synaptic localization of two major gamma-aminobutyric acid type A receptor alpha subunits on hippocampal pyramidal cells. *Proc. Natl. Acad. Sci.* 93, 11939–11944. doi: 10.1073/pnas.93.21.11939

Nyíri, G., Freund, T. F., and Somogyi, P. (2001). Input-dependent synaptic targeting of α2-subunit-containing GABAA receptors in synapses of hippocampal pyramidal cells of the rat. *Eur. J. Neurosci.* 13, 428–442. doi: 10.1046/j.1460-9568.2001.01407.x

Oh, W. C., Lutzu, S., Castillo, P. E., and Kwon, H.-B. (2016). De novo synaptogenesis induced by GABA in the developing mouse cortex. *Science* 353, 1037–1040. doi: 10.1126/science.aaf5206

Ohtaka-Maruyama, C. (2020). Subplate neurons as an Organizer of Mammalian Neocortical Development. *Front. Neuroan.* 14:8. doi: 10.3389/fnana.2020.00008

Okaty, B. W., Miller, M. N., Sugino, K., Hempel, C. M., and Nelson, S. B. (2009). Transcriptional and electrophysiological maturation of neocortical fast-spiking GABAergic interneurons. *J. Neurosci.* 29, 7040–7052. doi: 10.1523/JNEUROSCI.0105-09.2009

Owens, D. F., Liu, X., and Kriegstein, A. R. (1999). Changing properties of GABAA receptor–mediated signaling during early neocortical development. *J. Neurophysiol.* 82, 570–583. doi: 10.1152/jn.1999.82.2.570

Paxinos, G. (2007). *Atlas of the Developing Mouse Brain at E17.5, P0 and P6*. Amsterdam; Boston, MA: Elsevier.

Paxinos, G., and Franklin, K. B. J. (2004). *The Mouse Brain in Stereotaxic Coordinates*. San Diego, CA: Elsevier Academic Press.

Paysan, J., and Fritschy, J. M. (1998). $GABA_A$-receptor subtypes in developing brain: actors or spectators? *Perspect. Dev. Neurobiol* 5, 179–192.

Paysan, J., Kossel, A., Bolz, J., and Fritschy, J. M. (1997). Area-specific regulation of gamma-aminobutyric acid type A receptor subtypes by thalamic afferents in developing rat neocortex. *Proc. Natl. Acad. Sci. U S A* 94, 6995–7000. doi: 10.1073/pnas.94.13.6995

Peerboom, C., and Wierenga, C. J. (2021). The postnatal GABA shift: a developmental perspective. *Neurosci. Biobehav. Rev.* 124, 179–192. doi: 10.1016/j.neubiorev.2021.01.024

Peng, Z., Huang, C. S., Stell, B. M., Mody, I., and Houser, C. R. (2004). Altered expression of the delta subunit of the GABAA receptor in a mouse model of temporal lobe epilepsy. *J. Neurosci.* 24, 8629–8639. doi: 10.1523/JNEUROSCI.2877-04.2004

Picton, A. J., and Fisher, J. L. (2007). Effect of the alpha subunit subtype on the macroscopic kinetic properties of recombinant GABA(A) receptors. *Brain Res.* 1165, 40–49. doi: 10.1016/j.brainres.2007.06.050

Pirker, S., Schwarzer, C., Wieselthaler, A., Sieghart, W., and Sperk, G. (2000). $GABA_A$ receptors: immunocytochemical distribution of 13 subunits in the adult rat brain. *Neuroscience* 101, 815–850. doi: 10.1016/S0306-4522(00)00442-5

Preibisch, S., Saalfeld, S., and Tomancak, P. (2009). Globally optimal stitching of tiled 3D microscopic image acquisitions. *Bioinformatics* 25, 1463–1465. doi: 10.1093/bioinformatics/btp184

Qu, G. J., Ma, J., Yu, Y. C., and Fu, Y. (2016). Postnatal development of GABAergic interneurons in the neocortical subplate of mice. *Neuroscience* 322, 78–93. doi: 10.1016/j.neuroscience.2016.02.023

Rahmati, N., Normoyle, K. P., Glykys, J., Dzhala, V. I., Lillis, K. P., Kahle, K. T., et al. (2021). Unique actions of GABA arising from cytoplasmic chloride microdomains. *J. Neurosci.* 41, 4957–4975. doi: 10.1523/JNEUROSCI.3175-20.2021

Renzel, R., Sadek, A. R., Chang, C. H., Gray, W. P., Seifert, G., and Steinhauser, C. (2013). Polarized distribution of AMPA, but not GABAA, receptors in radial glia-like cells of the adult dentate gyrus. *Glia* 61, 1146–1154. doi: 10.1002/glia.22505

Riquelme, R., Miralles, C. P., and De Blas, A. L. (2002). Bergmann glia $GABA_A$ receptors concentrate on the glial processes that wrap inhibitory synapses. *J. Neurosci.* 22, 10720–10730. doi: 10.1523/JNEUROSCI.22-24-10720.2002

Rivera, C., Voipio, J., Payne, J. A., Ruusuvuori, E., Lahtinen, H., Lamsa, K., et al. (1999). The K+/Cl- co-transporter KCC2 renders GABA hyperpolarizing during neuronal maturation. *Nature* 397, 251–255. doi: 10.1038/16697

Rula, E. Y., Lagrange, A. H., Jacobs, M. M., Hu, N., Macdonald, R. L., and Emeson, R. B. (2008). Developmental modulation of GABA(A) receptor function by RNA editing. *J. Neurosci.* 28, 6196–6201. doi: 10.1523/JNEUROSCI.0443-08.2008

Schambra, U. B., and Schambra, U. B. (2008). *Prenatal Mouse Brain Atlas. 2nd ed*. New York: Springer. doi: 10.1007/978-0-387-47093-1

Schneider Gasser, E. M., Straub, C. J., Panzanelli, P., Weinmann, O., Sassoe-Pognetto, M., and Fritschy, J. M. (2006). Immunofluorescence in brain sections: simultaneous detection of presynaptic and postsynaptic proteins in identified neurons. *Nat. Protoc.* 1, 1887–1897. doi: 10.1038/nprot.2006.265

Scimemi, A., Semyanov, A., Sperk, G., Kullmann, D. M., and Walker, M. C. (2005). Multiple and plastic receptors mediate tonic $GABA_A$ receptor currents in the hippocampus. *J. Neurosci.* 25:10016. doi: 10.1523/JNEUROSCI.2520-05.2005

Sebe, J. Y., Looke-Stewart, E. C., Estrada, R. C., and Baraban, S. C. (2010). Robust tonic GABA currents can inhibit cell firing in mouse newborn neocortical pyramidal cells. *Eur. J. Neurosci.* 32, 1310–1318. doi: 10.1111/j.1460-9568.2010.07373.x

Sedmak, G., Jovanov-Milosevic, N., Puskarjov, M., Ulamec, M., Kruslin, B., Kaila, K., et al. (2016). Developmental expression patterns of KCC2 and functionally associated molecules in the human brain. *Cereb Cortex* 26, 4574–4589. doi: 10.1093/cercor/bhv218

Serwanski, D. R., Miralles, C. P., Christie, S. B., Mehta, A. K., Li, X., and De Blas, A. L. (2006). Synaptic and nonsynaptic localization of GABAA receptors containing the alpha5 subunit in the rat brain. *J. Compar. Neurol.* 499, 458–470. doi: 10.1002/cne.21115

Sinha, R., Grimes, W. N., Wallin, J., Ebbinghaus, B. N., Luu, K., Cherry, T., et al. (2021). Transient expression of a GABA receptor subunit during early development is critical for inhibitory synapse maturation and function. *Curr. Biol.* 31:4314. doi: 10.1016/j.cub.2021.07.059

Stefanits, H., Milenkovic, I., Mahr, N., Pataraia, E., Hainfellner, J. A., Kovacs, G. G., et al. (2018). GABA(A) receptor subunits in the human amygdala and hippocampus: immunohistochemical distribution of 7 subunits. *J. Comp. Neurol.* 526, 324–348. doi: 10.1002/cne.24337

Stein, V., Hermans-Borgmeyer, I., Jentsch, T. J., and Hubner, C. A. (2004). Expression of the KCl cotransporter KCC2 parallels neuronal maturation and the emergence of low intracellular chloride. *J. Comp. Neurol.* 468, 57–64. doi: 10.1002/cne.10983

Sun, C., Zhu, H., Clark, S., and Gouaux, E. (2023). Cryo-EM structures reveal native GABA(A) receptor assemblies and pharmacology. *Nature* 622, 195–201. doi: 10.1038/s41586-023-06556-w

Takayama, C., and Inoue, Y. (2010). Developmental localization of potassium chloride co-transporter 2 (KCC2), GABA and vesicular GABA transporter (VGAT) in the postnatal mouse somatosensory cortex. *Neurosci. Res.* 67, 137–148. doi: 10.1016/j.neures.2010.02.010

Tonon, M. C., Vaudry, H., Chuquet, J., Guillebaud, F., Fan, J., Masmoudi-Kouki, O., et al. (2020). Endozepines and their receptors: structure, functions and pathophysiological significance. *Pharmacol. Ther.* 208:107386. doi: 10.1016/j.pharmthera.2019.06.008

Torres-Reveron, J., and Friedlander, M. J. (2007). Properties of persistent postnatal cortical subplate neurons. *J. Neurosci.* 27, 9962–9974. doi: 10.1523/JNEUROSCI.1536-07.2007

Unichenko, P., Kirischuk, S., and Luhmann, H. J. (2015). GABA transporters control GABAergic neurotransmission in the mouse subplate. *Neuroscience* 304, 217–227. doi: 10.1016/j.neuroscience.2015.07.067

Uvarov, P., Ludwig, A., Markkanen, M., Pruunsild, P., Kaila, K., Delpire, E., et al. (2007). A novel N-terminal isoform of the neuron-specific K-Cl cotransporter KCC2. *J. Biol. Chem.* 282, 30570–30576. doi: 10.1074/jbc.M705095200

Uvarov, P., Ludwig, A., Markkanen, M., Soni, S., Hübner, C. A., Rivera, C., et al. (2009). Coexpression and heteromerization of two neuronal K-Cl cotransporter isoforms in neonatal brain. *J. Biol. Chem.* 284, 13696–13704. doi: 10.1074/jbc.M807366200

Vanhatalo, S., Palva, J. M., Andersson, S., Rivera, C., Voipio, J., and Kaila, K. (2005). Slow endogenous activity transients and developmental expression of K+-Cl- cotransporter 2 in the immature human cortex. *Eur. J. Neurosci.* 22, 2799–2804. doi: 10.1111/j.1460-9568.2005.04459.x

Virtanen, M. A., Uvarov, P., Hübner, C. A., and Kaila, K. (2020). NKCC1, an elusive molecular target in brain development: making sense of the existing data. *Cells* 9:2607. doi: 10.3390/cells9122607

Virtanen, M. A., Uvarov, P., Mavrovic, M., Poncer, J. C., and Kaila, K. (2021). The multifaceted roles of KCC2 in cortical development. *Trends Neurosci.* 44, 378–392. doi: 10.1016/j.tins.2021.01.004

Viswanathan, S., Sheikh, A., Looger, L. L., and Kanold, P. O. (2016). Molecularly defined subplate neurons project both to thalamocortical recipient layers and thalamus. *Cerebr. Cortex* 27, 4759–4768. doi: 10.1093/cercor/bhw271

Wang, D. D., and Kriegstein, A. R. (2008). GABA regulates excitatory synapse formation in the neocortex via NMDA receptor activation. *J. Neurosci.* 28, 5547–5558. doi: 10.1523/JNEUROSCI.5599-07.2008

Wang, D. D., and Kriegstein, A. R. (2011). Blocking early GABA depolarization with bumetanide results in permanent alterations in cortical circuits and sensorimotor gating deficits. *Cerebr. Cortex* 21, 574–587. doi: 10.1093/cercor/bhq124

Wang, L. P., Kempermann, G., and Kettenmann, H. (2005). A subpopulation of precursor cells in the mouse dentate gyrus receives synaptic GABAergic input. *Mol. Cell Neurosci.* 29, 181–189. doi: 10.1016/j.mcn.2005.02.002

Warm, D., Schroer, J., and Sinning, A. (2022). Gabaergic interneurons in early brain development: conducting and orchestrated by cortical network activity. *Front. Molec. Neurosci.* 14:807969. doi: 10.3389/fnmol.2021.807969

Yamada, J., Furukawa, T., Ueno, S., Yamamoto, S., and Fukuda, A. (2007). Molecular basis for the GABAA receptor-mediated tonic inhibition in rat somatosensory cortex. *Cereb. Cortex* 17, 1782–1787. doi: 10.1093/cercor/bhl087

Yang, J.-M. M., Zhang, J., Yu, Y.-Q. Q., Duan, S., and Li, X.-M. M. (2014). Postnatal development of 2 microcircuits involving fast-spiking interneurons in the mouse prefrontal cortex. *Cereb. Cortex* 24, 98–109. doi: 10.1093/cercor/bhs291

Zavalin, K., Hassan, A., Fu, C., Delpire, E., and Lagrange, A. H. (2022). Loss of KCC2 in GABAergic neurons causes seizures and an imbalance of cortical interneurons. *Front. Molec. Neurosci.* 15:826427. doi: 10.3389/fnmol.2022.826427

Zeller, A., Arras, M., Jurd, R., and Rudolph, U. (2007). Mapping the contribution of β3-containing GABAA receptors to volatile and intravenous general anesthetic actions. *BMC Pharmacol.* 7:2. doi: 10.1186/1471-2210-7-2

frontiers | Frontiers in Cellular Neuroscience

TYPE Original Research
PUBLISHED 18 July 2024
DOI 10.3389/fncel.2024.1423471

OPEN ACCESS

EDITED BY
Goichi Miyoshi,
Gunma University, Japan

REVIEWED BY
Katsuhiko Tabuchi,
Shinshu University, Japan
Dongqing Shi,
University of Michigan, United States

*CORRESPONDENCE
Jasmina N. Jovanovic
✉ j.jovanovic@ucl.ac.uk

RECEIVED 25 April 2024
ACCEPTED 02 July 2024
PUBLISHED 18 July 2024

CITATION
Sui Y, Mortensen M, Yuan B, Nicholson MW, Smart TG and Jovanovic JN (2024) $GABA_A$ receptors and neuroligin 2 synergize to promote synaptic adhesion and inhibitory synaptogenesis.
Front. Cell. Neurosci. 18:1423471.
doi: 10.3389/fncel.2024.1423471

$GABA_A$ receptors and neuroligin 2 synergize to promote synaptic adhesion and inhibitory synaptogenesis

Yusheng Sui[1], Martin Mortensen[2], Banghao Yuan[1], Martin W. Nicholson[1], Trevor G. Smart[2] and Jasmina N. Jovanovic[1]*

[1]Department of Pharmacology, School of Pharmacy, University College London, London, United Kingdom, [2]Department of Neuroscience, Physiology and Pharmacology, Division of Biosciences, University College London, London, United Kingdom

$GABA_A$ receptors (γ-aminobutyric acid-gated receptors type A; $GABA_A$Rs), the major structural and functional postsynaptic components of inhibitory synapses in the mammalian brain, belong to a family of GABA-gated Cl^-/HCO_3^- ion channels. They are assembled as heteropentamers from a family of subunits including: α (1–6), β(1–3), γ(1–3), δ, ε, π, θ and ρ(1–3). $GABA_A$Rs together with the postsynaptic adhesion protein Neuroligin 2 (NL2) and many other pre- and post-synaptic proteins guide the initiation and functional maturation of inhibitory GABAergic synapses. This study examined how $GABA_A$Rs and NL2 interact with each other to initiate the formation of synapses. Two functionally distinct $GABA_A$R subtypes, the synaptic type α2β2γ2-$GABA_A$Rs versus extrasynaptic type α4β3δ-$GABA_A$Rs were expressed in HEK293 cells alone or together with NL2 and co-cultured with striatal GABAergic medium spiny neurons to enable innervation of HEK293 cells by GABAergic axons. When expressed alone, only the synaptic α2β2γ2-$GABA_A$Rs induced innervation of HEK293 cells. However, when $GABA_A$Rs were co-expressed with NL2, the effect on synapse formation exceeded the individual effects of these proteins indicating a synergistic interaction, with α2β2γ2-$GABA_A$R/NL2 showing a significantly greater synaptogenic activity than α4β3δ-$GABA_A$R/NL2 or NL2 alone. To investigate the molecular basis of this interaction, different combinations of $GABA_A$R subunits and NL2 were co-expressed, and the degree of innervation and synaptic activity assessed, revealing a key role of the γ2 subunit. In biochemical assays, the interaction between NL2 and α2β2γ2-$GABA_A$R was established and mapped to the large intracellular domain of the γ2 subunit.

KEYWORDS

inhibition, GABAergic synapse, synaptic, extrasynaptic, stable cell lines, medium spiny neurons, immunocytochemistry, protein domains

1 Introduction

$GABA_A$ receptors are the essential structural and functional postsynaptic components of inhibitory synapses in the mammalian brain. They belong to a diverse family of GABA-gated Cl^-/HCO_3^- permeable ion channels that promote neuronal differentiation and synaptogenesis in the developing brain by increasing neuronal excitability (Owens and Kriegstein, 2002;

Raimondo et al., 2017; Cherubini and Ben-Ari, 2023). In contrast, in the adult brain, $GABA_A$Rs mediate inhibitory neurotransmission by decreasing neuronal excitability in a process that is fundamental to normal brain function and information processing (Schofield et al., 1987; Olsen and Sieghart, 2009; Smart and Stephenson, 2019; Sallard et al., 2021).

$GABA_A$Rs are hetero-pentameric assemblies of subunits selected from: α (1–6), β (1–3), γ (1–3), δ, ε, π, θ and ρ(1–3), in which two α, two β and one γ subunit are required for the formation of fully functional synaptic receptors (Olsen and Sieghart, 2009; Chua and Chebib, 2017; Scott and Aricescu, 2019). The subtypes of $GABA_A$Rs which incorporate α1-3 and 5, β2-3 and γ2 subunits are spatially, functionally, and pharmacologically distinct from those containing the α4, 6, β2-3 and δ subunits (Farrant and Nusser, 2005; Smart and Mortensen, 2023). The presence of the γ2 subunit is obligatory for synaptic $GABA_A$Rs because it governs their localization and clustering at the postsynaptic membrane, allowing for the rapid and robust neurotransmission in all GABAergic synapses (Olsen and Sieghart, 2009; Lorenz-Guertin et al., 2018). However, the γ2-containing $GABA_A$Rs translocate in and out of synapses as part of their lifecycle. Thus, they are not solely a synaptic feature, but do also transit through the extrasynaptic space (Thomas et al., 2005; Hannan et al., 2020). In contrast, the subtypes of $GABA_A$Rs lacking the γ2 subunit (αβ isoforms), or those incorporating the δ subunit are predominantly located outside of synapses where they can be activated by low levels of ambient GABA to mediate tonic inhibition (Farrant and Nusser, 2005; Smart and Mortensen, 2023). While the incorporation of the β subunit is required for the expression of $GABA_A$Rs at the neuronal cell surface (Connolly et al., 1996a,b; Nguyen and Nicoll, 2018), some α subunits are selectively assembled at specific inhibitory synapses where they support the formation and function of neuronal circuits involved in specific brain physiology, such as anxiety, sedation, arousal, and others (Klausberger et al., 2002; Rudolph and Mohler, 2006; Thomson and Jovanovic, 2010).

How, where, and when inhibitory synapses are formed is tightly regulated during brain development by genetic and environmental factors and guided by specialized protein–protein interactions leading to the formation of transsynaptic complexes between the pre-and postsynaptic elements. Multiple proteins have been shown to participate in the initiation and functional maturation of inhibitory synapses, including the postsynaptic adhesion protein NL2 together with its presynaptic partners α and β neurexins (Sudhof, 2017; Sudhof, 2018; Ali et al., 2020), as well as other synaptic partners, such as SLITRK3, β-dystroglycan, IgSF9b, GARLH4/LHFPL4 (Connor and Siddiqui, 2023). $GABA_A$Rs themselves participate in inhibitory synaptogenesis as structural (Fuchs et al., 2013; Brown et al., 2014, 2016; Duan et al., 2019) and signaling (Pallotto and Deprez, 2014; Arama et al., 2015; Cherubini and Ben-Ari, 2023) components and contribute to the functional specialization of synapses via the incorporation of specific receptor subtypes with distinct physiological properties (Thomson and Jovanovic, 2010; Fritschy et al., 2012; Fritschy and Panzanelli, 2014).

Constitutive and inducible gene knockout studies of individual proteins involved in synapse formation in mice, including NL2, have revealed subtle deficits in inhibitory synapses, without causing a global impairment of GABAergic synaptogenesis (Fritschy et al., 2012; Sudhof, 2018). This suggests that the process of synapse initiation and functional maturation relies on multiple protein complexes and, importantly, their specific interactions which incrementally and cooperatively contribute to this process. While molecular details of these interactions remain largely unknown, their importance has been demonstrated in the developing hippocampus where cooperative interaction between NL2 and SLITRK3 is required for the formation and functional maturation of inhibitory synapses (Li et al., 2017).

Our initial studies have demonstrated a cooperative interaction between $GABA_A$Rs and NL2 in promoting the formation and strengthening of synaptic connections in a co-culture model in which HEK293 cells expressing $GABA_A$Rs and NL2 were cultured together with GABAergic medium spiny neurons (Fuchs et al., 2013). Here, we have explored this cooperativity further to uncover the molecular details of the $GABA_A$R/NL2 interaction. Our experiments demonstrate that the prototypical synaptic α2β2γ2-$GABA_A$Rs have a significantly greater effect in facilitating the NL2-dependent induction of synapses than the prototypical extrasynaptic α4β3δ-$GABA_A$Rs. Furthermore, we demonstrate that the synergism between $GABA_A$Rs and NL2 is mediated by the γ2 subunit interaction with NL2, and we map this interaction to the intracellular domain of this subunit.

2 Materials and methods

2.1 Cell lines, primary neuronal cultures and co-cultures

Human embryonic kidney cells (ATCC) were maintained using Dulbecco's Minimum Essential Medium (DMEM; Thermo Fischer) supplemented with 10% v/v fetal bovine serum (FBS; 10082–147, Thermo Fischer), 10 mM L-Glutamine (25030–024, Thermo Fischer), 50 units/mL penicillin and 50 µg/mL streptomycin (15140–148, Thermo Fischer). HEK293 cell lines stably expressing $GABA_A$Rs were kept in complete DMEM with the addition of 800 µg/mL Geneticin G418 sulfate (11811023, Thermo Fischer), 800 µg/mL Zeocin (R25001, Gibco), and 800 µg/mL hygromycin B (10687010, Invitrogen) for selection of α2 and α4 subunits, β2 and β3 subunits, and γ2 and δ subunits, respectively. The α2β2γ2-$GABA_A$R stable cell line was described previously (Brown et al., 2014) and in Supplementary Figure S1.

The GABAergic medium spiny neuron cultures were prepared from the striatum of ~ day E17 embryonic Sprague–Dawley rats (UCL-BSU) housed and sacrificed according to United Kingdom Home Office guidelines as previously described (Brown et al., 2014). Briefly, brains were dissected in sterile Ca^{2+} and Mg^{2+} – free HEPES-buffered saline solution (HBSS; 14180–046, Thermo Fischer) to obtain striata. Neurons were dissociated using fire-polished Pasteur glass pipettes, counted using a hemocytometer, and plated onto poly-D-lysine (0.1 mg/mL, P1149-10MG, Sigma Aldrich) coated tissue culture dishes (Z707686, TPP) for biochemical experiments, or poly-L-lysine (0.1 mg/mL, P6282-5MG, Sigma Aldrich) coated 13 mm glass coverslips (631-0148P, VWR) for immunolabeling and electrophysiology. Neuronal cultures and co-cultures with HEK293 cells were maintained in Neurobasal medium (21103–049, Gibco) containing B27 supplement (17504–044, Gibco), glutamine (2 mM, 25030–024, Gibco), penicillin (50 units/mL, 15070–63, Gibco), streptomycin (50 g/mL, 15070–063, Gibco), and glucose (6 mM, G8769, Sigma).

In order to generate a HEK293 neuronal co-culture, adherent HEK293 cells (control or stably expressing $GABA_A$Rs) were first transfected with the cDNA of proteins of interest using Effectene (301425, Qiagen), and 24 h later these cells were transferred to the medium spiny neuron culture for a further 24–48 h of incubation. as described previously (Brown et al., 2014).

2.2 Construction of HEK293 cell line stably expressing α4β3δ-$GABA_A$Rs

$GABA_A$R α4, β3 and δ cDNAs were cloned into pcDNA3-G418 (Invitrogen), pcDNA3.1-zeocin (Invitrogen) and pcDNA3.1-hygromycin (Invitrogen), respectively, for antibiotic-selective expression. Lipofectamine LTX (15338–030, Invitrogen) was used for the two-stage stable transfection. For the first stage, α4 and β3 cDNAs were transfected into HEK293 cells followed by G418 and zeocin antibiotic selection. For the second stage, the HEK293 cell line clone expressing both subunits was transfected with δ cDNA followed by G418, zeocin, and hygromycin antibiotic selection. Stable expression of the subunits was confirmed by immunoblotting and immunolabeling using subunit-specific antibodies and their functional properties were assessed using whole-cell recordings (Supplementary Figure S2).

2.3 Cell surface ELISA

HEK293 cells stably expressing $GABA_A$Rs were transfected with HA-tagged NL2 cDNA (Poulopoulos et al., 2009) using Effectene (301,425, Qiagen), and incubated in 24-well plates coated with 0.1 mg/mL poly-D-lysine (P1149, Sigma Aldrich) in the 37°C 5% CO2 humidified incubator for 24 h. The cells were fixed with 4% paraformaldehyde (PFA)/4% sucrose w/v in PBS for 10 min at room temperature and subsequently washed with PBS and HBSS (14185–052, Gibco). Cells were blocked in 1% bovine serum albumin (BSA, BP9704-100, Fisher Scientific) in HBSS for 30 min at room temperature and subsequently incubated with anti-HA tag primary antibody (1,10,000 in blocking solution, ab184643, Abcam) for 2 h at room temperature or overnight at 4°C. For assessing the total expression of proteins, cells were permeabilized with 0.5% Triton X-100 (A16046, Alfa-Aesar) in HBSS for 10 min at room temperature before the blocking step. After incubation, cells were washed, blocked in 1% BSA in HBSS for 30 min at room temperature, and incubated with the secondary antibody conjugated to horseradish peroxide (HRP) (31,460, Thermo Fisher) in 1% BSA/ HBSS (1,2,500) for 1 h at room temperature. The cells were washed with HBSS and the HRP activity was detected using tetramethylbenzidine reagent (TMB, 34028, Thermo Scientific). The oxidation of TMB produced blue color, the absorbance of which was measured at 650 nm by DU800 spectrophotometer (Beckman Coulter).

2.4 Immunocytochemistry

The cells plated on 13 mm coverslips coated with poly-L-lysine were briefly washed with PBS and fixed with 4% PFA/4% sucrose in PBS for 10 min at room temperature. For assessing the activity of the presynaptic terminals, Cy5-labeled anti-synaptotagmin 1 luminal domain-specific antibody (1,50, 105311C5, Synaptic Systems) was added to the culture and incubated in the 37°C 5% CO2 humidified incubator for 30 min before fixation. The PFA was aspirated, and the cells were washed thoroughly with PBS. The residual aldehyde groups of PFA were blocked with 0.3 M glycine in PBS for 10 min at room temperature, followed by multiple washes with PBS. The cells were blocked in 1% BSA in PBS for 30 min at room temperature. The primary antibodies: anti-VGAT (1,500, 131,003, Synaptic Systems), anti-$GABA_A$R α2 subunit (1,500, 224,103, Synaptic Systems), anti-$GABA_A$R α4 subunit (1,200, Hörtnagl et al., 2013), anti-$GABA_A$R β2/3 subunit (1,500, MAB341, Sigma Aldrich), anti-$GABA_A$R γ2 subunit (1,2,500, Fritschy and Mohler, 1995), anti-$GABA_A$R δ subunit (1,200, 868-GDN, PhosphoSolutions), and anti-Bassoon (1,500, MA1-20689, Thermo Fischer) were diluted in 1% BSA in PBS, added to the cells, and incubated for 2 h at room temperature or overnight at 4°C. After incubation, the cells were rinsed twice and washed multiple times with PBS. For labeling of intracellular proteins, the cells were permeabilized with 0.5% Triton-X-100 in PBS for 10 min at room temperature prior to the addition of the primary antibody mix. The cells were washed and blocked again with 1% BSA in PBS for 30 min at room temperature. Fluorescently-labeled secondary antibodies (AlexaFluor, Invitrogen) were diluted in 1% BSA in PBS (1,750) and added to the cells for 1 h at room temperature protected from light. The coverslips were washed with PBS and mounted on glass slides with ProLong Gold antifade reagent (P36930, Invitrogen). The slides were dried at room temperature protected from light and kept at 4°C in boxes.

2.5 Confocal imaging and analysis

The coverslips were imaged using a Zeiss confocal microscope LSM 700, 710, or 880 with 63× oil immersion objective and analyzed using ImageJ (National Institute of Health) as described previously (Brown et al., 2016). Images were acquired at 12-bit depth from 10 to 15 cells from each co-culture. For each image, a series of z-stack images were acquired from the bottom to the top of HEK293 cells with optimal intervals of 0.7 µm. ImageJ software was utilized for the analysis of contacts formed between presynaptic GABAergic terminals of cultured neurons and HEK293 cells. The co-localization was obtained by the *Process → Image Calculator* function using the option *and* which produced an image showing all the pixels that appeared in both channels. The threshold of the image was adjusted by the *Auto-Threshold* function. The data for co-localization were obtained by the *Analyze → Analyze Particles* function. For quantitative assessment of synaptic contacts formed between presynaptic GABAergic terminals and HEK293 cells, the *% area* was selected because this parameter represents the surface area of each HEK293 cell with co-localized pixels normalized to the total surface area of the cell, which therefore accounts for the difference in size of individual HEK293 cells. These parameters were imported into Origin Pro software for statistical analysis and graphical presentation of the data. The data were plotted with Box-and-Whisker plots showing the median, standard deviation, and outliers. The normal (Gaussian) distribution of the data was first tested using the Shapiro–Wilk normality test. Non-normally distributed data were subjected to non-parametric Mann–Whitney test or Kruskal Wallis ANOVA followed by Dunn's test for multiple

comparisons. Normally distributed data were analyzed using a two-tailed Student's t-test to determine the statistical significance.

2.6 Super-resolution imaging and analysis

The samples were prepared in the same way as for the confocal imaging. The $GABA_A$Rs were labeled with α2 (1,500, 224,103, Synaptic Systems) or α4 (1,200, Hörtnagl et al., 2013) subunit-specific antibodies, respectively. The synaptic contacts were labeled with presynaptic active zone marker Bassoon-specific antibody (MA1-20689, Thermo Fischer). Images were acquired using ELYRA PS.1 SIM (Carl Zeiss) at 63x oil lens following chromatic shift correction by recording fluorescent beads. A 4 µm z-stack with 0.110 µm intervals of the samples was acquired to keep the z-range in focus. The images were then processed by the Structured Illumination and Channel Alignment function in Zen 2012 Software. The images were deconvolved and analyzed using SVI Huygens Professional software. After deconvolution, the background was eliminated using the Costes Optimized method (Coastes et al., 2004). The z-stack images were rendered to 3-dimensional images for colocalization analysis and Manders coefficients were calculated to show the level of overlapping signals, with M1 indicating the proportion of Bassoon overlapping with $GABA_A$Rs and M2 indicating the proportion of $GABA_A$Rs overlapping with Bassoon.

2.7 Immunoblotting

Cultured cells were lysed with 2% SDS and the protein concentration determined using the BCA assay (Thermo Fisher Scientifics). Proteins were separated on 10% SDS-poly-acrylamide separation gels and transferred onto a solid nitrocellulose membrane (Whatman). For the detection of proteins, the following primary antibodies were used: anti-HA tag (1,1,000, ab184643, Abcam), anti-$GABA_A$R α1 subunit (1,500, Duggan and Stephenson, 1990), anti $GABA_A$R β3 subunit (1:200, UCL 74, (Tretter et al., 1997)), anti-$GABA_A$R δ subunit (1,200, 868-GDN, PhosphoSolutions) and anti NL2 (1,800, 129,203, Synaptic Systems). Anti-alkaline phosphatase-conjugated secondary antibodies: anti-rabbit (1,1,000, A16099, Invitrogen) and anti-mouse (1,200, 31,450, Invitrogen) were used for visualization of the protein bands.

2.8 Co-immunoprecipitation

Protein lysates were obtained from adult male rat cortex or HEK293 cells expressing $GABA_A$Rs/NL2 via homogenization in lysis buffer (20 mM HEPES pH 7.4, 100 mM NaCl, 1% Triton X-100, 2 mM $CaCl_2$, 1 mM $MgCl_2$), containing phenylmethylsulfonyl fluoride (PMSF;10 µM), leupeptin, chymostatin, pepstatin (5 µg/mL each, Peptide Institute). The concentration of the protein lysates was determined by Bradford assay (Bio-Rad). The input (1 mg total protein) was incubated with 10 µg of $GABA_A$R α1 or α2 subunit-specific antibodies (Duggan and Stephenson, 1990), or anti-HA tag (ab184643, Abcam) or anti-c-myc antibody (2 µg/mL, 05–724, Millipore) or non-immune control antibodies (31,243, Invitrogen, from the same species as the specific antibody) followed by 1% BSA coated Protein-G-Sepharose beads (50 µL, NB-45-00037-5, Generon). The beads were pulled down by centrifugation after extensive washing and denatured with Laemmli SB (62.5 mM Tris, pH 8.0, 2% SDS, 10% glycerol, 0.0025% Bromophenol Blue, 100 mM DTT) for SDS/PAGE and immunoblotting.

2.9 Electrophysiology

Coverslips with cells (transfected HEK293, stable HEK293 cell lines, neurons or HEK293/neuron co-cultures) were transferred into a recording chamber on a Nikon Eclipse FN1 microscope, where cells were continuously perfused with Krebs solution containing (mM): 140 NaCl, 4.7 KCl, 1.2 $MgCl_2$, 2.52 $CaCl_2$, 11 Glucose and 5 HEPES (pH 7.4). Patch pipettes (thin-walled filamented borosilicate glass capillaries; TW150F-4; WPI, United States; 3–4 MΩ) were filled with an intracellular solution containing (mM): 140 CsCl, 2 NaCl, 2 $MgCl_2$, 5 EGTA, 10 HEPES, 0.5 $CaCl_2$, 2 Na-ATP and 0.5 Na-GTP (pH 7.2). To record functional current $GABA_A$R responses, drugs were applied to cells using a Y-tube delivery system (Mortensen and Smart, 2007).

HEK293 cells were voltage-clamped at −40 mV using an Axopatch 200B amplifier (Molecular Devices, United States), and whole-cell currents (IPSCs or drug-activated) were filtered at 5 kHz (−36 dB), digitized at 50 kHz via a Digidata 1322A (Molecular Devices), and recorded to a Dell Optiplex 990 using Clampex 10.2 (Molecular Devices). Series resistance was compensated at 70%, and only data with less than 20% deviation in series resistance was included in subsequent analyses.

3 Results

3.1 Synergistic interaction between $GABA_A$Rs and NL2 in synapse formation

We have demonstrated previously that stable expression of synaptic α1β2γ2-$GABA_A$Rs in HEK293 cells promotes the adhesion of GABAergic axons and the formation of functional synapses when these cells are co-cultured with the GABAergic medium spiny neurons (Fuchs et al., 2013; Brown et al., 2014, 2016). When $GABA_A$Rs were co-expressed with NL2 in this system, the effect on synapse formation exceeded the individual effects of these two proteins both in the number and transmission efficacy of the synapses ascertained by electrophysiological recordings (Fuchs et al., 2013). To investigate the degree of HEK293 cell innervation induced by another synaptic $GABA_A$R type and possible synergistic interaction with NL2, in the current study, we have expressed and functionally characterized the HEK293 stable cell line expressing the α2β2γ2-$GABA_A$R (Supplementary Figures S1A,B; Brown et al., 2014). These cells were fluorescently labeled by transiently expressing the green fluorescent protein (GFP) and co-cultured with GABAergic medium spiny neurons (Figure 1A). The control HEK293 cells were also labeled with GFP. The cells were fixed and immunolabeled with a VGAT-specific antibody to detect GABAergic terminals forming contacts with HEK293 cells using confocal microscopy. Synaptic contacts were defined based on signal colocalization between the VGAT and GFP (green and blue channels in Figure 1A) and analyzed using Image J as described in the Methods and previously (Brown et al., 2014).

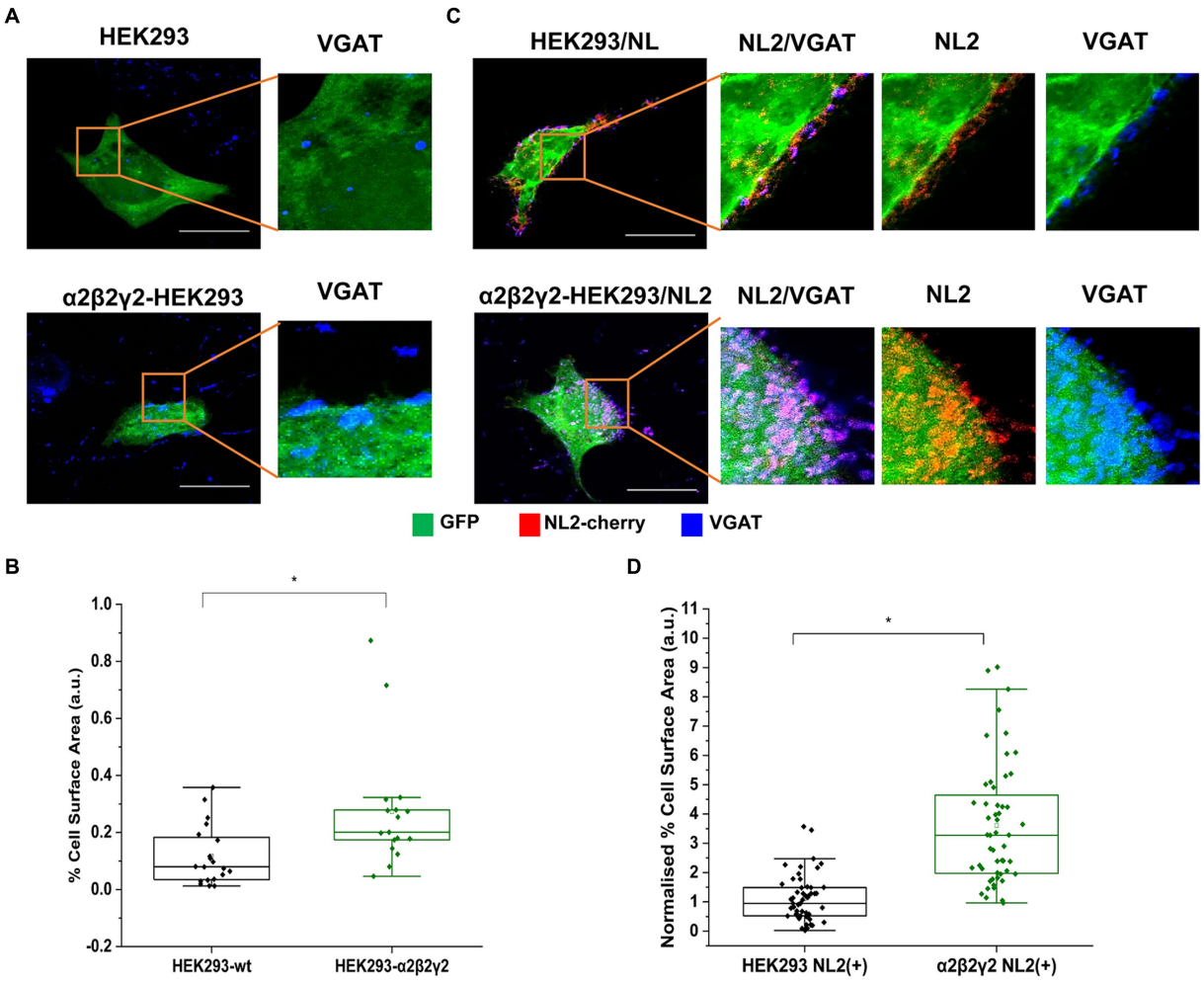

FIGURE 1
α2β2γ2-GABA$_A$Rs induce synaptic contact formation and potentiate the induction of contacts by NL-2. Synaptic contact formation in co-culture of embryonic medium spiny neurons and **(A)** HEK293 (wt; upper panels) or α2β2γ2-GABA$_A$R-expressing HEK293 cells (lower panels), or **(C)** HEK293/NL2 cells (wt; upper panels) or α2β2γ2-GABA$_A$R/NL2-expressing cells (lower panels). The HEK293 cell body was visualized by GFP (green), GABAergic terminals were labeled with an anti-VGAT antibody (blue) and NL2 was mcherry-tagged (red). Scale bar = 20 μm. Fluorescent imaging was done using Zeiss 700 confocal microscope at 63 × magnification with image size 1,024 × 1,024. Max intensity projection of the z-stack images was shown. The enlarged images are 10 × zoom in. Quantitative analysis of synapses expressed as % area of co-localized pixels that represent contacts between VGAT terminals and in **(B)** HEK293 or α2β2γ2-GABA$_A$R-expressing cells (n = 21 and n = 18, respectively; N = 2 independent experiments, p = 0.002), or **(D)** HEK293/NL2 cells or α2β2γ2-GABA$_A$R/NL2 expressing cells (n = 53 and n = 52 cells, respectively; N = 3 independent experiments, $p < 0.00001$ (4.7×10^{-13})). The box and whisker plot show the mean (square dot with no fill), median (horizontal line), and standard deviation (whiskers). Shapiro–Wilk normality test was used to test the normal distribution of the data and Mann–Whitney test was used to analyze statistical significance of the difference (*$p < 0.05$).

Quantification of the % area of co-localized pixels that represent contacts between VGAT terminals and HEK293 cells revealed a significant increase in synaptic contact formation in the presence of α2β2γ2-GABA$_A$Rs in comparison with the control HEK293 cell line (median = 0.20%; IQR = 0.16 - 0.30%; n = 17 cells vs. median = 0.08%; IQR = 0.03 - 0.21%; n = 21 cells, respectively; from N = 2 independent experiments, p = 0.002, Figure 1B).

To investigate how the co-expression of GABA$_A$Rs and NL2 in HEK293 cells may regulate the formation of synaptic contacts, HEK293 cells stably expressing α2β2γ2-GABA$_A$Rs or the control HEK293 cells were transfected with GFP and cherry-tagged NL2 cDNAs, and co-cultured with the medium spiny neurons (Figure 1C). Expression of NL2 in control HEK293 cells induced synaptic contact formation in agreement with the published literature [median = 0.95%; IQR = 0.52 - 1.49%; n = 53 cells from N = 3 independent experiments; $p < 0.00001$ ($p = 3.5 \times 10^{-9}$)]; (Scheiffele et al., 2000) but when NL2 was expressed in the α2β2γ2-GABA$_A$R stable cell line, the formation of contacts was significantly greater [median = 3.28%; IQR = 1.96 - 4.78%; n = 52 cells from N = 3 independent experiments; $p = < 0.00001$ ($p = 4.7 \times 10^{-13}$); Figure 1D]. In this analysis, the value of the % area of co-localized pixels for each HEK293 cell was divided by the fluorescence value of NL2 measured in the same cell because of the high degree of variation in expression of NL2 following transient transfection. These results support the previously described (Fuchs et al., 2013) strong synergistic interaction between GABA$_A$Rs and NL2 during the formation of synaptic contacts.

The α4β3δ-GABA$_A$Rs are generally localized outside of GABAergic synapses and they mediate tonic inhibition (Farrant and

10.3389/fncel.2024.1423471

Nusser, 2005). These receptors were also expressed in HEK293 cells to create a stable cell line which was characterized using immunolabeling and voltage-clamp electrophysiology. The ubiquitous expression of all three subunits at the cell surface was confirmed by confocal imaging (Supplementary Figures S2A,B). Pharmacological responses of these receptors to GABA and the modulator DS2 (αβδ specific) in whole-cell recordings indicated that the receptors expressing the δ subunit were functional (Supplementary Figures S2C,D). To test whether these receptors can induce the adhesion of GABAergic terminals, the HEK293 cell line or control HEK293 cells were transiently transfected with GFP and co-cultured with the medium spiny neurons (Figure 2A). Quantification of the % area of co-localized pixels which represents contacts between VGAT terminals and HEK293 cells demonstrated no significant difference between the control and α4β3δ-GABA$_A$R HEK293 cells (median = 0.28%; IQR = 0.04–0.42%; $n = 19$ cells vs. median = 0.35%; IQR = 0.23–0.45%; $n = 17$ cells, respectively; from $N = 2$ independent experiments, $p = 0.2$, Figure 2B). These results indicate that α4β3δ-GABA$_A$Rs do not promote the formation of inhibitory synapses in these cultures, indicating that this activity is a characteristic of the synaptic GABA$_A$R subtypes (Brown et al., 2016). However, when α4β3δ-GABA$_A$R-HEK293 cells or control HEK293 cells were transiently transfected with GFP and cherry-tagged NL2 cDNAs and co-cultured with the medium spiny neurons (Figure 2C), we detected a significant increase in contacts induced by NL2 in the presence of α4β3δ-GABA$_A$Rs (median = 1.81%; IQR = 1.25 - 3.02%; $n = 52$ cells versus the no α4β3δ expressing control median = 0.95%; IQR = 0.52 - 1.49%; $n = 53$ cells, respectively; from N = 3 independent experiments; $p < 0.00001$ ($p = 8.4 \times 10^{-7}$); Figure 2D). The value of the % area of co-localized pixels for each cell was normalized to the expression of NL2 as described above. These

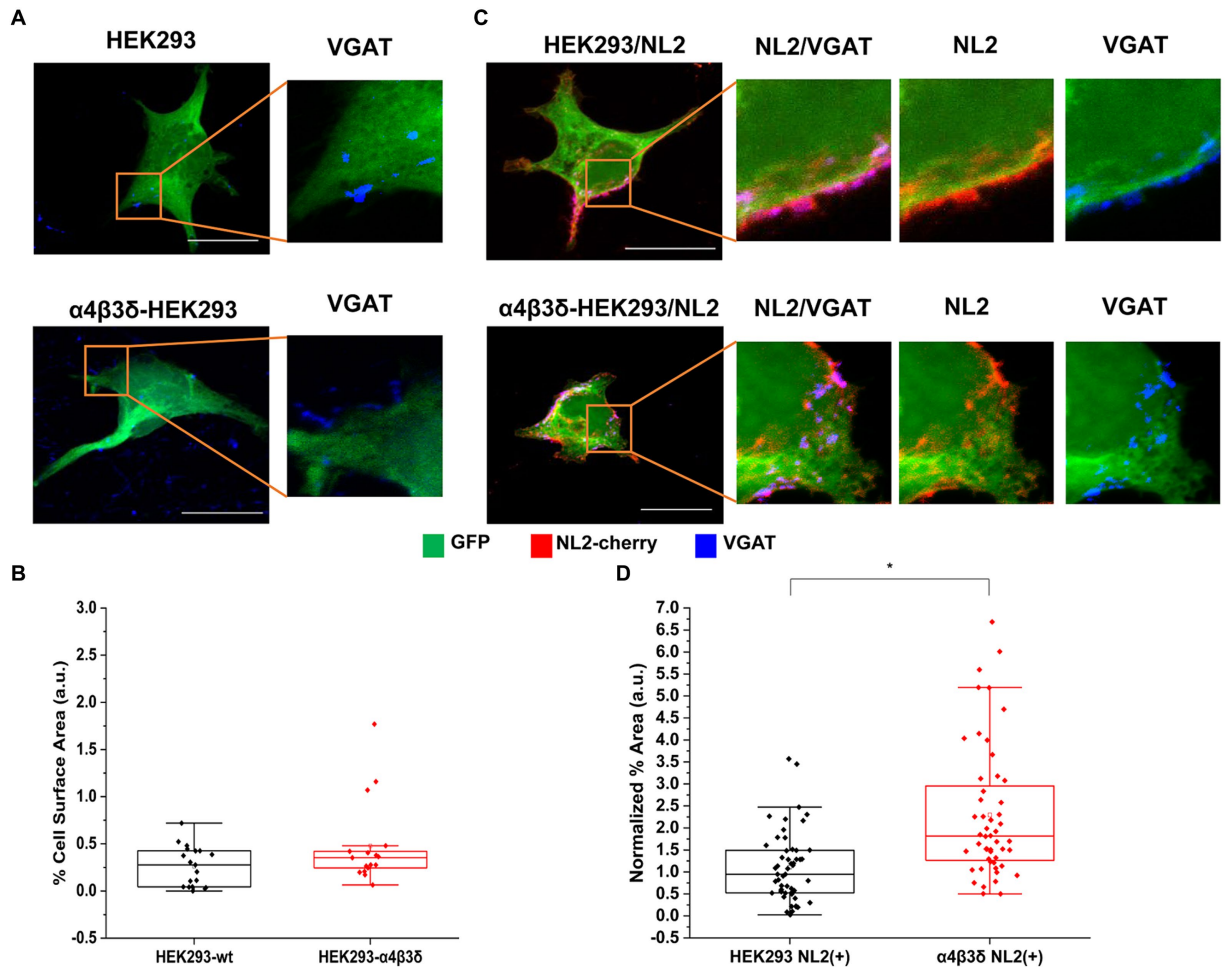

FIGURE 2
α4β3δ-GABA$_A$Rs do not induce synaptic contact formation but potentiate the induction of contacts by NL-2. Synaptic contact formation in co-culture of embryonic medium spiny neurons and **(A)** HEK293 (wt; upper panels) or α4β3δ-GABA$_A$R-expressing HEK293 cells (lower panels), or **(B)** HEK293/NL2 cells (wt; upper panels) or α4β3δ-GABA$_A$R/NL2-expressing cells (lower panels). The HEK293 cell body was visualized by GFP (green), GABAergic terminals were labeled with an anti-VGAT antibody (blue) and NL2 was mcherry-tagged (red). Scale bar = 20 μm. Fluorescent imaging was done using Zeiss 700 confocal microscope at 63 × magnification with image size 1,024 × 1,024. Max intensity projection of the z-stack images was shown. The enlarged images are 10 × zoom in. Quantitative analysis of synapses expressed as % area of co-localized pixels that represent contacts between VGAT terminals and in **(C)** HEK293 or α4β3δ-GABA$_A$R-expressing cells ($n = 21$ and $n = 17$, respectively; $N = 2$ independent experiments, $p = 0.2$), or **(D)** HEK293/NL2 cells or α2β2γ2-GABA$_A$R/NL2 expressing cells ($n = 53$ and $n = 52$ cells, respectively; $N = 3$ independent experiments, $p < 0.00001$ (8.4×10^{-7})). The box and whisker plot show the mean (square dot with no fill), median (horizontal line), and standard deviation (whiskers). Shapiro–Wilk normality test was used to test the normal distribution of the data and Mann–Whitney test was used to analyze statistical significance of the difference. (*$p < 0.05$).

results indicate that extrasynaptic $GABA_ARs$ can facilitate the NL2-dependent induction of synapses although their effect is significantly weaker than the effect observed for synaptic $GABA_ARs$.

To test whether the observed potentiation of NL2 effects by $GABA_ARs$ may be a consequence of increased expression of NL2, we have transfected the HA-tagged NL2 cDNA into the control, α4β3δ-$GABA_AR$- or α2β2γ2-$GABA_AR$-expressing HEK293 cells and carried out ELISA using an HA tag-specific antibody (Supplementary Figure S3). However, the surface or total expression of NL2 showed no difference between these conditions, indicating that other molecular mechanisms may mediate the observed cooperative interaction between NL2 and $GABA_ARs$.

The $GABA_AR$- and NL2- induced synaptic contacts were further characterized using immunolabeling and super-resolution imaging to measure the degree of co-localization between the α2β2γ2-$GABA_ARs$ or α4β3δ-$GABA_ARs$ and the presynaptic active vesicular release zone protein Bassoon. In these experiments, the α2β2γ2-$GABA_AR$/NL2- or α4β3δ-$GABA_AR$/NL2-expressing HEK293 cells in co-culture with the medium spiny neurons were immunolabeled with an α2- or α4-subunit-specific antibody, respectively, in combination with a Bassoon-specific antibody. While both $GABA_AR$ subtypes showed predominantly punctate distribution at the cell surface, their colocalization with Basson-positive terminals appeared greater for the α2β2γ2-$GABA_AR$ than α4β3δ-$GABA_AR$, which was in agreement with our confocal imaging data (Figures 3A,B). This was confirmed by a significantly higher M1 coefficient value obtained for the Bassoon/α2β2γ2-$GABA_AR$ co-localization in synaptic contacts than Bassoon/α4β3δ-$GABA_ARs$ co-localization (median = 0.27; IQR = 0.24–0.42; $n = 8$ cells versus median = 0.17; IQR = 0.10–0.25; $n = 8$ cells, respectively; from $N = 2$ independent experiments, $p = 0.04$; Figure 3C). In contrast, the M2 coefficient appeared higher but without reaching significance for the α2β2γ2-$GABA_AR$ overlapping with Bassoon than the α4β3δ-$GABA_AR$ (median = 0.73; IQR = 0.24–0.81; $n = 8$ cells vs. median = 0.51; IQR = 0.36–0.66; $n = 8$ cells, respectively; from $N = 2$ independent experiments; Figure 3D). These results indicate that NL2-induced formation of synapses is more likely to occur in the proximity of the α2β2γ2-$GABA_AR$ than α4β3δ-$GABA_AR$.

3.2 Structural and functional characterization of synaptic contacts induced by co-expression of $GABA_ARs$ and NL2

Functional characterization of synaptic contacts formed with the control/NL2, α2β2γ2-$GABA_AR$/NL2- or α4β3δ-$GABA_AR$/NL2-expressing HEK293 cells was first carried out by assessing the activity of their presynaptic components, GABAergic terminals, in synaptotagmin-antibody uptake assay (Fernández-Alfonso, Kwan and

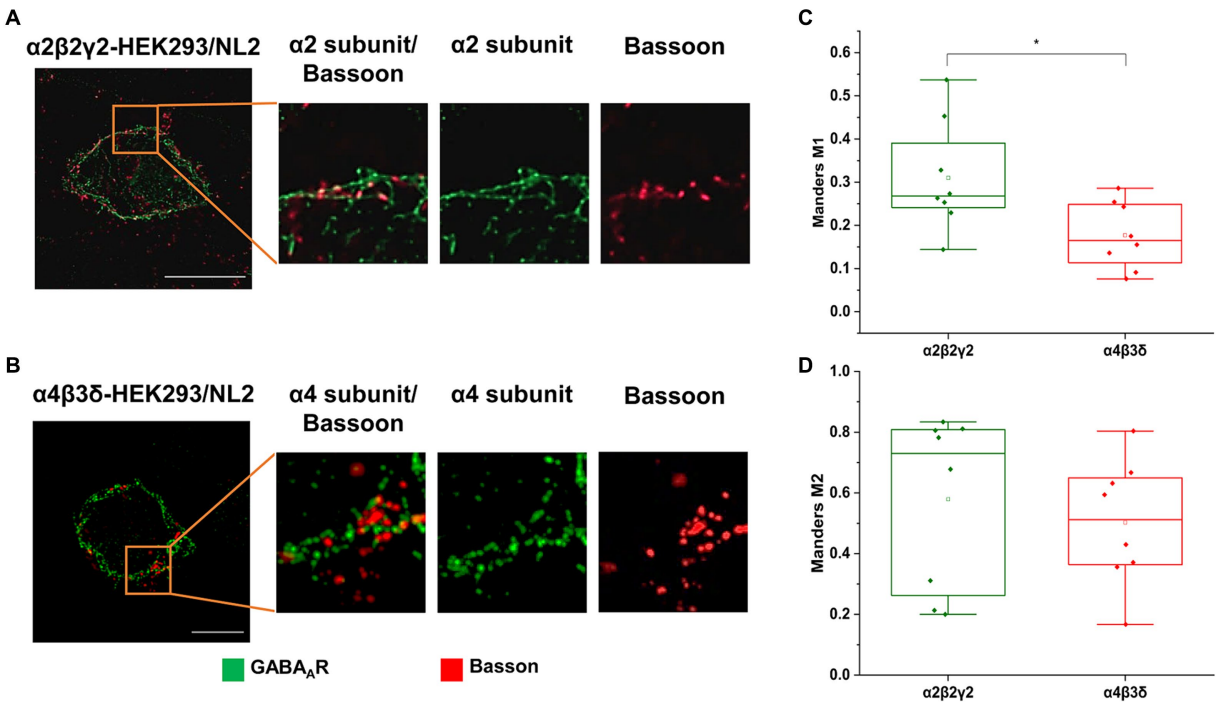

FIGURE 3
Co-localization of the presynaptic marker Bassoon and $GABA_A$ receptors on the surface of **(A)** $\alpha_2\beta_2\gamma_2$-$GABA_AR$, or **(B)** $\alpha_4\beta_3\delta$-$GABA_AR$-expressing HEK293 cells in co-culture with the embryonic medium spiny neurons. $GABA_AR$ α_2 or α_4 subunits (green) and Basson (red) were visualized using specific antibodies. Images were acquired using Zeiss ELYRA PS.1 SIM at 63 x magnification. Scale bar = 10 μm. **(C,D)** Quantitative analysis of colocalization between presynaptic marker Bassoon and $GABA_AR$ α2/4 subunits using Manders' coefficient M1, which indicates the proportion of Bassoon signals that overlap with $GABA_A$ receptor α2/4 subunits **(C)**, and Manders' coefficient M2, which indicates the proportion of α2/4 subunit signals that overlap with Bassoon signals **(D)**. The M1 coefficient is significantly higher in α2β2γ2-$GABA_AR$/NL2 expressing cell than in α4β3δ-$GABA_AR$/NL2 expressing cells (*t*-test, $p = 0.04$). The M2 coefficient is higher in α2β2γ2-$GABA_AR$ cells than in α4β3δ-$GABA_AR$ cells, but this difference is not statistically significant. Data from n = 8 cells from $N = 2$ independent experiments.

Ryan, 2006). In this assay, active presynaptic terminals were fluorescently labeled with a Cy5-tagged anti-synaptotagmin 1 vesicle-luminal domain-specific antibody (1,50, see Methods). The cells were fixed, permeabilized and immunolabeled with the VGAT-specific antibody, allowing us to visualize both active and inactive terminals forming contacts with HEK293 cells and quantify their ratio (Figures 4A–C). Quantification of the % area of co-localized pixels that represent contacts between synaptotagmin-positive and VGAT-positive terminals and the control HEK293 cells, confirmed that NL2 can induce the adhesion of active terminals in the absence of $GABA_A$Rs (median = 0.12%; IQR = 0.03 - 0.22%; $n = 30$ cells; from $N = 3$ independent experiments; Figures 4A,D). However, in the presence of α4β3δ-$GABA_A$Rs, NL2 had a significantly greater effect (median = 0.52%; IQR = 0.18 - 0.95%; $n = 21$ cells; from $N = 2$ independent experiments, $p = 0.0006$; Figures 4B,D). Moreover, in the presence of α2β2γ2-$GABA_A$Rs, NL2 was even more effective and the number of active synapses was significantly larger [$p < 0.00001$ ($p = 6.4 \times 10^{-10}$)] than the number obtained in the absence of $GABA_A$Rs or presence of α4β3δ-$GABA_A$Rs (median = 1.32%; IQR = 0.78 - 2.03%; $n = 21$ cells; from $N = 2$ independent experiments, $p = 0.04$, Figures 4C,D). The percentage of synapses incorporating active terminals in these experiments was ~10% (control/NL2), 24% (α4β3δ-$GABA_A$R/NL2), and 30% (α2β2γ2-$GABA_A$R/NL2).

Electrophysiological analysis of the whole-cell recordings of inhibitory postsynaptic currents (IPSCs) in $GABA_A$R- or $GABA_A$R/NL2 expressing HEK293 cells revealed that GABA-mediated synaptic transmission could be detected reproducibly only in the presence of the α2β2γ2-$GABA_A$Rs (Figure 5). In the absence of NL2, the IPSCs were detected in 60% of the α2β2γ2-$GABA_A$R-HEK293 cells (Figures 5A,G,H; 9 out of 15), in which 8 cells were detected with <0.1 Hz IPSC and 1 cell with >0.1 Hz, which supports the results of the structural analysis presented in Figure 1A. When NL2 was co-expressed, IPSCs were detected in 93.3% of α2β2γ2-$GABA_A$R/HEK293 cells (14 out of 15), in which 2 cells were detected with <0.1 Hz IPSC and 12 cells with >0.1 Hz (Figures 5B,G,H). In the absence of NL2, no IPSCs were detected in the α4β3δ-$GABA_A$R/HEK293 cells (11 cells, Figures 5D,G,H), while in the presence of NL2, IPSCs were detected in only 1 α4β3δ-$GABA_A$R-HEK293 cell out of 15 (> 0.1 Hz; Figures 5E,G,H). These data show that expression of NL2 increases the frequency of GABAergic IPSCs in the presence of synaptic α2β2γ2-$GABA_A$Rs. However, synaptic contacts induced by NL2 alone or the presence of α4β3δ-$GABA_A$Rs (Figures 2–4) fail to differentiate into active synapses and remain functionally silent (~95% of cells; 1/15).

Given a clear difference in the number and activity of NL2-induced synaptic contacts in the presence of α2β2γ2- and α4β3δ-$GABA_A$Rs, we were keen to establish which of the $GABA_A$R subunits may play a key role in these processes. To test different subunit combinations, we transiently transfected into the β3-expressing HEK293 stable cell line (B2 clone) combinations of α2, α4, γ2 or δ subunits cDNAs to form the following $GABA_A$R subtypes: α2β3γ2, α4β3δ, α4β3γ2 or α2β3δ. These cells were also co-transfected with cherry-NL2 cDNA. The cells were co-cultured with medium spiny neurons and synaptic activity in HEK293 cells was examined using whole-cell recordings. Compared to the α2β2γ2-$GABA_A$R/NL2-expressing HEK293 cells, a similar level of activity was detected in 7 out of 8 of the α4β3γ2-$GABA_A$R/NL2-expressing HEK293 cells with IPSC frequencies >0.1 Hz (Figures 5C,G,H). However, in 8 out of 10 of the α2β3δ-$GABA_A$R/NL2-expressing HEK293 cells, no IPSCs were detected, indicating that the majority of synaptic contacts formed in these conditions were also functionally silent (Figures 5F–H).

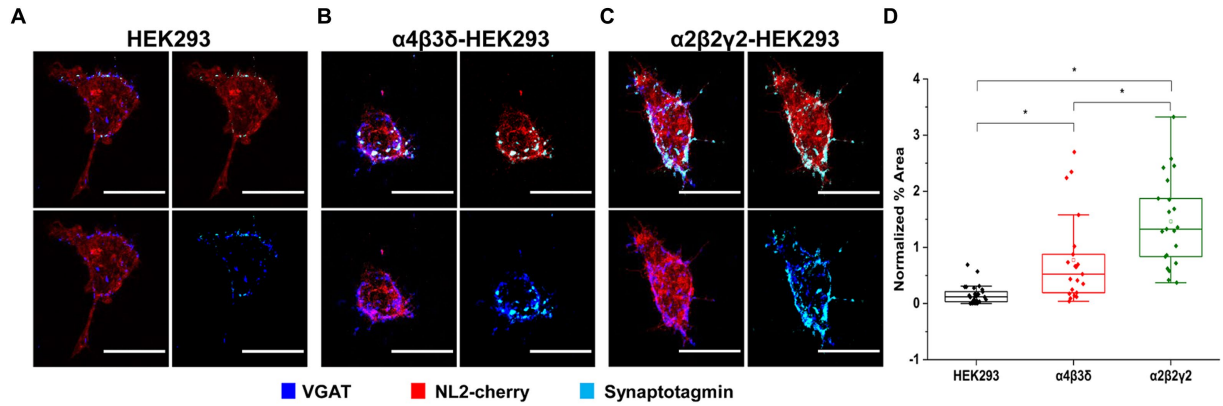

FIGURE 4
$GABA_A$R and NL2 co-expression induces the adhesion of active GABAergic terminals. Presynaptic activity is detected in synapses formed with **(A)** wt/NL2-expressing HEK293 cells, **(B)** α4β3δ-$GABA_A$R/NL2-expressing HEK293 cells, or **(C)** α2β2γ2/NL2-$GABA_A$R-expressing HEK293 cells in co-culture with embryonic medium spiny neurons. Active presynaptic terminals were visualized with the Cy5-labeled anti-synaptotagmin luminal domain-specific antibody (cyan), while all presynaptic terminals were visualized with an anti-VGAT-specific antibody (blue). NL2 was tagged with mCherry tag (red). Scale bar = 20 μm. Fluorescent imaging was done using Zeiss 700 confocal microscope at 63 × magnification with image size 512 × 512. Max intensity projection of the z-stack images was shown. The enlarged images are 10 × zoom in. **(D)** Quantitative analysis of active synaptic contacts in which the % area was normalized to the expression level of NL2. The box and whisker plot shows the mean (square dot with no fill), median (horizontal line), and standard deviation of the mean (whiskers). Data from HEK293 cells ($n = 30$, from $N = 3$ independent experiments), α4β3δ-$GABA_A$R-expressing HEK293 cells ($n = 22$, from $N = 2$ independent experiments) and α2β2γ2-$GABA_A$R-expressing HEK293 cells ($n = 22$, from $N = 2$ independent experiments). Significant difference was detected between HEK293 cells and α4β3δ-$GABA_A$R-expressing HEK293 cells ($p = 0.0006$), HEK293 cells and α2β2γ2-$GABA_A$R-expressing HEK293 cells (6.4×10^{-10}) and α4β3δ-$GABA_A$R-expressing HEK293 cells and α2β2γ2-$GABA_A$R-expressing HEK293 cells ($p = 0.04$). Shapiro–Wilk normality test was used to test the normal distribution of the data and Kruskal Wallis ANOVA followed by Dunn's test was used to analyze the statistical significance (*$p < 0.05$).

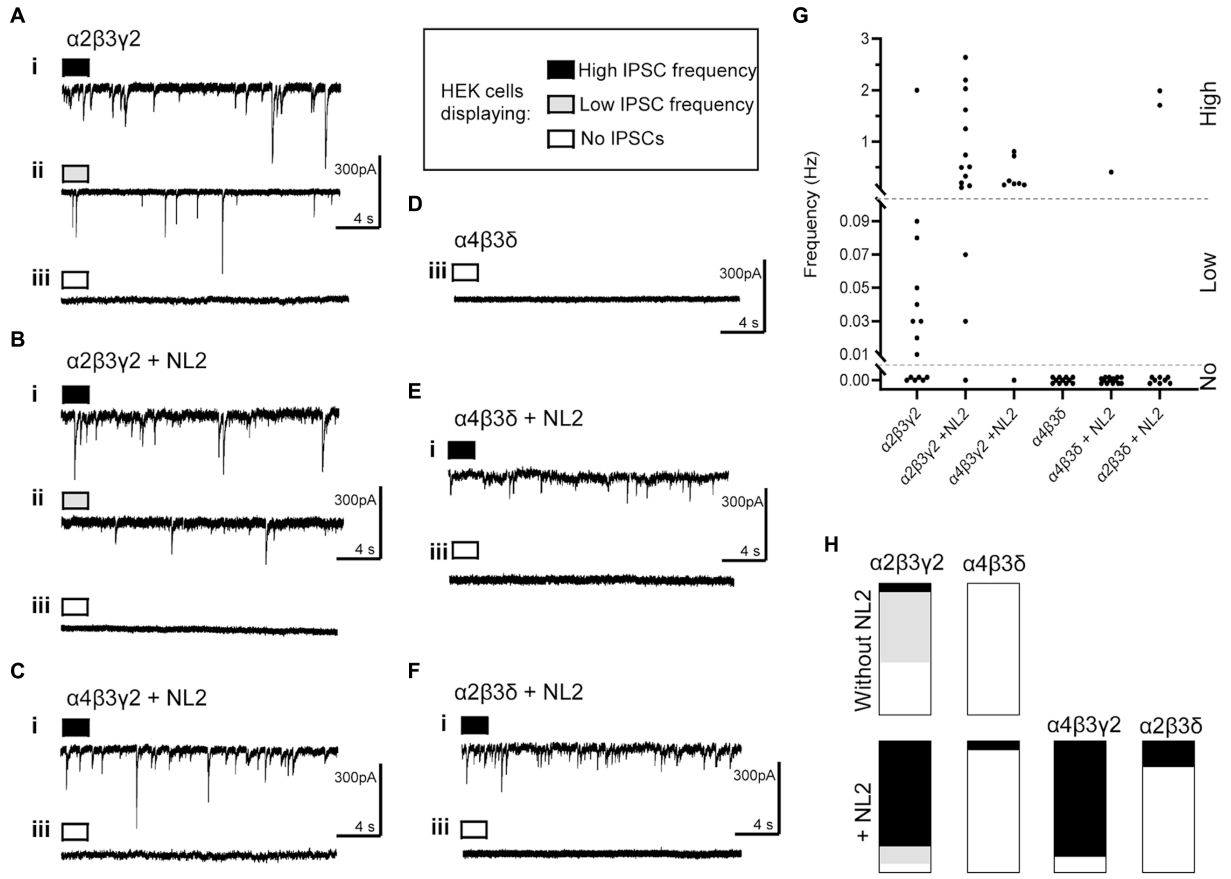

FIGURE 5
Whole cell recordings of IPSCs in co-culture of HEK293 cells and embryonic medium spiny neurons. Representative examples of voltage-clamp recordings of IPSCs in HEK cells expressing **(A)** α2β3γ2-GABA$_A$Rs without NL2, **(B)** α2β3γ2 with NL2, **(C)** α4β3γ2 with NL2, **(D)** α4β3δ without NL2, **(E)** α4β3δ with NL2, and **(F)** α2β3δ with NL2. Examples of three levels of IPSC frequency are shown as (i) high, >0.1 Hz, black; (ii) low, <0.1 Hz, gray; or **(iii)** no IPSCs, white. **(G)** Scatter-plot showing individual IPSC frequencies in each group. **(H)** Parts-of-whole histograms show the prevalence of observing a high, low or zero IPSC frequency, with the following number of cells appearing in each plot (high/low/none-total): α2β3γ2-NL2: 1/8/6–15, α2β3γ2 + NL2: 12/2/1–15, α4β3γ2 + NL2: 7/0/1–8, α4β3δ-NL2: 0/0/11–11, α4β3δ + NL2: 1/0/14–15, α2β3δ + NL2: 2/0/8–10.

To investigate these differences further, we have also carried out immunolabeling experiments to characterize the degree of innervation of HEK293 cells expressing different subunit combinations (Figures 6A–D). Synaptic contacts were defined based on signal colocalization between the presynaptic Bassoon and postsynaptic NL2 (cyan and red channel in Figures 6A–D) and analyzed using ImageJ as described in the Methods. Quantification of the % area of co-localized pixels that represent contacts between the Bassoon-positive terminals and NL2 demonstrated that the level of presynaptic innervation was significantly higher in the presence of α2β3γ2-GABA$_A$Rs (median = 1.22%; IQR = 0.54 – 1.96%; $n = 45$) than α2β3δ- (median = 0.62%; IQR = 0.17 – 1.19%; $n = 43$, $p = 0.003$) or α4β3δ-GABA$_A$Rs (median = 0.69%; IQR = 0.34 – 1.01%; $n = 43$, $p = 0.03$) (from $N = 3$ independent experiments; Figure 6E). The lower innervation for α4β3γ2 combination, detected by imaging, was surprising given its ability to mediate IPSCs in the presence of NL2 (Figures 5C,G,H), possibly reflecting the greater sensitivity of electrophysiology for detecting active synapses.

Together, our results point to a key role of the γ2 subunit in facilitating the NL2-induced synapse formation and functional maturation in this co-culture model. Although adhesion of active GABAergic terminals can be induced by NL2 in the presence of other GABA$_A$R subunit combinations, the highest degree of innervation and the tight functional coupling between the presynaptic release of GABA and the postsynaptic responses require the cooperation between the γ2 subunit-containing GABA$_A$Rs and NL2.

3.3 The synergism between GABA$_A$Rs and NL2 does not require GABA$_A$R activity

To test if the GABA$_A$R activation by GABA may be required for the observed effects, the control, α2β2γ2-GABA$_A$R or α4β3δ-GABA$_A$R-expressing HEK293 cells were transiently transfected with GFP and cherry-NL2 cDNAs and platted together with the medium spiny neurons in the absence or presence of bicuculline, a GABA$_A$R competitive antagonist (Supplementary Figure S4). Quantification of the % area of co-localized VGAT and GFP pixels that represent contacts showed potentiation of NL2 effects by α2β2γ2-GABA$_A$Rs irrespective of whether the cultures were incubated with DMSO (control HEK293/NL2 cells: median = 1.68%; IQR = 0.54 – 2.57%; $n = 20$; α2β2γ2-GABA$_A$R/NL2 cells: median = 4.21%; IQR = 2.00

10.3389/fncel.2024.1423471

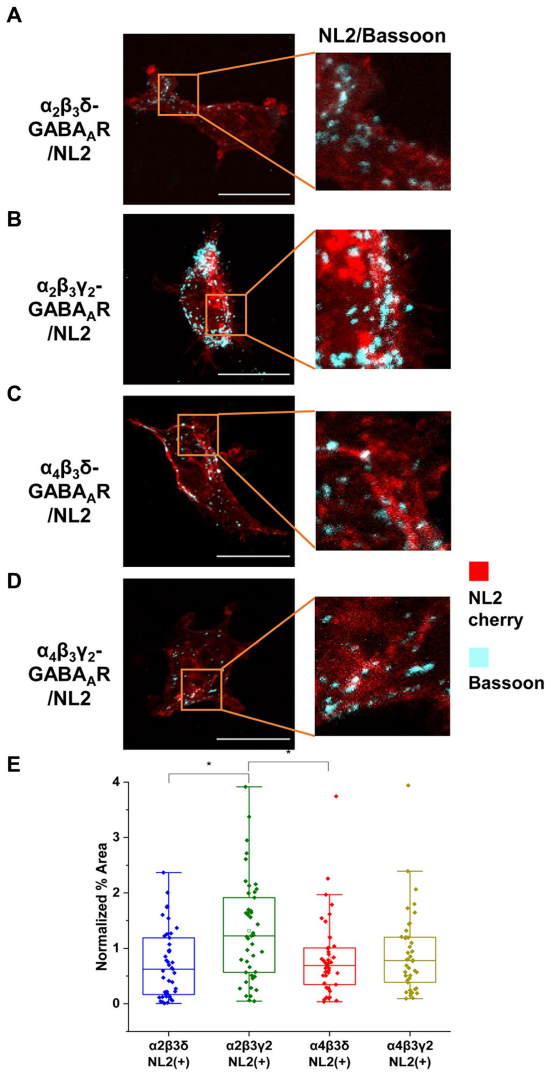

FIGURE 6
α2β3γ2-GABA$_A$R and NL2 co-expression is the most potent combination in inducing synaptic contacts. HEK293 cells expressing **(A)** α2β3δ-, **(B)** α2β3γ2-, **(C)** α4β3δ-, or **(D)** α4β3γ2-GABA$_A$R and NL2 were co-cultured with embryonic medium spiny neurons. NL2 was tagged with mCherry (red) while GABAergic terminals were labeled an anti-Bassoon-specific antibody (cyan). Scale bar = 20 μm. Fluorescent imaging was done using 63 × magnification with image size 1,024 × 1,024. Max intensity projection of the z-stack images was shown. The enlarged images are 10 × zoom in. **(E)** Quantitative analysis of synapses expressed as % area of colocalised pixels that represent contacts between Basson-positive terminals and HEK293 expressing α2β3δ-, α2β3γ2-, α4β3δ- or α4β3γ2-GABA$_A$ receptors and NL2. The % area was normalized to the expression level of NL2 for each cell. The box and whisker plot shows the mean (square dot with no fill), median (horizontal line), and standard deviation of the mean (whiskers), with filled dots representing individual cells. Data from $N = 3$ independent experiments. Significant difference was detected between α2β3γ2-GABA$_A$R- and α2β3δ-GABA$_A$R-expressing HEK293 cells ($p = 0.003$) or α4β3δ-GABA$_A$R-expressing HEK293 cells ($p = 0.03$). Shapiro–Wilk normality test was used to test the normal distribution of the data and Kruskal Wallis ANOVA followed by Dunn's test was used to analyze the statistical significance of the difference. (*$p < 0.05$).

– 7.11%; $n = 20$; from $N = 2$ independent experiments, $p = 0.01$) or bicuculline (control HEK293/NL2 cells: median = 1.11%; IQR = 0.43 – 2.00%; $n = 21$; α2β2γ2-GABA$_A$R/NL2 cells: median = 2.28%; IQR = 1.34 – 4.22%; $n = 20$, respectively; from $N = 2$ independent experiments, $p = 0.009$; Supplementary Figures S4A,C).

Similar results were obtained in co-cultures of control HEK293/NL2 and α4β3δ-GABA$_A$R/NL2-expressing HEK293 cells in the absence or presence of bicuculline (Supplementary Figures S4B,D). Quantification of the % area of co-localized pixels of VGAT and GFP that represent contacts between the presynaptic terminals and HEK293 cells showed a significant increase in NL2 induction in the presence of α4β3δ-GABA$_A$Rs in both DMSO-treated cultures (control HEK293/NL2 cells: median = 1.05% IQR = 0.52 – 1.72%; $n = 20$; α4β3δ-GABA$_A$R/NL2 cells: median = 2.89% IQR = 1.77 – 4.99%; $n = 20$; from $N = 2$ independent experiments, $p = 0.03$) and bicuculline-treated cultures (control HEK293/NL2 cells: median = 1.05% IQR = 0.27 – 1.27%; $n = 20$; from $N = 2$ independent experiments; α4β3δ-GABA$_A$R/NL2 cells: median = 3.23% IQR = 1.36 – 4.79%; $n = 20$; from $N = 2$ independent experiments, $p = 0.03$; Supplementary Figure S4D).

3.4 GABA$_A$Rs and NL2 synergism is mediated by the TM3-4 intracellular loop of the γ2 subunit

To investigate the mechanisms underlying the observed synergistic effects of α2β2γ2-GABA$_A$Rs and NL2 in synapse formation, we first assessed whether the extracellular N-terminal domains (ECDs) of GABA$_A$R α2, β2 or γ2 subunits may be involved given that they were previously shown to contribute to the GABAergic synapse formation in the absence of NL2 (Figure 7; Brown et al., 2016).

To test this, 4 μg of either the α2 (Figure 7B), β2 (Figure 7C), or γ2 ECD (Figure 7D; 0.29–0.32 μM), purified from SF9 cells (Brown et al., 2016) were applied to the co-culture of α2β2γ2-GABA$_A$R/GFP/NL2-expressing HEK293 cells and medium spiny neurons. An equivalent amount of untransfected SF9 cell extract (4 μg), following the same purification procedure as the extracts expressing ECDs, was used as a control (Figure 7A). Quantification of the % area of co-localized pixels of VGAT and GFP that represent synaptic contacts showed no significant change with the application of ECDs (Figure 7E). With SF9 extract control, the median was 5.82% (IQR = 3.96 - 6.90%, n = 19 cells from N = 2 independent experiments). Application of β2 ECD slightly decreased the synapse formation albeit not significantly (median = 4.67%; IQR = 2.67 – 7.35%; $n = 20$ cells; from $N = 2$ independent experiments). No change was observed with the application of α2 (median = 6.03%; IQR = 4.04 – 7.58%; $n = 20$ cells; from $N = 2$ independent experiments) or γ2 (median = 6.22%; IQR = 4.05 – 7.33%; $n = 20$ cells; from $N = 2$ independent experiments) ECDs.

These results indicate that cooperation between α2β2γ2-GABA$_A$Rs and NL2 may be mediated by the subunit intracellular domains. To test this hypothesis, we took advantage of previously characterized δ-γ2 subunits chimera (Hannan et al., 2020), in which the large intracellular loop (ICL) (TM 3–4) of the δ subunit was replaced with the equivalent domain of the γ2 subunit (δγ2ICL). HEK293 cells stably expressing β3 subunits were transiently transfected with the cherry-NL2 and α2 + γ2 (Figure 8A), or α2 + δγ2ICL (Figure 8B), or α2 + δ (Figure 8C) cDNAs and cultured with medium spiny neurons for 24 h. Quantification of the % area of co-localized pixels that represent contacts between presynaptic Bassoon and NL2 demonstrated no significant difference in NL2-dependent induction

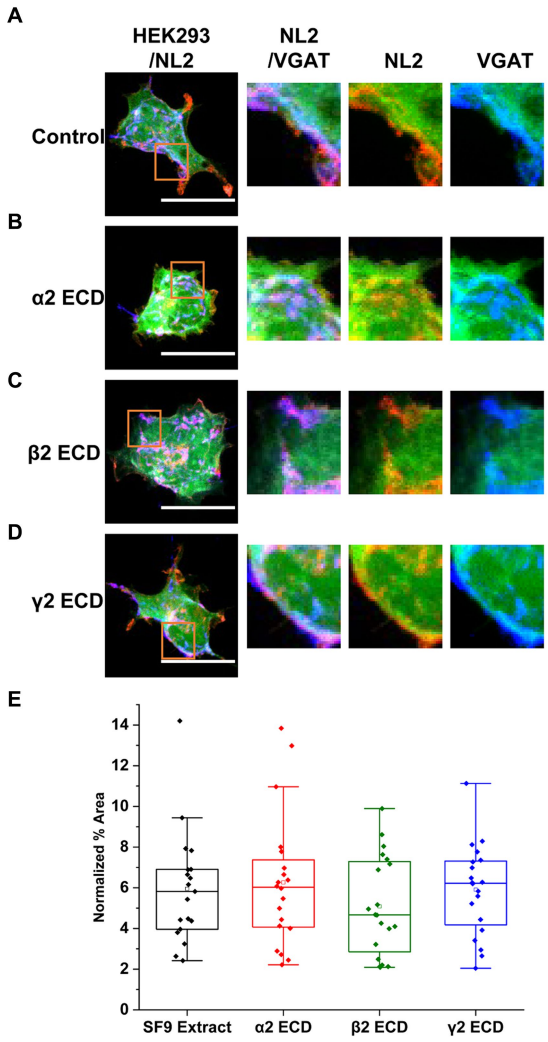

FIGURE 7
The N-terminal extracellular domains (ECDs) of $GABA_AR$ subunits do not mediate the induction of synaptic contacts by $GABA_AR$ and NL2 co-expression. **(A)** Synaptic contact formation in co-culture of α2β2γ2-$GABA_AR$/mCherry-NL2/GFP–expressing HEK293 cells and embryonic medium spiny neurons in the presence of **(A)** SF9 cell extracts, **(B)** α2 subunit ECD, **(C)** β2 subunit ECD or **(D)** γ2 subunit ECD. HEK293 cell body was visualized with GFP (green), NL2 was labeled with mCherry (red), and the presynaptic terminals were visualized with an anti-VGAT-specific antibody (blue). Scale bar = 20 μm. Fluorescent imaging was done using 63 × magnification with image size 512 × 512. Max intensity projection of the z-stack images was shown. The enlarged images are 10 × zoom in. **(E)** Quantitative analysis of the % area of synaptic contacts formed with α2β2γ2-$GABA_A$ receptor/NL2-expressing HEK293 cells. The % area values were normalized to the expression of NL2 for each cell. The box and whisker plot shows the mean (square dot with no fill), median (horizontal line), and standard deviation of the mean (whiskers). Data from $n = 19$ α2β2γ2-$GABA_A$/NL2-expressing HEK293 cells treated with SF9, $n = 20$ treated with α2 subunit ECD, $n = 20$ treated with β2 subunit ECD, and $n = 20$ treated with γ2 subunit ECD; from $N = 2$ independent experiments. Shapiro–Wilk normality test was used to test the normal distribution of the data and Kruskal Wallis ANOVA followed by Dunn's test was used to analyze the statistical significance of the difference.

of synaptic contacts between the α2β3γ2/NL2 and α2β3δγ2ICL/NL2 (median = 2.72%; IQR = 1.63 – 5.15%; $n = 31$ cells, versus median = 2.42%; IQR = 1.12 – 4.06%; $n = 32$ cells; $N = 2$ independent experiments). In both conditions, the NL2 effects were significantly greater than in the presence of α2β3δ-$GABA_A$Rs (median = 1.42%; IQR = 0.78 – 2.49%; $n = 30$ cells, respectively, $p = 0.003$ for α2β3γ2/NL2, $p = 0.047$ for α2β3δγ2ICL/NL2; $N = 2$ independent experiments; Figure 8D). Thus, the TM3-4 intracellular loop of the γ2 subunit mediates the cooperativity between $GABA_A$Rs and NL2. Whether the large intracellular loop of the γ2 subunit mediated a direct interaction between the $GABA_A$Rs and NL2 remained unclear.

To address this question, we have carried out co-immunoprecipitation experiments using the lysates of HEK293 cells expressing Myc-tagged α2β3γ2-$GABA_A$Rs and HA-tagged NL2. Using either the Myc-antibody, followed by immunoblotting with the NL2-specific antibody (Figure 9A), or, conversely, HA-tag antibody, followed by immunoblotting with β3 subunit-specific antibody (Figure 9B), we confirmed that $GABA_A$Rs and NL2 can be co-immunoprecipitated and thus can interact with each other. Furthermore, to assess if the ICL of γ2 subunit mediates this interaction, α2β3γ2-, or α2β3δγ2ICL- or α2β3δ-$GABA_A$Rs were co-expressed with HA-tagged NL2 in HEK293 cells, and subjected to co-immunoprecipitation with the Myc-antibody followed by immunoblotting with the NL2-antibody or β3-subunit antibody. In α2β3γ2-$GABA_A$R precipitates, a clear band corresponding to the molecular weight for NL2 was detected while no such band was detected in α2β3δ-$GABA_A$R precipitates (Figure 9C, upper panel). In the α2β3δγ2ICL-$GABA_A$R precipitates, a weaker band corresponding to NL2 was also detected (Figure 9C, upper panel). Immunoblotting with the β3 subunit antibody showed that the amount of precipitated $GABA_A$Rs was comparable in three different conditions (Figure 9C, lower panel). To test if NL2 can bind directly to the large intracellular domain of the γ2 subunit, GST-tagged ICL was expressed and purified from *E. coli* and incubated with the lysates of HEK293 cells transfected with HA-NL2. However, the binding between NL2 and the TM 3–4 ICL of the γ2 subunit (Figure 9D) could not be detected, indicating that $GABA_A$Rs and NL2 interaction may be indirect and likely mediated by another protein, the nature of which remains to be established. Nevertheless, $GABA_A$Rs and NL2 can interact *in vivo* as demonstrated by their co-immunoprecipitation from rat brain lysates prepared under non-denaturing conditions (Figure 9E).

4 Discussion

$GABA_A$Rs and NL2 are co-expressed in many GABAergic inhibitory synapses in the mammalian brain with both proteins being implicated in synaptic initiation and functional maturation (Ali et al., 2020). It is now evident that together with many other proteins, $GABA_A$Rs and NL2 undergo complex interactions to facilitate synaptic contact formation but how these interactions are coordinated in time and space to lead to the establishment of fully functional inhibitory synapses remains to be described in detail. This is important because genetic mutations and alterations in NL2 and $GABA_A$Rs expression and function found in patients have been directly associated with their neurological and psychiatric symptoms, often showing a degree of overlap (Ali et al., 2020; Thompson, 2024). In many such cases, deficits in inhibitory synaptic connections have been implicated as the leading cause of the symptoms that patients experience. However, the intricate details of molecular interactions with a clear functional read-out are difficult to study in complex *in vivo* or *in vitro* systems in which these

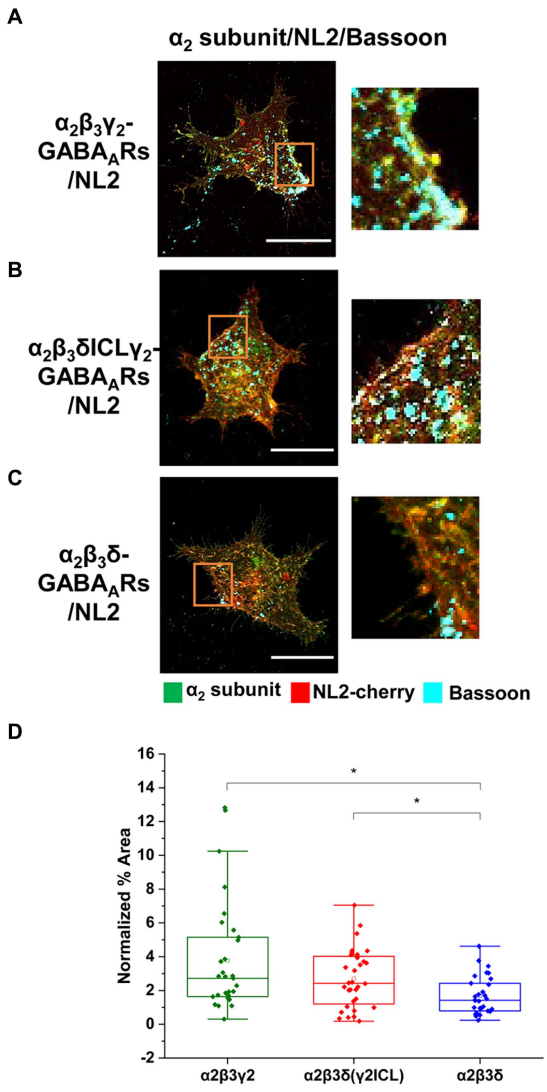

FIGURE 8
Cooperative interaction between $GABA_A$Rs and NL2 is mediated by the γ2 subunit intracellular loop. **(A)** Synaptic contact formation in co-culture of α2β3γ2-$GABA_A$R/NL2-, **(B)** α2β3δγ2ICL-$GABA_A$R/NL2- or **(C)** α2β3δ-$GABA_A$R/NL2-expressing HEK293 cells and embryonic medium spiny neurons. NL2 was tagged with mCherry (red), synaptic terminals were labeled with an anti-Bassoon antibody (cyan), and $GABA_A$Rs were visualized with an anti-α2 subunit specific antibody (green). Scale bar=20μm. Fluorescent imaging was done using Zeiss 700 confocal microscope at 63×magnification with image size 512×512. Max intensity projection of the z-stack images was shown. The enlarged images are 10×zoom in. **(D)** Quantitative analysis of the % area of synaptic contacts which was normalized to the expression of NL2 for each cell. The box and whisker plot shows the mean (square dot with no fill), median (horizontal line), and standard deviation of the mean (whiskers). Data from n=31 α2β3γ2-$GABA_A$R/NL2-, n=32 α2β3δγ2ICL-$GABA_A$R/NL2-, and n=30 α2β3δ-$GABA_A$R/NL2-expressing HEK293 cells, from N=2 independent experiments. Significant difference was detected between α2β3γ2-$GABA_A$R/NL2- and α2β3δ-$GABA_A$R/NL2-expressing HEK293 cells (p=0.003) or α2β3δγ2ICL- and α2β3δ-$GABA_A$R/NL2-expressing HEK293 cells (p=0.047). Shapiro–Wilk normality test was used to test the normal distribution of the data and Kruskal Wallis ANOVA followed by Dunn's test was used to analyze the statistical significance of the difference. (*p<0.05).

and many other proteins coexist. The current study therefore aimed to investigate whether and how the interaction between $GABA_A$Rs and NL2 may lead to the establishment of functional synapses in the absence of other synaptic proteins using a reduced *in vitro* co-culture system. Although far from the situation *in vivo* and subject to the limitations of any study in a reduced system, this approach has revealed a synergism between $GABA_A$Rs and NL2 in inducing synaptic formations for which the presence of the γ2 subunit and specifically its TM3-4 intracellular domain-mediated interaction between these proteins are required.

We also know that the phosphorylation status of NL2 is important for its surface stability and for regulating synaptic $GABA_A$R numbers at synapses (Halff et al., 2022). Furthermore, we and others have previously shown that the number of synaptic contacts could be enhanced significantly by co-expression of NL2 and $GABA_A$Rs in heterologous co-culture models (Fuchs et al., 2013) and cultured neurons (Fu and Vicini, 2009). Moreover, in functional experiments, synaptic responses including spontaneous IPSC and miniature IPSC amplitudes detected in the presence of NL2 (and $GABA_A$Rs) indicated that each nerve terminal elicits a more efficacious postsynaptic response and that each axon forms more functional synapses. Our current study largely confirms these findings but also draws an important distinction between the synaptic and extrasynaptic subtypes of $GABA_A$Rs in their ability to synergize with NL2. The synaptic $GABA_A$Rs, those more closely associated with NL2 *in vivo*, show a significantly stronger synergism with NL2 in synaptic initiation and pre-and post-synaptic coupling leading to the formation of fully functional synapses. The extrasynaptic δ-$GABA_A$Rs, although able to potentiate the synaptogenic effects of NL2 to some extent, do not generate the same postsynaptic responses as their γ2 counterparts, probably due to their largely perisynaptic localization rather than their intrinsic channel properties given that they have a higher affinity for GABA and slower desensitization rate than synaptic $GABA_A$Rs (Farrant and Nusser, 2005; Mortensen et al., 2011). This infers that synaptic $GABA_A$Rs may have a stronger physical association with NL2 than the extrasynaptic receptors which is indeed supported by our biochemical experiments showing that NL2 could be detected only in precipitated protein complexes of synaptic $GABA_A$Rs.

Our current study also confirms the previously reported synaptogenic activity of synaptic $GABA_A$Rs in the absence of NL2 (Fuchs et al., 2013; Brown et al., 2014, 2016). These *in vitro* findings are supported by the *in vivo* evidence from $GABA_A$R α1, α3 or γ2 subunit knock-out mice demonstrating that the lack of these subunits in certain brain regions leads to prominent structural changes in specific types of inhibitory synapses (Schweizer et al., 2003; Li et al., 2005; Fritschy and Panzanelli, 2006; Studer et al., 2006). Moreover, genetic deletion of $GABA_A$Rs using CRISPR-Cas9 technology in a single hippocampal neuron was shown to cause a substantial reduction in GABAergic synapses received by this cell (Duan et al., 2019), further supporting the critical role of $GABA_A$Rs in inhibitory synapse development.

NL2 has been viewed as a chief synaptic adhesion mediator based on its well-characterized interactions with the presynaptic proteins Neurexins (Sudhof, 2008), although many other adhesion proteins have also been shown to facilitate the initiation of synaptic contacts (Connor and Siddiqui, 2023). However, the presence of $GABA_A$Rs is the key requirement for these contacts to develop into functional synapses. Moreover, in the presence of synaptic $GABA_A$Rs and NL2 at the postsynaptic membrane, significantly more presynaptic GABAergic terminals show the activity-dependent uptake of synaptotagmin luminal domain-specific antibodies indicating that their ability to release GABA is enhanced in comparison with the

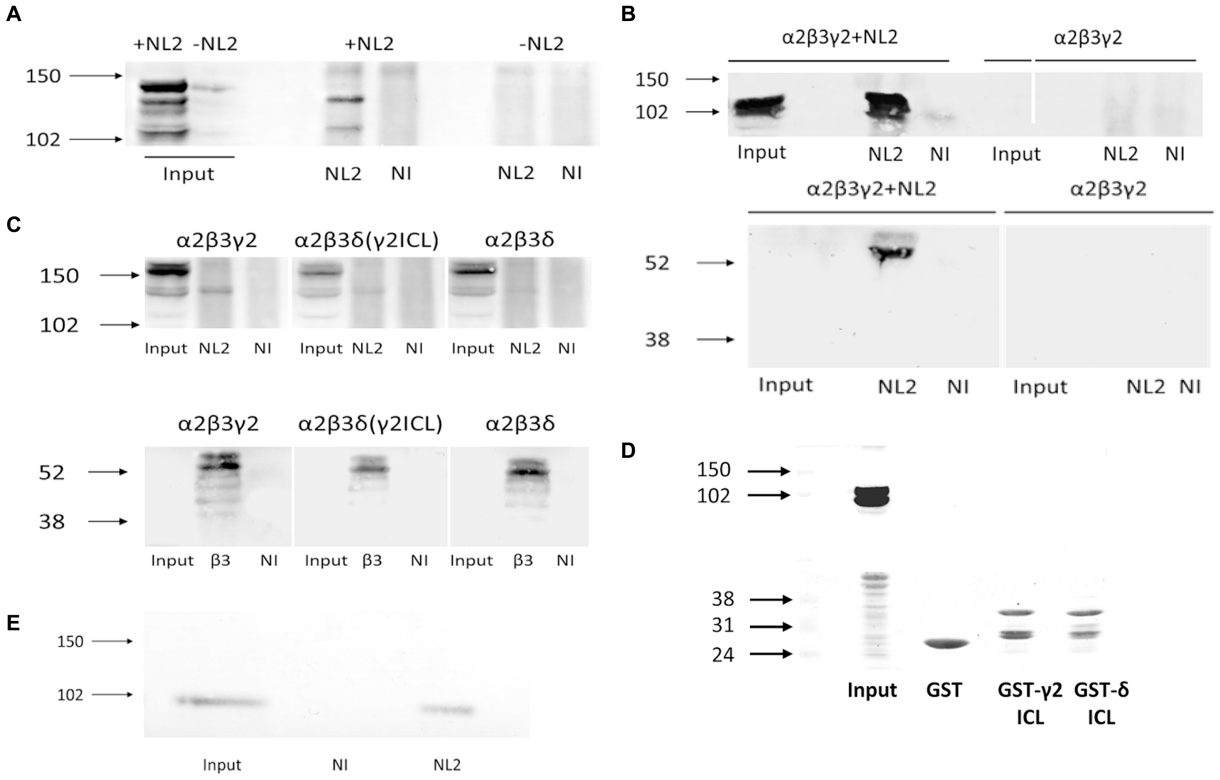

FIGURE 9
GABA$_A$R and NL2 interaction is mediated by the γ2 subunit intracellular loop. **(A)** Myc-tagged GABA$_A$Rs were immunoprecipitated using a myc-specific antibody, followed by detection of NL2 by immunoblotting using an anti-NL2-specific antibody. **(B)** HA-tagged NL2 was immunoprecipitated with a HA-specific antibody and subsequently detected by immunoblotting with the same antibody (upper panel), while the presence of GABA$_A$Rs in precipitates was detected by immunoblotting with an anti-β3 specific antibody (lower panel). **(C)** NL2-GABA$_A$ receptor interaction in the presence of the γ2 subunit intracellular TM 3–4 loop domain detected by co-immunoprecipitation. The β3 subunit was myc-tagged. The immunoprecipitation was carried out with an anti-myc-specific antibody. NL2 was detected in precipitates using an anti-NL2-specific antibody (upper panel), while GABA$_A$ receptors were detected using an anti-β3 subunit-specific antibody (lower panel). **(D)** NL2 does not bind to the purified GST-γ2 ICL or GST-δ ICL *in vitro* (upper panel). Purified GST fusion proteins were detected by Ponceau S (lower panel). **(E)** NL2 interacts with GABA$_A$Rs in the adult male rat cortex. Co-immunoprecipitation was carried out with an anti-α1 subunit C-terminal-specific antibody, followed by detection of NL2 by immunoblotting using an anti-NL2-specific antibody. In all immunoblotting experiments, the binding of primary antibodies was visualized using alkaline phosphatase-conjugated secondary antibody and NBT/BCIP color substrate reaction. Blots are representative of $N = 2$ independent experiments for each experimental paradigm.

conditions where only NL2 or GABA$_A$Rs are expressed. This suggests that GABA$_A$Rs also influence presynaptic maturation regulated by NL2 either directly, by interacting with the presynaptic proteins such as Neurexins (Zhang et al., 2010) and/or other proteins involved in this process (Brown et al., 2016), or they act indirectly, by facilitating the NL2 interactions with its presynaptic partners. However, direct interactions of GABA$_A$Rs with presynaptic proteins in this context are less likely to contribute because introducing the purified N-terminal ECDs of individual subunits as blocking reagents into our co-cultures did not affect the synergism between GABA$_A$Rs and NL2. Nevertheless, it remains possible that GABA$_A$Rs may still engage directly via interactions that require the fully assembled heteropentameric N-terminals ECDs rather than ECDs of individual subunits used in our experiments or they may act via their C-terminal ECDs. The indirect facilitation of presynaptic maturation by GABA$_A$Rs is supported by our findings as well as by previous studies. Our results indicate that the intracellular TM3-4 loop of the γ2 subunits is required for the cooperativity between GABA$_A$Rs and NL2 in synaptic formation but also for the association between GABA$_A$Rs and NL2. However, the TM 3–4 ICL may not be sufficient for binding to occur, given that no binding to NL2 was detected when the purified GST-fusion of the γ2 TM3-4 intracellular loop was tested in binding assays *in vitro*. It is therefore likely that this association is mediated by another protein that can bind directly to both the γ2 TM3-4 intracellular loop and NL2. While there may be several proteins involved, one of the two main candidates is the tetraspanin LHFPL4, also known as GARLH4, which interacts with the γ2 subunit to link GABA$_A$Rs and NL2 (Davenport et al., 2017; Yamasaki et al., 2017; Han et al., 2021). However, the attempts to detect this protein in our HEK293 cell lines using immunoblotting with specific antibodies were unsuccessful (data not shown), which leads us to conclude that this protein is unlikely to play a role in the synergism between GABA$_A$Rs and NL2 observed in this study. The other main candidate for this role is the postsynaptic scaffold protein gephyrin which was shown previously to directly interact with the TM3-4 intracellular loops of multiple GABA$_A$Rs subunits, including the γ2 subunit (Tretter et al., 2008; Maric et al., 2011; Mukherjee et al., 2011; Tretter et al., 2011; Kowalczyk et al., 2013; Maric et al., 2014), but also NL2 (Antonelli

et al., 2014; Nguyen et al., 2016). Gephyrin is expressed in our HEK293 cell lines in abundance (data not shown) which suggests that the observed interaction between NL2 and $GABA_A$Rs may be at least in part mediated by this protein.

It is also likely that multiple interactions between gephyrin and α (1, 2, 3 or 5), β (2 or 3) and γ2 subunits incorporated into the synaptic subtypes of $GABA_A$Rs occur at the same time and cumulatively contribute to a strong and stable binding of the receptor to gephyrin and NL2, which may be required for the initiation of synapses. In contrast, the extrasynaptic $GABA_A$R subtypes may still engage in interactions with gephyrin and indirectly with NL2 via their β subunits given that α4, α6, or δ do not bind gephyrin, but this interaction is likely to be weaker and transient and therefore insufficient to stabilize the complex between $GABA_A$Rs and NL2 to the extent required for the formation of new functional synapses. This could potentially explain the findings that the initiation of contacts is still increased in the presence of extrasynaptic $GABA_A$R and NL2, but these contacts do not develop into functional synapses. The perisynaptic localization of these receptors shown in our study and previously (Wei et al., 2003; Farrant and Nusser, 2005) is in agreement with this hypothesis. Moreover, the transient nature of these interactions and the ability of extrasynaptic $GABA_A$Rs to migrate laterally into and out of synapses even when synapses are established and fully functional has been demonstrated in a study which also showed that the TM3-4 loop of γ2 subunit plays a key role in regulating the degree of lateral migration of synaptic $GABA_A$Rs (Hannan et al., 2020). Finally, the apparent correlation between the degree of synergism between $GABA_A$Rs and NL2 and the establishment of functional synapses led us to assess whether $GABA_A$R channel activity may contribute to these developmental processes as described previously (Chattopadhyaya et al., 2007; Arama et al., 2015; Oh et al., 2016). In the presence of bicuculline, the synergism between synaptic or extrasynaptic $GABA_A$R and NL2 in synaptic contact formation was unaffected which further supports our hypothesis that $GABA_A$Rs not only mediate synaptic transmission in the brain but also participate together with NL2 in the initiation and maturation of synaptic contacts as structural proteins.

Data availability statement

The raw data supporting the conclusions of this article will be made available by the authors, without undue reservation.

Ethics statement

The animal study was approved by Ethics Committee University College London. The study was conducted in accordance with the local legislation and institutional requirements.

Author contributions

YS: Writing – review & editing, Methodology, Investigation, Formal analysis, Data curation, Conceptualization. MM: Writing – review & editing, Methodology, Investigation, Formal analysis, Data curation. BY: Writing – review & editing, Methodology, Investigation, Formal analysis. MN: Writing – review & editing, Methodology. TS: Funding acquisition, Writing – review & editing, Supervision, Conceptualization. JJ: Writing – review & editing, Writing – original draft, Supervision, Project administration, Methodology, Funding acquisition, Formal analysis, Conceptualization.

Funding

The author(s) declare that financial support was received for the research, authorship, and/or publication of this article. This work was supported by the Medical Research Council United Kingdom (G0800498; JJ) and Medical Research Council United Kingdom MR/T002581/1 (TS) and Wellcome Trust 217199/Z/19/Z (TS).

Acknowledgments

We would like to thank Professor Alex Thomson for her support and Professor Talvinder Sihra for proof reading the manuscript.

Conflict of interest

The authors declare that the research was conducted in the absence of any commercial or financial relationships that could be construed as a potential conflict of interest.

The author(s) declared that they were an editorial board member of Frontiers, at the time of submission. This had no impact on the peer review process and the final decision.

Publisher's note

Supplementary material

The Supplementary material for this article can be found online at: https://www.frontiersin.org/articles/10.3389/fncel.2024.1423471/full#supplementary-material

References

Ali, H., Marth, L., and Krueger-Burg, D. (2020). Neuroligin-2 as a central organizer of inhibitory synapses in health and disease. *Sci. Signal.* 13:379. doi: 10.1126/scisignal.abd8379

Antonelli, R., Pizzarelli, R., Pedroni, A., Fritschy, J. M., Del Sal, G., Cherubini, E., et al. (2014). Pin1-dependent signalling negatively affects GABAergic transmission by modulating neuroligin2/gephyrin interaction. *Nat. Commun.* 5:5066. doi: 10.1038/ncomms6066

Arama, J., Abitbol, K., Goffin, D., Fuchs, C., Sihra, T. S., Thomson, A. M., et al. (2015). GABAA receptor activity shapes the formation of inhibitory synapses between

developing medium spiny neurons. *Front. Cell. Neurosci.* 9:290. doi: 10.3389/fncel.2015.00290

Brown, L. E., Fuchs, C., Nicholson, M. W., Stephenson, F. A., Thomson, A. M., and Jovanovic, J. N. (2014). Inhibitory synapse formation in a co-culture model incorporating GABAergic medium spiny neurons and HEK293 cells stably expressing GABAA receptors. *J. Vis. Exp.* 93:e52115. doi: 10.3791/52115

Brown, L. E., Nicholson, M. W., Arama, J. E., Mercer, A., Thomson, A. M., and Jovanovic, J. N. (2016). Gamma-aminobutyric acid type a (GABAA) receptor subunits play a direct structural role in synaptic contact formation via their N-terminal extracellular domains. *J. Biol. Chem.* 291, 13926–13942. doi: 10.1074/jbc.M116.714790

Chattopadhyaya, B., Di Cristo, G., Wu, C. Z., Knott, G., Kuhlman, S., Fu, Y., et al. (2007). GAD67-mediated GABA synthesis and signaling regulate inhibitory synaptic innervation in the visual cortex. *Neuron* 54, 889–903. doi: 10.1016/j.neuron.2007.05.015

Cherubini, E., and Ben-Ari, Y. (2023). GABA signaling: therapeutic targets for neurodegenerative and neurodevelopmental disorders. *Brain Sci.* 13:1240. doi: 10.3390/brainsci13091240

Chua, H. C., and Chebib, M. (2017). GABA(a) receptors and the diversity in their structure and pharmacology. *Adv. Pharmacol.* 79, 1–34. doi: 10.1016/bs.apha.2017.03.003

Connolly, C. N., Krishek, B. J., Mcdonald, B. J., Smart, T. G., and Moss, S. J. (1996a). Assembly and cell surface expression of heteromeric and homomeric gamma-aminobutyric acid type a receptors. *J. Biol. Chem.* 271, 89–96. doi: 10.1074/jbc.271.1.89

Connolly, C. N., Wooltorton, J. R., Smart, T. G., and Moss, S. J. (1996b). Subcellular localization of gamma-aminobutyric acid type a receptors is determined by receptor beta subunits. *Proc. Natl. Acad. Sci. U. S. A.* 93, 9899–9904. doi: 10.1073/pnas.93.18.9899

Connor, S. A., and Siddiqui, T. J. (2023). Synapse organizers as molecular codes for synaptic plasticity. *Trends Neurosci.* 46, 971–985. doi: 10.1016/j.tins.2023.08.001

Davenport, E. C., Pendolino, V., Kontou, G., Mcgee, T. P., Sheehan, D. F., Lopez-Domenech, G., et al. (2017). An essential role for the Tetraspanin LHFPL4 in the cell-type-specific targeting and clustering of synaptic GABA(a) receptors. *Cell Rep.* 21, 70–83. doi: 10.1016/j.celrep.2017.09.025

Duan, J., Pandey, S., Li, T., Castellano, D., Gu, X., Li, J., et al. (2019). Genetic deletion of GABA(a) receptors reveals distinct requirements of neurotransmitter receptors for GABAergic and glutamatergic synapse development. *Front. Cell. Neurosci.* 13:217. doi: 10.3389/fncel.2019.00217

Farrant, M., and Nusser, Z. (2005). Variations on an inhibitory theme: phasic and tonic activation of GABA(a) receptors. *Nat. Rev. Neurosci.* 6, 215–229. doi: 10.1038/nrn1625

Fritschy, J. M., and Panzanelli, P. (2006). Molecular and synaptic organization of GABAA receptors in the cerebellum: effects of targeted subunit gene deletions. *Cerebellum* 5, 275–285. doi: 10.1080/14734220600962805

Fritschy, J. M., and Panzanelli, P. (2014). GABAA receptors and plasticity of inhibitory neurotransmission in the central nervous system. *Eur. J. Neurosci.* 39, 1845–1865. doi: 10.1111/ejn.12534

Fritschy, J. M., Panzanelli, P., and Tyagarajan, S. K. (2012). Molecular and functional heterogeneity of GABAergic synapses. *Cell. Mol. Life Sci.* 69, 2485–2499. doi: 10.1007/s00018-012-0926-4

Fu, Z., and Vicini, S. (2009). Neuroligin-2 accelerates GABAergic synapse maturation in cerebellar granule cells. *Mol. Cell. Neurosci.* 42, 45–55. doi: 10.1016/j.mcn.2009.05.004

Fuchs, C., Abitbol, K., Burden, J. J., Mercer, A., Brown, L., Iball, J., et al. (2013). GABA(a) receptors can initiate the formation of functional inhibitory GABAergic synapses. *Eur. J. Neurosci.* 38, 3146–3158. doi: 10.1111/ejn.12331

Halff, E. F., Hannan, S., Kwanthongdee, J., Lesept, F., Smart, T. G., and Kittler, J. T. (2022). Phosphorylation of neuroligin-2 by PKA regulates its cell surface abundance and synaptic stabilization. *Sci. Signal.* 15:eabg2505. doi: 10.1126/scisignal.abg2505

Han, W., Shepard, R. D., and Lu, W. (2021). Regulation of GABA(a)Rs by transmembrane accessory proteins. *Trends Neurosci.* 44, 152–165. doi: 10.1016/j.tins.2020.10.011

Hannan, S., Minere, M., Harris, J., Izquierdo, P., Thomas, P., Tench, B., et al. (2020). GABA(a)R isoform and subunit structural motifs determine synaptic and extrasynaptic receptor localisation. *Neuropharmacology* 169:107540. doi: 10.1016/j.neuropharm.2019.02.022

Klausberger, T., Roberts, J. D., and Somogyi, P. (2002). Cell type- and input-specific differences in the number and subtypes of synaptic GABA(a) receptors in the hippocampus. *J. Neurosci.* 22, 2513–2521. doi: 10.1523/JNEUROSCI.22-07-02513.2002

Kowalczyk, S., Winkelmann, A., Smolinsky, B., Forstera, B., Neundorf, I., Schwarz, G., et al. (2013). Direct binding of GABAA receptor beta2 and beta3 subunits to gephyrin. *Eur. J. Neurosci.* 37, 544–554. doi: 10.1111/ejn.12078

Li, J., Han, W., Pelkey, K. A., Duan, J., Mao, X., Wang, Y. X., et al. (2017). Molecular dissection of Neuroligin 2 and Slitrk3 reveals an essential framework for GABAergic synapse development. *Neuron* 96:e8. doi: 10.1016/j.neuron.2017.10.003

Li, R. W., Yu, W., Christie, S., Miralles, C. P., Bai, J., Loturco, J. J., et al. (2005). Disruption of postsynaptic GABA receptor clusters leads to decreased GABAergic innervation of pyramidal neurons. *J. Neurochem.* 95, 756–770. doi: 10.1111/j.1471-4159.2005.03426.x

Lorenz-Guertin, J. M., Bambino, M. J., and Jacob, T. C. (2018). gamma2 GABA(a)R trafficking and the consequences of human genetic variation. *Front. Cell. Neurosci.* 12:265. doi: 10.3389/fncel.2018.00265

Maric, H. M., Kasaragod, V. B., Hausrat, T. J., Kneussel, M., Tretter, V., Stromgaard, K., et al. (2014). Molecular basis of the alternative recruitment of GABA(a) versus glycine receptors through gephyrin. *Nat. Commun.* 5:5767. doi: 10.1038/ncomms6767

Maric, H. M., Mukherjee, J., Tretter, V., Moss, S. J., and Schindelin, H. (2011). Gephyrin-mediated gamma-aminobutyric acid type a and glycine receptor clustering relies on a common binding site. *J. Biol. Chem.* 286, 42105–42114. doi: 10.1074/jbc.M111.303412

Mortensen, M., Patel, B., and Smart, T. G. (2011). GABA potency at GABA(a) receptors found in synaptic and Extrasynaptic zones. *Front. Cell. Neurosci.* 6:1. doi: 10.3389/fncel.2012.00001

Mortensen, M., and Smart, T. G. (2007). Single-channel recording of ligand-gated ion channels. *Nat. Protoc.* 2, 2826–2841. doi: 10.1038/nprot.2007.403

Mukherjee, J., Kretschmannova, K., Gouzer, G., Maric, H. M., Ramsden, S., Tretter, V., et al. (2011). The residence time of GABA(a)Rs at inhibitory synapses is determined by direct binding of the receptor alpha1 subunit to gephyrin. *J. Neurosci.* 31, 14677–14687. doi: 10.1523/JNEUROSCI.2001-11.2011

Nguyen, Q. A., Horn, M. E., and Nicoll, R. A. (2016). Distinct roles for extracellular and intracellular domains in neuroligin function at inhibitory synapses. *eLife* 5:236. doi: 10.7554/eLife.19236

Nguyen, Q. A., and Nicoll, R. A. (2018). The GABA(a) receptor beta subunit is required for inhibitory transmission. *Neuron* 98:e3. doi: 10.1016/j.neuron.2018.03.046

Oh, W. C., Lutzu, S., Castillo, P. E., and Kwon, H. B. (2016). De novo synaptogenesis induced by GABA in the developing mouse cortex. *Science* 353, 1037–1040. doi: 10.1126/science.aaf5206

Olsen, R. W., and Sieghart, W. (2009). GABA a receptors: subtypes provide diversity of function and pharmacology. *Neuropharmacology* 56, 141–148. doi: 10.1016/j.neuropharm.2008.07.045

Owens, D. F., and Kriegstein, A. R. (2002). Is there more to GABA than synaptic inhibition? *Nat. Rev. Neurosci.* 3, 715–727. doi: 10.1038/nrn919

Pallotto, M., and Deprez, F. (2014). Regulation of adult neurogenesis by GABAergic transmission: signaling beyond GABAA-receptors. *Front. Cell. Neurosci.* 8:166. doi: 10.3389/fncel.2014.00166

Raimondo, J. V., Richards, B. A., and Woodin, M. A. (2017). Neuronal chloride and excitability - the big impact of small changes. *Curr. Opin. Neurobiol.* 43, 35–42. doi: 10.1016/j.conb.2016.11.012

Rudolph, U., and Mohler, H. (2006). GABA-based therapeutic approaches: GABAA receptor subtype functions. *Curr. Opin. Pharmacol.* 6, 18–23. doi: 10.1016/j.coph.2005.10.003

Sallard, E., Letourneur, D., and Legendre, P. (2021). Electrophysiology of ionotropic GABA receptors. *Cell. Mol. Life Sci.* 78, 5341–5370. doi: 10.1007/s00018-021-03846-2

Scheiffele, P., Fan, J., Choih, J., Fetter, R., and Serafini, T. (2000). Neuroligin expressed in nonneuronal cells triggers presynaptic development in contacting axons. *Cell* 101, 657–669. doi: 10.1016/S0092-8674(00)80877-6

Schofield, P. R., Darlison, M. G., Fujita, N., Burt, D. R., Stephenson, F. A., Rodriguez, H., et al. (1987). Sequence and functional expression of the GABA a receptor shows a ligand-gated receptor super-family. *Nature* 328, 221–227. doi: 10.1038/328221a0

Schweizer, C., Balsiger, S., Bluethmann, H., Mansuy, I. M., Fritschy, J. M., Mohler, H., et al. (2003). The gamma 2 subunit of GABA(a) receptors is required for maintenance of receptors at mature synapses. *Mol. Cell. Neurosci.* 24, 442–450. doi: 10.1016/S1044-7431(03)00202-1

Scott, S., and Aricescu, A. R. (2019). A structural perspective on GABA(a) receptor pharmacology. *Curr. Opin. Struct. Biol.* 54, 189–197. doi: 10.1016/j.sbi.2019.03.023

Smart, T. G., and Mortensen, M. (2023). $GABA_A$ receptors in textbook of ion channels volume II: Properties, function, and pharmacology of the Superfamilies. Boca Raton, FL: CRC Press.

Smart, T. G., and Stephenson, F. A. (2019). A half century of gamma-aminobutyric acid. *Brain Neurosci. Adv.* 3:58249. doi: 10.1177/2398212819858249

Studer, R., Von Boehmer, L., Haenggi, T., Schweizer, C., Benke, D., Rudolph, U., et al. (2006). Alteration of GABAergic synapses and gephyrin clusters in the thalamic reticular nucleus of GABAA receptor alpha3 subunit-null mice. *Eur. J. Neurosci.* 24, 1307–1315. doi: 10.1111/j.1460-9568.2006.05006.x

Sudhof, T. C. (2008). Neuroligins and neurexins link synaptic function to cognitive disease. *Nature* 455, 903–911. doi: 10.1038/nature07456

Sudhof, T. C. (2017). Synaptic Neurexin complexes: a molecular code for the logic of neural circuits. *Cell* 171, 745–769. doi: 10.1016/j.cell.2017.10.024

Sudhof, T. C. (2018). Towards an understanding of synapse formation. *Neuron* 100, 276–293. doi: 10.1016/j.neuron.2018.09.040

Thomas, P., Mortensen, M., Hosie, A. M., and Smart, T. G. (2005). Dynamic mobility of functional GABAA receptors at inhibitory synapses. *Nat. Neurosci.* 8, 889–897. doi: 10.1038/nn1483

Thompson, S. M. (2024). Modulators of GABA(a) receptor-mediated inhibition in the treatment of neuropsychiatric disorders: past, present, and future. *Neuropsychopharmacology* 49, 83–95. doi: 10.1038/s41386-023-01728-8

Thomson, A. M., and Jovanovic, J. N. (2010). Mechanisms underlying synapse-specific clustering of GABA(a) receptors. *Eur. J. Neurosci.* 31, 2193–2203. doi: 10.1111/j.1460-9568.2010.07252.x

Tretter, V., Ehya, N., Fuchs, K., and Sieghart, W. (1997). Stoichiometry and assembly of a recombinant GABAA receptor subtype. *J. Neurosci.* 17, 2728–2737. doi: 10.1523/JNEUROSCI.17-08-02728.1997

Tretter, V., Jacob, T. C., Mukherjee, J., Fritschy, J. M., Pangalos, M. N., and Moss, S. J. (2008). The clustering of GABA(a) receptor subtypes at inhibitory synapses is facilitated via the direct binding of receptor alpha 2 subunits to gephyrin. *J. Neurosci.* 28, 1356–1365. doi: 10.1523/JNEUROSCI.5050-07.2008

Tretter, V., Kerschner, B., Milenkovic, I., Ramsden, S. L., Ramerstorfer, J., Saiepour, L., et al. (2011). Molecular basis of the gamma-aminobutyric acid a receptor alpha3 subunit interaction with the clustering protein gephyrin. *J. Biol. Chem.* 286, 37702–37711. doi: 10.1074/jbc.M111.291336

Wei, W., Zhang, N., Peng, Z., Houser, C. R., and Mody, I. (2003). Perisynaptic localization of delta subunit-containing GABA(a) receptors and their activation by GABA spillover in the mouse dentate gyrus. *J. Neurosci.* 23, 10650–10661. doi: 10.1523/JNEUROSCI.23-33-10650.2003

Yamasaki, T., Hoyos-Ramirez, E., Martenson, J. S., Morimoto-Tomita, M., and Tomita, S. (2017). GARLH family proteins stabilize GABA(a) receptors at synapses. *Neuron* 93:e6. doi: 10.1016/j.neuron.2017.02.023

Zhang, C., Atasoy, D., Arac, D., Yang, X., Fucillo, M. V., Robison, A. J., et al. (2010). Neurexins physically and functionally interact with GABA(a) receptors. *Neuron* 66, 403–416. doi: 10.1016/j.neuron.2010.04.008

frontiers | Frontiers in Cellular Neuroscience

TYPE Review
PUBLISHED 24 July 2024
DOI 10.3389/fncel.2024.1414955

OPEN ACCESS

EDITED BY
Anirban Paul,
The Pennsylvania State University,
United States

REVIEWED BY
Alexei Morozov,
Virginia Tech, United States
Dongqing Shi,
University of Michigan, United States

*CORRESPONDENCE
Robert Machold
robert.machold@nyulangone.org

RECEIVED 09 April 2024
ACCEPTED 08 July 2024
PUBLISHED 24 July 2024

CITATION
Machold R and Rudy B (2024) Genetic approaches to elucidating cortical and hippocampal GABAergic interneuron diversity. *Front. Cell. Neurosci.* 18:1414955. doi: 10.3389/fncel.2024.1414955

Genetic approaches to elucidating cortical and hippocampal GABAergic interneuron diversity

Robert Machold[1]* and Bernardo Rudy[1,2,3]

[1]Neuroscience Institute, New York University Grossman School of Medicine, New York, NY, United States, [2]Department of Neuroscience and Physiology, New York University Grossman School of Medicine, New York, NY, United States, [3]Department of Anesthesiology, Perioperative Care and Pain Medicine, New York University Grossman School of Medicine, New York, NY, United States

GABAergic interneurons (INs) in the mammalian forebrain represent a diverse population of cells that provide specialized forms of local inhibition to regulate neural circuit activity. Over the last few decades, the development of a palette of genetic tools along with the generation of single-cell transcriptomic data has begun to reveal the molecular basis of IN diversity, thereby providing deep insights into how different IN subtypes function in the forebrain. In this review, we outline the emerging picture of cortical and hippocampal IN speciation as defined by transcriptomics and developmental origin and summarize the genetic strategies that have been utilized to target specific IN subtypes, along with the technical considerations inherent to each approach. Collectively, these methods have greatly facilitated our understanding of how IN subtypes regulate forebrain circuitry via cell type and compartment-specific inhibition and thus have illuminated a path toward potential therapeutic interventions for a variety of neurocognitive disorders.

KEYWORDS

GABAergic interneurons, intersectional genetics, transgenic, cortex, hippocampus, subtypes

Introduction

The marvelous diversity of locally projecting GABAergic inhibitory interneurons (INs) has been appreciated for over a century, beginning with the detailed morphological observations of Ramón y Cajal. In recent years, our understanding of the molecular and circuit specialization of cortical and hippocampal INs has increased dramatically, and there are a number of excellent reviews to recommend on this subject (Klausberger and Somogyi, 2008; Tremblay et al., 2016; Bandler et al., 2017; Pelkey et al., 2017; Wamsley and Fishell, 2017; Feldmeyer et al., 2018; Lim et al., 2018; Huang and Paul, 2019; Fishell and Kepecs, 2020; Gutman-Wei and Brown, 2021; Kullander and Topolnik, 2021; Topolnik and Tamboli, 2022; Kessaris and Denaxa, 2023). The discovery of molecular markers corresponding to the distinct electrophysiological and morphological properties of IN subpopulations has greatly facilitated work on elucidating IN subtype functionality (Kawaguchi and Kubota, 1996; Kawaguchi and Kubota, 1997; Kubota et al., 2011; Rudy et al., 2011; Taniguchi et al., 2011; Pfeffer et al., 2013; He et al., 2016; Gouwens et al., 2020; Bugeon et al., 2022) and has guided the implementation of genetic strategies to experimentally target and manipulate molecularly defined cell subtypes

(Urban and Rossier, 2012; Huang et al., 2014; Taniguchi, 2014; He and Huang, 2018; Hanson and Wester, 2022). Over the last few decades, a remarkable toolkit for genetic targeting of cell populations in the mouse has been developed, including transgenic and knock-in approaches to express recombinases (e.g., Cre or Flp) under the control of specific marker genes (driver lines), as well as reporter lines to express fluorescent proteins or other actuators in response to recombinase activity (Madisen et al., 2010, 2012, 2015; Taniguchi et al., 2011; He et al., 2016; Daigle et al., 2018). In parallel, there has been a revolution in recombinant AAV (rAAV)-based viral vectors to target IN cell populations, including recombinase-dependent constructs (e.g., AAV-DIO) as well as the ongoing discovery and implementation of cell type-specific short promoters in mouse and other species (Dimidschstein et al., 2016; Haery et al., 2019; Hrvatin et al., 2019; Mehta et al., 2019; Nair et al., 2020; Vormstein-Schneider et al., 2020; Duba-Kiss et al., 2021; Graybuck et al., 2021; Hoshino et al., 2021; Mich et al., 2021; Challis et al., 2022; Pouchelon et al., 2022; Campos et al., 2023; Niibori et al., 2023).

The emergence of technologies to evaluate single-cell transcriptomes (scRNAseq) has revolutionized our understanding of molecular cell type heterogeneity and, in particular, has provided deep insights into mouse forebrain GABAergic IN subtype diversity (Zeisel et al., 2015; Tasic et al., 2016; Paul et al., 2017; Harris et al., 2018; Munoz-Manchado et al., 2018; Saunders et al., 2018; Tasic et al., 2018; Gouwens et al., 2020; Yao et al., 2021). In this review, we present an exposition of the transcriptomic analysis of cortical and hippocampal INs published recently by the Allen Institute (Yao et al., 2021; portal.brain-map.org/atlases-and-data/rnaseq; 10x genomics with 10x smart-seq taxonomy). This extensive dataset, comprised of scRNAseq profiles from roughly 170,000 curated INs clustered into 123 bins, provides an exceptionally high-resolution view of IN transcriptomic identity and serves as a useful framework for the discussion of subtype-specific genetic targeting strategies (Figure 1). Along this framework, we have aligned individual heatmaps of gene expression, with transcript levels represented as color intensity corresponding to trimmed mean (25–75%) counts per million (CPM) on a log2 scale.[1] From a bird eye view, this approach illustrates the main contours of IN subtype diversity, with five primary markers covering the vast majority of INs: Meis2, Id2, Vip, Sst, and Pvalb (Figure 1; see abbreviations list at the end of the manuscript). The relative abundance of each primary IN group varies across different cortical/hippocampal areas (Kim et al., 2017; Yao et al., 2021), but in somatosensory barrel field cortex, the proportions are approximately Id2 (18%), VIP (12%), Sst (30%), and Pvalb (40%) (Rudy et al., 2011; Tremblay et al., 2016; Machold et al., 2023). We have also included scatterplots (see footnote 1) of the overall IN landscape to highlight the locales of selected IN subtypes. It is important to note that the study by Yao et al. (2021) includes data on the proportions of each individual IN subtype across different cortical and hippocampal areas, as well as a mapping of the previous transcriptomic clusters described in a study by Tasic et al. (2018) to the bins in this expanded dataset.

Within several of these primary marker groups, we have delineated specific subpopulations that are fundamentally distinct based on their transcriptomic properties as well as other features described in the literature. For example, the Id2 group (Mayer et al., 2018; Machold et al., 2023) encompasses neurogliaform cells (NGFC), α7/canopy cells (Schuman et al., 2019), Serpinf1 cells (a subset of CCK+ INs; Tasic et al., 2018), NtnG1 cells (a hippocampal-specific population that expresses NDNF; see Figure 2), and Sncg cells (CCK+ basket cells). VIP cells here are represented as one main group, with some of the VIP cells clustering in the Serpinf1 and Sncg groups (see Figure 3 for further details). The SST INs exhibit extensive diversity overall (see Figure 4), but a primary distinction is between the SST long range (SST LR) subtype and the other SST INs. Likewise, PV INs can be initially delineated into PV (basket type) and PV axo-axonic (AAC) or chandelier cells (ChC; see Figure 5). Note that while these primary markers are reasonably thorough in tiling the overall IN population, there are notable areas of some overlap (e.g., PV/SST; Figures 4, 5), as well as certain minor populations that do not appear to express any of the markers (e.g., Igfbp6 Calb2 INs within the VIP group; see Figure 3).

Developmental origins

Cortical, hippocampal, and striatal INs arise during embryonic development from two primary germinal zones in the ventral telencephalon, namely, the medial ganglionic eminence (MGE) and the caudal ganglionic eminence (CGE), and undergo an extensive migration to reach their final locations (Bandler et al., 2017; Hu et al., 2017; Wamsley and Fishell, 2017; Lim et al., 2018; Llorca and Deogracias, 2022; Bandler and Mayer, 2023; Kessaris and Denaxa, 2023). All INs are specified from progenitors that express Ascl1 (Mash1) during neurogenesis (Casarosa et al., 1999) and acquire their GABAergic IN identity via expression of a cascade of Dlx homeobox transcription factors (Anderson et al., 1997, 1999; Eisenstat et al., 1999; Stuhmer et al., 2002). The Dlx genes (Dlx1 and 2, and Dlx5 and 6) are organized into two genetic loci, with each pair sharing an intergenic enhancer that was found to be sufficient in transgenic mice to drive expression of reporters or recombinases in newly born INs (Zerucha et al., 2000; Ghanem et al., 2003, 2007). Thus, all INs can be labeled developmentally using Dlx5/6-Cre (Dlx6a-Cre) (Monory et al., 2006) or Dlx5/6-Flpe (Miyoshi et al., 2010) transgenic drivers in combination with reporter lines. More recently, a number of pan-GABAergic knock-in drivers have been made that allow for targeting of all cortical and hippocampal INs, for example, Slc32a1-Cre (VGAT-Cre) (Vong et al., 2011), Slc32a1-Flpo (Vgat-Flpo) (Daigle et al., 2018), and Gad2-Cre (Taniguchi et al., 2011). Of particular interest, rAAV constructs utilizing promoters based on the Dlx intergenic enhancers have been shown to be effective in targeting INs from development through adult ages, both in rodents and other species including non-human primates (Dimidschstein et al., 2016). Other broad GABAergic-specific promoters recently shown to function in rAAVs include mGAD65a (Hoshino et al., 2021). Given the potential translational utility of IN-specific viral vectors, this is an area of exciting ongoing innovation (Duba-Kiss et al., 2021; Campos et al., 2023).

INs originating from the MGE include all PV and SST subtypes, as well as a subset of Id2 NGFC; these MGE lineages all arise from progenitors that express the homeobox transcription factor Nkx2.1 (Sussel et al., 1999). While most cortical and hippocampal MGE INs

1 portal.brain-map.org/atlases-and-data/rnaseq

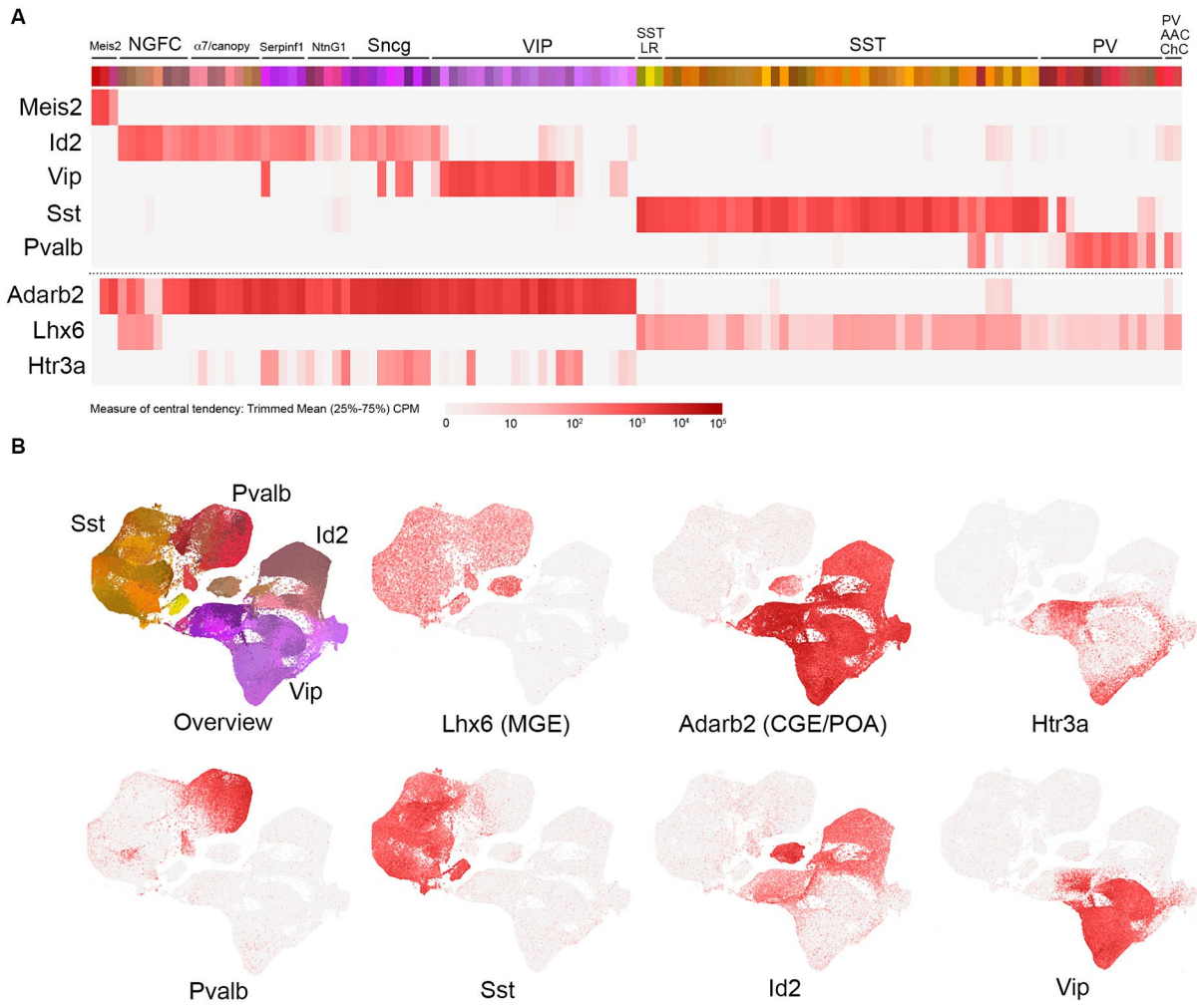

FIGURE 1
Overview of cortical and hippocampal IN transcriptomic subtypes. **(A)** Schematic view of the total GABAergic IN scRNAseq data from Yao et al. (2021) [portal.brain-map.org/atlases-and-data/rnaseq; whole cortex and hippocampus—10x genomics (2020) with 10x smart-seq taxonomy (2021)]. Each colored bin represents a subpopulation of cells clustered as described by Yao et al. (2021). Groups of related bins are annotated here based on gene expression and putative cell type assignment, with heatmaps of the primary gene marker mRNA levels represented as trimmed means (counts per million: CPM, with color intensity reflecting log2 scale as indicated) aligned below. These primary markers are as follows(from left to right): Meis2, Id2, Vip, Sst, and Pvalb. The Id2 IN population encompasses neurogliaform cells (NGFCs), α7/canopy cells, Serpinf1, NtnG1, and Sncg subtypes (detailed in Figure 2). The VIP group is represented as one group here, with details elaborated in Figure 3. The Sst group is represented as two main groups: Sst long-range (Sst LR) and other Sst subtypes (detailed in Figure 4). Likewise, the Pvalb group is represented as PV and PV axo-axonic/chandelier (PV AAC/ChC) subtypes (detailed in Figure 5). To complement these primary IN markers, heatmaps for Adarb2 (CGE/POA) and Lhx6 (MGE) are shown, along with Htr3a. **(B)** Scatterplots of the total IN population from Yao et al. (2021) illustrate the transcriptomic diversity of IN subtypes in reduced dimensional space. The color scheme of the bins in A is maintained in the cell representations shown in the overview, and the general locations of the four main IN groups (Id2, Vip, Sst, and Pvalb) are indicated. Individual scatterplots for Lhx6 (MGE), Adarb2 (CGE/POA), Htr3a, Pvalb, Sst, Id2, and Vip are shown, with the red color intensity reflecting the trimmed mean CPM values (log2 scale) as in **(A)**.

rapidly downregulate Nkx2.1 expression immediately following their specification (Marin et al., 2000), they maintain expression of Lhx6, a homeobox transcription factor whose expression is induced by Nkx2.1 (Du et al., 2008), into adulthood, at least at low levels (Figure 1). Thus, in principle, all MGE-derived INs can be targeted using Nkx2.1 or Lhx6 cumulative genetics. BAC transgenic cre driver lines have been generated for both Nkx2.1 (Xu et al., 2008) and Lhx6 (Fogarty et al., 2007). The Nkx2-1(BAC)-Cre driver efficiently labels the vast majority of MGE-derived INs when paired with a cre reporter line (e.g., Ai14), albeit with somewhat less efficiency for SST INs arising from the dorsal MGE, likely due to a genomic positional effect on the expression of the BAC transgene (see "Caveats and other considerations" section below). However, the dorsal MGE can be targeted with an Nkx6.2-CreER driver (Sousa et al., 2009; He et al., 2016). In addition to Nkx2.1(BAC)-Cre, an Nkx2.1-Flpo knock-in line has been generated that efficiently labels all MGE-derived INs when paired with a flp-dependent reporter line (He et al., 2016).

While recent efforts to identify a progenitor marker similar to Nkx2.1 that is selective for the CGE have been promising (Lee et al., 2022), this is still a work in progress; however, the expression of Adarb2 appears to mark all CGE-derived INs in the adult (Figure 1). Broad labeling of CGE INs has been achieved using an Htr3a(BAC)-EGFP transgenic line (DH30Gsat) (Lee et al., 2010;

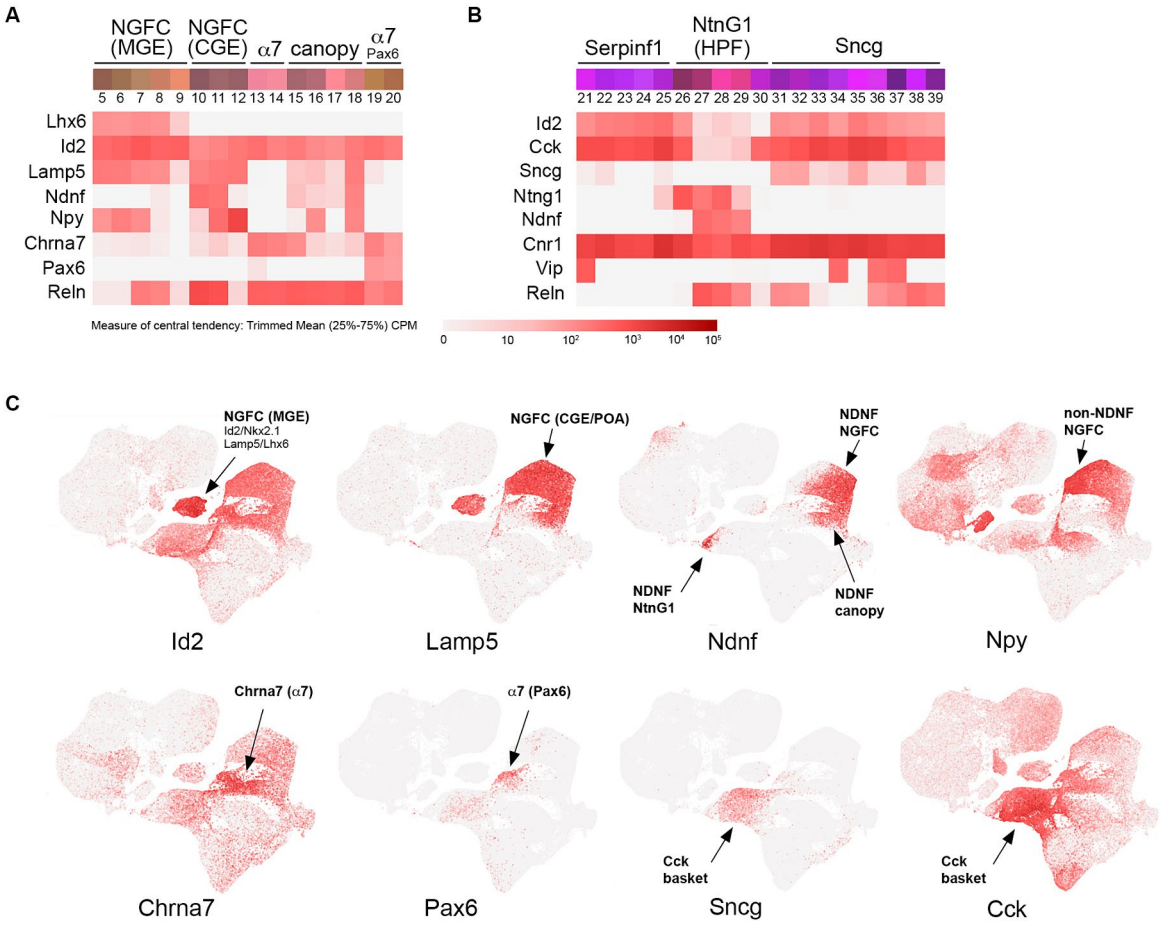

FIGURE 2
Id2-Lamp5-Sncg transcriptomic subtypes. **(A)** INs corresponding to MGE-derived NGFC (Lhx6+; bins 5–9), CGE-derived NGFC (non-Lhx6+; bins 10–12), α7 cells (bins 13–14 and Pax6+ bins 19–20), and canopy cells (bins 15–18). Heatmaps for Lhx6, Id2, Lamp5, Ndnf, Npy, Chrna7, Pax6, and Reln transcripts are aligned below (trimmed mean CPM in each bin is represented by red color intensity on a log2 scale, as indicated by the guide located below the heatmaps). **(B)** INs corresponding to Serpinf1 (bins 21–25), NtnG1 (bins 26–30), and Sncg (bins 31–39) cells. Heatmaps for Id2, Cck, Sncg, NtnG1, Ndnf, Cnr1, Vip, and Reln are aligned below. **(C)** Individual scatterplots for Id2, Lamp5, Ndnf, Npy, Chrna7, Pax6, Sncg, and Cck are shown, with annotation and arrows highlighting the approximate location of the indicated IN subtypes. HPF, hippocampal formation.

Vucurovic et al., 2010), with the latter being an effective means to distinguish all CGE INs from MGE INs in postnatal animals (Rudy et al., 2011). However, the pan-CGE IN labeling observed in this high copy number BAC transgenic line is a distortion of the endogenous Htr3a expression pattern, which is largely restricted to a CCK+ subset of VIP and Sncg INs in the adult mouse brain (Figure 1) (Ferezou et al., 2002; Machold et al., 2023). This discrepancy likely arises from the widespread but transient nature of Htr3a (5HT3aR) expression in most CGE INs, consistent with a developmental role for 5HT3aR during early migration of CGE INs into the cortex (Murthy et al., 2014). Additional Htr3a driver lines include an Htr3a(BAC)-Cre line (NO152) (Gerfen et al., 2013; Miyoshi et al., 2015) and an Htr3a-Flpo knock-in line (Schuman et al., 2019); the latter driver lines each label a subset of CGE INs in somatosensory barrel field cortex as compared to Htr3a(BAC)-EGFP (Machold et al., 2023) [Htr3a(BAC)-Cre; Ai9: ~90%; Htr3a-Flpo (het); Ai65F: ~30%; Htr3a-Flpo (hom); Ai65F: ~60%]. Other broad markers for CGE INs expressed during development include Prox1 (Rubin and Kessaris, 2013; Miyoshi et al., 2015) and Sp8/Sp9 (Ma et al., 2012; Wei et al., 2019).

Meis2

INs expressing the homeobox transcription factor Meis2 have not been well characterized to date. These INs likely originate from the lateral ganglionic eminence (LGE), where Meis2 expression is highly expressed in comparison to the MGE (Toresson et al., 1999). Meis2 INs have been described in the olfactory bulb (Allen et al., 2007) and are sparsely present in the cortical white matter (Frazer et al., 2017), along with a heterogeneous population of interstitial INs (von Engelhardt et al., 2011). While a full discussion of the origins and diversity of olfactory bulb INs is beyond the scope of this review, it is worth mentioning that these INs (Meis2 and non-Meis2 subtypes) arise from the LGE during embryogenesis (Stenman et al., 2003) and continue to be generated postnatally

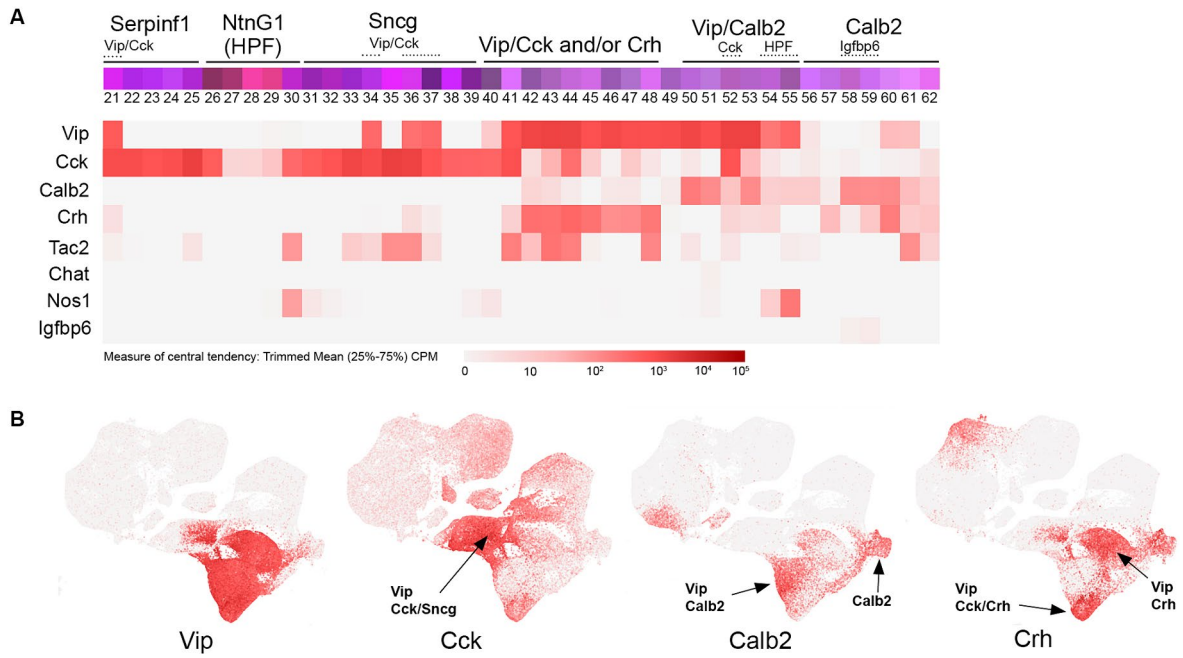

FIGURE 3
VIP transcriptomic subtypes. **(A)** Overview of VIP IN transcriptomic diversity, with heatmaps for Vip, Cck, Calb2, Crh, Tac2, Chat, Nos1, and Igfbp6 transcripts shown below (trimmed mean CPM in each bin is represented by red color intensity on a log2 scale, as indicated by the guide located below the heatmaps). Several subgroups of VIP INs are annotated above the colored bins, including Vip/Cck, Vip/Crh, Vip/Calb2, and Calb2 (non-VIP) cells. **(B)** Individual scatterplots for Vip, Cck, Calb2, and Crh are shown, with annotation and arrows highlighting the approximate location of the indicated IN subtypes. HPF, hippocampal formation.

from neurogenic niches along the subventricular zone, following which they migrate along the rostral migratory stream to populate the olfactory bulb (Lledo et al., 2008).

Id2

The population of CGE INs has been recognized for some time to include both VIP+ and non-VIP+ cells, with Reelin (Reln) being a marker for the latter group (Lee et al., 2010; Miyoshi et al., 2010; Rudy et al., 2011; Tremblay et al., 2016). However, since Reln is also expressed in the majority of SST INs (Miyoshi et al., 2010; Pohlkamp et al., 2014), it is not ideal for identifying non-VIP+ CGE INs, particularly in deeper cortical layers. Although less studied, this group represents a significant fraction of the INs in superficial layers: 90% in L1 and 27% in L2/3 (more abundant than SST INs in these layers). The main IN species in this non-VIP+ CGE group is the neurogliaform cell (NGFC), an IN subtype with distinctive spider-like axonal morphology and extensive local output connectivity due to its cloud-like volume release of GABA (Olah et al., 2009; Overstreet-Wadiche and McBain, 2015). NGFCs have been identified in slice preparations by their high levels of NPY expression (Kubota et al., 2011), and through the use of an NPY(BAC)-hrGFP transgenic line (Chittajallu et al., 2013; Neske et al., 2015; Schuman et al., 2019), but as with Reelin, NPY is also expressed in the majority of SST INs (e.g., see Figure 4). Thus, in the absence of a specific marker such as PV, SST, or VIP, NGFC have been overlooked in many IN studies due to the lack of molecular tools to target this unique IN population. Interestingly though, in contrast to other IN subtypes, NGFC INs were found to arise from both Nkx2.1+ (MGE) and non-Nkx2.1+ lineages, with the majority of hippocampal NGFCs being of MGE origin (Tricoire et al., 2011; Pelkey et al., 2017). The embryonic origin of non-Nkx2.1+ NGFCs (the overwhelming majority of cortical NGFCs) has been proposed to be the preoptic area (POA), based on the use of an Nkx5.1(BAC)-Cre transgenic line (Hmx3-iCre) (Gelman et al., 2009). Since the POA is largely derived from Nkx2.1+ progenitors (He et al., 2016), it remains to be determined which non-Nkx2.1+ germinal zone within the POA or ventral CGE territories gives rise to cortical NGFCs. Nevertheless, this Nkx5.1(BAC)-iCre transgenic line has been useful for targeting and characterizing the development of the cortical NGFC population (Niquille et al., 2018; Gomez et al., 2023).

In addition to NGFC, a number of other understudied IN species within the umbrella of non-VIP/non-SST/non-PV INs (i.e., the fourth major group) have been identified and characterized to date. These include a sparse CCK+ basket cell type that was initially described in the hippocampus (Katona et al., 1999; Klausberger and Somogyi, 2008) and studied in the cortex using a GAD65-EGFP transgenic line (Galarreta et al., 2004). Furthermore, studies on the INs residing in cortical layer 1 (L1) have revealed that these cells included NGFCs but also other distinctive IN cell types (Ibrahim et al., 2020; Schuman et al., 2021; Huang et al., 2024). Examination of single-cell transcriptomic data to uncover differentially expressed genes in IN subpopulations has revealed a number of new markers for these IN subtypes, including Lamp5 and Sncg as putative markers for NGFC and CCK basket cells, respectively (Tasic et al., 2016, 2018; Gouwens et al., 2020; Dudok et al., 2021a). Within the Lamp5 population, NDNF was identified as a marker selectively expressed in the majority of L1 INs, including L1 NGFCs (Tasic et al., 2016) and a distinct L1

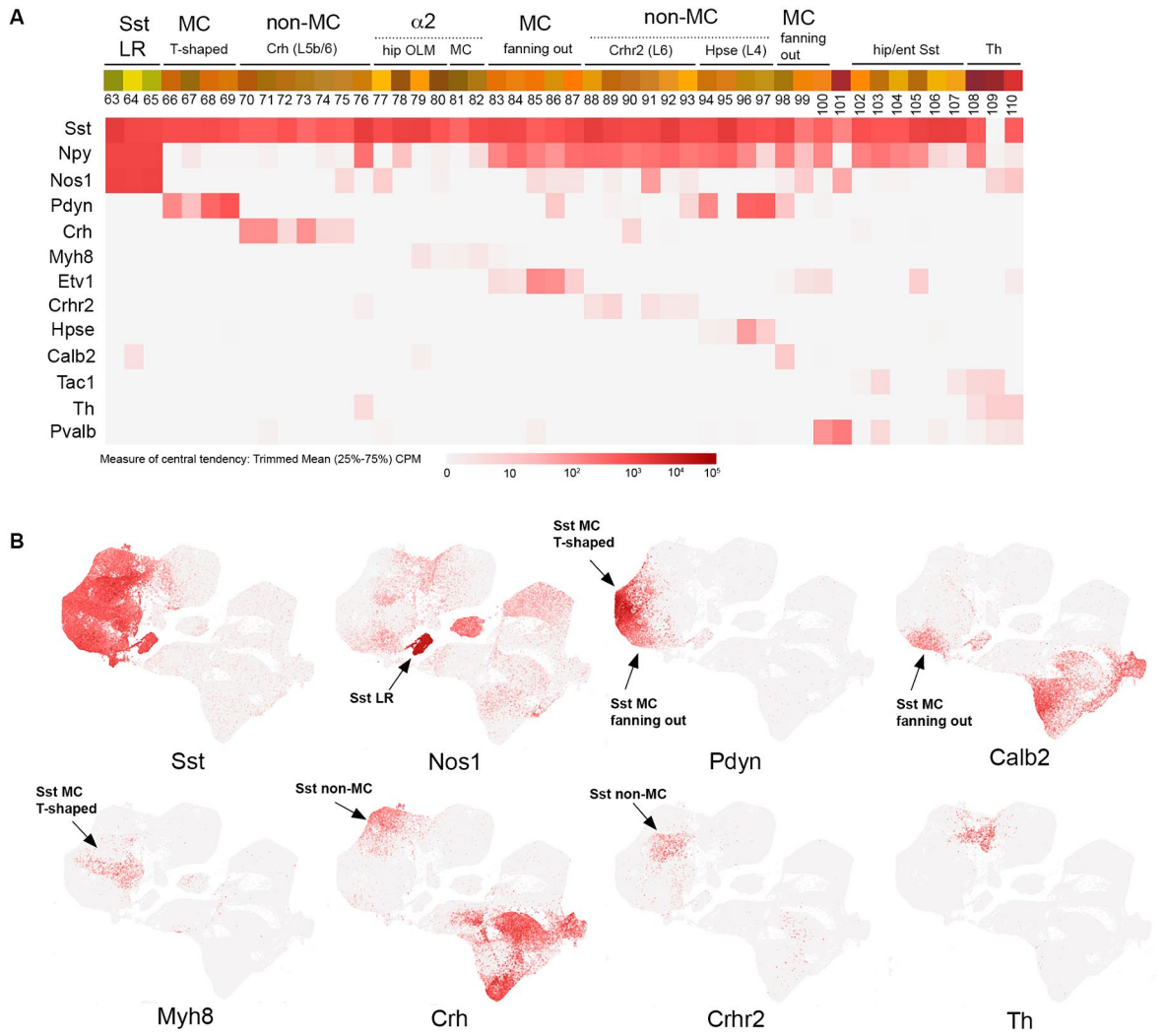

FIGURE 4
SST transcriptomic subtypes. **(A)** Overview of SST IN transcriptomic diversity, with heatmaps for Sst, Npy, Nos1, Pdyn, Crh, Myh8, Etv1, Crhr2, Hpse, Calb2, Tac1, Th, and Pvalb transcripts shown below (trimmed mean CPM in each bin is represented by red color intensity on a log2 scale, as indicated by the guide located below the heatmaps). Different subgroups of SST INs are annotated above the colored bins, including Sst LR (long range), MC (Martinotti), non-MC (non-Martinotti), α2 (Chrna2-expressing OLM and MC cells), hippocampal/entorhinal Sst cells, and Th cells. **(B)** Individual scatterplots for Sst, Nos1, Pdyn, Calb2, Myh8, Crh, Crhr2, and Th are shown, with annotation and arrows highlighting the approximate location of the indicated IN subtypes.

NDNF IN population given the name canopy cells based on their superficial location and extended horizontal axonal morphology (Schuman et al., 2019). In addition to NDNF INs, the population of L1 INs was also found to include cells with high levels of α7 nAChR (Chrna7) expression (Schuman et al., 2019), a cell type that roughly corresponds to the "single bouquet cell" (Lee et al., 2015; Zhu, 2023). Recently, the gene Id2 was identified as a marker whose expression encompasses the vast majority of INs within this heterogeneous fourth group (Machold et al., 2023).

To a first approximation, Id2 INs represent ~18% of total INs in the cortex and are roughly comprised of NGFC (~80%) and non-NGFC (~20%) subtypes (Machold et al., 2023). Examination of the IN clusters from Yao et al. (2021) reveals the different IN species from the cortex and hippocampus that make up the Id2 IN group (Figure 2). First, within the NGFC INs, there is a fundamental lineage split between those that are MGE-derived, that is, arising from Nkx2.1+ progenitors, as evidenced by residual Lhx6 expression (Figure 2A, bins 5–9), and those that are CGE (or non-Nkx2.1+ POA) derived (Figure 2A, bins 10–12). In the overall IN scatterplot, these Id2/Nkx2.1 (or Lamp5/Lhx6) cells form a distinct cluster away from other NGFCs (Figure 2C). Interestingly, these MGE-derived NGFCs are mostly found within the hippocampus where they comprise the majority of NGFCs, in contrast to the cortex where most NGFCs are CGE/POA derived (Overstreet-Wadiche and McBain, 2015; Yao et al., 2021). These MGE-origin NGFCs have been targeted using intersectional genetics with an Id2-CreER driver line combined with Nkx2.1-Flpo (e.g., Id2-CreER; Nkx2.1-Flpo; Ai65 for tdTomato labeling) and in mouse cortex were found to be a sparse NGFC population located mainly in deep cortical layers (Krienen et al., 2020; Valero et al., 2021). By optotagging these cells (Id2-CreER; Nkx2.1-Flpo; Ai80), they could be identified during silicon probe recordings and were found to exhibit a uniquely anti-correlated activity profile

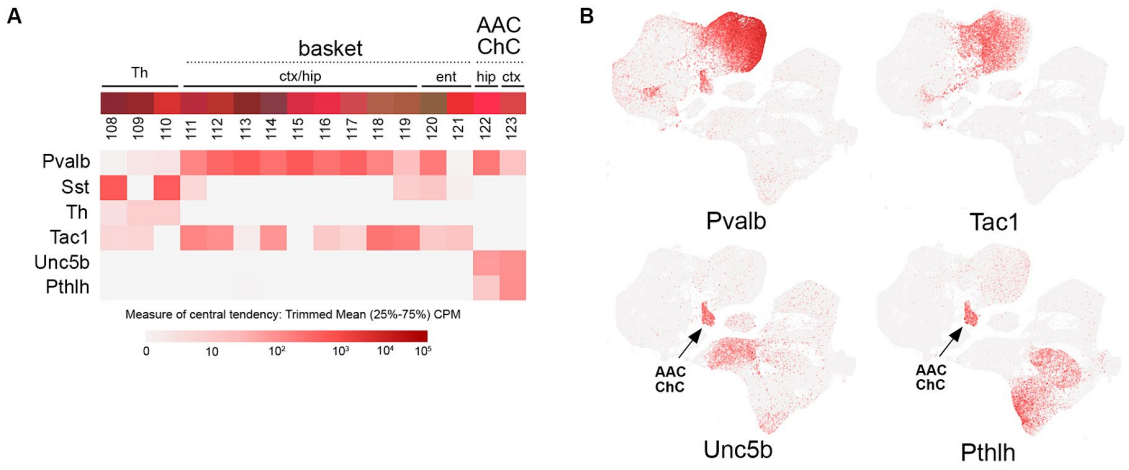

FIGURE 5
PV transcriptomic subtypes. **(A)** Overview of PV (Pvalb) IN transcriptomic diversity, with heatmaps for Pvalb, Sst, Th, Tac1, Unc5b, and Pthlh transcripts shown below (trimmed mean CPM in each bin is represented by red color intensity on a log2 scale, as indicated by the guide located below the heatmaps). The two main groups of PV INs (basket; bins 111–119, and axo-axonic/chandelier; bins 122–123) are annotated above the colored bins. **(B)** Individual scatterplots for Pvalb, Tac1, Unc5b, and Pthlh are shown, with annotation and arrows highlighting the axo-axonic/chandelier (AAC/ChC) cluster.

during cortical down states in sleep (Valero et al., 2021). Also of interest is the observation from comparative studies that this IN type is proportionally more abundant in the primate cortex compared to the mouse (Hodge et al., 2019; Krienen et al., 2020).

NGFCs of CGE origin are comprised of two main subtypes: those that express NDNF and are mostly located within L1 (or hippocampal SLM), and those that are non-NDNF that are located in L2-6. The primary NDNF+ NGFC population (bin 11) expresses moderate levels of NPY (bin 10, located mainly in the frontal cortex, has relatively low levels of NPY) but high levels of Reln; this is in contrast to the non-NDNF NGFC population (bin 12) that expresses very high levels of NPY but is only weakly Reln+ (Figure 2A). In addition to the NDNF NGFC INs, there are two other distinct branches of NDNF+ INs (bins 15–18, Figure 2A, and bins 27–29, Figure 2B). The first branch (bins 15–18) likely encompasses the NDNF canopy cell population identified in L1 via the use of an NPY(BAC)-hrGFP transgenic reporter line to distinguish NDNF NGFC from NDNF canopy cells (Schuman et al., 2019). However, endogenous NPY expression level alone does not appear to be sufficient to resolve NDNF IN subtype heterogeneity (Gouwens et al., 2020). Consistent with this, intersectional genetic targeting with NDNF-Flpo and NPY-Cre does not distinguish L1 NGFC from canopy cells (Hartung et al., 2024), likely due to low levels of NPY expression in the latter. Thus, a multifactorial genetic approach is necessary to fully appreciate NDNF IN diversity, especially across species (Chartrand et al., 2023). The second NDNF+ branch (bins 27–29; Figure 2B) is distinguished by the expression of NtnG1 and its selective hippocampal location (HPF), but the identity of these cells is presently unknown. Several NDNF driver lines have been developed for targeting NDNF cells, including NDNF-dgCre (destabilized cre) (Tasic et al., 2016), NDNF-Cre (Schuman et al., 2019), NDNF-CreER, and NDNF-Flpo (Abs et al., 2018).

In addition to NDNF INs, cortical L1 also harbors a smaller population of INs that can be distinguished by their high levels of Chrna7 expression (α7 cells) (Boyle et al., 2011; Schuman et al., 2019). These α7 INs are largely restricted to L1 and express Reln and Cck, but for the most part, do not express NDNF (Figure 2). Interestingly, even within this α7+ IN population, there are two distinct branches, with one expressing the paired box transcription factor Pax6 (bins 19–20), a marker previously identified in a subset of L1 cells (Zeisel et al., 2015). The other α7 branch (bins 13–14) can be distinguished by the expression of Egln3 and Deptor (Yao et al., 2021; Chartrand et al., 2023), two markers that are also expressed in an adjacent canopy cell type (bin 15), perhaps indicative of some molecular continuity between α7 and canopy cell types. Targeting of α7 cells using an existing Chrna7-Cre knock-in driver line (Rogers et al., 2012) or with two separate knock-in lines made by us (Chrna7-CreER and Chrna7-ires-dgCre) was not successful due to misexpression of Cre in all cases, indicating that the endogenous regulation of Chrna7 transcription is particularly sensitive to sequence alterations introduced during driver line construction.

Beyond α7 INs, there exists an astonishing degree of transcriptomic diversity in strongly Cck+INs (Figure 2B), despite their relative sparseness (~3% of total INs). Two main molecular groups of Cck INs have been distinguished by the Allen Institute in their transcriptomic analyses: Serpinf1 and Sncg (Tasic et al., 2018; Yao et al., 2021). Both the Serpinf1 (bins 21–25) and Sncg (bins 31–39) express high levels of Cck and Cnr1, which encodes for the CB1 cannabinoid receptor. These cells likely correspond to the CCK basket cell type identified in the hippocampus (Klausberger and Somogyi, 2008) and cortex (Galarreta et al., 2004) that exhibits the unusual property of DSI (depolarization-induced suppression of inhibition) mediated by retrograde signaling via endocannabinoids released by pyramidal neurons (Wilson and Nicoll, 2001). Intriguingly, a subset of these basket cells express the vesicular glutamate transporter VGLUT3 (Somogyi et al., 2004; Fasano et al., 2017; Pelkey et al., 2020). Recently, a Sncg-Flpo line has been described that enables genetic targeting of these CCK basket cells (Lee et al., 2021; Dudok et al.,

2021a). Some of the subtypes within the Serpinf1 and Sncg groups express VIP (bins 21, 34, 36, and 37) and thus would be included in VIP/CCK intersectional targeting (see below).

VIP

VIP INs comprise a diverse population of CGE-derived cells mostly located in cortical layers 2–4 (Pronneke et al., 2015; Apicella and Marchionni, 2022) that include interneuron-selective (IS) subtypes, that is, INs that mainly target other INs instead of pyramidal neurons. Consistent with this, VIP INs have been shown to play an important role in mediating cortical disinhibition during arousal (e.g., during active exploration), primarily via the inhibition of SST INs (Lee et al., 2013; Pi et al., 2013; Tremblay et al., 2016; Kullander and Topolnik, 2021). While VIP IN subtype diversity has not yet been fully characterized, a fundamental distinction between VIP/CCK and VIP/CR (Calb2) subtypes has emerged. Using intersectional genetic approaches with a VIP-Flpo driver line combined with either CCK-Cre or CR (Calb2)-Cre, VIP/CCK INs were found to include cells with multipolar morphologies that exhibited output to both pyramidal neurons and other INs, whereas VIP/CR cells possessed bipolar morphologies and targeted efferents to INs (mainly Sst) exclusively (He et al., 2016; Paul et al., 2017; Guet-McCreight et al., 2020). Examination of the transcriptomic profile of VIP INs reveals a complex array of subtypes (Figure 3), even within the VIP/CCK subpopulation which as described above includes some INs from the Sncg and Serpinf1 groups (bins 21, 34, 36, and 37) in addition to those within the main VIP group (bins 41, 44, and 52). A comparative transcriptomic analysis of VIP/CCK and VIP/CR subtypes (Paul et al., 2017) with the overall VIP population revealed the existence of a third group of VIP INs that do not express either Cck or Calb2 (Tasic et al., 2018); some of the markers that exhibit overlap with this group include Crh (Harris et al., 2018; Riad et al., 2022), Tac2 and Cxcl14 (Wu et al., 2022), and Pcdh11x (Tasic et al., 2018). Other markers for subsets of VIP INs include Chat (Dudai et al., 2021), Mybpc1 and Parm1 (Jiang et al., 2023), and Nos1 in hippocampal VIP INs (bins 54 and 55). Of note, there is a largely uncharacterized population of Calb2 INs within the VIP group that are weakly or non-VIP expressing (bins 56–62), some of which are marked by Igfbp6 (bins 58–59) (Tasic et al., 2016), underscoring the diversity of Calb2 INs in the cortex (Cauli et al., 2014).

SST

SST INs as a group exhibit a tremendous amount of transcriptomic diversity (Figure 4), consistent with the emerging evidence for specialized circuit functions of individual SST IN subtypes (Xu et al., 2013; Tremblay et al., 2016; Muñoz et al., 2017; Schwiedrzik and Freiwald, 2017; Green et al., 2023; Hostetler et al., 2023; Wu et al., 2023; Chamberland et al., 2024). In the sensory cortex, in contrast to VIP cells, most SST IN somas are located in deep layers (L5-6) (reviewed in Tremblay et al., 2016). To a first approximation, SST INs can be divided into long range (LR), Martinotti (MC), and non-Martinotti (non-MC) groups that diverge early in development (Fisher et al., 2024), with additional subtypes evident within each category by adulthood (Figure 4). SST LR INs are characterized by extensive axonal projections that can span cortical and even extracortical areas; thus, they are actually GABAergic projection neurons rather than INs *per se* (Caputi et al., 2013). These cells (bins 63–65) express particularly high levels of Nos1 (nNos) and have been targeted using Sst/Nos1 intersectional genetics, pairing Sst-Flpo with a Nos1-CreER driver that with one dose of tamoxifen selects for these strongly Nos1+ SST cells (He et al., 2016). Intriguingly, the transcriptome of SST LR cells is so distinct that they cluster away from the rest of the Sst IN population (Figure 4B). Martinotti SST INs, loosely defined as SST INs that project axons to superficial cortical layers (L1-3) and target the apical dendrites of pyramidal cells (in addition to other INs), can be delineated as T-shaped (most of the ascending axon in L1) or fanning-out (axon in L2/3 and L1), with each type exhibiting distinct activity profiles in somatosensory cortex during whisking behavior (Muñoz et al., 2017). In the hippocampus, the analogous SST population are the oriens-lacunosum moleculare (OLM) INs, which characteristically extend their axons from the oriens to SLM to target pyramidal neuron apical dendrites (Klausberger and Somogyi, 2008; Caroni, 2015).

A number of recent studies have begun to illuminate the diversity of SST MC, non-MC, and OLM IN populations using intersectional genetic approaches (He et al., 2016; Nigro et al., 2018; Gouwens et al., 2020; Wu et al., 2023; Chamberland et al., 2024). However, the insights from earlier work using mouse lines (GIN, X94, and X98) with short promoter GAD67-EGFP transgenic insertions that labeled different subsets of SST INs due to remarkably specific founder effects should not be overlooked as this approach enabled the first characterization of non-MC and MC subtypes (Ma et al., 2006; Xu et al., 2013; Hostetler et al., 2023). Currently, there are a variety of genetic approaches to target SST IN subtypes. A subset of L5 MC with T-shaped morphology and OLM INs can be labeled using a Chrna2(BAC)-Cre line with excellent specificity (Hilscher et al., 2017; Siwani et al., 2018; Hilscher et al., 2023; Chamberland et al., 2024); this population (bins 77–82) includes the SST/Myh8 subtype in cortex (Wu et al., 2023). A distinct T-shaped MC population (bins 66–69) can be targeted by using a Pdyn-CreER driver and excluding SST/NPY+ cells by taking advantage of the cre-dependent reporter Ai9 design, in which Flp activity removes reporter expression (Pdyn-CreER; NPY-Flpo; Ai9) (Wu et al., 2023). Fanning-out MC subtypes can be targeted using intersectional genetics with Sst-Flpo, for example, SST/CR (bin 98), which labels a fanning-out subtype primarily located in L2/3, likely corresponding to the GIN population (Ma et al., 2006; He et al., 2016; Nigro et al., 2018). A distinct deep layer fanning-out subtype can be targeted with SST/Etv1 intersectional genetics (bins 83–87) (Wu et al., 2023). SST non-MC INs are also surprisingly diverse, with Sst/Crh (L5b-6; bins 70–76), Sst/Crhr2 (L6; bins 88–93), and Sst/Hpse (L4; bins 94–97) subtypes (Wu et al., 2023). Of note, there is some degree of continuity between the Sst and Pvalb IN clusters, with a Th + subtype forming a bridge of cells between the two main groups (Figure 4B). Tac1 is a marker for most Pvalb INs (Pfeffer et al., 2013) (Figure 5A), but there is an Sst/Tac1 subtype described recently in the hippocampus that interestingly exhibits a high degree of output selectivity for PV INs vs. pyramidal cells (Chamberland et al., 2024), supporting the idea that in addition to VIP/CR INs, some SST IN subtypes may act in a disinhibitory manner (Xu et al., 2013).

PV

Despite being the most abundant IN population, PV INs appear to possess less transcriptomic diversity than the other IN groups (Figure 5). However, there is a fundamental division in the PV group between the basket cell (bins 111–121) and axo-axonic cell (AAC) or chandelier cell (ChC; bins 122–123) subtypes, reflected by the distinct clustering of AAC from other PV INs (Figure 5B). Cortical PV basket cells are located across L2-6, where their axons form extensive perisomatic baskets on pyramidal neurons (reviewed in Tremblay et al., 2016). In contrast, cortical PV ChC INs are mostly located in L2, where they extend their axons horizontally to target the axon initial segments of pyramidal neurons (Taniguchi et al., 2013; Inan and Anderson, 2014). Targeting of PV INs as a group can be achieved with Pvalb-Cre or Flp driver lines, or by use of rAAVs with PV IN-specific promoters (e.g., E2) (Vormstein-Schneider et al., 2020). Expression of PV itself in basket cells can vary across cortical areas; for example, most entorhinal/perirhinal fast-spiking basket cells express little to no PV (Nigro et al., 2021). Selective targeting of ChC was first achieved by taking advantage of the distinct developmental trajectories of ChC and PV basket cells. Interestingly, while most MGE INs (including PV basket cells) rapidly downregulate Nkx2.1 expression following their specification, ChC are born relatively late during embryogenesis and also maintain Nkx2.1 expression for a few days during their tangential migration (~E18-P3). Thus, ChC can be targeted using an Nkx2.1-CreER (tamoxifen-inducible cre) knock-in driver to selectively label Nkx2.1+ ChC INs at late embryonic stages (Taniguchi et al., 2011, 2013). To improve experimental access to ChC in adult animals, this developmental Nkx2.1-CreER strategy was paired with a Cre-dependent Flp reporter line (R26-CAG-loxP-stop-loxP-Flpo), thereby resulting in permanent Flp expression in ChC (Lu et al., 2017). In combination with Flp-dependent rAAV injection (rAAV-fDIO-EGFP), this approach enabled the robust labeling and fine reconstruction of individual ChC INs (Wang et al., 2019). More recently, ChC/AAC INs have been successfully targeted with Unc5B-CreER in the hippocampus (Dudok et al., 2021b) and brain-wide using intersectional genetics with Unc5B-CreER; Nkx2.1-Flpo or Pthlh-Flpo; and Nkx2.1-Cre pairing (Raudales et al., 2024).

Drivers and reporters

Many years of diligent work by numerous laboratories (but particularly the Huang Lab and the Zeng/Allen Institute group) have led to a truly impressive genetic toolkit of driver and reporter lines for targeting IN cell types (Madisen et al., 2010, 2012, 2015; Taniguchi et al., 2011; He et al., 2016; Daigle et al., 2018). A summary of some of the main Cre and Flp driver lines presently available that are relevant for IN studies is shown in Table 1. Along with many other terrific resources provided by the Allen Institute, the transgenic characterization page is highly recommended as it provides an extensive collection of images across the brain of the cumulative cell labeling arising from a variety of driver lines, in addition to the acute expression pattern of each driver[2] (Harris et al., 2014). Along with the development of driver lines, an extensive array of reporter lines has been established, enabling the conditional expression of a wide range of actuators, including fluorescent proteins, Ca^{2+} activity indicators, engineered channelrhodopsins (ChR), and chemogenetic tools (Table 1). These include the popular Cre-dependent tdTomato reporter lines made by the Allen Institute Ai9 and Ai14 (same reporter as Ai9, except with the neo selection cassette removed) and Ai32 (ChR2/EYFP). For intersectional genetics, building on the pioneering work from the Dymecki Lab (Dymecki et al., 2002; Branda and Dymecki, 2004; Dymecki and Kim, 2007; Jensen and Dymecki, 2014), there is now an expanding range of Cre- and Flp-dependent reporters, including Ai65 (Cre + Flp ➔ tdTomato), Ai80 (Cre + Flp ➔ CatCh ChR), RC::FPSit (Cre + Flp ➔ synaptophysin-YFP), R26-dual-tTA (Cre + Flp ➔ tet activator), RC::FL-hM3Dq (Cre + Flp ➔ Gq DREADD), RC::FL-hM4Di (Cre + Flp ➔ Gi DREADD), and recently developed TIGRE-based lines such as Ai195 (Cre + Flp ➔ GCaMP7s) and Ai211 (Cre + Flp ➔ ChrimsonR ChR). In addition, several intersectional/subtractive reporters have been made that enable dual fluorescent labeling of complementary cell populations: RC::FLTG (Flp ➔ tdTomato; Flp + Cre ➔ EGFP) and IS (Cre ➔ tdTomato; Cre + Flp ➔ EGFP). For viral-based reporters, there is an extensive collection of Cre-dependent (rAAV-DIO or rAAV-flex) or Flp-dependent (rAAV-fDIO) constructs available (e.g., Addgene.org), as well as ongoing innovation in intersectional AAV design (Fenno et al., 2020; Pouchelon et al., 2022; Hughes et al., 2024). Resources for animal husbandry, colony management, and genotyping methods are available from vendors/repositories such as Jackson Laboratories and Taconic Biolabs.

Caveats and other considerations

A fundamental consideration in the use of transgenic targeting strategies is the nature of the transgenic driver line itself, with different caveats to bear in mind when working with short transgenes (e.g., Dlx6a-Cre), BAC transgenic lines (e.g., Htr3a(BAC)-Cre), or knock-in lines. Short transgenes constructed using defined enhancer elements typically less than ~2 kb assemble into multicopy concatemers prior to genomic integration and can exhibit dramatic positional effects on expression that vary from founder to founder depending on the location of the transgene insertion (Palmiter and Brinster, 1986). As described above in the SST IN section, the EGFP expressing transgenic lines X94 and GIN that, respectively, label non-MC and L2/3 MC SST subsets originated from founders harboring Gad67-EGFP transgene insertions subject to remarkably specific but unpredictable positional effects (Ma et al., 2006). Transgenic lines constructed using the Dlx5/6 intergenic enhancer (e.g., Dlx6a-Cre and Dlx5/6-Flpe) benefit from being driven by endogenous Dlx1/2 expression and thus may be more resistant to genomic positional effects; this might account at least in part for the success of rAAV-pDlx constructs (Dimidschstein et al., 2016). BAC transgenic approaches entail the inclusion of typically 50–100 kb of 5′ and 3′ sequence flanking the gene of interest to recapitulate the expression pattern exhibited by the endogenous gene and minimize positional effects (Heintz, 2000); this approach has led to a vast collection of transgenic EGFP and cre driver lines via the GENSAT project (Gong et al., 2003; Gerfen et al., 2013). However, BAC transgenic lines can still exhibit founder effects arising from variation in transgene copy number and the location of genomic

2 connectivity.brain-map.org/transgenic

TABLE 1 Driver lines and intersectional reporters.

Driver line	Nature of transgene	Jax/MMRRC stock #	Reference	PMID
Calb2-ires-Cre	KI	010774	Taniguchi et al. (2011)	21943598
Cck-ires-Cre	KI	012706	Taniguchi et al. (2011)	21943598
Chrna2(BAC)-Cre	BAC tg	MMRRC_036502-UCD	Gerfen et al. (2013)	24360541
Crh-ires-Cre	KI	021704	Taniguchi et al. (2011)	21943598
Crh-ires-Flpo	KI	031559	Salimando et al. (2020)	32277042
Dlx6a-Cre	Tg	008199	Monory et al. (2006)	16908411
Dlx5/6-Flpe	Tg	010815	Miyoshi et al. (2010)	20130169
Gad2-ires-Cre	KI	028867	Taniguchi et al. (2011)	21943598
GIN	Tg	003718	Ma et al. (2006)	16687498
Hmx3(BAC)-Cre	BAC tg	n/a	Gelman et al. (2009)	19625528
Htr3a(BAC)-Cre	BAC tg (NO152Gsat)	MMRRC_036680-UCD	Gerfen et al. (2013)	24360541
Htr3a(BAC)-EGFP	BAC tg (DH30Gsat)	MMRRC_000273-UNC	Lee et al. (2010)	21159951
Htr3a-ires-Flpo	KI	030755	Schuman et al. (2019)	30413647
Id2-CreER	KI	016222	Rawlins et al. (2009)	19855016
Lamp5-P2A-Flpo	KI	037340	n/a	n/a
Ndnf-ires-Cre	KI	030757	Schuman et al. (2019)	30413647
Ndnf-ires-dgCre	KI	028536	Tasic et al. (2016)	26727548
Ndnf-ires-CreERT2	KI	034875	Abs et al. (2018)	30269988
Ndnf-ires-Flpo	KI	034876	Abs et al. (2018)	30269988
Nkx2.1(BAC)-Cre	BAC tg	008661	Xu et al. (2008)	17990269
Nkx2.1-CreER	KI	014552	Taniguchi et al. (2011)	21943598
Nkx2.1-ires-Flpo	KI	028577	He et al. (2016)	27618674
Nos1-CreER	KI	014541	Taniguchi et al. (2011)	21943598
Npy-ires-Cre	KI	027851	Milstein et al. (2015)	26402609
Npy-ires-Flpo	KI	030211	Daigle et al. (2018)	30007418
Npy(BAC)-hrGFP	BAC tg	006417	van den Pol et al. (2009)	19357287
Pvalb-ires-Cre	KI	017320	Hippenmeyer et al. (2005)	15836427
Pvalb-T2A-Cre	KI	012358	Madisen et al. (2010)	20023653
Slc32a1-ires-Cre	KI	028862	Vong et al. (2011)	21745644
Slc32a1-ires-Flpo	KI	029591	Daigle et al. (2018)	30007418
Sncg-ires-Flpo	KI	034424	Lee et al. (2021)	34387544
Sst-ires-Cre	Ki	013044	Taniguchi et al. (2011)	21943598
Sst-ires-Flpo	KI	031629	He et al. (2016)	27618674
Vip-ires-Cre	KI	010908	Taniguchi et al. (2011)	21943598
Vip-ires-Flpo	KI	028578	He et al. (2016)	27618674
X94	Tg	006334	Ma et al. (2006)	16687498

Intersectional reporter line	Genomic locus	Jax/MMRRC stock #	Reference	PMID
Ai65 (tdTomato)	R26	021875	Madisen et al. (2015)	25741722
Ai80 (CatCh)	R26	025109	Daigle et al. (2018)	30007418
Ai195 (jGCaMP7s)	TIGRE	034112	Allen Institute	n/a
Ai211 (ChrimsonR)	TIGRE	037379	Allen Institute	n/a
RC::FPSit (synaptophysin-YFP)	R26	030206	Niederkofler et al. (2016)	27851959
RC:: FLTG (tdTomato/EGFP)	R26	026932	Plummer et al. (2015)	26586220
IS (tdTomato/EGFP)	R26	028582	He et al. (2016)	27618674
R26-dual-tTA (tTA)	R26	036304	Matho et al. (2021)	34616069
RC::FL-hM4Di	R26	MMRRC 043516-UCD	Lusk et al. (2022)	35086530
RC::FL-hM3Dq	R26	026942	Sciolino et al. (2016)	27264177

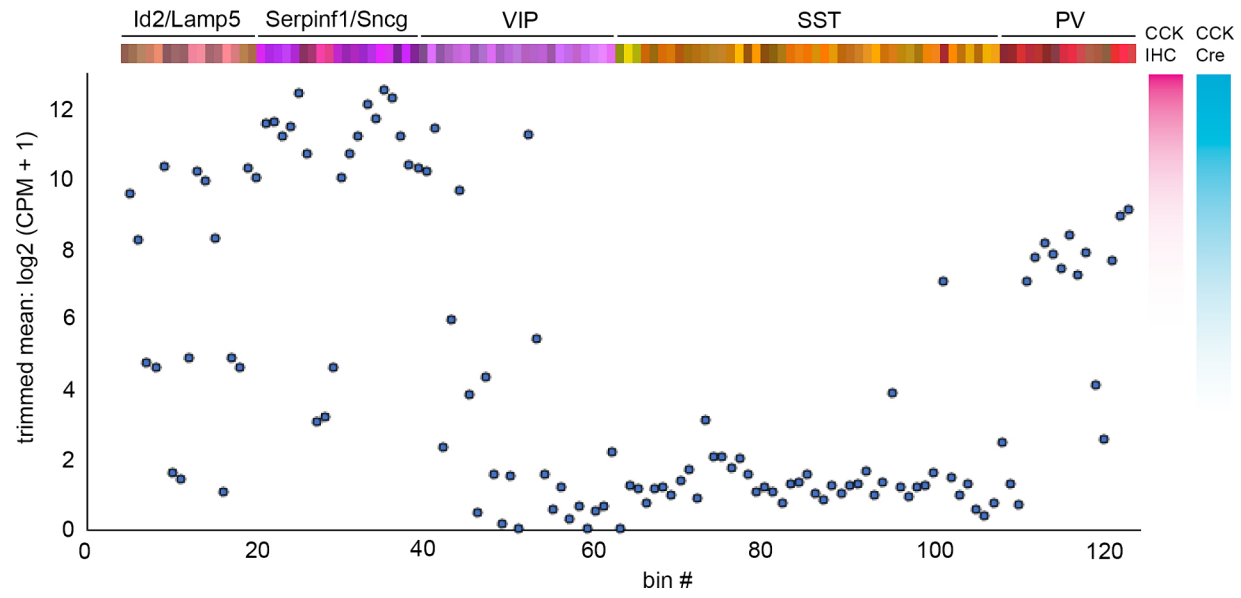

FIGURE 6
Cck mRNA expression levels across INs. Plot of trimmed mean log2 (CPM + 1) Cck mRNA transcript levels for each IN bin using values from Yao et al. (2021). To the right of the plot are illustrative comparisons of the hypothetical degree of cell labeling using CCK immunohistochemistry (IHC) or Cck-Cre; reporter cumulative genetic labeling. Note that the latter method labels a substantial number of Id2/Lamp5 and PV INs (Machold et al., 2023).

insertion, as evidenced within the GENSAT collection[3] and observed with the Htr3a(BAC)-EGFP and Htr3a(BAC)-Cre lines (Machold et al., 2023). Furthermore, BAC transgenic lines may overexpress genes that are within the BAC genomic region that flanks the gene of interest, for example, there is ectopic Htr3b expression in the Htr3a(BAC)-Cre line (Winterer et al., 2019).

Also of fundamental importance when using driver lines expressing recombinases such as Cre or Flp is the spatiotemporal expression trajectory of the driver gene itself. For many of the commonly used IN driver lines, the cumulative recombination pattern obtained by pairing driver and reporter lines aligns well with the mature expression profile (Harris et al., 2014). However, certain genes may exhibit developmental expression that then results in much broader reporter expression beyond the intended target population (e.g., NDNF; Schuman et al., 2019). In those cases, it is necessary to use Cre- or Flp-dependent viral reporters that can be injected at adult ages (e.g., rAAV-DIO or rAAV-fDIO constructs) or to design driver lines with destabilized cre recombinases (NDNF-dgCre; Tasic et al., 2016) or tamoxifen-inducible CreER (NDNF-CreER; Abs et al., 2018). Furthermore, it is crucial to consider the relative specificity of a driver gene's expression across different cell types. An example of this is Cck, which is expressed at high levels in a subset of VIP and Sncg/Serpinf1 INs but also at lower levels in NGFC as well as PV cells (Figure 6), resulting in significant labeling of those INs in Cck-Cre intersectional crosses (Machold et al., 2023). Another example of this is the "off-target" labeling of a subset of PV INs in Sst-Cre; Ai14 animals (Hu et al., 2013), which is not an artifact of genetics but instead a reflection of the existence of a small population of PV cells with sufficient Sst expression to drive reporter expression, also evident in the transcriptome data (Figures 4, 5). A critical caveat with both PV and SST drivers is that both genes are expressed at low levels in subsets of pyramidal cells: PV in L5 PCs (Hafner et al., 2019; Palicz et al., 2024) and SST in CA3 hippocampal PCs (Muller-Komorowska et al., 2020). Thus, future studies that target PV or SST INs should strongly consider using intersectional approaches (e.g., by using rAAV-pDlx DIO constructs instead of those with pan-neuronal promoters) to avoid incidental expression in PCs.

It is difficult to predict the level of recombinase expression that will result in a particular reporter being expressed, although in general, cre recombinase is somewhat more efficient than flp (Zhao et al., 2023). The efficiency of recombination of different reporters can vary substantially depending on the loxP and/or frt flanked transcriptional stop cassettes (or DIO/fDIO design); for example, we have observed that the intersectional tdTomato reporter Ai65 is more sensitive and labels more cells when compared with RC::FLTG. A key consideration with any recombinase-conditional or enhancer-dependent approach is the leakiness of the expression system. Genetic tdTomato reporter lines such as Ai9/Ai14 or Ai65 exhibit excellent signal-to-noise ratios (i.e., recombinase-dependent expression vs. leakiness), but a low level of background expression that is difficult to detect with fluorescent proteins may be more consequential with reporters expressing sensitive actuators such as other recombinases. In contrast to genetic reporter lines which are typically present as single copies, viral reporters are usually injected at high titer, with multiplicity of infection rates $>10^3$ depending on the distance from the injection site. Both rAAV-DIO and rAAV-fDIO constructs have been found to exhibit some leakiness depending on the viral preparation and other variables (Fischer et al., 2019; Botterill et al., 2021); thus, it is essential to include control injections in non-transgenic animals (i.e., not expressing recombinase) to assess off-target expression. Finally, while rAAVs engineered with cell type-specific promoters and/or enhancers show great promise, leakiness and specificity issues must be carefully evaluated. For example, the CamK2 promoter that is widely used for pyramidal neuron targeting in rAAV constructs has recently been shown to exhibit some leaky expression in INs (Veres et al., 2023). As observed previously with

3 gensat.org

short enhancer-based transgenes (Hostetler et al., 2023), short promoters in rAAV constructs (e.g., pSst44; Hrvatin et al., 2019) may display a remarkable degree of specificity for subpopulations of INs that exhibit shared circuit properties (Green et al., 2023) but may not drive expression in the entire IN group being targeted (in this case, SST INs).

An important consideration, perhaps of a more philosophical nature, is how to think about cell type diversity and its relationship to transcriptomic variation. Overall, there appears to be some degree of transcriptomic continuity across certain cortical and hippocampal IN subtypes (Harris et al., 2018; Scala et al., 2021; Yao et al., 2021), supporting the idea that the specific genetic identity of individual INs within a subtype is influenced by local context or even stochastic events during their developmental trajectory and circuit integration. While the transcriptomic properties of each IN likely underlie their morphological and electrophysiological attributes to a large extent, the relationship is complex (e.g., Paul et al., 2017; Gouwens et al., 2020), and there are many additional variables that could be considered when defining an IN "cell type" (Petilla Interneuron Nomenclature Group et al., 2008; Zeng, 2022; Mao and Staiger, 2024). Fundamental attributes of an IN include its input/output organization, which is determined in large part by the morphology and location of its dendrites and axons, but also by molecular interactions between a diverse assortment of cell surface and secreted proteins that begin during early development (Honig and Shapiro, 2020; Sanes and Zipursky, 2020). Many different types of proteins can contribute to an IN's responsiveness to a specific input in addition to the ion channels and other cell surface molecules that regulate intrinsic membrane properties, including those that participate in downstream intracellular signaling pathways, or protein trafficking to specific cellular compartments. Last but not least, the engagement of a specific IN population during a particular behavioral context can be strongly influenced by the expression of receptors for neuromodulators such as acetylcholine, norepinephrine, and serotonin, or for peptidergic signaling (e.g., oxytocin). Thus, when delineating IN cell subtypes, it ultimately comes down to deciding which attributes to prioritize and which are the most critical in determining the cell's functional role in brain circuitry.

Why has evolution favored inhibitory IN subtype diversity? The most straightforward explanation lies in the increasingly complex structure of neocortical pyramidal neurons from mice to humans, particularly of their distinctive apical dendrites whose branching complexity has expanded in tandem with the superficial cortical layers (L1-3) that support cortical–cortical connectivity (Schmidt and Polleux, 2021; Galakhova et al., 2022). Considering that even mouse pyramidal neurons each receive on the order of thousands of excitatory inputs, the specialization of GABAergic inputs to different pyramidal neuron compartments and other IN subtypes allows for enhanced control over the integration of information streams arriving at the apical dendrites and soma/basal dendrites [top-down and bottom-up inputs, respectively; reviewed in Schuman et al., 2021]. With regard to human health, there is an emerging consensus that dysfunction of specific IN subtypes may contribute to a wide range of neurocognitive disorders (Ferguson and Gao, 2018; Gallo et al., 2020; Goff and Goldberg, 2021; Yang et al., 2022), including autism (Lunden et al., 2019; Contractor et al., 2021), epilepsy (Jiang et al., 2016), schizophrenia (Dienel and Lewis, 2019), depression (Fogaca and Duman, 2019), and Alzheimer's disease (Hernandez-Frausto et al., 2023). Furthermore, the elaborate developmental trajectory of INs may lead them to be particularly susceptible to environmental perturbations (Pai et al., 2023) or toxic insults (Ansen-Wilson and Lipinski, 2017). It is our hope that a deeper understanding of the marvelous diversity of INs will help illuminate the inner workings of the brain and facilitate the elucidation of novel therapeutic approaches for treating neurological diseases.

Author contributions

RM: Conceptualization, Data curation, Visualization, Writing – original draft, Writing – review & editing. BR: Funding acquisition, Resources, Supervision, Writing – review & editing.

Funding

The author(s) declare financial support was received for the research, authorship, and/or publication of this article. This study was supported by NIH grants P01NS074972 and R01NS133751 (PI: BR).

Acknowledgments

We thank Gord Fishell and members of the Rudy Lab for their helpful comments and discussions.

Conflict of interest

The authors declare that the research was conducted in the absence of any commercial or financial relationships that could be construed as a potential conflict of interest.

Publisher's note

References

Abs, E., Poorthuis, R. B., Apelblat, D., Muhammad, K., Pardi, M. B., Enke, L., et al. (2018). Learning-related plasticity in dendrite-targeting layer 1 interneurons. *Neuron* 100, 684–699. doi: 10.1016/j.neuron.2018.09.001

Allen, Z. J. 2nd, Waclaw, R. R., Colbert, M. C., and Campbell, K. (2007). Molecular identity of olfactory bulb interneurons: transcriptional codes of periglomerular neuron subtypes. *J. Mol. Histol.* 38, 517–525. doi: 10.1007/s10735-007-9115-4

Anderson, S. A., Eisenstat, D. D., Shi, L., and Rubenstein, J. L. (1997). Interneuron migration from basal forebrain to neocortex: dependence on Dlx genes. *Science* 278, 474–476. doi: 10.1126/science.278.5337.474

Anderson, S., Mione, M., Yun, K., and Rubenstein, J. L. (1999). Differential origins of neocortical projection and local circuit neurons: role of dlx genes in neocortical interneuronogenesis. *Cereb. Cortex* 9, 646–654. doi: 10.1093/cercor/9.6.646

Ansen-Wilson, L. J., and Lipinski, R. J. (2017). Gene-environment interactions in cortical interneuron development and dysfunction: A review of preclinical studies. *Neurotoxicology* 58, 120–129. doi: 10.1016/j.neuro.2016.12.002

Apicella, A. J., and Marchionni, I. (2022). Vip-expressing GABAergic neurons: Disinhibitory vs. inhibitory motif and its role in communication across neocortical areas. *Front. Cell. Neurosci.* 16:811484. doi: 10.3389/fncel.2022.811484

Bandler, R. C., and Mayer, C. (2023). Deciphering inhibitory neuron development: the paths to diversity. *Curr. Opin. Neurobiol.* 79:102691. doi: 10.1016/j.conb.2023.102691

Bandler, R. C., Mayer, C., and Fishell, G. (2017). Cortical interneuron specification: the juncture of genes, time and geometry. *Curr. Opin. Neurobiol.* 42, 17–24. doi: 10.1016/j.conb.2016.10.003

Botterill, J. J., Khlaifia, A., Walters, B. J., Brimble, M. A., Scharfman, H. E., and Arruda-Carvalho, M. (2021). Off-target expression of Cre-dependent adeno-associated viruses in wild-type C57BL/6J mice. *eNeuro* 8:Eneuro.0363–21.2021. doi: 10.1523/ENEURO.0363-21.2021

Boyle, M. P., Bernard, A., Thompson, C. L., Ng, L., Boe, A., Mortrud, M., et al. (2011). Cell-type-specific consequences of Reelin deficiency in the mouse neocortex, hippocampus, and amygdala. *J. Comp. Neurol.* 519, 2061–2089. doi: 10.1002/cne.22655

Branda, C. S., and Dymecki, S. M. (2004). Talking about a revolution: the impact of site-specific recombinases on genetic analyses in mice. *Dev. Cell* 6, 7–28. doi: 10.1016/S1534-5807(03)00399-X

Bugeon, S., Duffield, J., Dipoppa, M., Ritoux, A., Prankerd, I., Nicoloutsopoulos, D., et al. (2022). A transcriptomic axis predicts state modulation of cortical interneurons. *Nature* 607, 330–338. doi: 10.1038/s41586-022-04915-7

Campos, L. J., Arokiaraj, C. M., Chuapoco, M. R., Chen, X., Goeden, N., Gradinaru, V., et al. (2023). Advances in Aav technology for delivering genetically encoded cargo to the nonhuman primate nervous system. *Curr Res Neurobiol* 4:100086. doi: 10.1016/j.crneur.2023.100086

Caputi, A., Melzer, S., Michael, M., and Monyer, H. (2013). The long and short of GABAergic neurons. *Curr. Opin. Neurobiol.* 23, 179–186. doi: 10.1016/j.conb.2013.01.021

Caroni, P. (2015). Inhibitory microcircuit modules in hippocampal learning. *Curr. Opin. Neurobiol.* 35, 66–73. doi: 10.1016/j.conb.2015.06.010

Casarosa, S., Fode, C., and Guillemot, F. (1999). Mash1 regulates neurogenesis in the ventral telencephalon. *Development* 126, 525–534. doi: 10.1242/dev.126.3.525

Cauli, B., Zhou, X., Tricoire, L., Toussay, X., and Staiger, J. F. (2014). Revisiting enigmatic cortical calretinin-expressing interneurons. *Front. Neuroanat.* 8:52. doi: 10.3389/fnana.2014.00052

Challis, R. C., Ravindra Kumar, S., Chen, X., Goertsen, D., Coughlin, G. M., Hori, A. M., et al. (2022). Adeno-associated virus toolkit to target diverse brain cells. *Annu. Rev. Neurosci.* 45, 447–469. doi: 10.1146/annurev-neuro-111020-100834

Chamberland, S., Grant, G., Machold, R., Nebet, E. R., Tian, G., Stich, J., et al. (2024). Functional specialization of hippocampal somatostatin-expressing interneurons. *Proc. Natl. Acad. Sci. U. S. A.* 121:e2306382121. doi: 10.1073/pnas.2306382121

Chartrand, T., Dalley, R., Close, J., Goriounova, N. A., Lee, B. R., Mann, R., et al. (2023). Morphoelectric and transcriptomic divergence of the layer 1 interneuron repertoire in human versus mouse neocortex. *Science* 382:eadf0805. doi: 10.1126/science.adf0805

Chittajallu, R., Pelkey, K. A., and Mcbain, C. J. (2013). Neurogliaform cells dynamically regulate somatosensory integration via synapse-specific modulation. *Nat. Neurosci.* 16, 13–15. doi: 10.1038/nn.3284

Contractor, A., Ethell, I. M., and Portera-Cailliau, C. (2021). Cortical interneurons in autism. *Nat. Neurosci.* 24, 1648–1659. doi: 10.1038/s41593-021-00967-6

Daigle, T. L., Madisen, L., Hage, T. A., Valley, M. T., Knoblich, U., Larsen, R. S., et al. (2018). A suite of transgenic driver and reporter mouse lines with enhanced brain-cell-type targeting and functionality. *Cell* 174, 465–480. doi: 10.1016/j.cell.2018.06.035

Dienel, S. J., and Lewis, D. A. (2019). Alterations in cortical interneurons and cognitive function in schizophrenia. *Neurobiol. Dis.* 131:104208. doi: 10.1016/j.nbd.2018.06.020

Dimidschstein, J., Chen, Q., Tremblay, R., Rogers, S. L., Saldi, G. A., Guo, L., et al. (2016). A viral strategy for targeting and manipulating interneurons across vertebrate species. *Nat. Neurosci.* 19, 1743–1749. doi: 10.1038/nn.4430

Du, T., Xu, Q., Ocbina, P. J., and Anderson, S. A. (2008). Nkx2.1 specifies cortical interneuron fate by activating Lhx6. *Development* 135, 1559–1567. doi: 10.1242/dev.015123

Duba-Kiss, R., Niibori, Y., and Hampson, D. R. (2021). GABAergic gene regulatory elements used in adeno-associated viral vectors. *Front. Neurol.* 12:745159. doi: 10.3389/fneur.2021.745159

Dudai, A., Yayon, N., Soreq, H., and London, M. (2021). Cortical Vip(+) /chat(+) interneurons: from genetics to function. *J. Neurochem.* 158, 1320–1333. doi: 10.1111/jnc.15263

Dudok, B., Klein, P. M., Hwaun, E., Lee, B. R., Yao, Z., Fong, O., et al. (2021a). Alternating sources of perisomatic inhibition during behavior. *Neuron* 109, 997–1012. doi: 10.1016/j.neuron.2021.01.003

Dudok, B., Szoboszlay, M., Paul, A., Klein, P. M., Liao, Z., Hwaun, E., et al. (2021b). Recruitment and inhibitory action of hippocampal axo-axonic cells during behavior. *Neuron* 109, 3838–3850. doi: 10.1016/j.neuron.2021.09.033

Dymecki, S. M., and Kim, J. C. (2007). Molecular neuroanatomy's "three Gs": a primer. *Neuron* 54, 17–34. doi: 10.1016/j.neuron.2007.03.009

Dymecki, S. M., Rodriguez, C. I., and Awatramani, R. B. (2002). Switching on lineage tracers using site-specific recombination. *Methods Mol. Biol.* 185, 309–334. doi: 10.1385/1-59259-241-4:309

Eisenstat, D. D., Liu, J. K., Mione, M., Zhong, W., Yu, G., Anderson, S. A., et al. (1999). Dlx-1, Dlx-2, and Dlx-5 expression define distinct stages of basal forebrain differentiation. *J. Comp. Neurol.* 414, 217–237. doi: 10.1002/(SICI)1096-9861(19991115)414:2<217::AID-CNE6>3.0.CO;2-I

Fasano, C., Rocchetti, J., Pietrajtis, K., Zander, J. F., Manseau, F., Sakae, D. Y., et al. (2017). Regulation of the hippocampal network by Vglut3-positive Cck- GABAergic basket cells. *Front. Cell. Neurosci.* 11:140. doi: 10.3389/fncel.2017.00140

Feldmeyer, D., Qi, G., Emmenegger, V., and Staiger, J. F. (2018). Inhibitory interneurons and their circuit motifs in the many layers of the barrel cortex. *Neuroscience* 368, 132–151. doi: 10.1016/j.neuroscience.2017.05.027

Fenno, L. E., Ramakrishnan, C., Kim, Y. S., Evans, K. E., Lo, M., Vesuna, S., et al. (2020). Comprehensive dual- and triple-feature intersectional single-vector delivery of diverse functional payloads to cells of behaving mammals. *Neuron* 107:e11, 836–853. doi: 10.1016/j.neuron.2020.06.003

Ferezou, I., Cauli, B., Hill, E. L., Rossier, J., Hamel, E., and Lambolez, B. (2002). 5-Ht3 receptors mediate serotonergic fast synaptic excitation of neocortical vasoactive intestinal peptide/cholecystokinin interneurons. *J. Neurosci.* 22, 7389–7397. doi: 10.1523/JNEUROSCI.22-17-07389.2002

Ferguson, B. R., and Gao, W. J. (2018). Pv interneurons: critical regulators of E/I balance for prefrontal cortex-dependent behavior and psychiatric disorders. *Front Neural Circuits* 12:37. doi: 10.3389/fncir.2018.00037

Fischer, K. B., Collins, H. K., and Callaway, E. M. (2019). Sources of off-target expression from recombinase-dependent AAV vectors and mitigation with cross-over insensitive Atg-out vectors. *Proc. Natl. Acad. Sci. USA* 116, 27001–27010. doi: 10.1073/pnas.1915974116

Fishell, G., and Kepecs, A. (2020). Interneuron types as attractors and controllers. *Annu. Rev. Neurosci.* 43, 1–30. doi: 10.1146/annurev-neuro-070918-050421

Fisher, J., Verhagen, M., Long, Z., Moissidis, M., Yan, Y., He, C., et al. (2024). Cortical somatostatin long-range projection neurons and interneurons exhibit divergent developmental trajectories. *Neuron* 112:e8, 558–573. doi: 10.1016/j.neuron.2023.11.013

Fogaca, M. V., and Duman, R. S. (2019). Cortical GABAergic dysfunction in stress and depression: new insights for therapeutic interventions. *Front. Cell. Neurosci.* 13:87. doi: 10.3389/fncel.2019.00087

Fogarty, M., Grist, M., Gelman, D., Marin, O., Pachnis, V., and Kessaris, N. (2007). Spatial genetic patterning of the embryonic neuroepithelium generates GABAergic interneuron diversity in the adult cortex. *J. Neurosci.* 27, 10935–10946. doi: 10.1523/JNEUROSCI.1629-07.2007

Frazer, S., Prados, J., Niquille, M., Cadilhac, C., Markopoulos, F., Gomez, L., et al. (2017). Transcriptomic and anatomic parcellation of 5-Ht(3A)R expressing cortical interneuron subtypes revealed by single-cell RNA sequencing. *Nat. Commun.* 8:14219. doi: 10.1038/ncomms14219

Galakhova, A. A., Hunt, S., Wilbers, R., Heyer, D. B., De Kock, C. P. J., Mansvelder, H. D., et al. (2022). Evolution of cortical neurons supporting human cognition. *Trends Cogn. Sci.* 26, 909–922. doi: 10.1016/j.tics.2022.08.012

Galarreta, M., Erdelyi, F., Szabo, G., and Hestrin, S. (2004). Electrical coupling among irregular-spiking GABAergic interneurons expressing cannabinoid receptors. *J. Neurosci.* 24, 9770–9778. doi: 10.1523/JNEUROSCI.3027-04.2004

Gallo, N. B., Paul, A., and Van Aelst, L. (2020). Shedding light on chandelier cell development, connectivity, and contribution to neural disorders. *Trends Neurosci.* 43, 565–580. doi: 10.1016/j.tins.2020.05.003

Gelman, D. M., Martini, F. J., Nobrega-Pereira, S., Pierani, A., Kessaris, N., and Marin, O. (2009). The embryonic preoptic area is a novel source of cortical GABAergic interneurons. *J. Neurosci.* 29, 9380–9389. doi: 10.1523/JNEUROSCI.0604-09.2009

Gerfen, C. R., Paletzki, R., and Heintz, N. (2013). Gensat bac cre-recombinase driver lines to study the functional organization of cerebral cortical and basal ganglia circuits. *Neuron* 80, 1368–1383. doi: 10.1016/j.neuron.2013.10.016

Ghanem, N., Jarinova, O., Amores, A., Long, Q., Hatch, G., Park, B. K., et al. (2003). Regulatory roles of conserved intergenic domains in vertebrate Dlx bigene clusters. *Genome Res.* 13, 533–543. doi: 10.1101/gr.716103

Ghanem, N., Yu, M., Long, J., Hatch, G., Rubenstein, J. L., and Ekker, M. (2007). Distinct cis-regulatory elements from the Dlx1/Dlx2 locus mark different progenitor cell populations in the ganglionic eminences and different subtypes of adult cortical interneurons. *J. Neurosci.* 27, 5012–5022. doi: 10.1523/JNEUROSCI.4725-06.2007

Goff, K. M., and Goldberg, E. M. (2021). A role for vasoactive intestinal peptide interneurons in neurodevelopmental disorders. *Dev. Neurosci.* 43, 168–180. doi: 10.1159/000515264

Gomez, L., Cadilhac, C., Prados, J., Mule, N., Jabaudon, D., and Dayer, A. (2023). Developmental emergence of cortical neurogliaform cell diversity. *Development.* 150:dev201830. doi: 10.1242/dev.201830

Gong, S., Zheng, C., Doughty, M. L., Losos, K., Didkovsky, N., Schambra, U. B., et al. (2003). A gene expression atlas of the central nervous system based on bacterial artificial chromosomes. *Nature* 425, 917–925. doi: 10.1038/nature02033

Gouwens, N. W., Sorensen, S. A., Baftizadeh, F., Budzillo, A., Lee, B. R., Jarsky, T., et al. (2020). Integrated Morphoelectric and transcriptomic classification of cortical GABAergic cells. *Cell* 183:e19, 935–953. doi: 10.1016/j.cell.2020.09.057

Graybuck, L. T., Daigle, T. L., Sedeno-Cortes, A. E., Walker, M., Kalmbach, B., Lenz, G. H., et al. (2021). Enhancer viruses for combinatorial cell-subclass-specific labeling. *Neuron* 109:e13, 1449–1464. doi: 10.1016/j.neuron.2021.03.011

Green, J., Bruno, C. A., Traunmuller, L., Ding, J., Hrvatin, S., Wilson, D. E., et al. (2023). A cell-type-specific error-correction signal in the posterior parietal cortex. *Nature* 620, 366–373. doi: 10.1038/s41586-023-06357-1

Guet-Mccreight, A., Skinner, F. K., and Topolnik, L. (2020). Common principles in functional Organization of VIP/Calretinin cell-driven Disinhibitory circuits across cortical areas. *Front. Neural. Circuits* 14:32. doi: 10.3389/fncir.2020.00032

Gutman-Wei, A. Y., and Brown, S. P. (2021). Mechanisms underlying target selectivity for cell types and subcellular domains in developing neocortical circuits. *Front. Neural. Circuits* 15:728832. doi: 10.3389/fncir.2021.728832

Haery, L., Deverman, B. E., Matho, K. S., Cetin, A., Woodard, K., Cepko, C., et al. (2019). Adeno-associated virus technologies and methods for targeted neuronal manipulation. *Front. Neuroanat.* 13:93. doi: 10.3389/fnana.2019.00093

Hafner, G., Witte, M., Guy, J., Subhashini, N., Fenno, L. E., Ramakrishnan, C., et al. (2019). Mapping brain-wide afferent inputs of Parvalbumin-expressing GABAergic neurons in barrel cortex reveals local and Long-range circuit motifs. *Cell Rep.* 28, 3450–3461. doi: 10.1016/j.celrep.2019.08.064

Hanson, M. A., and Wester, J. C. (2022). Advances in approaches to study cell-type specific cortical circuits throughout development. *Front. Cell. Neurosci.* 16:1031389. doi: 10.3389/fncel.2022.1031389

Harris, J. A., Hirokawa, K. E., Sorensen, S. A., Gu, H., Mills, M., Ng, L. L., et al. (2014). Anatomical characterization of Cre driver mice for neural circuit mapping and manipulation. *Front. Neural. Circuits* 8:76. doi: 10.3389/fncir.2014.00076

Harris, K. D., Hochgerner, H., Skene, N. G., Magno, L., Katona, L., Bengtsson Gonzales, C., et al. (2018). Classes and continua of hippocampal CA1 inhibitory neurons revealed by single-cell transcriptomics. *PLoS Biol.* 16:e2006387. doi: 10.1371/journal.pbio.2006387

Hartung, J., Schroeder, A., Perez Vazquez, R. A., Poorthuis, R. B., and Letzkus, J. J. (2024). Layer 1 NDNF interneurons are specialized top-down master regulators of cortical circuits. *Cell Rep.* 43:114212. doi: 10.1016/j.celrep.2024.114212

He, M., and Huang, Z. J. (2018). Genetic approaches to access cell types in mammalian nervous systems. *Curr. Opin. Neurobiol.* 50, 109–118. doi: 10.1016/j.conb.2018.02.003

He, M., Tucciarone, J., Lee, S., Nigro, M. J., Kim, Y., Levine, J. M., et al. (2016). Strategies and tools for combinatorial targeting of GABAergic neurons in mouse cerebral cortex. *Neuron* 91, 1228–1243. doi: 10.1016/j.neuron.2016.08.021

Heintz, N. (2000). Analysis of mammalian central nervous system gene expression and function using bacterial artificial chromosome-mediated transgenesis. *Hum. Mol. Genet.* 9, 937–943. doi: 10.1093/hmg/9.6.937

Hernandez-Frausto, M., Bilash, O. M., Masurkar, A. V., and Basu, J. (2023). Local and long-range GABAergic circuits in hippocampal area Ca1 and their link to Alzheimer's disease. *Front. Neural. Circuits* 17:1223891. doi: 10.3389/fncir.2023.1223891

Hilscher, M. M., Leao, R. N., Edwards, S. J., Leao, K. E., and Kullander, K. (2017). Chrna2-Martinotti cells synchronize layer 5 type A pyramidal cells via rebound excitation. *PLoS Biol.* 15:e2001392. doi: 10.1371/journal.pbio.2001392

Hilscher, M. M., Mikulovic, S., Perry, S., Lundberg, S., and Kullander, K. (2023). The alpha2 nicotinic acetylcholine receptor, a subunit with unique and selective expression in inhibitory interneurons associated with principal cells. *Pharmacol. Res.* 196:106895. doi: 10.1016/j.phrs.2023.106895

Hippenmeyer, S., Vrieseling, E., Sigrist, M., Portmann, T., Laengle, C., Ladle, D., et al. (2005). A developmental switch in the response of DRG neurons to ETS transcription factor signaling. *PLoS Biol.* 3:e159. doi: 10.1371/journal.pbio.0030159

Hodge, R. D., Bakken, T. E., Miller, J. A., Smith, K. A., Barkan, E. R., Graybuck, L. T., et al. (2019). Conserved cell types with divergent features in human versus mouse cortex. *Nature* 573, 61–68. doi: 10.1038/s41586-019-1506-7

Honig, B., and Shapiro, L. (2020). Adhesion protein structure, molecular affinities, and principles of cell-cell recognition. *Cell* 181, 520–535. doi: 10.1016/j.cell.2020.04.010

Hoshino, C., Konno, A., Hosoi, N., Kaneko, R., Mukai, R., Nakai, J., et al. (2021). GABAergic neuron-specific whole-brain transduction by AAV-PHP.B incorporated with a new Gad65 promoter. *Mol. Brain* 14:33. doi: 10.1186/s13041-021-00746-1

Hostetler, R. E., Hu, H., and Agmon, A. (2023). Genetically defined subtypes of somatostatin-containing cortical interneurons. *eNeuro* 10:Eneuro.0204–23.2023. doi: 10.1523/ENEURO.0204-23.2023

Hrvatin, S., Tzeng, C. P., Nagy, M. A., Stroud, H., Koutsioumpa, C., Wilcox, O. F., et al. (2019). A scalable platform for the development of cell-type-specific viral drivers. *eLife* 8:e48089. doi: 10.7554/eLife.48089

Hu, H., Cavendish, J. Z., and Agmon, A. (2013). Not all that glitters is gold: off-target recombination in the somatostatin-Ires-Cre mouse line labels a subset of fast-spiking interneurons. *Front. Neural. Circuits* 7:195. doi: 10.3389/fncir.2013.00195

Hu, J. S., Vogt, D., Sandberg, M., and Rubenstein, J. L. (2017). Cortical interneuron development: a tale of time and space. *Development* 144, 3867–3878. doi: 10.1242/dev.132852

Huang, Z. J., and Paul, A. (2019). The diversity of GABAergic neurons and neural communication elements. *Nat. Rev. Neurosci.* 20, 563–572. doi: 10.1038/s41583-019-0195-4

Huang, Z. J., Taniguchi, H., He, M., and Kuhlman, S. (2014). Genetic labeling of neurons in mouse brain. *Cold Spring Harb. Protoc.* 2014, 150–160. doi: 10.1101/pdb.top080374

Huang, S., Wu, S. J., Sansone, G., Ibrahim, L. A., and Fishell, G. (2024). Layer 1 neocortex: gating and integrating multidimensional signals. *Neuron* 112, 184–200. doi: 10.1016/j.neuron.2023.09.041

Hughes, A. C., Pittman, B. G., Xu, B., Gammons, J. W., Webb, C. M., Nolen, H. G., et al. (2024). A single-vector intersectional Aav strategy for interrogating cellular diversity and brain function. *Nat. Neurosci.* 27, 1400–1410. doi: 10.1038/s41593-024-01659-7

Ibrahim, L. A., Schuman, B., Bandler, R., Rudy, B., and Fishell, G. (2020). Mining the jewels of the cortex's crowning mystery. *Curr. Opin. Neurobiol.* 63, 154–161. doi: 10.1016/j.conb.2020.04.005

Inan, M., and Anderson, S. A. (2014). The chandelier cell, form and function. *Curr. Opin. Neurobiol.* 26, 142–148. doi: 10.1016/j.conb.2014.01.009

Jensen, P., and Dymecki, S. M. (2014). Essentials of recombinase-based genetic fate mapping in mice. *Methods Mol. Biol.* 1092, 437–454. doi: 10.1007/978-1-60327-292-6_26

Jiang, S. N., Cao, J. W., Liu, L. Y., Zhou, Y., Shan, G. Y., Fu, Y. H., et al. (2023). Sncg, Mybpc1, and Parm1 classify subpopulations of Vip-expressing interneurons in layers 2/3 of the somatosensory cortex. *Cereb. Cortex* 33, 4293–4304. doi: 10.1093/cercor/bhac343

Jiang, X., Lachance, M., and Rossignol, E. (2016). Involvement of cortical fast-spiking parvalbumin-positive basket cells in epilepsy. *Prog. Brain Res.* 226, 81–126. doi: 10.1016/bs.pbr.2016.04.012

Katona, I., Sperlagh, B., Sik, A., Kafalvi, A., Vizi, E. S., Mackie, K., et al. (1999). Presynaptically located Cb1 cannabinoid receptors regulate GABA release from axon terminals of specific hippocampal interneurons. *J. Neurosci.* 19, 4544–4558. doi: 10.1523/JNEUROSCI.19-11-04544.1999

Kawaguchi, Y., and Kubota, Y. (1996). Physiological and morphological identification of somatostatin- or vasoactive intestinal polypeptide-containing cells among GABAergic cell subtypes in rat frontal cortex. *J. Neurosci.* 16, 2701–2715. doi: 10.1523/JNEUROSCI.16-08-02701.1996

Kawaguchi, Y., and Kubota, Y. (1997). GABAergic cell subtypes and their synaptic connections in rat frontal cortex. *Cereb. Cortex* 7, 476–486. doi: 10.1093/cercor/7.6.476

Kessaris, N., and Denaxa, M. (2023). Cortical interneuron specification and diversification in the era of big data. *Curr. Opin. Neurobiol.* 80:102703. doi: 10.1016/j.conb.2023.102703

Kim, Y., Yang, G. R., Pradhan, K., Venkataraju, K. U., Bota, M., Garcia Del Molino, L. C., et al. (2017). Brain-wide maps reveal stereotyped cell-type-based cortical architecture and subcortical sexual dimorphism. *Cell* 171, 456–469. doi: 10.1016/j.cell.2017.09.020

Klausberger, T., and Somogyi, P. (2008). Neuronal diversity and temporal dynamics: the unity of hippocampal circuit operations. *Science* 321, 53–57. doi: 10.1126/science.1149381

Krienen, F. M., Goldman, M., Zhang, Q., del Rosario, R., Florio, M., Machold, R., et al. (2020). Innovations present in the primate interneuron repertoire. *Nature* 586, 262–269. doi: 10.1038/s41586-020-2781-z

Kubota, Y., Shigematsu, N., Karube, F., Sekigawa, A., Kato, S., Yamaguchi, N., et al. (2011). Selective coexpression of multiple chemical markers defines discrete populations of neocortical GABAergic neurons. *Cereb. Cortex* 21, 1803–1817. doi: 10.1093/cercor/bhq252

Kullander, K., and Topolnik, L. (2021). Cortical disinhibitory circuits: cell types, connectivity and function. *Trends Neurosci.* 44, 643–657. doi: 10.1016/j.tins.2021.04.009

Lee, B. R., Budzillo, A., Hadley, K., Miller, J. A., Jarsky, T., Baker, K., et al. (2021). Scaled, high fidelity electrophysiological, morphological, and transcriptomic cell characterization. *eLife* 10:e65482. doi: 10.7554/eLife.65482

Lee, S., Hjerling-Leffler, J., Zagha, E., Fishell, G., and Rudy, B. (2010). The largest group of superficial neocortical GABAergic interneurons expresses ionotropic serotonin receptors. *J. Neurosci.* 30, 16796–16808. doi: 10.1523/JNEUROSCI.1869-10.2010

Lee, S., Kruglikov, I., Huang, Z. J., Fishell, G., and Rudy, B. (2013). A disinhibitory circuit mediates motor integration in the somatosensory cortex. *Nat. Neurosci.* 16, 1662–1670. doi: 10.1038/nn.3544

Lee, D. R., Rhodes, C., Mitra, A., Zhang, Y., Maric, D., Dale, R. K., et al. (2022). Transcriptional heterogeneity of ventricular zone cells in the ganglionic eminences of the mouse forebrain. *eLife* 11:e71864. doi: 10.7554/eLife.71864

Lee, A. J., Wang, G., Jiang, X., Johnson, S. M., Hoang, E. T., Lante, F., et al. (2015). Canonical Organization of Layer 1 neuron-led cortical inhibitory and Disinhibitory Interneuronal circuits. *Cereb. Cortex* 25, 2114–2126. doi: 10.1093/cercor/bhu020

Lim, L., Mi, D., Llorca, A., and Marin, O. (2018). Development and functional diversification of cortical interneurons. *Neuron* 100, 294–313. doi: 10.1016/j.neuron.2018.10.009

Lledo, P. M., Merkle, F. T., and Alvarez-Buylla, A. (2008). Origin and function of olfactory bulb interneuron diversity. *Trends Neurosci.* 31, 392–400. doi: 10.1016/j.tins.2008.05.006

Llorca, A., and Deogracias, R. (2022). Origin, development, and synaptogenesis of cortical interneurons. *Front. Neurosci.* 16:929469. doi: 10.3389/fnins.2022.929469

Lu, J., Tucciarone, J., Padilla-Coreano, N., He, M., Gordon, J. A., and Huang, Z. J. (2017). Selective inhibitory control of pyramidal neuron ensembles and cortical subnetworks by chandelier cells. *Nat. Neurosci.* 20, 1377–1383. doi: 10.1038/nn.4624

Lunden, J. W., Durens, M., Phillips, A. W., and Nestor, M. W. (2019). Cortical interneuron function in autism spectrum condition. *Pediatr. Res.* 85, 146–154. doi: 10.1038/s41390-018-0214-6

Lusk, S. J., McKinney, A. E., Hunt, P. J., Fahey, P. J., Patel, J., Chang, A., et al. (2022). A CRISPR toolbox for generating intersectional genetic mouse models for functional, molecular, and anatomical circuit mapping. *BMC Biol.* 20:28. doi: 10.1186/s12915-022-01227-0

Ma, Y., Hu, H., Berrebi, A. S., Mathers, P. H., and Agmon, A. (2006). Distinct subtypes of somatostatin-containing neocortical interneurons revealed in transgenic mice. *J. Neurosci.* 26, 5069–5082. doi: 10.1523/JNEUROSCI.0661-06.2006

Ma, T., Zhang, Q., Cai, Y., You, Y., Rubenstein, J. L., and Yang, Z. (2012). A subpopulation of dorsal lateral/caudal ganglionic eminence-derived neocortical interneurons expresses the transcription factor Sp8. *Cereb. Cortex* 22, 2120–2130. doi: 10.1093/cercor/bhr296

Machold, R., Dellal, S., Valero, M., Zurita, H., Kruglikov, I., Meng, J. H., et al. (2023). Id2 GABAergic interneurons comprise a neglected fourth major group of cortical inhibitory cells. *eLife* 12:e85893. doi: 10.7554/eLife.85893

Madisen, L., Garner, A. R., Shimaoka, D., Chuong, A. S., Klapoetke, N. C., Li, L., et al. (2015). Transgenic mice for intersectional targeting of neural sensors and effectors with high specificity and performance. *Neuron* 85, 942–958. doi: 10.1016/j.neuron.2015.02.022

Madisen, L., Mao, T., Koch, H., Zhuo, J. M., Berenyi, A., Fujisawa, S., et al. (2012). A toolbox of Cre-dependent optogenetic transgenic mice for light-induced activation and silencing. *Nat. Neurosci.* 15, 793–802. doi: 10.1038/nn.3078

Madisen, L., Zwingman, T. A., Sunkin, S. M., Oh, S. W., Zariwala, H. A., Gu, H., et al. (2010). A robust and high-throughput Cre reporting and characterization system for the whole mouse brain. *Nat. Neurosci.* 13, 133–140. doi: 10.1038/nn.2467

Mao, X., and Staiger, J. F. (2024). Multimodal cortical neuronal cell type classification. *Pflugers Arch.* 476, 721–733. doi: 10.1007/s00424-024-02923-2

Marin, O., Anderson, S. A., and Rubenstein, J. L. (2000). Origin and molecular specification of striatal interneurons. *J. Neurosci.* 20, 6063–6076. doi: 10.1523/JNEUROSCI.20-16-06063.2000

Matho, K. S., Huilgol, D., Galbavy, W., He, M., Kim, G., An, X., et al. (2021). Genetic dissection of the glutamatergic neuron system in cerebral cortex. *Nature.* 598, 182–187. doi: 10.1038/s41586-021-03955-9

Mayer, C., Hafemeister, C., Bandler, R. C., Machold, R., Batista Brito, R., Jaglin, X., et al. (2018). Developmental diversification of cortical inhibitory interneurons. *Nature* 555, 457–462. doi: 10.1038/nature25999

Mehta, P., Kreeger, L., Wylie, D. C., Pattadkal, J. J., Lusignan, T., Davis, M. J., et al. (2019). Functional access to neuron subclasses in rodent and primate forebrain. *Cell Rep.* 26, 2818–2832. doi: 10.1016/j.celrep.2019.02.011

Mich, J. K., Graybuck, L. T., Hess, E. E., Mahoney, J. T., Kojima, Y., Ding, Y., et al. (2021). Functional enhancer elements drive subclass-selective expression from mouse to primate neocortex. *Cell Rep.* 34:108754. doi: 10.1016/j.celrep.2021.108754

Milstein, A. D., Bloss, E. B., Apostolides, P. F., Vaidya, S. P., Dilly, G. A., Zemelman, B. V., et al. (2015). Inhibitory gating of input comparison in the CA1 microcircuit. *Neuron.* 87, 1274–1289. doi: 10.106/j.neuron.2015.08.025

Miyoshi, G., Hjerling-Leffler, J., Karayannis, T., Sousa, V. H., Butt, S. J., Battiste, J., et al. (2010). Genetic fate mapping reveals that the caudal ganglionic eminence produces a large and diverse population of superficial cortical interneurons. *J. Neurosci.* 30, 1582–1594. doi: 10.1523/JNEUROSCI.4515-09.2010

Miyoshi, G., Young, A., Petros, T., Karayannis, T., Mckenzie Chang, M., Lavado, A., et al. (2015). Prox1 regulates the subtype-specific development of caudal ganglionic Eminence-derived GABAergic cortical interneurons. *J. Neurosci.* 35, 12869–12889. doi: 10.1523/JNEUROSCI.1164-15.2015

Monory, K., Massa, F., Egertova, M., Eder, M., Blaudzun, H., Westenbroek, R., et al. (2006). The endocannabinoid system controls key epileptogenic circuits in the hippocampus. *Neuron* 51, 455–466. doi: 10.1016/j.neuron.2006.07.006

Muller-Komorowska, D., Opitz, T., Elzoheiry, S., Schweizer, M., Ambrad Giovannetti, E., and Beck, H. (2020). Nonspecific expression in limited excitatory cell populations in interneuron-targeting Cre-driver lines can have large functional effects. *Front. Neural. Circuits* 14:16. doi: 10.3389/fncir.2020.00016

Muñoz, W., Tremblay, R., Levenstein, D., and Rudy, B. (2017). Layer-specific modulation of neocortical dendritic inhibition during active wakefulness. *Science* 355, 954–959. doi: 10.1126/science.aag2599

Munoz-Manchado, A. B., Bengtsson Gonzales, C., Zeisel, A., Munguba, H., Bekkouche, B., Skene, N. G., et al. (2018). Diversity of interneurons in the dorsal striatum revealed by single-cell RNA sequencing and PatchSeq. *Cell Rep.* 24, 2179–2190. doi: 10.1016/j.celrep.2018.07.053

Murthy, S., Niquille, M., Hurni, N., Limoni, G., Frazer, S., Chameau, P., et al. (2014). Serotonin receptor 3A controls interneuron migration into the neocortex. *Nat. Commun.* 5:5524. doi: 10.1038/ncomms6524

Nair, R. R., Blankvoort, S., Lagartos, M. J., and Kentros, C. (2020). Enhancer-driven gene expression (edge) enables the generation of viral vectors specific to neuronal subtypes. *iScience* 23:100888. doi: 10.1016/j.isci.2020.100888

Neske, G. T., Patrick, S. L., and Connors, B. W. (2015). Contributions of diverse excitatory and inhibitory neurons to recurrent network activity in cerebral cortex. *J. Neurosci.* 35, 1089–1105. doi: 10.1523/JNEUROSCI.2279-14.2015

Niederkofler, V., Asher, T. E., Okaty, B. W., Rood, B. D., Narayan, A., Hwa, L. S., et al. (2016). Identification of serotonergic neuronal modules that affect aggressive behavior. *Cell Rep.* 17, 1934–1949. doi: 10.1016/j.celrep.2016.10.063

Nigro, M. J., Hashikawa-Yamasaki, Y., and Rudy, B. (2018). Diversity and connectivity of layer 5 somatostatin-expressing interneurons in the mouse barrel cortex. *J. Neurosci.* 38, 1622–1633. doi: 10.1523/JNEUROSCI.2415-17.2017

Nigro, M. J., Kirikae, H., Kjelsberg, K., Nair, R. R., and Witter, M. P. (2021). Not all that is gold glitters: Pv-Ires-Cre mouse line shows low efficiency of labeling of Parvalbumin interneurons in the Perirhinal cortex. *Front. Neural. Circuits* 15:781928. doi: 10.3389/fncir.2021.781928

Niibori, Y., Duba-Kiss, R., Bruder, J. T., Smith, J. B., and Hampson, D. R. (2023). In silico prediction and in vivo testing of promoters targeting GABAergic inhibitory neurons. *Mol. Ther. Methods Clin. Dev.* 28, 330–343. doi: 10.1016/j.omtm.2023.01.007

Niquille, M., Limoni, G., Markopoulos, F., Cadilhac, C., Prados, J., Holtmaat, A., et al. (2018). Neurogliaform cortical interneurons derive from cells in the preoptic area. *eLife* 7:e32017. doi: 10.7554/eLife.32017

Olah, S., Fule, M., Komlosi, G., Varga, C., Baldi, R., Barzo, P., et al. (2009). Regulation of cortical microcircuits by unitary GABA-mediated volume transmission. *Nature* 461, 1278–1281. doi: 10.1038/nature08503

Overstreet-Wadiche, L., and Mcbain, C. J. (2015). Neurogliaform cells in cortical circuits. *Nat. Rev. Neurosci.* 16, 458–468. doi: 10.1038/nrn3969

Pai, E. L., Stafford, A. M., and Vogt, D. (2023). Cellular signaling impacts upon GABAergic cortical interneuron development. *Front. Neurosci.* 17:1138653. doi: 10.3389/fnins.2023.1138653

Palicz, R., Pater, B., Truschow, P., Witte, M., and Staiger, J. F. (2024). Intersectional strategy to study cortical inhibitory parvalbumin-expressing interneurons. *Sci. Rep.* 14:2829. doi: 10.1038/s41598-024-52901-y

Palmiter, R. D., and Brinster, R. L. (1986). Germ-line transformation of mice. *Annu. Rev. Genet.* 20, 465–499. doi: 10.1146/annurev.ge.20.120186.002341

Paul, A., Crow, M., Raudales, R., He, M., Gillis, J., and Huang, Z. J. (2017). Transcriptional architecture of synaptic communication delineates GABAergic neuron identity. *Cell* 171, 522–539. doi: 10.1016/j.cell.2017.08.032

Pelkey, K. A., Calvigioni, D., Fang, C., Vargish, G., Ekins, T., Auville, K., et al. (2020). Paradoxical network excitation by glutamate release from VgluT3(+) GABAergic interneurons. *eLife* 9:e51996. doi: 10.7554/eLife.51996

Pelkey, K. A., Chittajallu, R., Craig, M. T., Tricoire, L., Wester, J. C., and Mcbain, C. J. (2017). Hippocampal GABAergic inhibitory interneurons. *Physiol. Rev.* 97, 1619–1747. doi: 10.1152/physrev.00007.2017

Petilla Interneuron Nomenclature GroupAscoli, G. A., Alonso-Nanclares, L., Anderson, S. A., Barrionuevo, G., Benavides-Piccione, R., et al. (2008). Petilla terminology: nomenclature of features of GABAergic interneurons of the cerebral cortex. *Nat. Rev. Neurosci.* 9, 557–568.

Pfeffer, C. K., Xue, M., He, M., Huang, Z. J., and Scanziani, M. (2013). Inhibition of inhibition in visual cortex: the logic of connections between molecularly distinct interneurons. *Nat. Neurosci.* 16, 1068–1076. doi: 10.1038/nn.3446

Pi, H. J., Hangya, B., Kvitsiani, D., Sanders, J. I., Huang, Z. J., and Kepecs, A. (2013). Cortical interneurons that specialize in disinhibitory control. *Nature* 503, 521–524. doi: 10.1038/nature12676

Plummer, N. W., Evsyukova, I. Y., Robertson, S. D., de Marchena, J., Tucker, C. J., Jensen, P., et al. (2015). Expanding the power of recombinase-based labeling to uncover cellular diversity. *Development.* 142, 4385–93. doi: 10.1242/dev.129981

Pohlkamp, T., David, C., Cauli, B., Gallopin, T., Bouche, E., Karagiannis, A., et al. (2014). Characterization and distribution of Reelin-positive interneuron subtypes in the rat barrel cortex. *Cereb. Cortex* 24, 3046–3058. doi: 10.1093/cercor/bht161

Pouchelon, G., Vergara, J., Mcmahon, J., Gorissen, B. L., Lin, J. D., Vormstein-Schneider, D., et al. (2022). A versatile viral toolkit for functional discovery in the nervous system. *Cell. Rep. Methods* 2:100225. doi: 10.1016/j.crmeth.2022.100225

Pronneke, A., Scheuer, B., Wagener, R. J., Mock, M., Witte, M., and Staiger, J. F. (2015). Characterizing Vip neurons in the barrel cortex of Vipcre/tdTomato mice reveals layer-specific differences. *Cereb. Cortex* 25, 4854–4868. doi: 10.1093/cercor/bhv202

Raudales, R., Kim, G., Kelly, S. M., Hatfield, J., Guan, W., Zhao, S., et al. (2024). Specific and comprehensive genetic targeting reveals brain-wide distribution and synaptic input patterns of GABAergic axo-axonic interneurons. *bioRxiv*:2023.11.07.566059.

Rawlins, E. L., Clark, C. P., Xue, Y., and Hogan, B. L. M. (2009). The Id2+ distal tip lung epithelium contains individual multipotent embryonic progenitor cells. *Development.* 136, 3741–5. doi: 10.1242/dev.037317

Riad, M. H., Park, K., Ibanez-Tallon, I., and Heintz, N. (2022). Local production of corticotropin-releasing hormone in prefrontal cortex modulates male-specific novelty exploration. *Proc. Natl. Acad. Sci. USA* 119:e2211454119. doi: 10.1073/pnas.2211454119

Rogers, S. W., Tvrdik, P., Capecchi, M. R., and Gahring, L. C. (2012). Prenatal ablation of nicotinic receptor alpha7 cell lineages produces lumbosacral spina bifida the severity of which is modified by choline and nicotine exposure. *Am. J. Med. Genet. A* 158A, 1135–1144. doi: 10.1002/ajmg.a.35372

Rubin, A. N., and Kessaris, N. (2013). Prox1: a lineage tracer for cortical interneurons originating in the lateral/caudal ganglionic eminence and preoptic area. *PLoS One* 8:e77339. doi: 10.1371/journal.pone.0077339

Rudy, B., Fishell, G., Lee, S., and Hjerling-Leffler, J. (2011). Three groups of interneurons account for nearly 100% of neocortical GABAergic neurons. *Dev. Neurobiol.* 71, 45–61. doi: 10.1002/dneu.20853

Salimando, G. J., Hyun, M., Boyt, K. M., and Winder, D. G. (2020). BNST GluN2D-containing NMDA receptors influence anxiety- and depressive-like behaviors and modulate cell-specific excitatory/inhibitory synaptic balance. *J. Neurosci.* 40, 3949–3968. doi: 10.1523/JNEUROSCI.0270-20.2020

Sanes, J. R., and Zipursky, S. L. (2020). Synaptic specificity, recognition molecules, and assembly of neural circuits. *Cell* 181, 536–556. doi: 10.1016/j.cell.2020.04.008

Saunders, A., Macosko, E. Z., Wysoker, A., Goldman, M., Krienen, F. M., De Rivera, H., et al. (2018). Molecular diversity and specializations among the cells of the adult mouse brain. *Cell* 174, 1015–1030. doi: 10.1016/j.cell.2018.07.028

Scala, F., Kobak, D., Bernabucci, M., Bernaerts, Y., Cadwell, C. R., Castro, J. R., et al. (2021). Phenotypic variation of transcriptomic cell types in mouse motor cortex. *Nature* 598, 144–150. doi: 10.1038/s41586-020-2907-3

Schmidt, E. R. E., and Polleux, F. (2021). Genetic mechanisms underlying the evolution of connectivity in the human cortex. *Front. Neural. Circuits* 15:787164. doi: 10.3389/fncir.2021.787164

Schuman, B., Dellal, S., Pronneke, A., Machold, R., and Rudy, B. (2021). Neocortical layer 1: an elegant solution to top-down and bottom-up integration. *Annu. Rev. Neurosci.* 44, 221–252. doi: 10.1146/annurev-neuro-100520-012117

Schuman, B., Machold, R. P., Hashikawa, Y., Fuzik, J., Fishell, G. J., and Rudy, B. (2019). Four Unique Interneuron Populations Reside in Neocortical Layer 1. *J. Neurosci.* 39, 125–139. doi: 10.1523/JNEUROSCI.1613-18.2018

Schwiedrzik, C. M., and Freiwald, W. A. (2017). High-level prediction signals in a low-level area of the macaque face-processing hierarchy. *Neuron* 96, 89–97. doi: 10.1016/j.neuron.2017.09.007

Sciolino, N. R., Plummer, N. W., Chen, Y., Alexander, G. M., Robertson, S. D., Dudek, S. M., et al. (2016). Recombinase-dependent mouse lines for chemogenetic activation of genetically defined cell types. *Cell Rep.* 15, 2563–73. doi: 10/1016/j.celrep.2016.05.034

Siwani, S., Franca, A. S. C., Mikulovic, S., Reis, A., Hilscher, M. M., Edwards, S. J., et al. (2018). Olmalpha2 cells Bidirectionally modulate learning. *Neuron* 99, 404–412. doi: 10.1016/j.neuron.2018.06.022

Somogyi, J., Baude, A., Omori, Y., Shimizu, H., El Mestikawy, S., Fukaya, M., et al. (2004). GABAergic basket cells expressing cholecystokinin contain vesicular glutamate transporter type 3 (Vglut3) in their synaptic terminals in hippocampus and isocortex of the rat. *Eur. J. Neurosci.* 19, 552–569. doi: 10.1111/j.0953-816X.2003.03091.x

Sousa, V. H., Miyoshi, G., Hjerling-Leffler, J., Karayannis, T., and Fishell, G. (2009). Characterization of Nkx6-2-derived neocortical interneuron lineages. *Cereb. Cortex* 19, i1–i10. doi: 10.1093/cercor/bhp038

Stenman, J., Toresson, H., and Campbell, K. (2003). Identification of two distinct progenitor populations in the lateral ganglionic eminence: implications for striatal and olfactory bulb neurogenesis. *J. Neurosci.* 23, 167–174. doi: 10.1523/JNEUROSCI.23-01-00167.2003

Stuhmer, T., Anderson, S. A., Ekker, M., and Rubenstein, J. L. (2002). Ectopic expression of the dlx genes induces glutamic acid decarboxylase and dlx expression. *Development* 129, 245–252. doi: 10.1242/dev.129.1.245

Sussel, L., Marin, O., Kimura, S., and Rubenstein, J. L. (1999). Loss of Nkx2.1 homeobox gene function results in a ventral to dorsal molecular respecification within the basal telencephalon: evidence for a transformation of the pallidum into the striatum. *Development* 126, 3359–3370. doi: 10.1242/dev.126.15.3359

Taniguchi, H. (2014). Genetic dissection of GABAergic neural circuits in mouse neocortex. *Front. Cell. Neurosci.* 8:8. doi: 10.3389/fncel.2014.00008

Taniguchi, H., He, M., Wu, P., Kim, S., Paik, R., Sugino, K., et al. (2011). A resource of Cre driver lines for genetic targeting of GABAergic neurons in cerebral cortex. *Neuron* 71, 995–1013. doi: 10.1016/j.neuron.2011.07.026

Taniguchi, H., Lu, J., and Huang, Z. J. (2013). The spatial and temporal origin of chandelier cells in mouse neocortex. *Science* 339, 70–74. doi: 10.1126/science.1227622

Tasic, B., Menon, V., Nguyen, T. N., Kim, T. K., Jarsky, T., Yao, Z., et al. (2016). Adult mouse cortical cell taxonomy revealed by single cell transcriptomics. *Nat. Neurosci.* 19, 335–346. doi: 10.1038/nn.4216

Tasic, B., Yao, Z., Graybuck, L. T., Smith, K. A., Nguyen, T. N., Bertagnolli, D., et al. (2018). Shared and distinct transcriptomic cell types across neocortical areas. *Nature* 563, 72–78. doi: 10.1038/s41586-018-0654-5

Topolnik, L., and Tamboli, S. (2022). The role of inhibitory circuits in hippocampal memory processing. *Nat. Rev. Neurosci.* 23, 476–492. doi: 10.1038/s41583-022-00599-0

Toresson, H., Mata De Urquiza, A., Fagerstrom, C., Perlmann, T., and Campbell, K. (1999). Retinoids are produced by glia in the lateral ganglionic eminence and regulate striatal neuron differentiation. *Development* 126, 1317–1326. doi: 10.1242/dev.126.6.1317

Tremblay, R., Lee, S., and Rudy, B. (2016). GABAergic interneurons in the neocortex: from cellular properties to circuits. *Neuron* 91, 260–292. doi: 10.1016/j.neuron.2016.06.033

Tricoire, L., Pelkey, K. A., Erkkila, B. E., Jeffries, B. W., Yuan, X., and Mcbain, C. J. (2011). A blueprint for the spatiotemporal origins of mouse hippocampal interneuron diversity. *J. Neurosci.* 31, 10948–10970. doi: 10.1523/JNEUROSCI.0323-11.2011

Urban, A., and Rossier, J. (2012). Genetic targeting of specific neuronal cell types in the cerebral cortex. *Prog. Brain Res.* 196, 163–192. doi: 10.1016/B978-0-444-59426-6.00009-4

Valero, M., Viney, T. J., Machold, R., Mederos, S., Zutshi, I., Schuman, B., et al. (2021). Sleep down state-active Id2/Nkx2.1 interneurons in the neocortex. *Nat. Neurosci.* 24, 401–411. doi: 10.1038/s41593-021-00797-6

van den Pol, A. N., Yao, Y., Fu, L., Foo, K., Huang, H., Coppari, R., et al. (2009). Neuromedin B and gastrin-releasing peptide excite arcuate nucleus neuropeptide Y neurons in a novel transgenic mouse expressing strong Renilla green fluorescent protein in NPY neurons. *J. Neurosci.* 29, 4622–39. doi: 10.1523/JNEUROSCI.3249-08.2009

Veres, J. M., Andrasi, T., Nagy-Pal, P., and Hajos, N. (2023). Camkiialpha promoter-controlled circuit manipulations target both pyramidal cells and inhibitory interneurons in cortical networks. *eNeuro*, 10:Eneuro.0070–23.2023. doi: 10.1523/ENEURO.0070-23.2023

Von Engelhardt, J., Khrulev, S., Eliava, M., Wahlster, S., and Monyer, H. (2011). 5-Ht(3A) receptor-bearing white matter interstitial GABAergic interneurons are functionally integrated into cortical and subcortical networks. *J. Neurosci.* 31, 16844–16854. doi: 10.1523/JNEUROSCI.0310-11.2011

Vong, L., Ye, C., Yang, Z., Choi, B., Chua, S. Jr., and Lowell, B. B. (2011). Leptin action on GABAergic neurons prevents obesity and reduces inhibitory tone to Pomc neurons. *Neuron* 71, 142–154. doi: 10.1016/j.neuron.2011.05.028

Vormstein-Schneider, D., Lin, J. D., Pelkey, K. A., Chittajallu, R., Guo, B., Arias-Garcia, M. A., et al. (2020). Viral manipulation of functionally distinct interneurons in mice, non-human primates and humans. *Nat. Neurosci.* 23, 1629–1636. doi: 10.1038/s41593-020-0692-9

Vucurovic, K., Gallopin, T., Ferezou, I., Rancillac, A., Chameau, P., Van Hooft, J. A., et al. (2010). Serotonin 3A receptor subtype as an early and protracted marker of cortical interneuron subpopulations. *Cereb. Cortex* 20, 2333–2347. doi: 10.1093/cercor/bhp310

Wamsley, B., and Fishell, G. (2017). Genetic and activity-dependent mechanisms underlying interneuron diversity. *Nat. Rev. Neurosci.* 18, 299–309. doi: 10.1038/nrn.2017.30

Wang, X., Tucciarone, J., Jiang, S., Yin, F., Wang, B. S., Wang, D., et al. (2019). Genetic single neuron anatomy reveals fine granularity of cortical Axo-Axonic cells. *Cell Rep.* 26, 3145–3159. doi: 10.1016/j.celrep.2019.02.040

Wei, S., Du, H., Li, Z., Tao, G., Xu, Z., Song, X., et al. (2019). Transcription factors Sp8 and Sp9 regulate the development of caudal ganglionic eminence-derived cortical interneurons. *J. Comp. Neurol.* 527, 2860–2874. doi: 10.1002/cne.24712

Wilson, R. I., and Nicoll, R. A. (2001). Endogenous cannabinoids mediate retrograde signalling at hippocampal synapses. *Nature* 410, 588–592. doi: 10.1038/35069076

Winterer, J., Lukacsovich, D., Que, L., Sartori, A. M., Luo, W., and Foldy, C. (2019). Single-cell Rna-Seq characterization of anatomically identified olm interneurons in different transgenic mouse lines. *Eur. J. Neurosci.* 50, 3750–3771. doi: 10.1111/ejn.14549

Wu, S. J., Sevier, E., Dwivedi, D., Saldi, G. A., Hairston, A., Yu, S., et al. (2023). Cortical somatostatin interneuron subtypes form cell-type-specific circuits. *Neuron* 111:e9, 2675–2692. doi: 10.1016/j.neuron.2023.05.032

Wu, J., Zhao, Z., Shi, Y., and He, M. (2022). Cortical Vip(+) interneurons in the upper and deeper layers are transcriptionally distinct. *J. Mol. Neurosci.* 72, 1779–1795. doi: 10.1007/s12031-022-02040-8

Xu, H., Jeong, H. Y., Tremblay, R., and Rudy, B. (2013). Neocortical somatostatin-expressing GABAergic interneurons disinhibit the thalamorecipient layer 4. *Neuron* 77, 155–167. doi: 10.1016/j.neuron.2012.11.004

Xu, Q., Tam, M., and Anderson, S. A. (2008). Fate mapping Nkx2.1-lineage cells in the mouse telencephalon. *J. Comp. Neurol.* 506, 16–29. doi: 10.1002/cne.21529

Yang, J., Yang, X., and Tang, K. (2022). Interneuron development and dysfunction. *FEBS J.* 289, 2318–2336. doi: 10.1111/febs.15872

Yao, Z., Van Velthoven, C. T. J., Nguyen, T. N., Goldy, J., Sedeno-Cortes, A. E., Baftizadeh, F., et al. (2021). A taxonomy of transcriptomic cell types across the isocortex and hippocampal formation. *Cell* 184, 3222–3241. doi: 10.1016/j.cell.2021.04.021

Zeisel, A., Munoz-Manchado, A. B., Codeluppi, S., Lonnerberg, P., La Manno, G., Jureus, A., et al. (2015). Brain structure. Cell types in the mouse cortex and hippocampus revealed by single-cell Rna-seq. *Science* 347, 1138–1142. doi: 10.1126/science.aaa1934

Zeng, H. (2022). What is a cell type and how to define it? *Cell* 185, 2739–2755. doi: 10.1016/j.cell.2022.06.031

Zerucha, T., Stuhmer, T., Hatch, G., Park, B. K., Long, Q., Yu, G., et al. (2000). A highly conserved enhancer in the Dlx5/Dlx6 intergenic region is the site of cross-regulatory interactions between dlx genes in the embryonic forebrain. *J. Neurosci.* 20, 709–721. doi: 10.1523/JNEUROSCI.20-02-00709.2000

Zhao, C., Ries, C., Du, Y., Zhang, J., Sakimura, K., Itoi, K., et al. (2023). Differential Crh expression level determines efficiency of Cre- and Flp-dependent recombination. *Front. Neurosci.* 17:1163462. doi: 10.3389/fnins.2023.1163462

Zhu, J. J. (2023). Architectural organization of approximately 1,500-neuron modular minicolumnar disinhibitory circuits in healthy and Alzheimer's cortices. *Cell Rep.* 42:112904. doi: 10.1016/j.celrep.2023.112904

Glossary

AAC	Axo-axonic cell
Ai	Allen Institute
BAC	Bacterial artificial chromosome
Calb2/CR	Calbindin-2 (calretinin)
CamK2	Ca2+/calmodulin-dependent protein kinase 2
Cck	Cholecystokinin
CGE	Caudal ganglionic eminence
ChC	Chandelier cell
Chrna2	Cholinergic receptor nicotinic alpha 2 subunit
Crh	Corticotropin-releasing hormone
DIO	Double-floxed (loxP) inverse ORF
Dlx	Distal-less homeobox
DREADD	Designer receptors exclusively activated by designer drugs
fDIO	Double-flrted (frt) inverse ORF
Gad2	Glutamate decarboxylase 2
Htr3a	5-hydroxytryptamine receptor 3a
Id2	Inhibitor of DNA binding 2
IN	GABAergic interneuron
KI	Knock-in
Lamp5	Lysosomal associated membrane protein family member 5
L1	Layer 1
LR	Long range
Ndnf	Neuron-derived neurotrophic factor
NGFC	Neurogliaform cell
Nkx2.1	Nk2 homeobox 1
Nos1	Nitric oxide synthase 1
NPY	Neuropeptide Y
MC	Martinotti cell
MGE	Medial ganglionic eminence
OLM	Oriens-lacunosum moleculare
ORF	Open reading frame
PMID	PubMed identifier
POA	Preoptic area
Pvalb/PV	Parvalbumin
rAAV	Recombinant adeno-associated virus
Slc32a1	Solute carrier family 32 member 1
Sncg	Synuclein gamma
Sst	Somatostatin
Tg	Transgenic
Vip	Vasoactive intestinal peptide

frontiers | Frontiers in Cellular Neuroscience

TYPE Brief Research Report
PUBLISHED 12 September 2024
DOI 10.3389/fncel.2024.1465836

OPEN ACCESS

EDITED BY
Yasufumi Hayano,
The Ohio State University, United States

REVIEWED BY
Dongqing Shi,
University of Michigan, United States
Roberto de la Torre Martinez,
Karolinska Institutet (KI), Sweden

*CORRESPONDENCE
Renata Batista-Brito
✉ renata.brito@einsteinmed.edu

RECEIVED 16 July 2024
ACCEPTED 23 August 2024
PUBLISHED 12 September 2024

CITATION
Sabri E and Batista-Brito R (2024) Vasoactive intestinal peptide-expressing interneurons modulate the effect of behavioral state on cortical activity.
Front. Cell. Neurosci. 18:1465836.
doi: 10.3389/fncel.2024.1465836

Vasoactive intestinal peptide-expressing interneurons modulate the effect of behavioral state on cortical activity

Ehsan Sabri[1] and Renata Batista-Brito[1,2,3]*

[1]Dominick P. Purpura Department of Neuroscience, Albert Einstein College of Medicine, Bronx, NY, United States, [2]Department of Psychiatry and Behavioral Sciences, Albert Einstein College of Medicine, Bronx, NY, United States, [3]Department of Genetics, Albert Einstein College of Medicine, Bronx, NY, United States

Animals live in a complex and changing environment with various degrees of behavioral demands. Behavioral states affect the activity of cortical neurons and the dynamics of neuronal populations, however not much is known about the cortical circuitry behind the modulation of neuronal activity across behavioral states. Here we show that a class of GABAergic inhibitory interneurons that express vasoactive intestinal peptide-expressing interneurons (VIP), namely VIP interneurons, play a key role in the circuits involved in the modulation of cortical activity by behavioral state, as reflected in the mice facial motion. We show that inhibition of VIP interneurons reduces the correlated activity between the behavioral state of the animal and the spiking of individual neurons. We also show that VIP inhibition during the quiet state decreases the synchronous spiking of the neurons but increases delta power and phase locking of spiking to the delta-band activity. Taken together our data show that VIP interneurons modulate the behavioral state-dependency of cortical activity across different time scales.

KEYWORDS

cortical state, behavioral state, VIP interneurons, spiking synchrony, delta power

1 Introduction

Behavioral states, also known as arousal states, can change from sleep to quiet wakefulness or to active exploration of the environment (McGinley et al., 2015; Stringer et al., 2019; Vinck et al., 2015). Transitions between alertness, quiet wakefulness, and sleep occur over a period of seconds, and the resultant states are highly correlated with specific rhythmic activity patterns in the neocortex (i.e., oscillatory activity, or cortical states) (Iwańczuk and Guźniczak, 2015; Saper et al., 2010). At the cortical level, these different arousal states are associated with specific oscillatory activities, which are often called "cortical states." For example, periods of active engagement and attention are associated with desynchronization, or suppression of low-frequency activity (McGinley et al., 2015). Alternately, during periods of slow-wave sleep (SWS), and periods of quiet wakefulness (e.g., tiredness or daydreaming), neocortical rhythms are synchronized, or dominated by low-frequency oscillations (McGinley et al., 2015). Cortical states have been shown to

influence information coding, dynamics of neuronal populations, and cognition (Batista-Brito et al., 2017, 2018; Cardin, 2018; McGinley et al., 2015) and a hallmark of many psychiatric disorders is disturbed behavioral states, however despite the importance of cortical states, little is known about the neuronal circuitry that controls their modulation across arousal states. Recent evidence suggests that GABAergic inhibitory neurons (INs) play a key role in the circuits involved in cortical state modulation (Batista-Brito et al., 2017, 2018; Cardin, 2018; McGinley et al., 2015), and INs in the cortex are increasingly linked to schizophrenia and the regulation of cortical states (Akbarian et al., 1996; Batista-Brito et al., 2017; Beasley et al., 2002; Cardin, 2018; Eastwood and Harrison, 2003).

Cortical circuits are composed of excitatory and inhibitory neurons. Inhibitory GABAergic interneurons function to maintain stability within local neural networks. During healthy cortical activity, excitation is balanced by inhibition. GABAergic signaling not only prevents pathology, such as the runaway excitation observed in seizure, but also regulates the dendritic integration of synaptic inputs, influences the precision of spike output, and facilitates the accurate encoding of sensory information. Nevertheless, a major challenge to understanding the contribution of inhibition to brain development and function is the diversity of cortical GABAergic interneurons, which can be subdivided into three distinct classes, namely: (1) fast-spiking cells that express parvalbumin (PV-INs) and target the cell bodies of excitatory pyramidal neurons (PNs), (2) low-threshold spiking cells that express the peptide somatostatin (SOM-INs) and target the distal dendrites of excitatory neurons, and (3) VIP-expressing interneurons (VIP-INs) that predominantly target other interneurons (Tremblay et al., 2016). VIP-INs are important regulators of cortical function (Fu et al., 2014; Karnani et al., 2016b,a; Lee et al., 2013; Pi et al., 2013). These cells receive local and long-range excitatory glutamatergic inputs as well as serotonergic and cholinergic afferents (Tremblay et al., 2016). The coordinated activity of mature VIP-INs is influenced by the behavioral state, as these cells are recruited by arousing events such as the onset of motor activity (Pi et al., 2013; Lee et al., 2013; Askew et al., 2019). VIP-INs of the sensory cortex are activated by the long-range corticocortical inputs from other cortical areas such as the motor cortex, and cholinergic and serotonergic projections from the basal forebrain (Lee et al., 2013). VIP-INs integrate into cortical circuits early in postnatal life (Miyoshi and Fishell, 2011) and genetic alterations of these cells lead to profound alteration of cortical state and sensory responses (Batista-Brito et al., 2017), however, very little is known about how these cells shape the behavioral state dependency of cortical activity.

Here we examined the role of VIP-INs in the function of cortical circuits. We perturbed VIP-IN function by silencing this cell type using chemogenetics. We find that disruption of VIP-INs interferes with the behavioral state-dependent regulation of cortical circuits. VIP inhibition in the quiet state reduces synchronous neuronal spiking while enhancing delta power of the local field potential (LFP), and increasing phase locking of cortical neurons to delta rhythm. Collectively, our findings suggest that VIP interneurons are critical for the regulation of behavioral state-dependent cortical activity across various time scales.

2 Results

2.1 Comparing the correlation pattern of facial motion and pupil size with mice neuronal spiking in V1

With advances in the simultaneous recording of neuronal population activity, it has been widely observed that spontaneous fluctuations in population spiking are correlated with behavioral measures of arousal such as locomotion and pupil size (Niell and Stryker, 2010; Vinck et al., 2015). The dynamics of pupil size is broader than locomotion in reflecting spontaneous activity in the cortex because it captures the smaller fluctuations that occur even when the animal is not moving. Changes in mouse facial motion have also been shown to be synchronized with spontaneous population spiking (Figure 1B; Stringer et al., 2019). In our recordings from mice V1, we observe the spiking activity of the majority of neurons is correlated with facial motion and pupil size changes (see an example window of simultaneous single neurons alongside facial motion and pupil size Figure 1B). Here we examine the temporal dynamics of the correlation pattern between pupil size, facial motion, and single-cell spiking to see which one of pupil size and facial motion is more accurate in reflecting the fluctuations of the neuronal spiking in V1. The dynamics of pupil size and facial motion are highly correlated; however, the cross-correlogram of pupil size and facial motion shows that the pupil size is 1 s delayed relative to the facial motion (Figure 1C). To examine the dynamics of correlation between single-neuron spiking and pupil size or facial motion, we calculated the spike-triggered average of each neuron on pupil size and facial motion (see Figure 1D for an example neuron). We observed that although both pupil and facial motion show strong correlations with single-neuron spiking, the pupil is consistently up to 1 s delayed relative to neuronal spiking in V1, while facial motion more synchronously follows neuronal spiking in V1 (Figures 1E, F).

2.2 How the suppression of VIP interneurons affect the correlation pattern of V1 neuronal spiking and mice facial motion

A large body of evidence suggests that neuromodulators such as Ach play a key role in the synchronized fluctuations in activity in the cortex (Harris and Thiele, 2011; Goard and Dan, 2009; Pi et al., 2013; Lee and Dan, 2012; Lohani et al., 2022). However, the circuitry of the cell types involved in relaying the effect of Ach remains largely unexplored. VIP-expressing interneurons are directly activated by Ach and provide a disinhibitory effect on the local network (Batista-Brito et al., 2017; Lee et al., 2013; Pi et al., 2013), making them a good candidate to play a key role in this circuit. To study the role of VIP interneurons here, we suppress the activity of these cells (Figure 2A) and examine how this changes the pattern of correlation between single-cell spiking and facial motion (Figure 2B). For this, we compared the spike-triggered activity of single neurons and facial motion before and after CNO injection to suppress the activity of VIP interneurons. We observed a decrease

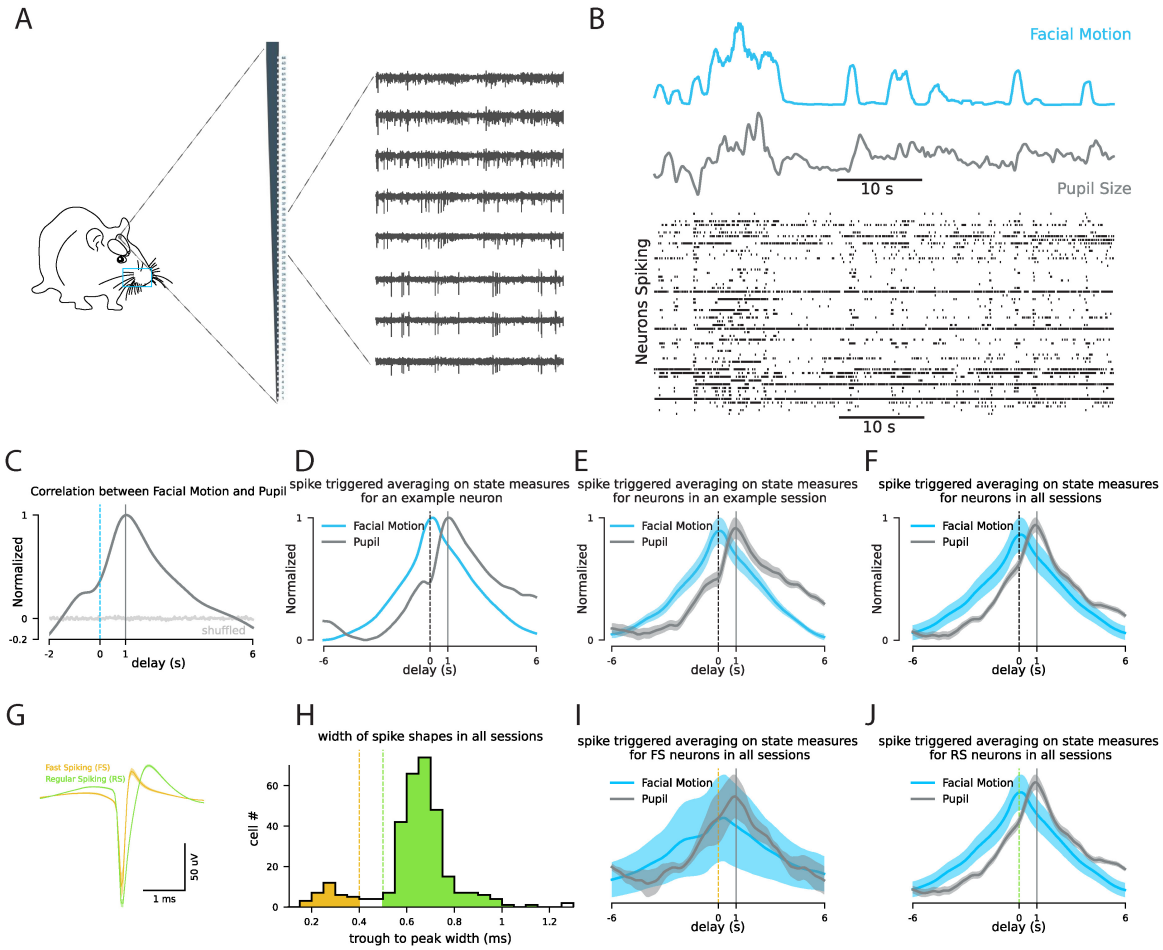

FIGURE 1
Facial motion has less delay compared to pupil size in following the neuronal spiking in mouse V1. **(A)** Experiment schematic. **(B)** Example window showing simultaneous changes in mouse facial motion energy, and pupil size alongside with the changes in the spiking of the recorded neurons in V1. **(C)** Correlation pattern between the pupil size and the facial motion energy. **(D)** The patterns of spike-triggered averaging on facial motion (blue) and pupil (gray) for an example neuron. **(E)** Same as panel **(D)** for average across all neurons in an example session. **(F)** Same as panel **(D)** for average across all neurons in all the recording sessions from control animals (n = 321). **(G)** The average shape of the putative fast spiking neurons (orange, width ¡ 0.4 ms) and putative regular spiking neurons (green, width ¿0.5 ms). **(H)** The distribution of trough to peak width for all the recorded neurons (n = 321). **(I)** Same as panel **(D)** for average across all the putative FS neurons (n = 37). **(J)** Same as panel **(D)** for average across all the putative RS neurons (n = 273). "delay" refers to the delay between the triggering spikes at 0 and the behavioral signals. "s" refers to seconds.

in the strength of the correlation between the spiking activity of neurons in V1 and facial motion after VIP suppression (Figures 2C–E). This observation suggests that VIP interneurons are part of the circuit to convey the effect of the behavioral state on the activity of the network. To further characterize the effect of VIP interneuons, we next examine the changes in the network activity after the VIP suppression in this experiment.

2.3 During the periods of no facial motion, how does suppression of VIP interneurons change the dynamics of neuronal activity in mice V1?

With the suppression of VIP interneurons in VIP-Cre x hM4Di mice, the facial motion significantly decreases ($p < 0.08$ across all the recording sessions). Because of that we next focused on the periods of neural activity in which there are no facial movement and compare the network dynamics before and after the suppression of the VIP interneurons. We observe that with the suppression of VIP interneurons there is a slight increase in the firing rate of neurons in V1 ($p = 0.12$, Figure 3A). However, after the VIP inhibition there is a significant change in the spectral components of the LFP across all layers. Most notably, we observe a decrease in the power of alpha-band oscillations and an increase in the power of slower delta-band oscillations (Figure 3B). This spectral shift is also reflected in the coherence between spiking and LFP. We measured the phase locking value between neuronal spiking and delta-band activity and we observed a higher synchrony to delta-band activity after the VIP suppression (Figure 3C). This shift in the network spectral component toward slower rhythms suggests more synchronized spiking across the network. However, by examining the spiking synchrony across neuronal pairs, we observe a decrease in the peak of spiking correlation patterns (Figure 3D) which suggests that

VIP suppression modulates the network activity differently across different time scales.

3 Discussion

To study the circuitry behind the effect of behavioral state on neural cortical dynamics we focused on the VIP interneurons. VIP interneurons are well studied for their disinhibitory effect on the network through the SST interneurons (Pi et al., 2013). They also receive neuromodulatory input (Tremblay et al., 2016) thus making them a good candidate to play a key role in this circuit. To quantify the network spiking fluctuations that are correlated with the behavioral state, we used spike-triggered averaging to show that facial motion follows the neural dynamics more temporally accurate than pupil size. Next, we used chemogenetics to silence the activity of the VIP interneurons and observed that the correlated dynamics of the neuronal spiking and facial motion is reduced by the suppression of the activity of the VIP interneurons. Finally, we focused on the periods of no facial motion, before and after the VIP interneuron suppression, to examine the changes in the neural activity because of VIP suppression in the absence of behavioral modulation. We observed that delta power in LFP increases after the VIP suppression, and although the firing rate of neurons remains largely unchanged the phase locking of the spiking to the delta oscillation increases. Further analysis of the spiking correlation across neurons showed that fast spiking synchrony between neurons has been reduced which suggests that VIP suppression effects the network differently in different time scales: VIP suppression induces more slow synchrony in the network but reduces fast synchronous spiking across neurons.

Response variability is one of the first observations in the study of cortical sensory processing. For several decades, spike recording in sensory cortices of mammals has puzzled systems neuroscientists about the source of trial-to-trial variability of neurons' responses to sensory stimulation (Werner and Mountcastle, 1963). This variability has initially been interpreted as noise (Shadlen and Newsome, 1994), however, recently its potential role has been studied in the efficient processing of sensory signals in the cortex (Kohn et al., 2016). It has been posited that changes in baseline activity, meaning the level of neuronal activity (i.e., internal state, cortical state) when the sensory signal arrives in the network, is the main source of variability. What is the source of fluctuations in the baseline activity (aka spontaneous activity)? Previous works by us and others have shown that behavioral measures of arousal (e.g., pupil size and locomotion) could explain (to some extent) sensory response variability, as well as the spontaneous fluctuations of neuronal activity (Figure 1; Vinck et al., 2015; Niell and Stryker, 2010). Simultaneous recordings of thousands of neurons have also shown that spontaneous neural activity fluctuations (i.e., cortical/behavioral state) are shared across the whole brain (Stringer et al., 2019). Taken together, all suggest that response variability in sensory cortices is caused by cortical/behavioral states that are manifested as changes in excitability across the brain.

A large body of evidence suggests that neuromodulators (especially Ach) play a key role in the synchronized fluctuations

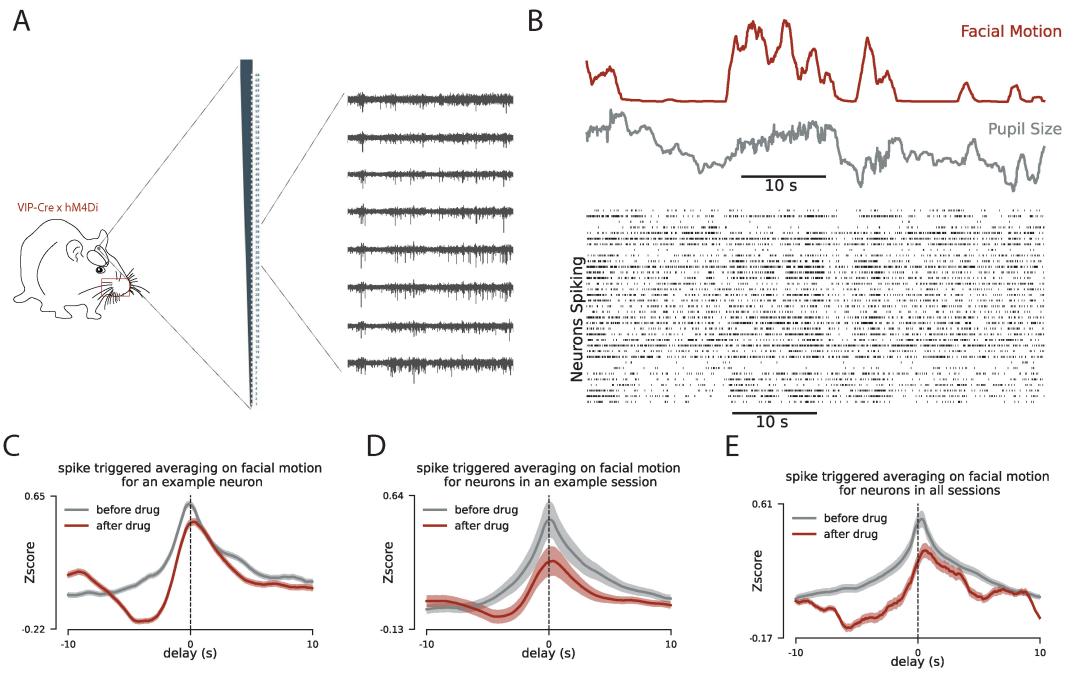

FIGURE 2
Inhibition of VIP interneurons reduces the correlated dynamics between mouse facial motion and V1 spiking. **(A)** Schematic for the experiment with chemogenetic inhibition of VIP interneurons. **(B)** Same as Figure 1B when the VIP interneurons are suppressed using DREADD. **(C)** The patterns of spike-triggered averaging on the facial motion before (gray) and after the CNO injection (drug) for an example neuron. *y*-axis is normalized relative to the chance level for each pattern. **(D)** Same as panel **(C)** for the average across all neurons in an example session. **(E)** Same as panel **(C)** for the average across all neurons in all recording sessions. In panels **(C–E)** the delay in the *x*-axis quantifies the delay between the spiking activity of neurons and the facial motion.

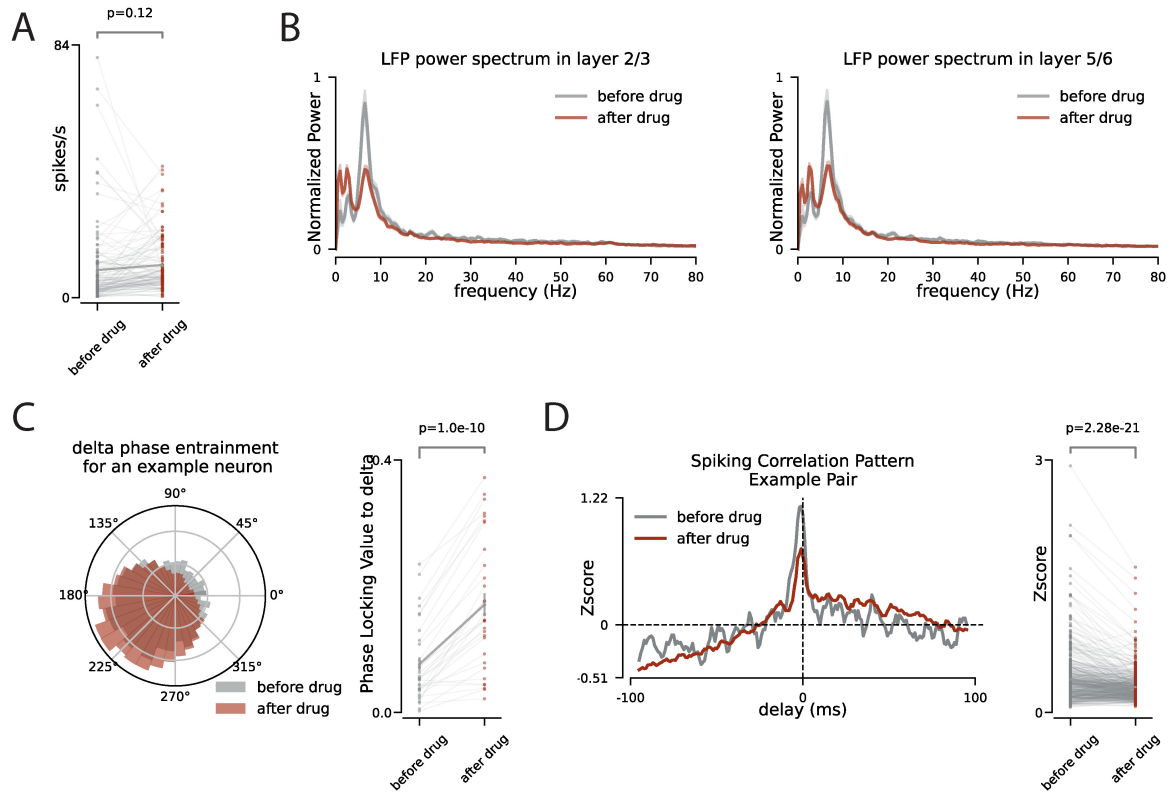

FIGURE 3
During no facial motion, VIP inhibition increases delta power and phase locking of spiking to the delta but decreases the synchronous spiking of the neurons. **(A)** During the no facial motion periods (stillness) the firing rate of neurons (n = 166) is compared before and after the CNO injection. **(B)** The power spectrum of the LFP during the no facial motion periods before (gray) and after (red) CNO injection, shaded area is s.e.m. **(C)** Left panel: the polar distribution of spiking of an example neuron relative to the phase of delta oscillation. Right panel: the change in phase locking value to the delta oscillation for all neurons with significant phase locking to the delta. **(D)** Left panel: The pattern of spiking synchrony between two example neurons before (gray) and after (red) CNO injection. The horizontal dashed line is the chance level. The y-axis is the z-score relative chance level. Right panel: The change in peak of the pairwise spiking synchrony before and after the CNO injection across all pairs of neurons that are recorded simultaneously.

in activity across the cortex (Harris and Thiele, 2011). However, the circuitry of the cell types involved in relaying the effect of Ach remains largely unexplored. Different types of inhibitory cell types have been shown to be activated during the mice locomotion (Fu et al., 2014; Lee et al., 2013), however, the more subtle changes in the behavioral state like fluctuations in pupil size or mice facial motion are also reflected in the activity of distinct inhibitory cell types (Muñoz et al., 2017). Here we showed that the activity of VIP-interneurons modulates the effect of the behavioral state on the neuronal spiking in V1. This observation fits well with the well-known disinhibitory effect of VIPs on the network through the SST interneurons (Pi et al., 2013). Because SST interneurons are active during the activated cortical state (Muñoz et al., 2017), they are likely to reduce the effect of direct excitation of Ach into the network. This is consistent with the idea that when VIPs are active, they suppress the inhibition from SSTs and so the Ach becomes more effective in boosting the network activity. Our study provides evidence for the role of VIP-Interneurons in the circuitry behind the correlation between neural activity in V1 and behavioral state, however, it remains to show if VIP-Interneurons play a similar role in other cortical regions. In this study, we have suppressed the activity of the VIP interneurons in the hole brain using chemogenetics in the transgenic animals. The short-range connectivity of VIP interneurons suggests that the observed effects on the network are induced by the local VIP interneurons, however, we need further experiments to completely rule out the possibility of effect of VIP interneurons in other regions by local inhibition of VIP interneurons.

4 Methods

4.1 Animals, headpost Surgery, and treadmill habituation

All animal handling procedures were performed under guidelines approved by the Albert Einstein College of Medicine Institutional Animal Care and Use Committee and federal guide. For the control experiments (1), we handled wild-type male mice (n = 5), aged 3–5 months, for 10–15 min daily for 3 days before headpost surgery. On the day of surgery, the mouse was anesthetized with isoflurane and the scalp was cleaned with Betadine solution. After making a midline incision, the scalp was resected to expose the skull. A tungsten wire (50 μm) was then inserted into the right cerebellum through a small hole.

This tungsten wire was connected to a gold-plated pin (World Precision Instruments) to serve as the ground/reference connection during electrophysiology recording. The reference pin and a custom 3D printed headpost were affixed to the skull using dental cement. However, the target recording site, left V1, was left free from cement and was merely sealed with vetbond. After surgery, analgesics were administered to help with recovery. Following a 3- to 5-day recovery period after surgery, the mice began treadmill training. Over the next 4 days, we gradually increased the time the mice were head-fixed on the treadmill, continuing until they appeared comfortable and started running without obvious stress. For VIP suppression experiments (2), we crossed Vip-IRES-cre (C57BL/6J) and R26-LSL-Gi-DREADD lines to express the inhibitory DREADD exclusively at VIP interneurons. Similar procedures as described for the wild-type animals were performed on the transgenic animals ($n = 4$).

4.2 Electrophysiology and behavioral state monitoring

Approximately 16–20 h before the recording, a small craniotomy was performed over the left V1 under light anesthesia using isoflurane, ensuring the dura remained intact. After craniotomy, the site was sealed with Kwik-Cast (World Precision Instruments), and the animal was allowed to recover in preparation for the recording session the next day. Single-shank 64-channel silicon probes (Sharpened H3, Cambridge NeuroTech) were used for the recordings. The probe was inserted 1200 μm deep from the dura at a rate of 1 μm/s and then retracted by 100 μm for faster stabilization. The broadband signal was recorded using an RHD USB interface board (Intan) at a rate of 20 k Sample/s. For the LFP, the broadband signal from each channel was low-pass filtered (<200 Hz) and downsampled to 2 k Sample/s. To reduce shared high-frequency noise, the signal from each channel was high-pass filtered (>300 Hz) and subtracted by the median of the high-pass filtered signals across the 64 channels at each time point. These median-corrected high-pass filtered signals were then processed to extract spike times using KiloSort (Pachitariu et al., 2024). The KiloSort output was manually curated to discard non-spike patterns. In VIP suppression experiments we injected 5 μg/kg of CNO in the second half of the experiment.

The left half of the mouse face was recorded with the BFLY-PGE-13S2M-CS camera (FLIR) at 30 frames/s under infrared illumination. The recorded frames were synchronized with the electrophysiology signal using the TTL pulses the camera sends out during each frame's lens opening. The facemap software was used to extract the pupil size and facial motion (Syeda et al., 2022). To track facial movement, a rectangular window containing the whiskers and nose was selected. At this frame rate (30 frames/s) the temporal resolution (~33 ms) is enough to capture neural dynamics as fast as beta and slower dynamics as we report in Figure 1. To evaluate the correlation dynamics between spiking activity and behavioral measures (pupil size and facial motion), we calculate the average of the behavioral measures in 20 s windows (±10 s) around each detected spike of each cell (Figures 2C–E). In Figure 1, we have zoomed around the delays up to 6 s to better show the difference between dynamics of pupil size and the facial motion.

To estimate the power spectrum using Fast Fourier Transform (FFT), we used the Welsh method implemented in the Python Scipy package. We applied this FFT estimation on non-overlapping windows of 5 s long. The estimated power spectrum was normalized by the total power of the signal and the spectrum was corrected for the 1/f component (Gerster et al., 2022).

Data availability statement

The raw data supporting the conclusions of this article will be made available by the authors, without undue reservation.

Ethics statement

The animal study was approved by the IUCAC from Albert Einstein College of Medicine. The study was conducted in accordance with the local legislation and institutional requirements.

Author contributions

ES: Conceptualization, Data curation, Formal analysis, Investigation, Methodology, Software, Writing – original draft, Writing – review and editing. RB-B: Conceptualization, Funding acquisition, Investigation, Project administration, Resources, Supervision, Writing – original draft, Writing – review and editing.

Funding

The author(s) declare that financial support was received for the research, authorship, and/or publication of this article. This work was supported by a NARSAD Young Investigator Award, a Simons Bridge to Independence Award, a Whitehall Award, and National Institutes of Health (NIH) grants R01EY034617, R21MH133097, and R01EY034310.

Conflict of interest

The authors declare that the research was conducted in the absence of any commercial or financial relationships that could be construed as a potential conflict of interest.

Publisher's note

References

Akbarian, S., Kim, J. J., Potkin, S. G., Hetrick, W. P., Bunney, W. E., and Jones, E. G. (1996). Maldistribution of interstitial neurons in prefrontal white matter of the brains of schizophrenic patients. *Arch. Gen. Psychiatry* 53, 425–436. doi: 10.1001/ARCHPSYC.1996.01830050061010

Askew, C. E., Lopez, A. J., Wood, M. A., and Metherate, R. (2019). Nicotine excites VIP interneurons to disinhibit pyramidal neurons in auditory cortex. *Synapse* 73:2116. doi: 10.1002/SYN.22116

Batista-Brito, R., Vinck, M., Ferguson, K. A., Chang, J. T., Laubender, D., Lur, G., et al. (2017). Developmental dysfunction of VIP interneurons impairs cortical circuits. *Neuron* 95, 884–895. doi: 10.1016/J.NEURON.2017.07.034

Batista-Brito, R., Zagha, E., Ratliff, J. M., and Vinck, M. (2018). Modulation of cortical circuits by top-down processing and arousal state in health and disease. *Curr. Opin. Neurobiol.* 52, 172–181. doi: 10.1016/J.CONB.2018.06.008

Beasley, C. L., Cotter, D. R., and Everall, I. P. (2002). Density and distribution of white matter neurons in schizophrenia, bipolar disorder and major depressive disorder: No evidence for abnormalities of neuronal migration. *Mol. Psychiatry* 7, 564–570. doi: 10.1038/sj.mp.4001038

Cardin, J. A. (2018). Inhibitory interneurons regulate temporal precision and correlations in cortical circuits. *Trends Neurosci.* 41, 689–700. doi: 10.1016/J.TINS.2018.07.015

Eastwood, S., and Harrison, P. (2003). Interstitial white matter neurons express less reelin and are abnormally distributed in schizophrenia: Towards an integration of molecular and morphologic aspects of the neurodevelopmental hypothesis. *Mol. Psychiatry* 8:769. doi: 10.1038/SJ.MP.4001399

Fu, Y., Tucciarone, J. M., Espinosa, J. S., Sheng, N., Darcy, D. P., Nicoll, R. A., et al. (2014). A cortical circuit for gain control by behavioral state. *Cell* 156, 1139–1152. doi: 10.1016/J.CELL.2014.01.050

Gerster, M., Waterstraat, G., Litvak, V., Lehnertz, K., Schnitzler, A., Florin, E., et al. (2022). Separating neural oscillations from aperiodic 1/f activity: Challenges and recommendations. *Neuroinformatics* 20:991. doi: 10.1007/S12021-022-09581-8

Goard, M., and Dan, Y. (2009). Basal forebrain activation enhances cortical coding of natural scenes. *Nat. Neurosci.* 11, 1444–1449. doi: 10.1038/nn.2402

Harris, K. D., and Thiele, A. (2011). Cortical state and attention. *Nat. Rev. Neurosci.* 12, 509–523. doi: 10.1038/nrn3084

Iwańczuk, W., and Guźniczak, P. (2015). Neurophysiological foundations of sleep, arousal, awareness and consciousness phenomena. Part 2. *Anaesthesiol. Intensive Ther.* 47, 168–174. doi: 10.5603/AIT 2015.0016

Karnani, M. M., Jackson, J., Ayzenshtat, I., Tucciarone, J., Manoocheri, K., Snider, W. G., et al. (2016b). Cooperative subnetworks of molecularly similar interneurons in mouse neocortex. *Neuron* 90, 86–100. doi: 10.1016/J.NEURON.2016.02.037

Karnani, M. M., Jackson, J., Ayzenshtat, I., Sichani, X. H., Manoocheri, K., Kim, S., et al. (2016a). Opening holes in the blanket of inhibition: Localized lateral disinhibition by VIP interneurons. *J. Neurosci.* 36, 3471–3480. doi: 10.1523/JNEUROSCI.3646-15.2016

Kohn, A., Coen-Cagli, R., Kanitscheider, I., and Pouget, A. (2016). Correlations and neuronal population information. *Annu. Rev. Neurosci.* 39, 237–256. doi: 10.1146/ANNUREV-NEURO-070815-013851/CITE/REFWORKS

Lee, S. H., and Dan, Y. (2012). Neuromodulation of brain states. *Neuron* 76, 209–222. doi: 10.1016/J.NEURON.2012.09.012

Lee, S., Kruglikov, I., Huang, Z. J., Fishell, G., and Rudy, B. (2013). A disinhibitory circuit mediates motor integration in the somatosensory cortex. *Nat. Neurosci.* 16, 1662–1670. doi: 10.1038/nn.3544

Lohani, S., Moberly, A. H., Benisty, H., Landa, B., Jing, M., Li, Y., et al. (2022). Spatiotemporally heterogeneous coordination of cholinergic and neocortical activity. *Nat. Neurosci.* 12, 1706–1713. doi: 10.1038/s41593-022-01202-6

McGinley, M. J., Vinck, M., Reimer, J., Batista-Brito, R., Zagha, E., Cadwell, C. R., et al. (2015). Waking state: Rapid variations modulate neural and behavioral responses. *Neuron* 87, 1143–1161. doi: 10.1016/J.NEURON.2015.09.012

Miyoshi, G., and Fishell, G. (2011). GABAergic interneuron lineages selectively sort into specific cortical layers during early postnatal development. *Cereb. Cortex* 21, 845–852. doi: 10.1093/CERCOR/BHQ155

Muñoz, W., Tremblay, R., Levenstein, D., and Rudy, B. (2017). Layer-specific modulation of neocortical dendritic inhibition during active wakefulness. *Science* 355, 954–959. doi: 10.1126/SCIENCE.AAG2599

Niell, C. M., and Stryker, M. P. (2010). Modulation of visual responses by behavioral state in mouse visual cortex. *Neuron* 65, 472–479. doi: 10.1016/j.neuron.2010.01.033

Pachitariu, M., Sridhar, S., Pennington, J., and Stringer, C. (2024). Spike sorting with Kilosort4. *Nat. Methods* 5, 914–921. doi: 10.1038/s41592-024-02232-7

Pi, H.-J., Hangya, B., Kvitsiani, D., Sanders, J. I., Huang, Z. J., and Kepecs, A. (2013). Cortical interneurons that specialize in disinhibitory control. *Nature* 503, 521–524.

Saper, C. B., Fuller, P. M., Pedersen, N. P., Lu, J., and Scammell, T. E. (2010). Sleep state switching. *Neuron* 68, 1023–1042. doi: 10.1016/J.NEURON.2010.11.032

Shadlen, M. N., and Newsome, W. T. (1994). Noise, neural codes and cortical organization. *Curr. Opin. Neurobiol.* 4, 569–579. doi: 10.1016/0959-4388(94)90059-0

Stringer, C., Pachitariu, M., Steinmetz, N., Reddy, C. B., Carandini, M., and Harris, K. D. (2019). Spontaneous behaviors drive multidimensional, brainwide activity. *Science* 364:255.

Syeda, A., Zhong, L., Tung, R., Long, W., Pachitariu, M., and Stringer, C. (2022). Facemap: A framework for modeling neural activity based on orofacial tracking. *bioRxiv* [Preprint]. doi: 10.1101/202211.03.515121bioRxiv:2022.11.03.515121

Tremblay, R., Lee, S., and Rudy, B. (2016). GABAergic interneurons in the neocortex: From cellular properties to circuits. *Neuron* 91:260. doi: 10.1016/J.NEURON.2016.06.033

Vinck, M., Batista-Brito, R., Knoblich, U., and Cardin, J. A. (2015). Arousal and locomotion make distinct contributions to cortical activity patterns and visual encoding. *Neuron* 86, 740–754.

Werner, G., and Mountcastle, V. B. (1963). The variability of central neural activity in a sensory system, and its implications for the central reflection of sensory events. *J. Neurophysiol.* 26, 958–977. doi: 10.1152/JN.1963.26.6.958

frontiers | Frontiers in Cellular Neuroscience

TYPE Mini Review
PUBLISHED 23 September 2024
DOI 10.3389/fncel.2024.1465821

OPEN ACCESS

EDITED BY
Anirban Paul,
The Pennsylvania State University,
United States

REVIEWED BY
Andrzej W. Cwetsch,
Instituto de Biotecnología y Biomedicina
Universidad de Valencia, Spain
Dhananjay Huilgol,
Duke University, United States

*CORRESPONDENCE
Renata Batista-Brito
✉ renata.brito@einsteinmed.edu

RECEIVED 16 July 2024
ACCEPTED 05 September 2024
PUBLISHED 23 September 2024

CITATION
Ward C, Sjulson L and Batista-Brito R (2024) The function of *Mef2c* toward the development of excitatory and inhibitory cortical neurons.
Front. Cell. Neurosci. 18:1465821.
doi: 10.3389/fncel.2024.1465821

The function of *Mef2c* toward the development of excitatory and inhibitory cortical neurons

Claire Ward[1], Lucas Sjulson[1,2] and Renata Batista-Brito[1,2,3]*

[1]Dominick P. Purpura Department of Neuroscience, Albert Einstein College of Medicine, Bronx, NY, United States, [2]Department of Psychiatry and Behavioral Sciences, Albert Einstein College of Medicine, Bronx, NY, United States, [3]Department of Genetics, Albert Einstein College of Medicine, Bronx, NY, United States

Neurodevelopmental disorders (NDDs) are caused by abnormal brain development, leading to altered brain function and affecting cognition, learning, self-control, memory, and emotion. NDDs are often demarcated as discrete entities for diagnosis, but empirical evidence indicates that NDDs share a great deal of overlap, including genetics, core symptoms, and biomarkers. Many NDDs also share a primary sensitive period for disease, specifically the last trimester of pregnancy in humans, which corresponds to the neonatal period in mice. This period is notable for cortical circuit assembly, suggesting that deficits in the establishment of brain connectivity are likely a leading cause of brain dysfunction across different NDDs. Regulators of gene programs that underlie neurodevelopment represent a point of convergence for NDDs. Here, we review how the transcription factor MEF2C, a risk factor for various NDDs, impacts cortical development. Cortical activity requires a precise balance of various types of excitatory and inhibitory neuron types. We use MEF2C loss-of-function as a study case to illustrate how brain dysfunction and altered behavior may derive from the dysfunction of specific cortical circuits at specific developmental times.

KEYWORDS

cortical development, MEF2C haploinsufficiency syndrome, autism spectrum disorder, GABA, interneurons

Introduction

Neurodevelopmental disorders (NDDs), such as autism spectrum disorder (ASD), intellectual disability, and schizophrenia, represent a leading cause of neuropsychiatric illness, affecting one in eight children in the US (Bitta et al., 2017). We remain far from understanding the complex biology underlying NDDs; however, recent human genetic studies have consistently shown large degrees of genetic overlap between distinct NDDs (International Schizophrenia Consortium et al., 2009; Williams et al., 2011; Cross-Disorder Group of the Psychiatric Genomics Consortium, 2013; Insel and Landis, 2013; Ruderfer et al., 2014; Cross-Disorder Group of the Psychiatric Genomics Consortium, 2019). Recent work shows that subtle genetic changes, especially during critical developmental periods, can cause diverse impairments in brain activity and behavior. NDD risk-associated genes are highly expressed during neonatal development, a sensitive period for NDDs notable for cortical circuit assembly and synaptic maturation (LeBlanc and Fagiolini, 2011; Willsey et al., 2013; Meredith, 2015; Marin, 2016; Satterstrom et al., 2020). These findings have introduced the possibility that changes to a small set of common signaling pathways might

result in various NDD phenotypes. The identification of these common signaling pathways is a fundamental aim of NDD research. Consistent with this idea, NDDs often present with a shared set of core symptoms and feature common biomarkers, such as changes in brain synchrony and cortical oscillations (Bartos et al., 2007; Milh et al., 2007; Lakatos et al., 2008; Allene and Cossart, 2010; Tan et al., 2013; Fryer et al., 2016; Hwang et al., 2016; Seibt et al., 2016).

Using bioinformatics and ever-growing genetic data, many known NDD-associated genes have been classified according to cellular and circuit functions. Numerous cellular processes are impaired across NDDs, including transcriptional and epigenetic regulation, neuronal proliferation, neuronal migration, neuronal survival, connectivity of both excitatory and inhibitory circuits (Rossignol, 2011; Meredith, 2015; Marin, 2016; Krol and Feng, 2018), and synaptic transmission (Chattopadhyaya and Cristo, 2012; Clement et al., 2012; Meredith et al., 2012; Estes et al., 2015; Meredith, 2015; Canitano and Pallagrosi, 2017; Krol and Feng, 2018; Parenti et al., 2020). Transcription factors, a group of proteins that interact with DNA and regulate gene expression through modulation of RNA synthesis, represent a major point of convergence for neurodevelopmental and neuropsychiatric diseases (Santos-Terra et al., 2021). One of such transcription factors is the myocyte enhancement factor 2c protein (MEF2C), which is encoded by the MEF2C gene in humans and the orthologous Mef2c gene in mice. MEF2C has been widely associated with various NDDs such as autism spectrum disorder (ASD), schizophrenia, bipolar disorder (Harrington et al., 2016; Rajkovich et al., 2017; Tu et al., 2017; Assali et al., 2019). In this review we will treat *Mef2c* as a test case for how changes in one gene can impact excitatory and inhibitory cortical circuits, and will focus on how dysfunction of *Mef2c* in different cortical circuits relates to pathological pattens of activity and altered behavior.

Mef2c and neurodevelopmental disorders

Human genome-wide association studies (GWAS) reveal that *MEF2C* is a common genetic risk factor for various neurodevelopmental and neuropsychiatric disorders (Gandal et al., 2018; Harrington et al., 2020; Fahey et al., 2023). Microdeletions or coding-region missense or nonsense mutations in *MEF2C* during development can lead to *MEF2C* haploinsufficiency syndrome, which often features intellectual disability, epilepsy, and autism spectrum disorder (Borlot et al., 2019; Chaudhary et al., 2021; Cooley Coleman et al., 2021; Cooley Coleman et al., 2022), and loss of *Mef2c* in rodent models leads to profound changes in behaviors associated with NDDs (Barbosa et al., 2008; Li H. et al., 2008; Adachi et al., 2016; Harrington et al., 2016; Deczkowska et al., 2017; Tu et al., 2017; Bjorness et al., 2020; Harrington et al., 2020; Li et al., 2023; Cho et al., 2024; Ward et al., 2024) (Figure 1A).

The symptom severity associated with MEF2C loss-of-function, along with the number of NDDs associated with it, underscore its necessity in regulating genetic programs during neurodevelopment. Gene ontology studies in mice revealed that *Mef2c* regulates processes such as neurogenesis, neuronal differentiation and morphogenesis, cell survival, and synapse development (Harrington et al., 2016; Tu et al., 2017; Harrington et al., 2020; Allaway et al., 2021). Indeed, *Mef2c* knockdown mice exhibit many cellular deficits, such as reduced neurogenesis, increased cell death, and increased excitatory to inhibitory (E/I) neurotransmission (Tu et al., 2017) (Figure 1B). In addition to the many cellular phenotypes, *Mef2c* knockdown mice exhibit behavioral phenotypes common to mouse models of NDDs, such as hyperactivity and deficits in social interactions (Tu et al., 2017; Harrington et al., 2020; Li et al., 2023), enabling us to investigate the circuits involved in *Mef2c*-related pathophysiology and behavior.

Mef2c regulates the cellular and synaptic development of excitatory and inhibitory neurons

Mef2c is highly expressed within the cerebral cortex throughout the life of an animal, including during embryonic development. *Mef2c* is broadly expressed in pyramidal cells, the principal excitatory cells of the cortex, and subsets of inhibitory interneurons (Assali et al., 2019). Within GABAergic cortical interneurons *Mef2c* is expressed in virtually all parvalbumin-expressing INs (PV-INs) and a subset of somatostatin expressing INs (SST-INs) (Mayer et al., 2018; Ward et al., 2024). Using conditional genetics, and with the increasing availability of mouse Cre-driver lines that can be used to target specific cell types across various stages of development, we have gained a granularity that allows for better understanding of how *Mef2c*-mediated gene regulation is critical for the development of excitatory and inhibitory circuits, as detailed in Table 1.

Neurogenesis, neuronal differentiation, and survival

The MEF2C transcription factor is critical during development and regulates neurogenesis, neuronal differentiation, and survival (Mao et al., 1999; Li H. et al., 2008; Li Z. et al., 2008) (Figure 1C). Removal of the *Mef2c* gene in Nestin-expressing neural stem/progenitor cells impairs neuronal proliferation and results in disrupted layer formation at embryonic day 18.5 (E18.5) and disorganized cortical plate at postnatal day 7 (P7) (Li H. et al., 2008). Deficits in neuronal migration may be a common feature in ASDs, and despite the distinct progenitor pools and migratory streams of excitatory and inhibitory neurons, deficits in *Mef2c* expression have been shown to affect both cell types (Li H. et al., 2008; Reiner et al., 2016). This effect appears to be dependent on factors such as cell type, dose, and developmental stage, as we highlight across many molecular and behavioral phenotypes in this review. Embryonic removal of *Mef2c* from excitatory neurons alone does not lead to gross changes in cortical structure, while overexpression of *Mef2c* in adult born neurons leads to mislocalization in the hippocampus (Harrington et al., 2016; Basu et al., 2024). MEF2C continues to be expressed in postmitotic pyramidal cells, where it promotes their survival by activating anti-apoptotic genes and inhibiting pro-apoptotic pathways, thus highlighting its protective role in the nervous system (Li Z. et al., 2008; Tu et al., 2017). MEF2C promotes differentiation by regulating the expression of genes involved in neuronal differentiation and maturation, such as *Bdnf* (Lyons et al., 2012; Harrington et al., 2016; Tu et al., 2017;

TABLE 1 Cellular and behavioral phenotypes in *Mef2c* mouse models.

Models		
Mef2c+/− (Haploinsufficiency model)	Single copy from all cells, embryonic	Tu et al., 2017; Harrington et al., 2020; Li et al., 2023
Nestin-Cre:*Mef2c*$^{F/null}$ or *Mef2c*$^{F/F}$	Neuronal progenitor, embryonic	Li H. et al., 2008; Chen et al., 2016
GFAP-Cre:*Mef2c*$^{F/F}$ (GFAP^{cKO})	Radial glial cells, embryonic	Barbosa et al., 2008
Emx1-Cre:*Mef2c*$^{F/F}$ (Emx1^{cKO})	Excitatory forebrain neurons, embryonic	Harrington et al., 2016
Emx1-Cre:*Mef2c*$^{F/+}$ (Emx1^{cHet})	""	Harrington et al., 2020
CAMKII-Cre:*Mef2c*$^{F/F}$ (CAMKII^{cKO})	Excitatory forebrain neurons, postnatal	Adachi et al., 2016
Ascl-CreER:*Mef2c*$^{F/F}$ (Aslc^{cKO})	Hippocampal adult born neurons	Basu et al., 2024
VGAT-Cre:*Mef2c*$^{F/+}$ (VGAT^{cHet})	GABAergic neurons, embryonic	Cho et al., 2024
Lhx6-Cre:*Mef2c*$^{F/F}$ (Lhx6^{cKO})	PV-IN and SST-IN progenitors, embryonic	Ward et al., 2024
Lhx6-Cre:*Mef2c*$^{F/+}$(Lhx6^{cHet})	""	Ward et al., 2024
PV-Cre:*Mef2c*$^{F/F}$ (PV^{cKO})	PV-INs, postnatal	Ward et al., 2024
PV-Cre:*Mef2c*$^{F/+}$ (PV^{cHet})	""	Harrington et al., 2020
SST-Cre:*Mef2c*$^{F/+}$ (SST^{cHet})	SST-INs, embryonic	Cho et al., 2024
VIP-Cre:*Mef2c*$^{F/+}$ (VIP^{cHet})	VIP-INs, embryonic	Cho et al., 2024
Cx3Cr1-Cre^{ER}:*Mef2c*$^{F/+}$ (Cx3Cr1^{cHet})	Microglia, embryonic	Deczkowska et al., 2017; Harrington et al., 2020
Cx3Cr1-Cre^{ER}:*Mef2c*$^{F/+}$ (Cx3Cr1^{cHet})	Microglia, embryonic	Harrington et al., 2020
Cellular phenotypes		
Dendritic Spines	= *Mef2c*$^{+/-}$	Harrington et al., 2020
	↓ *Mef2c*$^{+/-}$	Li et al., 2023
	↑ GFAP^{cKO}	Barbosa et al., 2008
	↓ Emx1^{cKO}	Harrington et al., 2016
	↑ CAMKII^{cKO}	Adachi et al., 2016
	↓ Aslc^{cKO}	Basu et al., 2024
sEPSC or mEPSC amplitude and frequency	↓ Amp ↑ Freq *Mef2c*$^{+/-}$	Tu et al., 2017
	↓ Amp ↑ Freq *Mef2c*$^{+/-}$ (Layer 2/3 cell)	Harrington et al., 2020
	↓ Amp = Freq *Mef2c*$^{+/-}$ (Layer 5 cell)	Harrington et al., 2020
	= Amp ↓Freq *Mef2c*$^{+/-}$	Li et al., 2023
	↓ Amp ↓ Freq Nestin-Cre:*Mef2c*$^{F/null}$	Li H. et al., 2008
	= Amp ↑ Freq GFAP^{cKO}	Barbosa et al., 2008
	↓ Amp ↓ Freq Emx1^{cKO}	Harrington et al., 2016
	↓ Amp ↓ Freq Emx1^{cHet}	Harrington et al., 2020
	= Amp ↓ Freq Aslc^{cKO}	Basu et al., 2024
	= Amp = Freq VGAT^{cHet}	Cho et al., 2024
	= Amp ↓ Freq Lhx6^{cKO}	Ward et al., 2024
	= Amp ↓ Freq Lhx6^{cHet}	Ward et al., 2024
	= Amp = Freq PV^{cKO}	Ward et al., 2024
	= Amp ↓ Freq Cx3Cr1^{cHet}	Harrington et al., 2020
Inhibitory cells and synaptic markers	↓ PV-INs *Mef2c*$^{+/-}$	Tu et al., 2017
	↓ PV-INs *Mef2c*$^{+/-}$	Li et al., 2023
	= PV-INs VGAT^{cHet}	Cho et al., 2024
	↓ PV-INs Lhx6^{cKO}	Ward et al., 2024

(Continued)

TABLE 1 (Continued)

		↓ PV-INs Lhx6^{cHet}	Ward et al., 2024
		= PV-INs PV^{cKO}	Ward et al., 2024
		↓ GAD65 *Mef2c*$^{+/-}$	Tu et al., 2017
		↑ GAD65 Emx1^{cKO}	Harrington et al., 2016
		↓ VGAT *Mef2c*$^{+/-}$	Tu et al., 2017
sIPSC or mIPSC amplitude and frequency		↓ Amp ↓ Freq *Mef2c*$^{+/-}$	Tu et al., 2017
		= Amp = Freq *Mef2c*$^{+/-}$	Harrington et al., 2020
		= Amp = Freq *Mef2c*$^{+/-}$	Li et al., 2023
		↑ Amp ↑ Freq Emx1^{cKO}	Harrington et al., 2016
		= Amp = Freq Aslc^{cKO}	Basu et al., 2024
		= Amp = Freq VGAT^{cHet}	Cho et al., 2024
		= Amp ↓ Freq Lhx6^{cKO}	Ward et al., 2024
		= Amp ↓ Freq Lhx6^{cHet}	Ward et al., 2024
Behavioral phenotypes			
Hyperactivity	Open field track length or beam breaks	= *Mef2c*$^{+/-}$	Tu et al., 2017
		↑ *Mef2c*$^{+/-}$	Harrington et al., 2020
		↑ *Mef2c*$^{+/-}$	Li et al., 2023
		= Nestin-Cre:*Mef2c*$^{F/null}$	Li H. et al., 2008
		= GFAP^{cKO}	Barbosa et al., 2008
		↑ Emx1^{cKO}	Harrington et al., 2016
		↑ Emx1^{cHet}	Harrington et al., 2020
		↑ CAMKII^{cKO}	Adachi et al., 2016
		= Aslc^{cKO}	Basu et al., 2024
		= VGAT^{cHet}	Cho et al., 2024
		↑ Lhx6^{cKO}	Ward et al., 2024
		= Lhx6^{cHet}	Ward et al., 2024
		= PV^{cKO}	Ward et al., 2024
		= SST^{cHet}	Cho et al., 2024
		= VIP^{cHet}	Cho et al., 2024
		= Cx3Cr1^{cKO}	Deczkowska et al., 2017
		= Cx3Cr1^{cHet}	Harrington et al., 2020
Hyperactivity	Jumping	↑ *Mef2c*$^{+/-}$	Harrington et al., 2020
		↑Emx1^{cKO}	Harrington et al., 2016
		↑ Emx1^{cHet}	Harrington et al., 2020
		= VGAT^{cHet}	Cho et al., 2024
		↑ Lhx6^{cKO}	Ward et al., 2024
		= Lhx6^{cHet}	Ward et al., 2024
		= PV^{cKO}	Ward et al., 2024
		= PV^{cHet}	Harrington et al., 2020
		= SST^{cHet}	Cho et al., 2024
		↑ VIP^{cHet}—Males only	Cho et al., 2024
		↑ Cx3Cr1^{cHet}—Males only	Harrington et al., 2020
Motor	Paw clasping	↑ *Mef2c*$^{+/-}$	Tu et al., 2017
		↑ Nestin-Cre:*Mef2c*$^{F/null}$	Li H. et al., 2008

(Continued)

TABLE 1 (Continued)

		↑ GFAP^{cKO}	Barbosa et al., 2008
		↑ CAMKII^{cKO}	Adachi et al., 2016
		↑ Lhx6^{cKO}	Ward et al., 2024
		= Lhx6^{cHet}	Ward et al., 2024
		= PV^{cKO}	Ward et al., 2024
Motor	Ex. Rotarod, balance beam	= *Mef2c*$^{+/-}$	Tu et al., 2017
		= *Mef2c*$^{+/-}$	Harrington et al., 2020
		↓ Emx1^{cKO}	Harrington et al., 2016
		↓ CAMKII^{cKO}	Adachi et al., 2016
Social	3-Chamber social preference Time spent with social stimuli	↓ *Mef2c*$^{+/-}$	Tu et al., 2017
		↓ *Mef2c*$^{+/-}$	Harrington et al., 2020
		= *Mef2c*$^{+/-}$	Li et al., 2023
		↓ Emx1^{cKO}	Harrington et al., 2016
		= Emx1^{cHet}	Harrington et al., 2020
		= CAMKII^{cKO}	Adachi et al., 2016
		= Aslc^{cKO}	Basu et al., 2024
		↓ VGAT^{cHet}—Females only	Cho et al., 2024
		↓ Lhx6^{cKO}	Ward et al., 2024
		= Lhx6^{cHet}	Ward et al., 2024
		= PV^{cKO}	Ward et al., 2024
		= PV^{cHet}	Harrington et al., 2020
		= SST^{cHet}	Cho et al., 2024
		= VIP^{cHet}	Cho et al., 2024
		↓ Cx3Cr1^{cHet}	Harrington et al., 2020
		↓ Cx3Cr1^{cKO}	Deczkowska et al., 2017
Social	Ultrasonic vocalizations	↓ *Mef2c*$^{+/-}$	Harrington et al., 2020
		↓ Emx1^{cKO}	Harrington et al., 2016
		↓ Nestin^{cKO}	Chen et al., 2016
		= VGAT^{cHet}	Cho et al., 2024
Exploration	Elevated plus maze Open arm time or track length	↑ *Mef2c*$^{+/-}$	Harrington et al., 2020
		↑ Nestin-Cre:*Mef2c*$^{F/null}$	Li H. et al., 2008
		= GFAP^{cKO}	Barbosa et al., 2008
		↑ Emx1^{cHet}	Harrington et al., 2020
		= PV^{cHet}	Harrington et al., 2020
		↑ VGAT^{cHet}—Females only	Cho et al., 2024
		↑ Lhx6^{cKO}	Ward et al., 2024
		= Lhx6^{cHet}	Ward et al., 2024
		= SST^{cHet}	Cho et al., 2024
		= VIP^{cHet}	Cho et al., 2024
Cognitive	Barnes maze	↑ *Mef2c*$^{+/-}$	Tu et al., 2017
	Escape latency	= *Mef2c*$^{+/-}$	Harrington et al., 2020

(Continued)

TABLE 1 (Continued)

Cognitive	Fear conditioning time spent freezing	= *Mef2c*$^{+/-}$	Harrington et al., 2020
		↑ Nestin-Cre:*Mef2c*$^{F/null}$	Li H. et al., 2008
		↓ GFAP^{cKO}	Barbosa et al., 2008
		↓ Emx1^{cKO}	Harrington et al., 2016
		↓ Aslc^{cKO}	Basu et al., 2024
		= VGAT^{cHet}	Cho et al., 2024
		↑ SST^{cHet}—Females only	Cho et al., 2024
		= VIP^{cHet}	Cho et al., 2024

Comparison of transgenic mouse models of *Mef2c* loss-of-function, with an emphasis on studies containing cellular characterizations within the cortex. *Mef2c* Haploinsufficiency models feature a disrupted expression of a single *Mef2c* allele in all cells, while conditional loss-of-function models are cell-type specific, with varied Cre-dependent removal times and numbers of affected alleles. Select cellular and behavioral characterizations common across mouse models are compared. No change in phenotype relative to wildtype animals is denoted as "=," while "↑" and "↓" indicate increases or decreases in a given cellular or behavioral phenotype, respectively.

Avarlaid et al., 2024), and has been shown to regulate excitatory neurons' dendritic arborization, and axonal guidance (Ma and Telese, 2015; Harrington et al., 2016; Tu et al., 2017; Basu et al., 2024). Embryonic overexpression of *Mef2c* increases basal dendritic arborization (Jung et al., 2016), while reduced *Mef2c* results in decreased arborization (Tu et al., 2017). MEF2C has been shown to positively modulate the expression of MECP2 (Zweier et al., 2010; Paciorkowski et al., 2013), a transcriptional regulator that facilitates expression of the KCC2 ion channel that is critical for developmental transition from the excitatory to inhibitory of action GABA (Tang et al., 2016; Oyarzabal et al., 2020), and it is possible that this aspect of cellular development could be affected by *Mef2c* loss of function as well. In addition, depletion of MEF2C leads to the defective activation of the mTOR pathway (Pereira et al., 2009) and mTOR positively regulates MEF2C (Wu et al., 2015). Furthermore, members of the MEF2C interactome are strongly linked to mTOR pathway activity, such as MECP2 (Ricciardi et al., 2011; Tsujimura et al., 2015; Rangasamy et al., 2016; Olson et al., 2018; Zhang et al., 2018) and FMR1 (Sharma et al., 2010; Casingal et al., 2020; Zhang et al., 2024). These serve as examples of the many gene regulatory networks implicated in neurodevelopmental disorders that are upstream or downstream of *Mef2c* (D'Haene et al., 2019; Zhang and Zhao, 2022). *Mef2c* is also expressed in cortical interneurons originating in the medial ganglionic eminence (MGE) (Mayer et al., 2018; Ward et al., 2024). *Mef2c* is expressed in cortical parvalbumin interneuron (PV-IN) precursors during embryonic development, where it functions as the earliest indicator of PV-IN fate and is necessary for the survival and molecular maturation of the PV-IN lineage (Mayer et al., 2018). *Mef2c* continues to be expressed in PV-INs throughout the animal's life, but postnatal removal of *Mef2c* using the PV^{Cre} mouse line does not impact PV-IN survival or differentiation (Ward et al., 2024). *Mef2c* is also expressed by roughly 30% of SST-INs, however, its loss does not impact SST-IN survival or differentiation (Ward et al., 2024).

Synapse development and function

Mef2c regulates synaptic transmission and plays a critical role in synapse development and plasticity of cortical pyramidal cells (Barbosa et al., 2008; Li H. et al., 2008; Adachi et al., 2016; Harrington et al., 2016; Rajkovich et al., 2017; Tu et al., 2017; Harrington et al., 2020; Basu et al., 2024). *Mef2c* influences the expression of synaptic proteins, such as Arc and SynGAP, which are involved in synaptic strength and plasticity (Flavell et al., 2006; Harrington et al., 2016; Tu et al., 2017; Puang et al., 2020); however, the role of *Mef2c* in synaptic development is complex. Selective loss of *Mef2c* in cortical pyramidal cells can result in either an increased (Barbosa et al., 2008; Adachi et al., 2016) or decreased (Harrington et al., 2016; Tu et al., 2017; Li et al., 2023) density of dendritic spines, with various changes in electrophysiological synaptic properties (Barbosa et al., 2008; Li Z. et al., 2008; Adachi et al., 2016; Harrington et al., 2016; Tu et al., 2017; Harrington et al., 2020; Ward et al., 2024). These seemingly opposing roles underscore the nuanced role of *Mef2c* in synapse maturation and/or maintenance, which is input- (local versus long-range) and activity-dependent (Rajkovich et al., 2017). *Mef2c* strengthens long-range inputs from the contralateral cortex and weakens local inputs (Rajkovich et al., 2017). Interestingly, *Mef2c* only results in weakened synaptic strength in the presence of sensory experience, highlighting the role of activity in *Mef2c*-dependent function. In addition to the role of sensory experience on *Mef2c* function, *Mef2c* activity is also dependent on sleep (Bjorness et al., 2020). Sleep deprivation leads to *Mef2c*-dependent upregulation of synapse-weakening genes and a reduction in synapse-strengthening genes, as well as changes in glutamatergic synaptic transmission and sleep-dependent synaptic remodeling (Bjorness et al., 2020). *Mef2c* is also necessary for the synaptic maturation of PV-INs (Ward et al., 2024). Embryonic loss of *Mef2c* in MGE INs (Lhx6-Cre:Mef2c$^{F/F}$) causes a massive reduction in glutamatergic synaptic transmission onto INs, but postnatal loss of *Mef2c* by using the line PV^{Cre} does not impact synaptic transmission onto PV-INs (Ward et al., 2024), thus highlighting the critical role of *Mef2c* during development.

E/I imbalance

Imbalances in excitatory and inhibitory synaptic transmission, particularly increased E/I balance, have been proposed to cause various NDDs, including ASD and schizophrenia (Rubenstein and Merzenich, 2003; Gao and Penzes, 2015; Sohal and Rubenstein, 2019; Liu et al., 2021). The E/I imbalance hypothesis was originally based on the observation that patients with NDDs have increased

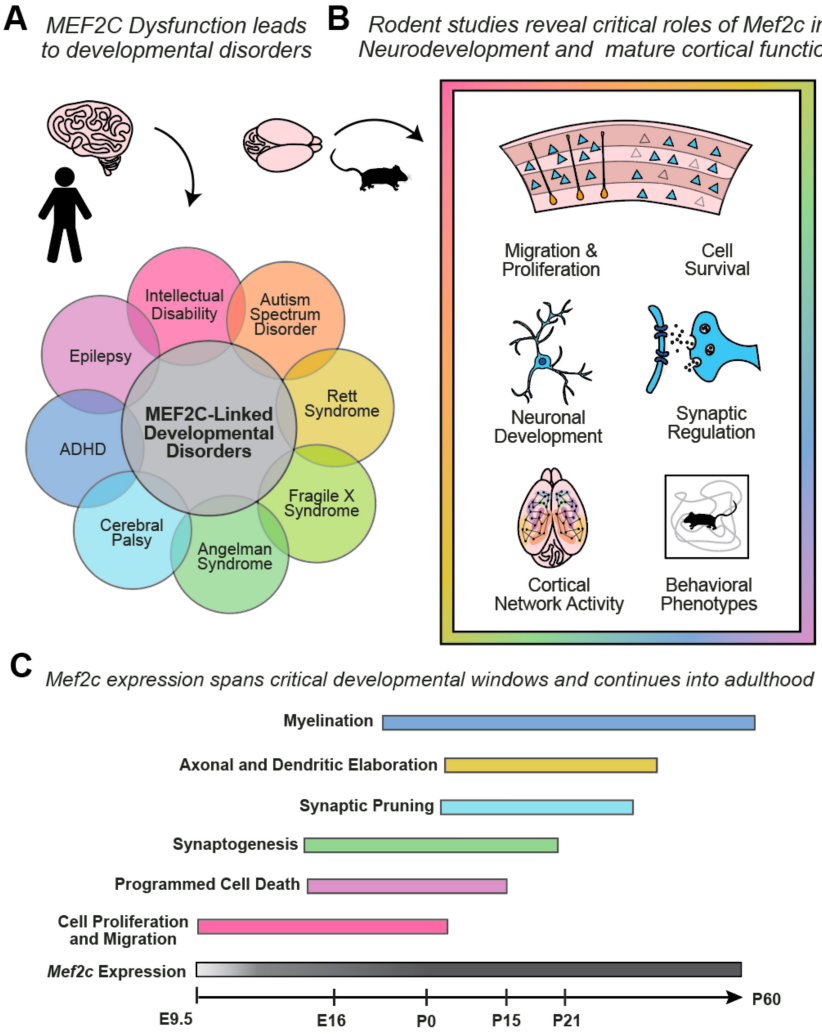

FIGURE 1
(A) Dysfunction of the *MEF2C* gene in humans can give rise to many neurodevelopmental disorders, which often are characterized by overlapping behavioral phenotypes. **(B)** Transgenic mouse studies of the *Mef2c* gene have identified MEF2C as a transcription factor that regulates gene programs that are critical to many cellular processes. Loss of *Mef2c* expression can give rise to impaired neuronal activity across cell populations and leads to behavioral phenotypes typical of mouse models of neurodevelopmental disorders, such as hyperactivity in an open field arena. **(C)** *Mef2c* is expressed from early embryonic development through adulthood, with roles in shaping gene expression during critical neurodevelopmental windows and regulating synapses in mature cortical circuits.

rates of epilepsy, which is true for *MEF2C* haploinsufficiency patients (Cooley Coleman et al., 2021; Wan et al., 2021; Cooley Coleman et al., 2022). However, $GABA_A$ agonists or positive allosteric modulators, which reduce E/I balance, do not alleviate the core symptoms of NDDs (Lingjaerde, 1991), and conditions that increase E/I balance, such as withdrawal from alcohol or sedative/hypnotics (Hendricson et al., 2007), do not cause syndromes resembling NDDs, calling this hypothesis into question. Increasingly, the field is moving away from the overly simplistic one-dimensional E/I imbalance hypothesis to more sophisticated models of cortical circuit dysfunction (O'Donnell et al., 2017; Sohal and Rubenstein, 2019) that incorporate multiple distinct excitatory and inhibitory cell types. The complex cell-type-dependent and temporally-specific effects of *MEF2C* haploinsufficiency provide a compelling illustration of why this more nuanced approach is necessary.

Impact of *Mef2c* on behavior

Despite their complex etiologies, NDDs feature overlapping behavioral traits. Most *Mef2c* loss-of-function mouse models include assays for behavioral domains affected in various NDDs (Table 1). While there is no set battery of tests conducted across NDD studies, there are several phenotypes that stand out across studies. Loss or reduction of *Mef2c* in both pyramidal cells and MGE interneurons leads to hyperactivity (Adachi et al., 2016; Harrington et al., 2016; Harrington et al., 2020; Li et al., 2023; Cho et al., 2024; Ward et al., 2024), paw clasping (Barbosa et al., 2008; Li H. et al., 2008; Adachi et al., 2016; Tu et al., 2017; Ward et al., 2024), and social deficits (Harrington et al., 2016; Deczkowska et al., 2017; Tu et al., 2017; Harrington et al., 2020; Li et al., 2023; Basu et al., 2024; Cho et al., 2024; Ward et al., 2024). *Mef2c*

haploinsufficiency mice (*Mef2c*$^{+/-}$) exhibited hyperactivity and social deficit phenotypes; however, not all assays were in agreement (Tu et al., 2017; Harrington et al., 2020; Li et al., 2023). One study reported that *Mef2c*$^{+/-}$ animals exhibit impaired spatial memory in the Barnes maze and Morris water maze (Tu et al., 2017), however, a separate study of *Mef2c*$^{+/-}$ animals revealed deficits in a battery of cognitive tests including fear conditioning, Barnes maze, y-maze, and an operant reward learning test (Harrington et al., 2020), thus illustrating the challenge comparing behavioral domains across studies.

An advantage of mouse models and the advent of conditional genetics is the ability to investigate how specific brain circuits contribute to pathological neuronal activity and altered behavior (see behavior phenotypes resulting from reduced *Mef2c* in various cell types in Table 1). For instance, Harrington and colleagues observed that both *Mef2c*$^{+/-}$ animals and animals with embryonic loss of *Mef2c* specifically in pyramidal cells (Emx1-Cre:*Mef2c*$^{F/F}$ animals) exhibit a significant reduction in the frequency of ultrasonic vocalizations in pups, with adult animals emitting fewer and less complex vocalizations (Harrington et al., 2016; Harrington et al., 2020). On the other hand, Emx1-Cre:*Mef2c*$^{F/F}$ animals exhibited cognitive deficits in contextual memory fear conditioning while none were observed in *Mef2c*$^{+/-}$ animals when tested on the same paradigm (Harrington et al., 2016; Harrington et al., 2020). Another important factor in considering how the loss of a gene impacts behavior is the age at which the loss occurred. For instance, early (embryonic) but not late (postnatal) removal of *Mef2c* from MGE interneurons leads to hyperactivity (Ward et al., 2024). Furthermore, some studies have found that some behavioral phenotypes are sex specific (Harrington et al., 2020; Cho et al., 2024). There is evidence to suggest that anxiety-like behavior correlates with *Mef2c* expression in a way that is influenced by sex and estrous cycle phase (Jaric et al., 2019; Hong et al., 2024), further underscoring the importance of considering sex as a biological variable. These findings provide an example of how relating gene dysfunction to behavior is extremely challenging; however, investment in relating changes in brain activity with target behaviors holds the promise of revealing the circuits underlying neurodevelopmental behaviors in NDDs.

Discussion

Brain development is a pivotal and meticulously orchestrated process, governed by numerous neurobiological pathways that lay the foundation for essential brain functions. It is likely that various NDDs share pathways and circuits that become altered during prenatal or early postnatal stages. A main challenge in NDD treatment is the fact that diagnosis often occurs after the most effective time for treatment. Early identification of biomarkers for NDDs is critical given its potential for early intervention. Another big challenge is that despite significant advancements in understanding the pathophysiology of NDDs, targeted and effective treatments are still rare. Identification of common NDD molecular pathways and circuit dysfunction could potentially serve as an early prognostic indicator for NDDs and allow for targeted therapies.

The convergence of genetic factors and the existence of critical periods of vulnerability for NDDs underscores the potential for drugs to target fundamental networks as soon as possible in order to prevent or mitigate clinical manifestations of NDDs. However, more work needs to be done to establish a causal link between molecular and circuit abnormalities, disease pathology, and abnormal behavior. Animal models offer the opportunity to comprehensively unravel the molecular, circuit, and temporal intricacies of NDDs, pinpointing potential therapeutic targets, and ultimately informing us about new treatment modalities. In particular, the mouse as a disease model can provide valuable tools in deciphering the intricate genetic landscape of NDDs as well as elucidating the molecular, cellular, and circuit impacts of diverse mutations toward brain development and disease physiology. Interestingly, pharmacological and gene therapy approaches have both been applied in *Mef2c*$^{+/-}$ models, rescuing both cellular and behavioral phenotypes (Tu et al., 2017; Li et al., 2023). Nonetheless, for animal models to be useful it is important to consider the fundamental differences between animal models and humans, especially during development.

Single-cell omics techniques, alongside non-invasive brain activity measures like EEGs, computational models, and bioinformatics network analysis, offer a pathway to delineate parallels between animal models and humans. These methodologies have the potential to unravel the intricate relationship between gene expression alterations during human brain neuronal development and the manifestation of behaviors associated with NDDs. This understanding holds promise for developing tailored therapeutic interventions, catalyzing a transition from the prevailing symptom-based approach toward more proactive, targeted, and effective treatments.

Author contributions

CW: Conceptualization, Writing – original draft, Writing – review & editing. LS: Writing – original draft, Writing – review & editing. RB-B: Conceptualization, Writing – original draft, Writing – review & editing.

Funding

The authors declare that financial support was received for the research, authorship, and/or publication of this article. This work was supported by a Ruth L. Kirschstein Predoctoral Fellowship F31HD101360 to CW; a NARSAD Young Investigator Award, a Simons Bridge to Independence Award, a Whitehall Award, and National Institutes of Health (NIH) grants R01EY034617, R21MH133097, and R01EY034310 to RB-B; DA051608 to LS.

Conflict of interest

The authors declare that the research was conducted in the absence of any commercial or financial relationships that could be construed as a potential conflict of interest.

Publisher's note

References

Adachi, M., Lin, P. Y., Pranav, H., and Monteggia, L. M. (2016). Postnatal loss of Mef2c results in dissociation of effects on synapse number and learning and memory. *Biol. Psychiatry* 80, 140–148. doi: 10.1016/j.biopsych.2015.09.018

Allaway, K. C., Gabitto, M. I., Wapinski, O., Saldi, G., Wang, C. Y., Bandler, R. C., et al. (2021). Genetic and epigenetic coordination of cortical interneuron development. *Nature* 597, 693–697. doi: 10.1038/s41586-021-03933-1

Allene, C., and Cossart, R. (2010). Early NMDA receptor-driven waves of activity in the developing neocortex: Physiological or pathological network oscillations? *J. Physiol.* 588, 83–91. doi: 10.1113/jphysiol.2009.178798

Assali, A., Harrington, A. J., and Cowan, C. W. (2019). Emerging roles for MEF2 in brain development and mental disorders. *Curr. Opin. Neurobiol.* 59, 49–58. doi: 10.1016/j.conb.2019.04.008

Avarlaid, A., Falkenberg, K., Lehe, K., Mudò, G., Belluardo, N., Di Liberto, V., et al. (2024). An upstream enhancer and MEF2 transcription factors fine-tune the regulation of the Bdnf gene in cortical and hippocampal neurons. *J. Biol. Chem.* 300:107411. doi: 10.1016/j.jbc.2024.107411

Barbosa, A. C., Kim, M. S., Ertunc, M., Adachi, M., Nelson, E. D., McAnally, J., et al. (2008). MEF2C, a transcription factor that facilitates learning and memory by negative regulation of synapse numbers and function. *Proc. Natl. Acad. Sci. U.S.A.* 105, 9391–9396. doi: 10.1073/pnas.0802679105

Bartos, M., Vida, I., and Jonas, P. (2007). Synaptic mechanisms of synchronized gamma oscillations in inhibitory interneuron networks. *Nat. Rev. Neurosci.* 8, 45–56. doi: 10.1038/nrn2044

Basu, S., Ro, E. J., Liu, Z., Kim, H., Bennett, A., Kang, S., et al. (2024). The Mef2c gene dose-dependently controls hippocampal neurogenesis and the expression of autism-like behaviors. *J. Neurosci.* 44:1058232023. doi: 10.1523/jneurosci.1058-23.2023

Bitta, M., Kariuki, S. M., Abubakar, A., and Newton, C. (2017). Burden of neurodevelopmental disorders in low and middle-income countries: A systematic review and meta-analysis. *Wellcome Open Res.* 2:121. doi: 10.12688/wellcomeopenres.13540.3

Bjorness, T. E., Kulkarni, A., Rybalchenko, V., Suzuki, A., Bridges, C., Harrington, A. J., et al. (2020). An essential role for MEF2C in the cortical response to loss of sleep in mice. *Elife* 9:e58331. doi: 10.7554/eLife.58331

Borlot, F., Whitney, R., Cohn, R. D., and Weiss, S. K. (2019). MEF2C-related epilepsy: Delineating the phenotypic spectrum from a novel mutation and literature review. *Seizure* 67, 86–90. doi: 10.1016/j.seizure.2019.03.015

Canitano, R., and Pallagrosi, M. (2017). Autism spectrum disorders and schizophrenia spectrum disorders: Excitation/inhibition imbalance and developmental trajectories. *Front. Psychiatry* 8:69. doi: 10.3389/fpsyt.2017.00069

Casingal, C. R., Kikkawa, T., Inada, H., Sasaki, Y., and Osumi, N. (2020). Identification of FMRP target mRNAs in the developmental brain: FMRP might coordinate Ras/MAPK, Wnt/β-catenin, and mTOR signaling during corticogenesis. *Mol. Brain* 13:167. doi: 10.1186/s13041-020-00706-1

Chattopadhyaya, B., and Cristo, G. D. (2012). GABAergic circuit dysfunctions in neurodevelopmental disorders. *Front. Psychiatry* 3:51. doi: 10.3389/fpsyt.2012.00051

Chaudhary, R., Agarwal, V., Kaushik, A. S., and Rehman, M. (2021). Involvement of myocyte enhancer factor 2c in the pathogenesis of autism spectrum disorder. *Heliyon* 7:e06854. doi: 10.1016/j.heliyon.2021.e06854

Chen, Y. C., Kuo, H. Y., Bornschein, U., Takahashi, H., Chen, S. Y., Lu, K. M., et al. (2016). Foxp2 controls synaptic wiring of corticostriatal circuits and vocal communication by opposing *Mef2c*. *Nat. Neurosci.* 19, 1513–1522. doi: 10.1038/nn.4380

Cho, J. Y., Rumschlag, J. A., Tsvetkov, E., Proper, D. S., Lang, H., Berto, S., et al. (2024). MEF2C hypofunction in GABAergic cells alters sociability and prefrontal cortex inhibitory synaptic transmission in a sex-dependent manner. *Biol. Psychiatry Glob. Open Sci.* 4:100289. doi: 10.1016/j.bpsgos.2024.100289

Clement, J. P., Aceti, M., Creson, T. K., Ozkan, E. D., Shi, Y., Reish, N. J., et al. (2012). Pathogenic SYNGAP1 mutations impair cognitive development by disrupting maturation of dendritic spine synapses. *Cell* 151, 709–723. doi: 10.1016/j.cell.2012.08.045

Cooley Coleman, J. A., Sarasua, S. M., Boccuto, L., Moore, H. W., Skinner, S. A., and DeLuca, J. M. (2021). Comprehensive investigation of the phenotype of MEF2C-related disorders in human patients: A systematic review. *Am. J. Med. Genet. A* 185, 3884–3894. doi: 10.1002/ajmg.a.62412

Cooley Coleman, J. A., Sarasua, S. M., Moore, H. W., Boccuto, L., Cowan, C. W., Skinner, S. A., et al. (2022). Clinical findings from the landmark MEF2C-related disorders natural history study. *Mol. Genet. Genom. Med.* 10:e1919. doi: 10.1002/mgg3.1919

Cross-Disorder Group of the Psychiatric Genomics Consortium (2013). Identification of risk loci with shared effects on five major psychiatric disorders: A genome-wide analysis. *Lancet* 381, 1371–1379. doi: 10.1016/S0140-6736(12)62129-1

Cross-Disorder Group of the Psychiatric Genomics Consortium (2019). Genomic relationships, novel loci, and pleiotropic mechanisms across eight psychiatric disorders. *Cell* 179:1469–1482.e1411. doi: 10.1016/j.cell.2019.11.020

D'Haene, E., Bar-Yaacov, R., Bariah, I., Vantomme, L., Van Loo, S., Cobos, F. A., et al. (2019). A neuronal enhancer network upstream of MEF2C is compromised in patients with Rett-like characteristics. *Hum. Mol. Genet*. 28, 818–827. doi: 10.1093/hmg/ddy393

Deczkowska, A., Matcovitch-Natan, O., Tsitsou-Kampeli, A., Ben-Hamo, S., Dvir-Szternfeld, R., Spinrad, A., et al. (2017). Mef2C restrains microglial inflammatory response and is lost in brain ageing in an IFN-I-dependent manner. *Nat. Commun.* 8:717. doi: 10.1038/s41467-017-00769-0

Estes, A., Zwaigenbaum, L., Gu, H., St John, T., Paterson, S., Elison, J. T., et al. (2015). Behavioral, cognitive, and adaptive development in infants with autism spectrum disorder in the first 2 years of life. *J. Neurodev. Disord.* 7: 24. doi: 10.1186/s11689-015-9117-6

Fahey, L., Ali, D., Donohoe, G., and Morris, D. W. (2023). Genes positively regulated by Mef2c in cortical neurons are enriched for common genetic variation associated with IQ and educational attainment. *Hum. Mol. Genet.* 32, 3194–3203. doi: 10.1093/hmg/ddad142

Flavell, S. W., Cowan, C. W., Kim, T. K., Greer, P. L., Lin, Y., Paradis, S., et al. (2006). Activity-dependent regulation of MEF2 transcription factors suppresses excitatory synapse number. *Science* 311, 1008–1012. doi: 10.1126/science.1122511

Fryer, S. L., Roach, B. J., Wiley, K., Loewy, R. L., Ford, J. M., and Mathalon, D. H. (2016). Reduced amplitude of low-frequency brain oscillations in the psychosis risk syndrome and early illness schizophrenia. *Neuropsychopharmacology* 41, 2388–2398. doi: 10.1038/npp.2016.51

Gandal, M. J., Zhang, P., Hadjimichael, E., Walker, R. L., Chen, C., Liu, S., et al. (2018). Transcriptome-wide isoform-level dysregulation in ASD, schizophrenia, and bipolar disorder. *Science* 362:aat8127. doi: 10.1126/science.aat8127

Gao, R., and Penzes, P. (2015). Common mechanisms of excitatory and inhibitory imbalance in schizophrenia and autism spectrum disorders. *Curr. Mol. Med.* 15, 146–167. doi: 10.2174/1566524015666150303003028

Harrington, A. J., Bridges, C. M., Berto, S., Blankenship, K., Cho, J. Y., Assali, A., et al. (2020). MEF2C hypofunction in neuronal and neuroimmune populations produces MEF2C haploinsufficiency syndrome-like behaviors in mice. *Biol. Psychiatry* 88, 488–499. doi: 10.1016/j.biopsych.2020.03.011

Harrington, A. J., Raissi, A., Rajkovich, K., Berto, S., Kumar, J., Molinaro, G., et al. (2016). MEF2C regulates cortical inhibitory and excitatory synapses and behaviors relevant to neurodevelopmental disorders. *Elife* 5:e20059. doi: 10.7554/eLife.20059

Hendricson, A. W., Maldve, R. E., Salinas, A. G., Theile, J. W., Zhang, T. A., Diaz, L. M., et al. (2007). Aberrant synaptic activation of N-methyl-D-aspartate receptors underlies ethanol withdrawal hyperexcitability. *J. Pharmacol. Exp. Ther.* 321, 60–72. doi: 10.1124/jpet.106.111419

Hong, Y., Hu, J., Zhang, S., Liu, J., Yan, F., Yang, H., et al. (2024). Integrative analysis identifies region- and sex-specific gene networks and Mef2c as a mediator of anxiety-like behavior. *Cell Rep.* 43:114455. doi: 10.1016/j.celrep.2024.114455

Hwang, K., Ghuman, A. S., Manoach, D. S., Jones, S. R., and Luna, B. (2016). Frontal preparatory neural oscillations associated with cognitive control: A developmental study comparing young adults and adolescents. *Neuroimage* 136, 139–148. doi: 10.1016/j.neuroimage.2016.05.017

Insel, T. R., and Landis, S. C. (2013). Twenty-five years of progress: The view from NIMH and NINDS. *Neuron* 80, 561–567. doi: 10.1016/j.neuron.2013.09.041

International Schizophrenia Consortium, Purcell, S. M., Wray, N. R., Stone, J. L., Visscher, P. M., O'Donovan, M. C., et al. (2009). Common polygenic variation contributes to risk of schizophrenia and bipolar disorder. *Nature* 460, 748–752. doi: 10.1038/nature08185

Jaric, I., Rocks, D., Greally, J. M., Suzuki, M., and Kundakovic, M. (2019). Chromatin organization in the female mouse brain fluctuates across the oestrous cycle. *Nat. Commun.* 10:2851. doi: 10.1038/s41467-019-10704-0

Jung, Y., Hsieh, L. S., Lee, A. M., Zhou, Z., Coman, D., Heath, C. J., et al. (2016). An epigenetic mechanism mediates developmental nicotine effects on neuronal structure and behavior. *Nat. Neurosci.* 19, 905–914. doi: 10.1038/nn.4315

Krol, A., and Feng, G. (2018). Windows of opportunity: Timing in neurodevelopmental disorders. *Curr. Opin. Neurobiol.* 48, 59–63. doi: 10.1016/j.conb.2017.10.014

Lakatos, P., Karmos, G., Mehta, A. D., Ulbert, I., and Schroeder, C. E. (2008). Entrainment of neuronal oscillations as a mechanism of attentional selection. *Science* 320, 110–113. doi: 10.1126/science.1154735

LeBlanc, J. J., and Fagiolini, M. (2011). Autism: A "critical period" disorder? *Neural Plast.* 2011:921680. doi: 10.1155/2011/921680

Li, H., Radford, J. C., Ragusa, M. J., Shea, K. L., McKercher, S. R., Zaremba, J. D., et al. (2008). Transcription factor MEF2C influences neural stem/progenitor cell differentiation and maturation in vivo. *Proc. Natl. Acad. Sci. U.S.A.* 105, 9397–9402. doi: 10.1073/pnas.0802876105

Li, Z., McKercher, S. R., Cui, J., Nie, Z., Soussou, W., Roberts, A. J., et al. (2008). Myocyte enhancer factor 2C as a neurogenic and antiapoptotic transcription factor in murine embryonic stem cells. *J. Neurosci.* 28, 6557–6568. doi: 10.1523/jneurosci.0134-08.2008

Li, W.-K., Zhang, S.-Q., Peng, W.-L., Shi, Y.-H., Yuan, B., Yuan, Y.-T., et al. (2023). Whole-brain in vivo base editing reverses behavioral changes in Mef2c-mutant mice. *Nat. Neurosci.* 27, 116–128. doi: 10.1038/s41593-023-01499-x

Lingjaerde, O. (1991). Benzodiazepines in the treatment of schizophrenia: An updated survey. *Acta Psychiatr. Scand.* 84, 453–459. doi: 10.1111/j.1600-0447.1991.tb03177.x

Liu, Y., Ouyang, P., Zheng, Y., Mi, L., Zhao, J., Ning, Y., et al. (2021). A selective review of the excitatory-inhibitory imbalance in schizophrenia: Underlying biology, genetics, microcircuits, and symptoms. *Front. Cell. Dev. Biol.* 9:664535. doi: 10.3389/fcell.2021.664535

Lyons, M. R., Schwarz, C. M., and West, A. E. (2012). Members of the myocyte enhancer factor 2 transcription factor family differentially regulate Bdnf transcription in response to neuronal depolarization. *J. Neurosci.* 32, 12780–12785. doi: 10.1523/jneurosci.0534-12.2012

Ma, Q., and Telese, F. (2015). Genome-wide epigenetic analysis of MEF2A and MEF2C transcription factors in mouse cortical neurons. *Commun. Integr. Biol.* 8:e1087624. doi: 10.1080/19420889.2015.1087624

Mao, Z., Bonni, A., Xia, F., Nadal-Vicens, M., and Greenberg, M. E. (1999). Neuronal activity-dependent cell survival mediated by transcription factor MEF2. *Science* 286, 785–790. doi: 10.1126/science.286.5440.785

Marin, O. (2016). Developmental timing and critical windows for the treatment of psychiatric disorders. *Nat. Med.* 22, 1229–1238. doi: 10.1038/nm.4225

Mayer, C., Hafemeister, C., Bandler, R. C., Machold, R., Batista Brito, R., Jaglin, X., et al. (2018). Developmental diversification of cortical inhibitory interneurons. *Nature* 555, 457–462. doi: 10.1038/nature25999

Meredith, R. M. (2015). Sensitive and critical periods during neurotypical and aberrant neurodevelopment: A framework for neurodevelopmental disorders. *Neurosci. Biobehav. Rev.* 50, 180–188. doi: 10.1016/j.neubiorev.2014.12.001

Meredith, R. M., Dawitz, J., and Kramvis, I. (2012). Sensitive time-windows for susceptibility in neurodevelopmental disorders. *Trends Neurosci.* 35, 335–344. doi: 10.1016/j.tins.2012.03.005

Milh, M., Kaminska, A., Huon, C., Lapillonne, A., Ben-Ari, Y., and Khazipov, R. (2007). Rapid cortical oscillations and early motor activity in premature human neonate. *Cereb. Cortex* 17, 1582–1594. doi: 10.1093/cercor/bhl069

O'Donnell, C., Gonçalves, J. T., Portera-Cailliau, C., and Sejnowski, T. J. (2017). Beyond excitation/inhibition imbalance in multidimensional models of neural circuit changes in brain disorders. *Elife* 6:e26724. doi: 10.7554/eLife.26724

Olson, C. O., Pejhan, S., Kroft, D., Sheikholeslami, K., Fuss, D., Buist, M., et al. (2018). MECP2 Mutation Interrupts Nucleolin-mTOR-P70S6K Signaling in Rett Syndrome Patients. *Front. Genet.* 9:635. doi: 10.3389/fgene.2018.00635

Oyarzabal, A., Xiol, C., Castells, A. A., Grau, C., O'Callaghan, M., Fernández, G., et al. (2020). Comprehensive analysis of GABA(A)-A1R developmental alterations in Rett syndrome: Setting the focus for therapeutic targets in the time frame of the disease. *Int. J. Mol. Sci.* 21:518. doi: 10.3390/ijms21020518

Paciorkowski, A. R., Traylor, R. N., Rosenfeld, J. A., Hoover, J. M., Harris, C. J., Winter, S., et al. (2013). MEF2C Haploinsufficiency features consistent hyperkinesis, variable epilepsy, and has a role in dorsal and ventral neuronal developmental pathways. *Neurogenetics* 14, 99–111. doi: 10.1007/s10048-013-0356-y

Parenti, I., Rabaneda, L. G., Schoen, H., and Novarino, G. (2020). Neurodevelopmental disorders: From genetics to functional pathways. *Trends Neurosci.* 43, 608–621. doi: 10.1016/j.tins.2020.05.004

Pereira, A. H., Clemente, C. F., Cardoso, A. C., Theizen, T. H., Rocco, S. A., Judice, C. C., et al. (2009). MEF2C silencing attenuates load-induced left ventricular hypertrophy by modulating mTOR/S6K pathway in mice. *PLoS One* 4:e8472. doi: 10.1371/journal.pone.0008472

Puang, S. J., Elanggovan, B., Ching, T., and Sng, J. C. G. (2020). MEF2C and HDAC5 regulate Egr1 and Arc genes to increase dendritic spine density and complexity in early enriched environment. *Neuronal. Signal.* 4:NS20190147. doi: 10.1042/NS20190147

Rajkovich, K. E., Loerwald, K. W., Hale, C. F., Hess, C. T., Gibson, J. R., and Huber, K. M. (2017). Experience-dependent and differential regulation of local and long-range excitatory neocortical circuits by postsynaptic Mef2c. *Neuron* 93, 48–56. doi: 10.1016/j.neuron.2016.11.022

Rangasamy, S., Olfers, S., Gerald, B., Hilbert, A., Svejda, S., and Narayanan, V. (2016). Reduced neuronal size and mTOR pathway activity in the Mecp2 A140V Rett syndrome mouse model. *F1000Res* 5:2269. doi: 10.12688/f1000research.8156.1

Reiner, O., Karzbrun, E., Kshirsagar, A., and Kaibuchi, K. (2016). Regulation of neuronal migration, an emerging topic in autism spectrum disorders. *J. Neurochem.* 136, 440–456. doi: 10.1111/jnc.13403

Ricciardi, S., Boggio, E. M., Grosso, S., Lonetti, G., Forlani, G., Stefanelli, G., et al. (2011). Reduced AKT/mTOR signaling and protein synthesis dysregulation in a Rett syndrome animal model. *Hum. Mol. Genet.* 20, 1182–1196. doi: 10.1093/hmg/ddq563

Rossignol, E. (2011). Genetics and function of neocortical GABAergic interneurons in neurodevelopmental disorders. *Neural Plast.* 2011:649325. doi: 10.1155/2011/649325

Rubenstein, J. L., and Merzenich, M. M. (2003). Model of autism: Increased ratio of excitation/inhibition in key neural systems. *Genes Brain Behav.* 2, 255–267. doi: 10.1034/j.1601-183x.2003.00037.x

Ruderfer, D. M., Fanous, A. H., Ripke, S., McQuillin, A., Amdur, R. L., Schizophrenia Working Group of the Psychiatric Genomics Consortium, et al. (2014). Polygenic dissection of diagnosis and clinical dimensions of bipolar disorder and schizophrenia. *Mol. Psychiatry* 19, 1017–1024. doi: 10.1038/mp.2013.138

Santos-Terra, J., Deckmann, I., Fontes-Dutra, M., Schwingel, G. B., Bambini-Junior, V., and Gottfried, C. (2021). Transcription factors in neurodevelopmental and associated psychiatric disorders: A potential convergence for genetic and environmental risk factors. *Int. J. Dev. Neurosci.* 81, 545–578. doi: 10.1002/jdn.10141

Satterstrom, F. K., Kosmicki, J. A., Wang, J., Breen, M. S., De Rubeis, S., An, J. Y., et al. (2020). Large-scale exome sequencing study implicates both developmental and functional changes in the neurobiology of autism. *Cell* 56:e523. doi: 10.1016/j.cell.2019.12.036

Seibt, J., Timofeev, I., Carrier, J., and Peyrache, A. (2016). Role of spindle oscillations across lifespan in health and disease. *Neural Plast.* 2016:8103439. doi: 10.1155/2016/8103439

Sharma, A., Hoeffer, C. A., Takayasu, Y., Miyawaki, T., McBride, S. M., Klann, E., et al. (2010). Dysregulation of mTOR signaling in fragile X syndrome. *J. Neurosci.* 30, 694–702. doi: 10.1523/jneurosci.3696-09.2010

Sohal, V. S., and Rubenstein, J. L. R. (2019). Excitation-inhibition balance as a framework for investigating mechanisms in neuropsychiatric disorders. *Mol. Psychiatry* 24, 1248–1257. doi: 10.1038/s41380-019-0426-0

Tan, H. R., Lana, L., and Uhlhaas, P. J. (2013). High-frequency neural oscillations and visual processing deficits in schizophrenia. *Front. Psychol.* 4:621. doi: 10.3389/fpsyg.2013.00621

Tang, X., Kim, J., Zhou, L., Wengert, E., Zhang, L., Wu, Z., et al. (2016). KCC2 rescues functional deficits in human neurons derived from patients with Rett syndrome. *Proc. Natl. Acad. Sci. U.S.A.* 113, 751–756. doi: 10.1073/pnas.1524013113

Tsujimura, K., Irie, K., Nakashima, H., Egashira, Y., Fukao, Y., Fujiwara, M., et al. (2015). miR-199a links MeCP2 with mTOR signaling and its dysregulation leads to Rett syndrome phenotypes. *Cell Rep.* 12, 1887–1901. doi: 10.1016/j.celrep.2015.08.028

Tu, S., Akhtar, M. W., Escorihuela, R. M., Amador-Arjona, A., Swarup, V., Parker, J., et al. (2017). NitroSynapsin therapy for a mouse MEF2C haploinsufficiency model of human autism. *Nat. Commun.* 8:1488. doi: 10.1038/s41467-017-01563-8

Wan, L., Liu, X., Hu, L., Chen, H., Sun, Y., Li, Z., et al. (2021). Genotypes and phenotypes of MEF2C haploinsufficiency syndrome: New cases and novel point mutations. *Front. Pediatr.* 9:664449. doi: 10.3389/fped.2021.664449

Ward, C., Nasrallah, K., Tran, D., Sabri, E., Vazquez, A., Sjulson, L., et al. (2024). Developmental disruption of Mef2c in medial ganglionic eminence-derived cortical inhibitory interneurons impairs cellular and circuit function. *Biol. Psychiatry* doi: 10.1016/j.biopsych.2024.05.021 [Epub ahead of print].

Williams, H. J., Norton, N., Dwyer, S., Moskvina, V., Nikolov, I., Carroll, L., et al. (2011). Fine mapping of ZNF804A and genome-wide significant evidence for its involvement in schizophrenia and bipolar disorder. *Mol. Psychiatry* 16, 429–441. doi: 10.1038/mp.2010.36

Willsey, A. J., Sanders, S. J., Li, M., Dong, S., Tebbenkamp, A. T., Muhle, R. A., et al. (2013). Coexpression networks implicate human midfetal deep cortical projection neurons in the pathogenesis of autism. *Cell* 155, 997–1007. doi: 10.1016/j.cell.2013.10.020

Wu, H., Ren, Y., Pan, W., Dong, Z., Cang, M., and Liu, D. (2015). The mammalian target of rapamycin signaling pathway regulates myocyte enhancer factor-2C phosphorylation levels through integrin-linked kinase in goat skeletal muscle satellite cells. *Cell Biol. Int.* 39, 1264–1273. doi: 10.1002/cbin.10499

Zhang, B., Zhang, J., Chen, H., Qiao, D., Guo, F., Hu, X., et al. (2024). Role of FMRP in AKT/mTOR pathway-mediated hippocampal autophagy in fragile X syndrome. *Prog. Neuropsychopharmacol. Biol. Psychiatry* 134:111036. doi: 10.1016/j.pnpbp.2024.111036

Zhang, W., Feng, G., Wang, L., Teng, F., Wang, L., Li, W., et al. (2018). MeCP2 deficiency promotes cell reprogramming by stimulating IGF1/AKT/mTOR signaling and activating ribosomal protein-mediated cell cycle gene translation. *J. Mol. Cell Biol.* 10, 515–526. doi: 10.1093/jmcb/mjy018

Zhang, Z., and Zhao, Y. (2022). Progress on the roles of MEF2C in neuropsychiatric diseases. *Mol. Brain* 15:8. doi: 10.1186/s13041-021-00892-6

Zweier, M., Gregor, A., Zweier, C., Engels, H., Sticht, H., Wohlleber, E., et al. (2010). Mutations in MEF2C from the 5q14.3q15 microdeletion syndrome region are a frequent cause of severe mental retardation and diminish MECP2 and CDKL5 expression. *Hum. Mutat.* 31, 722–733. doi: 10.1002/humu.21253

frontiers | Frontiers in Cellular Neuroscience

TYPE Original Research
PUBLISHED 15 January 2025
DOI 10.3389/fncel.2024.1513347

OPEN ACCESS

EDITED BY
Takeshi Kawauchi,
Kyoto University, Japan

REVIEWED BY
Laurent Nguyen,
University of Liège, Belgium
Masaaki Ogawa,
Shiga University of Medical Science, Japan

*CORRESPONDENCE
Goichi Miyoshi
✉ Goichi.Miyoshi@gmail.com

RECEIVED 18 October 2024
ACCEPTED 06 December 2024
PUBLISHED 15 January 2025

CITATION
Asano H, Arai M, Narita A, Kuroiwa T, Fukuchi M, Yoshimoto Y, Oya S and Miyoshi G (2025) Developmental regression of novel space preference in an autism spectrum disorder model is unlinked to GABAergic and social circuitry.
Front. Cell. Neurosci. 18:1513347.
doi: 10.3389/fncel.2024.1513347

Developmental regression of novel space preference in an autism spectrum disorder model is unlinked to GABAergic and social circuitry

Hirofumi Asano[1,2], Masaya Arai[1,3], Aito Narita[1], Takayuki Kuroiwa[1], Mamoru Fukuchi[3], Yuhei Yoshimoto[2], Soichi Oya[2] and Goichi Miyoshi[1]*

[1]Department of Developmental Genetics and Behavioral Neuroscience, Gunma University Graduate School of Medicine, Maebashi, Gunma, Japan, [2]Department of Neurosurgery, Gunma University Graduate School of Medicine, Maebashi, Gunma, Japan, [3]Laboratory of Molecular Neuroscience, Faculty of Pharmacy, Takasaki University of Health and Welfare, Takasaki, Gunma, Japan

Autism spectrum disorder (ASD) is characterized by social deficits and restricted behaviors, with developmental defects in GABAergic circuits proposed as a key underlying etiology. Here, we introduce the V-Y assay, a novel space preference test in which one arm of the Y-maze is initially hidden and later revealed as a novel space. Using an ASD mouse model with *FOXG1* haploinsufficiency, which exhibits ASD-like social impairments that can be either exacerbated or ameliorated by GABAergic circuit manipulations, we observed impaired novel space preference and exploratory behavior in the V-Y assay. Interestingly, unlike social phenotypes, novel space preference was initially established by 3 weeks of age but regressed by 6 weeks. Furthermore, alterations in GABAergic signaling via *Gad2* mutation did not affect novel space preference, in contrast to their impact on social behaviors. These findings reveal that the regression of novel space preference in ASD follows a distinct developmental trajectory from GABA-driven social impairments, providing new insights into the mechanisms underlying ASD.

KEYWORDS

GABAergic development, ASD model, novel space preference, regression, social behavior

Introduction

Autism spectrum disorder (ASD) is characterized by social communication deficits and restricted, repetitive behaviors (DSM-5), with a prevalence of 1–2% among children (CDC, United States). Abnormal inhibition mediated by cortical GABAergic interneurons has been implicated in ASD etiology. Postmortem studies of ASD patients have shown a loss of inhibitory neurons (Hashemi et al., 2017), and epilepsy is a common comorbidity in ASD. Moreover, ASD mouse models with conditional mutations in syndromic ASD genes within GABAergic populations often reproduce the behavioral phenotypes observed in straight-null animals (Chao et al., 2010; Judson et al., 2016). These findings support the current hypothesis that disruptions in GABAergic signaling are central to ASD pathology (Nelson and Valakh, 2015; Pizzarelli and Cherubini, 2011; Rubenstein and Merzenich, 2003).

In addition to core symptoms such as social and repetitive behavioral impairments, ASD patients often display deficits in spatial recognition. They tend to learn spatial regularities and

locations more slowly, relying on allocentric representations. These individuals also show reduced novel space preference, are less likely to explore environments thoroughly, and more likely to revisit previously explored locations (Smith, 2015). While visuospatial abilities are considered a strength in some ASD patients (Mottron et al., 2006; Stevenson and Gernsbacher, 2013), a growing body of evidence points to challenges in spatial processing (Bochynska et al., 2020).

Rett syndrome, caused by mutations in the *Mecp2* gene on the X chromosome, is classified as a syndromic form of ASD (Sztainberg and Zoghbi, 2016). In Rett syndrome, while the extent of X-inactivation in the nervous system of girls contributes to the severity of the disease, developmental regression is observed after a period of seemingly normal motor, cognitive, and social development in early infancy, followed by a severe loss of abilities around 1–2 years of age. Regression phenotypes are also observed in female mouse models of Rett syndrome (Mykins et al., 2024). A significant subgroup of ASD children also experience developmental regression, particularly in language and social communication (Williams et al., 2015), with approximately one-third losing previously acquired skills during their second year of life (Boterberg et al., 2019; Tammimies, 2019). Despite these observations, the relationship between GABAergic neuron development and the loss of previously acquired skills in ASD remains poorly understood.

To better understand ASD etiology and explore potential treatments, numerous transgenic mouse models have been developed to study social behavior impairments (Chao et al., 2010; Judson et al., 2016; Miyoshi et al., 2021; Nakatani et al., 2009; Peca et al., 2011; Schmeisser et al., 2012; Silverman et al., 2010). Spatial recognition deficits have also been studied in ASD models (Arbab et al., 2018; Kleijer et al., 2018), along with regression phenotypes (Kshetri et al., 2024). Our previous work focused on *FOXG1*, a transcription factor strongly associated with ASD (Mariani et al., 2015) and involved in GABAergic neurogenesis (Miyoshi et al., 2024). *FOXG1* dysregulation during development has been proposed as an endophenotype of idiopathic ASD, supported by patient iPS cell-derived brain organoids (Mariani et al., 2015). Both haploinsufficiency and gene duplication of *FOXG1* lead to the development of FOXG1 syndrome, classified to ASD (Brimble et al., 2023). The significance of precise *FOXG1* gene dosage is highlighted by its dynamic expression changes in migrating neuronal precursors, which are crucial for cortical circuit formation (Miyoshi and Fishell, 2012; Miyoshi et al., 2024). We recapitulated human *FOXG1* phenotypes by decreasing or increasing *FoxG1* levels in mouse neurons, thereby creating *FOXG1* ASD mouse models. Our findings highlight a critical developmental period during early juvenile stages in the emergence of ASD-related social impairments. Furthermore, we show that these social behaviors can be either exacerbated or ameliorated depending on the timing of GABAergic circuit manipulation (Miyoshi et al., 2021).

In this study, we modified the Y-maze (Hellyer and Straughan, 1961) to develop the V-Y maze, specifically designed to detect novel space preference in model mice. We found that the *FOXG1* haploinsufficiency ASD mouse model transiently forms a novel space preference during early juvenile stages, but this preference regresses by 6 weeks of age. Unlike social behavior impairments, which are highly dependent on GABAergic circuit development, the regression of novel space preference occurs independently of this pathway. Our findings highlight the distinct developmental trajectories of spatial recognition and social behaviors in ASD, shedding light on the differential role of the GABAergic system in these phenotypes.

Materials and methods

Animal experiments

All animal handling and experiments were performed in accordance with protocols approved by the Institutional Animal Care and Use Committees of the Gunma University Graduate School of Medicine. Animal cages are maintained at 22°C ± 1°C, 50 ± 15% humidity, with a 12-h light/dark cycle. ALPHA-dri bedding (Shepherd, Technical grade # L-2307-1178 AD06123) and a pellet diet (Rodent Diet CE-2, gamma irradiated, CLEA) were used to maintain the mouse colony. After mating, the morning plug observed was considered embryonic day 0. Pups were typically delivered on embryonic day 19, corresponding to postnatal day 0 (P0). We conducted behavioral experiments in male mice; therefore, female pups were removed at P0. The dam was kept in either a small (W140 × D320 × H140mm, KN-60105-TPX, Natsume Seisakusho) or medium-sized cage (W215.8 × D316.8 × H150mm, KN-600U-TPX, Natsume Seisakusho). When pups reached postnatal day 14 (P14), the entire litter was placed in a medium-sized cage with a few pellet diets on the floor. At postnatal day 21, the whole litter was weaned and placed into a larger cage (W270 × D440 × H187mm, KN-601-TPX, Natsume Seisakusho). Genotyping of the animals by tail PCR was typically performed by postnatal week 2. After completing battery of behavioral analyses, tail PCR was repeated to assure the genotypes.

The ASD model and the control wildtype littermate animals were generated by crossing a male mouse heterozygous for the *FoxG1 LacZ* knock-in null allele (Xuan et al., 1995) with a wildtype female. A small proportion of ASD model mice exhibited spinning behavior in the home cage and were therefore excluded from the behavioral study. Pups were genotyped using PCR with three primers: FoxG1 10960F (AAGGGCAACTACTGGATGCTCGAC), Neo 1531F (TTGAATGGAAGGATTGGAGCTAC) and FoxG1 11611R (ACAGTCCTGTCGTAAAACTTGGC), which produced wildtype (652 bp) and mutant (~400 bp) bands (Miyoshi et al., 2021). We reduced GABAergic tone during development by utilizing a mutant allele of *Gad2*, the enzyme responsible for GABA synthesis. To perform littermate studies for *FoxG1*; *Gad2* compound mutants, double-heterozygous male *FoxG1-LacZ*; *Gad2-null* animals were crossed with female *Gad2-null* heterozygotes (Yanagawa et al., 1999). Pups carrying the *Gad2-null* heterozygous allele were removed after genotyping (Miyoshi et al., 2021).

Behavioral assays

V-Y assays for 2-, 3-, and 6-week-old male mice were conducted on independent sets of animals at P15–P17, P22–P24, and P43–P45, respectively. The three-chamber assay was performed on P21 and P42 for the 3-and 6-week-old mice, respectively, prior to the V-Y assay. Behavioral assays were conducted in a soundproof room (S-1520 DX, STAR LITE), with mouse behavior in each specific arena recorded by a Progressive Scan CMOS camera (USB 3.1 Blackfly S, Monochrome Camera, BFS-U3-51S5-C, FLIR) at 15 frames per second and saved as

M-JPEG files with 75% compression using Spinnaker camera software 2.7.0.128 (FLIR). Prior to recording, the test animal's information—such as the date of filming, animal number, and presence or absence of a social animal—was written on a small whiteboard (24 × 30 cm) and placed in the testing area. After video recording began, the whiteboard was removed, and the test animal was placed in the arena, or the starting dome was removed to release the animal. Once testing commenced, the experimenter quickly left the soundproof chamber and quietly closed the door to provide an undisturbed environment during the assay. After completing the video recording, the test animal was returned to a new cage containing previously tested littermate animals. The experimenter was always blind to the genotype of the test animals. Video files were later analyzed using ANY-maze video tracking software 7.4 (Stoelting, United States), with video analysis typically starting after the door was closed. All behavioral analysis data are presented as mean ± SEM.

V-Y maze novel space preference task

The Y-maze (YM-03M, Muromachi) consists of a 40 mm triangular center region with each arm measuring 40 mm wide floor and 415 mm in length. The top of the wall is 100 mm wide, and the vertical height is 100 mm. Both the Y-maze and the movable wall block used for the V-maze assay are made from gray vinyl chloride. A video recording was initiated for 11 min at a resolution of 2,200 × 1,948, with a frame rate of 15 frames per second. After the whiteboard was removed and the test animal was placed at the end of the V2 arm, the experimenter quickly and quietly left the soundproof chamber and closed the door. After 5 min and 30 s of recording, the experimenter quickly entered the soundproof chamber, removed the movable wall unit to allow access to all three arms of the Y-maze (V-Y assay), and then exited the chamber quietly, closing the door. Data were analyzed over the 5-min session, measuring time spent, distance traveled, and entry counts for the arms and center based on body location. We used identical analysis methods for the V-maze and V-Y assays in the Any-maze software. For the center region of the V-maze, small portions of the third arm region adjacent to the center area were also included in the analysis (see the scheme for the center region in Figure 1A). For entry counts into the arms, transitions such as V1-Center-V1 and V2-Center-V1 were both counted as a single entry event into the V1 arm. Additionally, entry counts into the wall or floor of each arm were analyzed based on head position. Note that, at the end of each arm, the wall regions with a width equal to that of the floor were not considered walls in our analysis (Figure 1K). For the 2-week-old V-Y assay, 2 wildtype and 6 ASD model animals that did not leave the V2 start arm during the V-maze session were excluded from the analysis. Similarly, 2 *Gad2* null ASD model animals were excluded because they remained in the start arm during the V-maze assay.

Three-chamber social interaction assay

The apparatus consists of a gray acrylic-modified polyvinyl-chloride floor and three chambers (each 20 cm × 40 cm) connected by 5 cm wide × 7 cm high windows in transparent acrylic walls, 22 cm in height (SC-03M, Muromachi). The wire cages are 18.5 cm high with a 9 cm diameter circular base and top, connected by 16 wires, each 3 mm in diameter, placed in a circle with a 7 mm gap between them. Of the four wire cages, two were used to hold a stranger mouse, while the other two remained empty for the Habituation phase (first 10 min) and the non-social side of the Sociability session (second 10 min). The chambers and wire cages were cleaned and dried with paper towels between each test animal trial.

The test mouse was initially placed in a start dome (20 cm diameter circular transparent acrylic tube) in the middle chamber. A video recording was started at a resolution of 1,900 × 1,300, with a frame rate of 15 frames per second. Once the whiteboard and dome were removed, the experimenter quickly left the soundproof room, quietly closing the door. During the first session (Habituation), the animal was allowed to freely explore the three chambers, with two empty wire cages placed in the center of the lateral chambers. After 10 min and 30 s of video recording, the test animal was returned to the middle chamber and trapped in the start dome. In the second session (sociability), one of the empty wire cages was replaced with a cage containing an age-matched stranger mouse. Another 10 min and 30 s of video recording was obtained. The test animal was then again confined to the start dome. In the final session (Social Novelty), the remaining empty cage was replaced with a cage containing another stranger mouse. While 6-week-old animals normally do not climb on top of the wire cages, 3-week-old animals did. Therefore, we excluded animals that climbed on top of the wire cages (WT: 17 and ASD model: 3) from our analyses.

Results

The V-Y arm maze assay reveals a novel space preference and exploratory behavior

The Y-maze assay, which consistently presents two arm choices to test animals, is often used for analyzing repetitive entry behavior into the same arms. To evaluate whether a test mouse prefers to enter a newly revealed arm, we initially hid one arm of the Y-maze and then revealed it during the late phase of the assay (Figure 1A). To hide a single arm, we used specific movable walls (Figure 1B), which could later be removed to display three arm choices. We analyzed the behavior of 6-week-old (6w) mice over a 5-min period during the V-maze phase (Figure 1C), which consisted of two arms, to assess differences in time spent (Figure 1D), distance traveled (Figure 1E), and entry counts (Figure 1F) between the two arms (V1 and V2) (see schematic in Figure 1A). The analysis indicated no significant differences between V1 and V2 arms in these metrics. Upon removing the movable walls for the Y-maze phase (Figure 1G), we compared the familiar V arms (V1 and V2, averaged) with the newly revealed novel arm over a 5-min period (Figures 1A,B). We found that the test animals showed an increase in time spent, distance traveled, and number of entries in the novel arm compared to the familiar arms (Figures 1H–J). This strongly suggests that our V-Y assay effectively demonstrates a preference for novel space in the animals.

Next, using the head position of the animals (Figure 1K, green dots), we assessed whether the animals preferred to stay on the floor or stand against the wall during the assay. Crossing of the head position from the floor into the wall domain (Figure 1K) were counted as wall entries (Figure 1L). We found that wall entry counts were comparable during both the initial V-maze phase and the novel arm

10.3389/fncel.2024.1513347

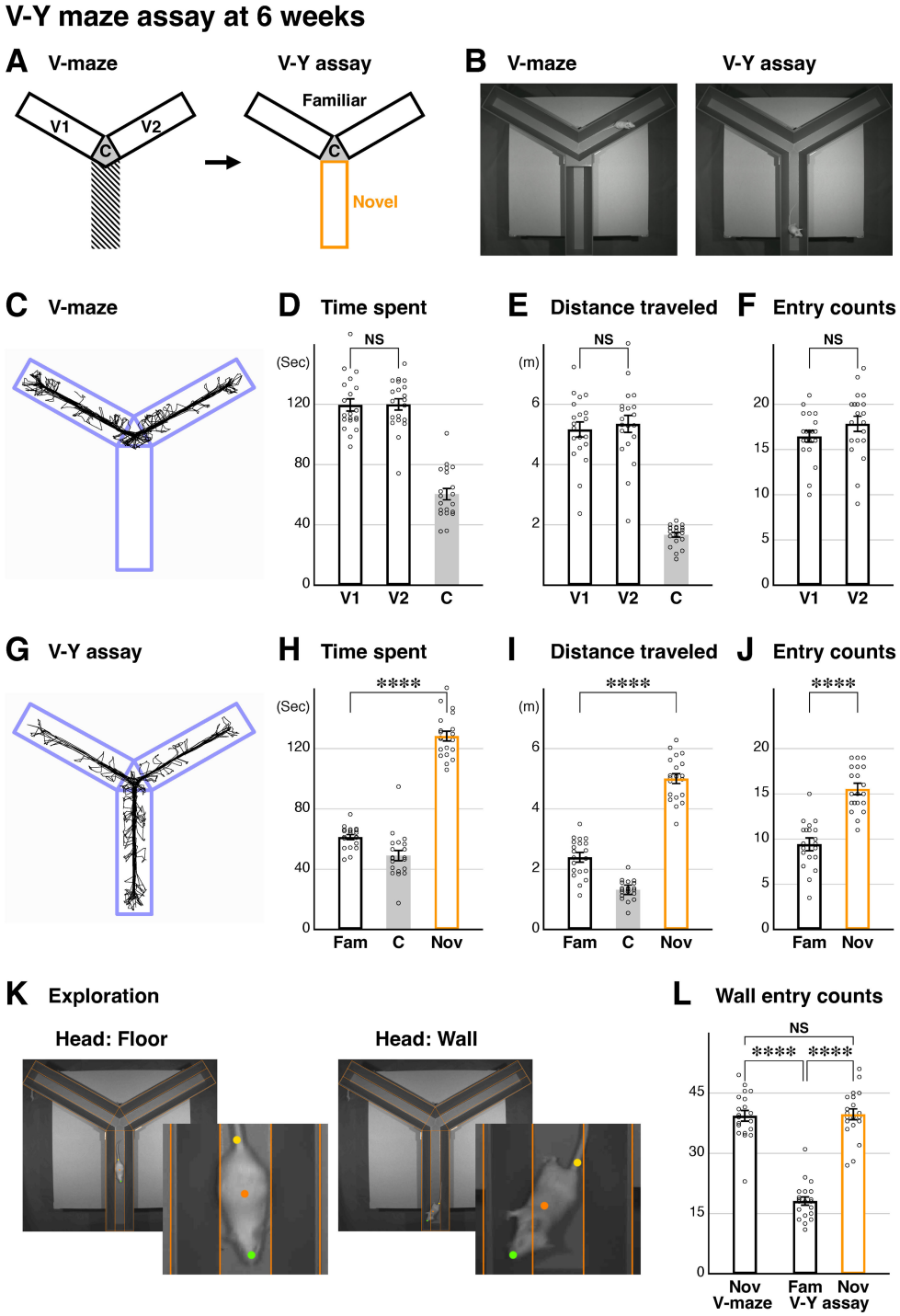

FIGURE 1
Development of the V-Y maze assay for analyzing novel space preference and exploratory behavior in mice. **(A)** A schematic of the V-Y maze assay. During the initial V-maze phase, arms V1, V2, and the center (C) are analyzed separately. In the subsequent V-Y maze phase, the previous V1 and V2 arms become familiar arms, while a newly introduced arm becomes the novel arm. **(B)** Representative video images from the V-maze and V-Y assays at 6 weeks (P43-45). A custom movable wall block was designed to create continuous V-shaped arms in the center region. **(C–F)** A representative behavioral trace of the test animal's body **(C)**. Analysis of the V-maze phase (n = 20). Time spent (**D**, p = 0.950), distance traveled (**E**, p = 0.623), and entries (**F**, p = 0.186) in the V1 and V2 arms were comparable. **(G–J)** A representative behavioral trace of the test animal's body during the V-Y assay phase **(G)**. Analysis during the V-Y phase (n = 20). Time spent [**H**, p = 2.78×10(–17)****], distance traveled [**I**, p = 1.52×10(–14)****], and entries [**J**, p = 3.46×10(–9)****] in the novel arm were significantly increased compared to the familiar arms (average of V1 and V2). **(K,L)** Exploratory behavior of the test animals was analyzed based on head positions (**K**, green dots), and the entries into the walls are presented **(L)**. Note that the central regions of the wall at the end of each arm were not included in the analysis **(K)**. Higher magnification views of the body and head positions are also shown **(K)**. While entries into the wall domain were comparable between the novel arms of the V-maze and V-Y assays (p = 0.768), both were significantly increased compared to the familiar arms [p = 2.07×10(–12)**** for V-maze and p = 9.78×10(–15)**** for V-Y assay], suggesting that the mice are actively exploring the novel arm. Data are mean ± SEM, p-values are from two-tailed t-tests, except for the V and V-Y comparison in **(L)**, which is from a paired two-tailed t-test.

of the V-Y assay (Figure 1L). However, wall entries were significantly decreased in the familiar arms of the V-Y assay compared to both the V-maze arms and the novel arm of the V-Y assay (Figure 1L). This suggests that when animals explore a novel environment, they tend to spend more time seeking the walls. In conclusion, our V-Y maze assay highlights a preference for novel space in animals, as indicated by increased time spent in the novel arm and enhanced wall-seeking exploratory behavior.

Both novel space preference and exploratory behavior are attenuated in the ASD mouse model

After establishing our V-Y assay, we investigated novel space preference in a mouse model related to ASD. A heterozygous mouse for the transcription factor *FoxG1* (Xuan et al., 1995) shows impaired social behavior, reduced gamma frequency EEG power in the prefrontal cortex, and has been characterized as an ASD mouse model (Miyoshi et al., 2021). We thus utilized 6-week-old *FoxG1-LacZ* heterozygous ASD model animals and compared them with littermate wildtype (WT) controls. During the initial V-maze phase (Figure 2A), the time spent in the two V arms was comparable within both the wildtype and ASD model groups (Figure 2B). However, the mean speed, measured based on body position, was increased in the ASD model compared to the control wildtypes (Figure 2C). In the V-Y assay phase (Figure 2D), which investigates novel space preference, we found that, unlike the control littermates, the time spent, distance traveled, and number of entries for the novel arm were comparable to the familiar arms in the ASD model (Figures 2E–G). We observed a similar trend in mean speed during the V and V-Y assays (Figure 2C, and data not shown). This strongly suggests that the ASD model does not show a novel space preference, in addition to impairments in social behavior (Miyoshi et al., 2021). Consistent with this finding, when exploratory behavior of the ASD model was analyzed, we found that head entries into the wall domain were comparable between the familiar and novel arms during the V-Y assay phase (Figure 2H). We conclude that the ASD model demonstrates a lack of interest in novel space, even though it has been shown to display spatial preference (Narita et al., 2024).

The ASD model acquires novel space preference during the juvenile stage and subsequently regresses during development

To understand the developmental process for the acquisition of novel space preference, we performed our V-Y maze assay at 2 weeks (P15-17, Figures 3A,C) and 3 weeks (P22-24, Figures 3B,D), in addition to the analysis conducted at 6 weeks of age (Figure 2). At 2 weeks, the time spent in the familiar and novel arms was comparable in wildtype animals (Figure 3E). However, at 3 weeks, the time spent in the novel arm was significantly increased compared to the familiar arm (Figure 3E). These data suggest that mice generally acquire novel space preference during juvenile developmental stages between 2 and 3 weeks and maintain it through 6 weeks (Figures 1H, 3E) and into adulthood. In the ASD model, we found that the time spent in the familiar and novel arms at 2 weeks was comparable, similar to littermate wildtype controls (Figure 3E). However, at 3 weeks, the time spent in the novel arm was significantly increased compared to the familiar arm, strongly suggesting that the ASD model acquires novel space preference between postnatal 2–3 weeks (Figure 3E). Later, at 6 weeks, the ASD model does not show a preference for novel space (Figures 2E, 3E). These data indicate that the ASD model develops a preference for novel space by postnatal 3 weeks, similar to wildtype animals, but subsequently loses this preference by 6 weeks of age.

We next analyzed wall entry counts during the V-Y assay to investigate the exploratory behavior of the animals. At 2 weeks, both wildtype and ASD model displayed comparable entries between the familiar and novel arms (Figure 3F). However, by 3 weeks, both models showed an increase in wall entry counts in the novel arm compared to the familiar arms (Figure 3F). Since wall entries in the ASD model become comparable between the familiar and novel arms by 6 weeks (Figures 2H, 3F), the exploratory behavior of the ASD model appears to be transiently established by postnatal 3 weeks and subsequently regresses during development. Altogether, we conclude that novel space preference is acquired between postnatal weeks 2 and 3. In the ASD model, this preference is initially transiently established but subsequently regresses, disappearing by 6 weeks of age.

The regression of spatial preference in the ASD model occurs independently of GABAergic neuron development

These results raised the possibility that the social behavioral deficit observed in the ASD model at 6 weeks (Miyoshi et al., 2021) could also be properly established earlier at 3 weeks. To test this, we conducted a three-chamber social behavioral assay for the ASD model and the control littermate wildtypes at 3 weeks (P21), following the same protocol as our study for 6-week-old animals (Miyoshi et al., 2021). After 10 min of habituation in the arena (Figure 4A), sociability was assessed by offering the choice between a chamber containing a stranger mouse and an empty chamber (Figure 4A). In the subsequent session, a second stranger mouse was placed in the previously empty chamber, giving the animals the choice between a familiar and a novel mouse to assess social novelty (Figure 4A). We found that wildtype animals spent more time in the chamber containing a stranger mouse during the sociability session and preferred to spend time in the chamber with the novel mouse over the familiar mouse during the social novelty session (Figure 4B). These data suggest that sociability and social novelty are established in wildtype mice by 3 weeks of age. In contrast, the ASD model spent comparable amounts of time in the chamber with the stranger mouse and the empty chamber during the sociability session, and also showed no preference between the familiar and novel mice during the social novelty session (Figure 4B), resulting in significantly lower social scores (Figure 4C). Furthermore, the time spent in the center chamber during the social novelty session was significantly increased in the ASD model compared to control animals, suggesting that the ASD model avoids interacting with other mice (Figure 4B). These data indicate that sociability is impaired in the ASD model by 3 weeks and that this deficit persists through 6 weeks into adulthood.

Given the observed difference between novel space and social preference at 3 weeks, we next examined the role of GABAergic

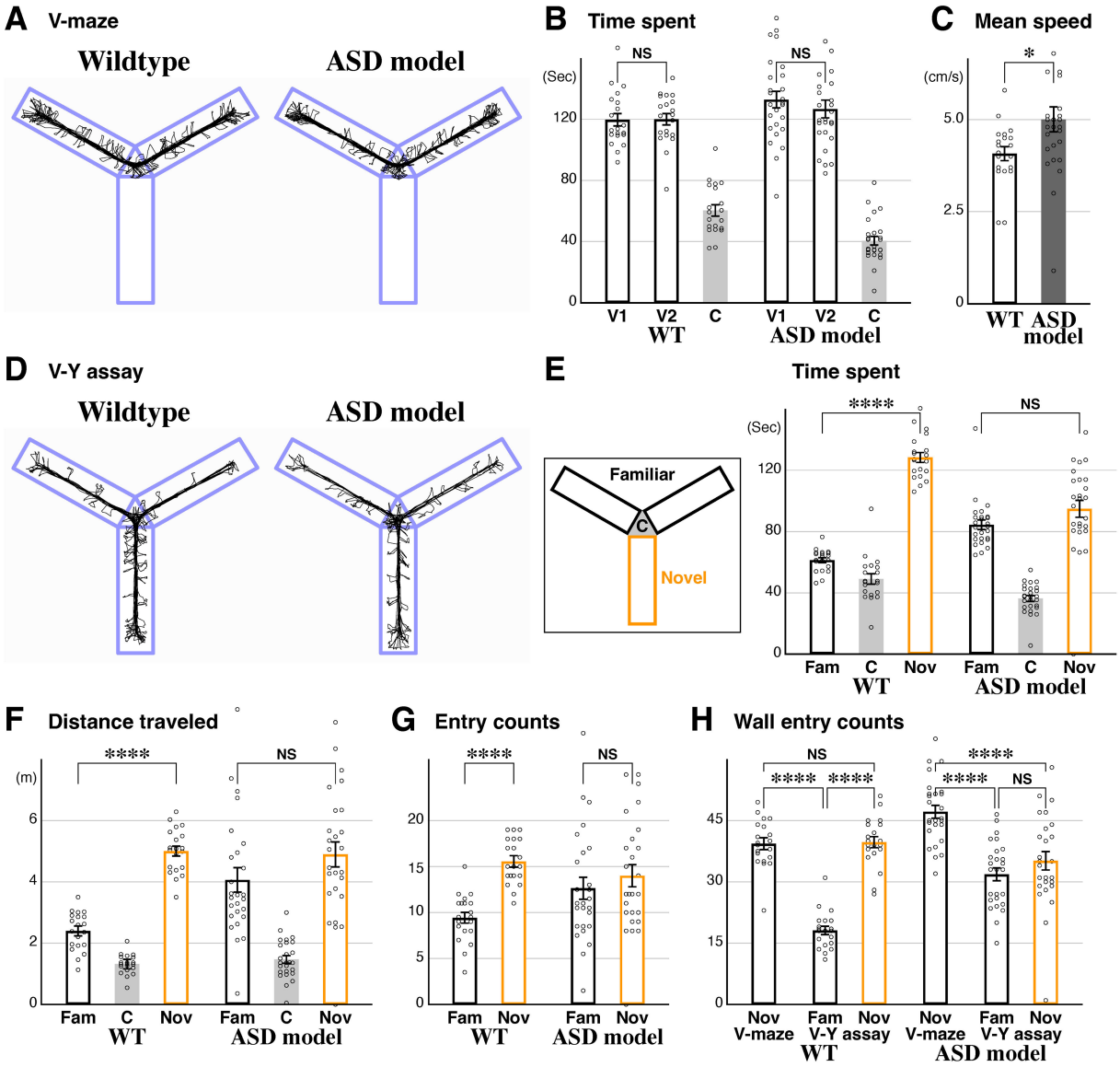

FIGURE 2
Autism spectrum disorder (ASD) model displays impairments in novel space preference and explorative behavior. The V-maze assay followed by the V-Y maze assay was carried out in littermate wildtype (n = 20) and ASD model (*FoxG1* heterozygous, n = 26) mice at postnatal 6 weeks (P43-45). **(A)** Representative traces of the two mouse models. **(B,C)** During the V-maze assay, the time spent in the V1 and V2 arms was comparable within each model (**B**, p = 0.445, ASD model). Mean speed was increased in the ASD model compared to wildtype animals (**C**, p = 0.0216*). **(D)** Representative traces during the V-Y assay. **(E–G)** While time spent, distance traveled, and entries in the novel arm were increased compared to the familiar arms in wildtype animals (same data as in Figures 1H–J), this was not the case in the ASD model (p = 0.110, 0.142, and 0.426, respectively). **(H)** Explorative behavior was analyzed based on head positions. Unlike the wildtype littermates (Figure 1L), the ASD model exhibited comparable wall entry counts between the familiar and novel arms during the V-Y assay (p = 0.232) and showed a significant decrease in the novel arm during the V-Y assay compared to the V-maze [p = 1.32×10(−5)****]. Additionally, wall entry counts in the V arms were significantly reduced during the V-Y assay in the ASD model animals [p = 6.87×10(−11)****]. These data suggest that the ASD model exhibits overall alterations in explorative behavior. The raw data points for 222.7 (**B**, V2, ASD), 7.9 and 10.5 (**C**, ASD) are not shown. Data are mean ± SEM, p-values are from two-tailed t-tests, except for the V and V-Y comparisons in **(H)**, which are from paired two-tailed t-tests.

neuron development in novel space preference. We used a transgenic mutant for *Gad2*, a gene encoding a synthetic enzyme for the GABA neurotransmitter. In the three-chamber social assay, reduced GABAergic tone via *Gad2* null mutation decreased the sociability score in wildtype animals and exacerbated ASD-like social impairments in the ASD model (Miyoshi et al., 2021). To investigate the impact of reduced GABAergic tone on novel space preference, we similarly combined *Gad2* mutant animals with the ASD model and conducted the V-Y assay at 6 weeks (P43-45, Figure 4D). Specifically, we crossed *FoxG1-LacZ*; *Gad2-null* double-heterozygous males with *Gad2-null* heterozygous females to generate the experimental animals. Similar to their wildtype littermates, *Gad2* mutants spent significantly more time in the novel arm compared to the familiar arms (Figure 4D). Furthermore, the time spent in the novel arm was comparable

10.3389/fncel.2024.1513347

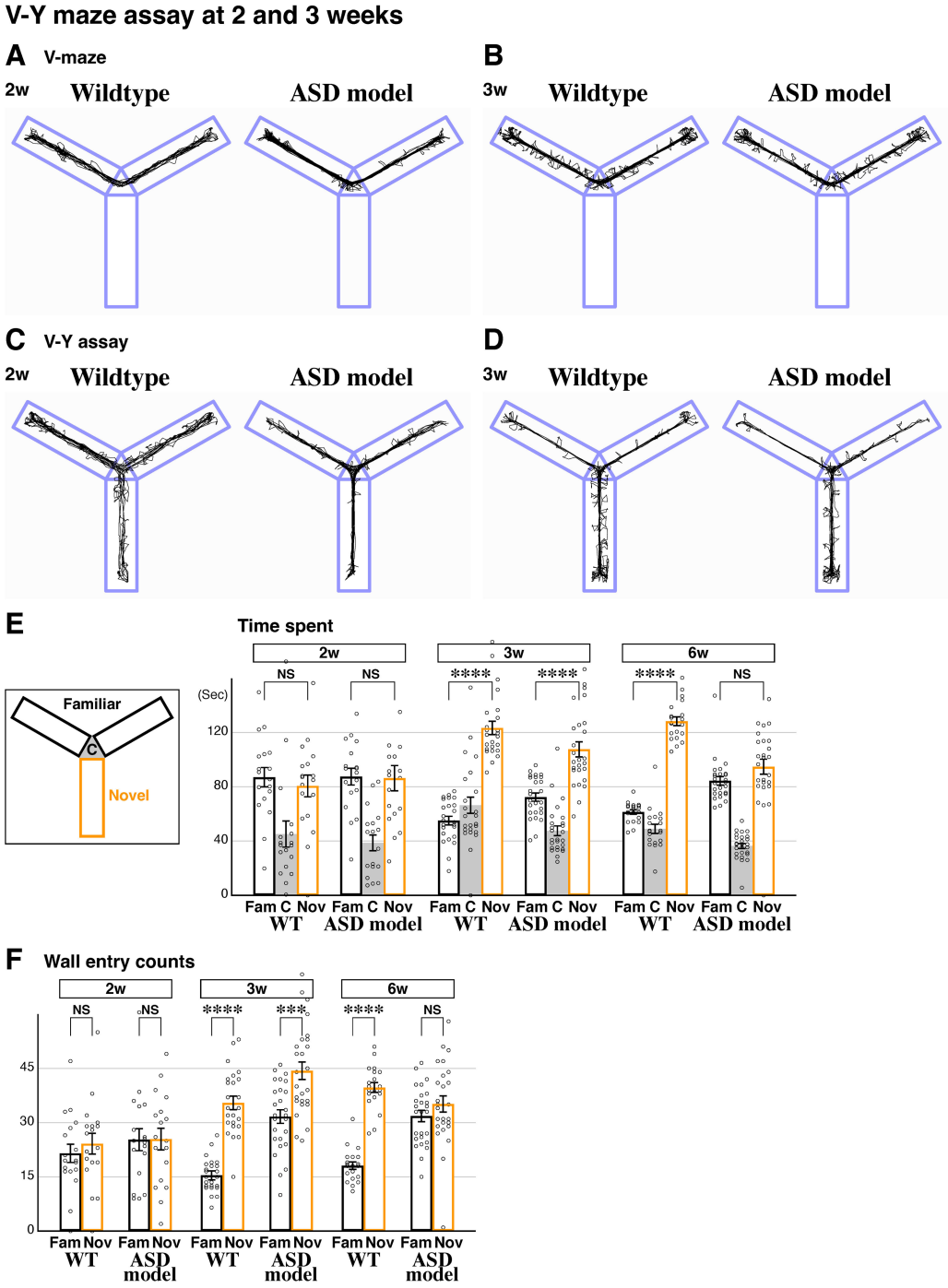

FIGURE 3
Developmental regression of novel space preference in the ASD model. **(A–D)** Representative behavioral traces of littermate wildtype and ASD model (*FoxG1* heterozygous) mice during the V-maze assay **(A,B)** and V-Y assay **(C,D)** at 2 (P15-17, **A,C**) and 3 weeks (P22-24, **B,D**). **(E)** Time spent in each arm during the V-Y assay. At postnatal 2 weeks, time spent in the familiar and novel arms was comparable in both wildtype (n = 18, p = 0.553) and ASD models (n = 18, p = 0.919), suggesting that novel space preference had not yet developed in either model at this age. At postnatal 3 weeks, unlike at 2 weeks, both models spent significantly more time in the novel arm compared to the familiar arms [n = 24, p = 2.12×10(–14)**** for wildtype and n = 26, p = 1.97×10(–6)**** for ASD]. At 6 weeks (P43-45), the ASD model no longer showed a preference for the novel arm (data from Figure 2E), indicating a regression of novel space preference by 6 weeks in the ASD model. **(F)** In 6-week-old wildtype mice, the number of head position entries into the wall was higher in the novel arm compared to the familiar arms (data from Figure 1L). This was similarly observed at 3 weeks [p = 3.36×10(–11)****] but not at 2 weeks (p = 0.489), indicating that exploratory behavior typically becomes evident by postnatal 3 weeks. However, in the ASD model, wall entries in the novel arm compared to the familiar arms increased only at 3 weeks [p = 1.50×10(–4)***] but not at 2 (p = 0.969) or 6 weeks (data from Figure 2H). This trend was similar to the time spent in each arm **(E)**, suggesting that the ASD model starts to exhibit defects in exploratory behavior after 3 weeks. The raw data point 198.8 (**E**, 2w, Nov, ASD) is not shown. Data are mean ± SEM, p-values are from two-tailed t-tests.

10.3389/fncel.2024.1513347

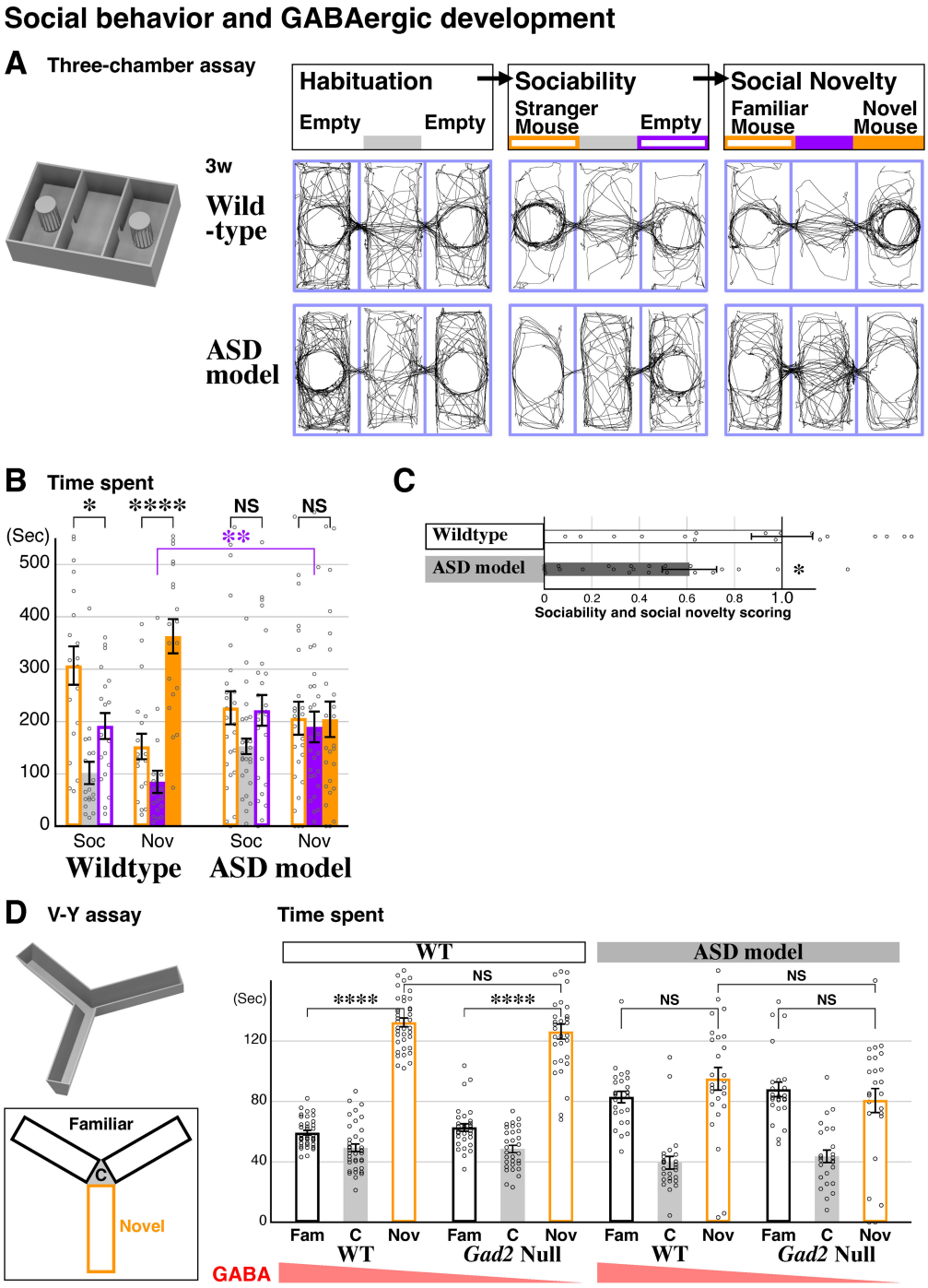

FIGURE 4
Novel space preference is formed independent of social and GABAergic pathways. **(A)** A 3-D model of the three-chamber social assay setup, and representative traces of 3-week-old (P21) animal body location are shown for both wildtype and *FoxG1* heterozygous (*LacZ* knock-in) littermates during each 10-min session of Habituation, Sociability, and Social Novelty. **(B,C)** Social behavior of the animals was analyzed by comparing the time spent in each chamber of the three-chamber assay. Wildtype animals preferred to spend time in the social side of the chambers (**B**, orange bar graphs), whereas ASD model animals did not exhibit a social preference (**B**, NS for left vs. right chamber). WT: n = 19, p = 0.0136*(Soc), p = 1.12x10(−5)****(Nov), Het: n = 25, p = 0.908(Soc), p = 0.962(Nov). Additionally, the ASD model preferred the middle chamber (filled purple bar graph, p = 0.00620**) during the social novelty session and avoided the two lateral chambers containing other mice. Social behavior scores **(C)** are calculated based on the time spent in the social side (orange bars in **B**) of the chambers (p = 0.0295*). **(D)** The V-Y maze assay was performed on 6-week-old (P43–45) littermate wildtype (n = 38), *Gad2* null (n = 31), *FoxG1* heterozygous (n = 26), and *Gad2* null; *FoxG1* heterozygous (n = 25) animals. Both wildtype and *Gad2* null animals spent significantly more time in the novel arm compared to the familiar arms [p = 8.39x10(−30)**** for WT and p = 6.21x10(−15)**** for *Gad2* null]. In the ASD model background, time spent in the familiar and novel arms was comparable for both wildtype (p = 0.159) and *Gad2* nulls (p = 0.431). Time spent in the novel arm was also comparable with *Gad2* mutation in both wildtype and ASD model backgrounds (p = 0.289 for wildtype and p = 0.193 for the ASD model). These results suggest that, unlike social behavior, the *Gad2* mutation does not affect novel space preference in either wildtype or ASD model animals, indicating that GABAergic development is not centrally involved in this behavior. The raw data points for 1.95, 1.97 (**C**, WT), 1.79, 1.91, 1.93 (**C**, ASD) and 188.9 (**D**, WT/*Gad2*, Nov) are not shown. Data are mean ± SEM, p values are from two-tailed t-tests.

between wildtype and *Gad2* null animals, suggesting that reduced GABAergic tone has no impact on novel space preference. Similarly, when we compared the ASD model (*FoxG1* heterozygous) with the ASD model carrying reduced GABAergic tone (*FoxG1* heterozygous and *Gad2* null), we found no significant differences in novel space preference. Consistent with our earlier findings (Figure 2E), the time spent in the novel and familiar arms was comparable in the ASD model, and this trend was similar in the *Gad2* null ASD model (Figure 4D). In addition, the time spent in the novel arm was also comparable between these two genotypes. These data strongly suggest that a reduction in GABAergic tone during development does not impact novel space preference, even in the ASD model. Altogether, our findings demonstrate that novel space preference in the ASD model undergoes a unique pattern of developmental regression that occurs independently of overall GABAergic tone and is distinct from the development of social behavior circuits.

Discussion

In summary, we developed a novel V-Y maze assay suitable for detecting novel space preference and exploratory behavior in both juvenile and adult mouse models. We demonstrated that novel space preference is established during early juvenile stages but subsequently regresses by postnatal 6 weeks in our ASD mouse model. This regression occurs independently of GABAergic circuit development, unlike the social behavior impairments observed in this model.

We modified the classic Y-maze to develop a novel space preference V-Y assay by blocking one arm of the Y-maze during the initial half of the assay. Through this approach, we were able to directly compare novel space preference between wildtype and ASD model mice. In addition to assessing novel space preference, this assay enabled us to investigate exploratory behavior by analyzing wall-seeking tendencies based on how often the animals' heads were oriented toward the wall. Furthermore, we found that this assay is well-suited for studying developmental processes in juvenile mice. Specifically, we analyzed postnatal 2-and 3-week-old animals and demonstrated that novel space preference is established by 3 weeks of age but subsequently regresses by 6 weeks in our ASD model.

In our V-Y maze assay, we focused on novel space preference, but how is working memory affected in the ASD model? In a previous study, we found that the *FoxG1* haploinsufficiency ASD model displays working memory deficits using an 8-arm maze with water droplets as a reward (Miyoshi et al., 2021). Interestingly, while social behavior impairments were either exacerbated or ameliorated depending on the modulation of GABAergic tone, working memory remained unaffected. It is possible that the novel space preference phenotype observed in this study may correlate with the working memory of the animals. Similarly, preference for a novel object was also found to be impaired in the adult *FoxG1* haploinsufficiency model (Younger et al., 2022) using a *Cre* knock-in *FoxG1* allele (Hebert and McConnell, 2000). Other ASD models, including those with syndromic gene mutations, have been shown to exhibit spatial and/or working memory deficits (Berkowicz et al., 2016; Boku et al., 2018; Lim et al., 2017; Nakamura et al., 2021; Rendall et al., 2016). Therefore, it may be reasonable to investigate the developmental trajectory of working memory and novel object recognition in our ASD model at postnatal week 3 to determine whether these abilities are initially acquired but subsequently regress by week 6. In terms of spatial preference, while ASD model animals exhibited a similar environmental preference to wildtypes, interestingly, this preference was initially suppressed but became more pronounced and comfortable over time in the ASD model (Narita et al., 2024). These findings align with observations in human ASD individuals, who may initially struggle to process spatial information but can still distinguish their surroundings and identify comfortable spaces (Smith, 2015).

Which brain region regulates novel space preference? Novelty detection and association are processed by hippocampal networks (Knight, 1996; Kumaran and Maguire, 2007). Spatial navigation in a novel environment is primarily handled by hippocampus, with the posterior hippocampal regions showing a greater response to environmental novelty than to object novelty (Kaplan et al., 2014). Moreover, theta rhythms in prefrontal regions are thought to facilitate the integration of new information into memory through communication with the hippocampus (Chrastil et al., 2022). Interestingly, ASD patients who experience navigation difficulties often retain intact spatiotemporal memory but exhibit impairments in upstream multisensory information processing (Laidi et al., 2023). Additionally, language and spatial working memory are coded separately in the brain, which may explain why some ASD patients show language impairments while visual memory and processing speed remain unaffected (Hill et al., 2015). In our previous study, we identified a transient increase in the excitatory/inhibitory (E/I) ratio in the medial prefrontal cortex (mPFC) of our ASD model at 2 weeks (P14). To address this, we bilaterally transplanted embryonic GABAergic neuronal precursors into the P7 mPFC, aiming to enhance GABA tone within this region. This intervention ameliorated the social impairments observed in the ASD model. Conversely, *Gad2* mutation, which globally reduced GABAergic tone from early development, further exacerbated the social behavioral impairments in the ASD model (Miyoshi et al., 2021). In the present study, using the same *Gad2* manipulation, we found that the reduction of GABAergic tone had no effect on novel space preference, as assessed by our V-Y assay (Figure 4D). We attribute these findings to differences in the requirements for GABAergic tone. However, it is also possible that social behavior and novel space preference have distinct thresholds for GABA. Alternatively, the brain circuits underlying these behaviors may be differentially affected by a similar decrease in GABA tone due to the *Gad2* mutation.

In this study, we utilized the *FoxG1* heterozygous null ASD model; however, how can our findings be generalized to ASD? This model exhibits impairments in both sociability and social novelty, characterized by avoidance of stranger animals (Miyoshi et al., 2021). Additionally, *FoxG1* heterozygous null mice display increased activity levels (open field), anxiolytic behavior (elevated plus maze), reduced working memory (8-arm radial maze), and decreased gamma EEG power in the mPFC (Miyoshi et al., 2021). Furthermore, studies using Cre knock-in *FoxG1* heterozygous animals have demonstrated defects in novel object recognition and fear memory, along with increased anxiety in the open field (Younger et al., 2022). Abnormal locomotion and impairments in contextual fear conditioning were first identified in tTA knock-in *FoxG1* heterozygous animals (Shen et al., 2006). Thus, *FoxG1* heterozygous mice exhibit a characteristic behavioral profile, including these deficits in addition to social impairments. Moreover, *FOXG1* dysregulation has been linked not only to ASD but also to neuropsychiatric disorders such as schizophrenia (Won et al., 2016). It would be highly informative to assess how other established syndromic ASD mouse models, as well as

valproic acid-induced ASD models (Chaliha et al., 2020; Nicolini and Fahnestock, 2018), perform in our V-Y assay. Of particular interest is the *Mecp2* mutant model, to determine whether it exhibits a regression in scores similar to the regression observed in Rett syndrome patients (Sztainberg and Zoghbi, 2016).

In our V-Y maze assay, the 6-week-old ASD model not only shows diminished novel space preference but also exhibits reduced exploratory behavior, as indicated by a decrease in wall-seeking. It has been reported that ASD individuals exhibit reduced novel space preference, are less likely to explore environments thoroughly, and are more likely to revisit previously explored locations (Smith, 2015). We propose that the V-Y maze assay is a suitable tool for simultaneously analyzing novel space preference and exploratory behavior in ASD models (Bourgeron, 2015; Del Pino et al., 2018; Fuccillo, 2016; Golden et al., 2018; Mullins et al., 2016; Sztainberg and Zoghbi, 2016; Takumi et al., 2020). Here, we demonstrate that social behavior and novel space preference are regulated by independent brain networks, with only the former depending on proper GABAergic circuit development (Fishell and Kepecs, 2020; Kupferschmidt et al., 2022; Lunden et al., 2019; Miyoshi, 2019; Tang et al., 2021). We propose that distinct approaches must be taken to address both social behavior impairments and novel space preference/exploration deficits in the treatment of individuals with ASD.

Data availability statement

The original contributions presented in the study are included in the article/supplementary material, further inquiries can be directed to the corresponding author.

Ethics statement

The animal study was approved by Institutional Animal Care and Use Committees of the Gunma University Graduate School of Medicine. The study was conducted in accordance with the local legislation and institutional requirements.

Author contributions

HA: Data curation, Formal analysis, Investigation, Methodology, Software, Validation, Visualization, Writing – original draft, Writing – review & editing. MA: Writing – review & editing, Data curation, Formal analysis. AN: Methodology, Software, Validation, Visualization, Writing – review & editing. TK: Validation, Writing – review & editing. MF: Writing – review & editing. YY: Writing – review & editing. SO: Writing – review & editing. GM: Conceptualization, Funding acquisition, Investigation, Methodology, Project administration, Resources, Supervision, Validation, Visualization, Writing – original draft, Writing – review & editing.

Funding

The author(s) declare that financial support was received for the research, authorship, and/or publication of this article. This work was supported by Grants-in-Aid for Scientific Research JP23H04211 and JP23H02683, the Astellas Foundation for Research on Metabolic Disorders, Kawano Masanori Memorial Public Interest Incorporated Foundation for Promotion of Pediatrics, FOXG1 Research Foundation, Takeda Science Foundation, The Mitsubishi Foundation, Gunma Foundation for Medicine and Health Science, and The Sumitomo Foundation (GM).

Acknowledgments

We thank Eseng Lai and Carina Hanashima for kindly sharing *FoxG1-LacZ* knock-in mutant animal. We thank Naomi Fukashiro for technical assistance. We acknowledge the Miyoshi lab members for their support and constructive input on this project.

Conflict of interest

The authors declare that the research was conducted in the absence of any commercial or financial relationships that could be construed as a potential conflict of interest.

The author(s) declared that they were an editorial board member of Frontiers, at the time of submission. This had no impact on the peer review process and the final decision.

Generative AI statement

The authors declare that no Generative AI was used in the creation of this manuscript.

Publisher's note

References

Arbab, T., Pennartz, C. M. A., and Battaglia, F. P. (2018). Impaired hippocampal representation of place in the Fmr1-knockout mouse model of fragile X syndrome. *Sci. Rep.* 8:8889. doi: 10.1038/s41598-018-26853-z

Berkowicz, S. R., Featherby, T. J., Qu, Z., Giousoh, A., Borg, N. A., Heng, J. I., et al. (2016). Brinp1(−/−) mice exhibit autism-like behaviour, altered memory, hyperactivity and increased parvalbumin-positive cortical interneuron density. *Mol. Autism.* 7:22. doi: 10.1186/s13229-016-0079-7

Bochynska, A., Coventry, K. R., Vulchanov, V., and Vulchanova, M. (2020). Tell me where it is: selective difficulties in spatial language on the autism spectrum. *Autism* 24, 1740–1757. doi: 10.1177/1362361320921040

Boku, S., Izumi, T., Abe, S., Takahashi, T., Nishi, A., Nomaru, H., et al. (2018). Copy number elevation of 22q11.2 genes arrests the developmental maturation of working memory capacity and adult hippocampal neurogenesis. *Mol. Psychiatry* 23, 985–992. doi: 10.1038/mp.2017.158

Boterberg, S., Charman, T., Marschik, P. B., Bolte, S., and Roeyers, H. (2019). Regression in autism spectrum disorder: a critical overview of retrospective findings and recommendations for future research. *Neurosci. Biobehav. Rev.* 102, 24–55. doi: 10.1016/j.neubiorev.2019.03.013

Bourgeron, T. (2015). From the genetic architecture to synaptic plasticity in autism spectrum disorder. *Nat. Rev. Neurosci.* 16, 551–563. doi: 10.1038/nrn3992

Brimble, E., Reyes, K. G., Kuhathaas, K., Devinsky, O., Ruzhnikov, M. R. Z., Ortiz-Gonzalez, X. R., et al. (2023). Expanding genotype-phenotype correlations in FOXG1 syndrome: results from a patient registry. *Orphanet J. Rare Dis.* 18:149. doi: 10.1186/s13023-023-02745-y

Chaliha, D., Albrecht, M., Vaccarezza, M., Takechi, R., Lam, V., Al-Salami, H., et al. (2020). A systematic review of the Valproic-acid-induced rodent model of autism. *Dev. Neurosci.* 42, 12–48. doi: 10.1159/000509109

Chao, H. T., Chen, H., Samaco, R. C., Xue, M., Chahrour, M., Yoo, J., et al. (2010). Dysfunction in GABA signalling mediates autism-like stereotypies and Rett syndrome phenotypes. *Nature* 468, 263–269. doi: 10.1038/nature09582

Chrastil, E. R., Rice, C., Goncalves, M., Moore, K. N., Wynn, S. C., Stern, C. E., et al. (2022). Theta oscillations support active exploration in human spatial navigation. *NeuroImage* 262:119581. doi: 10.1016/j.neuroimage.2022.119581

Del Pino, I., Rico, B., and Marin, O. (2018). Neural circuit dysfunction in mouse models of neurodevelopmental disorders. *Curr. Opin. Neurobiol.* 48, 174–182. doi: 10.1016/j.conb.2017.12.013

Fishell, G., and Kepecs, A. (2020). Interneuron types as attractors and controllers. *Annu. Rev. Neurosci.* 43, 1–30. doi: 10.1146/annurev-neuro-070918-050421

Fuccillo, M. V. (2016). Striatal circuits as a common node for autism pathophysiology. *Front. Neurosci.* 10:27. doi: 10.3389/fnins.2016.00027

Golden, C. E., Buxbaum, J. D., and De Rubeis, S. (2018). Disrupted circuits in mouse models of autism spectrum disorder and intellectual disability. *Curr. Opin. Neurobiol.* 48, 106–112. doi: 10.1016/j.conb.2017.11.006

Hashemi, E., Ariza, J., Rogers, H., Noctor, S. C., and Martinez-Cerdeno, V. (2017). The number of Parvalbumin-expressing interneurons is decreased in the medial prefrontal cortex in autism. *Cereb. Cortex* 27, 1931–1943. doi: 10.1093/cercor/bhw021

Hebert, J. M., and McConnell, S. K. (2000). Targeting of cre to the Foxg1 (BF-1) locus mediates loxP recombination in the telencephalon and other developing head structures. *Dev. Biol.* 222, 296–306. doi: 10.1006/dbio.2000.9732

Hellyer, S., and Straughan, J. H. (1961). Alternation as function of preliminary training and type of deprivation. *Science* 133, 1422–1423. doi: 10.1126/science.133.3462.1422

Hill, A. P., van Santen, J., Gorman, K., Langhorst, B. H., and Fombonne, E. (2015). Memory in language-impaired children with and without autism. *J. Neurodev. Disord.* 7:19. doi: 10.1186/s11689-015-9111-z

Judson, M. C., Wallace, M. L., Sidorov, M. S., Burette, A. C., Gu, B., van Woerden, G. M., et al. (2016). GABAergic neuron-specific loss of Ube3a causes Angelman syndrome-like EEG abnormalities and enhances seizure susceptibility. *Neuron* 90, 56–69. doi: 10.1016/j.neuron.2016.02.040

Kaplan, R., Horner, A. J., Bandettini, P. A., Doeller, C. F., and Burgess, N. (2014). Human hippocampal processing of environmental novelty during spatial navigation. *Hippocampus* 24, 740–750. doi: 10.1002/hipo.22264

Kleijer, K. T. E., van Nieuwenhuize, D., Spierenburg, H. A., Gregorio-Jordan, S., Kas, M. J. H., and Burbach, J. P. H. (2018). Structural abnormalities in the primary somatosensory cortex and a normal behavioral profile in Contactin-5 deficient mice. *Cell Adhes. Migr.* 12, 5–18. doi: 10.1080/19336918.2017.1288788

Knight, R. (1996). Contribution of human hippocampal region to novelty detection. *Nature* 383, 256–259. doi: 10.1038/383256a0

Kshetri, R., Beavers, J. O., Hyde, R., Ewa, R., Schwertman, A., Porcayo, S., et al. (2024). Behavioral regression in shank3 (Deltaex4-22) mice during early adulthood corresponds to cerebellar granule cell glutamatergic synaptic changes. *Research Square,* rs-3. Available at: https://www.researchsquare.com/article/rs-4888950/v1

Kumaran, D., and Maguire, E. A. (2007). Which computational mechanisms operate in the hippocampus during novelty detection? *Hippocampus* 17, 735–748. doi: 10.1002/hipo.20326

Kupferschmidt, D. A., Cummings, K. A., Joffe, M. E., MacAskill, A., Malik, R., Sanchez-Bellot, C., et al. (2022). Prefrontal interneurons: populations, pathways, and plasticity supporting typical and disordered cognition in rodent models. *J. Neurosci.* 42, 8468–8476. doi: 10.1523/JNEUROSCI.1136-22.2022

Laidi, C., Neu, N., Watilliaux, A., Martinez-Teruel, A., Razafinimanana, M., Boisgontier, J., et al. (2023). Preserved navigation abilities and spatio-temporal memory in individuals with autism spectrum disorder. *Autism Res.* 16, 280–293. doi: 10.1002/aur.2865

Lim, C. S., Kim, H., Yu, N. K., Kang, S. J., Kim, T., Ko, H. G., et al. (2017). Enhancing inhibitory synaptic function reverses spatial memory deficits in Shank2 mutant mice. *Neuropharmacology* 112, 104–112. doi: 10.1016/j.neuropharm.2016.08.016

Lunden, J. W., Durens, M., Phillips, A. W., and Nestor, M. W. (2019). Cortical interneuron function in autism spectrum condition. *Pediatr. Res.* 85, 146–154. doi: 10.1038/s41390-018-0214-6

Mariani, J., Coppola, G., Zhang, P., Abyzov, A., Provini, L., Tomasini, L., et al. (2015). FOXG1-dependent dysregulation of GABA/glutamate neuron differentiation in autism Spectrum disorders. *Cell* 162, 375–390. doi: 10.1016/j.cell.2015.06.034

Miyoshi, G. (2019). Elucidating the developmental trajectories of GABAergic cortical interneuron subtypes. *Neurosci. Res.* 138, 26–32. doi: 10.1016/j.neures.2018.09.012

Miyoshi, G., and Fishell, G. (2012). Dynamic FoxG1 expression coordinates the integration of multipolar pyramidal neuron precursors into the cortical plate. *Neuron* 74, 1045–1058. doi: 10.1016/j.neuron.2012.04.025

Miyoshi, G., Ueta, Y., Natsubori, A., Hiraga, K., Osaki, H., Yagasaki, Y., et al. (2021). FoxG1 regulates the formation of cortical GABAergic circuit during an early postnatal critical period resulting in autism spectrum disorder-like phenotypes. *Nat. Commun.* 12:3773. doi: 10.1038/s41467-021-23987-z

Miyoshi, G., Ueta, Y., Yagasaki, Y., Kishi, Y., Fishell, G., Machold, R. P., et al. (2024). Developmental trajectories of GABAergic cortical interneurons are sequentially modulated by dynamic FoxG1 expression levels. *Proc. Natl. Acad. Sci. USA* 121:e2317783121. doi: 10.1073/pnas.2317783121

Mottron, L., Dawson, M., Soulieres, I., Hubert, B., and Burack, J. (2006). Enhanced perceptual functioning in autism: an update, and eight principles of autistic perception. *J. Autism Dev. Disord.* 36, 27–43. doi: 10.1007/s10803-005-0040-7

Mullins, C., Fishell, G., and Tsien, R. W. (2016). Unifying views of autism Spectrum disorders: a consideration of autoregulatory feedback loops. *Neuron* 89, 1131–1156. doi: 10.1016/j.neuron.2016.02.017

Mykins, M., Bridges, B., Jo, A., and Krishnan, K. (2024). Multidimensional analysis of a social behavior identifies regression and phenotypic heterogeneity in a female mouse model for Rett syndrome. *J. Neurosci.* 44:e1078232023. doi: 10.1523/JNEUROSCI.1078-23.2023

Nakamura, J. P., Gillespie, B., Gibbons, A., Jaehne, E. J., Du, X., Chan, A., et al. (2021). Maternal immune activation targeted to a window of parvalbumin interneuron development improves spatial working memory: implications for autism. *Brain Behav. Immun.* 91, 339–349. doi: 10.1016/j.bbi.2020.10.012

Nakatani, J., Tamada, K., Hatanaka, F., Ise, S., Ohta, H., Inoue, K., et al. (2009). Abnormal behavior in a chromosome-engineered mouse model for human 15q11-13 duplication seen in autism. *Cell* 137, 1235–1246. doi: 10.1016/j.cell.2009.04.024

Narita, A., Asano, H., Kudo, H., Miyata, S., Shutoh, F., and Miyoshi, G. (2024). A novel quadrant spatial assay reveals environmental preference in mouse spontaneous and parental behaviors. *Neurosci. Res.* 209, 18–27. doi: 10.1016/j.neures.2024.08.002

Nelson, S. B., and Valakh, V. (2015). Excitatory/inhibitory balance and circuit homeostasis in autism Spectrum disorders. *Neuron* 87, 684–698. doi: 10.1016/j.neuron.2015.07.033

Nicolini, C., and Fahnestock, M. (2018). The valproic acid-induced rodent model of autism. *Exp. Neurol.* 299, 217–227. doi: 10.1016/j.expneurol.2017.04.017

Peca, J., Feliciano, C., Ting, J. T., Wang, W., Wells, M. F., Venkatraman, T. N., et al. (2011). Shank3 mutant mice display autistic-like behaviours and striatal dysfunction. *Nature* 472, 437–442. doi: 10.1038/nature09965

Pizzarelli, R., and Cherubini, E. (2011). Alterations of GABAergic signaling in autism spectrum disorders. *Neural Plast.* 2011:297153, 1–12. doi: 10.1155/2011/297153

Rendall, A. R., Truong, D. T., and Fitch, R. H. (2016). Learning delays in a mouse model of autism Spectrum disorder. *Behav. Brain Res.* 303, 201–207. doi: 10.1016/j.bbr.2016.02.006

Rubenstein, J. L., and Merzenich, M. M. (2003). Model of autism: increased ratio of excitation/inhibition in key neural systems. *Genes Brain Behav.* 2, 255–267. doi: 10.1034/j.1601-183X.2003.00037.x

Schmeisser, M. J., Ey, E., Wegener, S., Bockmann, J., Stempel, A. V., Kuebler, A., et al. (2012). Autistic-like behaviours and hyperactivity in mice lacking ProSAP1/Shank2. *Nature* 486, 256–260. doi: 10.1038/nature11015

Shen, L., Nam, H. S., Song, P., Moore, H., and Anderson, S. A. (2006). FoxG1 haploinsufficiency results in impaired neurogenesis in the postnatal hippocampus and contextual memory deficits. *Hippocampus* 16, 875–890. doi: 10.1002/hipo.20218

Silverman, J. L., Yang, M., Lord, C., and Crawley, J. N. (2010). Behavioural phenotyping assays for mouse models of autism. *Nat. Rev. Neurosci.* 11, 490–502. doi: 10.1038/nrn2851

Smith, A. D. (2015). Spatial navigation in autism spectrum disorders: a critical review. *Front. Psychol.* 6:31. doi: 10.3389/fpsyg.2015.00031

Stevenson, J. L., and Gernsbacher, M. A. (2013). Abstract spatial reasoning as an autistic strength. *PLoS One* 8:e59329. doi: 10.1371/journal.pone.0059329

Sztainberg, Y., and Zoghbi, H. Y. (2016). Lessons learned from studying syndromic autism spectrum disorders. *Nat. Neurosci.* 19, 1408–1417. doi: 10.1038/nn.4420

Takumi, T., Tamada, K., Hatanaka, F., Nakai, N., and Bolton, P. F. (2020). Behavioral neuroscience of autism. *Neurosci. Biobehav. Rev.* 110, 60–76. doi: 10.1016/j.neubiorev.2019.04.012

Tammimies, K. (2019). Genetic mechanisms of regression in autism spectrum disorder. *Neurosci. Biobehav. Rev.* 102, 208–220. doi: 10.1016/j.neubiorev.2019.04.022

Tang, X., Jaenisch, R., and Sur, M. (2021). The role of GABAergic signalling in neurodevelopmental disorders. *Nat. Rev. Neurosci.* 22, 290–307. doi: 10.1038/s41583-021-00443-x

Williams, K., Brignell, A., Prior, M., Bartak, L., and Roberts, J. (2015). Regression in autism spectrum disorders. *J. Paediatr. Child Health* 51, 61–64. doi: 10.1111/jpc.12805

Won, H., de la Torre-Ubieta, L., Stein, J. L., Parikshak, N. N., Huang, J., Opland, C. K., et al. (2016). Chromosome conformation elucidates regulatory relationships in developing human brain. *Nature* 538, 523–527. doi: 10.1038/nature19847

Xuan, S., Baptista, C. A., Balas, G., Tao, W., Soares, V. C., and Lai, E. (1995). Winged helix transcription factor BF-1 is essential for the development of the cerebral hemispheres. *Neuron* 14, 1141–1152. doi: 10.1016/0896-6273(95)90262-7

Yanagawa, Y., Kobayashi, T., Ohnishi, M., Kobayashi, T., Tamura, S., Tsuzuki, T., et al. (1999). Enrichment and efficient screening of ES cells containing a targeted mutation: the use of DT-A gene with the polyadenylation signal as a negative selection maker. *Transgenic Res.* 8, 215–221. doi: 10.1023/A:1008914020843

Younger, S., Boutros, S., Cargnin, F., Jeon, S., Lee, J. W., Lee, S. K., et al. (2022). Behavioral phenotypes of Foxg1 heterozygous mice. *Front. Pharmacol.* 13:927296. doi: 10.3389/fphar.2022.927296

Frontiers in
Cellular Neuroscience

Leading research in cellular mechanisms underlying brain function and development

Part of the world's most cited neuroscience journal series that advances our understanding of the cellular mechanisms underlying cell function in the nervous system across all species.

Discover the latest Research Topics

See more →

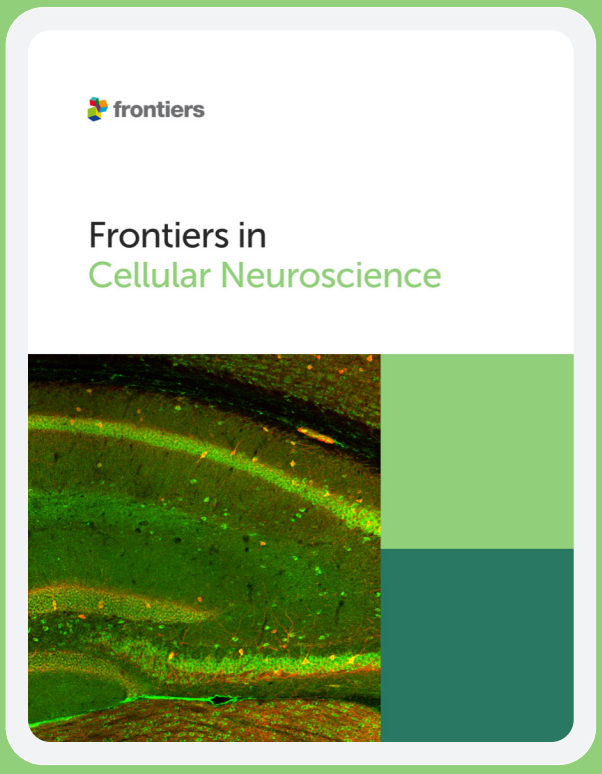

Frontiers

Avenue du Tribunal-Fédéral 34
1005 Lausanne, Switzerland
frontiersin.org

Contact us

+41 (0)21 510 17 00
frontiersin.org/about/contact